Aston University

Some pages of this thesis may have been removed for copyright restrictions.

If you have discovered material in Aston Research Explorer which is unlawful e.g. breaches copyright, (either yours or that of a third party) or any other law, including but not limited to those relating to patent, trademark, confidentiality, data protection, obscenity, defamation, libel, then please read our Takedown policy and contact the service immediately (openaccess@aston.ac.uk)

Investigation of Different Methods of Online Impedance Spectroscopy of Batteries

Mina Abedi Varnosfaderani

Doctor of Philosophy

ASTON UNIVERSITY

April 2017

© Mina Abedi Varnosfaderani, 2017

Mina Abedi Varnosfaderani asserts her moral right to be identified as the author of this thesis

This copy of the thesis has been supplied on condition that anyone who consults it is understood to recognise that its copyright belongs to its author and that no quotation from the thesis and no information derived from it may be published without appropriate permission or acknowledgement.

Thesis Summary

A key challenge in a battery energy storage system is understanding the availability and reliability of the system from the perspective of the end customer. A key task in this process is recognising when a battery or a module within a system starts to degrade and then mitigating against this using the control system or battery management system. Battery characterisation parameters such as internal impedance and state of health and state of charge of the battery are a useful representation of the battery conditions. This thesis investigates the feasibility of undertaking Electrochemical Impedance Spectroscopy (EIS) methods online to generate an understanding of battery impedance. In order to perform an EIS measurement, an excitation signal of fixed frequency must be generated and the voltage and current measured and used to calculate the impedance.

This thesis proposed different methods of generating a low-frequency excitation signal using hardware found in most battery systems to extract the harmonic impedance of a battery cell to aim towards a low cost on-line impedance estimation. This work focuses on producing impedance spectroscopy measurements through the power electronics system, a battery balancing system and the earth leakage monitoring system to attempt to get comparable results to off-line EIS measurements under similar conditions. To generate an excitation signal through the power electronic circuit, different control methods were used including varying; the duty cycle, the switching frequency and the starting position of the switched wave and the addition of an impulse type function. Although utilising a variable duty cycle to generate a harmonic impedance has been previously published in literature, the other techniques analysed within this these have not previously been considered.

The thesis looks at the theoretical analysis of the circuits and control techniques and then follows this up with simulation and experimental studies. The results showed that all the methods investigated have the capability to generate a low frequency perturbation signal to undertake on-line EIS measurement. However, there are potential trade-offs, for example increased inductor ripple current. Not all of the methods produce sufficiently accurate results experimentally. However, five of the methods were used to generate EIS plots similar to those undertaken off-line.

Dedicated to

Mohammad,

Maleehe

&

Meisam

Acknowledgements

I would take this opportunity to express my sincere gratitude to my supervisor Dr. Dani Strickland for her continuous support, invaluable guidance and advice throughout my PhD study. I am grateful for her motivation, immense knowledge and patience throughout my studies. It is with her precious support that this research was made possible.

I would like to express my gratitude towards my co-supervisor Dr. Andrew Cross for his immensely helpful advice, encouragement and insightful comments which helped me widen my research perspectives. I am also thankful to Dr. Jin yang, Mr. Steve Luke, Mr. Lee Jenkins, Dr. Zhengyu Lin and Prof. David Webb, and Dr. Kate Sugden for their help and support during my PhD study.

I also would like to thank my colleagues Dr. Hassan Taghizadeh Esfanjani, Mr. Arash Amiri, Dr. Laurence Chittack, and Mr. Zhi Qiao for their precious friendship and stimulating discussion.

I would like to thank our university staff and technicians: Mrs Helen Yard, Mr Paul Titmus, Mr Richard Reeves, and Mr Robert Abel for their support and assistance.

I would like to express my deepest gratitude towards my parents and my brother for supporting me spiritually throughout my PhD study and writing this thesis. I would like to thank them for their patience and encouragement throughout my life. Their love and support have always been my strength. I would like to thank my aunt and uncle who have supported me emotionally all along.

I would like to acknowledge the following organisations for their assistance in this thesis:

- Western Power Distribution for access to their battery data as part of project FALCON,
- OpalRT for their assistance in the use of their real time system,
- Petalite for access to their batteries,
- The EPSRC for funding the SOLATRON capital equipment needed to prove the off-line EIS results.

Contents

Contents 5
List of Figures 10
List of Tables 22
List of Symbols 25
List of Abbreviations 25
1 Introduction 26
2 Background 29
2.1 Energy Storage 29
2.2 Battery definitions 34
2.3 Battery parameter estimation 36
2.3.1 SOC estimation 36
2.3.2 SOH estimation 39
2.3.3 SOP, SOF and SOL estimation 41
2.3.4 Remaining Available Capacity estimation 43
2.3.5 Impedance estimation 44
2.4 Electrochemical impedance spectroscopy 45
2.4.1 Lithium-ion Batteries 52
2.4.2 Lead-acid Battery 55
2.4.3 Nickel Metal Batteries: 59
2.4.4 Super-capacitors (SC): 61
2.4.5 Solar panel: 63
2.4.6 Summary of published EIS 66
2.5 On-line EIS techniques 67
2.5.1 Separate Excitation 69
2.5.2 Existing Hardware – Battery balancing 71
2.5.3 Existing Hardware – AC/DC Power Electronics 72
2.5.4 Existing Hardware – DC/DC Power Electronics 74
2.6 EIS equivalent circuit models 76

2.6.1 Different models at 100% SOC 76
2.6.2 Different levels of degradation 79
2.7 Summary 83
3 Theoretical analysis of on-line EIS techniques 84
3.1 Introduction: 84
3.2 DC/DC Converter with variable duty cycle PWM 87
3.2.1 Harmonic analysis of gate drive circuit PWM 87
3.2.2 Harmonic analysis of variable duty cycle PWM Current waveform 92
3.2.3 Cross check of circuit boost ratio using variable duty cycle method 94
3.2.4 Inductor ripple calculation of variable duty cycle method 95
3.3 DC/DC Converter with variable switching frequency PWM 98
3.3.1 Harmonic analysis of gate drive circuit PWM 98
3.3.2 Harmonic analysis of variable switching frequency PWM current waveform . 100
3.3.3 Inductor ripple calculation of variable frequency 101
3.4 DC/DC Converter with variable starting point PWM 103
3.4.1 Harmonic analysis of gate drive circuit PWM 104
3.4.2 Harmonic analysis of variable starting point PWM current waveform 105
3.4.3 Inductor ripple calculation of varying start position 106
3.5 DC/DC Converter with an Impulse Function 109
3.5.1 Harmonic analysis of gate drive circuit PWM 111
3.5.2 Harmonic analysis of impulse PWM current waveform 114
3.5.3 Cross check of circuit boost ratio 115
3.5.4 Inductor ripple calculation of impulse method 116
3.6 Battery balancing circuit 118
3.6.1 Circuit Operation 121
3.6.2 Harmonic analysis of the battery balancing current waveform 123
3.6.3 Inductor ripple calculation of battery balancing method 125
3.7 Earth Leakage monitoring circuit 127
3.7.1 Circuit Operation 128

3.7.2 Harmonic analysis of the ELM current method waveform 132
3.7.3 Inductor ripple calculation of ELM 133
3.8 Summary 134
4 Simulation of on-line EIS techniques 138
4.1 Introduction 138
4.2 DC/DC Converter with varying duty cycle PWM 145
4.3 DC/DC Converter with varying frequency PWM 150
4.4 DC/DC Converter with variable starting point PWM 155
4.5 DC/DC Converter with an Impulse Function 160
4.6 Battery Balancing 164
4.7 Earth Leakage Monitoring 172
4.8 Summary 176
5 Experimental results of on-line EIS techniques 178
5.1 Experimental setup 178
5.2 DC/DC Converter operating with no low frequency component 180
5.2.1 Circuit operation 180
5.2.2 Harmonics 182
5.3 DC/DC Converter with varying duty cycle PWM 183
5.3.1 Circuit Operation 183
5.3.2 Harmonics 186
5.3.3 Inductor Ripple 186
5.3.4 EIS Calculation 189
5.4 DC/DC Converter with variable switching frequency PWM 191
5.4.1 Circuit Operation 191
5.4.2 Harmonics 194
5.4.3 Inductor Ripple 195
5.4.4 EIS Calculation 197
5.5 DC/DC Converter with variable starting point PWM 198
5.5.1 Circuit Operation 198

5.5.2 Harmonics 201
5.5.3 Inductor ripple 201
5.5.4 EIS Calculation 203
5.6 DC/DC Converter with an Impulse Function 206
5.6.1 Circuit Operation 206
5.6.2 Harmonics 208
5.6.3 Inductor ripple 209
5.6.4 EIS Calculation 211
5.7 Battery balancing circuit 213
5.7.1 Circuit Operation 213
5.7.2 Harmonics 217
5.7.3 Inductor ripple 217
5.7.4 EIS Calculation 219
5.8 Earth Leakage monitoring circuit 221
5.8.1 Circuit Operation 221
5.8.2 Harmonics 224
5.8.3 Inductor ripple 224
5.8.4 EIS Calculation 226
5.9 Summary 229
6 Practical implementation issues 230
6.1 Introduction 230
6.2 Applicability to other battery types 230
6.3 Applicability to PV panels 233
6.4 Measurements over variable SOC 241
6.5 Integrating into a battery management strategy 244
6.6 Investigating a degraded battery in a series battery connection 247
6.7 Closed loop control model 248
6.8 Summary 250
7 Conclusions and Future Work 251

7.1 Future work 254

8 References 258

Appendix A……..A1

Appendix B……..A8

Appendix C……....A20

List of Figures

Figure 2-1: Summary of installed global energy storage projects [9] 30
Figure 2-2: GB DNO Deployment of Electrical Energy storage (at 1st December 2014) [12] ... 30
Figure 2-3: 11kV feeder from Fox Mile Primary with five connected Energy Storage Sites..... 32
Figure 2-4: A short and long battery maintenance cycle. 33
Figure 2-5: Different methods of battery SOC monitoring 37
Figure 2-6 : Different methods of battery SOH monitoring 40
Figure 2-7: Different methods of battery SOP monitoring 42
Figure 2-8 : Different methods of available battery capacity estimation 43
Figure 2-9 : Different methods of impedance determination 44
Figure 2-10 *:* EIS Battery Terminal Connections [160] 46
Figure 2-11: Common Nyquist shapes found in literature 49
Figure 2-12 : Common equivalent circuits in literature, Note: the inductor component is ignored by some of the authors, especially when they are more interested in the low frequency behaviour 50
Figure 2-13: Summary of Equivalent circuit and Nyquist plots used by authors for different batteries, supercapacitors, and Solar cell 51
Figure 2-14 : Change in shape with SOC variation 54
Figure 2-15: Reported change in shape with temperature, cycle and charge 55
Figure 2-16: Change in shape with SOC variation, OCV, and bias voltage 57
Figure 2-17: Change in shape with cycle and discharge duration 58
Figure 2-18: Change in shape with SOC and OCV variation 60
Figure 2-19 : Change in shape with temperature, cycle and charge variation 61
Figure 2-20 :Change in shape with SOC and temperature variation 63
Figure 2-21 : Change in shape with voltage and temperature variation 65
Figure 2-22: Change in shape with degradation and illumination 66
Figure 2-23 :Different battery EIS methods 68
Figure 2-24: Separate excitation circuit topology for online impedance monitoring 69
Figure 2-25: converter with battery balancing topology for online impedance monitoring 71
Figure 2-26: Ladder circuit balancing operation 72
Figure 2-27: Charger (AC-DC converter) topology for online impedance monitoring 73
Figure 2-28: motor inverter topology for online impedance monitoring 74
Figure 2-29: Diagnostic mode of online EIS using a DC/DC converter 75
Figure 2-30: Operational mode of online EIS using a DC/DC converter with variable duty cycle 76

Figure 2-31: Ideal Equivalent circuit models of a lithium-ion battery at different SOC and degradation equivalent circuit. 77
Figure 2-32: Equivalent circuit model solar panel. 78
Figure 2-33 : proposed equivalent circuits a) comparison of Nyquist plot of EC (equivalent circuit models a, b, c, d, e, f, e, g, j) b) comparison of Nyquist plot of EC (equivalent circuit models k, l, m, q, r, s, u, v) for 100% of SOC 78
Figure 2-34 : EIS of new battery (blue line), degraded battery (yellow line), and very degraded battery over 1000 cycles (green). 80
Figure 2-35 : proposed equivalent circuits a) comparison of Nyquist plot of EC (equivalent circuit models a, b, c, d, e, f, e, g, j) b) comparison of Nyquist plot of EC (equivalent circuit models k, l, m, q, r, s, u, v) for degraded battery at 100% SOC 81
Figure 2-36 : proposed equivalent circuits a) comparison of Nyquist plot of EC (equivalent circuit models a, b, c, d, e, f, e, g, j) b) comparison of Nyquist plot of EC (equivalent circuit models k, l, m, q, r, s, u, v) for a very degraded battery at 100% SOC 82
Figure 3-1 : Block Diagram of a battery system showing where hardware may be used to inject a low frequency waveform..... 84
Figure 3-2 : DC/DC topology used in analysis of boost operation 85
Figure 3-3 : Comparison of a variable duty cycle (f_s = 2 kHz, f_0 = 125 Hz, A_d= 0.01) with a fixed duty cycle 88
Figure 3-4 : Periodic representation of a function (first function in red) and (second function in blue) through to Np functions. 88
Figure 3-5 : Time shift calculation for the m^{th} function 89
Figure 3-6 : Low frequency components of variable duty cycle a) Fourier coefficient C_n b) phase when f_0=125Hz , f_s =2kHz and A_d = 0.01 pu (the harmonic number = 1 relates to 125Hz) 91
Figure 3-7 : Low frequency components of fixed duty cycle Fourier coefficient C_n when f_0=125Hz , f_s =2kHz and A_d=0 (the harmonic number = 1 relates to 125Hz) 92
Figure 3-8 : Battery Current Waveform showing the Time shift calculation for the m^{th} function 93
Figure 3-9 : Theoretical harmonics of the Li-ion battery current signal at variable duty cycle with a low frequency of 125Hz with A_d= 0.01..... 94
Figure 3-10 : Converter current waveform in continuous mode 95
Figure 3-11 : Comparison of a variable frequency (f_{av} = 2 kHz, f_0 = 125 Hz) with a fixed frequency of 2kHz..... 98
Figure 3-12 : Time shift calculation for the m^{th} function 99
Figure 3-13 : Low frequency components of variable frequency Fourier coefficient Cn for an average switching frequency of 2kHz, a low frequency component of 125Hz and A_f = 400 ... 100
Figure 3-14 : Current Waveform for a variable switching frequency 101

Figure 3-15 : Theoretical harmonics of the Li-ion battery current signal at variable switching frequency with a low frequency of 125Hz with A_f= 400. 101
Figure 3-16 : Example of current ripple over a low frequency cycle..... 102
Figure 3-17 : Example showing limitation of A_t for a duty cycle of 0.6 in a switching frequency of 2kHz..... 103
Figure 3-18 : Example showing comparison of variable starting position and fixed starting position for a pulse with duty cycle of 0.6, a switching frequency of 2kHz and an A_t = 0.00005. 104
Figure 3-19 : Low frequency components of variable starting point Fourier coefficient Cn for an average switching frequency of 2kHz, a duty cycle of 0.6, a low frequency component of 125Hz and A_t= 0.00004. 105
Figure 3-20 : Current Waveform for a variable starting point 106
Figure 3-21 : Theoretical harmonics of the Li-ion battery current signal at variable starting point with a low frequency of 125Hz with A_t= 0.00004 and t_{av}= 0.00026 106
Figure 3-22 : Variation of starting position on ripple 107
Figure 3-23 : Example showing adding a low frequency impulse stream to the switching pattern with an OR and XOR function gate drive signal (low frequency wave 634Hz, switching frequency 2kHz, duty cycle = 0.6)..... 109
Figure 3-24 : Example showing adding a low frequency impulse stream to the switching pattern with an OR function for an integer value of high to low frequency pulses (low frequency 250Hz, switching frequency 2kHz) 110
Figure 3-25 : Example showing detecting a low frequency impulse stream to the switching pattern with an OR function for an integer value of high to low frequency pulses for different duty cycle of a) 0.02, b) 0.1 (low frequency 250Hz, switching frequency 2kHz)..... 110
Figure 3-26 : Impulse function combined with first pulse in series..... 111
Figure 3-27 : Low frequency components of PWM with an Impulse function Fourier coefficient $\boldsymbol{Cn}$ with a 125Hz impulse wave of width 0.0004s 113
Figure 3-28 : Example showing how the impulse width can be chosen for a) 10Hz, b) 125Hz, c) 1kHz..... 114
Figure 3-29 : Current Waveform for a PWM with an impulse function..... 115
Figure 3-30 : Harmonics of the Li-ion battery current signal with an impulse function added at 125Hz. 115
Figure 3-31 : Examples of switched capacitor balancing: a) Switched Capacitor, b) Single Switched Capacitor, c) Double-tiered Capacitor, d) Modularised Switched capacitor[136].... 120
Figure 3-32 : Switched capacitor battery balancing circuit..... 121
Figure 3-33 : Switching capacitor battery balancing circuit operation a) stage one b)stage two 122

Figure 3-34 : Charging and discharging voltage Waveform for the Balancing capacitor at the low frequency..... 123
Figure 3-35 : Current Waveform for a Battery Balancing method a) Battery 1 discharge current, b)Battery 2 charge current..... 124
Figure 3-36 : Theoretically derived harmonics of the Li-ion battery1 current signal with a balancing capacitor charge signal at a low frequency of 125Hz, V_{bat1}=3.2V, V_{bat2}= 3V 125
Figure 3-37 : Theoretically derived harmonics of the Li-ion battery2 current signal with a balancing capacitor discharge signal at a low frequency of 125Hz, V_{bat1}=3.2V, V_{bat2}= 3V 125
Figure 3-38 : A representation of Earth leakage monitoring circuit operation 127
Figure 3-39 : Different methods of generating an excitation signal through ELM equipment. 129
Figure 3-40 : An approximate circuit representation of the Earth leakage monitoring circuit under a) normal operation and b) under fault..... 131
Figure 3-41 : Current Waveform for a ELM method..... 132
Figure 3-42 : Theoretically derived harmonics of the Li-ion battery current signal with an ELM signal at a low frequency of 125Hz..... 133
Figure 3-43 : Ripple current through the inductor 134
Figure 4-1 : Lithium-ion phosphate battery EIS impedance plot and equivalent circuit model 138
Figure 4-2 : High level circuit simulation model with ideal components 139
Figure 4-3 : Simulated Li-ion battery Current and Voltage waveforms. The battery is excited with PWM at a fixed duty cycle of 0.6 and switching frequency of 2kHz. 143
Figure 4-4 : Simulated Load Current and output Voltage waveforms. The battery is excited with PWM at a fixed duty cycle of 0.6 and switching frequency of 2kHz. 143
Figure 4-5 : Simulated current harmonics at switching frequency of 2kHz, Where the fundamental frequency is defined as 125kHz to enable comparison with low frequency produced analysis. 144
Figure 4-6 : (a) Variable duty cycle gate drive control (b) generating PWM signal sub-block 145
Figure 4-7 : Simulated Li-ion battery Current and Voltage waveforms. The battery is excited with PWM with variable duty cycle at a low frequency of 125Hz with A_d = 0.01..... 147
Figure 4-8 : Simulated Load Current and Voltage (Vdc) waveforms. The battery is excited with PWM with variable duty cycle at a low frequency of 125Hz with A_d = 0.01..... 147
Figure 4-9 : Simulated Li-ion battery Current and Voltage waveforms. The battery is excited with PWM with variable duty cycle at a low frequency of 175Hz with A_d = 0.01..... 148
Figure 4-10 : Simulated Load Current and Voltage (Vdc) waveforms. The battery is excited with PWM with variable duty cycle at a low frequency of 175Hz with A_d = 0.01..... 148
Figure 4-11 : Simulated current harmonics at variable duty cycle of low frequency of 125Hz and switching frequency of 2kHz 149
Figure 4-12 : Simulated Variable frequency gate drive control..... 150

Figure 4-13 : The subsystem model for a variable frequency PWM generator 150
Figure 4-14 : Simulated Li-ion battery Current and Voltage waveforms. The battery is excited with PWM with variable frequency at a low frequency of 125Hz with A_f = 400..... 152
Figure 4-15 : Simulated Load Current and Voltage (Vdc) waveforms. The battery is excited with PWM with variable frequency at a low frequency of 125Hz with A_f = 400..... 152
Figure 4-16 : Simulated Li-ion battery Current and Voltage waveforms. The battery is excited with PWM with variable frequency at a low frequency of 175Hz with A_f = 400..... 153
Figure 4-17 : Simulated Load Current and Voltage (Vdc) waveforms. The battery is excited with PWM with variable frequency at a low frequency of 175Hz with A_f = 400..... 153
Figure 4-18 : Simulated current ripple at low frequency of 125Hz and switching frequency of 2kHz. A_f = 400. 154
Figure 4-19 : Example showing adding a low frequency variable starting point using a sawtooth waveform with frequency 2kHz and a sinewave with low frequency wave 175Hz, duty cycle = 0.6..... 155
Figure 4-20 : Simulation model of the gate drive circuit to generate a variable starting points pulse 155
Figure 4-21 : Simulated Li-ion battery Current and Voltage waveforms. The battery is excited with PWM with variable starting point at a low frequency of 125Hz with A_t= 0.00004..... 157
Figure 4-22 : Simulated Load Current and Voltage (Vdc) waveforms. The battery is excited with PWM with variable starting point at a low frequency of 125Hz with A_t= 0.00004..... 157
Figure 4-23 : Simulated Li-ion battery Current and Voltage waveforms. The battery is excited with PWM with variable starting point at a low frequency of 175Hz with A_t= 0.00004..... 158
Figure 4-24 : Simulated Load Current and Voltage (Vdc) waveforms. The battery is excited with PWM with variable starting point at a low frequency of 175Hz with A_t= 0.00004..... 158
Figure 4-25 : Simulated variable starting point current ripple at low frequency of 125Hz and switching frequency of 2kHz 159
Figure 4-26 : Example showing a simulation model for Impulse function..... 160
Figure 4-27 : Simulated Li-ion battery Current and Voltage waveforms. The battery is excited with an impulse signal at a low frequency of 125Hz with pulse duty cycle of 0.04..... 162
Figure 4-28 : Simulated Load Current and Voltage (Vdc) waveforms. The battery is excited with an impulse signal at a low frequency of 125Hz with pulse duty cycle of 0.04..... 162
Figure 4-29 : Simulated Li-ion battery Current and Voltage waveforms. The battery is excited with an impulse signal at a low frequency of 166.7Hz with pulse duty cycle of 0.06..... 163
Figure 4-30 : Simulated Load Current and Voltage (Vdc) waveforms. The battery is excited with an impulse signal at a low frequency of 166.7Hz with pulse duty cycle of 0.06..... 163
Figure 4-31 : Simulated PWM with an Impulse function current ripple at low frequency of 125Hz with pulse width of 0.0004s and switching frequency of 2kHz 164

Figure 4-32 : Example showing a simulation model for a switched capacitor battery balancing circuit connected to the converter 165
Figure 4-33 : Simulated Li-ion battery Current and Voltage waveforms. The battery is subject to battery balancing at a low frequency of 125Hz..... 167
Figure 4-34 : Simulated Load Current and Voltage (Vdc) waveforms. The battery is subject to battery balancing at a low frequency of 125Hz..... 168
Figure 4-35 : Simulated Li-ion battery Current and Voltage waveforms. The battery is subject to battery balancing at a low frequency of 166.7 Hz..... 168
Figure 4-36 : Simulated Load Current and Voltage (Vdc) waveforms. The battery is subject to battery balancing at a low frequency of 175Hz..... 169
Figure 4-37 : Simulated Li-ion battery Current and Voltage waveforms. The battery is subject to battery balancing at a low frequency of 125Hz. With V_{bat1} =3.18V and V_{bat2} =0.043V 170
Figure 4-38 : Simulated Load Current and Voltage (Vdc) waveforms. The battery is subject to battery balancing at a low frequency of 125Hz..... 170
Figure 4-39 : Simulated current ripple at a low frequency of 125Hz and a switching frequency of 2kHz using the battery balancing method. a) Battery 1 current harmonics, b) Battery 2 current harmonics 171
Figure 4-40 : Example showing a simulation model for Earth leakage monitoring battery connected to the converter. 172
Figure 4-41 : Simulated Li-ion battery Current and Voltage waveforms. The battery is excited with an Earth leakage Monitoring signal at a low frequency of 125Hz. 174
Figure 4-42 : Simulated Load Current and Voltage (Vdc) waveforms. The battery is excited with an Earth leakage Monitoring signal at a low frequency of 125Hz. 174
Figure 4-43 : Simulated Li-ion battery Current and Voltage waveforms. The battery is excited with an Earth leakage Monitoring signal at a low frequency of 175Hz. 175
Figure 4-44 : Simulated Load Current and Voltage (Vdc) waveforms. The battery is excited with an Earth leakage Monitoring signal at a low frequency of 175Hz. 175
Figure 4-45 : Simulated current harmonics at low frequency of 125Hz and switching frequency of 2kHz using the ELM method..... 176
Figure 5-1 : Experimental setup..... 178
Figure 5-2 : Integrated driver circuit..... 179
Figure 5-3 : Measured Li-ion battery Current (Green) and Voltage (Yellow) waveforms. The battery is excited with PWM at a fixed duty cycle of 0.6 and switching frequency of 2kHz (red). 180
Figure 5-4 : Measured Load Current (Green) and Voltage (Blue) waveforms. The battery is excited with PWM at a fixed duty cycle of 0.6 and switching frequency of 2kHz. 180

Figure 5-5 : a) Experimentally derived harmonics and b) simulated harmonics of the Li-ion battery current. The battery is excited with PWM at a fixed duty cycle of 0.6 and switching frequency of 2kHz. 182
Figure 5-6 : Measured Li-ion battery Current (Green) and Voltage (yellow) waveforms. The battery is excited with PWM with variable duty cycle at a low frequency of 125Hz with A_d = 0.01 (red). 183
Figure 5-7 : Measured Load Current (Green) and Voltage (Blue) waveforms. The battery is excited with PWM with variable duty cycle at a low frequency of 125Hz with A_d = 0.01. 183
Figure 5-8 : Measured Li-ion battery Current (Green) and Voltage (yellow) waveforms. The battery is excited with PWM with variable duty cycle at a low frequency of 175Hz with A_d = 0.01 (red). 184
Figure 5-9 : Measured Load Current (Green) and Voltage (Blue) waveforms. The battery is excited with PWM with variable duty cycle at a low frequency of 175Hz with A_d = 0.01. 184
Figure 5-10 : Experimentally derived harmonics of the Li-ion battery current signal with a variable duty cycle at a low frequency of 125Hz with A_d= 0.01. 186
Figure 5-11 : Comparison of the low frequency ripple at different low frequencies (a) f_0 = 125Hz, (b) f_0 = 175Hz, With d_{av} = 0.6 and A_d = 0.01. 187
Figure 5-12 : Comparison of the low frequency ripple at different A_d (a) A_d = 0.06, (b) A_d = 0.04, (c) A_d = 0.02, and (d) A_d = 0.01. With d_{av} = 0.6 and f_0 = 175Hz. 187
Figure 5-13 : Variation on current ripple with N_p with Theory (red) Simulation (black dash) Experimental (blue dots) 188
Figure 5-14 : battery current low frequency ripple with A_d = 0.1 at f_0 = 175Hz 189
Figure 5-15 : Impedance Nyquist plot of the lithium-ion phosphate battery with EIS (red), Simulation (black dash), and Experimental data (blue dots) for variable duty cycle..... 190
Figure 5-16 : Impedance Bode plot of the lithium-ion phosphate battery with EIS (red), Simulation (black), and Experimental data (blue dots) for variable duty cycle 190
Figure 5-17 : Impedance Bode plot of the lithium-ion phosphate battery with EIS (red), Simulation (black), and Experimental data (blue dots) for variable duty cycle 190
Figure 5-18 : Measured Li-ion battery Current (Green) and Voltage (Yellow) waveforms. The battery is excited with PWM (red) with variable switching frequency at a low frequency of 125Hz and A_f = 400. 191
Figure 5-19 : Measured Li-ion Battery setup, Load Current (Green) and Voltage (Blue). The battery is excited with PWM with variable switching frequency at a low frequency of 125Hz and A_f = 400. 192
Figure 5-20 : Li-ion battery Current (Green) and Voltage (Yellow) waveforms. Measured Li-ion battery Current (Green) and Voltage (Yellow) waveforms. The battery is excited with PWM (red) with variable switching frequency at a low frequency of 175Hz and A_f = 400. 192

Figure 5-21 : Li-ion Battery setup, Load Current (Green) and Voltage (Blue) waveforms. The battery is excited with PWM with variable switching frequency at a low frequency of 175Hz and $A_f = 400$. 192
Figure 5-22:a) Experimentally derived harmonics and b) simulated harmonics of the Li-ion battery current signal with a variable frequency at a low frequency of 125Hz with $A_f = 400$... 194
Figure 5-23 : Comparison of the low frequency ripple at different frequency (a) $A_f = 600$, (b) $A_f = 400$, (c) $A_f = 200$, and (d) $A_f = 100$. With $f_{av} = 2$kHz and $f_0 = 175$Hz..... 195
Figure 5-24 : Comparison of the low frequency ripple at different frequencies (a) $f_0 = 125$Hz, (b) $f_0 = 175$Hz, With $f_{av} = 2$kHz and $A_f = 400$. 196
Figure 5-25 : Comparison of the low frequency ripple at different frequencies using theory (Line), Simulation (dash), and Experiment (dots).$A_f = 400$ 196
Figure 5-26 : discontinuous battery current low frequency ripple with $A_f = 1500$ at $f_0 = 175$Hz 197
Figure 5-27 : Impedance Nyquist plot of the lithium-ion phosphate battery with Experimentally derived results 197
Figure 5-28 : Measured Li-ion battery Current (Green) and Voltage (yellow) waveforms. The battery is excited with PWM (red) with a variable starting point set to a low frequency of 125Hz and $A_t = 0.00004$s. 198
Figure 5-29 : Measured Load Current (Green) and Voltage (Blue) waveforms. The battery is excited with PWM (red) with a variable starting point set to a low frequency of 125Hz and $A_t = 0.00004$s. 199
Figure 5-30 : Measured Li-ion battery Current (Green) and Voltage (yellow) waveforms. The battery is excited with PWM (red) with a variable starting point set to a low frequency of 175Hz and $A_t = 0.00004$s. 199
Figure 5-31 : Load Current (Green) and Voltage (Blue) waveforms. The battery is excited with PWM with a variable starting point set to a low frequency of 175Hz and $A_t = 0.00004$s. 199
Figure 5-32 : Experimentally derived harmonics of the Li-ion battery current signal with a variable starting position at a low frequency of 125Hz with $A_t = 0.00004$s. 201
Figure 5-33 : Comparison of the low frequency ripple at different frequency (a)$A_t = 0.00008$, (b) $A_t = 0.00005$, (c) $A_t = 0.00004$, and (d) $A_t = 0.00002$. With $f_s = 2$kHz and $f_0 = 175$Hz 202
Figure 5-34 : Comparison of the low frequency ripple at different frequency (a) $f_0 = 125$Hz, (b) $f_0 = 175$Hz, With $t_{av} = 0.00026$s and $A_t = 0.00004$. 202
Figure 5-35 : Comparison of the low frequency ripple at different frequencies using theory (Line), Simulation (dash), and Experiment (dots) 203
Figure 5-36 : battery current low frequency ripple with $A_t = 0.0002$ at $f_0 = 175$Hz. 203
Figure 5-37 : Impedance Nyquist plot of the lithium-ion phosphate battery with EIS (red), Simulation (black), and Experimental data (blue dots)..... 204

Figure 5-38 : Amplitude bode plot of the lithium-ion phosphate battery with EIS (red), Simulation (black), and Experimental data (blue dots) 204
Figure 5-39 : Phase bode plot of the lithium-ion phosphate battery with EIS (red), Simulation (black), and Experimental data (blue dots) 205
Figure 5-40 : Measured Li-ion battery Current (Green) and Voltage (yellow) waveforms. The battery is excited with a PWM (red) with an impulse function at a Low frequency of 125Hz, with 4% impulse duty cycle. 206
Figure 5-41 : Measured Load Current (Green) and Voltage (Blue) waveforms. The battery is excited with a PWM (red) with an impulse function at a Low frequency of 125Hz, with 4% impulse duty cycle. 207
Figure 5-42 : Measured Li-ion battery Current (Green) and Voltage (yellow) waveforms. The battery is excited with a PWM (red) with an impulse function at a Low frequency of 166.7Hz, with 6% impulse duty cycle. 207
Figure 5-43 : Measured Load Current (Green) and Voltage (Blue) waveforms. The battery is excited with a PWM (red) with an impulse function at a Low frequency of 166.7Hz, with 6% impulse duty cycle. 207
Figure 5-44 : a) Experimentally derived harmonics and b) simulated harmonics of the Li-ion battery current signal with an impulse function at a low frequency of 125Hz with d=4%..... 209
Figure 5-45 : Comparison of the low frequency ripple at different frequency (a) $d_{impulse}$ = 0.06, (b) $d_{impulse}$ = 0.07, (c) $d_{impulse}$ = 0.08, and (d) $d_{impulse}$ = 0.1. With fs = 2kHz and f_0 =166.7Hz 210
Figure 5-46 : Comparison of the low frequency ripple at different frequency (a) f_0 =125Hz with $d_{impulse}$ = 0.04, (b) f_0 =166.7Hz with $d_{impulse}$ = 0.06 and fs = 2kHz. 210
Figure 5-47 : Comparison of the low frequency ripple at different frequencies using theory (Line), Simulation (dash), and Experiment (dots) 211
Figure 5-48 : Impedance Nyquist plot of the lithium-ion phosphate battery with EIS (red), Simulation (black), and Experimental data (blue dots)..... 212
Figure 5-49 : Impedance amplitude bode plot of the lithium-ion phosphate battery with EIS (red), Simulation (black), and Experimental data (blue dots)..... 212
Figure 5-50 : Impedance phase bode plot of the lithium-ion phosphate battery with EIS (red), Simulation (black), and Experimental data (blue dots)..... 212
Figure 5-51 : Experimental setup..... 213
Figure 5-52 : Li-ion battery1 Current (Green), Li-ion battery2 Current (blue), Li-ion battery1 Voltage (yellow), and Li-ion battery2 Voltage (red) waveforms, at Low frequency of 125Hz.214
Figure 5-53 : Load Current (Green) and output Voltage (blue) waveforms, the battery is excited at Low frequency of 125Hz. (need to do this again)..... 214
Figure 5-54 : Li-ion battery1 Current (Green), Li-ion battery2 Current (blue), Li-ion battery1 Voltage (yellow), and Li-ion battery2 Voltage (red) waveforms, at Low frequency of 125Hz.215

Figure 5-55 : Load Current (Green) and output Voltage (blue) waveforms, the battery is excited at Low frequency of 166Hz..... 215
Figure 5-56 : Experimentally derived harmonics of the Li-ion battery current signal with battery balancing at a low frequency of 125Hz (a) battery1 (b) battery2. 217
Figure 5-57 : Comparison of the low frequency ripple at different voltage difference (a) V_{diff} = 2.27V, (b) V_{diff} = 2.67V, (c)V_{diff} = 2.74V, and (d) V_{diff} = 3.15V. With f_s = 2kHz and f_0 = 166.7Hz 218
Figure 5-58 : Comparison of the low frequency ripple at different frequency (a) f_0 = 125Hz, (b) f_0 = 166.7Hz, With f_s = 2kHz at V_{diff} = 3.15V 219
Figure 5-59 : Comparison of the low frequency ripple at different frequencies using theory (Line), Simulation (dash), and Experiment (dots) 219
Figure 5-60 : Impedance Nyquist plot of the lithium-ion phosphate battery1 with EIS (red), Simulation (black), and Experimental data (blue dots)..... 220
Figure 5-61 : Impedance amplitude bode plot of the lithium-ion phosphate battery1 with EIS (red), Simulation (black), and Experimental data (blue dots)..... 220
Figure 5-62 : Impedance phase bode plot of the lithium-ion phosphate battery1 with EIS (red), Simulation (black), and Experimental data (blue dots)..... 220
Figure 5-63 : Experimental setup of ELM method 221
Figure 5-64 : Li-ion battery Current (Green) and Voltage (yellow) waveforms. The battery is excited with fixed duty cycle PWM (red) and a low ELM signal at 125Hz. 222
Figure 5-65 : Load Current (Green) and Voltage (blue) waveforms. The battery is excited with fixed duty cycle PWM and a low ELM signal at 125Hz. 222
Figure 5-66 : Li-ion battery Current (Green) and Voltage (yellow) waveforms. The battery is excited with fixed duty cycle PWM (red) and a low ELM signal at 175Hz. 222
Figure 5-67 : Load Current (Green) and Voltage (blue) waveforms. The battery is excited with fixed duty cycle PWM and a low ELM signal at 175Hz. 223
Figure 5-68 :a) Experimentally derived harmonics b)simulated harmonics of the Li-ion battery current signal with an ELM signal at a low frequency of 125Hz..... 224
Figure 5-69 : Comparison of the low frequency ripple at different frequency (a)V_{ELM} = 3.5V, (b)V_{ELM} = 5V, (c) V_{ELM} = 8V, and (d) V_{ELM} = 12V. With f_s = 2kHz and f_0 = 175Hz..... 225
Figure 5-70 : Comparison of the low frequency ripple at different frequency (a) f_0 = 125Hz, (b) f_0 = 175Hz 226
Figure 5-71 : Comparison of the low frequency ripple at different frequencies using theory (Line), Simulation (dash), and Experiment (dots) 226
Figure 5-72 : Impedance Nyquist plot of the lithium-ion phosphate battery with EIS (red), Simulation (black), and Experimental data (blue dots)..... 227

Figure 5-73 : Impedance amplitude bode plot of the lithium-ion phosphate battery with EIS (red), Simulation (black), and Experimental data (blue dots) 227
Figure 5-74 : Impedance phase bode plot of the lithium-ion phosphate battery with EIS (red), Simulation (black), and Experimental data (blue dots) 228
Figure 6-1 : NiMH battery EIS impedance plot and equivalent circuit model 230
Figure 6-2 : Impedance Nyquist plot of the NiMH battery with EIS (red), Simulation (black), and Experimental Validation (blue dots) 231
Figure 6-3 : Impedance Bode plot of the NiMH battery with EIS (red), Simulation (black), and Experimental Validation (blue dots) 232
Figure 6-4 : Impedance Bode plot of the NiMH battery with EIS (red), Simulation (black), and Experimental Validation (blue dots) 232
Figure 6-5: Solar Panel current (blue) and power rating (red) characteristic 233
Figure 6-6 : Photovoltaic solar panel EIS impedance plot and equivalent circuit model 234
Figure 6-7 : Solar panel Experimental Set Up 235
Figure 6-8 : Solar Current (Green) and Voltage (yellow) waveforms, the panel is excited with variable duty cycle with a low frequency component of 10 kHz, A_d= 0.012 236
Figure 6-9 : Solar Current (Green) and Voltage (yellow) waveforms, the panel is excited with constant duty cycle (no low frequency ripple is included) 236
Figure 6-10 : Impedance Nyquist plot of solar panel with EIS (blue), Simulation (black), and Experimental Validation (red dots) operation at A 238
Figure 6-11 : Impedance Nyquist plot of solar panel with EIS (blue), Simulation (black), and Experimental Validation (red dots). operation at MPP 238
Figure 6-12 : Impedance phase Bode plots of solar panel with EIS (blue), Simulation (black), and Experimental Validation (red dots) operation at A 239
Figure 6-13 : Impedance Amplitude Bode plots of solar panel with EIS (blue), Simulation (black), and Experimental Validation (red dots) operation at MPP 239
Figure 6-14: Impedance phase Bode plots of solar panel with EIS (blue), Simulation (black), and Experimental Validation (red dots) operation at A 240
Figure 6-15 : Impedance phase Bode plots of solar panel with EIS (blue), Simulation (black), and Experimental Validation (red dots) operation at MPP 240
Figure 6-16 : Path of measured values to information 241
Figure 6-17 : Real time EIS data continuously changes over a low frequency excitation sweep 242
Figure 6-18 : Battery Impedance Nyquist plot for different state of charge 243
Figure 6-19 : Battery Impedance Amplitude bode plot for different state of charge 243
Figure 6-20 : Battery Impedance Phase bode plot for different state of charge 244
Figure 6-21 : comparison of different fitting curves 246

Figure 6-22 : Battery Impedance Nyquist plot, impedance of two batteries in series connection experiment (blue dots), EIS of two batteries in series (red line), EIS of degraded battery (black dash), EIS of new battery (yellow dash) 247
Figure 6-23 : Battery Impedance Amplitude bode plot of two batteries in series connection experiment (blue dots), EIS of two batteries in series (yellow line), EIS of degraded battery (black line), EIS of new battery (yellow line) 248
Figure 6-24 : Battery Impedance Phase bode plot of two batteries in series connection experiment (blue dots), EIS of two batteries in series (yellow line), EIS of degraded battery (black line), EIS of new battery (yellow line) 248
Figure 6-25 :Typical control system model 249
Figure 6-26 : Current (Green), PWM signal (yellow), fixed duty cycle and switching frequency using closed loop control 249
Figure 6-27 : Current (Green), PWM signal (yellow), variable duty cycle at low frequency of 125Hz using closed loop control 249

List of Tables

Table 2-1: Definition of terminology 34
Table 2-2 : summary of SOC determination techniques 38
Table 2-3 : example summary of SOH determination techniques 40
Table 2-4: example summary of SOP determination techniques 42
Table 2-5: Summary of remaining available capacity determination techniques 43
Table 2-6 : example summary of battery impedance determination techniques 45
Table 2-7: Lithium-ion EIS testing Conditions used by various Authors 52
Table 2-8: Lead-Acid Battery EIS Test Condition 56
Table 2-9: Nickel Meta/Cadmium Battery EIS Test Condition 59
Table 2-10:Super-capacitor EIS testing condition used by various Authors 62
Table 2-11:Solar Cells EIS testing condition used by various Authors 64
Table 3-1 : key parameters for theoretical analysis of current harmonics 93
Table 3-2: Comparison of using integer and non-integer low frequency in PWM with an Impulse function simulation model 111
Table 3-3: capacitor based battery balancing method comparison 119
Table 3-4: low frequency excitation method comparison 135
Table 4-1: Battery Model component specifications 139
Table 4-2 : Boost converter component specifications 142
Table 4-3: Simulated results of fixed duty cycle 142
Table 4-4: Comparison of simulated results of fixed and variable duty cycle at 125Hz with A_d =0.01, ... 146
Table 4-5: Comparison of simulated results of fixed and variable duty cycle at 175Hz with A_d =0.01 146
Table 4-6: Comparison of simulated results of fixed and variable switching frequency at 125Hz with A_f = 400 151
Table 4-7: Comparison of simulated results of fixed and variable switching frequency at 175Hz with A_f = 400 151
Table 4-8: Comparison of simulated PWM with variable starting point at 125Hz effects on Current and Voltage ripple 156
Table 4-9: Comparison of simulated PWM with variable starting point at 175Hz effects on Current and Voltage ripple 156
Table 4-10: Comparison of simulated PWM with Impulse (OR-4 %) at 125Hz effects on Current and Voltage ripple 161
Table 4-11: Comparison of simulated PWM with Impulse (OR-6%) at 166.7Hz effects on Current and Voltage ripple 161

Table 4-12: Comparison of simulated battery balancing excited signal at 125Hz effects on Current and Voltage ripple 166
Table 4-13: Comparison of simulated battery balancing excited signal at 166.7 Hz effects on Current and Voltage ripple 166
Table 4-14: Comparison of simulated Earth leakage Monitoring excited signal at 125Hz effects on Current and Voltage ripple 173
Table 4-15: Comparison of simulated Earth leakage Monitoring excited signal at 175Hz effects on Current and Voltage ripple 173
Table 4-16: key results from simulation 177
Table 5-1: Experimental results of fixed duty cycle 181
Table 5-2: Simulated results of fixed duty cycle 181
Table 5-3: Simulated results of fixed duty cycle using non-ideal component 181
Table 5-4: Comparison of experimental results of fixed and variable duty cycle at 125Hz with A_d =0.01 185
Table 5-5: Comparison of experimental results of fixed and variable duty cycle at 175Hz with A_d = 0.01. 185
Table 5-6: Comparison of simulated results of fixed and variable duty cycle at 125Hz with A_d =0.01, ... 185
Table 5-7: Calculated increase in current ripple as a % with variable duty cycle compared to a fixed duty cycle 188
Table 5-8: Comparison of experimental results of fixed and variable frequency at 125Hz with A_f = 400. 193
Table 5-9: Comparison of experimental results of fixed and variable frequency at 175Hz with A_f = 400 193
Table 5-10: Calculated increase in current ripple as a % with variable duty cycle compared to a fixed duty cycle 195
Table 5-11: Comparison of PWM with variable starting point at 125Hz effects on Current and Voltage ripple 200
Table 5-12: Comparison of PWM with variable starting point at 175Hz effects on Current and Voltage ripple 200
Table 5-13: Comparison of simulated PWM with variable starting point at 125Hz effects on Current and Voltage ripple 200
Table 5-14: Calculated increase in current ripple as a % with variable starting position compared to a fixed starting position for a switching frequency of 2kHz and a t_{av} = 0.00026 201
Table 5-15: Comparison of PWM with Impulse (OR-4%) at 125Hz effects on Current and Voltage ripple 208

Table 5-16: Comparison of PWM with Impulse (OR-6%) at 166.7Hz effects on Current and Voltage ripple 208
Table 5-17: Calculated increase in current ripple as a % with pulse function compared to a fixed Pulse for a switching frequency of 2kHz 209
Table 5-18: Comparison of the based circuit data with battery balancing at 125Hz effects on Current and Voltage ripple 216
Table 5-19: Comparison of the based circuit data with battery balancing at 166Hz effects on Current and Voltage ripple 216
Table 5-20: Comparison of simulated battery balancing excited signal at 125Hz effects on Current and Voltage ripple 216
Table 5-21: Calculated increase in current ripple as a % with battery balancing method compared to the base case for a switching frequency of 2kHz 218
Table 5-22: Comparison of the based circuit data with the ELM circuit at 125Hz effects on Current and Voltage ripple 223
Table 5-23: Comparison of the based circuit data with the ELM 175Hz effects on Current and Voltage ripple 224
Table 5-24: Calculated increase in current ripple as a % with ELM circuit compared to the base case for a switching frequency of 2kHz 225
Table 5-25: key results from experimentally derived data 229
Table 6-1: Battery Model component specifications 231
Table 6-2: Solar panel Equivalent Circuit Model component specifications 234
Table 6-3: Boost converter component specifications 235
Table 6-4: Comparison of fixed duty cycle with variable duty cycle at 10 kHz effects on Current and Voltage ripple 237
Table 6-5: Equivalent circuit components variation 246

List of Symbols

f_s	Switching frequency	Hz
f_0	Low frequency spectroscopy waveform	Hz
ω_0	Low frequency component (e.g. $2\pi f_0$)	Hz
T_s	Time between switched pulses	s
T_0	Period of the low frequency waveform	s
d_{av}	Average duty cycle	
d	Duty cycle	
$d(t)$	Duty cycle at time t	
f_{av}	Average switching frequency	Hz
T_{av}	Average time between switched pulses	s
$f_s(t)$	Switching frequency at time t	Hz
τ_m	The width of m^{th} pulse	s
τ_{or}	width of the "OR" of the impulse and pulse train	s
N_p	Number of high frequency pulses per low frequency cycle	
V_{bat}	Battery voltage	V
V_{dc}	Load output voltage	V
$\tilde{v}_{dc}$	Load output voltage ripple	V
$\tilde{v}_{ELM}$	AC ripple of the ELM voltage	V
$\tilde{\imath}_{ELM}$	AC ripple of the ELM current	A
I_L	Inductor current	A
C_b	Balancing Capacitor	F
Z_{PE}	Impedance of power electric converter	Ω
R_L	Load Resistor	Ω

List of Abbreviations

EIS	Electrochemical Impedance Spectroscopy
SOC	State of Charge
SOH	State of Health
OCV	Open Circuit Voltage
ELM	Earth Leakage Monitoring
WPD	Western Power Distribution
DNO	Distribution Network Operators
LCNF	Low Carbon Network Fund
IFI	Innovation Funding Incentive

1 Introduction

There is increasing pressure for society to move towards a low carbon economy. To enable low efficiency, carbon dioxide producing power plant to be removed from the energy cycle, it is necessary to invest in renewable energy sources. The intermittent and indeterminate nature of the renewable generation means that to enable the grid to operate reliably and stably with a large proportion of renewables it is necessary to consider adding energy storage to the system. For an energy storage system to be of long-term value to the distribution network operators (DNO) it needs to be reliable and have a high degree of availability.

A key challenge in a battery energy storage system is understanding the availability and reliability of the system from the perspective of the end customer. A key task in this process is recognising when a battery or a module within a system starts to degrade and then mitigating against this using the control system or battery management system. Battery characterisation parameters such as internal impedance and state of health (SOH) and state of charge (SOC) of the battery are a useful representation of the battery conditions.

The quantity of published literature in reputable journals indicates that EIS measurements may be a valuable tool in determining the impedance and the subsequent states of the battery. This measurement is mostly undertaken off-line but some attempt has been made in recent years to reproduce an on-line version. This thesis investigates the feasibility of undertaking Electrochemical Impedance Spectroscopy (EIS) methods online to generate an understanding of battery impedance. In order to perform an EIS measurement, an excitation signal of fixed frequency must be generated and the voltage across and current through the battery measured and used to calculate the impedance.

The aim of this thesis is to therefore to investigate the feasibility of different methods of undertaking EIS measurements online using existing hardware found within the system. As part of this, it is necessary to look at how the excitation signal is generated from a theoretical perspective, to ensure that the circuit operates as expected through the use of simulation and then to undertake experimental measurements to confirm the operations of these circuits. To help with this an appropriate equivalent circuit model of the battery under different conditions has been chosen to allow the EIS methods to be simulated with this model.

The work in this thesis has been undertaken in parallel to most of the published literature in this field. The rapid independent development of knowledge in this area has meant there is a need for classification of these methods. This thesis, classifies the different methods according to the hardware and control used to provide the excitation signal.

The proposed methods used in this thesis included: a) using DC-DC converter hardware with variable duty cycle, b) using DC-DC converter hardware with variable switching frequency, c) using DC-DC converter hardware with variable pulse starting position, d) using DC-DC converter hardware with an added impulse function, e) using capacitive battery balancing hardware, and f) using Earth Leakage Monitoring hardware. In all these methods, the DC-DC converter was operated in continuous mode with a fixed duty cycle and load to allow comparable analysis between the techniques. Although utilising variable duty cycle to generate a harmonic impedance has been previously published in the literature, the other 5 techniques analysed within this these have not previously been considered. This represents a novelty in the knowledge in this field.

The remainder of this thesis is divided into five different sections; theoretical analysis of on-line EIS techniques, Simulation of on-line EIS techniques, experimental validation of on-line EIS techniques, practical implementation issues, and conclusions and future work.

Chapter 2 establishes the background for why this research is necessary along with current knowledge of energy storage systems, battery parameters estimation methods, and previously published works on electrochemical impedance spectroscopy measurement methods for different types of energy storage system.

Chapter 3 looks at different methods of injecting low-frequency waveforms into the battery for impedance measurement of the battery using existing circuit hardware. For impedance calculation, the voltage and current waveforms are converted to the frequency domain using Fourier analysis. This section represents a detailed analysis of the current ripple, converter boost ratio, Fourier analysis is used to estimate the harmonics of the gate drive signal and battery and converter ripple current.

Chapter 4 presents the modelling of these methods using MATLAB Simulink using an EIS equivalent circuit (EC) calculated representation of the battery. These simulated waveforms are compared with the theory. The impedance of the battery over the frequency range is then reverse calculated through the circuit and compared to that measured data by the laboratory EIS equipment.

Chapter 5 validates these techniques experimentally. A controller unit was used to generate the control PWM signal and inject the low-frequency excitation signals. The battery waveforms are then analysed to calculate the impedance over the frequency range of 1Hz - 2kHz. The experimental data is compared to theory and simulation.

Chapter 6 looks at practical issues including the applicability of this technique to different battery chemistries and a solar panel. The thesis goes on to investigate what is required from a

practical perspective to move this work forward from proof of concept to demonstrator by commenting on issues such as measurement through to data analysis. This includes practical considerations for measurement implementation issues such as prediction of the state of charge of the battery, prediction of the equivalent circuit component value using a least square method, and exploring the possibility of detecting a poor battery cell from within a string using measured impedance of the battery pack system.

Chapter 7 gives the conclusions of this thesis and suggests possible future work.

2 Background

2.1 Energy Storage

There is increasing pressure for society to move towards a low carbon economy [1]. To enable low efficiency, carbon dioxide producing power plant to be removed from the energy cycle it is necessary to invest in renewable energy sources (RESs) such as the wind or solar power or larger plant such as nuclear power [2]. With the social pressure and long lead times around nuclear generation [3], there is a strong focus on renewable generation and in particular low scale distributed energy resources (DERs) such as wind power and solar panels. The intermittent and indeterminate nature of the renewable generation means that to enable the grid to operate reliably and stably with a large proportion of renewables it is necessary to consider adding energy storage to the system [4]. This can be based on long-term storage (storing power when the wind is blowing and releasing when it is not) to intermittent storage (responding to grid frequency and assisting with maintaining grid stability) [5]–[7]. Where the generation is within the distribution system, energy storage may also be used to help prevent constraints (such as thermal ratings of lines/cables or voltage constraints at busbars) as alternatives to Network reinforcement. Energy storage can come in many forms, such as pumped storage, flywheels, compressed air and chemical storage such as batteries and fuel cells. In particular, battery energy storage deployment is increasing, partly, because it can react very quickly and therefore assist with grid stability much better than some of the other forms of storage [8]. The increase in all forms of stored energy globally including that from battery energy storage is shown in Figure 2-1 [9]. This uses Data derived from the Department of Energy (DOE), global energy storage database in the USA [10] which currently lists 1630 current energy storage projects at a total rating of 193GW. These figures illustrate an increasing trend in the uptake of energy storage.

In the UK, the introduction of the Innovation Funding Incentive (IFI) and Low Carbon Network Fund (LCNF) by the electricity supply regulator OFGEM [11] has facilitated research into electrical energy storage within the grid system through a number of funded projects in conjunction with the Distribution Network Operators (DNOs). In 2015 this scheme was replaced with the Network Innovation Allowance (NIA) to allow Network Innovation to continue. A number of electrical energy storage projects were trialled under this funding. A summary of these is shown in Figure 2-2 [12].

Figure 2-1: Summary of installed global energy storage projects [9]

Figure 2-2: GB DNO Deployment of Electrical Energy storage (at 1st December 2014) [12]

The lessons learnt from undertaking research by DNO's on Electrical Energy Storage in the UK was collected together by EA Technology [12] in the form of a good practice guide. For an energy storage system to be of long-term value to the DNO it needs to be reliable and has a high degree of availability.

Conventional reinforcement of distribution networks has traditionally been designed for an anticipated peak demand and can potentially be over engineered, expensive, disruptive and

inefficient. The Western Power Distribution (WPD) led FALCON project (Flexible Approaches to Low Carbon Networks) looked at flexible ways to optimise the Network, by focussing on the 11kV Network around the Milton Keynes area. Six alternative techniques were deployed to investigate alternatives to conventional reinforcement. One of these techniques is the inclusion of energy storage on the 11kV distribution network. Data was collected from the energy storage facility listed in Figure 2-2 as the Milton Keynes (250kW, 500kWh) project in order to investigate the reliability and availability of the energy storage facility from the perspective of a Utility customer [13]–[16].

As-installed, this project comprised of five energy storage units (inverter and battery module) connected at existing substations on a single 11kV feeder as shown in Figure 2-3. The five sites were set up with 50kW/100kWh energy storage batteries (Sodium Nickel) and inverters located at the substations highlighted in Figure 2-3.

These units charge or discharge the batteries at designated times or triggers:

- As specified manually;
- At specified times regardless of network conditions;
- When substation load is above a specified trigger point (peak shaving operations); or
- When grid frequency is above or below pre-specified trigger points.

In addition, the inverters can also import or export reactive power, influencing voltage at the point of connection.

A key method of ensuring continued battery system operation and accurate available capacity reporting is to have the battery undertake a maintenance cycle. This is an operation through the battery control system which takes the batteries offline and re-calibrates key parameters. This maintenance cycle typically discharges and recharges the battery system. The necessity of running batteries through a maintenance cycle, therefore, impacts on the availability of the battery to the Network Operator.

A maintenance cycle on the five Milton Keynes battery sites was recommended by the manufacturer to be run every week. The maintenance cycle is different for different battery chemistries and the manufacturer will advise on request. This maintenance cycle was started at a fixed time each week however, the control system decides how the cycle will proceed. Results from two maintenance cycles are shown in Figure 2-4, which is the AC feeder rms current with time. This results in two key unknowns;

1. Although the cycle may be set to a fixed time slot – the decision to discharge or charge the battery by the control system could occur at any time after this.

2. The maintenance cycle period, if it occurs, is not a fixed time period as shown by the red arrows in Figure 2-4, and can vary from less than an hour to 12 hours.

It is not possible to know in advance if the battery will be undertaking a twelve-hour maintenance cycle or none at all. From an availability perspective – this means the battery cannot be relied upon for service over the twelve hour period from the control system start of a maintenance cycle.

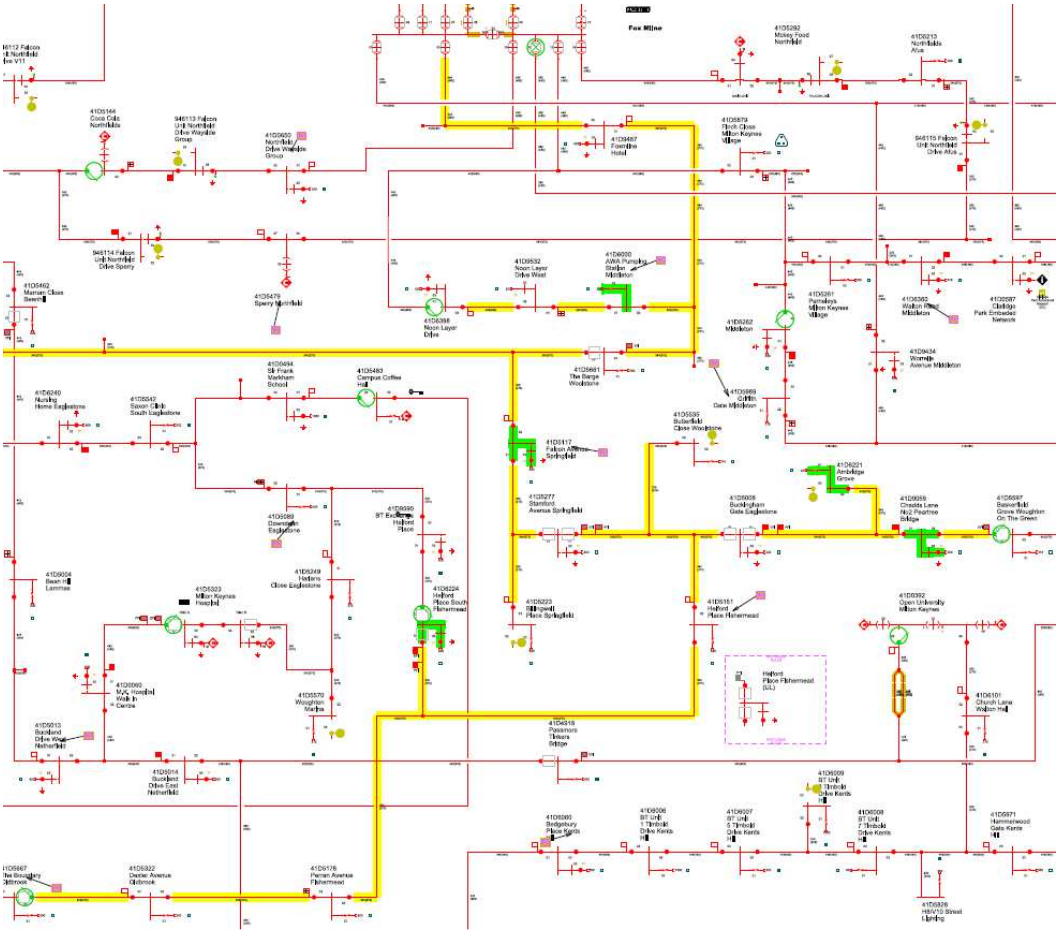

Figure 2-3: 11kV feeder from Fox Mile Primary with five connected Energy Storage Sites.

Battery maintenance cycles play an important role in the re-calibration of the batteries for operational purposes. The maintenance cycle reported on the FALCON batteries are more extensive than typically reported for large scale installations. However, they usefully illustrate the key point that to understand and manage the performance of a battery system, a battery management system needs to understand and control the state of the battery as accurately as possible to minimise the requirement for battery re-calibration and subsequent availability downtime.

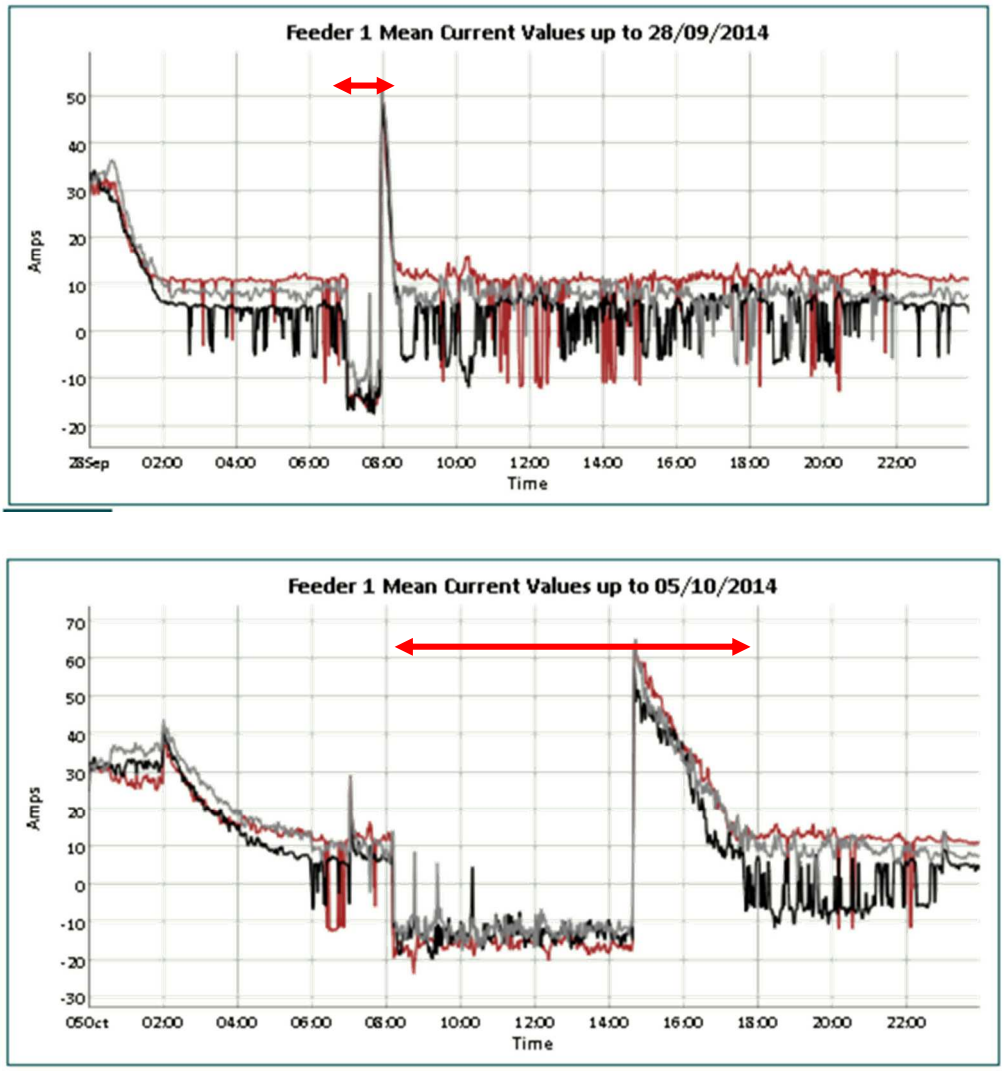

Figure 2-4: A short and long battery maintenance cycle.

With the decarbonisation of the transport sector, additional energy storage capability for grid support applications may also be available through electric or plug-in hybrid electric vehicles [17]. Additional schemes such as hybrid energy schemes with a mixture of generation and storage are becoming more widely available including schemes using second life batteries [18]–[20]. A second life battery is a battery which has been originally been used within an automotive application, but where the capacity of the battery has reduced below 80% of the nominal reported capacity of the new battery. Understanding the states of the key parameters of a battery energy storage system are key to its control and reliability regardless of the battery chemistry.

2.2 Battery definitions

There are a number of different terminologies in use to describe different characteristics of a battery system. This section lists a definition of terms as used within this thesis to ensure clarity of understanding.

Table 2-1: Definition of terminology

Term	Abbreviation	Definition as used in this thesis
Battery Cell		A single battery cell.
Battery String		A series connection of battery cells.
Battery Module		A series/parallel connection of strings.
Battery System		A combination of battery modules.
Nominal Battery Capacity		The capacity of the battery in Ah or Wh as specified by the manufacturer at point of manufacture. This value may be charge /discharge rate dependent. In this document, this is considered to be the capacity available to the user rather than the capacity of the battery where some of the capacity is unavailable.
Maximum Available Battery Capacity		The maximum capacity of the battery in Ah or Wh after the battery has been in use and may have degraded when it is fully charging. In this document, this is considered to be the capacity available to the user.
Remaining Battery Available Capacity		The remaining capacity of the battery in Ah or Wh after the battery has partially discharged. In this document, this is considered to be the capacity available to the user.
Charge and discharge rate		The rate at which the battery charges or discharges with time in A/s or W/s.
Safe operating envelope		The battery operational limits as defined by its maximum and minimum voltages, charge and discharge rates, temperature and any other key parameter as defined by the manufacturer.
State of charge	SOC	There are a number of definitions of SOC in literature [21], [22]. In this work, this is defined as the ratio of the remaining available battery

		capacity to the maximum available battery capacity.
Depth of Discharge	DOD	The percentage of a battery that has been discharged expressed as a percentage of the Maximum available battery capacity.
State of health	SOH	There are a number of definitions of SOH in literature. This term relates to the ability of the battery to provide specific performance in comparison with a new equivalent battery. This relates to the difference between the Nominal battery capacity and the Maximum available battery capacity and is a measure of power and/or energy fade. The power capability fades as the internal impedance of the battery increase while the energy fade occurs when the battery loses capacity. These factors may be calendric (dependent on age) or cyclic (dependent on operational characteristic).
State of Power	SOP	The available power that the battery can deliver at a given time to the user.
State of Function	SOF	A flag indicating that the battery is available to undertake a predetermined function [23]. Various alternative definitions are available [24]–[26].
State of Life or Remaining useful life	SOL or RUL	Indication of remaining estimated life in the battery based on pre-defined charging and discharging patterns maybe tied to DOD.

To understand and manage the battery performance in a battery system a battery management system (BMS) is typically used. In an energy storage system, many battery cells may be connected in series and parallel in order to generate the required power and energy levels. The role of the battery management system may therefore include;

- Data Acquisition: measuring, collecting and collating battery data
- Cell protection: ensure that the battery cells remain within the safe operating envelope
- Cell balancing: equalise the charge across battery cells to maximise the capacity of the system

- Thermal management: control cooling systems or temperature gradients within systems
- Energy management: control the flow of energy into and out of the battery cells to meet operational requirements
- Battery parameter estimation: determine key characteristics of the battery for use by the energy management function. This may include any combination of SOC, SOH, SOP, SOF, SOL, remaining available capacity and impedance determination.

The following section includes a review as to published methods of estimating the battery parameters for use by the BMS.

2.3 Battery parameter estimation

2.3.1 SOC estimation

A selection of different SOC measurement techniques are shown in Figure 2-5. These come in two categories; direct and indirect. If the SOC is estimated straight from a measurement variable this is known as a direct technique. If the SOC is found through calculation of combinations of variables then this is classed in this thesis as an indirect technique. The methods may also be on-line or off-line. The former results in better battery availability, while the latter may be more accurate. In other word, the availability of the battery depends on minimisation of the battery re-calibration and subsequent availability downtime requirements. This is possible by estimating and controlling the state of the battery such as SOC as accurately as possible.

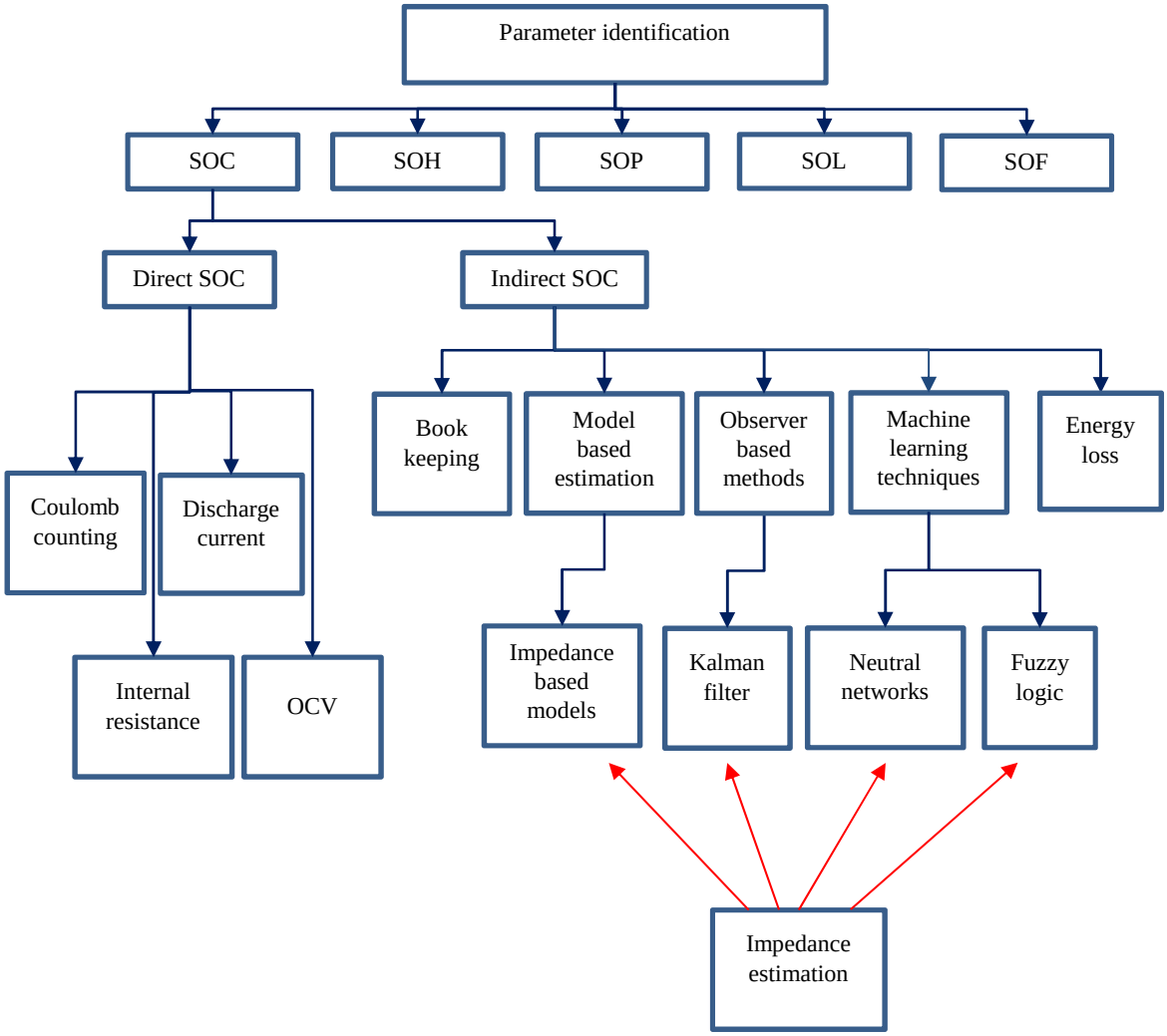

Figure 2-5: Different methods of battery SOC monitoring

Table 2-2 briefly summarises how these different methods work.

SOC is a function of many different parameters including battery state, capacity, charge and discharge rate, temperature and therefore its estimation is difficult and can be inaccurate.

The main direct techniques are the coulomb counting method and the OCV methods. The former method may suffer from sensor noise and initialisation-induced offsets, while the latter requires a period of disconnection to establish an accurate measurement for the battery's OCV. Consequently, these two methods are often combined in practice to form the basis for the indirect model-based SOC estimation techniques. The impedance estimation is required for state of charge calculation using some indirect methods as shown by the red arrows in Figure 2-5. The coulomb counting can also be considered as an input for the book-keeping method for SOC prediction.

Table 2-2 : summary of SOC determination techniques

Technique	Summary	On/ offline
Direct		
Discharge [27]	The batteries are discharged with a fixed small rate of current until the battery voltage reaches a threshold value. The SOC is estimated as a product of discharge duration and current rate.	Offline
Coulomb counting [28]–[34]	The state of charge is estimated by integrating current over the charge/discharge duration time from an initial SOC of the battery.	Online
Open Circuit Voltage (OCV) [35]–[40]	SOC is estimated using an OCV SOC look up table. The OCV maybe estimated using the terminal voltage and a battery circuit model.	Online
Internal resistance [41]–[47]	As small current ripple is used to measure internal impedance at a fixed frequency point to provide a value of impedance. This is then used in conjunction with an impedance SOC lookup table to generate SOC.	Online
Indirect		
Book Keeping Methods [21], [48]–[52]	Uses pre-characterised lookup tables which relate different battery characteristics to SOC. These may include parameters such as the coulomb counting data, battery discharge rate, cycle life, temperature rate.	Online
Model-based Estimation eg impedance based model estimation [21], [41], [53]–[57]	Measurements are used as inputs to a model (for example an impedance based equivalent circuit) which is then used to determine the OCV of the battery for use with an OCV-SOC lookup table. An impedance based estimation approach may use an offline generated impedance spectrum of the battery to produce an impedance model (equivalent circuit) to estimate the circuit parameters. The variation of these under different condition is used to estimate the SOC of the battery.	Online
Observer-based methods eg Kalman filter	Predicts the battery SOC using the components of a battery model. It works in two steps, prediction and measurement. Predict the model parameters and compares them with the measured one. This process is updated once a corruption occurs between the predicted and	Online

[37], [58]–[72]	measured data. The corrupted data can be minimised by using a weighted average.	
Machine learning	This includes techniques such as Neural Networks [51], [73]–[80] - The SOC current of the battery is estimated using pre-defined data such as the battery current, voltage, and SOC. It is a multilayer network system and uses pre-training data as an input. At each layer different functions are used to analyse the incoming data from the battery to estimate the battery SOC. Fuzzy logic [21], [81]–[87] - uses input parameters such as AC impedance and voltage recovery measurement, to estimate the battery SOC through fuzzy logic.	Online
Energy Loss [42], [88]	The internal resistor depends on the heat generated from the battery, when there is no other side reactions (i.e. under high current condition). This generated energy can be calculated using the calculated difference between charge and discharge energy.	Online

2.3.2 SOH estimation

The state of health is commonly used to report an indicator of the health condition of the battery. It does not relate to one physical quantity and there is no single rule in industry on how this should be specified. It is however set on an arbitrary set of rules based on what the battery designers deem to be suitable. This may include combinations of values such as the ratio of the battery capacity to the new battery nominal capacity or the ratio of the aged battery internal resistance to the new battery resistance. Within industry this calculation tends to be kept confidential. There are a number of parameters and techniques used to help estimate the SOH of a battery and these are summarised in Figure 2-6 with examples of these methods summarised in Table 2-3. These are similar to those used within the SOC calculation. SOC, OCV, and internal resistance of the battery all appear to be key parameters of SOH estimation [89]–[91]. The health condition of the battery depends on a number of factors including but not limited to; recharging time, SOC, internal impedance, voltage drop in discharge, temperature and output energy under DOD [90], [92].

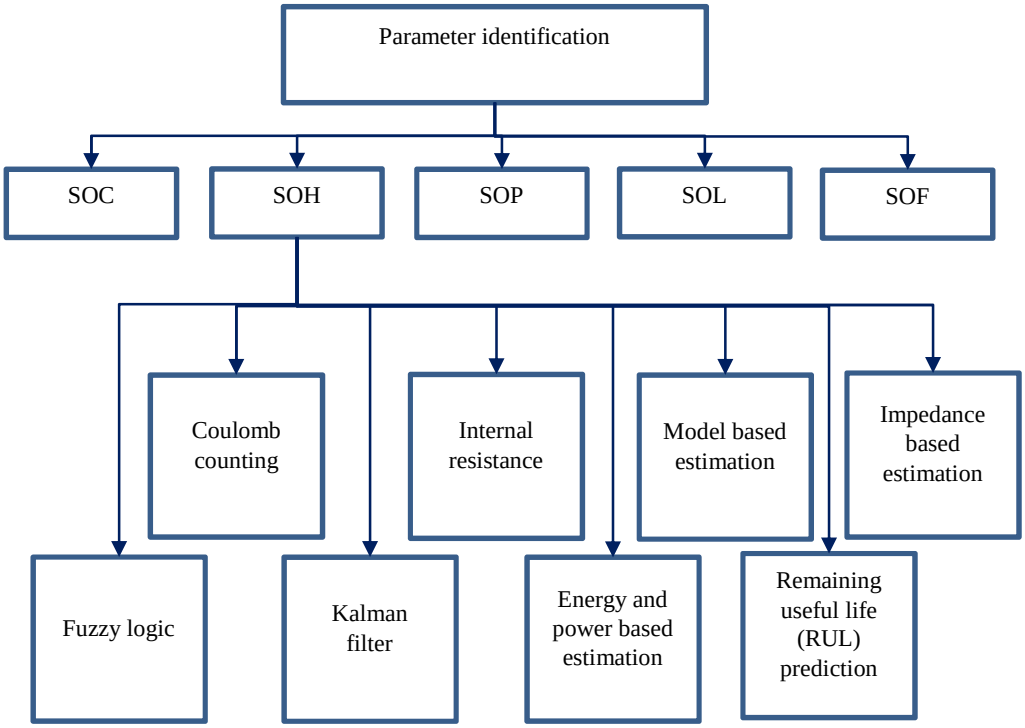

Figure 2-6 : Different methods of battery SOH monitoring

Table 2-3 : example summary of SOH determination techniques

Technique	Summary	On/offline
Fuzzy logic [84], [93]–[95]	The fuzzy logic system is used to model the relationship between the maximum capacity and the internal resistance to estimate the SOH. In this method a combination of coulomb counting and OCV have been used. The battery current and voltage were used as input parameters to the fuzzy logic system to measure the internal resistance and maximum capacity of the battery.	Online
Kalman filter [91], [96]–[98]	The Kalman filter has been combined with coulomb counting to measure the internal resistance based on a battery model and battery capacity to estimate SOH based.	Online
Model-based estimation [99]–[102]	Based on the battery type an equivalent circuit model is proposed and used. SOH can be estimated from the measurement of the battery circuit model components with the battery terminal voltage variation.	Online
Coulomb counting [103]–[106]	The maximum capacity of the battery is calculated each time the battery is discharged to its minimum voltage level (cut-off	Online

	voltage). The state of health is predicted from the ratio of the measured capacity to the maximum capacity of the battery at the beginning of life.	
Internal resistance [104], [105]	As the SOH of the battery decreases the internal impedance of the battery increases. This uses the OCV of the battery to measure the internal impedance. The SOH is predicted from the measured internal resistance and initial charge state of the battery.	Online
Remaining useful life (RUL) prediction [107]–[112]	The terminal voltage and current of the battery are measured and used with parameter estimation methods such as a nonlinear least square method to produce a battery equivalent circuit model parameters to predict the SOH. The estimated SOH and other properties of the battery as a function of time and/or number of cycles are used to predict the end of life of the battery.	Mostly Offline
Neural networks algorithms [89], [90]	The battery voltage, output energy and temperature are used as inputs to the neural network system to predict the SOH.	Online
Energy and power based estimation	As the battery degraded, its impedance and capacity increased and reduced respectively. The battery impedance and capacity is then used to measure the power and energy based SOH of the battery. The impedance and capacity of the battery can be estimated using the methods mentioned in the following sections.	Online

2.3.3 SOP, SOF and SOL estimation

These parameters are more recent in definition and a summary is shown in Figure 2-7 and described in Table 2-4. The battery SOP in normally defined as an amount of power that is available to the user. The state of power of the battery suffers from the issues of temperature variation, battery SOC, battery voltage limits (minimum voltage limit given by the manufacturer), sensitivity to the noise, and aging of the battery. The SOP of the battery has been reported to be estimated using the two methods of model based and the book keeping methods. The state of function of the battery is commonly used to monitor whether the available power of the battery can exceed the minimum threshold value required for the battery system application to accomplish the process. Reference [23]

represented the SOF estimation as a comparison of the available battery power peak (SOP) to the minimum required power. The SOF estimation depends on the open circuit voltage, SOC and the impedance voltage drop of the battery [113]. The State of life (SOL) or Remaining Useful Life (RUL) is described in literature as the remaining time before the battery must be replaced or as a function of the number of remaining charge/discharge cycles. Recent works on such RUL prediction approaches include [96], [107]–[112], [114], [115]. The main task is to estimate a SOH and then use this in a model which looks at RUL possibly based on pre-determined data obtained through battery aging and a predicted load profile.

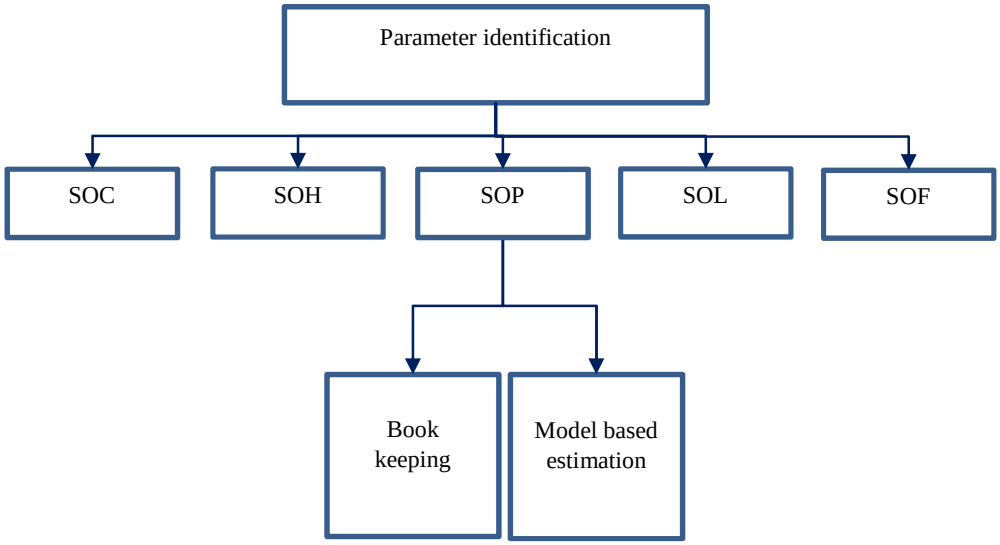

Figure 2-7: Different methods of battery SOP monitoring

Table 2-4: example summary of SOP determination techniques

Technique	Summary	On/offline
Model-based estimation [113], [116]–[123]	One method used to estimate the battery parameter is a kalman filter approach which adapts from the equivalent model based of the battery. The state of power of the battery is then calculated from the obtained parameter.	Online
Book keeping [21], [48]–[50], [52], [124]	This method uses the discharge current of the battery and integrates it over time. It uses the current data and other properties of battery (e.g. cycle, SOC, capacity loss, and etc) to estimate the SOP of the battery.	Online

2.3.4 Remaining Available Capacity estimation

Battery capacity is used as a factor to estimate the SOH, SOC, and SOP of the battery. This is because the battery capacity rate changes depending on battery aging and different operational conditions. There are a number of online and offline methods of estimating the remaining available capacity of a battery. These are summarised in Figure 2-8 and summarised in Table 2-5.

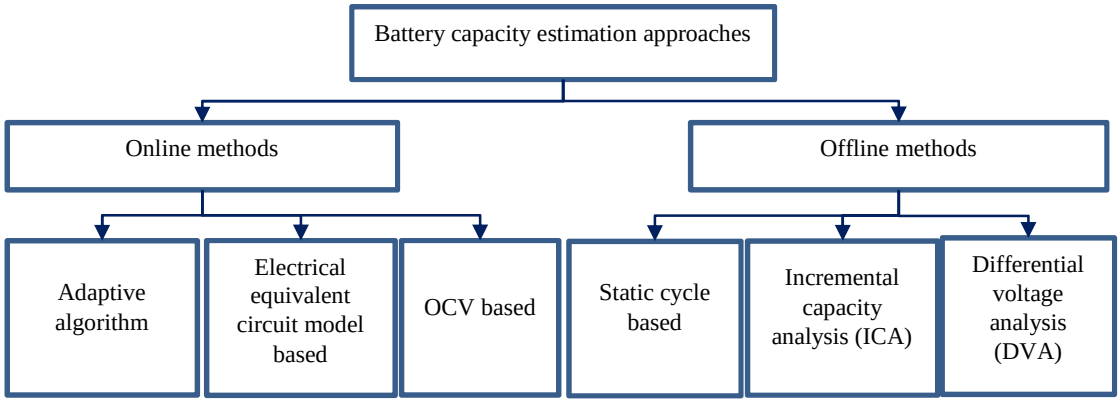

Figure 2-8 : Different methods of available battery capacity estimation

Table 2-5: Summary of remaining available capacity determination techniques

Technique	Summary
Online	
OCV [36]–[40], [125], [126]	The OCV of the battery changes due to the variation of the SOC over the charge/discharge cycle. The capacity can be calculated from the initial SOC value and the integrated battery current over the charge/ discharge time.
Adaptive algorithm [29], [30], [60], [127]–[129]	The mentioned adaptive algorithm in section 1.3.1 and 1.3.2 such as kalman filter and coulomb counting methods can be used to calculate the battery capacity from the battery dynamic model structure.
Equivalent circuit model based [21], [41], [53]	An equivalent circuit model is used to calculate the battery OCV. The OCV value is applied to lookup table parameter to estimate the battery capacity and its SOC.
Offline	
Static cycle based	This measures the amount of charge that battery loses after a full charge and discharge cycle.
Differential voltage analysis (DVA) and Incremental capacity analysis (ICA)[130]–[134]	A low constant current is used to discharge and charge the battery to calculate the battery SOC. Then it calculates the gradual changes of the battery cell behaviour using the incremental capacity (IC) or differential voltage (DV) curves as a function of temperature variation and battery SOC to once the OCV reaches to its final equilibrium value.

2.3.5 Impedance estimation

As mentioned in section 1.3.1 and 1.3.2, the impedance of the battery can be considered as a parameter for use in the estimation of battery SOH, SOC, SOP, SOL, and SOF. The impedance of the battery changes based on different factors of SOC level, capacity fade, self-discharge rate differences, varying operation conditions, and temperature difference across the cells [135]–[137]. Various methods have been published to measure the impedance of the batteries. These methods are categorised into electrochemical modelling, electrical equivalent circuit and EIS methods which are applied online and/or offline. There are a number of methods of estimating the battery impedance. These are shown in Figure 2-9 and examples are summarised in Table 2-6.

The electrochemical modelling uses numerical analysis of the underlying physical and chemical equations to describe the battery behaviour. These are mostly described through sets of partial differential equations. The equations can be solved in a number of ways including least square, particle filters, and gradient-based methods. The results of this can be used to look at battery dynamics directly or to estimate battery impedance for a given set of conditions. These methods can be complex and don't easily relate to physical quantities which are more easily understood.

Electrical equivalent circuit models (ECM) are commonly used in online battery state estimation methods. There are a large number of equivalent circuit models as discussed later in this chapter and they can be set up to represent discrete parameters eg corrosion. This method takes measured data (eg voltage and current) and then uses mathematical techniques to turn this data into an equivalent circuit.

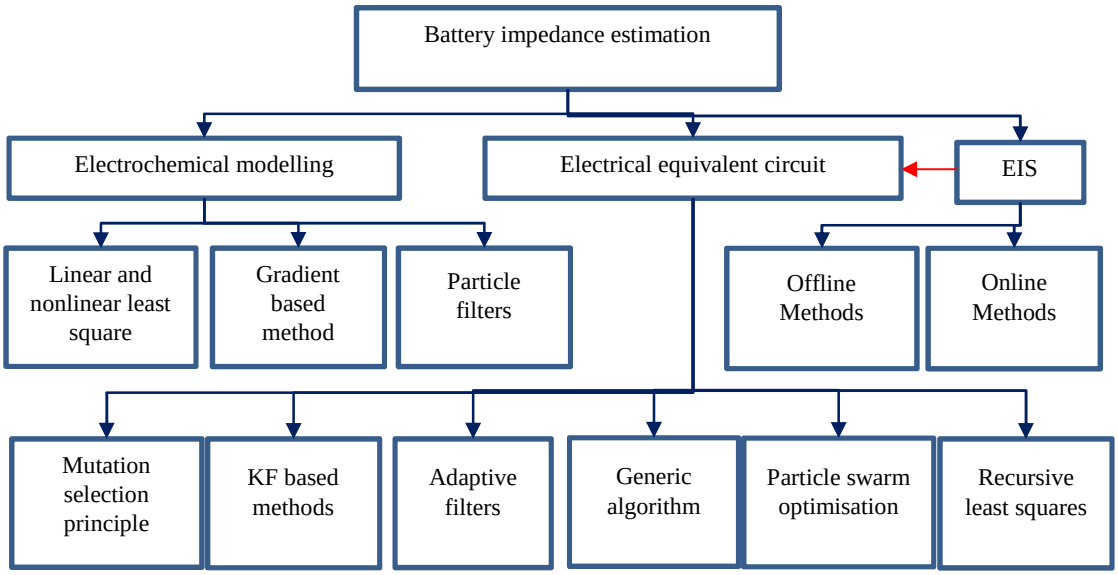

Figure 2-9 : Different methods of impedance determination

The Electrochemical impedance spectroscopy (EIS) method can be used in two ways, it can be used to generate data for equivalent circuit models or it can be used to look at processes and their time constants. EIS is usually undertaken offline, but more recent research has shown that this could be a valid on-line technique [53], [56], [138]–[140]. The offline EIS methods are performed when the battery system is disconnected from the system, and usually use expensive laboratory EIS equipment to measure the battery state and impedance. Various methods to replicate EIS online are presented in section 2.5.

Table 2-6 : example summary of battery impedance determination techniques

Technique	Summary	On/offline
Linear/nonlinear least square [141]–[145]	This method is used to fit the battery EC impedance parameters to the impedance curve of the battery. The parameters are predicted based on reducing the error between the observed data and the fitted data. The least square method can be applied in nonlinear models as well as linear one. This method is used in this work to predict the battery parameter in Chapter 6.	Offline
Particle filters [146]–[148]	This method predicts the impedance based on representing various sampled values from the unknown state space with a set of associated weights.	Offline
Particle swarm optimisation [149]–[151]	This method is similar to particle filter but have simpler programming and requires fewer adjusting points.	Online
Impedance spectroscopy [152]–[156]	A small AC signal is used to excite the battery and the impedance is measured over the frequency range.	Mostly Offline

EIS provides a mechanism for highly accurate impedance determination and is widely used. The next section contains a summary of published EIS results in conjunction with energy storage impedance determination.

2.4 Electrochemical impedance spectroscopy

Electrochemical impedance spectroscopy (EIS) is a method of data measurement which looks at the electrical characteristics of a material or electrical component such as a battery or solar cells. It is mainly used because of its high level of accuracy and subsequent analysis allows indication of different chemical processes. An online EIS technique could offer a possible method of determining remaining charge in a battery while enabling the degradation process to be characterised and an indication of state of health of the system to be output to the control system

for power management or to the owner/operator of the system. The high accuracy of the offline EIS technique allows it to be used as a benchmark to validate other techniques.

Electrochemical impedance spectroscopy measurements have been around since 1999 [157] and can be undertaken through a couple of different methods; these include analogue analysis and processing of the systems in the time and frequency domain or digital computation using the EIS equipment [158]. The main basis for the method is to measure the frequency response of a test piece to understand how its impedance changes over the frequency domain. Digital instrumentation has a better signal to noise rejection and easier data post processing than the analogue. The digital equipment used within this thesis, comprises an electrochemical interface EI (the Solartron 1287) with frequency response analyser (FRA), and impedance analyser (the Solartron 1260).

An EIS test is usually performed by applying a small AC excitation signal (AC potential or current signal) into the electrochemical cell. Then the impedance value of the system, is the ratio of the applied signal and response, and is independent of amplitude and phase of the excitation signal. The EIS technique can be a time-consuming measurement method depending on the frequency ranges and the system should ideally remain in the same state during the measurement time interval. A 4-wire measurement method is used as shown in Figure 2-10 to ensure the impedance of the connections, which can be of comparable magnitude, to the sample, are not included in the overall measurement. In this measurement; the current passage across the battery electrodes including a working electrode (WE) and a counter electrode (CE) causes the potential difference between two reference electrodes (RE_1 and RE_2) [159]. Reference electrodes provide the measurement of voltage between the terminals.

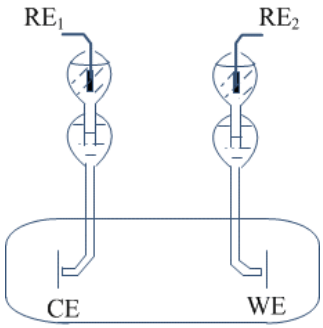

Figure 2-10 : EIS Battery Terminal Connections [160]

EIS measurements can determine the resistive, inductive, and capacitive behaviour of electrodes and electrolyte material under different conditions. The EIS data can be manipulated through equivalent circuits to represent theoretical system reactions in which the extracted results are correlated to a complex variable (e.g. corrosion, dielectric properties, and material conductance). An EIS characterisation procedure involves: (i) analysis of experimentally obtained impedance data of the materials by applying analytical methods, (ii) prediction of equivalent

circuit model, and (iii) data fitting method for validating experimental data. It can be difficult to analyse a system behaviour based on an equivalent circuit of the measured impedance using ordinary circuit elements because they present ideal electrical response[158]. Traditional electric circuit elements cannot always be used to describe imperfect chemical process such as corrosion and diffusion of the electric sources. Therefore it is usually necessary to use a complex combination of elements to demonstrate the imperfect behaviour.

In an EIS process the quantified response of the system to an excitation signal present in the time-domain, can be converted to the frequency domain using Fourier transforms.

$$F(j\omega) = \frac{1}{\sqrt{2\pi}} \int_{-\infty}^{\infty} F(t) e^{-j\omega t}\, dt \qquad \text{Equation 2-1}$$

The impedance value is equal to the ratio of the output response and the input response:

$$Z(j\omega) = \frac{E(j\omega)}{I(j\omega)} \qquad \text{Equation 2-2}$$

Where E and I are potential and current measured in the frequency domain, jω is the complex frequency and Z is an impedance function. If the input potential is expressed as $E = E_0 \sin \omega t$, then the output current is a function of time with different amplitude and phase shift ; $I = I_0 \sin(\omega t + \phi)$,

The impedance can be written as:

$$Z = \frac{E}{I} = Z_0 e^{-j\phi} = Z_0(\cos \omega t + j \sin \omega t) = Z_{Re} + jZ_{Im} \qquad \text{Equation 2-3}$$

The real component is often represented using $Z^{'}$, while the imaginary term by $Z^{''}$. The results of the EIS measurements can be expressed in a number of different ways. Typical methods include as a 3-D plot, Nyquist, and bode plot. In the Nyquist plot, the real and imaginary components of impedance are plotted over the range of frequencies. Plotting the imaginary and real component of impedance in the complex plane diagram commonly produces semicircle based diagrams. Some common impedance and their Nyquist equivalent plots are shown in Appendix A as these are useful to understand the Nyquist plots obtained later in this thesis. Appendix A includes representation of common components such as constant phase element (CPE), and Warburg impedance, which represent impurity in capacitance behaviour and frequency distribution that are presented in the impedance data [143], and adsorption and diffusion effect.

Once impedance has been calculated as a function of frequency this can then be represented using equivalent circuit models. Equivalent circuits are a useful pictorial representation of a real life system. They are made up of electrical components resistors, capacitors, and inductors and are widely used to represent the characterisation of electrochemical cell. Connection of electrical

elements can be estimated by considering the arc of impedance and the shape of the curve in a complex plot.

Some common shapes of plots for different elements such as batteries and PV panels from literature are shown in Figure 2-11. These shapes have been represented as a variety of equivalent circuit models as shown in Figure 2-12 from published literature. Within Figure 2-12 the CPE constant phase element and Warburg impedance are presented as a “Q” element in some of this literature. A summary of the equivalent circuits used by different researchers for different batteries and other systems are summarised in Figure 2-13. Where the equivalent circuit model is not specified in the literature this is shown as “no proposed EC model”. Many of the researchers have published a Nyquist plot shape similar to curve 3 from Figure 2-11 for different types of batteries and supercapacitors. However, they have used different equivalent circuit model representations for this curve. For a solar cell, curve 2 from Figure 2-11 is described by most of the researchers in conjunction with equivalent circuit of p and q from Figure 2-13.

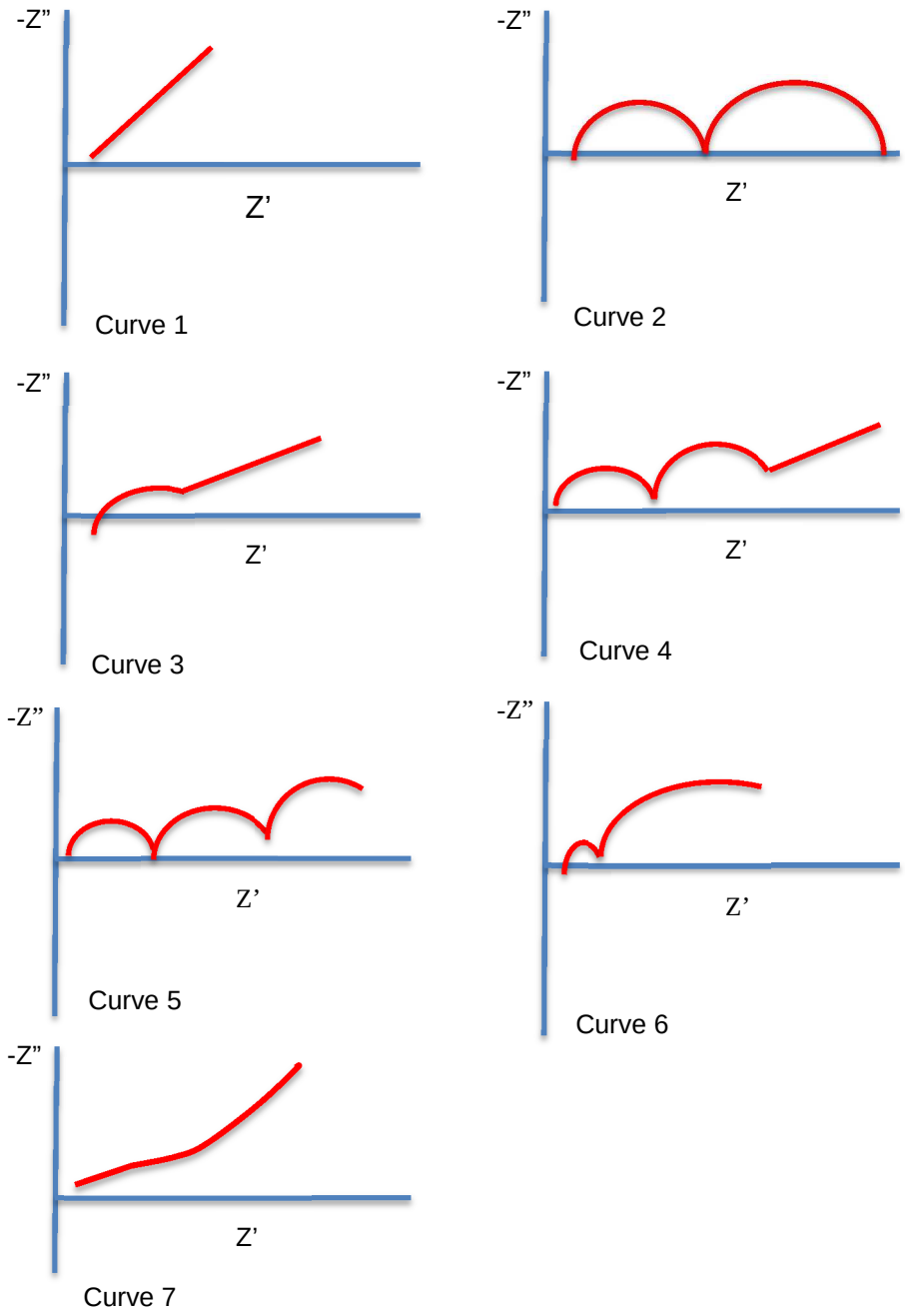

Figure 2-11: Common Nyquist shapes found in literature

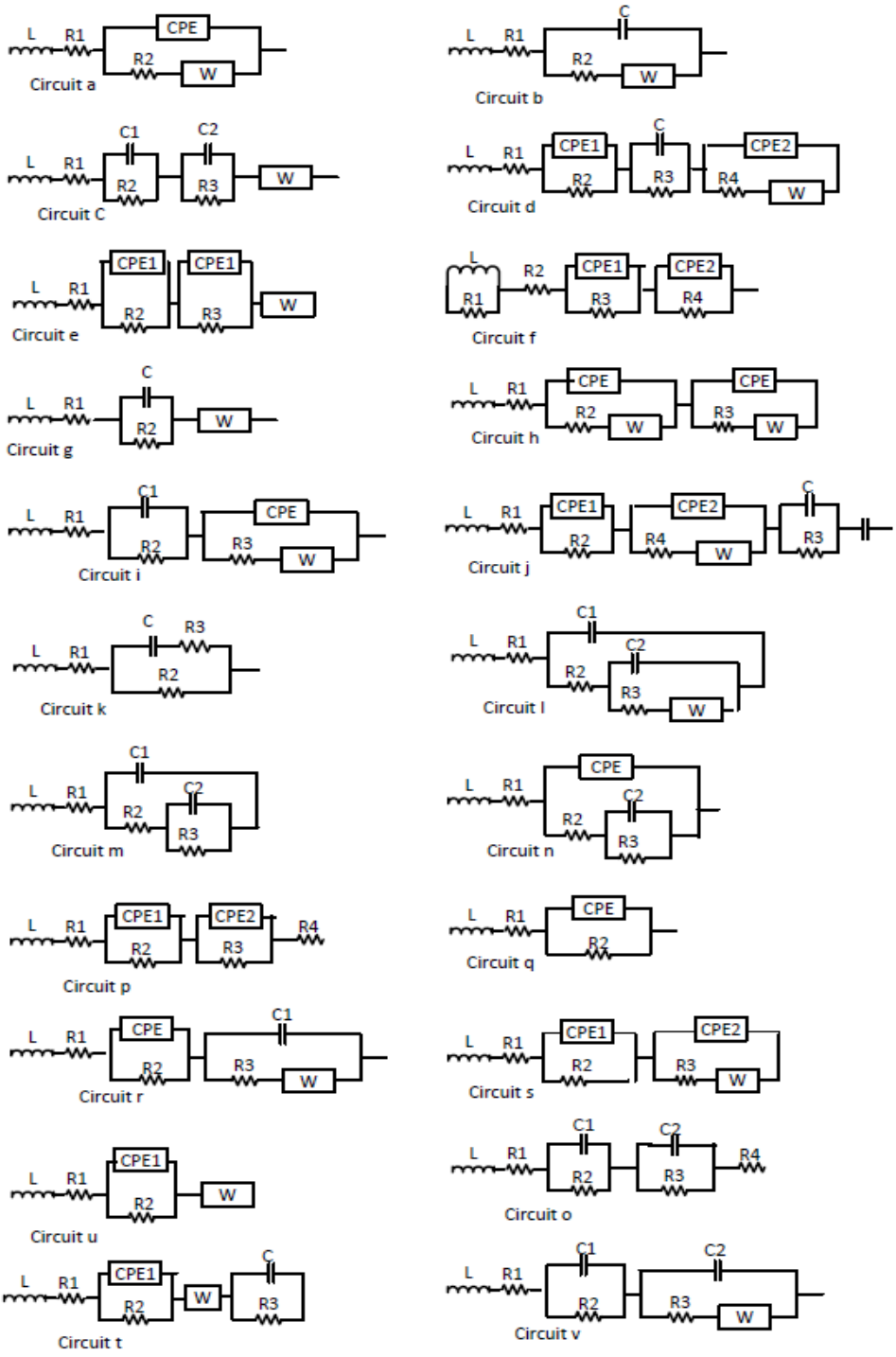

Figure 2-12 : Common equivalent circuits in literature, Note: the inductor component is ignored by some of the authors, especially when they are more interested in the low frequency behaviour

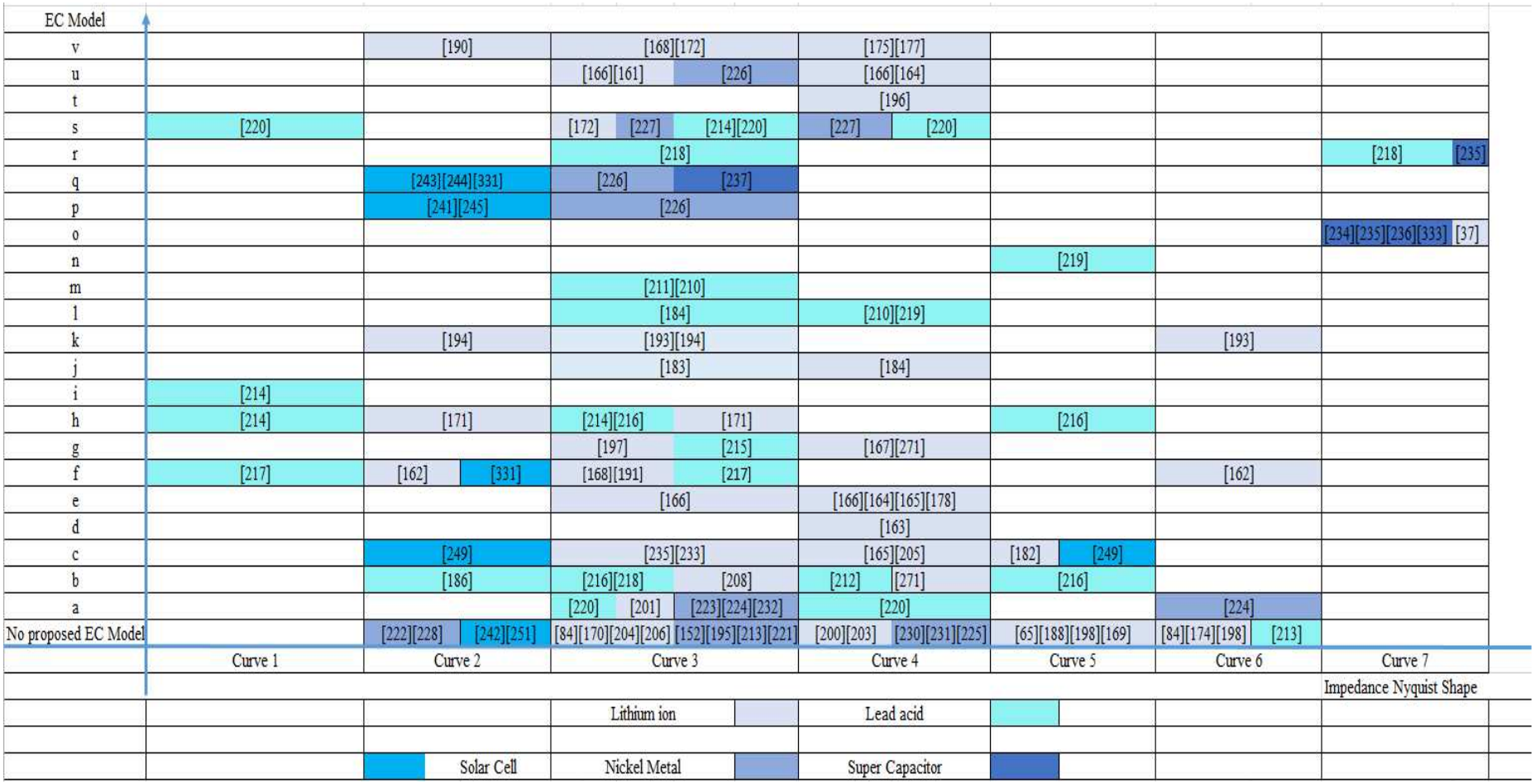

Figure 2-13: Summary of Equivalent circuit and Nyquist plots used by authors for different batteries, supercapacitors, and Solar cell

2.4.1 Lithium-ion Batteries

Work published in references [35], [37], [60], [65], [83], [84], [153], [161]–[208] is based on lithium-ion EIS characterisation. The excitation conditions are described in Table 2-7 where explicitly reported.

Table 2-7: Lithium-ion EIS testing Conditions used by various Authors

References	Frequency Range	Excitation Amplitude	Research investigation of
[161]	3mHz - 3 MHz	10mV	Various SOC
[162]	25mHz - 100kHz	5mV	Various SOC
[163]	10mHz - 100kHz	5mV	Variant Temperature 30, 60, 45, 20°
[84]	0.1 Hz - 65 kHz	3A	Different temperatures (0°C, 25°C/77°F and 45°C),
[164]	5mHz - 100kHz	10mV	40%, 20%, 80% of SOC
[165]	0.01 Hz - 10 kHz	10 mV, 20 mV	different temperatures (25˚ C, 35 ˚C, and 45 ˚C), SOCs 0% and 100%,
[166]	1mHz - 10 kHz	5mV	Different discharge state
[167]	0.01 Hz - 100 kHz	5mV	Different alloy
[168]	10mHz - 5kHz	0.1A to 1A	Temperature and SOC
[170]	10mHz - 5 kHz	10mA	Temperature, SOC
[171]	100mHz - 1 kHz	3mV	Temperature
[172]	0.1 Hz - 100 kHz	5mV	Temperature
[175]	0.1Hz - 100 kHz	5 mV	Temperature
[178]	3mHz and 10 kHz	10mV	Degradation
[83]	0.1 Hz - 65 kHz 0.1 Hz - 10 kHz	3A	Various SOC, and Temperature
[193]	0.1 Hz - 1638.4 Hz	62.5mA	Various SOC
[194]	0.1 Hz - 2 kHz	20mV	DOD

A summary of the change reported in Nyquist plot shape with SOC, temperature, cycling and starting charge are sketched from this published research is shown in Figure 2-14 and Figure 2-15. These are general summaries made by condensing the information from the references below. The frequency ranges represented by authors were chosen based on the test conditions and there was no specific correlation of frequency range with battery chemistry.

References [37], [65], [83], [84], [161]–[164], [166], [178]–[181], [185], [190], [192], [202] studied the impedance behaviour at different state of charge. The effect of the temperature on the impedance spectra has been investigated by [35], [37], [161], [163], [165], [170]–[172], [175], [176], [178], [190], [199], [204], [208]. Authors [167], [173], [174], [177], [182], [185]–[189], [195]–[197], [201], [202], [205], [206] characterised the lithium-ion batteries at different cycles of degradation. Variation of the impedance data at different open circuit voltages is reported by [166], [183], [192], [200]. References [164], [165], studied the electrochemical characteristic of different electrode/electrolyte alloys used in lithium-ion.

In general it is to be expected from literature that the impedance increases with the number of cycles, a reduction in temperature, a reduction in SOC and a decreasing charge. When the battery is degraded the conductivity of the electrolyte decreases because of electrolyte decomposition with battery aging. Therefore battery impedance increases [167]. This also leads to increase of battery internal impedance. The battery chemical process is affected with variation in temperature. Therefore when the battery is operating at low temperature the chemical reactions decrease due to the low kinetic energy of ions (i.e. ions conduct slower in electrolyte), which leads to increase of battery impedance. In SOC characterisation, when the battery SOC decreases, battery voltage decreases. A decrease in voltage causes the charge transfer to be slower which manifests itself as an increased impedance. At low charge rate the capacity of the battery decreases due to limitation in active ions transformation due to current drop, which is explained by [209]. Reduction in charge rate increases battery impedance. This result is potentially helpful because as the SOC reduces the impedance of the battery will look higher and the battery may assume a lower share of the power depending on battery configuration. However the accuracy with which the power sharing could occur will be reduced because of the uncertainty as to what is causing the changes.

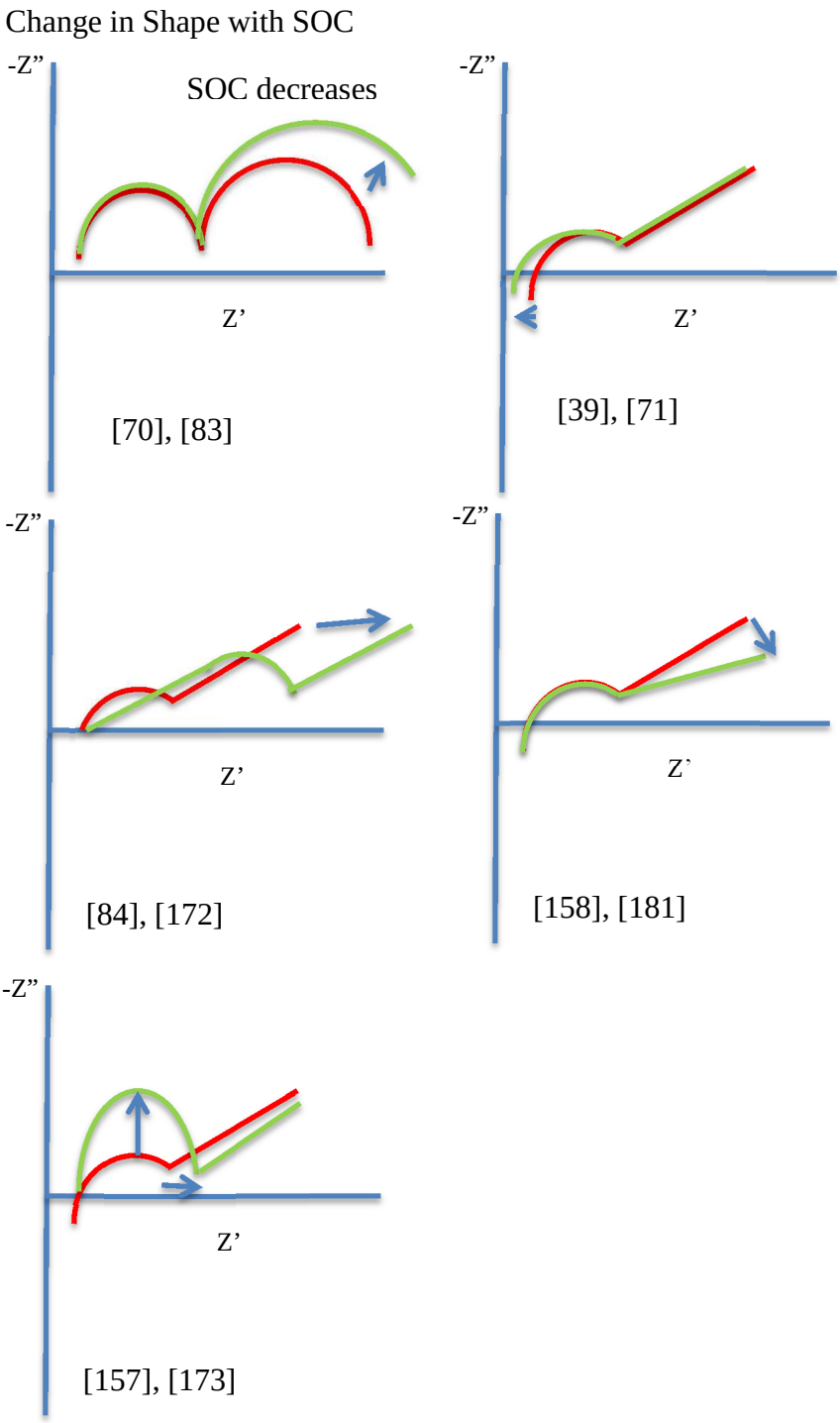

Figure 2-14 : Change in shape with SOC variation

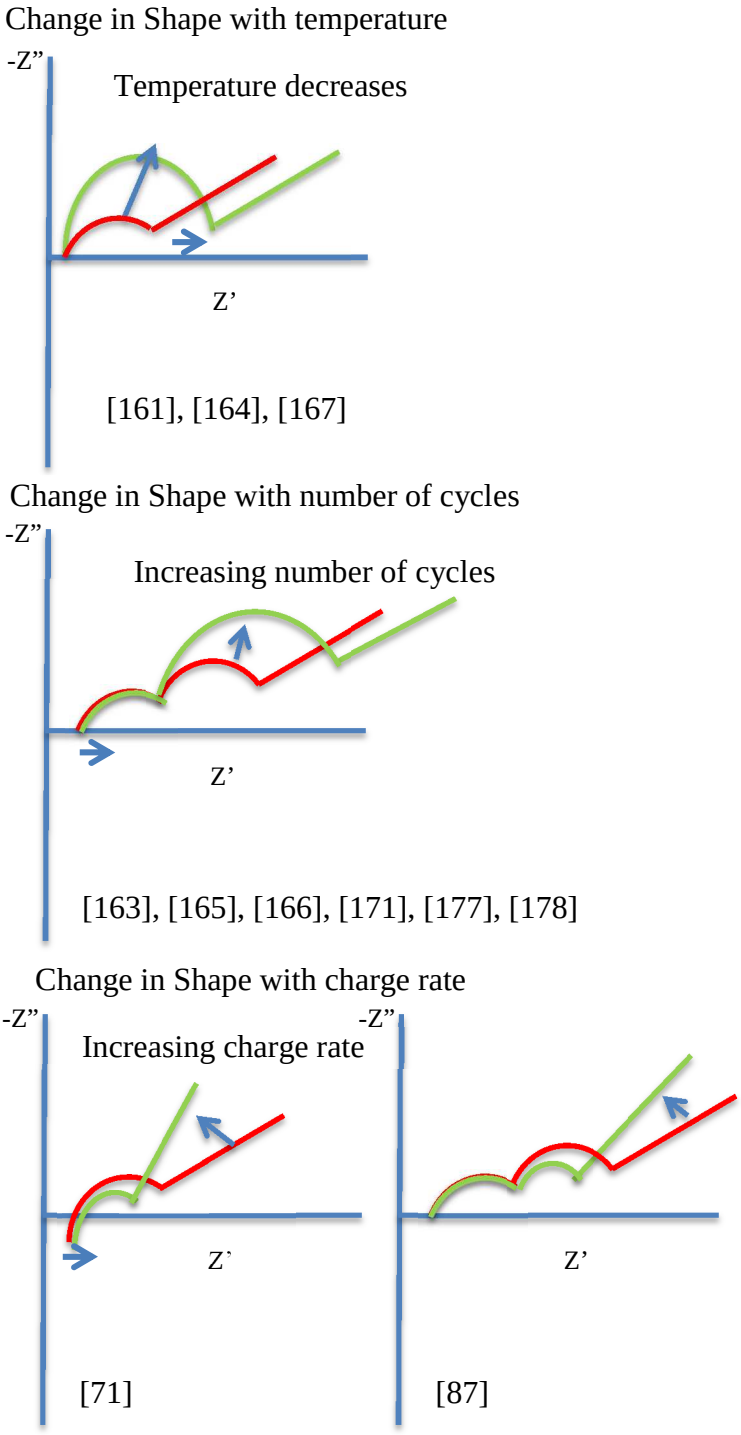

Figure 2-15: Reported change in shape with temperature, cycle and charge

2.4.2 Lead-acid Battery

Lead acid batteries are an older type of rechargeable battery. Authors [210]–[220] have performed EIS test methods to investigate the appropriate model parameter of the battery according to their chemical process under various conditions of different SOC, open circuit voltages, and charge/discharge current. Table 2-8 shows a summary of the applied EIS testing conditions reportedly undertaken by these authors.

Table 2-8: Lead-Acid Battery EIS Test Condition

Reference	Frequency	Excitation	Test Condition
[210]	10mHz - 10 kHz	10mV	SOC
[211]	1mHz - 100 kHz	10mV	Different SOC (100–10%) and potential.
[212]	10 Hz - 10MHz	5mV	Different Alloys
[213]	0.1 Hz - 10kHz	0.1 A	Discharge
[214]	0.1 Hz - 10kHz	10mV	SOC
[215]	0.1 Hz - 1kHz	10mV	SOH
[217]	0.65 Hz - 65 kHz	5mV	Different charge and discharge Cycle
[218]	0.1 Hz - 50 kHz	5mV	SOC
[219]	0.1 Hz - 100kHz	10mV	Different Potential
[220]	10mHz - 10kHz	60mA	Fully charge 5mA (bias), fully discharge

A summary of the change in Nyquist plot with SOC, OCV, and bias voltage (Figure 2-16), temperature, cycling and discharge duration are sketched below (Figure 2-17). Some authors report changes to curve shape and subsequent change in equivalent circuit leading on from this [210], [211], [214], [217], [220].

A summary is that the impedance increases with the number of cycles, duration of discharge rate, a reduction in OCV, a reduction in SOC and increasing discharge duration. Increasing the voltage of the battery leads to forcing more ions and charge to transfer. This causes an increases in internal temperature and an increase in the chemical processes (which may damage the battery cell [209]), therefore battery impedance decreases. This is in contrast with the charge rate effect on the impedance of the battery which is mentioned in section 2.4.1. as the discharge rate increase the impedance increases.

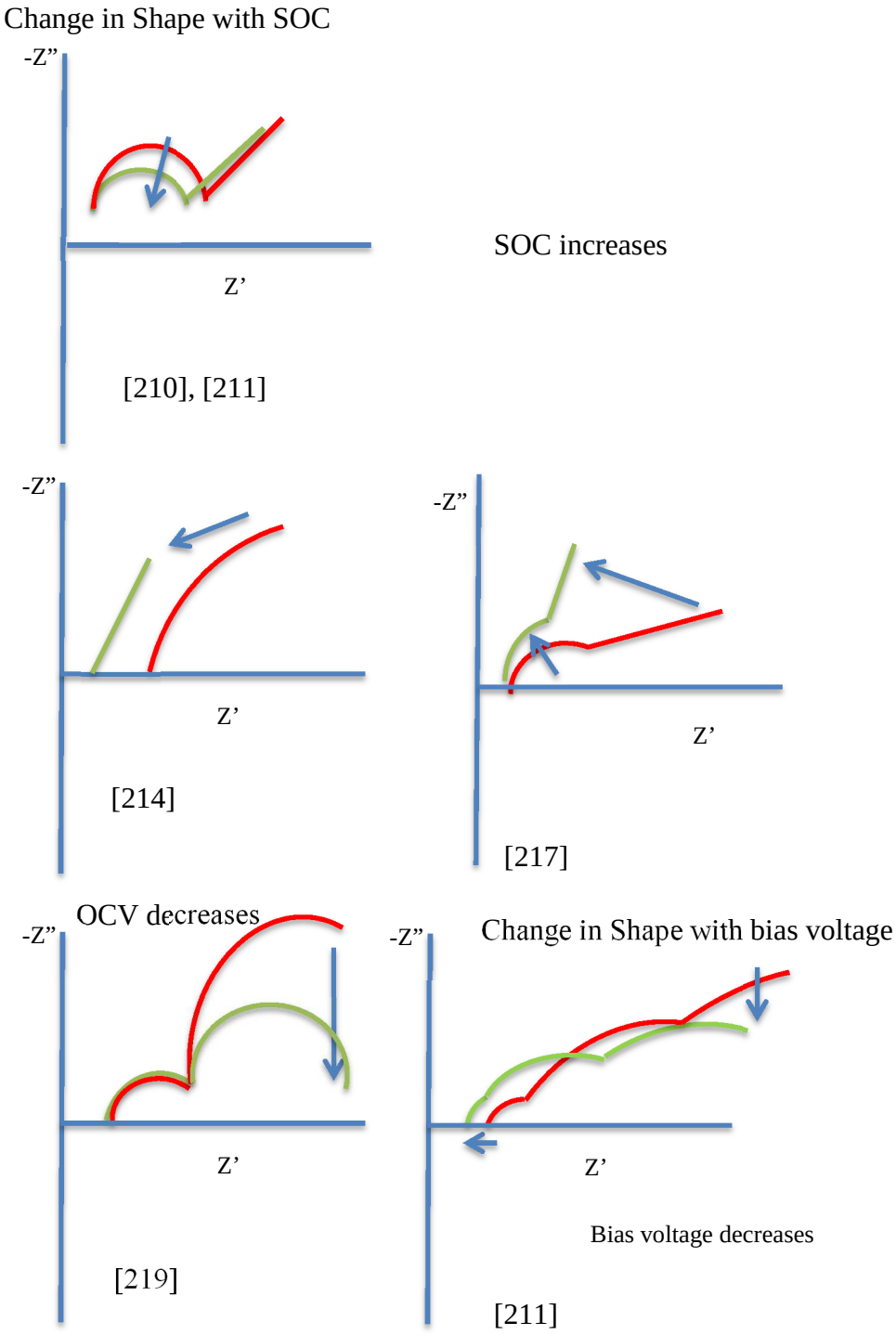

Figure 2-16: Change in shape with SOC variation, OCV, and bias voltage

Change in Shape with number of discharge cycles

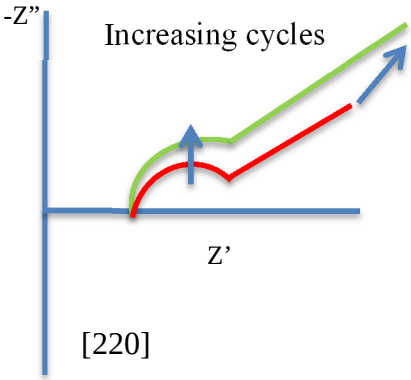

Change in Shape with number of charge cycles

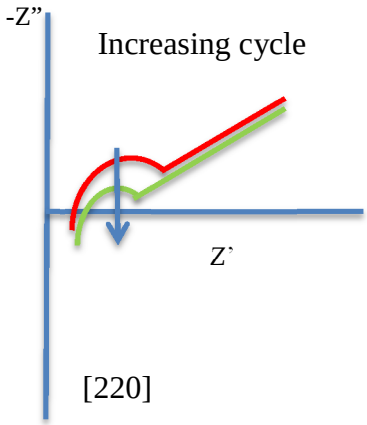

Change in Shape with discharge duration

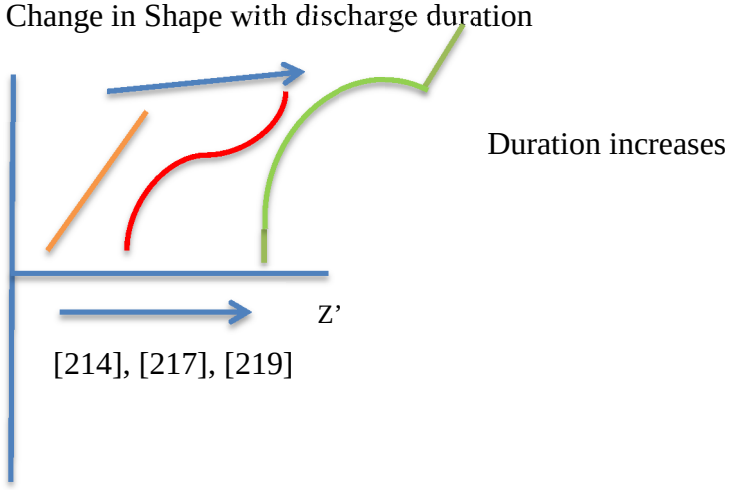

Figure 2-17: Change in shape with cycle and discharge duration

2.4.3 Nickel Metal Batteries:

Nickel metal/hybrid batteries are rechargeable batteries with nickel oxide-hydroxide as the cathode electrode and metal/iron/cadmium as the negative electrode. However, they are increasingly being replaced with other rechargeable battery types because of their low energy rate, poor charge life cycle, and high cost. They are mentioned here for completeness. Authors [152], [221]–[232] performed EIS tests on nickel batteries under condition of different SOC, temperature, discharge, open circuit voltage, and life cycle. Table 2-9 displays a summary of the applied EIS testing conditions undertaken by these authors.

Table 2-9: Nickel Meta/Cadmium Battery EIS Test Condition

Reference	Frequency Range	Excitation Amplitude	Test Conditions
[152]	60mHz - 600 Hz	100 mA	Various SOC
[221]	0.01 Hz - 100 KHz	10 mV	Additional Alloy
[222]	1mHz - 50 kHz	±5 mV	Different temperatures (13, 23, 33 °C)
[223]	10mHz - 100kHz	25 mV	25 °C and 70 °C
[224]	1mHz - 10kHz	10mV	Cycling
[225]	1mHz - 1 kHz 0.5 Hz - 1 kHz	10mV	Depth of discharge (DOD)
[226]	1 Hz - 100 kHz	10mV	Different SOC
[227]	5mHz - 10M Hz	5mV	OCV
[228]	10mHz - 10 kHz	10mV	Different Temperature
[230]	10mHz - 5 kHz	40mA	Different SOC, Life Cycle
[231]	0.01 Hz - 3 kHz	3mV	Different SOC
[232]	50 µHz - 10 KHz	5mV	Different SOC

References [152], [222], [223], [224], [225], [228], [231] investigate the variation of the impedance curve of the nickel batteries under the conditions of temperature variation, different SOC level, depth of charge and charge/discharge cycle. A summary of the change in Nyquist plot with SOC, OCV, and bias voltage (Figure 2-18), temperature, cycling and discharge duration are sketched below (Figure 2-19).

A summary is that the impedance increases with the number of cycles, a reduction in temperature, a reduction in SOC, a decreasing charge and depth of charge rise.

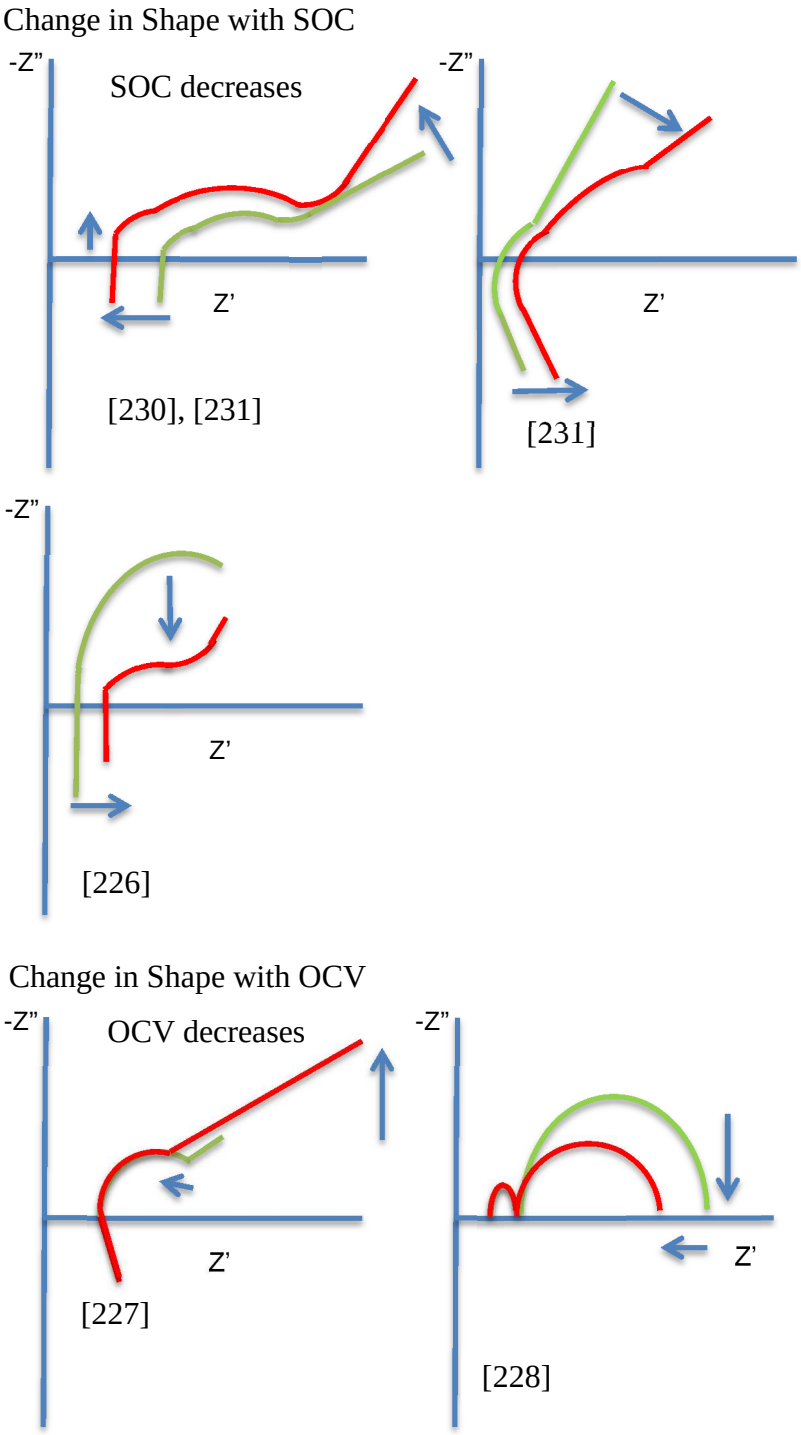

Figure 2-18: Change in shape with SOC and OCV variation

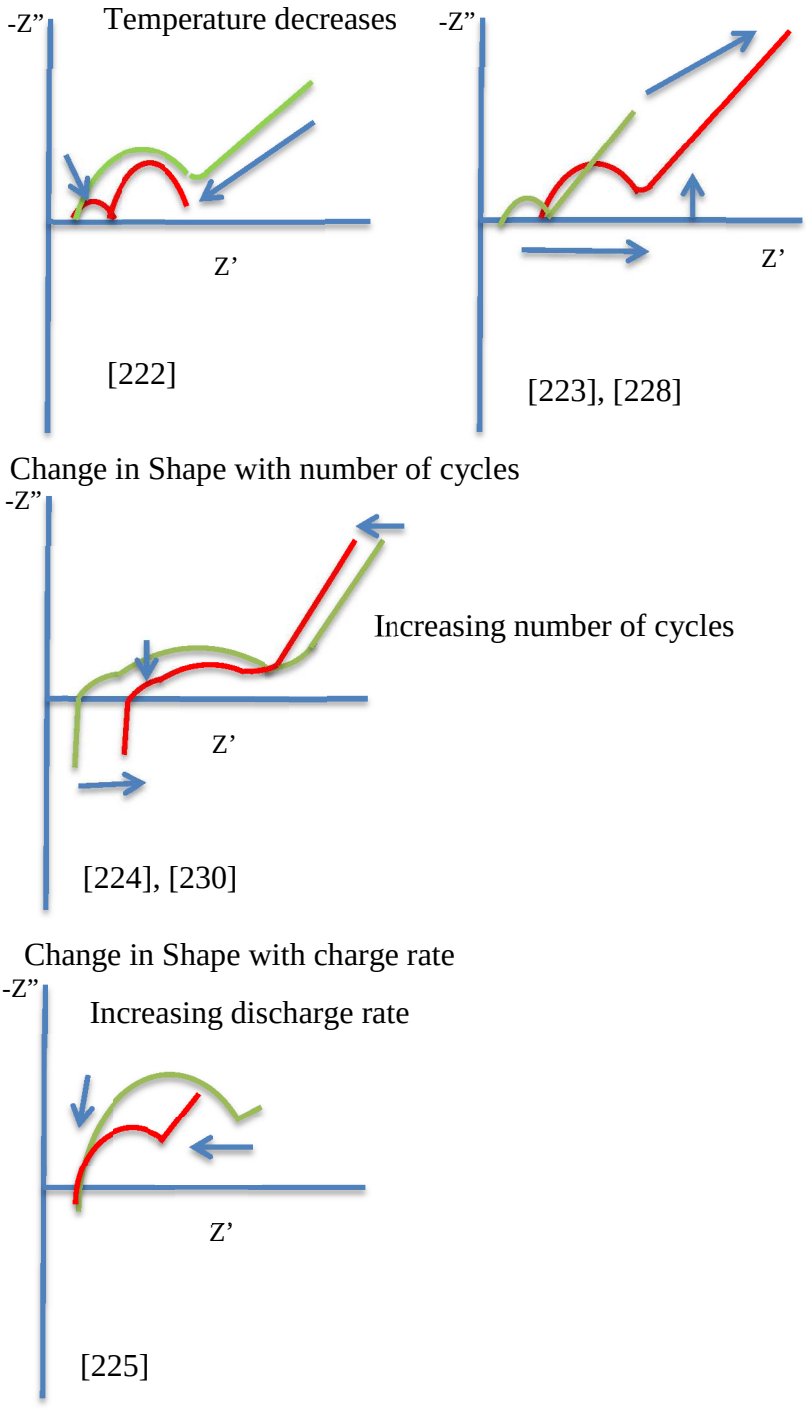

Figure 2-19 : Change in shape with temperature, cycle and charge variation

2.4.4 Super-capacitors (SC):

The summary of examples of applied EIS testing conditions on supercapacitors as reported in literature is shown in Table 2-10.

Table 2-10:Super-capacitor EIS testing condition used by various Authors

Reference	Rated Capacitance	Frequency Range	Excitation Amplitude	Test Condition
[233]	52 F	25mHz - 60kHz	10mV	Different SOC
[234]	1400 F	10µHz - 6 kHz	10mV	Temperature and different Voltage
[235]	1400 F	160mHz - 70Hz		Different SOC, Temperature
[236]	2600 F	10mHz - 1 kHz	10mV	Different Voltage and different alloy
[237]	2600 F	10mHz - 1kHz	10mV	Different SOC

A summary of the change in Nyquist plot with SOC and temperature (are sketched in Figure 2-20).

A summary is that the impedance increases with a reduction in temperature, and a reduction in SOC. This result is good because as the SOC reduces the impedance will look higher and the supercapacitor may assume a lower share of the power depending configuration. However the accuracy with which the power sharing occurs will be reduced because of the uncertainty as to what is causing the changes.

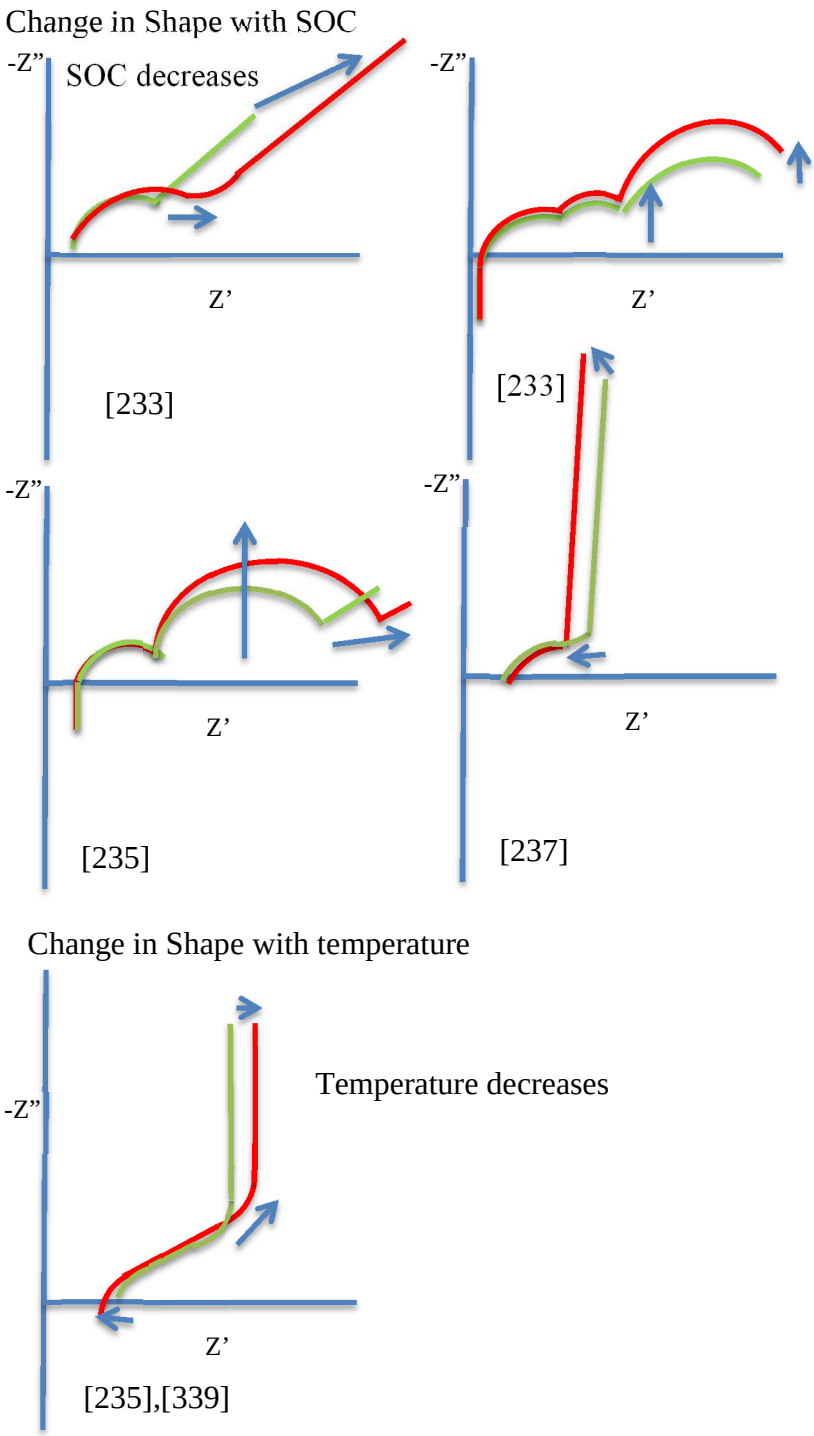

Figure 2-20 :Change in shape with SOC and temperature variation

2.4.5 Solar panel:

In addition to energy storage devices, solar cell analysis has also been subject to EIS testing. R. Anil Kumar et al [238], Fabregat et al [239], [240], Hyunwoong Seo et al [241], and Mehdi Lohrasbi [242], and other authors [243]–[254] used EIS test technique to characterize the dye-sensitized solar cell. The EIS testing conditions of these authors are shown in Table 2-11. All authors performed the EIS test by applying the same ac amplitude also been undertaken in different frequency ranges.

Table 2-11:Solar Cells EIS testing condition used by various Authors

Reference	Ac amplitude	Frequency range	DC bias
[238]	10mV	1 Hz - 60 kHz	0.1- 5 V
[239]	10mV	1 Hz - 5mHz	0
[240]	10mV	10mHz - 10 kHz	0
[241]	10mV	10mHz - 1 MHz	0
[242]	10mV	0.1 Hz - 100 kHz.	0
[244]	10mV	20 Hz - 10 kHz	0
[245]	20mV	0.01 Hz - 400 kHz	0
[246]	10mV	1MHz - 5MHz	0
[248]	10mV	100mHz - 100kHz	0 - 0.8 V
[243]	10mV	5 Hz - 105 Hz	0-1V
[249]	10mV	0.1 Hz - 1 MHz	0.4 - 0.75V
[250]	10mV	0.05 Hz - 100 KHz	0.925 - 1.225 V
[251]	10mV	100 Hz - 10 kHz	0.1 - 0.9V
[252]	10mV	0.1 Hz -100 kHz.	0
[253]	10mV	10mHz - 100 kHz	0

A summary of the change in Nyquist plot with voltage and temperature (Figure 2-21), and degradation are sketched below (Figure 2-22). A summary is that the impedance increases with the number of cycles and a reduction in voltage.

Change in Shape with voltage

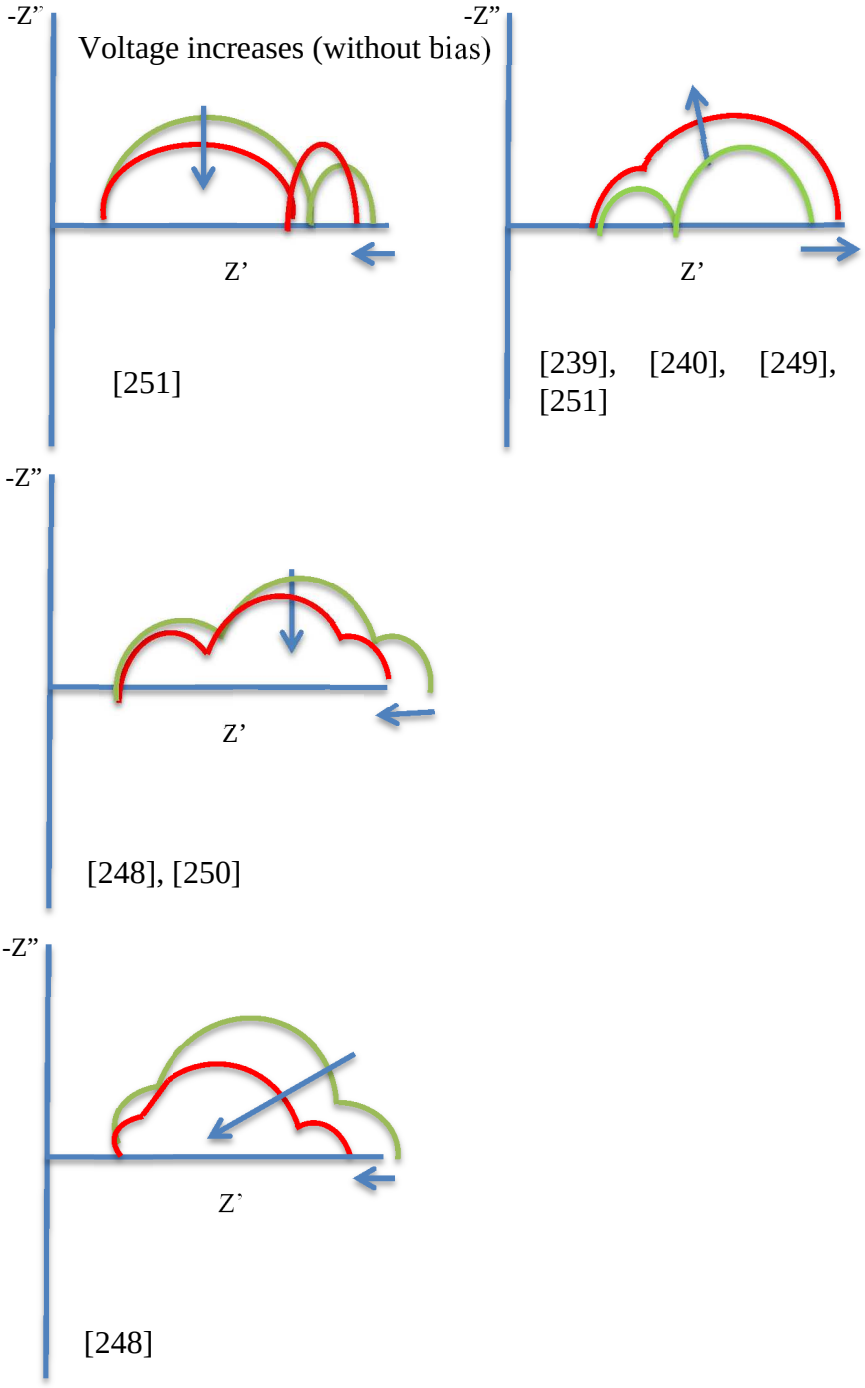

Figure 2-21 : Change in shape with voltage and temperature variation

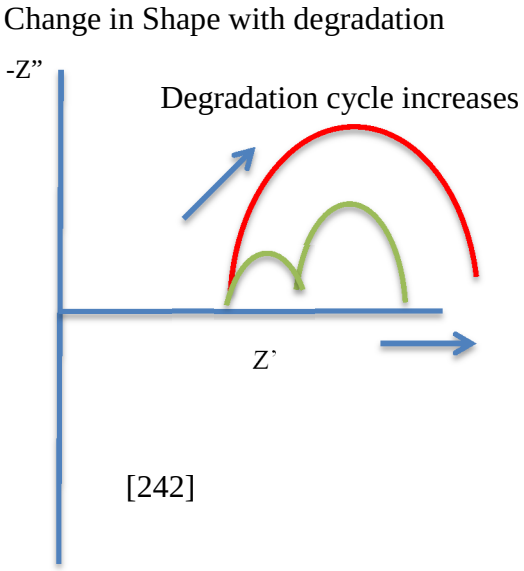

Figure 2-22: Change in shape with degradation and illumination

2.4.6 Summary of published EIS

There is significant body of research looking at EIS measurements of electrochemical devices. The value of having such data available is therefore important to the research community. This thesis is therefore interested in developing this technique into an on-line version of impedance determination. A summary of the findings in literature is listed below:

1. The range of measured impedance values published in batteries literature range vary from 0.3mΩ to 40MΩ, -450mΩ to 1.2kΩ, -10mΩ to 120Ω, -50mΩ to 170Ω for lithium-ion batteries, Lead acid batteries, Nickel Metal Batteries, and Super capacitors respectively. There is suspicion that some of the units are reported incorrectly on the graphs in some of the references.
2. The range of values published in Solar cells literature range from 0mΩ to 25kΩ. These values are higher than those quoted for the batteries and consequently the fault current available from solar cells will be much lower.
3. The experimental work within this thesis deliberately uses excitation conditions to be within the ranges published.
4. The EIS measurements show a variety of shapes. These shapes can be represented by a number of different equivalent circuits all of which will provide a “curve fit” type solution that is representative of the shapes.
5. Curve 2 and 5 are the most common shapes found in Solar cells literature and Curve 3 is the most common found in battery and super capacitors literature but authors have used a variety of models

to represent this shape. The EIS shape associated with batteries are subject to change in temperature and model.

6. The EIS shape associated with a particular solar panel can change as it undergoes a change in temperature, charge or degradation. The upshot of this is that the model around that solar panel is then also subject to change.

2.5 On-line EIS techniques

Some attempts to replicate an EIS method on-line have been undertaken [53], [56], [142], [215], [255]–[258]. Much of this work is recent in nature (within the last two years) and has been developed independently and in parallel with the work undertaken within this thesis. Some of these techniques are not specifically related to batteries but may be adapted. The offline techniques have mostly been used to generate the results described in section 2.4. This section looks at the body of work looking to replicate the EIS functionality on-line and shows where the work in this thesis fits and also where future work will in all probability take place. As the on-line techniques are varied in nature, some means of categorizing them has been attempted as shown in Figure 2-23.

The techniques are split first in offline and on-line. The on-line techniques are then split into those that require a separate excitation circuit and those that use existing hardware as a source of the excitation.

The boxes with red text highlight the areas where work has been undertaken within the thesis and has not been previously reported. The boxes with green text indicates where previously published work exists and has been built upon.

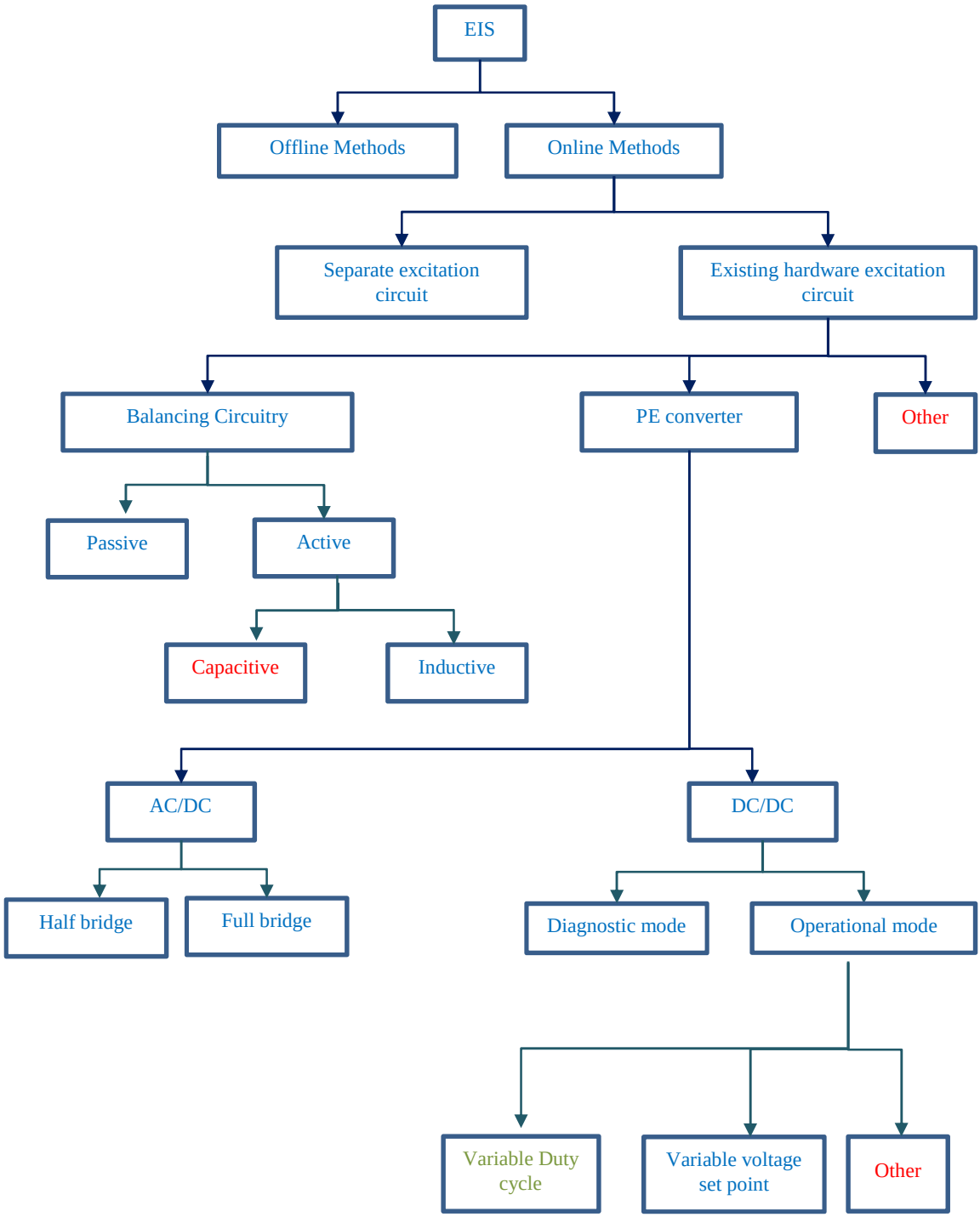

Figure 2-23 :Different battery EIS methods

2.5.1 Separate Excitation

Figure 2-24 shows the main features of an online EIS system with separate excitation hardware circuitry designed to run in parallel with the existing hardware. There are known examples of commercially available systems designed to be connected to the battery under operation but these can be expensive.

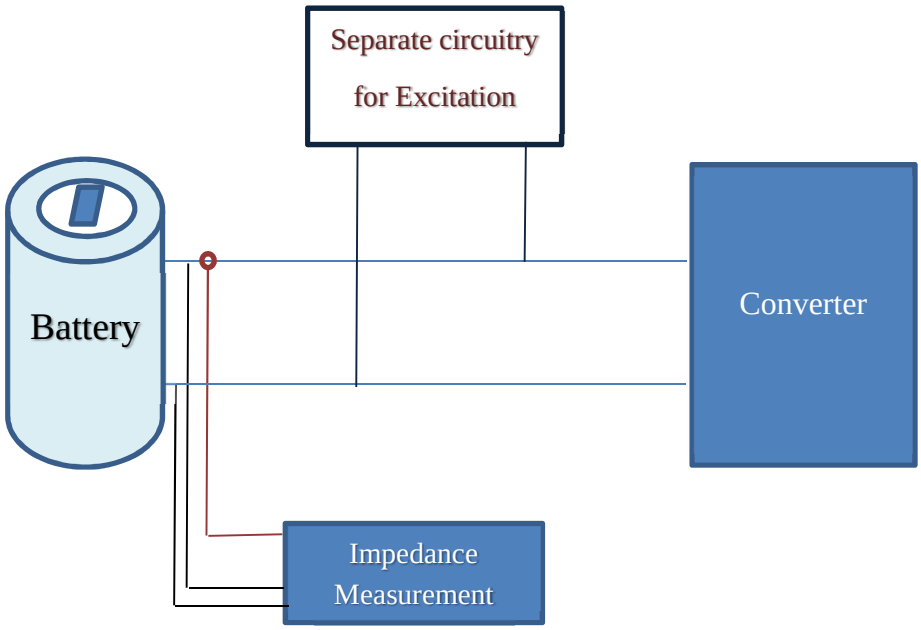

Figure 2-24: Separate excitation circuit topology for online impedance monitoring

A number of researchers have tried to overcome this high cost by designing lower cost bespoke systems. [259] used a separate excitation circuit specifically for EIS excitation. This work was undertaken on a three phase induction machine rather than a battery. This method was used to calculate the turns insulation parameters of the motor from the experimentally measured impedance data. In this literature, the excitation signal was reported as being generated between phase and ground using a coupling circuit. The impedance of the motor was then calculated from measured data from the measurement equipment. This injecting signal method was chosen because of the possibility of injecting a signal over a wide frequency range. The authors claimed that the choice of the injected amplitude (i.e. small enough to not disturb the operation of the motor, large enough to make the measurement possible), small signal to noise ratio as a result of the low supply impedance are the main challenges of this method.

[260] used a signal processing circuit to inject an EIS excitation signal directly to a battery. The signal processing circuit converted a voltage signal generated from the Labview software into a current signal and measured the voltage response to calculate the impedance of the battery. The current excitation

signal is injected each time with a different frequency. Sampling equipment was used to collect and analysed the battery voltage response and current excitation signals to calculate the impedance of the battery through Labview. The key challenge of this published method reported by the authors is that the impedance values depend on the accuracy of the sampling equipment and the designed circuit cannot be undertaken under high frequency ranges.

[261] used a power amplifier and separate excitation circuit. The current excitation signal was generated using the power amplifier as the battery perturbation unit. Similar to [260] the impedance of the battery was calculated by sampling the voltage and current data through the signal processing but differs in processing application unit.

There has been mention of sinusoidal charging of batteries using sinusoidal ripple current (SRC) as opposed to CV and CC (constant voltage and constant current) as a means improving charging performance [262]. This is done by adding a separate AC excitation signal to the battery system. Recent work [263] has looked at the possibility of using this to undertake EIS measurements. The methodology lacks detail in the published literature. Although, an EIS diagram is produced, it is not clear whether the method behind its production is online. This is because the EIS plot is shown for three OCV conditions. However, there is no perceptible barrier as to why this shouldn't be made online.

[264] also appeared to use a separate excitation circuit. In this work, an amplifier is used to generate and inject the current excitation signal and the impedance is calculated using a digital signal processing method. The digitised voltage and current response of the battery are used to calculate the impedance. Impedance data from a laboratory EIS unit is used as pre-trained data for the impedance calculation from the measured voltage and current signals. The impedance values vary depending on the correction results. The author claims that the implementation of the published measurement algorithm is a key challenge and needs to be improved.

Reference [265] and [266] employed a pseudo-random binary sequence (PRBS) current pulse perturbation to measure the impedance of the battery online. This method used a band limited pseudo-random noise signal to excite the battery current and then measure the voltage response of the battery. This noise signal can be superimposed either as an addition to the control signal or in isolation to excite the battery. The main disadvantage of this method is the small signal to noise ratio as a result of the smaller amplitude of the measured battery voltage frequency response compared to the amplitude of the noise signal. This can be improved by using a very large input which results in nonlinear behavior of the system. Therefore this method is not commonly used with literatures for impedance estimation.

Although a separate excitation circuit appears to work there are extra costs involved with the implementation. Therefore this thesis chose to focus on using existing hardware within the circuit to generate an EIS excitation signal.

2.5.2 Existing Hardware – Battery balancing

Battery balancing can be undertaken in a variety of ways. These are typically classified as passive (using resistors) to equalise charge and active (using switches in conjunction with energy storage components)

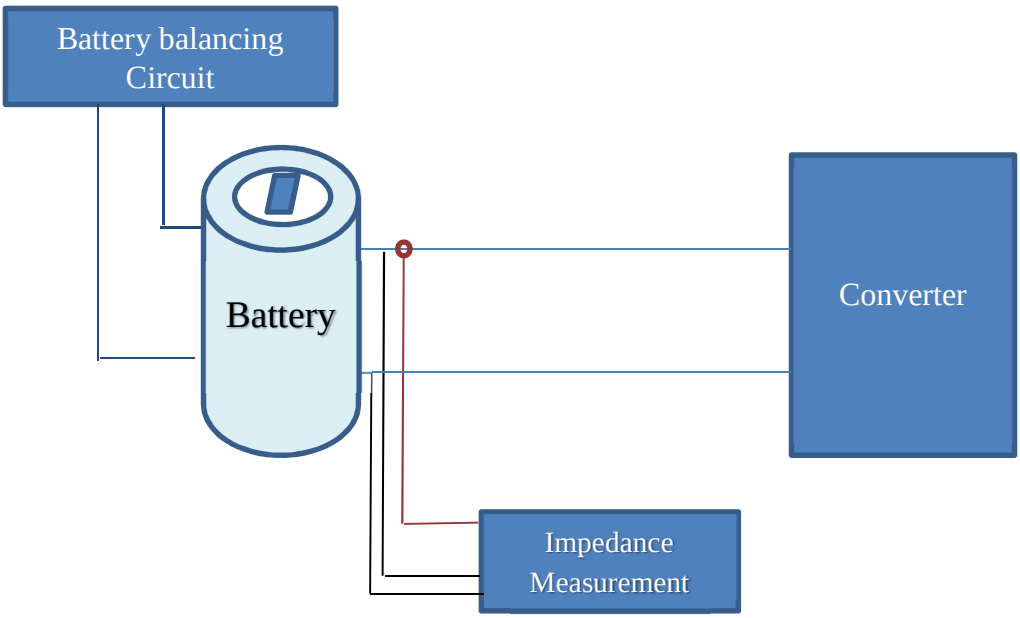

Figure 2-25: converter with battery balancing topology for online impedance monitoring

Koch et al [138] introduces three methods of on-line impedance measurement. One of these uses using battery balancing as a means of producing an excitation signal, to estimate the battery impedance over the specific frequency range. In battery balancing, a balancing resistor with a switch was used to excite the battery. This method is sensitive to the balancing current, which results in SOC changes after each measurement. This is because the balancing circuit can only discharge the battery.

References [142] and [267] are work by the same authors who used an inductive based battery balancing system for online EIS measurement. Two battery cells were connected to a ladder inductor battery balancing circuit using a switched-inductor bidirectional buck-boost converter as a building block of a ladder converter. The perturbation signal was generated by a digital signal synchronised in an FPGA and injected by the controller to the switches in the ladder circuit as shown in Figure 2-26. When switch M1 is on, battery 1 is connected in parallel with the converter and the converter operates for time DT_s . The converter is connected in parallel with battery 2 to shuffle the energy when switch

M2 is on for a time $(1-D)T_s$, where D is duty cycle that the balancing switches are operates with. The impedance of the battery was calculated from the measured voltage and current signals passed through the digital processing chain. The authors report a good performance.

Other forms of battery balancing have not yet been considered for on-line EIS measurement. However this thesis considers the use of a capacitive based balancing method for looking at on-line EIS measurements.

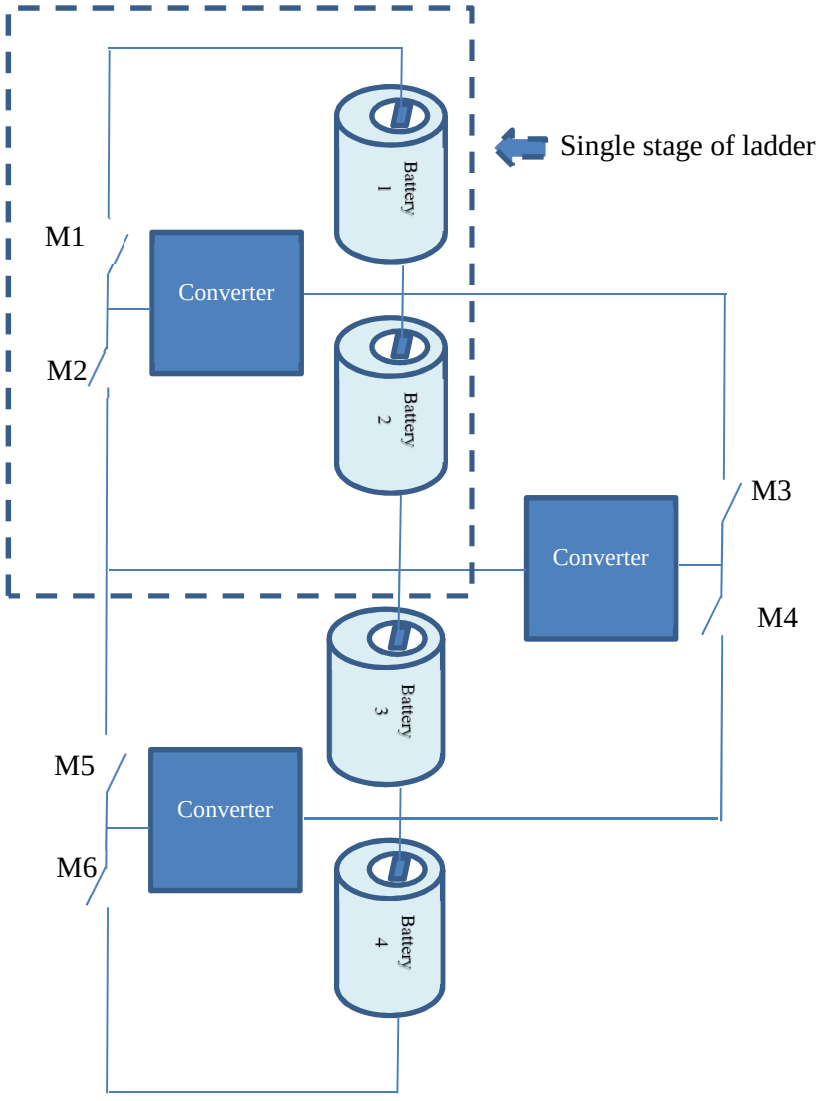

Figure 2-26: Ladder circuit balancing operation

2.5.3 Existing Hardware – AC/DC Power Electronics

[53] and [138] are published works by the same authors, who use a half bridge AC/DC converter to inject the EIS signals to a battery. This process is uni-directional and is undertaken on battery charging

only. The battery charger is connected to a number of battery cells and excites the battery cells by injecting a carrier frequency excitation signal to the converter switches. The authors reported that the synchronisation of the battery current during the measure is a disadvantage of the method (ie the battery cannot simultaneously charge and discharge) as the current needs to be measured.

Koch et al [138] also described a half bridge converter circuit (similar to [53]).

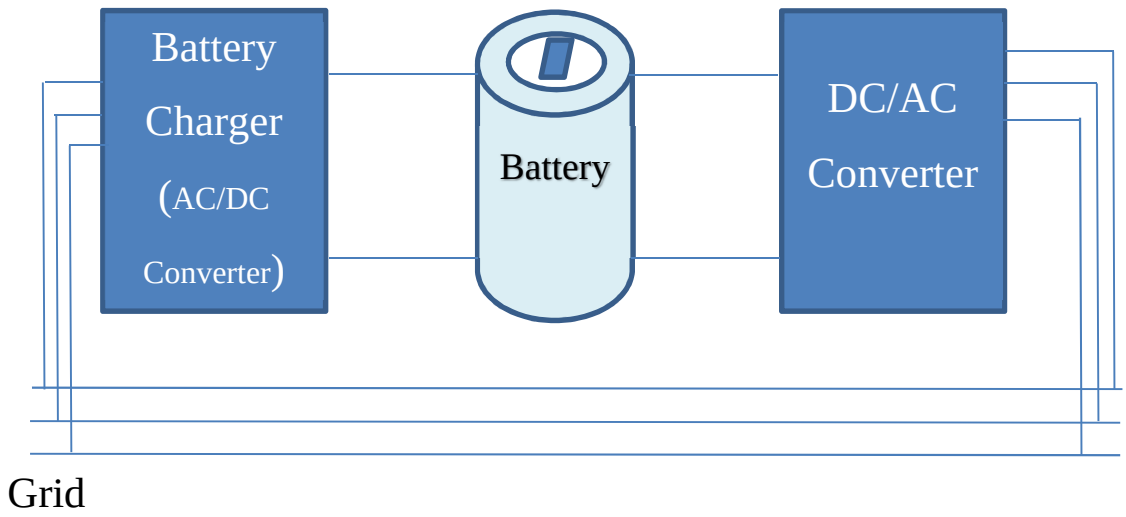

Figure 2-27: Charger (AC-DC converter) topology for online impedance monitoring

Reference [255] measured the impedance of the battery by using a motor inverter to generate the low-frequency excitation required to look at battery impedance as shown in Figure 2-28. The authors used the motor inverter to generate and excite the battery with the generated current perturbation signal. They have used a shunt resistor to measure the battery current from the voltage response of the battery and calculated the impedance from the captured data. The key disadvantage of the methods is that the excitation current is at the fundamental frequency of the converter. So for example, the frequency cannot be swept across a range of values under operation of a motor and this will affect the driving or it requires a separate excitation circuit. The tradeoff between the average and maximum amplitude of the current signal which results in the signal to noise ratio is another reported challenge of this published method.

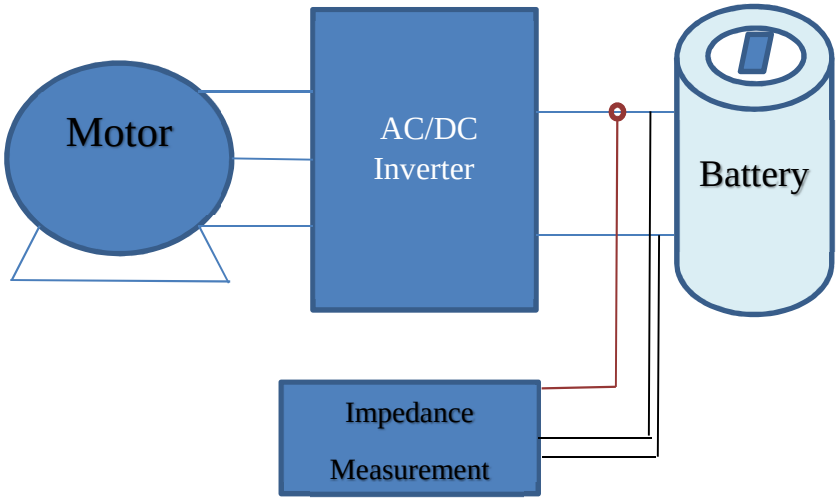

Figure 2-28: motor inverter topology for online impedance monitoring

2.5.4 Existing Hardware – DC/DC Power Electronics

The technique uses energy storage connected to a power electronics system (DC-DC converter), which form an interface between an electricity source such as a battery and the grid system to understand if the power electronics can be used to implement an EIS equivalent analysis. This research focuses on the methods and impact of measuring battery impedance through the power electronics. The method of introducing a small excitation signal through the DC/DC power electronics is primarily a function of different forms of control. These methods can be split into diagnostic mode and normal operational mode.

Diagnostic mode

[268] used dc/dc converter hardware to control a fuel cell under normal operating conditions and also to provide an AC excitation signal under a diagnostic setting when the fuel cell was not operational as shown in Figure 2-29 . The method was also applied to different fuel cells and the results appeared to show good agreement with the offline measured impedance values. However, if this method were to be applied to a battery it would need to be taken off-line to undertake the diagnostics.

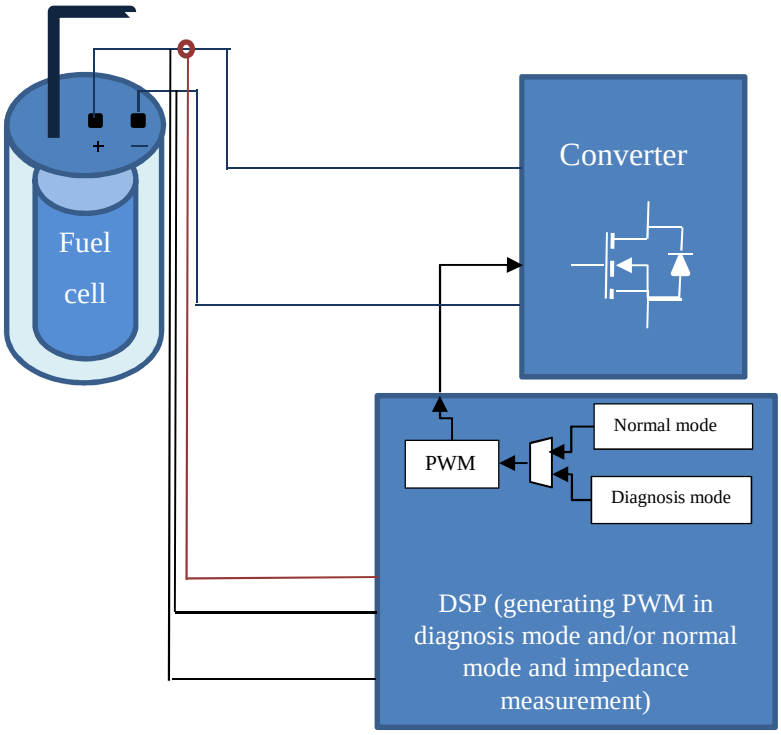

Figure 2-29: Diagnostic mode of online EIS using a DC/DC converter

Operational mode – variable voltage set point

Nguyen et al [215] uses a bidirectional converter circuit with a control system to generate small excitation signal for impedance measurement and SOH estimation with no additional excitation hardware. The excitation signal is a sinusoidal voltage signal added by the voltage controller loop to excite the battery over the frequency range. This method was introduced for the SOH prediction of the battery, the impedance is measured only after the battery is fully charged.

Operational mode – variable duty cycle

Similar to [268], references [256], [258] introduced a method of low-frequency harmonics injection to estimate the impedance and SOC of the batteries in operational mode. This is shown in Figure 2-30. In this method, the battery impedance is calculated from the measured battery voltage response and excited current signal. The current is excited with excitation signal is injected to the converter by varying the duty cycle of the switching PWM signal. This method is explained in more details in chapter 3 (section 2.2).

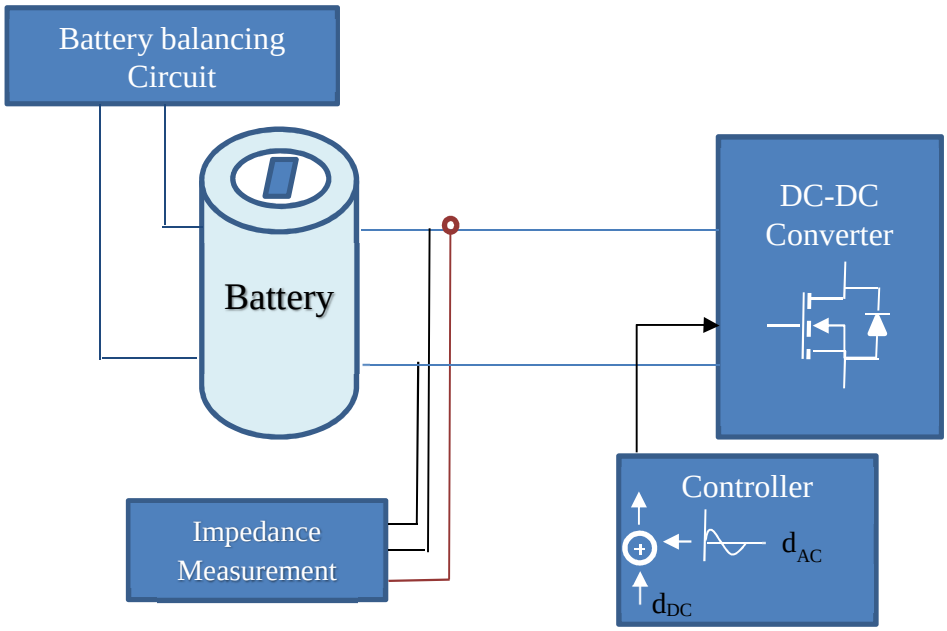

Figure 2-30: Operational mode of online EIS using a DC/DC converter with variable duty cycle

Reference [257] uses the same method, but uses multi-sine signals to measure the impedance of the battery with multiple harmonics at the same time rather than at a single frequency point each time. For example, the authors added three sinusoidal perturbation signals with different frequencies at once to calculate the impedance. [269] used the same hardware but used the control system to add a change to the output voltage set point to create a perturbation of multiple frequencies to capture more data over a shorter period of time. The proposed method suffers from the lack accuracy as the frequency order increases. Generated impedance values showed similar variation as the measured impedance value with the electrochemical equipment.

2.6 EIS equivalent circuit models

2.6.1 Different models at 100% SOC

As indicated in Figure 2-12 there are many published equivalent circuits with respect to the variation of the electrochemical reactions of the power sources under different conditions of temperature, state of charge, and degradation. Some authors suggested single equivalent circuit model for all different conditions they researched. While other reported literature suggested that the equivalent circuit model should change with operating conditions. Within this thesis it is required to use an equivalent circuit to represent the electrochemical devices in simulation

models to understand how the electrical circuits are behaving. The curve shapes from the experimental work conducted later in this thesis match those obtained by authors [161], [165], [166], [171], [172], [242] who use popular models with high citation indexes. Future work could consider alternatives to these. The models in Figure 2-12 were tested for suitability with the Nano-phosphate lithium-ion battery type used in this thesis.

Figure 2-31 shows an example of the change of equivalent circuit model of a battery for different state of charge and different aging cycles. These models are proposed as possible models for use in this work based on the reported literature and a comparison of the EIS measured data for different battery SOC.

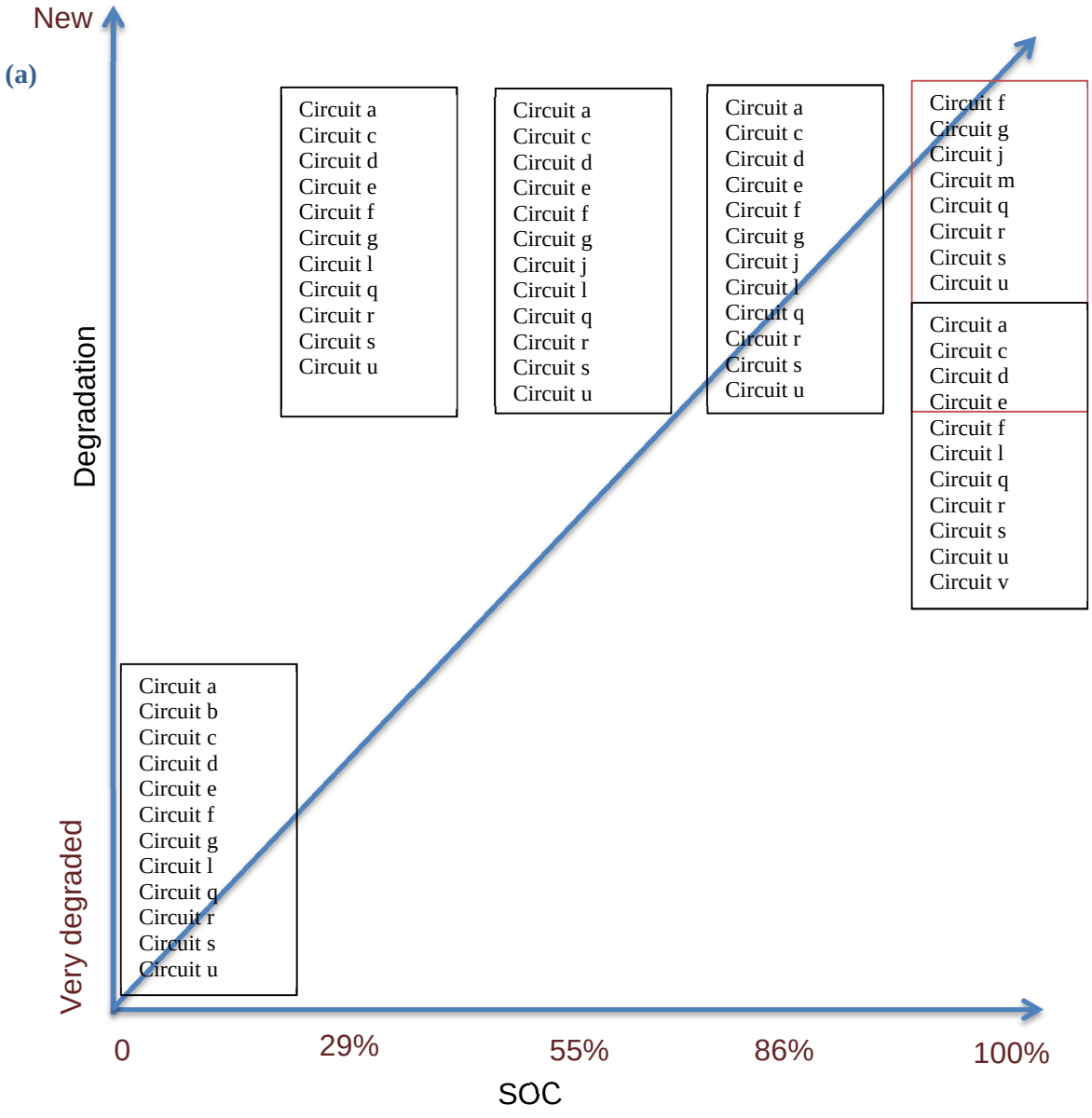

Figure 2-31: Ideal Equivalent circuit models of a lithium-ion battery at different SOC and degradation equivalent circuit.

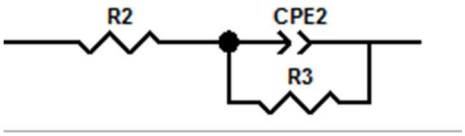

Figure 2-32: Equivalent circuit model solar panel.

The equivalent circuit model of a solar panel is shown in Figure 2-32. In this research data fitting Zview software is used to find the best parameter fit of the equivalent circuit to the measured impedance curve for the frequency range of 1Hz to 2 kHz.

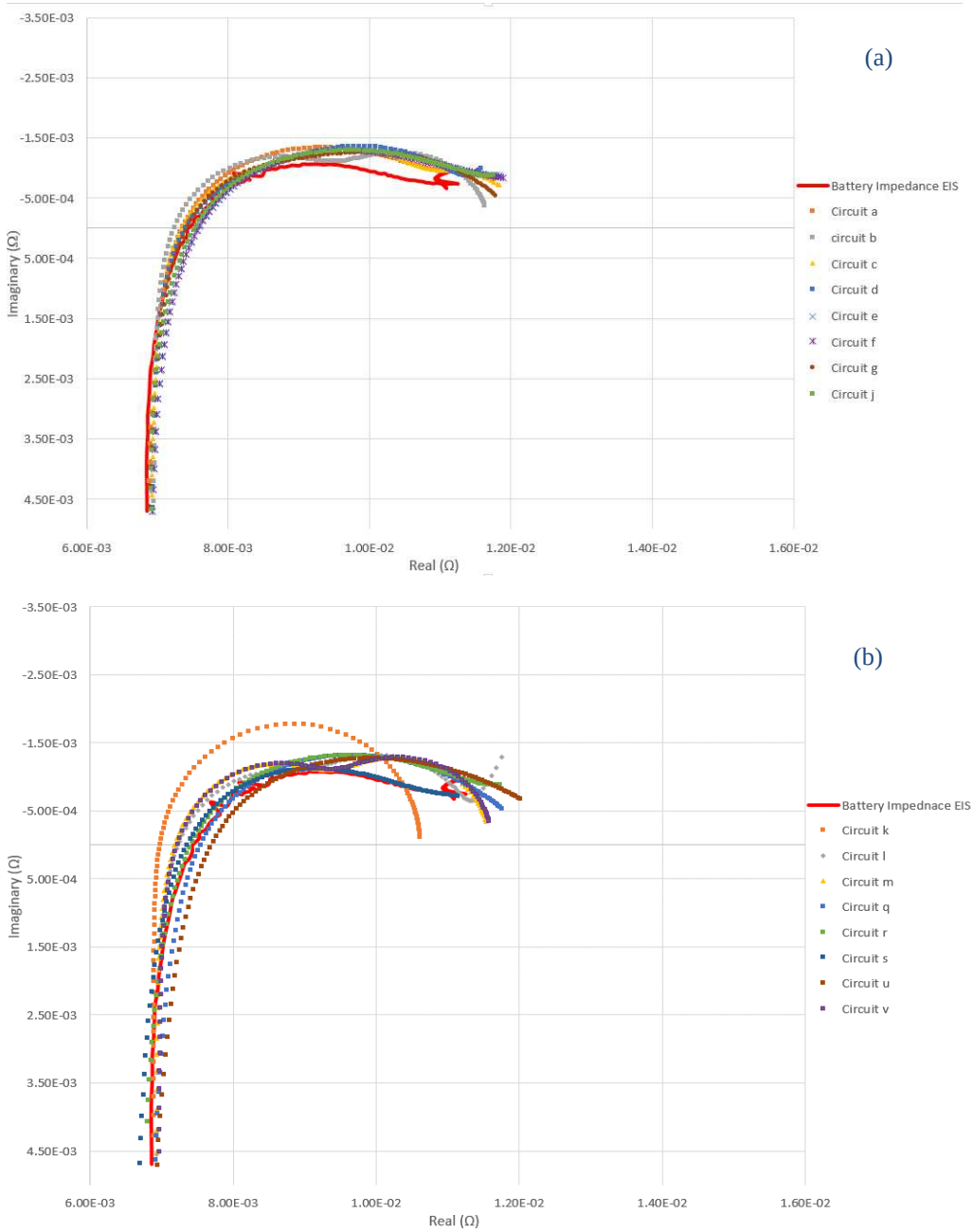

Figure 2-33 : proposed equivalent circuits a) comparison of Nyquist plot of EC (equivalent circuit models a, b, c, d, e, f, e, g, j) b) comparison of Nyquist plot of EC (equivalent circuit models k, l, m, q, r, s, u, v) for 100% of SOC

The graphs show that most of the equivalent circuit models proposed by the literature from Figure 2-12 give a reasonable match to the Nyquist plot of the original measured graphs, which is experimentally derived at 100% SOC. However, in this work, the circuit s is used because it is more practical for use with Matlab and is used by a large number of authors. The equivalent circuit models k, m and v weren't suitable for this battery impedance curve as they didn't match the impedance curve.

2.6.2 Different levels of degradation

In order to avoid a sudden failure of the battery system and to improve the reliability of the battery, it is useful to monitor the impedance as it degrades. The performance of rechargeable batteries deteriorates due to the capacity fade[270]. The capacity fading of the battery described by Vetter et al [173] can be divided in two principles of calendar storage ageing (over the years) and cycle aging. This is presented as the ability of the battery to store and release the charge. The cycle life of the battery cell results in capacity decrease due to the number of complete charging and discharging cycle. Over discharging or/and over charging and elevated temperature, can accelerate the degradation of the battery. This can be assigned to the loss of Li or other active materials and balance between electrodes, electrode conductivity, formation of a passive film layer, material decomposition at battery cells, and active material dissolution [187], [271], [272]. The SOH of the battery has a reported nonlinear relationship with these factors [215]. The impedance of the battery can be used to estimate the SOH of the battery [53], [57], [153], [156]. Therefore the aging process of the battery can be monitored by periodically measuring the impedance of the battery.

Different reported methods to investigate the battery life cycle have been published:

- Stored and held the battery at the same charge level at constant temperature [273], [274], in this test the battery life is influenced by the temperature level and the number of cycles that the battery is charged.
- Fully charged and discharged the battery to evaluate the effect of the temperature variation on battery lifespan to compare with different battery cells. There are different numbers of published battery cycling test reports including those from IEC [165] and IEA [166]. In this test procedure the battery cell is continuously charged and discharge till its capacity falls below 80% of its nominal capacity.
- Accelerating degradation method with consideration of overheating the battery[174], [189], [273], [277], deeper depth of discharge, and higher charge rate depending on type of application[187], [278]. This will accelerate the formation of the surface film on electrodes and increase the internal impedance of the battery.

In this research an A123 Nano-phosphate lithium-ion battery with a capacity of 2.5Ah 3.2V nominal voltage was used. A comparison of the Nyquist spectrum of a lithium-ion phosphate battery for different number of charge and discharge cycles is presented in Figure 2-34. To study the effect of the

degradation on the battery electrochemical reactions the new battery was charged/discharged a different number of charging/discharging cycles. The cycling test of the lithium battery cell was run at high charge and discharge rate to accelerate the aging of the battery. The cycling test was run by Petalite Company, the number of cycles for degraded and very degraded batteries was not given by the company for commercial purposes. The EIS tests at different cycles were carried out in the same conditions of full state of charge, constant room temperature, an EIS frequency range of (1Hz-2kHz) using a constant discharge current of 1.15A (the same as experiment discharge current represented in chapter 6). The Nyquist plot indicates that the series resistor of the battery increased and the impedance shows more capacitive behaviour over the frequency range.

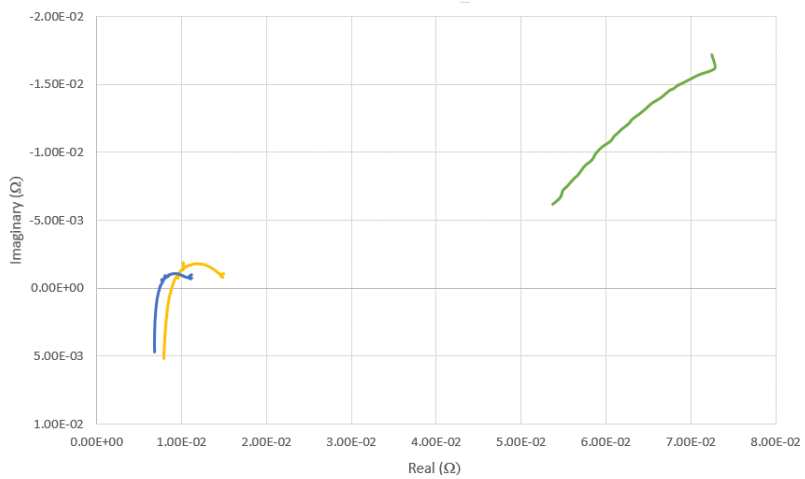

Figure 2-34 : EIS of new battery (blue line), degraded battery (yellow line), and very degraded battery over 1000 cycles (green).

The results of curve fitting the different circuits from Figure 2-12 to the degraded battery is shown below.

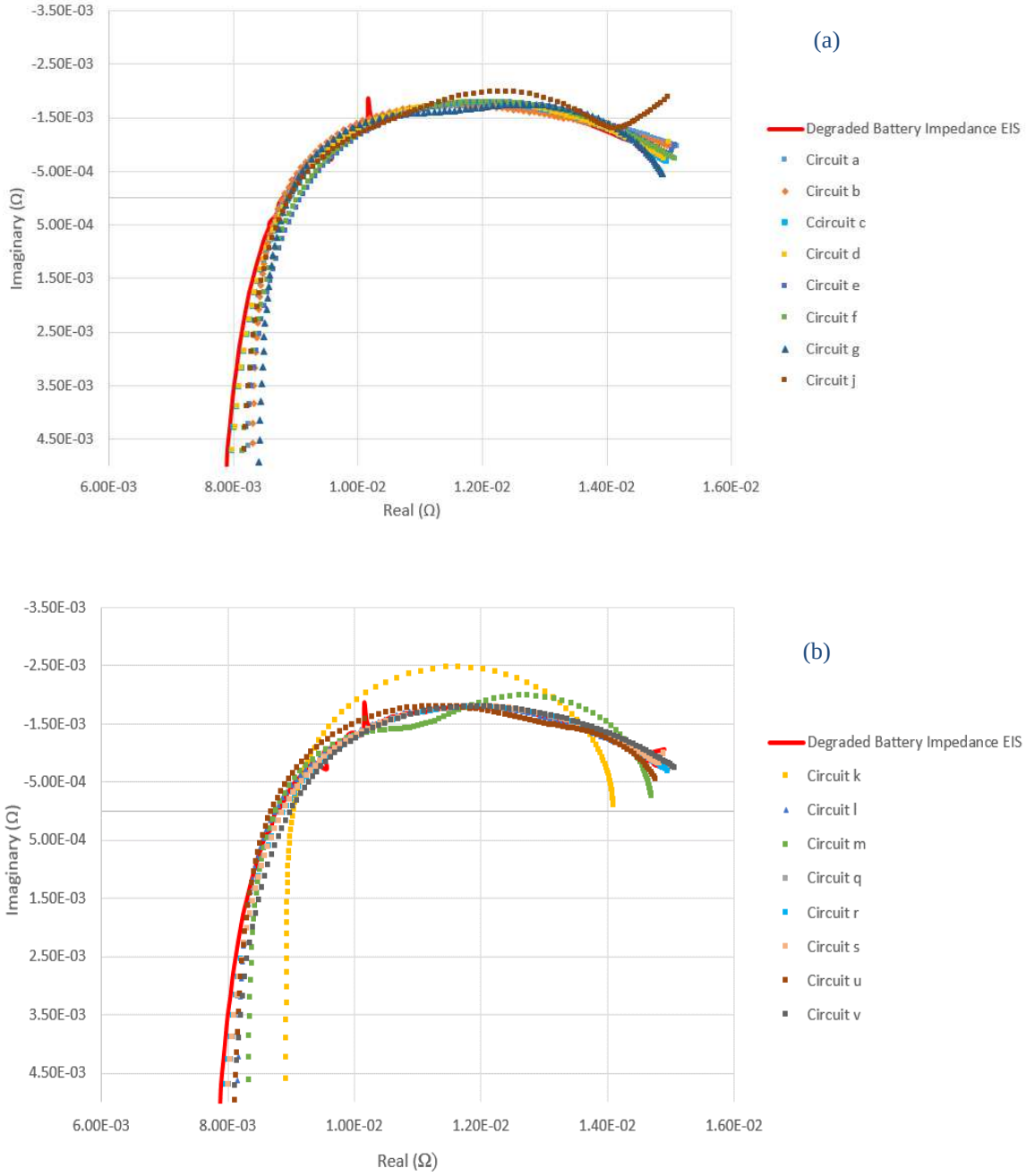

Figure 2-35 : proposed equivalent circuits a) comparison of Nyquist plot of EC (equivalent circuit models a, b, c, d, e, f, e, g, j) b) comparison of Nyquist plot of EC (equivalent circuit models k, l, m, q, r, s, u, v) for degraded battery at 100% SOC

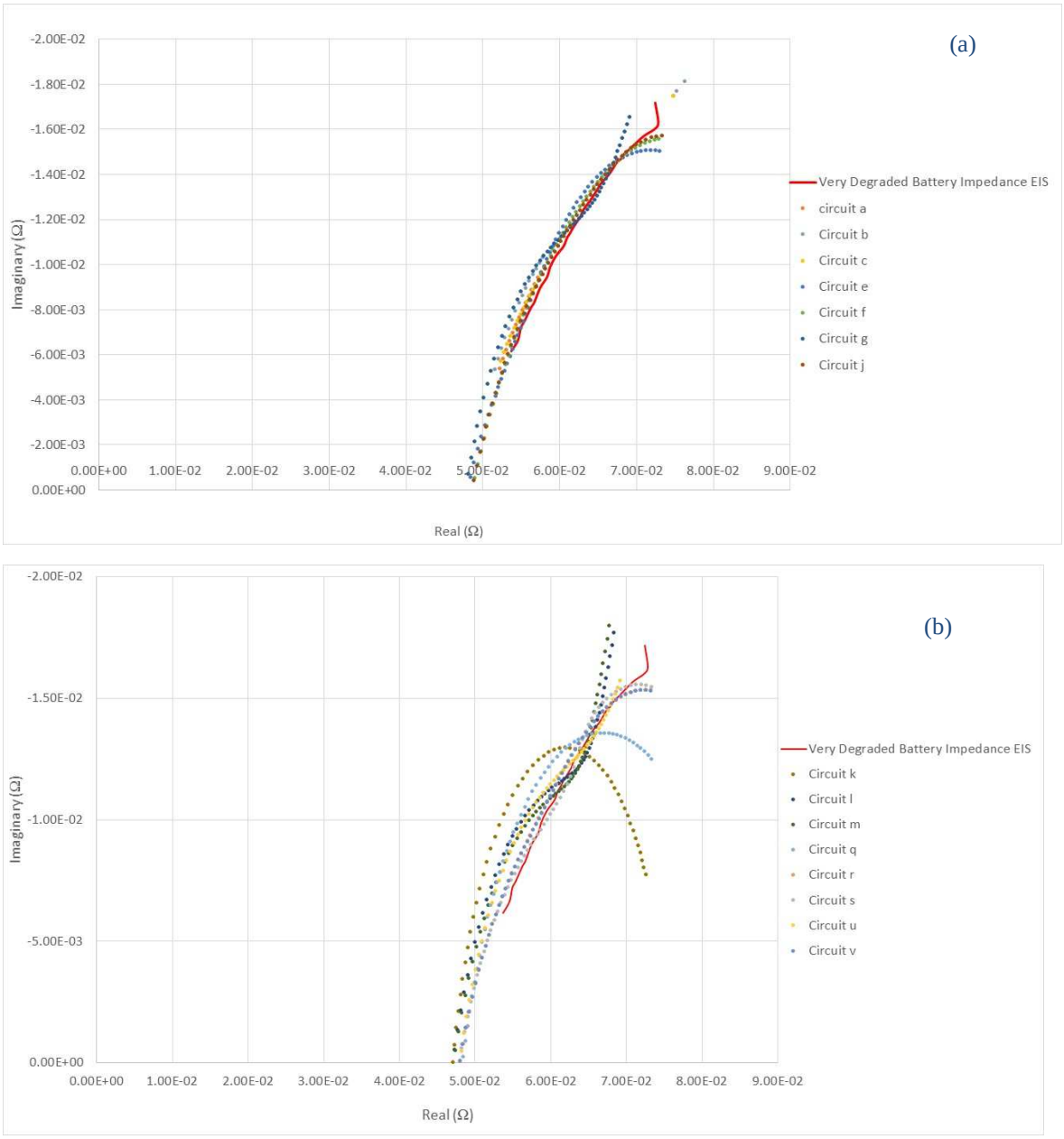

Figure 2-36 : proposed equivalent circuits a) comparison of Nyquist plot of EC (equivalent circuit models a, b, c, d, e, f, e, g, j) b) comparison of Nyquist plot of EC (equivalent circuit models k, l, m, q, r, s, u, v) for a very degraded battery at 100% SOC

Based on experimental results for the Li-ion battery used in this thesis – Model "s" has been chosen as an acceptable means of representing the battery at both different state of charge and different degradation. Different battery chemistries may require additional investigative work.

2.7 Summary

This chapter described the use of energy storage on the electricity grid systems and its inherent limitations and problems. These issues may be better understood and dealt with through advancements in battery management systems. Different parameters for understanding the state of the battery have been described and compared. The quantity of published literature in reputable journals indicates that EIS measurements may be a valuable tool in determining the impedance and the subsequent state of the battery. This measurement is mostly under taken off-line but some attempt has been made in recent years to reproduce an on-line version. High costs of commercial products have resulted in some attempt at using existing hardware to replicate the functionality.

3 Theoretical analysis of on-line EIS techniques

3.1 Introduction:

This chapter investigates the theory behind using existing battery hardware to implement an on-line impedance spectroscopy technique with the ultimate aim of helping to understand the state of the battery in real time, look for signs of degradation and to help control the power flows into and out of the battery pack which includes second life batteries. This could help with reliability and availability issues which may impact large scale adoption. The key to this is to determine how best to inject a low frequency waveform into the battery without the use of additional excitation hardware. Figure 3-1 shows a block diagram representation of a typical battery system showing where a low frequency waveform may be sourced from existing hardware found in a system. A key requirement of all the methods described below are; that they have to generate a low frequency waveform of variable frequency (swept across a range) while at the same time not impacting and minimising usual operation and using the hardware already in-situ.

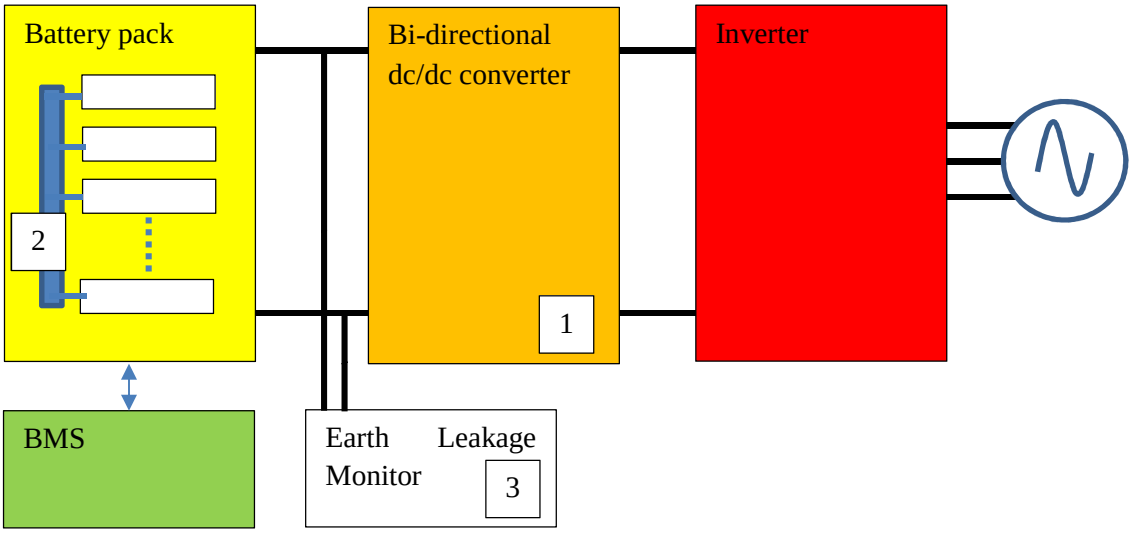

Figure 3-1 : Block Diagram of a battery system showing where hardware may be used to inject a low frequency waveform

Three possible locations include;

- The dc/dc power electronics
- The battery balancing circuitry
- The Earth Leakage Monitor

An Earth Leakage monitor is a requirement of the IET Wiring Regulations [279] for systems above 50V that are unearthed. It is usual to leave the battery pack floating through high impedance resistors or capacitors so that the dc bus is suitable for connection through an inverter to any ac system. In particular within the USA, it is not usual to have a corner grounded LV system [280], [281] which would not allow for direct connection of an inverter, without a transformer, adding additional cost, if the battery were grounded. This chapter considers all of the locations in Figure 3-1 in turn and considers different methods for injecting a low frequency wave using the existing hardware. The chapter describes each method, shows how the operation of the circuit compares to traditional operation and then shows that a low frequency harmonic has been introduced through Fourier analysis. There are always trade-offs within Engineering and the impact of using existing hardware to inject a low frequency excitation signal is that additional harmonics and dc ripple current are introduced. This chapter looks at quantifying these effects so that they can be considered at a circuit design phase. Chapter 4 and 5 then looks at how these methods work from a simulation and experimental perspective.

The first hardware location under consideration is the dc/dc power electronic converter, which usually connects the battery to a drive train or an electrical grid system through an inverter. This work is based on using the hardware available in a standard bi-directional dc-dc converter topology. However, for convenience, boost operation is examined in detail using the simplified circuit shown in Figure 3-2. This is used to analyse the effect of discharging mode on the battery performance for the different presented methods in this work. A similar analysis can be used for the charging mode by considering the buck operation but not presented in this work.

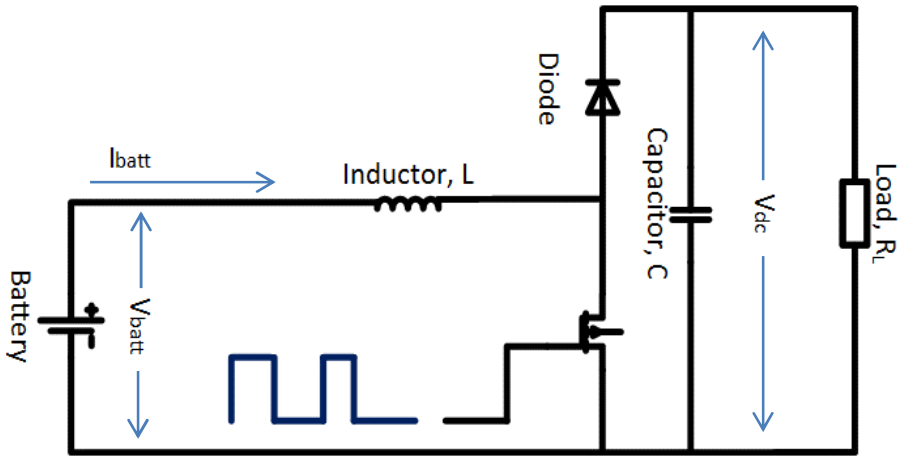

Figure 3-2 : DC/DC topology used in analysis of boost operation

Under normal operation, the duty cycle would be used to set the output voltage of the converter. The battery voltage is considered to be varying slowly, therefore under steady state operation, the duty cycle can be considered constant for a fixed switching frequency giving a fixed boost ratio. The aim of the work is to inject a low frequency signal and then sweep this frequency across a range to replicate the functionality of the EIS without the need for a separate excitation circuit. However, at the same time

the circuit should continue to produce a high frequency pulse train to boost the voltage. There are a number of methods of injecting harmonics within a converter. This chapter will consider four different methods;

1. Varying the duty cycle
2. Varying the switching frequency
3. Varying the time within a pulse when the circuit is on
4. Injecting a low frequency impulse train

Following the addition of a low frequency excitation signal, the battery voltage and current can then be measured and used to determine the harmonic impedance. Within the analysis of the dc/dc converter, this work looks at how the low frequency component is injected into the gate drive circuit controlling the dc/dc converter and compares this to a more traditional case with no injection. The work is then extended to show how the gate drive circuit switching allows injection of this low frequency signal into the circuit by deriving the harmonic equations for the circuit. Within Chapter 5, the measured harmonics are compared to those calculated using these equations. The impact of operation is examined with the extra ripple component through the inductor being derived where possible as an explicit expression.

The other methods presented in this chapter investigate using the battery balancing and ELM circuits to inject a low frequency signal. In each of these methods, the sections are divided into:

- Theoretical proof that a low frequency component has been introduced by Fourier analysis,
- Theoretical impact on inductor ripple,
- Operational characteristics of the converter circuit.

Harmonic analysis of gate drive signals and resulting sawtooth waveform at the output of the converter has previously been undertaken [282]–[285]. This thesis derives the formula from first principles because of the complexity of the waveforms. The analysis is based on an ideal case with no losses and linear operation.

3.2 DC/DC Converter with variable duty cycle PWM

The boost converter is operated such that the average duty cycle is considered constant (as if the system were operating in steady state), but the instantaneous duty cycle is varied to add a low frequency component in order to induce a low frequency harmonic into the circuit as described in Equation 3-1. Reference [256] introduced this method of low frequency harmonics injection to estimate the impedance and SOC of the batteries. However, this was produced as a proof of concept and looked at a single value point with no follow through to EIS. The work in this thesis extends this proof of concept into a more rigorous analysis. The duty cycle of the gate drive is varied as:

$$d(t) = d_{av} + A_d cos(\omega_o t) \quad \text{Equation 3-1}$$

Where d_{av} is average duty cycle, A_d is the offset amplitude, and ω_o is the low frequency component. This gate drive duty cycle is used in the following sub-sections to look at how the converter would operate under this switching pattern and to confirm a low frequency component has been introduced to the circuit.

3.2.1 Harmonic analysis of gate drive circuit PWM

A high frequency switching frequency,f_s (switching time period of T_s) is used in conjunction with the low frequency component f_o with a time period of T_o. The number of high frequency pulses in one low frequency cycle can be written as:

$$N_p = \frac{T_o}{T_s} \quad \text{Equation 3-2}$$

It is assumed that each pulse is switched at 2kHz and every T_s stays on for a period defined by $d(t)T_s$. The duty cycle varies from a maximum value of $d_{av} + A_d$ to the minimum value of $d_{av} - A_d$ (this is to ensure a symmetrical waveform and continues operation). The value of A_d was chosen according to the design calculation in section 4.1 and was confirmed with the experiment. An example of the switching pattern of the proposed waveform defined by $d(t)$ compared to a fixed duty cycle is shown in Figure 3-3.

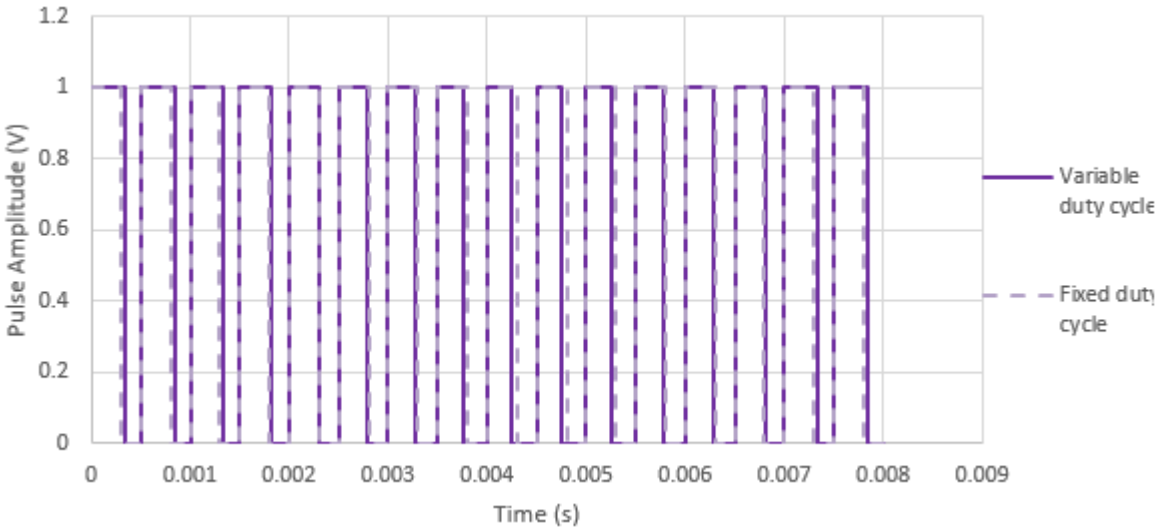

Figure 3-3 : Comparison of a variable duty cycle (f_s = 2 kHz, f_0 = 125 Hz, A_d= 0.01) with a fixed duty cycle

As the average duty cycle is set equal to a fixed duty cycle the boost ratio over time will be the same. However additional ripple and harmonics have been introduced. These can be calculated using the Fourier transform property of linearity as shown in Equation 3-3.

$$af_1(t) + bf_2(t) = aF_1(\omega) + bF_2(\omega) \qquad \text{Equation 3-3}$$

The repeating pulse signal train can be considered as a summation of N_p periodic functions as shown in Figure 3-4. The full derivation of the harmonic calculation is detailed in Appendix B, with only key results replicated within this chapter.

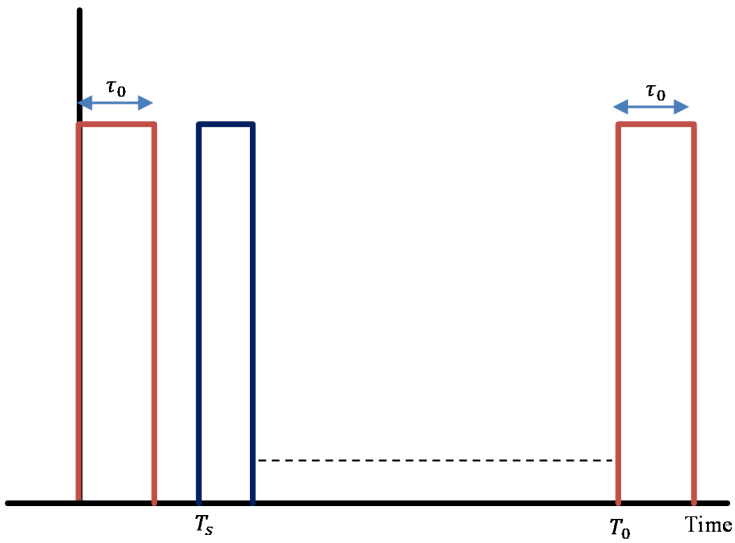

Figure 3-4 : Periodic representation of a function (first function in red) and (second function in blue) through to Np functions.

The first function is a periodic square wave starting at the origin and repeating after time T_o as shown in red in Figure 3-4, with a Fourier series representation of

$$f_0(t) = \left(\frac{2A\tau_0}{T_0} + \frac{2A}{\omega_0 T_0}\sum_n \frac{1}{n}(\sin(n\omega_0\tau_0)\cos(n\omega_o t) + \frac{1}{n}(1-\cos(n\omega_0\tau_0))\sin(n\omega_o t))\right) \quad \text{Equation 3-4}$$

where:

A = Fourier series coefficient amplitude,

τ_0 = The width of the first pulse, and

T_o = The low frequency waveform period.

While the harmonic spectrum of the first function is:

$$C_{0,n} = \frac{2A}{\omega_0 T_0}\sum_n \frac{1}{n}(\sin(n\omega_0\tau_0)\cos(n\omega_o t) - j\frac{1}{n}(1-\cos(n\omega_0\tau_0))\sin(n\omega_o t)) \quad \text{Equation 3-5}$$

Each subsequent periodic pulse, m (up to N_p -1), can be defined as a time shifted square wave with a different pulse width τ_m. The fourier series of the other functions can be found using the time shift property of Fourier analysis from Equation 3-6 :

$$f(t - t_{dtm}) = F(\omega)e^{-j\omega t_{dtm}} \quad \text{Equation 3-6}$$

As:

$$f(t_m) = \left(\frac{2A\tau_m}{T_0} + \frac{2A}{\omega_0 T_0}\sum_n \frac{1}{n}(\sin(n\omega_0\tau_m)\cos(n\omega_o t) + \frac{1}{n}(1 - \cos(n\omega_0\tau_m))\sin(n\omega_o t)\right)e^{-jn\omega_o t_{dtm}} \quad \text{Equation 3-7}$$

As the time shift is relative to the start of the first pulse, the time delay t_{dtm}, needs to be calculated from Equation 3-8 (see Figure 3-5).

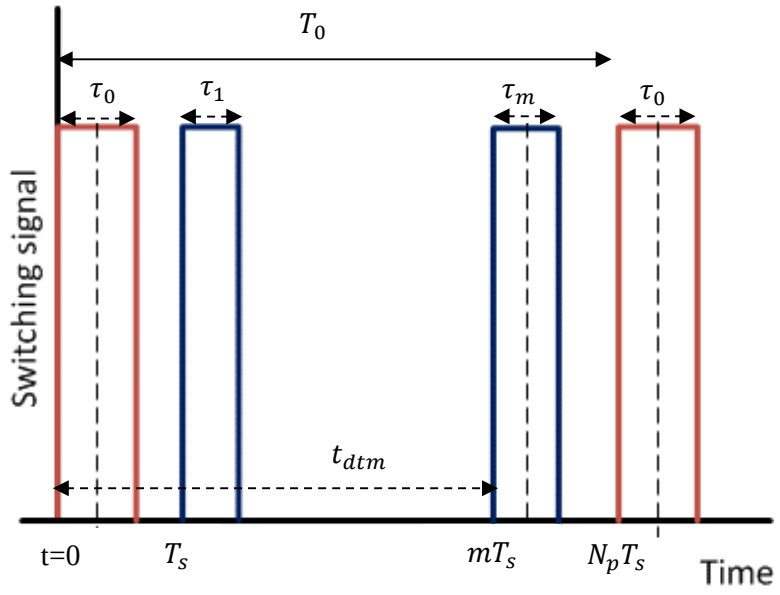

Figure 3-5 : Time shift calculation for the m[th] function

$$t_{dtm} = mT_s$$ Equation 3-8

Thus the frequency spectrum can be generalised to:

$$c_0 = \sum_{m=0}^{N_p-1} \frac{2A\tau_m}{T_0}$$ Equation 3-9

$$c_n = \sum_{m=0}^{N_p-1} \frac{2A}{n\omega_0 T_0} (\sin n\omega_0\tau_m - j(1 - \cos n\omega_0\tau_m))e^{-jn\omega_0(m)T_s}$$ Equation 3-10

T_s and T_o remains the same but the value of τ_m changes to represent the adjusted duty cycle in each pulse as:

$$\tau_m = T_s d_m(t)$$ Equation 3-11

Where $d_m(t)$ = the duty cycle at time equal to: mT_s and equals:

$$d_m(t) = d_{av} + A_d\, cos(\omega m T_s) = d_{av} + A_d cos(2\pi m/N_p)$$ Equation 3-12

It should be noted that using a fixed duty cycle (setting A_d to 0) causes C_o and C_n of Equation 3-9 and Equation 3-10 to simplify back to the standard expression of a periodic rectangular waveform. An example of the results of the variable duty cycle pulse analysis solved using the expressions above (Equation 3-10) at low-frequency of 125Hz, switching frequency of 2kHz and A_d of 0.01 pu within Matlab is shown in Figure 3-6. The Fourier analysis of a rectangular waveform of fixed switching frequency is shown in Figure 3-7. There is no low frequency component Figure 3-7, but the horizontal axis has been made the same as that in Figure 3-6 for easy comparison. The fundamental harmonic of the normal switching signal is therefore shown as a 16th harmonic number.

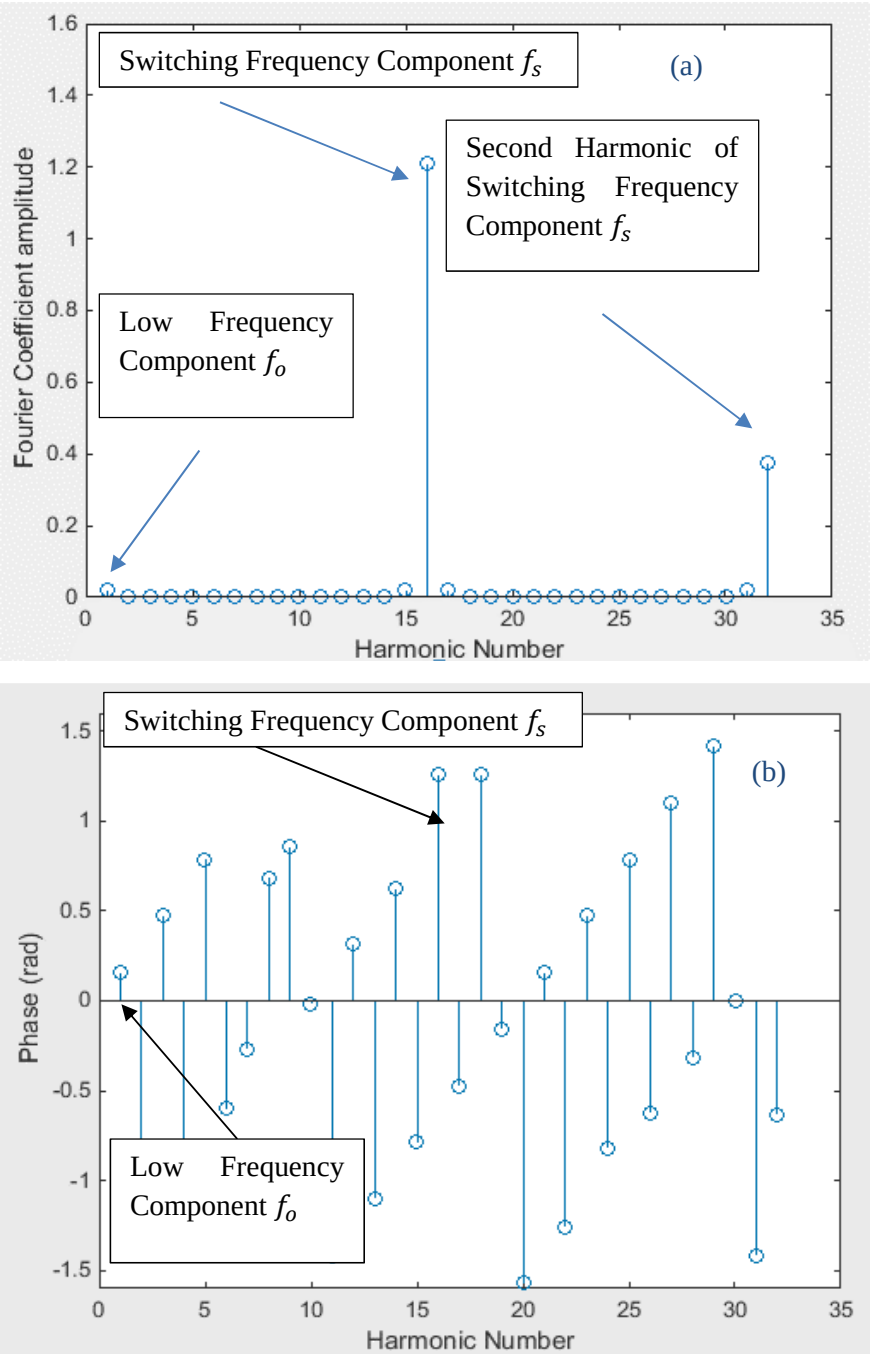

Figure 3-6 : Low frequency components of variable duty cycle a) Fourier coefficient C_n b) phase when f_0=125Hz , f_s =2kHz and A_d = 0.01 pu (the harmonic number = 1 relates to 125Hz)

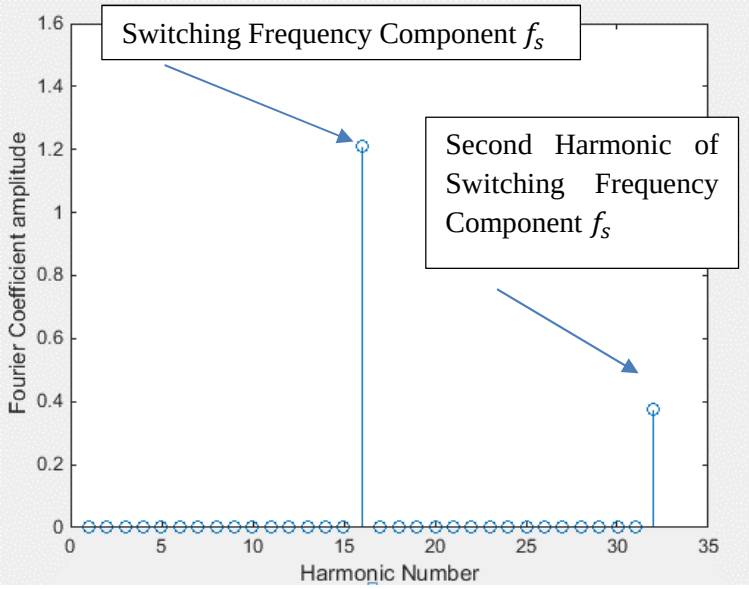

Figure 3-7 : Low frequency components of fixed duty cycle Fourier coefficient C_n when f_0=125Hz , f_s =2kHz and A_d=0 (the harmonic number = 1 relates to 125Hz)

The comparison of both figures above shows that a low frequency component of f_0 is injected into the PWM switching pattern of converter by varying the duty cycle. Although it is clear that a low frequency component is being introduced into the gate drive circuit, it is necessary to follow through the analysis to the circuit and look at the impact on the saw tooth waveform generated as a result of boost operation.

Note: If the number of high frequency pulses in a low frequency cycle N_p is not an integer then the Fourier analysis needs extending to the number related to the lowest common multiplier of the two time periods.

3.2.2 Harmonic analysis of variable duty cycle PWM Current waveform

Fourier analysis can also be used to study the current waveform seen from the battery as shown in Figure 3-8 . The first function is a periodic sawtooth function with a period of T_o and duration τ_0 from u_o to v_o. The second function is a periodic sawtooth wave with the opposite slope with a period of T_o but shifted with respect to the first waveform by d_mT_s from v_o to u_1. The second function is identical to the first one but has an additional time shift. The harmonic spectrum of the m^{th} function is shown in Appendix C in full.

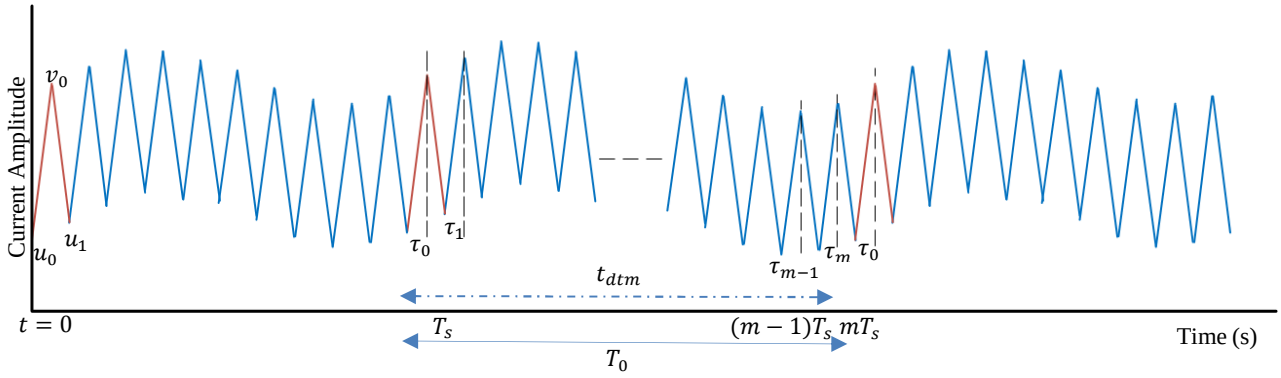

Figure 3-8 : Battery Current Waveform showing the Time shift calculation for the m[th] function

Where $m_{on,m}$ and $m_{off,m}$ are the gradients of the current and can be expressed as:

$$m_{on,m} = \frac{v_m - u_m}{d_m T_s} = \frac{1}{L} V_{bat} \qquad \text{Equation 3-13}$$

$$m_{off,m} = \frac{u_{m+1} - v_m}{(T_s - d_m T_s)} = \frac{1}{L}(V_{bat} - V_{dc}) \qquad \text{Equation 3-14}$$

Where:

V_{bat} = battery voltage, and

V_{dc} = the converter output voltage.

L = boost inductor.

It is assumed that the V_{bat} and V_{dc} are constant. Figure 3-9 shows the FFT analysis using a MATLAB script for a current waveform with 125Hz low-frequency ripple.

The key parameters used in the Matlab script were obtained from the hardware that was designed for the experimental validation described later in section 4.1. Results were also cross checked against a model in excel to ensure no coding errors.

Table 3-1 : key parameters for theoretical analysis of current harmonics

Boost Converter Components	**Specifications**
L	380µH,
V_{bat}	3.21
V_{dc}	8.03
Switching frequency f_s	2kHz

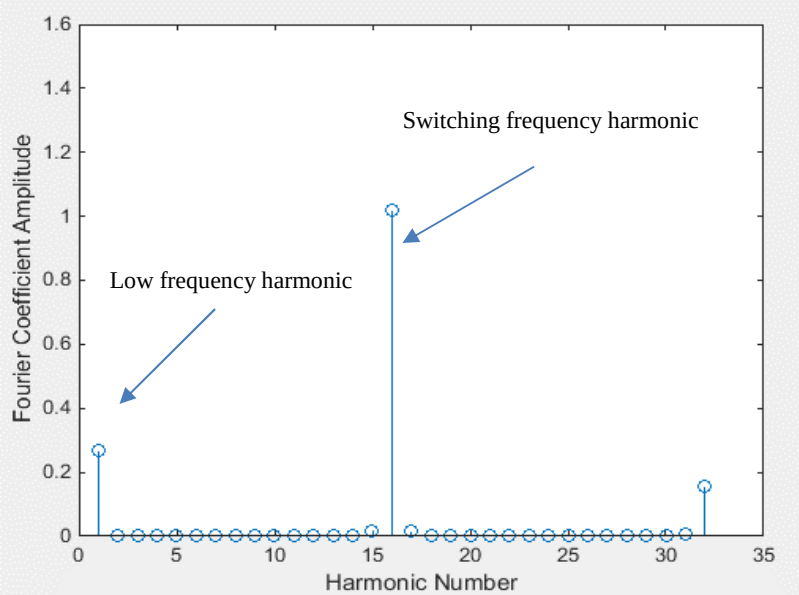

Figure 3-9 : Theoretical harmonics of the Li-ion battery current signal at variable duty cycle with a low frequency of 125Hz with A_d= 0.01.

3.2.3 Cross check of circuit boost ratio using variable duty cycle method

The gain and variation in ripple in the circuit compared to a fixed duty cycle can be calculated by considering the equations of the circuit. In the variable duty cycle switching method the current is not in equilibrium over one on and off switch cycle. It is in equilibrium over N_p cycles.

In steady state condition the inductor current over one switching cycle in boost mode in an ideal converter can be calculated as by using Equation 3-15 and Equation 3-16

$$\Delta i_{on,m} = \frac{1}{L} V_{bat} d_m T_s \quad \text{Equation 3-15}$$

$$\Delta i_{off,m} = \frac{1}{L}(V_{bat} - V_{dc})(T_s - d_m T_s) \quad \text{Equation 3-16}$$

where V_{bat} is battery voltage, V_{dc} is the converter output voltage, T_s is the switching period, $\Delta i_{on,m}$ increasing inductor current, and $\Delta i_{off,m}$ decreasing inductor current over the m^{th} switching cycle period, mT_s. In equilibrium the change in inductor current over a low frequency cycle is zero:

$$\frac{1}{2} L \sum_{m=0}^{N_p-1} \Delta i_{L_m}^2 = 0 \quad \text{Equation 3-17}$$

$$\sum_{m=0}^{N_p-1} \Delta i_{on,m} + \sum_{m=0}^{N_p-1} \Delta i_{off,m} = 0 \quad \text{Equation 3-18}$$

$$\sum_{m=0}^{N_p-1} \Delta i_{on,m} = \frac{1}{L} V_{bat} \sum_{m=0}^{N_p-1} d_m T_s = \frac{1}{L} V_{bat} N_p d_{av} T_s \quad \text{Equation 3-19}$$

$$\sum_{m=0}^{N_p-1} \Delta i_{off,m} = \sum_{m=0}^{N_p-1} \frac{1}{L}(V_{bat} - V_{dc})(T_s - d_m T_s) \quad \text{Equation 3-20}$$

$$\sum_{m=0}^{N_p-1} \Delta i_{off,m} = \frac{T_s}{L} N_p (V_{bat} - V_{dc})(1 - d_{av}) \quad \text{Equation 3-21}$$

Summing the duty cycle over N_p pulses is the same as $N_p d_{av}$, therefore $\sum_{m=0}^{N_p-1} d_m T_s = N_p d_{av} T_s$,

$$\frac{1}{L} V_{bat} N_p d_{av} T_s + \frac{1}{L} T_s N_p (V_{bat} - V_{dc})(1 - d_{av}) = 0 \quad \text{Equation 3-22}$$

Simplifying gives:

$$(\frac{1}{L} T_s N_p V_{bat} - \frac{1}{L} V_{dc} T_s N_p + \frac{1}{L} V_{dc} d_{av} T_s N_p) = 0 \quad \text{Equation 3-23}$$

$$V_{bat} - V_{dc} + V_{dc} d_{av} = 0 \quad \text{Equation 3-24}$$

$$\frac{V_{dc}}{V_{bat}} = \frac{1}{(1 - d_{av})} \quad \text{Equation 3-25}$$

The boost ratio is identical to a fixed duty cycle wave of the same average duty cycle. However, the peak to peak ripple compared to a fixed boost ratio varies.

3.2.4 Inductor ripple calculation of variable duty cycle method

Prior to choosing an inductor value, the additional gain in ripple in the circuit compared to a fixed duty cycle can be estimated by considering the equations with ideal components. The boost ratio is identical to a fixed duty cycle wave of the same average duty cycle. However, the peak to peak ripple compared to a fixed boost ratio varies as shown in Figure 3-10.

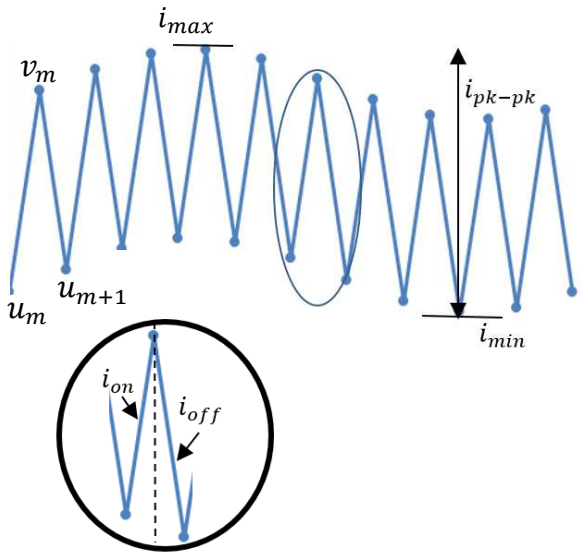

Figure 3-10 : Converter current waveform in continuous mode

Assume that a circuit with a fixed duty cycle has a ripple current of magnitude 1pu over a switching time period 1pu, such that on each interval $[m/N_p \; to \; (m+d)/N_p]$ the current increases at a steady

rate of 1/ d_{av} and in each interval $\left[(m+d)/N_p\ to\ (m+1)/N_p\right]$ the current decreases at a steady rate of $1/(1-d_{av})$.

A ripple is now applied to the duty cycle as per Equation 3-1. On each interval $\left[m/N_p\ to\ (m+d_m)/N_p\right]$ the current increases at a steady rate of 1/ d_{av} and in each interval $\left[(m+d_m)/N_p\ to\ (m+1)/N_p\right]$ the current decreases at a steady rate of 1/(1-d_{av}). The rate is the same as for the fixed rate above, but applied for a different time period. Over a time interval equal to one low frequency cycle, the total change in current is zero and is the sum of all the on and all the off currents.

$$0=\sum_{m=0}^{N_p-1}\left(\frac{d_m}{d_{av}}-\frac{1-d_m}{1-d_{av}}\right) \qquad \text{Equation 3-26}$$

Substituting for d_m gives

$$0=\sum_{m=0}^{N_p-1}\left(\frac{d_{av}+A_d cos(2\pi m/N_p)}{d_{av}}-\frac{1-d_{av}-A_d cos(2\pi m/N_p)}{1-d_{av}}\right) \qquad \text{Equation 3-27}$$

Over an interval of 1pu time the function increases from u_m to v_m, then decreases from v_m to u_{m+1}. Thus the minimum will be one of the values of u_m at time period k, and the maximum will be one of the values of v_m at time period n. In a similar manner to Equation 3-27 the function to calculate the minimum current can be written as:

$$u_k=\sum_{m=0}^{k-1}\left(\frac{d_{av}+A_d cos(2\pi m/N_p)}{d_{av}}-\frac{1-d_{av}-A_d cos(2\pi m/N_p)}{1-d_{av}}\right) \qquad \text{Equation 3-28}$$

$$u_k=\frac{A_d}{d_{av}(1-d_{av})}\sum_{m=0}^{k-1} cos(2\pi m/N_p) \qquad \text{Equation 3-29}$$

This can be simplified by putting $\omega=e^{\pi j/N_p}$ so that $\cos\left(2\pi m/N_p\right)=(\omega^{2m}+\omega^{-2m})/2$ and the geometric progressions are

$$\sum_{m=0}^{k-1}\omega^{2m}=\frac{\omega^{2k}-1}{\omega^2-1}=\frac{\omega^{2k-1}-\omega^{-1}}{\omega-\omega^{-1}} \qquad \text{Equation 3-30}$$

$$\sum_{m=0}^{k-1}\omega^{-2m}=\frac{\omega^{-2k}-1}{\omega^{-2}-1}=\frac{\omega-\omega^{-1-2k}}{\omega-\omega^{-1}} \qquad \text{Equation 3-31}$$

Giving

$$\sum_{m=0}^{k-1}\cos\left(2\pi m/N_p\right)=\frac{\omega^{2k-1}-\omega^{-1}+\omega-\omega^{-1-2k}}{2(\omega-\omega^{-1})} \qquad \text{Equation 3-32}$$

$$\sum_{m=0}^{k-1}\cos\left(2\pi m/N_p\right)=\frac{\sin\left((2k-1)\pi/N_p\right)}{2sin(\pi/N_p)}+\frac{1}{2} \qquad \text{Equation 3-33}$$

Substituting into Equation 3-33gives

$$u_k = \frac{A_d}{2d_{av}(1-d_{av})}\left(\frac{\sin\left((2k-1)\pi/N_p\right)}{sin(\pi/N_p)} + 1\right) \quad \text{Equation 3-34}$$

Note that $\sin(\pi/N_p)$ is π/N_p plus terms of order $(\pi/N_p)^3$. In practice $N_p>10$ so $\sin(\pi/N_p)$ can be well approximated by π/N_p giving

$$u_k = \frac{A_d}{2d_{av}(1-d_{av})}\left(\frac{N_p}{\pi}\sin\left((2k-1)\pi/N_p\right) + 1\right) \quad \text{Equation 3-35}$$

To minimize this, k needs to be the closest integer to $(3N_p+2)/4$ so that $(2k-1)\pi/N_p$ will be close to $3\pi/2$ and so $\sin\left((2k-1)\pi/N_p\right)$ will be close to -1. Provided that N_p is reasonably large the +1 term can be ignored giving

$$u_{min} \approx \frac{-A_d N_p}{2d_{av}(1-d_{av})\pi} \quad \text{Equation 3-36}$$

Similarly we have

$$u_{max} \approx \frac{+A_d N_p}{2d_{av}(1-d_{av})\pi} \quad \text{Equation 3-37}$$

V_m is reached by starting at u_m and increasing at a rate of $1/d_{av}$ for a time d_m, so

$$v_m = u_m + \frac{d_m}{d_{av}} = u_m + 1 + \frac{A_d}{d_{av}}cos(2\pi m/N_p) \quad \text{Equation 3-38}$$

The last term has no N_p in the numerator so it will be small compared to the other terms. Thus we have

$$v_{max} \approx u_{max} + 1 \approx 1 + \frac{A_d N_p}{2d_{av}(1-d_{av})\pi} \quad \text{Equation 3-39}$$

This gives a pu ripple magnitude above that for a fixed duty cycle of

$$v_{max} - u_{min} \approx 1 + \frac{A_d N_p}{d_{av}(1-d_{av})\pi} \quad \text{Equation 3-40}$$

The value of theoretical inductor ripple is compared to experimental and simulation results and further analysed in Section 5.3.

The purpose of this analysis is to understand the extra ripple the inductor could be subject to prior to understanding the design calculations. This value could be obtained from the Fourier analysis results but requires that the inductor value is already pre-specified. Similar analysis can be used for the battery voltage ripple variation. The voltage ripple variation also depends on the low-frequency and A_d variation.

3.3 DC/DC Converter with variable switching frequency PWM

In this method of injecting a low frequency component to the battery circuit, the same power electronic system is used. However, the switching frequency is no longer fixed but is allowed to vary. The change of frequency changes the inductor reactance. However, the calculations below are based on inductance rather than reactance, which is unchanging, so this variation has been accounted for. Any additional impact of the changing reactance would be considered future work. The switching frequency has the same average value but now oscillates around this value with a low frequency to induce a low frequency into the gate drive circuit according to Equation 3-41.

$$f_s(t) = f_{av} + A_f \cos(\omega_0 t) \qquad \text{Equation 3-41}$$

Where f_{av} = the average switching frequency, and A_f = the amplitude of the offset.

3.3.1 Harmonic analysis of gate drive circuit PWM

To analyse the gate drive harmonics, the same assumptions as described in section 3.2.1 are used. However, the duty cycle is now fixed and the switching period is allowed to vary, so the time that the pulses are on for is varying. The pulses are switched on at the start of each switching period and stay on for a period defined by $dT_s(t)$. Where $T_s(t) = 1/f_s(t)$. An example of a switching pattern for the proposed waveform defined by $f_s(t)$ compared to a fixed frequency, f_s is shown in Figure 3-11.

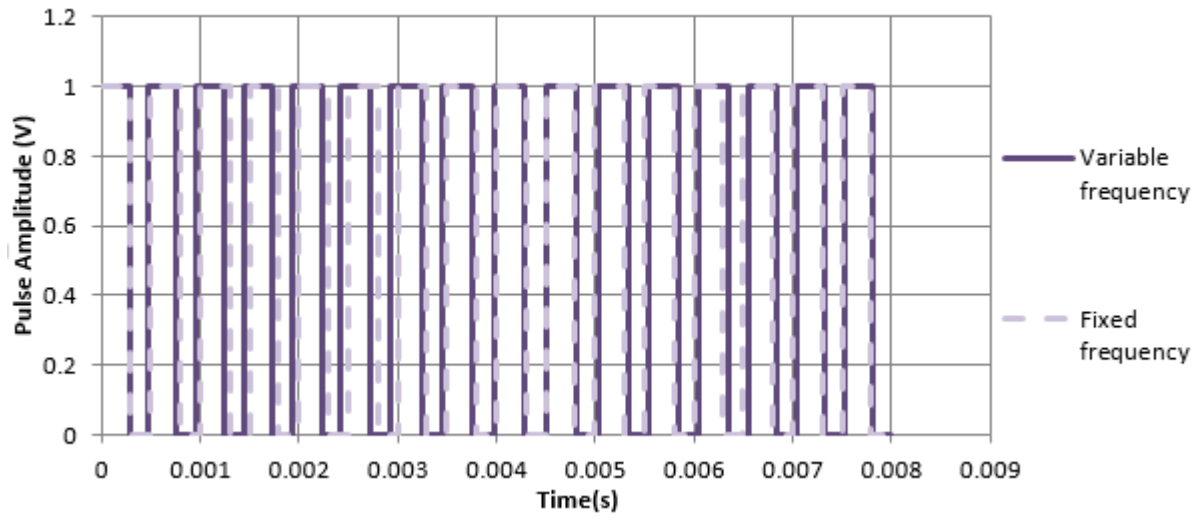

Figure 3-11 : Comparison of a variable frequency (f_{av} = 2 kHz, f_0 = 125 Hz) with a fixed frequency of 2kHz

The PWM signal is a summation of m separate functions as shown in Figure 3-12.

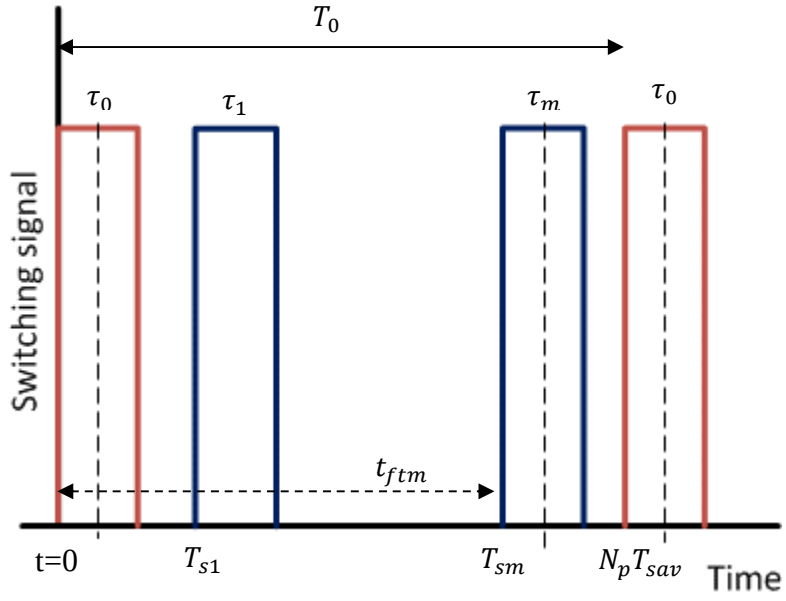

Figure 3-12 : Time shift calculation for the m[th] function

τ_0 is the on time for the first function and τ_{m-1} is the on time for the m^{th} function. The same definitions as for section 3.2.1 are used to calculate the first function of the periodic function starting at origin with period of T_0 and the second function is a periodic square wave, shifted by time t_{ftm} with a period of T_0.

$$f(t - t_{ftm}) = F(\omega)e^{-j\omega t_{ftm}} \quad \text{Equation 3-42}$$

The Fourier series of a periodic square wave in this analysis is therefore:

$$f(t_{ftm}) = \left(\frac{2A\tau_m}{T_0} + \frac{2A}{\omega_0 T_0}\sum_n \frac{1}{n}(\sin(n\omega_0\tau_m)\cos(n\omega_o t) + \frac{1}{n}(1 - \cos(n\omega_0\tau_m))\sin(n\omega_o t)\right)e^{-jn\omega_o t_{ftm}} \quad \text{Equation 3-43}$$

Where τ_m = the width of the rectangular pulse train, and T_0 the low frequency time period. The time shift delay is t_{ftm} for the m^{th} function with T_0 , the time between switching this function. This time delay for the m^{th}function can be defined as:

$$t_{ftm} = \sum_{n=0}^{m-1} T_{sm} \quad \text{Equation 3-44}$$

The pulse width of rectangle wave can be calculated as:

$$\tau_m = d \times T_{sm} \quad \text{Equation 3-45}$$

Where d is fixed and

$$T_{sm} = \frac{1}{f_s(t)} = \frac{1}{f_{av} + A_f \cos(\omega_0 t)} \quad \text{Equation 3-46}$$

Thus the frequency spectrum is equal to:

$$C_0 = \sum_{m=0}^{N_p-1} \left(\frac{A\tau_m}{T_o}\right)$$ Equation 3-47

$$C_n = \sum_{m=0}^{N_p-1} \left(\frac{2A}{n\omega_0 T_0}(\sin(n\omega_0\tau_m) - j(1-\cos(n\omega_0\tau_m)))\right) e^{-jn\omega_o t_{ftm}}$$ Equation 3-48

The calculated frequency magnitude is shown in Figure 3-13 using Equation 3-48 for two low-frequency cycles T_0 for an example case. In comparison with Figure 3-7 the low frequency component of f_0 is induced in the PWM signal and the switching frequency is now spread over a range defined by $f_{av} \pm A_f$ as expected. The first harmonic represents the injected low frequency component and the sixteenth harmonic represent the switching frequency harmonic.

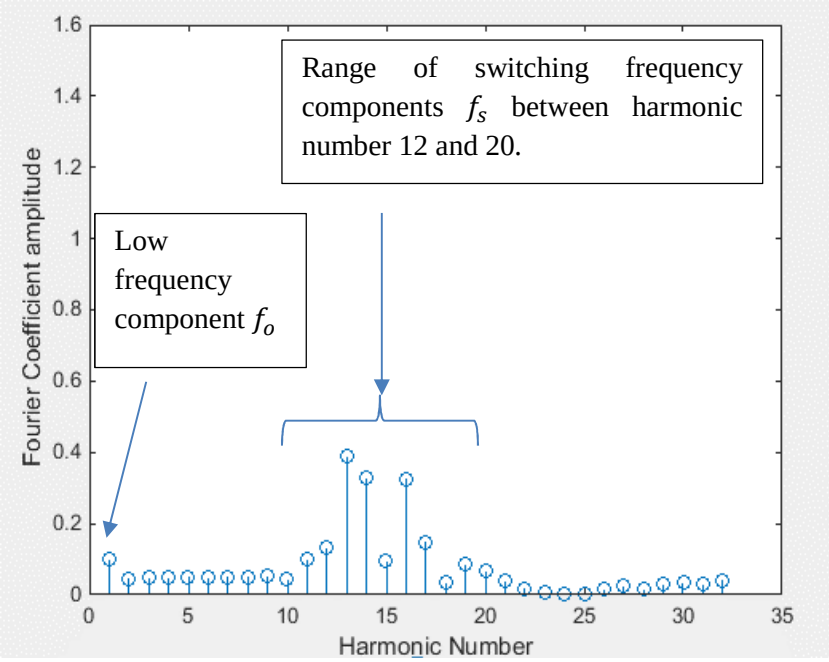

Figure 3-13 : Low frequency components of variable frequency Fourier coefficient Cn for an average switching frequency of 2kHz, a low frequency component of 125Hz and A_f = 400

3.3.2 Harmonic analysis of variable switching frequency PWM current waveform

The current waveform analysis is undertaken as a summation of sawtooth functions. The first function is a periodic sawtooth with a positive slope with period of T_0. The second function is a periodic saw tooth wave with the negative slope with a period of T_o but shifted with respect to the first waveform by dT_{sm} from v_o to u_1. The second function is similar to the first one but has an additional time shift and the "on"/"off" pulse time will have changed with the variable frequency. Figure 3-14 shows a sketch of the current waveform with variable frequency. In this figure, τ_0 is the "on" time for the first function and τ_{m-1} is the "on" time for the m^{th} function.

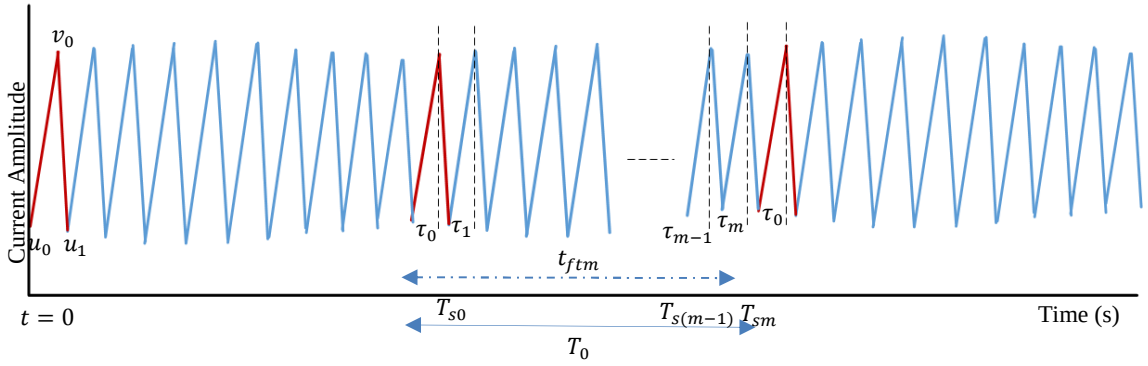

Figure 3-14 : Current Waveform for a variable switching frequency

The Fourier series of the periodic sawtooth function is shown in Appendix C. The harmonic spectrum using the values set in hardware using Table 3-1 is shown in Figure 3-15 using Equation C-61 for two low-frequency cycles.

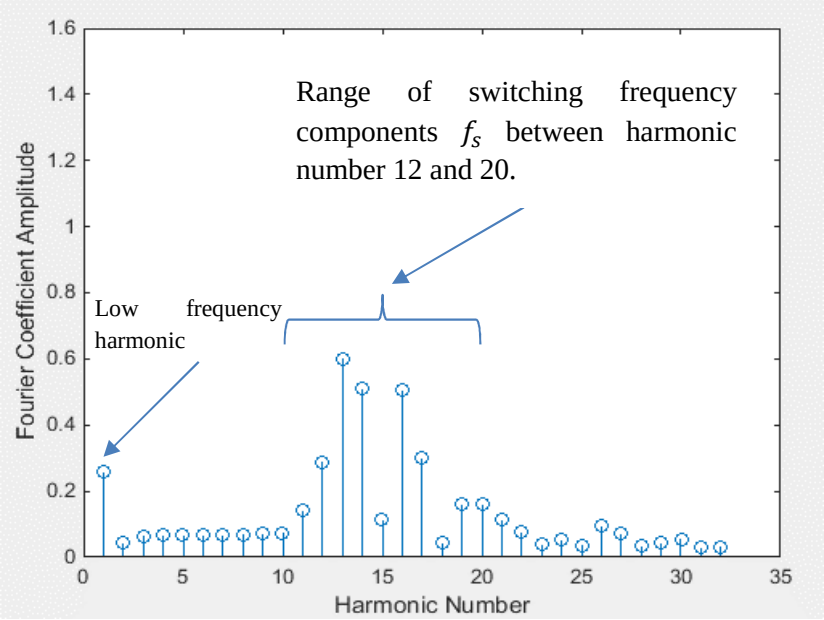

Figure 3-15 : Theoretical harmonics of the Li-ion battery current signal at variable switching frequency with a low frequency of 125Hz with A_f= 400.

3.3.3 Inductor ripple calculation of variable frequency

The boost ratio is identical to a fixed frequency switching period as the duty cycle has not changed. However, the peak to peak ripple compared to a fixed switching frequency varies. The current ripple in this interval is dependent on the switching frequency as shown in Figure 3-16. When the frequency is lower than the average, the time period for that pulse is longer than average and therefore the inductor current increase and decreases for a longer time relative to the fixed duty cycle. The peak to peak ripple is therefore the ripple of the lowest frequency from Equation 3-41 ($f_{av} – A_f$).

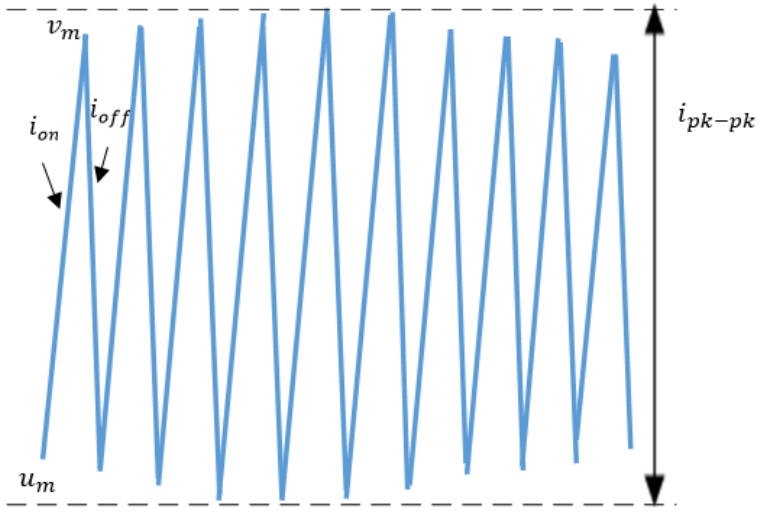

Figure 3-16 : Example of current ripple over a low frequency cycle

Assume that a circuit with a fixed switching frequency and duty cycle has a ripple current of magnitude 1pu over a switching time period 1pu, such that on each interval $[m/N_p \; to \; (m+d)/N_p]$ the current increases at a steady rate of $1/d$ and in each interval $[(m+d)/N_p \; to \; (m+1)/N_p]$ the current decreases at a steady rate of $1/(1-d)$. The duty cycle stays the same but the switching period in pu now increases to a maximum with the reduction in switching frequency to a minimum giving:

$$ripple\ ratio = \frac{f_{av}}{f_{av} - A_f}$$ **Equation 3-49**

The per unit current therefore both increases and decreases at the same steady rates but for the longer time period than a fixed switching signal:

$$I_{on,max} = \frac{1}{d}\,\frac{f_{av}}{f_{av} - A_f}$$ **Equation 3-50**

$$I_{off,max} = \frac{1}{1-d}\,\frac{f_{av}}{f_{av} - A_f}$$ **Equation 3-51**

Therefore the ripple increases by

$$ripple\ increase = \frac{f_{av}}{f_{av} - A_f}$$ **Equation 3-52**

Since the duty cycle and average frequency are constant, the increased theoretical ripple current is only a function of A_f. As this increases then the ripple current increases and there is no dependency on N_p.

3.4 DC/DC Converter with variable starting point PWM

In this method of injecting a low frequency component to the battery circuit, the same power electronic system is used. The switching frequency is fixed as is the duty cycle, but the starting position of the "on" signal varies within the switching period. Previously the pulse was turned on at the start of the switching period. However this starting position has been shifted to allow a sinusoidal variation about the midpoint of the switching time period. This variation is shown in Equation 3-53.

$$t_{ph}\,(t) = t_{av} + A_t \cos(\omega_0 t) \qquad \text{Equation 3-53}$$

Where t_{av} = an average switching on time, A_T = the amplitude of the position offset and ω_0 = the modulated frequency.

This method of introducing a low frequency harmonic is restrictive in nature because the "on" pulse shouldn't cross over to either of the adjacent switching periods, so the value of A_t is limited by this. Figure 3-17shows an example of this concept. The red lines are the start of each switching period, while the green dotted line is the average time in the cycle when the pulse is turned on. The blue lines show the pulse at the start of the switching period and the end of the switching period indicating the range of starting positions. In this case, if the switching frequency is 2kHz and the duty cycle is 0.6, the starting position equation has a maximum variation (not taking into account deadband) of:

$$t_{ph}\,(t) = 0.0001 + 0.0001 \cos(\omega_0 t) \qquad \text{Equation 3-54}$$

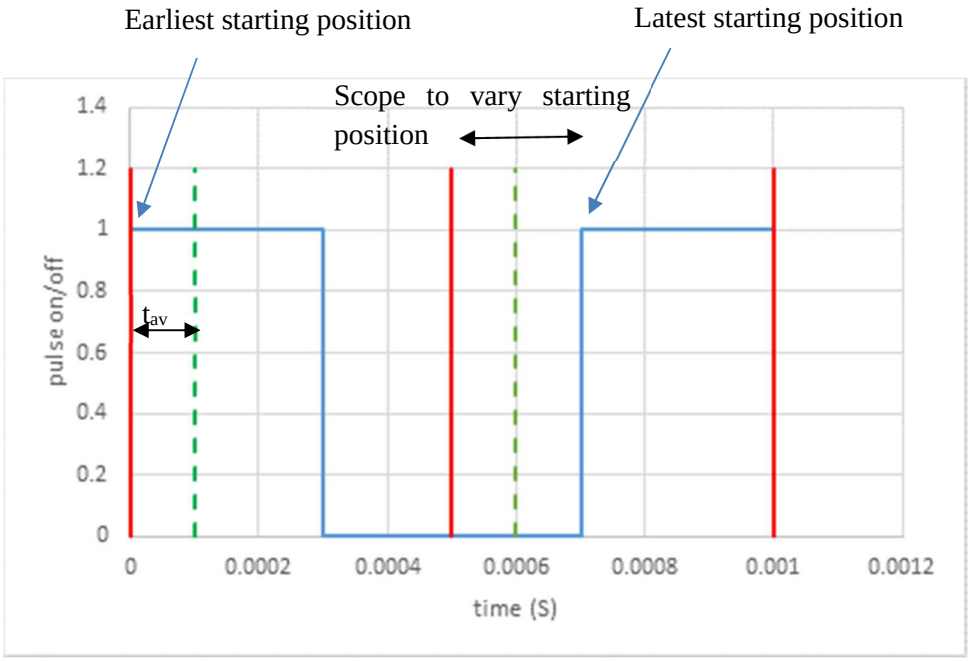

Figure 3-17 : Example showing limitation of A_t for a duty cycle of 0.6 in a switching frequency of 2kHz

3.4.1 Harmonic analysis of gate drive circuit PWM

Similar to sections 3.2.1 and 3.3.1 the harmonic analysis is considered as a sum of a set of rectangular pulses with period of T_o shifted based on the starting position of the pulse and with "on" duration fixed by duty cycle and switching frequency (dT_s). An example of the comparison of the time shifted pulse with a regular fixed start PWM signal is shown in Figure 3-18.

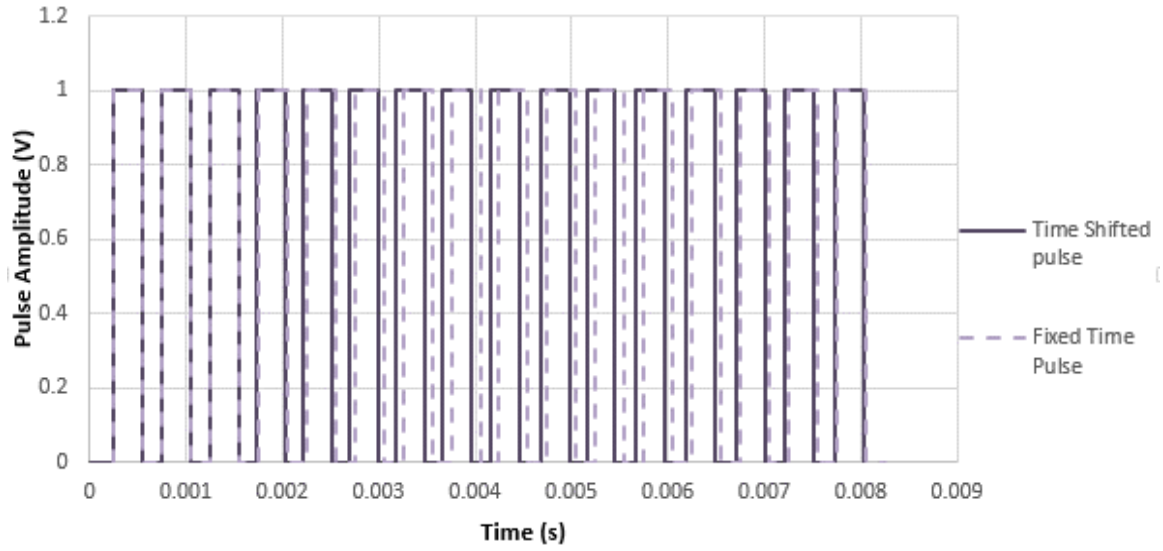

Figure 3-18 : Example showing comparison of variable starting position and fixed starting position for a pulse with duty cycle of 0.6, a switching frequency of 2kHz and an A_t = 0.00005.

In this case, because of the definition of the starting point in Equation 3-54, the first pulse does not start at the origin but is shifted by the delay in turn on. The Fourier series of a periodic square wave (equivalent to the first rectangular pulse train) is

$$f_0(t) = \left(\frac{2A\tau}{T_0} + \frac{2A}{\omega_0 T_0}\sum_n \frac{1}{n}(\sin(n\omega_0\tau)\,cos(n\omega_o t) + \frac{1}{n}(1 - \cos(n\omega_0\tau))sin(n\omega_o t))\right) e^{-jn\omega_o t_{phtm}} \quad \text{Equation 3-55}$$

Where τ = the width of the rectangular pulse train and T_o = the time period and $t_{pht0=}\, t_{av} + A_t$ is the time delay of the first pulse switching on.

The harmonic spectrum for this function is

$$C_{0,n=}\left(\frac{2A}{\omega_0 T_0}\sum_n \frac{1}{n}(\sin(n\omega_0\tau)\,cos(n\omega_o t) + (1 - \cos(n\omega_0\tau))sin(n\omega_o t)\right) e^{-jn\omega_o t_{phtm}} \quad \text{Equation 3-56}$$

The time delay for the m^{th} function can be represented as:

$$t_{phtm} = mT_s + t_{ph}(t) = mT_s + t_{av} + A_t\cos(\omega_0 t) \quad \text{Equation 3-57}$$

The resulting m^{th} function is as follows

$$f(t_m) = \left(\frac{2A\tau}{T_0} + \frac{2A}{\omega_0 T_0}\sum_n \frac{1}{n}(\sin(n\omega_0\tau)\,cos(n\omega_o t) + (1-\cos(n\omega_0\tau))sin(n\omega_o t))\right) e^{-jn\omega_o t_{phtm}} \quad \text{Equation 3-58}$$

The frequency spectrum is therefore equal to

$$C_0 = \sum_{m=0}^{N_p-1}\left(\frac{2A\tau}{T_0}\right) \quad \text{Equation 3-59}$$

$$c_n = \sum_{k=0}^{N_p-1}\frac{2A}{n\omega_0 T_0}(\sin n\omega_0\tau - j(1-\cos n\omega_0\tau))e^{-jn\omega_0(t_{phk}+(k)T_s)} \quad \text{Equation 3-60}$$

The full Fourier analysis calculations are presented in Appendix B. Figure 3-19 shows an example of the harmonics of the gate drive signal for a variation of the starting point with a low frequency harmonic using Equation 3-60. As can be seen, a low frequency component is visible.

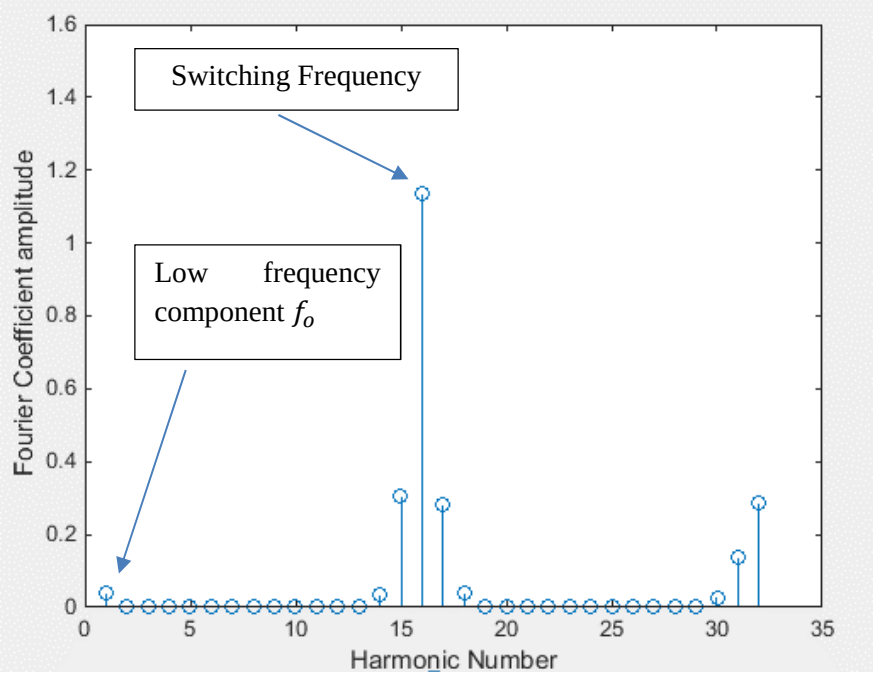

Figure 3-19 : Low frequency components of variable starting point Fourier coefficient Cn for an average switching frequency of 2kHz, a duty cycle of 0.6, a low frequency component of 125Hz and A_t= 0.00004.

3.4.2 Harmonic analysis of variable starting point PWM current waveform

Similar to the variable duty cycle method, fourier analysis can be used to study the current waveform seen from the battery as shown in Figure 3-20 . The first function is a periodic sawtooth function with a period of T_0 and duration τ from u_o to v_o with the time shift of tph_0. The second function is a periodic sawtooth wave with the opposite slope with a period of T_o but shifted with respect to the first waveform by dT_s+tph_0 from v_o to u_1. The second function is identical to the first one but has an additional time shift and the "on"/"off" pulse time will remain the same with the variable starting point. The harmonic spectrum of the m^{th} function is shown in Appendix C in full.

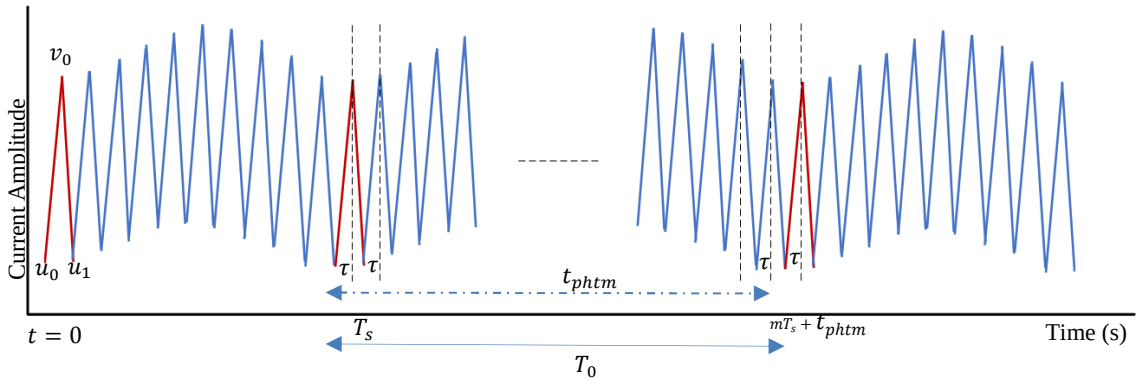

Figure 3-20 : Current Waveform for a variable starting point

The current as seen by the battery follows a saw tooth pattern dependent on the switching pattern. The harmonics of this waveform (which looks very similar to that in Figure 3-8 but are not identical due to the different methodology) can be analysed in a similar way. The derivation of the harmonic co-efficient is shown in Appendix C. This produces a harmonic spectrum as shown in Figure 3-21.

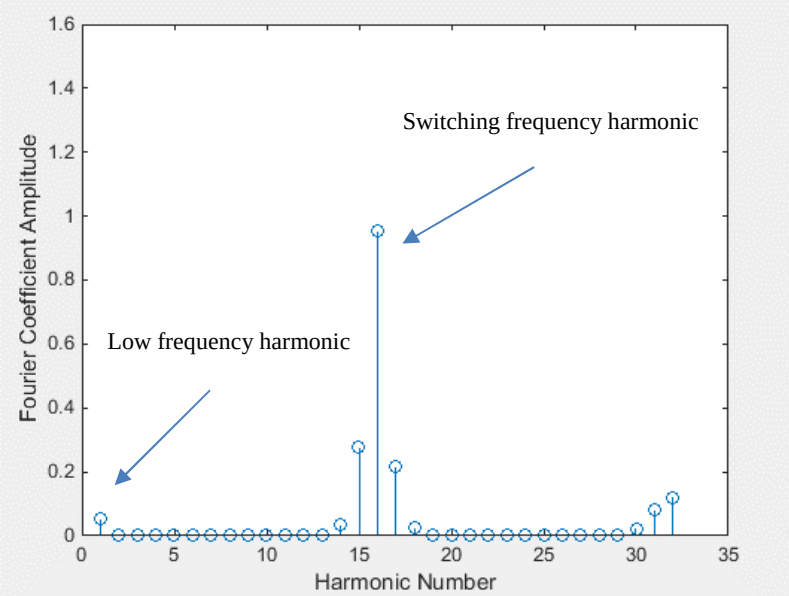

Figure 3-21 : Theoretical harmonics of the Li-ion battery current signal at variable starting point with a low frequency of 125Hz with A_t= 0.00004 and t_{av}= 0.00026 .

3.4.3 Inductor ripple calculation of varying start position

The analysis of the current peak to peak value can be found by considering a similar process to that used to calculate ripple in the variable duty cycle current peak to peak ripple case.

Assume that a circuit with a fixed duty cycle, fixed switching frequency and fixed starting position has a ripple current of magnitude 1pu over a switching time period 1pu, such that on each interval d the current increases at a steady rate of 1/ d and in each interval $d - 1$ the current decreases at a steady rate of $1/(1 - d)$. Over the period of a high frequency pulse in equilibrium the net current is zero.

A change in starting position is applied within this pulse as shown in Figure 3-19. However, the total pu time that the pulse is on is unchanged at *d* and over this interval the current continues to increase at a steady rate of 1/*d* as shown by the red trace (on for the same amount of time in each pulse with the same gradient). The total pu time that the current decreases remains constant at 1-d and the rate of decrease remains constant at 1/(1-d). However, because of the change of start position, this decrease can now be thought of as split into two sections as shown in Figure 3-19. Over the period of a pulse the net current remains zero as shown by the thick black line, and the total change in current over a pulse period remains unchanged at 1pu as shown by the blue arrow. However, the effect of starting position of the pulse introduces an increased ripple component – shown by the thick red arrow. The worst case scenario (when the starting position changes between a minimum and a maximum position) as shown in Figure 3-17 means that this can be as high as 2pu. However, if the starting position doesn't vary by this amount then the ripple can be calculated by considering the extreme cases from Equation 3-53.

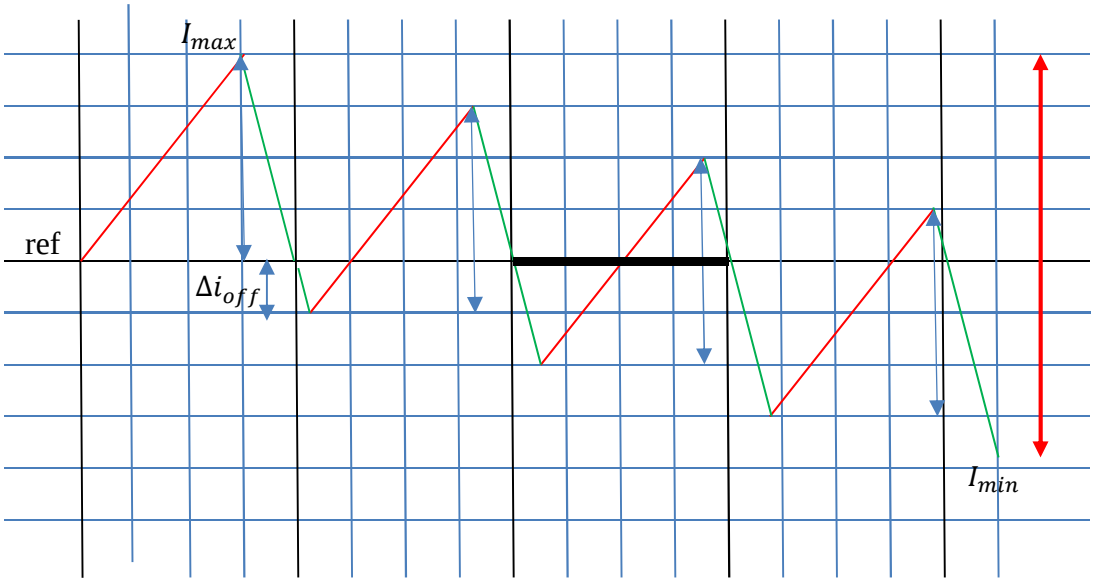

Figure 3-22 : Variation of starting position on ripple

The peak current will be found when $t_{ph}(t)$ is a minimum and the minimum current will be found when $t_{ph}(t)$ is a maximum. The peak current is found when the starting phase is at a minimum and therefore the smallest reduction in current occurs before the current starts to increase plus the increase in current. This value is equal to the minimum pu period of time the current is reducing, times the rate of reduction (1/(1-d)) plus the 1pu increases over time 1/d (the current increase).

$$I_{max} = 1 - \frac{t_{av} - A_t}{(1-d)T_s}$$ **Equation 3-61**

The minimum current is found at the time where the starting phase is at a maximum and before the current starts to increase. This is the pu time that the current is reducing times the rate of reduction.

Equation 3-62

$$I_{min} = -\frac{t_{av} + A_t}{(1-d)T_s}$$

The total pu ripple current is therefore the peak value over the ref plus the minimum value below the ref.

Equation 3-63

$$ripple\ increase = I_{max} - I_{min} = 1 - \frac{t_{av} - A_t}{(1-d)T_s} + \frac{t_{av} + A_t}{(1-d)T_s}$$

Equation 3-64

$$ripple\ increase = 1 + \frac{2A_t}{(1-d)T_s}$$

The ripple current for a fixed starting position is 1. Therefore the pu increase in ripple current between a fixed starting position of t_{av} and variable staring position is $\frac{2A_t}{(1-d)T_s}$.

3.5 DC/DC Converter with an Impulse Function

An alternative method of adding a low frequency harmonic into the gate drive circuit is to add in one directly. Ideally it would be useful to add a low frequency impulse function. However, it's not possible within the control system to add an impulse function directly, but rather a low frequency square wave pulse train with as small a width as possible could be considered. There are several different ways of doing this as shown in Figure 3-23. The first is that the impulse function is combined in an OR function with the usual switching frequency waveform. However, because the impulse function is on for a finite amount of time, the circuit is switched on for longer than the normal switching frequency duty cycle and therefore the average duty cycle with time over several periods of a low frequency pulse increases causing a change to the boost ratio. To overcome this issue, either the duty cycle needs to be reduced or an XOR function can be used so that the time the impulse function is on is both added and subtracted at different times resulting in no net change to the average duty cycle.

These methods are okay as long as the impulse function frequency isn't a multiple of the switching frequency such that the impulse function isn't then invisible to the gate drive circuit as shown in Figure 3-24.

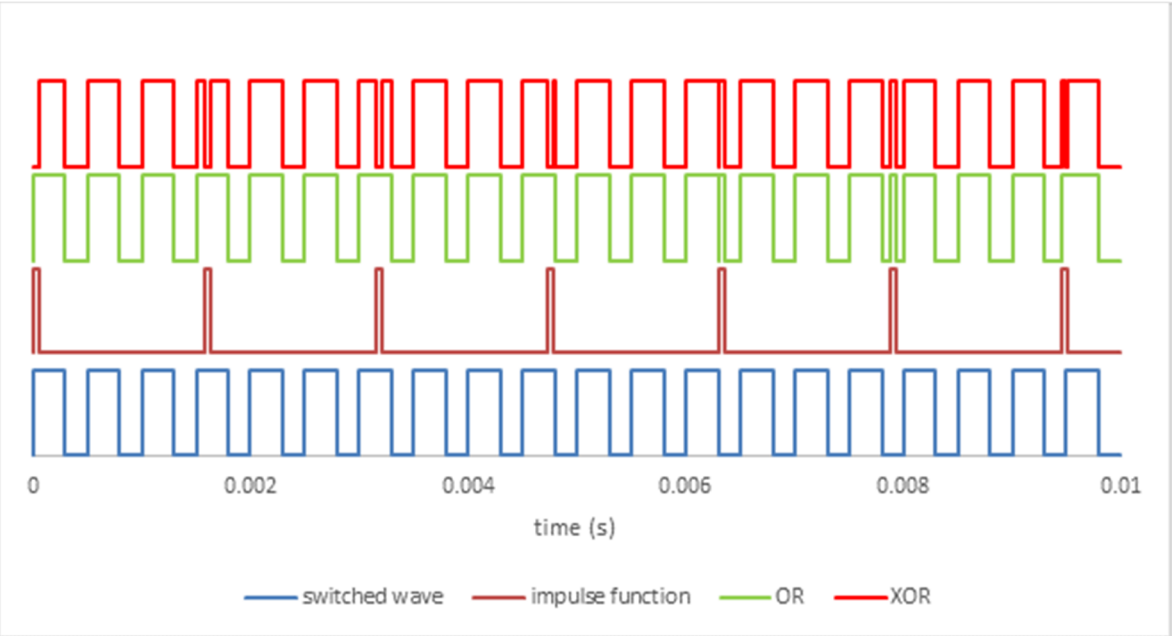

Figure 3-23 : Example showing adding a low frequency impulse stream to the switching pattern with an OR and XOR function gate drive signal (low frequency wave 634Hz, switching frequency 2kHz, duty cycle = 0.6)

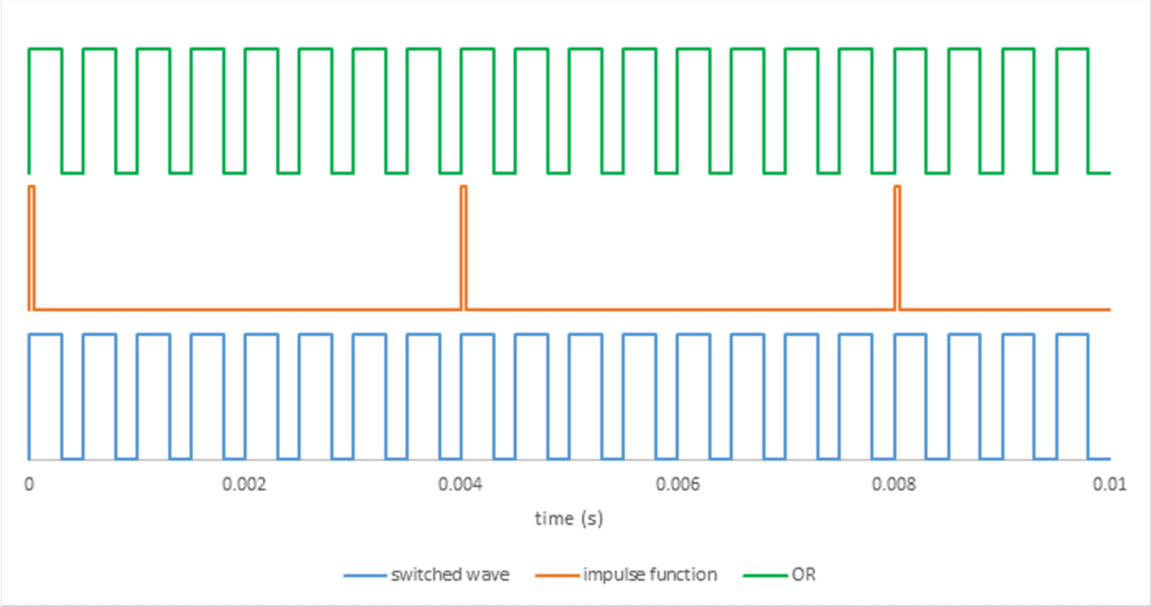

Figure 3-24 : Example showing adding a low frequency impulse stream to the switching pattern with an OR function for an integer value of high to low frequency pulses (low frequency 250Hz, switching frequency 2kHz)

Care is needed under this scenario to match the impulse function timing to the switching frequency. When the low switched wave is a function of the switching frequency, one method is to increase the size of the "impulse function" so it forms a square wave pulse that has a low frequency, but the duty cycle is just sufficient so that when passed through an OR function with the pulse train it results in an increase in the pulse width as shown in Figure 3-25

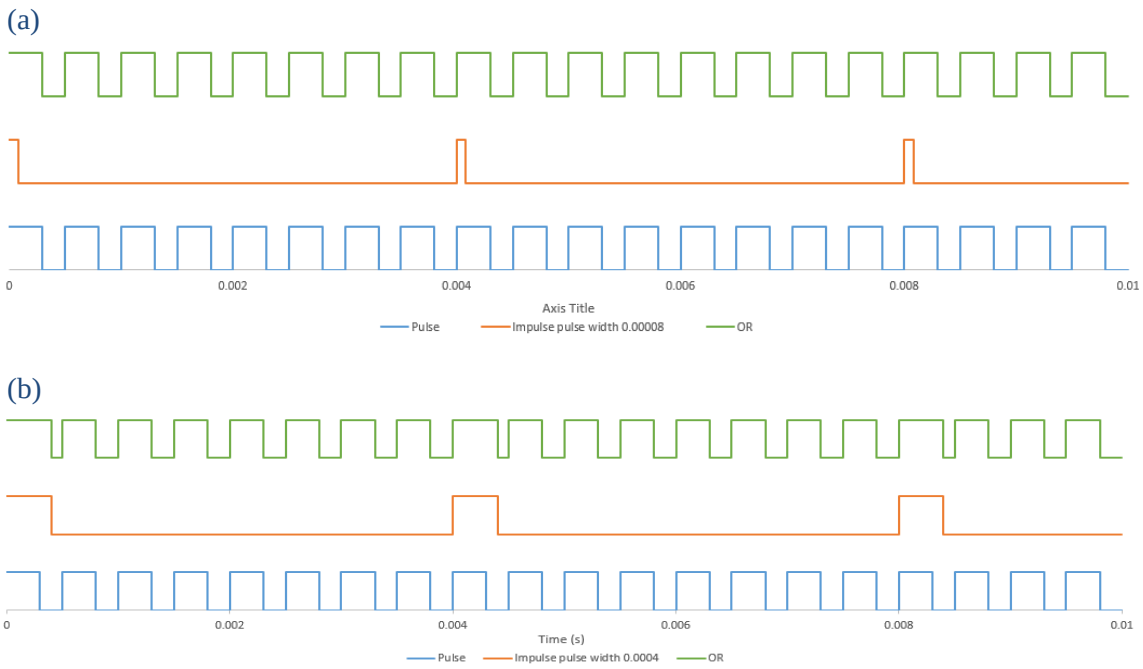

Figure 3-25 : Example showing detecting a low frequency impulse stream to the switching pattern with an OR function for an integer value of high to low frequency pulses for different duty cycle of a) 0.02, b) 0.1 (low frequency 250Hz, switching frequency 2kHz)

It is easier to analyse the impact of an impulse function when it is at a low frequency that is an integer value of the switching frequency as this can be done explicitly for comparison purposes with other sections having a non-integer values of N_p results in an analysis which need to be undertaken in code because of the complexity of the pulse formation with an OR or XOR function. Therefore the analysis in this thesis will look only at integer values of low frequency waveforms for convenience in conjunction with an OR function.

Table 3-2: Comparison of using integer and non-integer low frequency in PWM with an Impulse function simulation model

	Current ripple OR combination	Current ripple XOR combination	Fourier analysis
f_0 as an integer multiple of f_s	Increase average duty cycle due to additional impact of pulse width	Not practical	Straight forward Fourier analysis
f_0 as a non-integer multiple of f_s		No addition to average boost ratio	Complex Fourier analysis

3.5.1 Harmonic analysis of gate drive circuit PWM

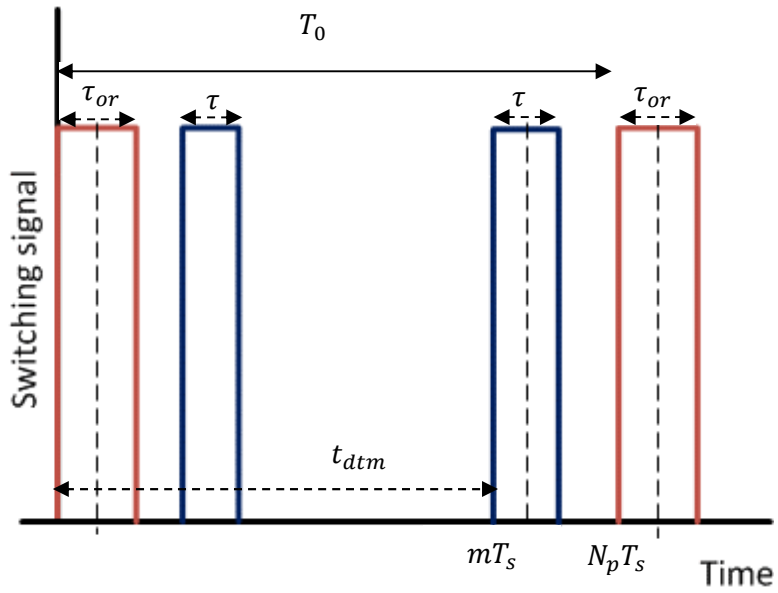

Figure 3-26 : Impulse function combined with first pulse in series

When the low frequency is an integer of the switching frequency then the Fourier series of a periodic square wave where the first function is the combination of the impulse function and normal pulse train as shown in Figure 3-26 is:

$$f_0(t) = \frac{2A\tau_{or}}{T_0} + \frac{2A}{\omega_0 T_0}\sum_n \frac{1}{n}(\sin(n\omega_0\tau_{or})\, cos(n\omega_o t) + \frac{1}{n}(1 - \cos(n\omega_0\tau_{or}))sin(n\omega_o t))$$ Equation 3-65

Where τ_{or} is the width of the "OR" of the impulse and pulse train which re-occurs again after time, T_o The harmonic spectrum for this first function is

$$C_{1,n=} \frac{2A}{\omega_0 T_0}\left(\sum_n \frac{1}{n}(\sin(n\omega_0\tau_{or})\, cos(n\omega_o t) + \frac{1}{n}(1 - \cos(n\omega_0\tau_{or}))sin(n\omega_o t)\right)$$ Equation 3-66

The remaining functions are made up of the regular rectangular pulse train with a time delay t_{dtm}, which can be calculated from:

$$t_{dtm} = mT_s$$ Equation 3-67

These functions have a different pulse width to the first one as they have no impulse component as:

$$f(t_m) = \left(\frac{2A\tau}{T_0} + \frac{2A}{\omega_0 T_0}\left(\sum_n \frac{1}{n}(\sin(n\omega_0\tau)\, cos(n\omega_o t) + \frac{1}{n}(1 - \cos(n\omega_0\tau))sin(n\omega_o t)\right)\right)e^{-jn\omega_o t_{dtm}}$$ Equation 3-68

The combined frequency spectrum of all the pulses is therefore equal to

$$C_0 = \frac{2A\tau_{or}}{T_0} + \sum_{k=1}^{N_p-1}\frac{2A\tau}{T_0}$$ Equation 3-69

$$C_n = \frac{2A}{\omega_0 T_0}(\sin n\omega_0\tau_{or} - j(1 - \cos n\omega_0\tau_{or})) + \frac{2A}{n\omega_0 T_0}\sum_{k=1}^{N_p-1}(\sin n\omega_0\tau - j(1 - \cos n\omega_0\tau))e^{-jn\omega_0(k)T_s}$$ Equation 3-70

The full Fourier analysis calculations are presented in Appendix B. Figure 3-27 shows an example of the harmonics of the gate drive signal for a variation of the starting point with a low frequency harmonic using Equation 3-70. As can be seen, a low frequency component is visible.

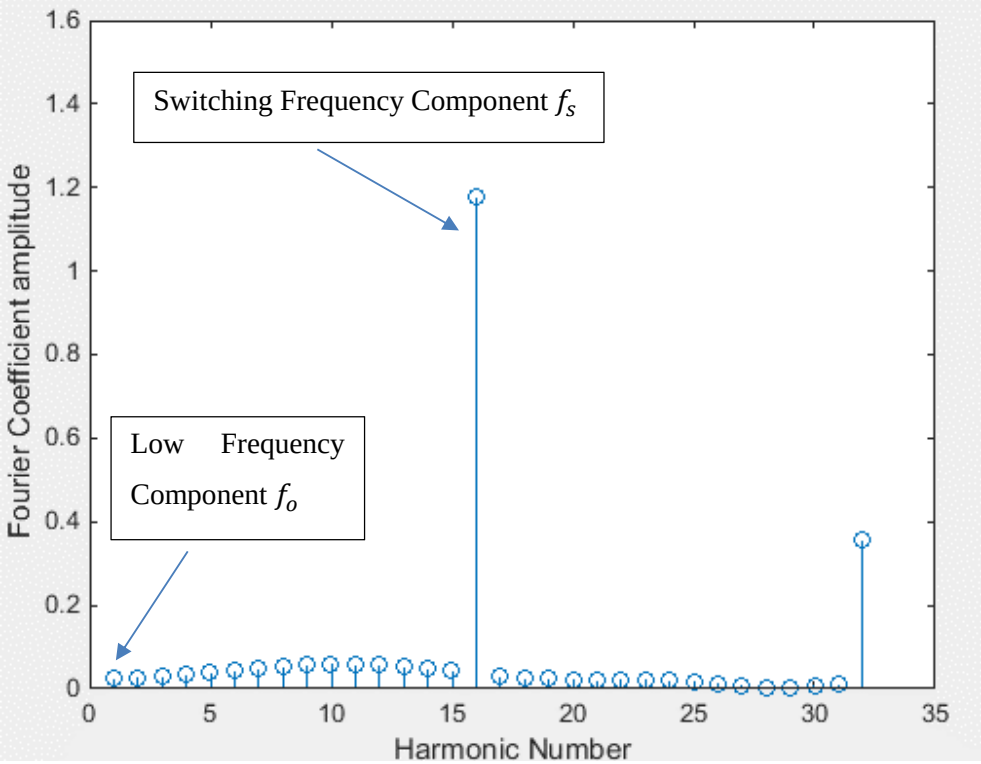

Figure 3-27 : Low frequency components of PWM with an Impulse function Fourier coefficient C_n with a 125Hz impulse wave of width 0.0004s

The width of the impulse function is dependent on the simulation and experimental hardware accuracy available. The work in this thesis uses an OpalRT real time controller to generate and capture waveforms operates, in real time with a fixed time step solver [286], [287], with a minimum fixed time step of 20μs. In order to get accurate and repeatable impulse type functions it is necessary to ensure that the pulse start, end and pulse width, over the defined low frequency duty cycle and period are all multiple integers of this minimum fixed time step. Some examples of this are shown in Figure 3-28. What this shows is that the duty cycle for the impulse function changes depending on the frequency of the pulse required. This complicates the coding when sweeping the frequency across a range to replicate EIS.

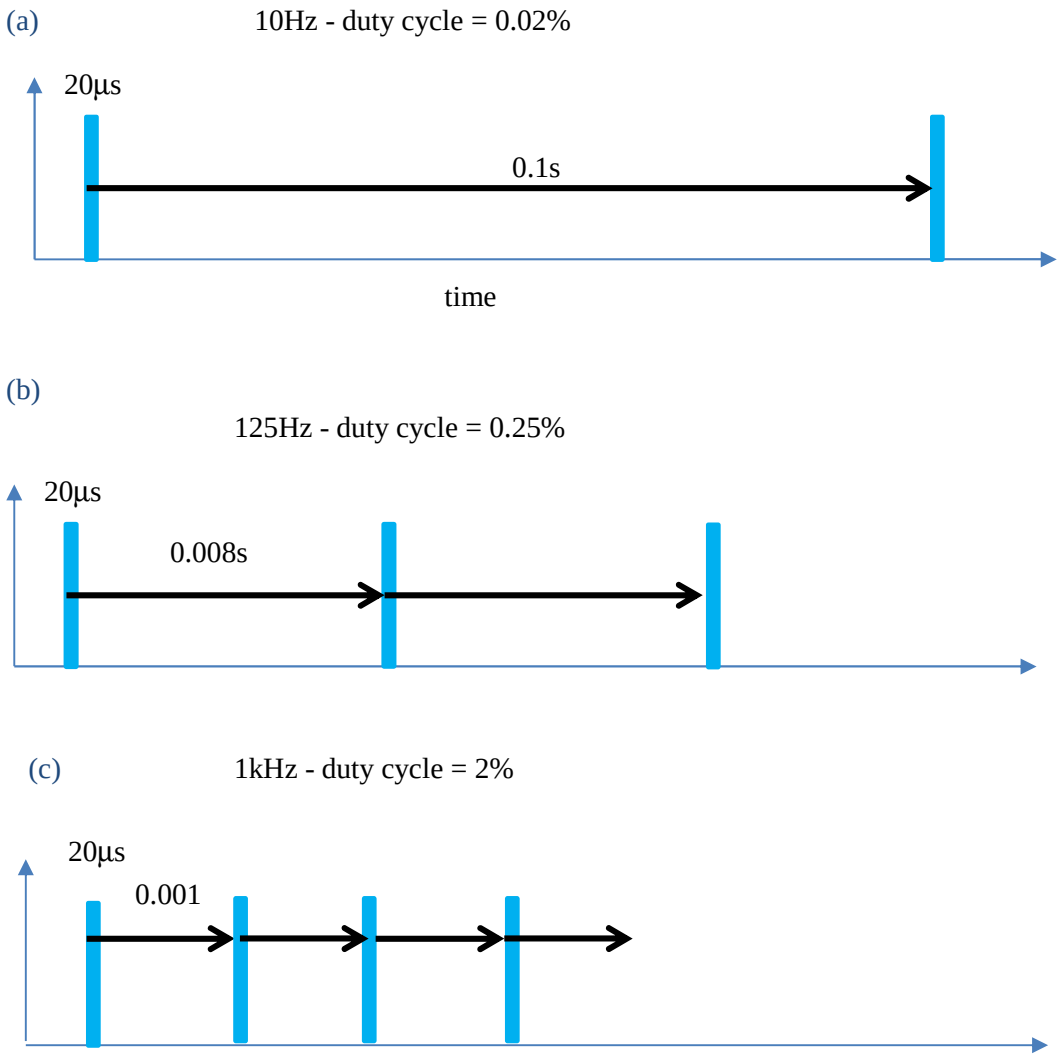

Figure 3-28 : Example showing how the impulse width can be chosen for a) 10Hz, b) 125Hz, c) 1kHz

3.5.2 Harmonic analysis of impulse PWM current waveform

The current waveform analysis is undertaken as a summation of sawtooth functions. The first function is a periodic sawtooth function with a period of T_0 and duration τ_{or} from u_o to v_o. The second function is a periodic sawtooth wave with the opposite slope with a period of T_o but shifted with respect to the first waveform by T_i+dT_s from v_o to u_1. The second function is identical to the first one but has an additional time shift. As shown in Figure 3-29 the battery current increased at each interval the impulse function is added seen by the extra rise time on the first pulse τ_{or}.

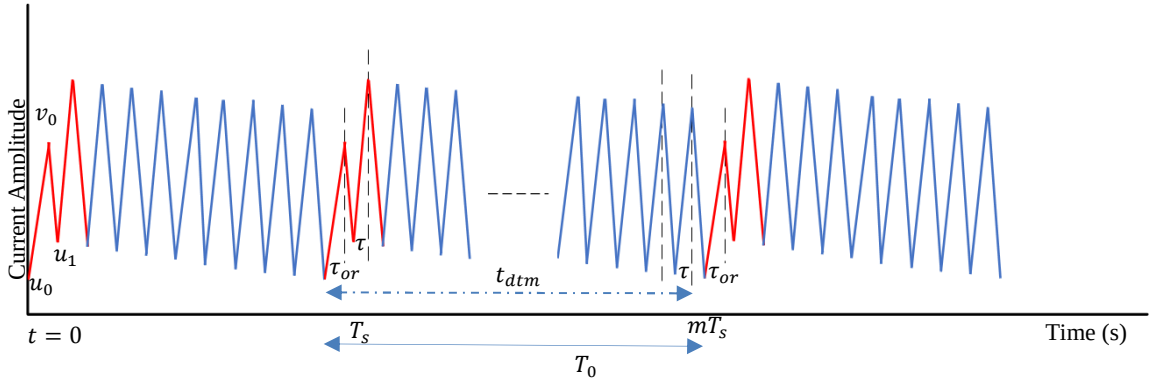

Figure 3-29 : Current Waveform for a PWM with an impulse function

The harmonic spectrum of the m^{th} function is shown in Appendix C in full. This produces a harmonic spectrum as shown in Figure 3-30 using Equation C-120.

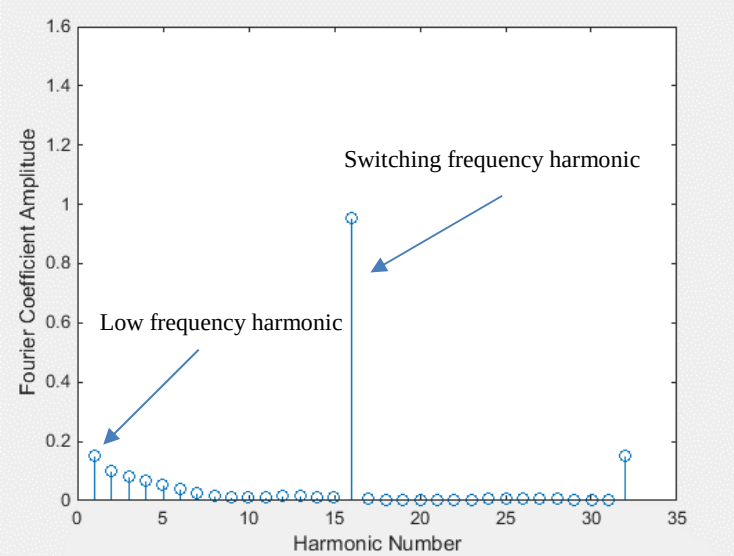

Figure 3-30 : Harmonics of the Li-ion battery current signal with an impulse function added at 125Hz.

3.5.3 Cross check of circuit boost ratio

The boost ratio for this method is higher than for a fixed duty cycle wave due to the extra "on" time of the pulse over one low frequency impulse. This can either be considered negligible and ignored or can be compensated for by reducing the boost ratio by a proportionate quantity. As the impulse function only operates once every low frequency cycle, its effects are transient in nature and the circuit then settles back to a steady state condition as shown in Figure 3-29.

In steady state condition the inductor current over the first switching cycle in boost mode in an ideal converter can be calculated as by using Equation 3-71 and Equation 3-72

$$\Delta i_{on,1} = \frac{1}{L} V_{bat}(dT_s + T_i)$$ Equation 3-71

$$\Delta i_{off,1} = \frac{1}{L}(V_{bat} - V_{dc})(T_s - T_i - dT_s)$$ Equation 3-72

where V_{bat} is battery voltage, V_{dc} is the converter output voltage, T_s is the switching period, T_i is the width of the impulse function, $\Delta i_{on,1}$ increasing inductor current and $\Delta i_{off,1}$ decreasing inductor current over the 1st switching cycle period. In equilibrium the change in inductor current over a low frequency cycle is zero:

$$\frac{1}{2} L \sum_{m=0}^{N_p-1} \Delta i_{L_m}^2 = 0$$ Equation 3-73

$$\sum_{m=0}^{N_p-1} \Delta i_{on,m} + \sum_{m=0}^{N_p-1} \Delta i_{off,m} = 0$$ Equation 3-74

$$\sum_{m=0}^{N_p-1} \Delta i_{on,m} = \frac{1}{L} V_{bat} \left((dT_s + T_i) + \sum_{m=1}^{N_p-1} dT_s \right) = \frac{1}{L} V_{bat} N_p dT_s + \frac{1}{L} V_{bat} T_i$$ Equation 3-75

$$\sum_{m=0}^{N_p-1} \Delta i_{off,m} = \frac{1}{L}(V_{bat} - V_{dc})(T_s - T_i - dT_s) + \sum_{m=1}^{N_p-1} \frac{1}{L}(V_{bat} - V_{dc})(T_s - dT_s)$$ Equation 3-76

$$\sum_{m=0}^{N_p-1} \Delta i_{off,m} = \frac{T_s}{L} N_p (V_{bat} - V_{dc})(1 - d) - \frac{T_i}{L}(V_{bat} - V_{dc})$$ Equation 3-77

Summing the current gives:

$$\frac{1}{L} V_{bat} N_p dT_s + \frac{1}{L} V_{bat} T_i + \frac{T_s}{L} N_p (V_{bat} - V_{dc})(1 - d) - \frac{T_i}{L}(V_{bat} - V_{dc}) = 0$$ Equation 3-78

Simplifying gives:

$$V_{bat} N_p T_s - V_{dc} N_p T_s + V_{dc} N_p T_s d + V_{dc} T_i = 0$$ Equation 3-79

setting T_i as a function of N_p and T_s by including a constant C_1 allows further simplification:

$$T_i = C_1 N_p T_s$$ Equation 3-80

$$V_{bat} - V_{dc} + V_{dc} d + C_1 V_{dc} = 0$$ Equation 3-81

$$\frac{V_{dc}}{V_{bat}} = \frac{1}{(1 - d - C_1)}$$ Equation 3-82

For example, at a low frequency of 125Hz in a 0.6 duty cycle, 2kHz switched waveform with a 20µs impulse pulse this equates to a constant C_1 of 12.5×10^{-3} and a boost ratio of 2.58 compared to 2.5 without the impulse function. The increase in duty cycle is dependent on the pulse width which is a function of the hardware.

3.5.4 Inductor ripple calculation of impulse method

The peak to peak ripple compared to a fixed boost ratio varies due to the extra "on" time of the pulse over one low frequency impulse. This can be calculated by considering the extra rise time on the first pulse. Assume that a circuit with a fixed duty cycle, fixed switching frequency and fixed starting

position has a ripple current of magnitude 1pu over a switching time period 1pu, such that on each interval d the current increases at a steady rate of 1/ d and in each interval $d-1$ the current decreases at a steady rate of $1/(1-d)$. The extra time on due to the impulse function increases the current at the same rate 1/d but for a longer time period. This period is dependent on the width of the "impulse" in relation to the regular switching pattern. The increase in ripple is therefore

$$\frac{\tau_{or}}{\tau} = \frac{dT_s+T_i}{dT_s}$$ **Equation 3-83**

3.6 Battery balancing circuit

This section looks at using hardware in the battery balancing circuiting to inject a low frequency excitation signal.

In battery systems, battery cells can be connected in series and/or parallel depending on the type of application they are used in. Charging and discharging battery cells as a series string can cause charge imbalance in the battery cells. This is because of the mismatch in battery internal impedance, different state of charge level, capacity range, self-discharge rate differences, varying operating conditions, and temperature difference across the cells [135]–[137]. Battery charge imbalance may result in over charging or over discharging of the cells with lower capacity. In imbalanced battery systems; the voltage of the individual battery cells could drift apart and lead to a decrease in lifespan and possible failure of the battery pack [137], [288], [289]. Therefore using an equaliser or balancing system, is usual in applications. Battery balancing uses extra hardware to equalise the battery series strings.

Battery balancing system can be categorised into two groups; passive and active balancing. In passive balancing [290]–[292], a resistor is used to dissipate the energy from the fully charged cell till its voltage reaches the same level as battery with lower voltage value. This is also known as shunt resistor balancing. This method is straightforward to implement at low-cost, but system energy is dissipated as heat within the resistors. Active balancing may be more expensive and may require a control system. In an active balancing group, battery cells are balanced by transferring the energy from the higher energy to the lower energy cell. This is subcategorised as capacitor based balancing [293]–[298], converter based balancing [299]–[303], and inductor/ transformer based balancing [304]–[311].

Authors [136], [137], [312]–[314] compared and reviewed current balancing methods. According to [136], [137], a capacitor based balancing topology requires more straightforward control methods and is well used compared to a converter based or transformer based balancing. In this research, a capacitor based balancing method is therefore chosen for proof of concept of the methodology. A comparison of different active capacitor based balancing is presented in Table 3-3. In inductor and transformer based balancing topologies, inductors and transformers are used to transfer the energy from single cells or group of cells with higher energies to the lower energies. These methods can be sub categorised as single/multi-inductor [293], [308], [309], single windings transformer , multi windings transformer [304], [310], [313]. This balancing approach is reported as being more expensive, with fast balancing speed with complex control systems and accurate voltage sensing. Energy converters namely: Cuk converter [315], buck or/and boost converter [316]–[318], flyback converter [319], [320], and ramp converter [321], [322] are described as alternative methods of cell balancing. These types of circuits are complex and may contain stacked converters. It is not clear at this stage if there is scope to introduce low frequency excitation through battery balancing aspect of the converter. There is scope for future work to look at alternative battery balancing methods to produce a low frequency excitation signal but this is considered beyond the scope of this these.

Table 3-3: capacitor based battery balancing method comparison

Balancing methods	Summary
Switched capacitor	Energy is transferred from the cell with higher energy to the lower energy cell through the switching capacitor. n-1 capacitors and 2n switching component are required to balance n cells. An example of the switched capacitor balancing for 3 battery cells is shown in Figure 3-31 a. and described in more detail below
Single Switched capacitor	Figure 3-31 b shows battery balancing using a single switched capacitor. Only one capacitor and n+5 switches are used to balance n battery cells. A control system is needed to detect the higher and lower voltage battery cells to transfer the energy between the cells using the corresponding switches.
Doubled-tiered capacitor	This balancing topology is similar to the switched capacitor method but requires n capacitors. As illustrated in Figure 3-31 c, the first capacitor tier is used to balance the battery cells and the second tier capacitor is used to speed up the balancing time.
Modularised Switched Capacitor	As shown in Figure 3-31 d, the battery cells are divided into modules, in each module the batteries are balanced with the sub-modules cells with a separate balancing system. In this technique n-1 capacitor and 2n+2m switches are required. Where n is number of battery cell and m is number of modules.

In this study, a straightforward switched capacitor balancing system is used to generate excitation low-frequency signal as a proof concept due to its popularity in literature. The schematic figure of two battery cells and converter with the switched capacitor balancing technique is shown in Figure 3-32. The switched capacitor system is connected to the battery and it is proposed to use this circuit to inject a low-frequency signal. The impedance of the battery is calculated by harmonic analysis of the measured battery current and voltage data at the frequency point, then the frequency is swept to generate the EIS impedance measurement over the frequency range.

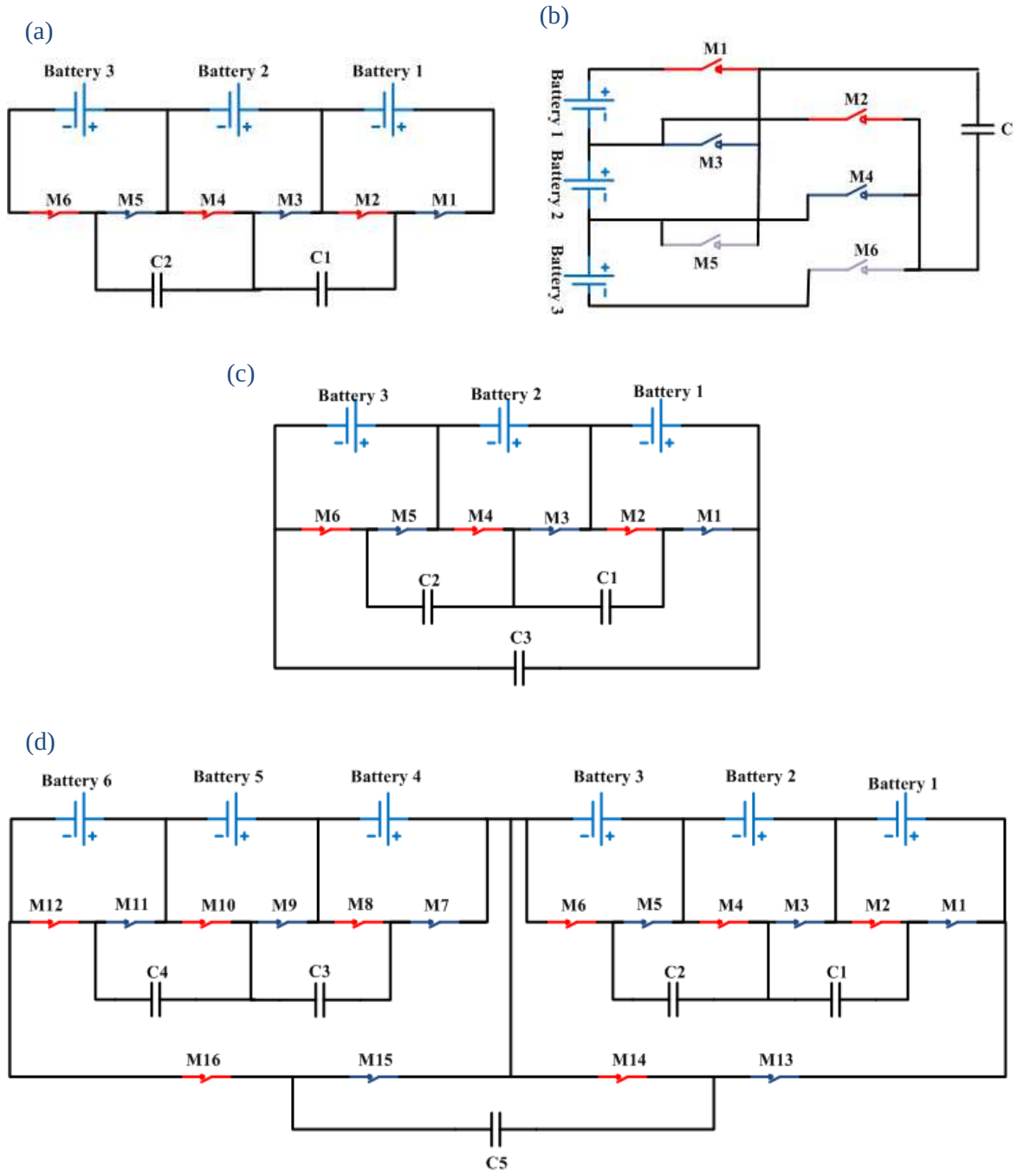

Figure 3-31 : Examples of switched capacitor balancing: a) Switched Capacitor, b) Single Switched Capacitor, c) Double-tiered Capacitor, d) Modularised Switched capacitor[136]

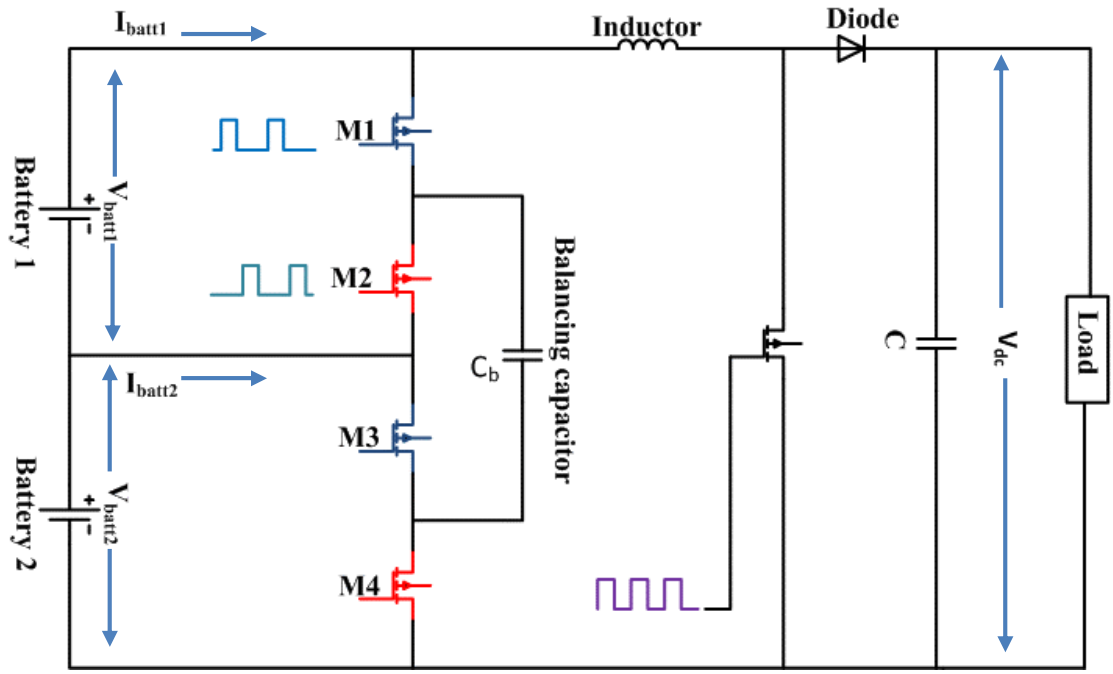

Figure 3-32 : Switched capacitor battery balancing circuit

3.6.1 Circuit Operation

For proof of concept, two series battery cells (as opposed to one, in contrast to the other methods in this thesis) are connected to the load through the boost converter while the terminals of each battery are connected to the balancing circuit (see Figure 3-32). In this battery balance circuit, one capacitor and four MOSFET (switches) are used. The switch M1 – M4 were operate to produce a low frequency excitation signal. The value of the capacitor was chosen so that the low frequency switching allows energy transfer between the two batteries. The time constant of the battery balancing system is set to approx. 0.3ms so over several high frequency switching operations the capacitor will have charged. This was done by assuming a circuit resistance of approx. 30mΩ made up of battery resistance, capacitor ESR, MOSFETs on resistance, leads and connectors and choosing a capacitor at 10mF. The system works in two stages as shown in Figure 3-33;

For example, when the voltage of the battery 1 is higher than battery 2.

1) Switch M1 and M3 are turned on and M2 and M4 are turned off, the capacitor will connected in parallel with the battery 1 through M1 and M3 (see Figure 3-33a). The capacitor then starts to charge from battery 1.
2) Switches M2 and M4 are turned on and M1 and M3 are turned off, the capacitor will be connected in parallel with the battery 2 through M2 and M4 (see Figure 3-33b). The capacitor starts to discharge to battery 2.

Two pulse signals with the duty cycle of less than 0.5 are used for controlling the switches M1-M4 [295]. The reason for choosing a duty cycle less than 0.5 is to avoid a short-circuit condition or current shoot-through when all switches are turned on at once. In this system, a duty cycle of 0.45 is used for the pulse signals. One pulse signal is used for charging the capacitor from the battery cell with higher voltage. The other pulse signal is used for discharging the capacitor to the battery cell with lower voltage. The frequency of the battery balancing is at a lower battery frequency than the boost converter switching frequency, to induce the low frequency excitation signal.

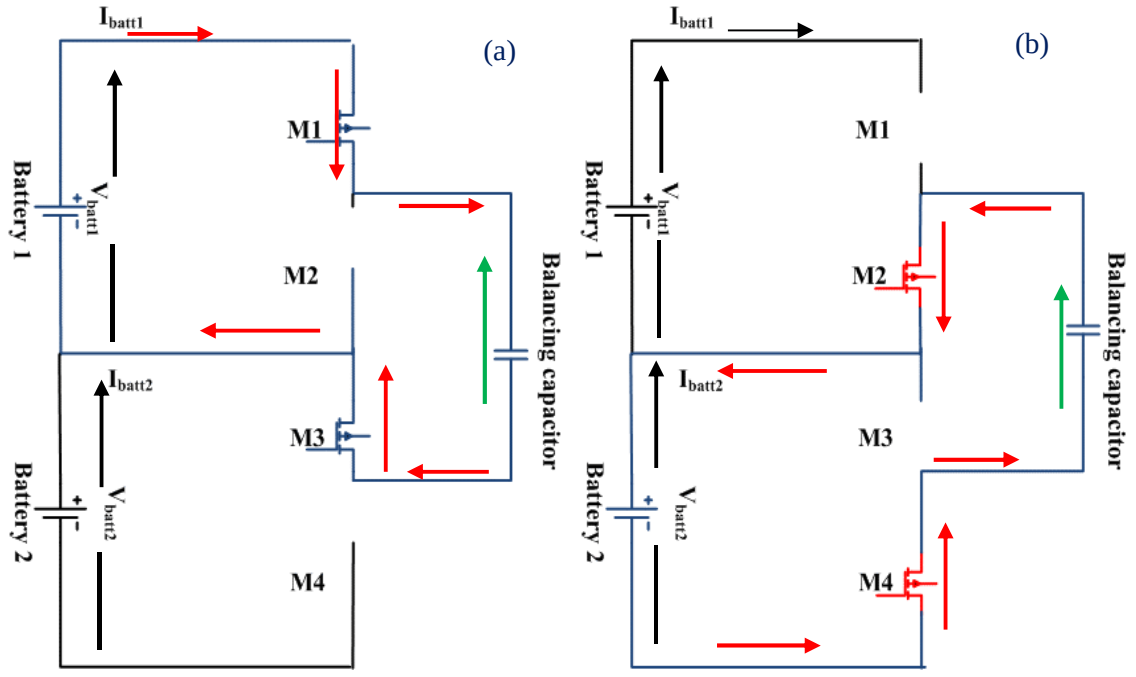

Figure 3-33 : Switching capacitor battery balancing circuit operation a) stage one b)stage two

In this thesis the duty cycle, d of the converter, is fixed giving a traditional sawtooth pattern through the inductor. However, the battery voltages are subject to a small perturbation caused by the balancing capacitor charging and discharging low frequency injection as shown in Figure 3-34. The minimum voltage of the balancing capacitor is equal to the battery with lower voltage value (V_{bat2}), and the maximum value of the balancing capacitor is equal to the battery with higher voltage value (V_{bat1}).

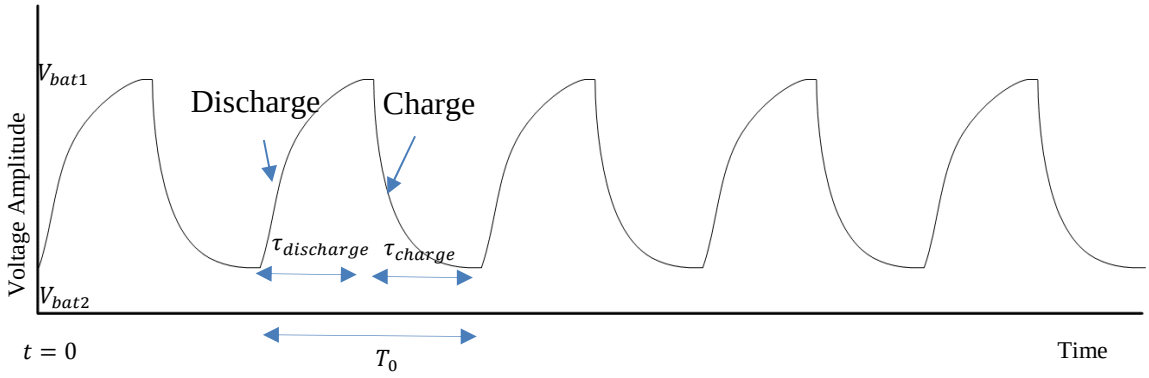

Figure 3-34 : Charging and discharging voltage Waveform for the Balancing capacitor at the low frequency

When the switches M1 and M3 are on the capacitor charges from battery 1 with a current equal to:

$$i_{cb_charge} = C\frac{(V_{bat1} - V_{bat2})}{\tau_c}\, e^{-\frac{t}{\tau_c}}$$ **Equation 3-84**

When the switches M2 and M4 are on the capacitor discharges to battery 2, with a current equal to:

$$i_{cb_discharge} = C\frac{dV_{c_{discharging}}}{dt} = -C\frac{(V_{bat1} - V_{bat2})}{\tau_c} e^{-\frac{t}{\tau_c}}$$ **Equation 3-85**

3.6.2 Harmonic analysis of the battery balancing current waveform

It is not necessary to look at the harmonics of the boost converter gate drive circuit as this is operating with a fixed duty cycle at fixed frequency. The harmonic analysis of the battery current is therefore undertaken by considering the superposition of the boost converter current and the current caused by the battery balancing circuit using the Fourier transform property of linearity. The current on the battery with the higher voltage increases at each interval f_0 as the capacitor current added to the boost converter current. While the current on the battery with the lower voltage decreases when connected to the capacitor. Figure 3-35 shows the charge and discharge current of battery 1 and battery 2. The current of each battery needs to be analysed separately for calculating the impedance of the individual cell.

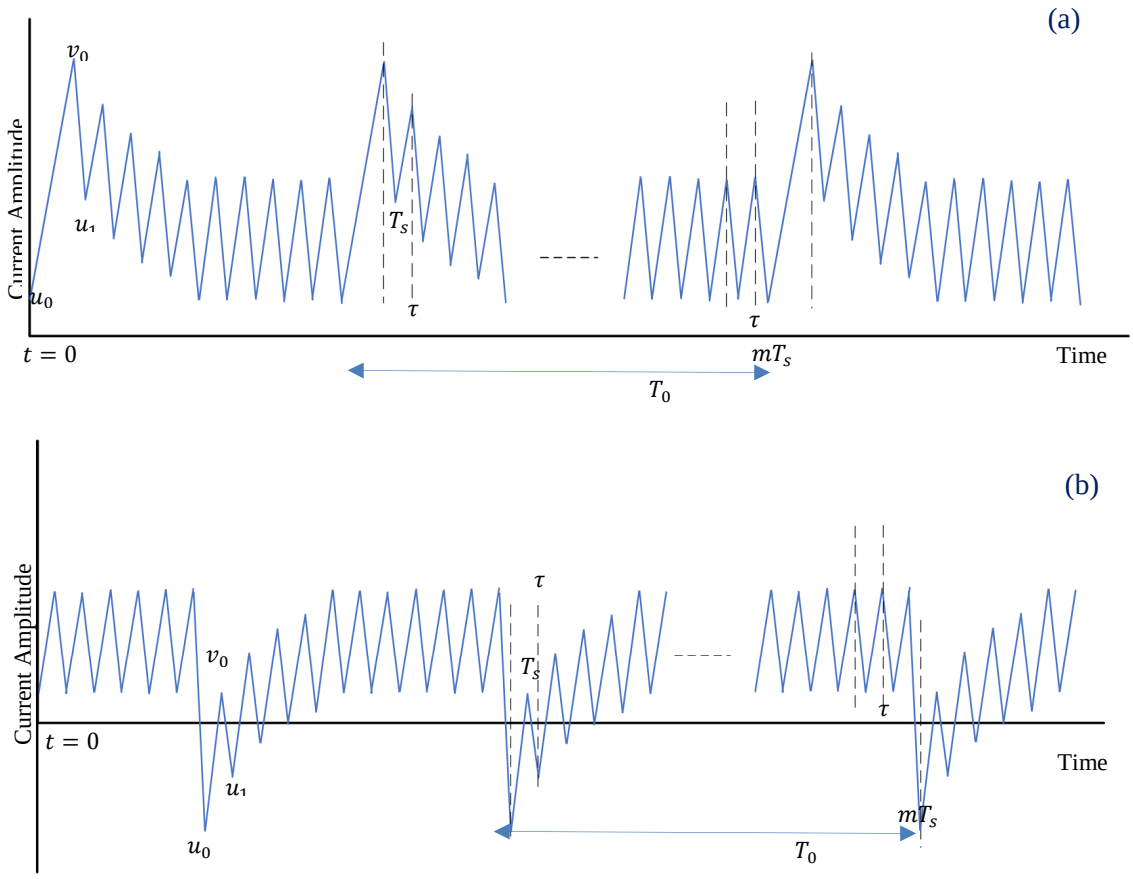

Figure 3-35 : Current Waveform for a Battery Balancing method a) Battery 1 discharge current, b)Battery 2 charge current

The converter current over one switching cycle in boost mode in an ideal converter for battery 1 can be calculated traditionally as:

$$\Delta i_{on} = \frac{1}{L}(V_{bat1} + V_{bat2})dT_s \quad \text{Equation 3-86}$$

$$\Delta i_{off} = \frac{1}{L}(V_{bat1} + V_{bat2} - V_{dc})(T_s - dT_s) \quad \text{Equation 3-87}$$

While the capacitor current is given by Equation 3-84 and Equation 3-85. The current waveform of the battery 1 is the sawtooth waveform with the exponential signal of the balancing capacitor. The harmonic spectrum of the current waveform is shown in Appendix C in full. This produces a harmonic spectrum as shown in Figure 3-36 and Figure 3-37 using Equation C-148.

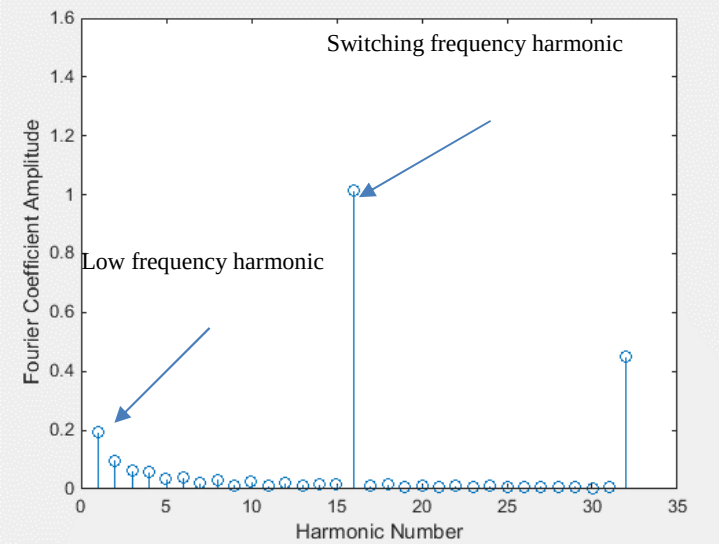

Figure 3-36 : Theoretically derived harmonics of the Li-ion battery1 current signal with a balancing capacitor charge signal at a low frequency of 125Hz, V_{bat1}=3.2V, V_{bat2}= 3V

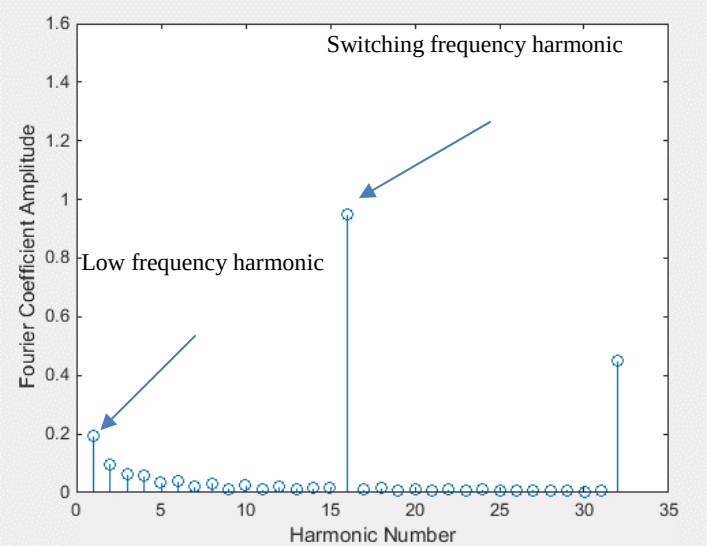

Figure 3-37 : Theoretically derived harmonics of the Li-ion battery2 current signal with a balancing capacitor discharge signal at a low frequency of 125Hz, V_{bat1}=3.2V, V_{bat2}= 3V

3.6.3 Inductor ripple calculation of battery balancing method

There is a negligible extra inductor current as the current from the capacitor will act to charge /discharge the batteries because of the low impedance path. This is dependent on the difference in battery voltage, so it is not fixed with time but varies as a function of the current. This gives rise to two points:

- The low frequency excitation is significantly reduced if the battery voltages are close. This is ok as monitoring is most valuable when a battery is degraded and therefore likely to be unbalanced.
- To keep this constant the low frequency which impacts the exponential decay through, can be altered based on the voltage difference to keep a constant ripple current.
- The method is dependent on a $\frac{dV}{dt}$ change in the capacitor. It is not clear if this technique can be used with a resistive balancing method similar to [138].

However, there is extra ripple current in each battery. This can be calculated by considering the increase in current due to the balancing capacitor current:

$$I_{cb} = C\frac{(V_{bat1} - V_{bat2})}{\tau_c}\, e^{-\frac{t}{\tau_c}}$$ **Equation 3-88**

3.7 Earth Leakage monitoring circuit

This section looks at a different method of injecting a low frequency excitation signal by manipulating Earth Leakage Monitoring (ELM) hardware that may be present in the system. In the UK, Earth leakage monitoring is required on any dc IT system, without an earth connection, with a voltage of over 50V [279]. There are a number of commercial earth leakage monitoring relay's on the market. These are split between devices which detect and monitor both ac and dc circuits [323], [324] and those that look only at dc systems [325]. An example of the operation for these devices (there are others) is shown in Figure 3-38. A low frequency power source applies a signal between the positive and negative terminals of the dc system and ground. This is designed so that negligible current flows through the monitor under normal operation when there is no fault. In the event of an earth fault, an earth leakage current is detected by the instrumentation.

This research looks at a new method of using an earth leakage monitoring system to inject the low frequency component necessary for on-line EIS measurement to the battery and then sweep this frequency across a range of values to replicate the functionality of the EIS without the need for a separate excitation circuit, while maintaining the earth leakage detection functionality. The battery, as in the other sub sections, is connected through a dc/dc converter to a load. The battery voltage and current are measured and used to determine the harmonic impedance. The technique is conducted on-line with the battery system operating under normal operation. The changes to the earth leakage monitoring method means that, similar to the case where there is a separate EIS excitation circuit, the power electronic circuit and boost inductor will see a harmonic component not present under traditional ELM operation.

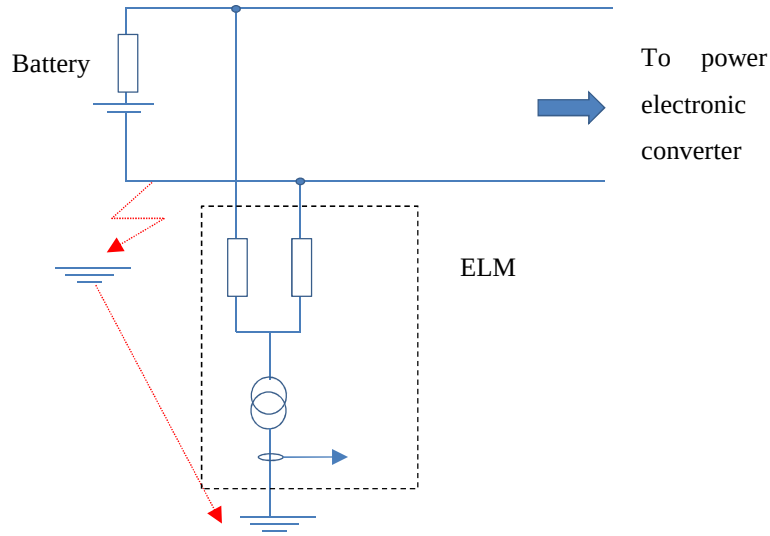

Figure 3-38 : A representation of Earth leakage monitoring circuit operation

3.7.1 Circuit Operation

The key requirement of this method is that it has to generate a low frequency waveform of variable frequency for the EIS calculation while at the same time ensuring normal operation of the remainder of the power system, in this case, a boost converter and the earth leakage monitoring system. The battery is connected to a boost converter, while the terminals of the battery are connected to an earth leakage monitor (ELM) to detect any leakage current between the battery terminals and ground. The key to using the ELM hardware is to generate a slightly different voltage across the terminal of the battery such that a low frequency signal can excite the circuit. Under normal operation there is a high impedance leakage to ground usually in the order of MΩ. This means that a small current exists in the circuit. Due to the low impedance of the battery (mΩ) it is difficult to pick up any current flowing through this in normal operation. Figure 3-39 shows some ways in which the circuit can be manipulated to increase the flow of leakage current through the battery system by deliberately skewing the current in the impedance connected to the positive and negative terminals of the battery. The circuit looks like a Wheatstone bridge circuit, and under traditional operation if the impedance in each leg of the ELM is set equal, the current through the battery would be zero as the leakage impedance from both terminals to ground is sufficiently high to be considered identical. A current source has a high impedance associated with it and therefore under normal battery operation there is a negligible DC current flowing from the battery through the ELM. The current source has been replaced in this thesis with a voltage source to tie up better with available laboratory equipment and the high impedance to dc is provided by a capacitor in series with the impedance in each leg of the ELM.

In this chapter the ELM is represented by the circuit in Figure 3-39c for convenience (this is assumed reasonable as many ELM devices are protection relays and therefore have multiple power sources). The AC sources have the same voltage amplitude but have a phase shift with respect to each other. The frequency of the ac source is swept over the frequency range for the EIS calculation. The ELM circuit also sees the input impedance of the power converter and load and therefore there is an additional ac component present in the power electronics.

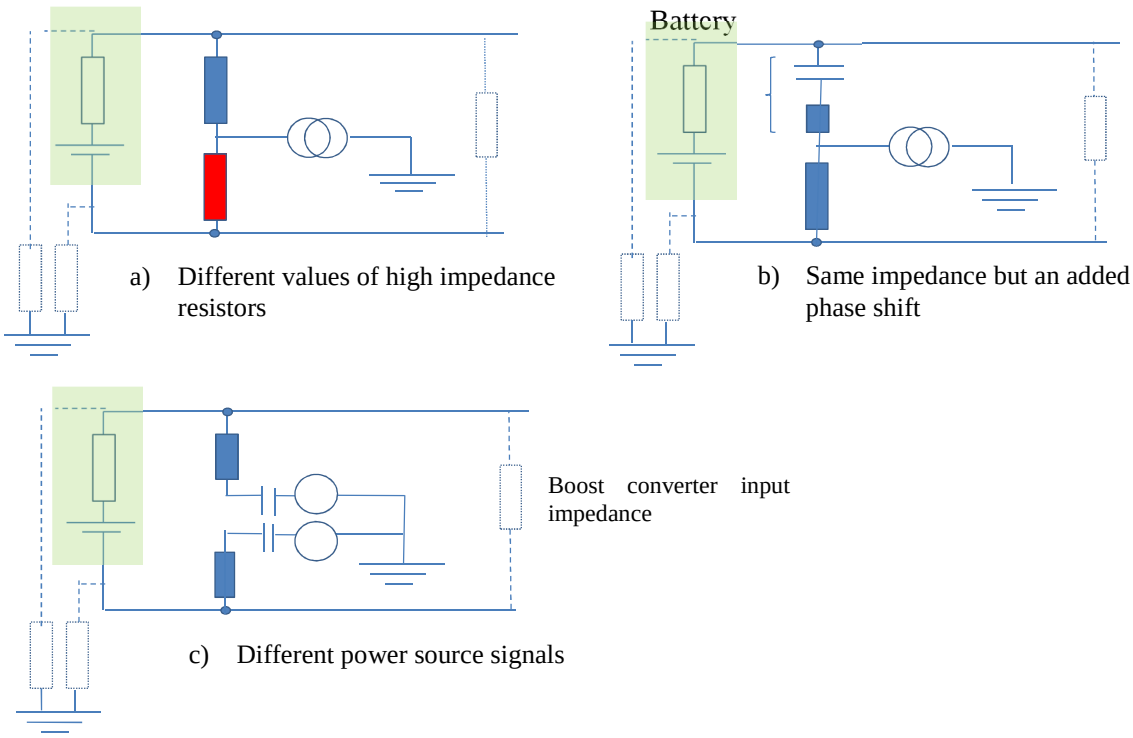

Figure 3-39 : Different methods of generating an excitation signal through ELM equipment

The ELM signal adds to the normal circuit operation through super-position to create additional ripple across the battery. To determine what this extra ripple will be – it is necessary to consider the small signal model of the boost converter under open loop control (in this case with ideal components).

When the switch is on:

$$V_{bat} = L\frac{dI_{bat}}{dt} \quad \text{Equation 3-89}$$

$$\frac{V_{dc}}{R_L} = -C\frac{dV_c}{dt} \quad \text{Equation 3-90}$$

When the switch is off:

$$V_{bat} = L\frac{dI_{bat}}{dt} + V_{dc} \quad \text{Equation 3-91}$$

$$\frac{V_{dc}}{R_L} = I_{bat} - C\frac{dV_{dc}}{dt} \quad \text{Equation 3-92}$$

For a small signal model, averaging, perturbation and linear approximation are used. The averaged equations are:

$$\bar{V}_{bat} = L\frac{d\,(\bar{I}_{bat})}{dt} + (1-\bar{d})\bar{V}_{dc} \quad \text{Equation 3-93}$$

$$\frac{\bar{V}_{dc}}{R_L} = (1-\bar{d})\bar{I}_{bat} - C\frac{d\bar{V}_{dc}}{dt} \quad \text{Equation 3-94}$$

In this thesis the duty cycle, d, is fixed, but the voltage V_{bat} can be considered subject to a small perturbation caused by the ELM low frequency injection.

$$\bar{V}_{bat} + \tilde{v}_{ELM} = L\frac{d\,(\bar{I}_{bat}+\tilde{\imath}_{ELM})}{dt} + (1-\mathrm{d})(\bar{V}_{dc}+\tilde{v}_{dc}) \quad \text{Equation 3-95}$$

$$\frac{\bar{V}_{dc}+\tilde{v}_{dc}}{R_L} = (1-d)(\bar{I}_{bat}+\tilde{\imath}_{ELM}) - C\frac{d(\overline{V}_{dc}+\tilde{v}_{dc})}{dt} \quad \text{Equation 3-96}$$

Using linearisation, a set of DC equations can be obtained as follows:

$$\bar{V}_{bat} = (1-\mathrm{d})\bar{V}_{dc} \quad \text{Equation 3-97}$$

$$\frac{\bar{V}_{dc}}{R_L} = (1-d)\bar{I}_{bat} \quad \text{Equation 3-98}$$

Giving a DC input impedance to the power electronic converter of:

$$\bar{Z}_{PE} = \frac{\bar{V}_{bat}}{\bar{I}_{bat}} = (1-\mathrm{d})^2 \mathrm{R}_L \quad \text{Equation 3-99}$$

From the parameters in the simulation chapter 4.7**.** This approximates to:

$$\bar{Z}_{PE} = 16(1-0.6)^2 \approx 2.56\Omega \gg Z_{BAT} \quad \text{Equation 3-100}$$

A similar set of equations for the AC signal can be obtained:

$$\tilde{v}_{ELM} = sL\tilde{\imath}_{ELM} + (1-\mathrm{d})\tilde{v}_{dc} \quad \text{Equation 3-101}$$

$$\frac{\tilde{v}_{dc}}{R_L} = (1-d)\tilde{\imath}_{ELM} - sC\tilde{v}_{dc} \quad \text{Equation 3-102}$$

Substituting gives

$$\frac{\frac{\tilde{v}_{ELM}-sL\tilde{\imath}_{ELM}}{(1-\mathrm{d})}}{R_L} = (1-d)\tilde{\imath}_{ELM} - sC\frac{\tilde{v}_{ELM}-sL\tilde{\imath}_{ELM}}{(1-\mathrm{d})} \quad \text{Equation 3-103}$$

$$\tilde{v}_{ELM} - sL\tilde{\imath}_{ELM} = R_L(1-d)^2\tilde{\imath}_{ELM} - sCR_L(\tilde{v}_{ELM} - sL\tilde{\imath}_{ELM}) \quad \text{Equation 3-104}$$

$$\tilde{v}_{ELM}(1+sCR_L) = R_L(1-d)^2\tilde{\imath}_{ELM} + sL\tilde{\imath}_{ELM} + sCR_{ELM}\,sL\tilde{\imath}_{ELM} \quad \text{Equation 3-105}$$

$$\tilde{Z}_{PE} = \frac{\tilde{v}_{ELM}}{\tilde{\imath}_{ELM}} = \frac{R_L(1-d)^2+sL+s^2CR_L\,L}{(1+sCR_L)} \quad \text{Equation 3-106}$$

At a value of 125Hz using the parameters from the simulation chapter (section 4) this results in an impedance of approximately:

$$\tilde{Z}_{PE} = \frac{16\times0.16+785\times3.8\times10^{-4}+785\times785\times0.0136\times16\times3.8\times10^{-4}}{(1+785\times0.0136\times16)} \quad \text{Equation 3-107}$$

$$\tilde{Z}_{PE} = \frac{2.56+0.3+51}{(1+170)} = 315m\Omega$$ Equation 3-108

This is again greater than the battery impedance. Therefore it can be assumed that the voltage produced by the ELM will produce negligible additional ripple on the current. The impedance of the circuit to the ac perturbation is shown in Figure 3-40. Which gives a voltage across the battery of approximately:

$$V_{bat,ac} \approx \frac{Z_{batt}}{Z_{batt}+20}\, 12\left(sin(\omega t) - \sin(\omega t + \frac{\pi}{4})\right)$$ Equation 3-109

$$V_{bat,ac} \approx \frac{Z_{batt}}{Z_{batt}+20}\, 24\left(sin\left(\omega t + \frac{\pi}{8}\right)\sin(-\frac{\pi}{8})\right)$$ Equation 3-110

$$V_{bat,ac} \approx \frac{Z_{batt}}{Z_{batt}+20}\, 9.2\left(sin\left(\omega t + \frac{\pi}{8}\right)\right)$$ Equation 3-111

This gives a peak of approximately 5mV which is small but detectable through the scope probes and of similar magnitude to EIS excitation signals in Table 2-7.

The earth leakage current in the event of a fault (as shown for example in Figure 3-39c) would register a current of approx. 2A rms:

$$I_{ELM} \approx 1.2\left(sin(\omega t) + \sin(\omega t + \frac{\pi}{4})\right)$$ Equation 3-112

$$I_{ELM} \approx 2.4\left(sin\left(\omega t + \frac{\pi}{8}\right)\cos(\frac{\pi}{8})\right)$$ Equation 3-113

$$I_{ELM} \approx 2.21\left(sin\left(\omega t + \frac{\pi}{8}\right)\right)$$ Equation 3-114

Within this circuit it is therefore possible to detect both an earth leakage current and a small EIS signal.

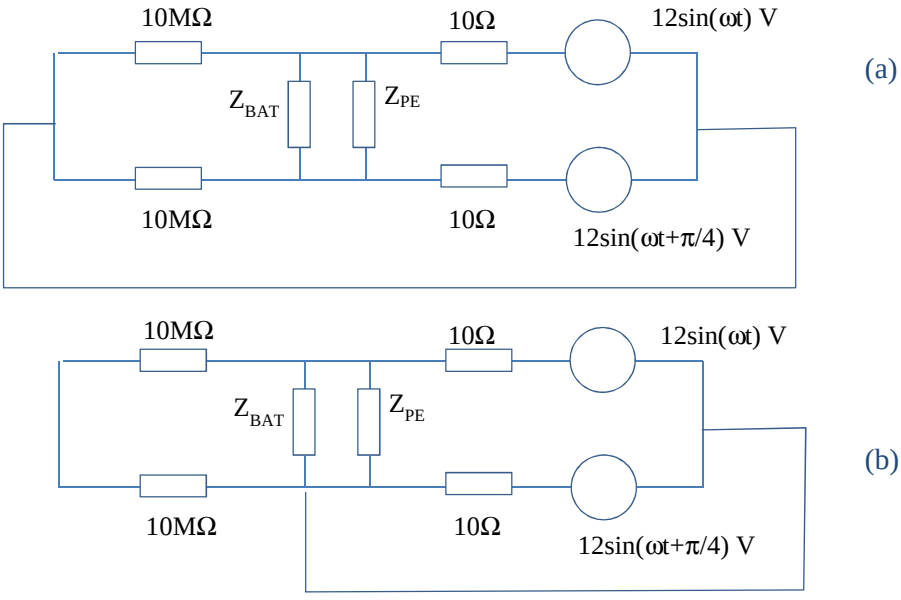

Figure 3-40 : An approximate circuit representation of the Earth leakage monitoring circuit under a) normal operation and b) under fault

3.7.2 Harmonic analysis of the ELM current method waveform

The current waveform seen from the battery using the ELM methods is the superposition of the ELM waveform and the sawtooth waveform. Fourier analysis can also be used to study the current waveform seen from the battery as shown in Figure 3-41. The harmonic spectrum of the current waveform is shown in Appendix C in full, but key equations are noted here.

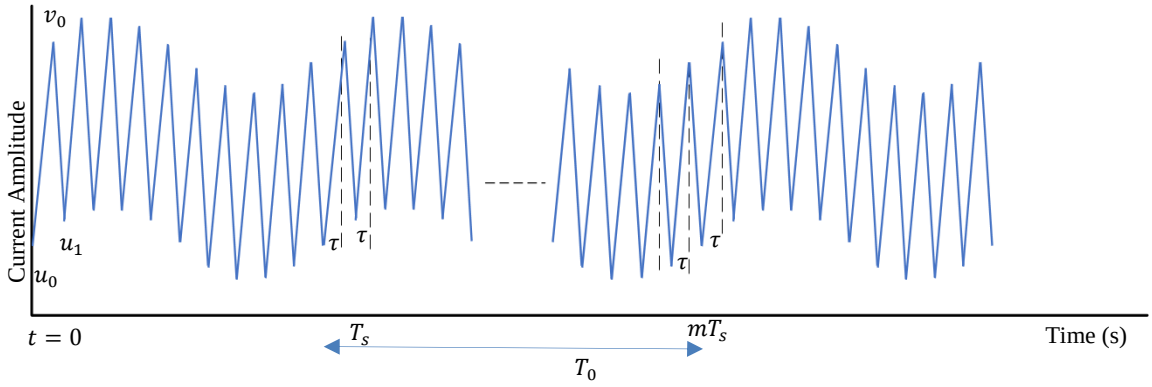

Figure 3-41 : Current Waveform for a ELM method

In steady state condition the inductor current over one switching cycle in boost mode in an ideal converter can be calculated as:

$$\Delta i_{on} = \frac{1}{L}(V_{bat} + \tilde{v}_{ELM})dT_s \quad \text{Equation 3-115}$$

$$\Delta i_{off} = \frac{1}{L}(V_{bat} + \tilde{v}_{ELM} - V_{dc})(T_s - dT_s) \quad \text{Equation 3-116}$$

$$\Delta i_{on} + \Delta i_{off} = \frac{1}{L}(V_{bat} + \tilde{v}_{ELM})dT_s + \frac{1}{L}(V_{bat} + \tilde{v}_{ELM} - V_{dc})(T_s - dT_s) \quad \text{Equation 3-117}$$

$$\Delta i_{on} + \Delta i_{off} = \frac{1}{L}V_{bat}dT_s + \frac{1}{L}\tilde{v}_{ELM}dT_s + \frac{1}{L}(V_{bat} - V_{dc})(T_s - dT_s) + \frac{1}{L}\tilde{v}_{ELM}(T_s - dT_s) \quad \text{Equation 3-118}$$

$$\Delta i_{on} + \Delta i_{off} = \frac{1}{L}V_{bat}dT_s + \frac{1}{L}(V_{bat} - V_{dc})(T_s - dT_s) + \frac{1}{L}\tilde{v}_{ELM}(T_s - dT_s) + \frac{1}{L}\tilde{v}_{ELM}dT_s \quad \text{Equation 3-119}$$

Simplification gives:

$$\Delta i_{on} + \Delta i_{off} = \frac{1}{L}V_{bat}dT_s + \frac{1}{L}(V_{bat} - V_{dc})(T_s - dT_s) + \frac{1}{L}\tilde{v}_{ELM}T_s \quad \text{Equation 3-120}$$

Where $\tilde{v}_{ELM}$ is the earth leakage voltage as seen by the battery and can be calculated using Equation 3-111:

$$\tilde{v}_{ELM} = \frac{Z_{batt}}{Z_{batt}+20}\ 9.2\left(sin\left(\omega t + \frac{\pi}{8}\right)\right)$$ Equation 3-121

Therefore Equation 3-119 can be defined as:

$$\Delta i_{on} + \Delta i_{off} = \frac{1}{L}V_{bat}dT_s + \frac{1}{L}(V_{bat} - V_{dc})(T_s - dT_s) + \frac{1}{L}\frac{Z_{batt}}{Z_{batt}+20}\ 9.2\left(sin\left(\omega t + \frac{\pi}{8}\right)\right)T_s$$ Equation 3-122

The Fourier analysis of the current waveform is shown in Appendix C. This produces a harmonic spectrum as shown in Figure 3-42 using Equation C-154.

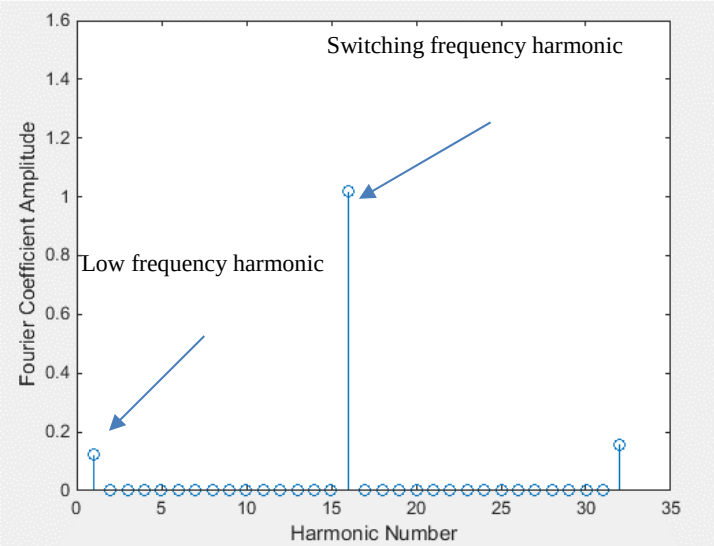

Figure 3-42 : Theoretically derived harmonics of the Li-ion battery current signal with an ELM signal at a low frequency of 125Hz

3.7.3 Inductor ripple calculation of ELM

The extra inductor ripple current is negligible. However, the increase in battery ripple current caused by the super-position of the ELM produced current in conjunction with the normal ripple current from the boost converter operation. This can be seen in Figure 3-43 which shows the ripple current through the inductor (blue) is equal to the super-position of the inductor current with no ELM (orange) and the small signal inductor current which is a function of the ELM (grey).

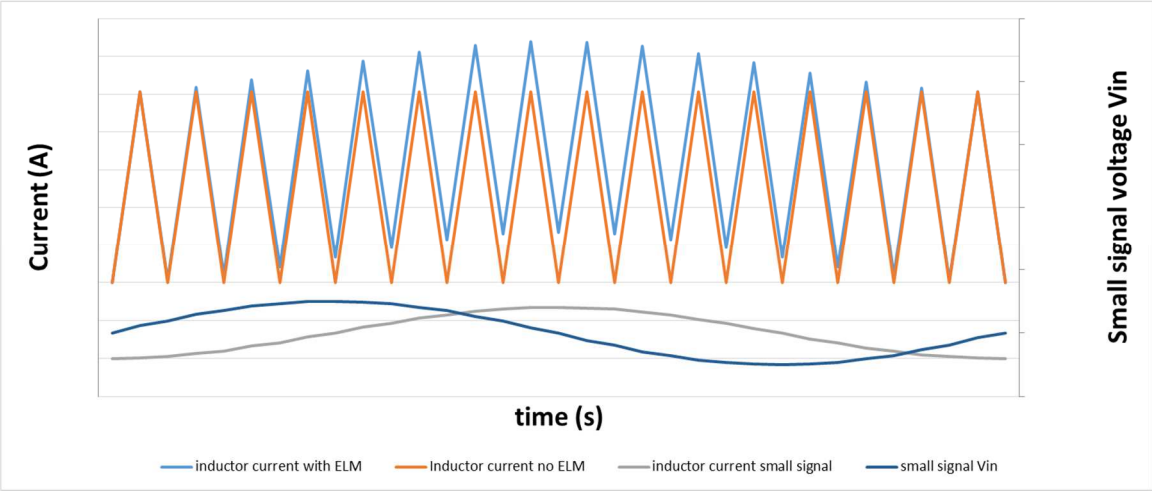

Figure 3-43 : Ripple current through the inductor

The increase in current compared to the scenario with no ELM is therefore:

$$ripple\ increase = 1 + \frac{\tilde{i}_{bat,ac}}{I_{bat}} = 1 + \frac{\frac{9.2}{Z_{bat}+20}}{\frac{1}{L}dT_sV_{bat}}$$ Equation 3-123

$$ripple\ increase = 1 + \frac{9.2L}{(Z_{batt}+20)dT_sV_{bat}}$$ Equation 3-124

The ripple increase is a function of the impedance of the battery. As the battery degrades this will increase allowing a less accurate calculation of impedance.

3.8 Summary

Six different methods of generating a low frequency excitation signal using hardware found in most battery systems have been analysed with regard to their applicability for use in an online EIS measurement system. These are:

1. Using existing dc/dc converter hardware but using variable duty cycle
2. Using existing dc/dc converter hardware but using variable frequency
3. Using existing dc/dc converter hardware but using variable pulse starting position
4. Using existing dc/dc converter hardware but adding an impulse function
5. Using battery balancing hardware converter hardware
6. Using Earth Leakage Monitoring hardware

Generating a low frequency excitation signal by varying the duty cycle in the dc-dc converter has been previously considered. However, the other methods (variable frequency, starting position and impulse function) have not previously been considered. The other techniques, in particular utilising the Earth Leakage Monitoring hardware and the battery balancing hardware in this manner have not been previously reported in literature and are a novel contribution of this thesis.

As part of the analysis, focus has been given to looking at determining the harmonic current through the battery using Fourier analysis and looking at the subsequent increased ripple current on the inductor. In all these methods, it was assumed that the DC-DC converter operates in continuous boost mode with a fixed duty cycle to allow comparable analysis. A summary of the key points in this chapter are shown in Table 3-4.

Table 3-4: low frequency excitation method comparison

Method	Battery current shape	Summary of Harmonics	Inductor ripple increase	Fourier co-efficient amplitude @125Hz
1	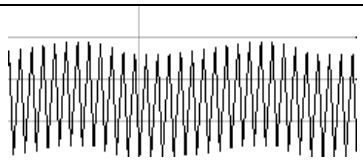 The current increases and decreases at fixed rates but over different time periods defined by the varying duty cycle within a fixed switching period.	Main harmonics f_s, f_o, $f_s \pm f_o$	Approximate expression dependent on frequency and duty cycle variation $1 + \frac{A_d N_p}{d_{av}(1-d_{av})\pi}$	0.27
2	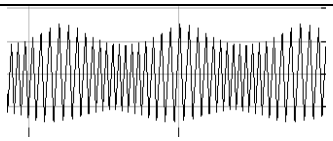 The duty cycle is fixed – so the current increases and decreases more at a lower frequency than a higher frequency.	Main harmonics f_o, harmonic spread f_s-$A_f \rightarrow f_s$+A_f, additional sidebands f_s-A_f –f_0 → f_s+A_f + f_0	Approximate expression dependent on frequency variation and average switching frequency $\frac{f_{av}}{f_{av} - A_f}$	0.26
3	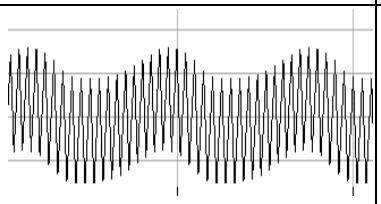 The duty cycle and switching frequency are fixed. Therefore the time the inductor is discharging is fixed but the time is split. This results is a skewed pattern compared to method 1	Main harmonics f_s, f_o, $f_s \pm f_o$	Approximate expression dependent on variable starting point variation, duty cycle and switching frequency $1 + \frac{2A_t}{(1-d)T_s}$	0.055

4	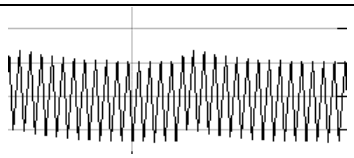 The duty cycle and switching frequency are fixed. However the first "on" time is higher and therefore this increases the current.	Main harmonics f_s, f_o, $f_s \pm f_o$ harmonic spread	Approximate expression dependent on the width of the impulse function and the "on" time of the signal $\frac{dT_s + T_i}{dT_s}$	0.15
5	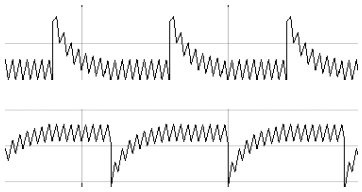 The duty cycle and switching frequency are fixed. However the battery current is the superposition of the dc-dc converter system and battery balancing circuit resulting in an increase in current in one battery and a decrease in the other in anti-switching.	Main harmonics f_s, f_o, $f_s \pm f_o$	Negligible increase in inductor ripple but increased battery current ripple.	0.2
6	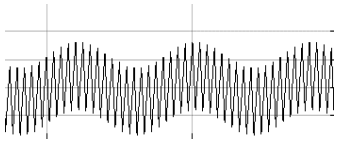 Although the shape of the waveform looks similar to method 1. It is not the same as formed by a different process and is the superposition of the boost converter saw tooth waveform and the sinusoidal ELM produce current	Main harmonics f_s, f_o,	Negligible increase in inductor current. Increase in ripple of battery current.	0.15

The theoretical results are a promising indicating that it is possible to generate a low frequency excitation signal in order to undertake on-line EIS measurement. However, there are potential trade-offs. The key trade-off is the increase in ripple current through the battery and inductor. There are however other issues, the variable frequency (method 2) produces a range of frequencies around the switching frequency. This may make it more difficult to deal with possible EMI issues. The results are also potentially subject to hardware limitations. In particular, the fixed time step operation of the controller at 20μs, limits the accuracy that can be obtained when adding an impulse function or

controlling where the starting position of a pulse may be. Using the impulse function may also result in an overall increase in the duty cycle which may need to be adjusted to compensate.

Chapter 3 looks at simulating these circuits using MATLAB Simulink to compare the theoretical derived expressions in this chapter with simulated ones. Chapter 4 then looks to determine equivalent values through experimental investigations.

4 Simulation of on-line EIS techniques

4.1 Introduction

In-order to help understand the operation of the circuit with respect to the theory and experimental work, it is necessary to look at modelling the circuit within a suitable package. For the purposes of this work Matlab SIMULINK (R2014b) was chosen. To undertake a circuit simulation the impedance of the battery was predetermined by EIS measurement and represented in a MATLAB simulation as an equivalent circuit in series with a dc voltage source which represents the battery voltage level. The different components of the circuit modelled include a Battery, the dc/dc converter and a load.

An A123 Lithium-ion phosphate battery with 2.5 Ah capacity and 3.2V nominal voltage was used in this work and the parameters were estimated using an EIS impedance analyser (solatron 1260 and 1287) as shown in Figure 4-1.

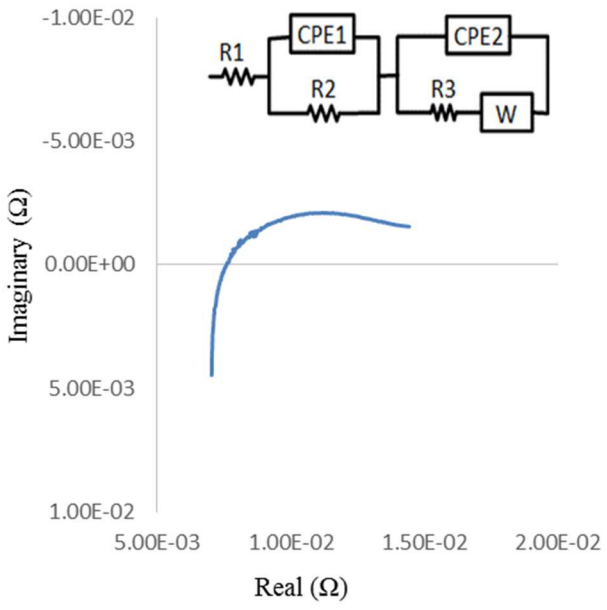

Figure 4-1 : Lithium-ion phosphate battery EIS impedance plot and equivalent circuit model

The equivalent circuit in Figure 4-1 is the closest and most common representation for this battery type [172]. There are alternative circuit model for CPE representations in literature [326]–[328]. This includes a cascade connection of multiple parallel RCs, a parallel connection of multiple cascade RC, and a multiple parallel RC in parallel connection. However, in this work, the CPE, which normally represents an impure capacitor element [143] is represented as a capacitor in MATLAB; to avoid

complexity in battery model within MATLAB. Table 4-1 represents the estimated values of these components, where C_1 is set equal to CPE_1 and C_2 is set equal to CPE_2.

Table 4-1: Battery Model component specifications

Components	Lithium-ion Battery
$R_1(\Omega)$	0.0069
$R_2(\Omega)$	0.0056
$R_3(\Omega)$	0.0000089
$CPE_1(S)$	2.36
$CPE_2(S)$	36.75

This battery model is included within an ideal component system model as shown in Figure 4-2.

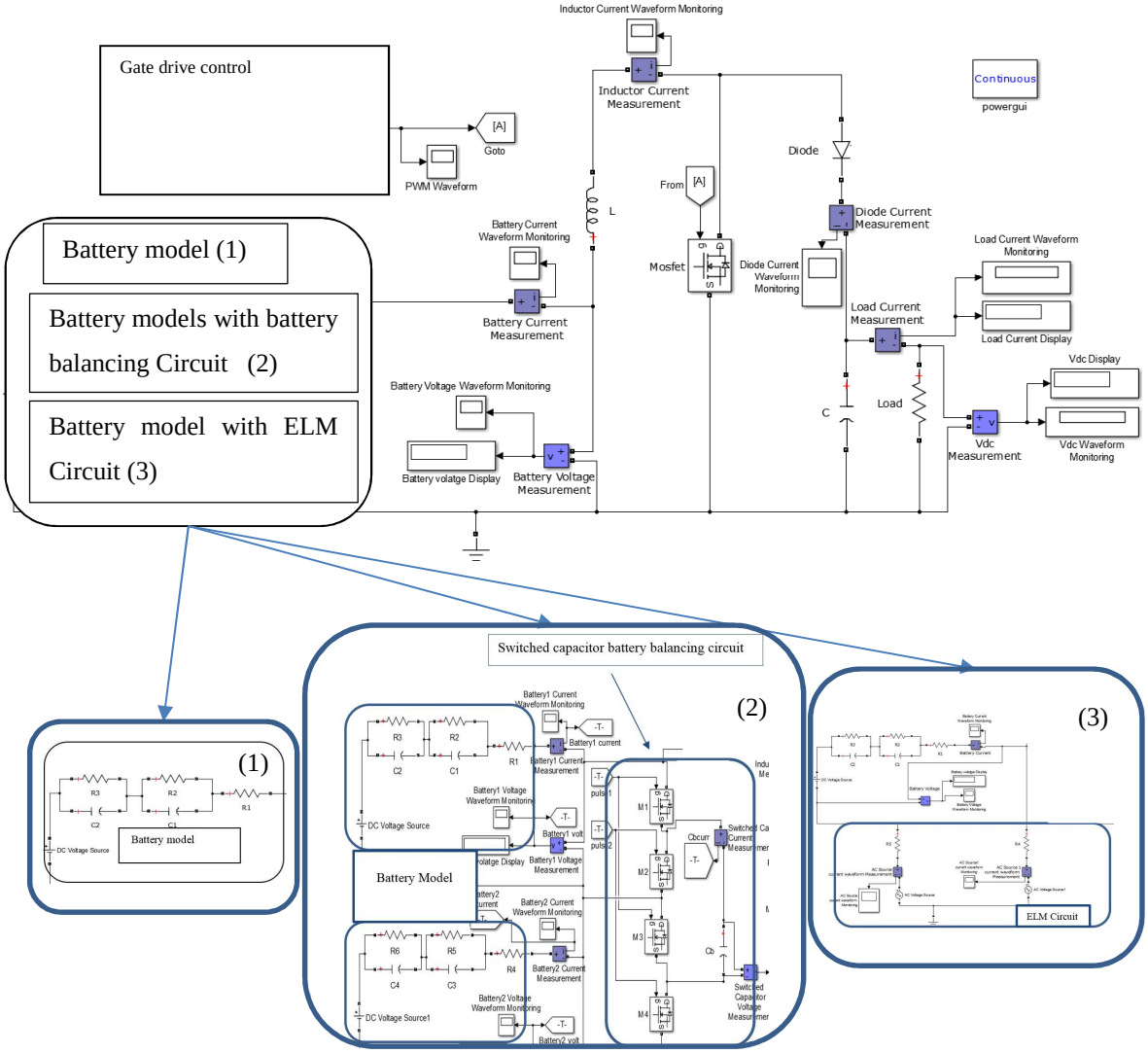

Figure 4-2 : High level circuit simulation model with ideal components

To determine the circuit components and dc-converter parameters the following design practice was used [329].

1. Key design parameters were specified
    - The input voltage range of the converter, V_{bat} is set to 3.2V to 2.8V (set by typical battery operating range)
    - The output voltage, V_{out} (voltage drop across diode V_D and load V_{dc}) was chosen to be approximately 8V to limit the boost ratio and avoid the complexities of a high boost ratio.
    - The ripple across the load Δv_{load} is targeted to be approximately 0.01V (approximately 1.5% of output voltage) as a typical figure.
    - The maximum Output current is set to 450mA to keep the total output power low in keeping with the low power rating of the battery.
    - The circuit is designed to operate in continuous mode so that the comparison with theory and experimental results is more straightforward.
    - A switching frequency of 2kHz was chosen as the controller struggles with complex calculations if the switching frequency is set to a higher value and to avoid other trade offs of a high switching frequency such as the switching loss of the switch itself and the gate drive and dropout voltage.

2. Inductor selection

This thesis is looking primarily at adjusting the ripple current to inject a low harmonic waveform and therefore the boost converter needs to be designed to deal with an unusually large ripple current in order to test all the different methods, as see the excitation signal.

Based on the inductor ripple increase from section 2.4 for the different methods of introducing a low frequency harmonic, a value of ripple current increase of approximately 200% of the output current has been chosen so that the low frequency ripple is visible.

$$\Delta I_L = 2\ x\ I_{out,max}\ x\ \frac{V_{out}}{V_{bat}} \approx 2.4\text{A} \qquad \textbf{Equation 4-1}$$

This enables the inductor value to be calculated.

$$L = \frac{V_{bat} x\ (V_{out} - V_{bat})}{\Delta I_L\ x\ f_s\ x\ V_{out}} = \frac{3\ x\ (8-3)}{2.4\ x\ 2000\ x\ 8} \approx 390\mu H \qquad \textbf{Equation 4-2}$$

The nearest available inductor size of $380\mu H$ was used.

3. Maximum switch current

Duty cycle, D is calculated from Equation 4-3 (assuming 100% efficiency)

$$D = 1 - \frac{V_{bat,min}}{V_{out}} = 1 - \frac{2.8}{8} \approx 0.65$$ **Equation 4-3**

A value of 0.6 was chosen so that there was more leeway to look at variable starting position as a method of introducing low frequency ripple.

The maximum switch current can then be calculated from

$$I = \frac{\Delta I_L}{2} + \frac{I_{out,max}}{1-D} \approx 2.4A$$ **Equation 4-4**

4. Rectifier Diode Selection

The forward current needs to be equal to the maximum output current and the power dissipation rating has to be at least

$$P_D = I_F \, x \, V_F$$ **Equation 4-5**

An HER204G Rectifier Diode with maximum 2A with a 1.1V forward voltage drop was used because of its fast recovery time and low forward voltage. It was convenient to use as this was available in the laboratory.

5. Output capacitor value

When the switch is on, the current of the capacitor at time, $t = \tau$, is equal to the load average current. Therefore, the voltage ripple of the capacitor can be calculated from:

$$\Delta v_{load} = \frac{1}{C}\int_0^{\tau} I_{out} = \frac{I_{out}\tau}{C}$$ **Equation 4-6**

The capacitor value can be calculated by substituting $\tau = \frac{D}{f_s}$ in Equation 4-6:

$$C = \frac{I_{out}D}{\Delta v_{load} f_s} = \frac{0.45 \; x \; 0.6}{0.01 \times 2000} = 13500 \; \mu F$$ **Equation 4-7**

A capacitor with value of the 13600µF was used in the hardware setup.

6. Output load resistor value

The load resistor is used to balance the capacitor voltage and also to provide a load to discharge the battery when the switch is off. The value of load resistor is therefore output voltage/output current

$$R_L = \frac{7}{0.45} \approx 16\Omega$$ Equation 4-8

The chosen components used in the experimental chapter 5 and replicated in simulation are summarised in Table 4-2. The mosfet used was available in the laboratory.

Table 4-2 : Boost converter component specifications

Boost Converter Components	**Specifications**
Inductance	380µH, 20 A ,Toroidal
Capacitance	13600µF, 16V Electrolytic
Load	16Ω resistor
Switch MOSFET	FDPF045N10A, 100 V, 67 A, 4.5 mΩ
Isolated dc/dc converter for derivers	IE0515S (15 V)
Drivers	HPCL 3140 (0.4A peak current driver)
Diode	HER204G Rectifier Diode with maximum 2A with a 1.1 forward voltage drop

Prior to investigating the different methods of introducing a low-frequency ripple, the base case with fixed duty cycle of 0.6 and fixed switching frequency of 2kHz was simulated. This provides a useful comparison to the methods under investigation in this thesis. Table 4-3 shows the simulated waveforms of this base case circuit. In this model, the circuit boosts at a ratio of 2.27 compared to the design equations, the simulated values of the load output voltage and ripple and the load current and ripple are as per the design equations. The battery voltage has been set to the upper level of the battery voltage range and the inductor ripple current is close to the calculated 2.4A from Equation 4-1. These results are referred to as the "base" results by which the other results from the methods of introducing a low frequency component of ripple will be compared.

Table 4-3: Simulated results of fixed duty cycle

	Simulation	
	Fixed Duty Cycle ideal component	
	Average Value	Peak-Peak ripple
I_{batt}	1.55 A	2.42 A
V_{batt}	3.21 V	16.8 mV
I_{load}	456 mA	0.7 mA
V_{dc}	7.3 V	11.1 mV

The simulated waveforms of the battery voltage, current, converter output voltage and load current are shown in Figure 4-3 and Figure 4-4. The waveforms show the circuit is operating in continuous mode as expected.

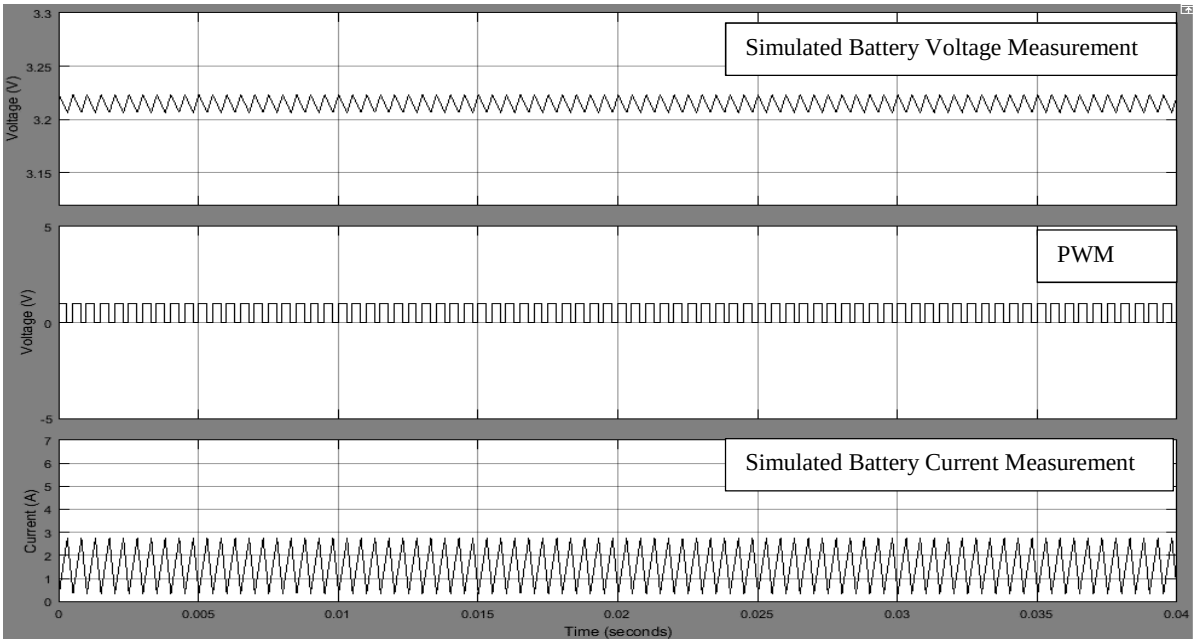

Figure 4-3 : Simulated Li-ion battery Current and Voltage waveforms. The battery is excited with PWM at a fixed duty cycle of 0.6 and switching frequency of 2kHz.

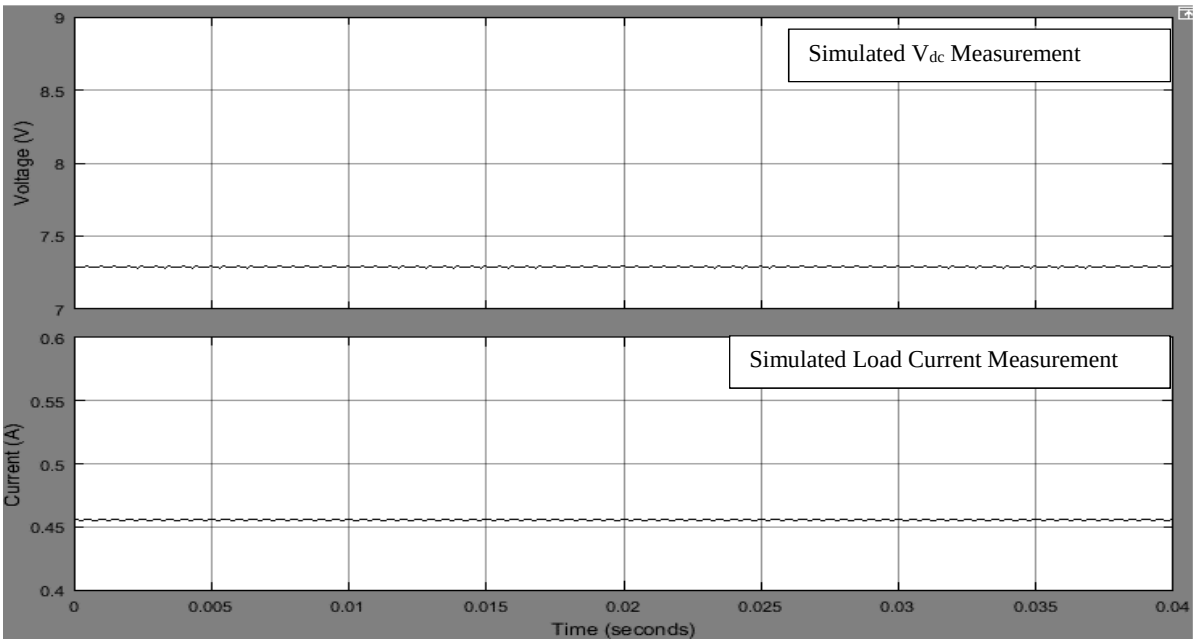

Figure 4-4 : Simulated Load Current and output Voltage waveforms. The battery is excited with PWM at a fixed duty cycle of 0.6 and switching frequency of 2kHz.

The calculated harmonics found from Fourier analysis of the battery current using the model from Figure 4-2 is shown in Figure 4-5 using the FFT calculation MATLAB code. Under the normal operation of the dc/dc converter, only the switching frequency harmonics are visible. This graph will

be compared to the other simulated curved with a low-frequency component and with theoretical and experimental values.

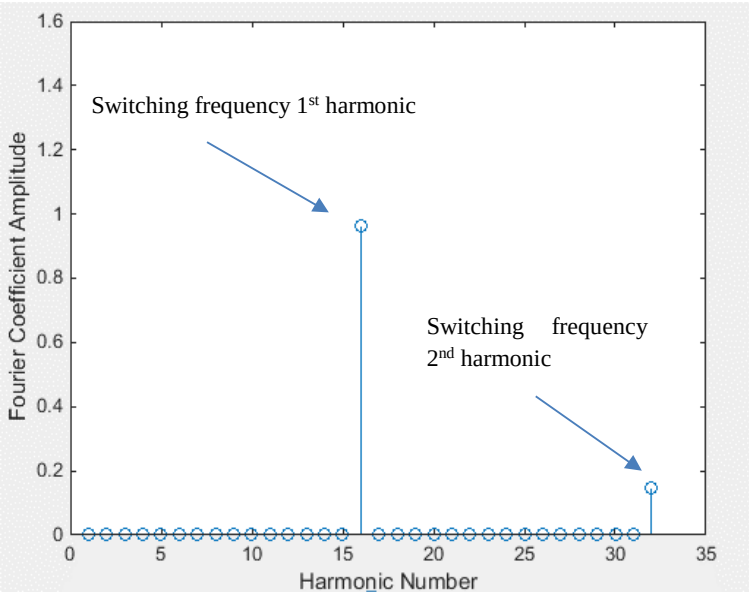

Figure 4-5 : Simulated current harmonics at switching frequency of 2kHz, Where the fundamental frequency is defined as 125kHz to enable comparison with low frequency produced analysis.

The following sections will look at simulating the different methods of introducing a low-frequency component into the battery.

4.2 DC/DC Converter with varying duty cycle PWM

To generate a low-frequency component by varying the duty cycle, the gate drive control is replaced with the model in Figure 4-6 (a). The gate drive includes a PWM generator block, a constant value, which represents the average duty cycle and a sinewave block to generate the low-frequency variation to the duty cycle. The PWM generator is a Simulink predefined function which creates a pulse signal based on an input duty cycle and the switching frequency, using a sawtooth function. In the sub block of the PWM generator block the output rectangular function is generated from the comparison of the scaled sawtooth signal with the input duty cycle.

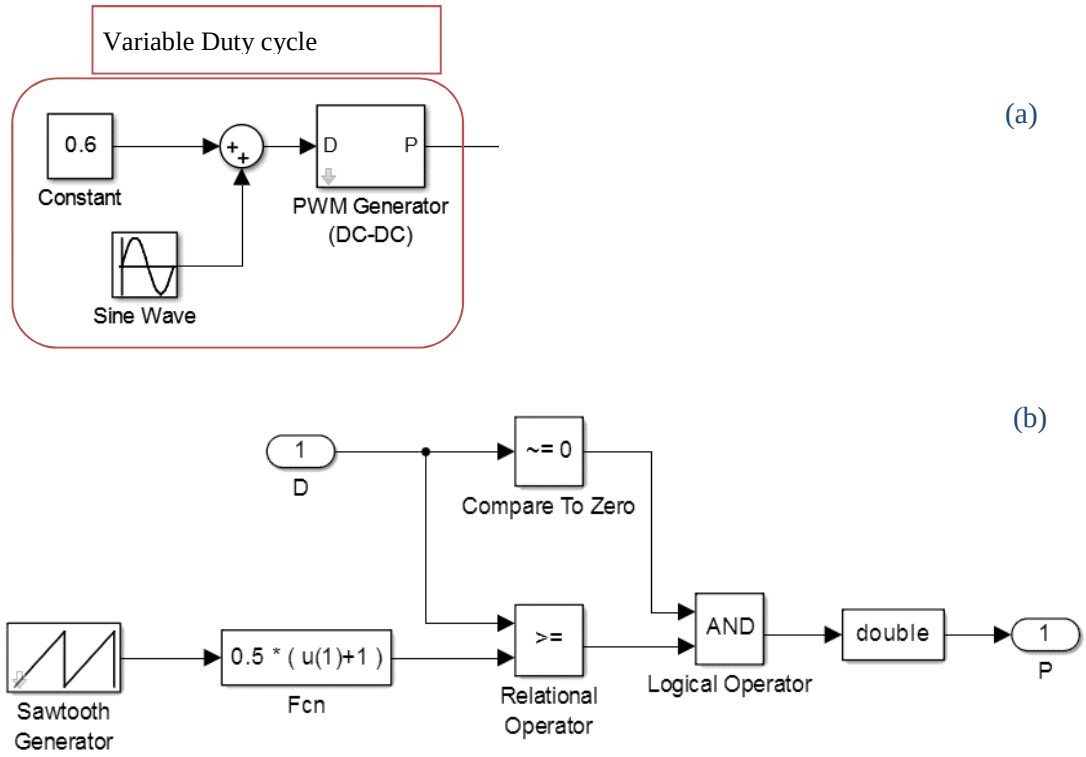

Figure 4-6 : (a) Variable duty cycle gate drive control (b) generating PWM signal sub-block

The circuit was simulated with 2kHz switching frequency and a duty cycle of 0.6 with a low frequency sine wave of amplitude of 0.01 to produce the variable duty cycle signal. The comparison of the simulated circuit data with a fixed duty cycle (from section 4.1) and this variable duty cycle at frequencies of 125Hz and 175 Hz are shown in Table 4-4 and Table 4-5 respectively.

Table 4-4: Comparison of simulated results of fixed and variable duty cycle at 125Hz with A_d =0.01,

	Simulation			
	Fixed Duty Cycle		Variable Duty Cycle	
	Average Value	Peak-Peak ripple	Average Value	Peak-Peak ripple
I_{batt}	1.55 A	2.42 A	1.55 A	2.72 A
V_{batt}	3.21 V	16.8 mV	3.21 V	18.8 mV
I_{load}	456 mA	0.7 mA	459 mA	1.5 mA
V_{dc}	7.3 V	11.1 mV	7.3 V	23.3 mV

Table 4-5: Comparison of simulated results of fixed and variable duty cycle at 175Hz with A_d =0.01

	Simulation			
	Fixed Duty Cycle		Variable Duty Cycle	
	Average Value	Peak-Peak ripple	Average Value	Peak-Peak ripple
I_{batt}	1.55 A	2.42 A	1.56 A	2.67 A
V_{batt}	3.21 V	16.8 mV	3.21 V	18.5 mV
I_{load}	456 mA	0.7 mA	458.2 mA	1.2 mA
V_{dc}	7.3 V	11.1 mV	7.3 V	18.7 mV

The results show that the load current and load voltage have the same average value but there is additional ripple on the current when the input current ripple is increased through the use of variable duty cycle. The simulated variable duty cycle converter boosts at the same ratio as the simulated base model circuit. The injected low-frequency signal added ripple to the battery and converter waveforms (Equation 3-40) which results in an increase in the peak to peak value of V_{batt}, I_{batt}, V_{dc}, and I_{load}. However, the added ripple reduced as Np value decreases (Equation 3-40). The battery current has the same average value, but there is an increase in ripple of 12% at 125Hz and 10% at 175Hz.

The simulated battery current and voltage, PWM, dc/dc boost converter load current, and output voltage waveforms at switching frequency of 2kHz and duty cycle of 0.6 are shown in Figure 4-7 to Figure 4-10. The waveforms clearly show an increase in the ripple on the battery current of the same shape as described in the theory section 3.2.4.

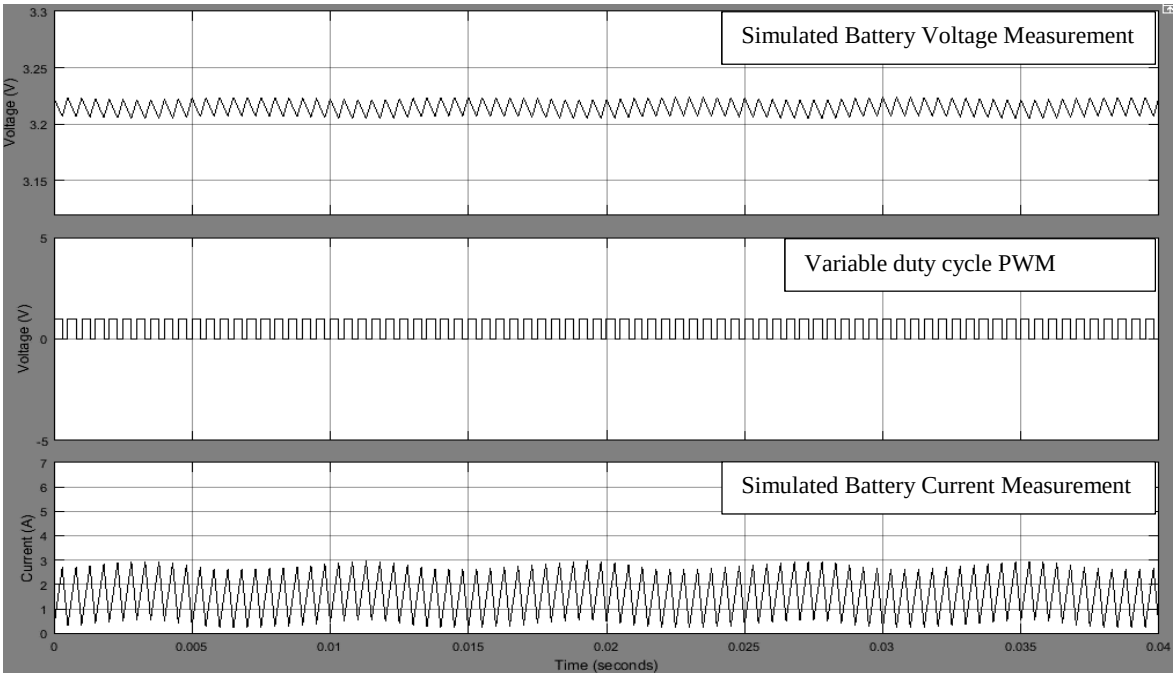

Figure 4-7 : Simulated Li-ion battery Current and Voltage waveforms. The battery is excited with PWM with variable duty cycle at a low frequency of 125Hz with A_d = 0.01.

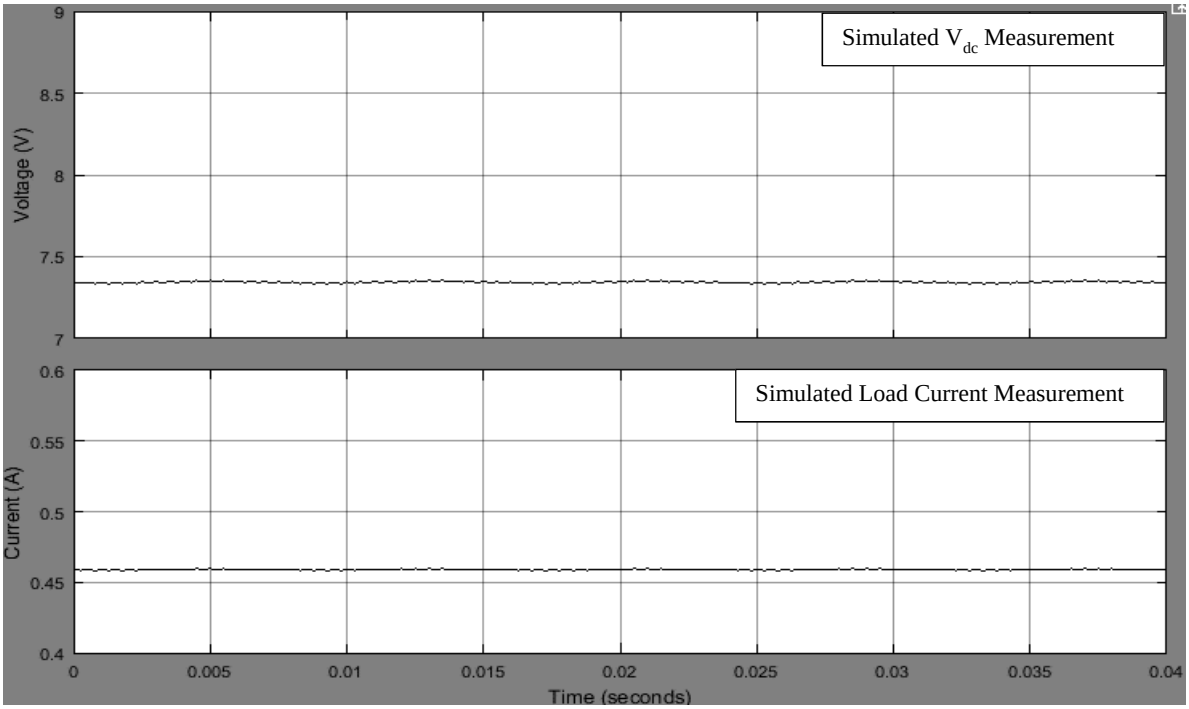

Figure 4-8 : Simulated Load Current and Voltage (Vdc) waveforms. The battery is excited with PWM with variable duty cycle at a low frequency of 125Hz with A_d = 0.01.

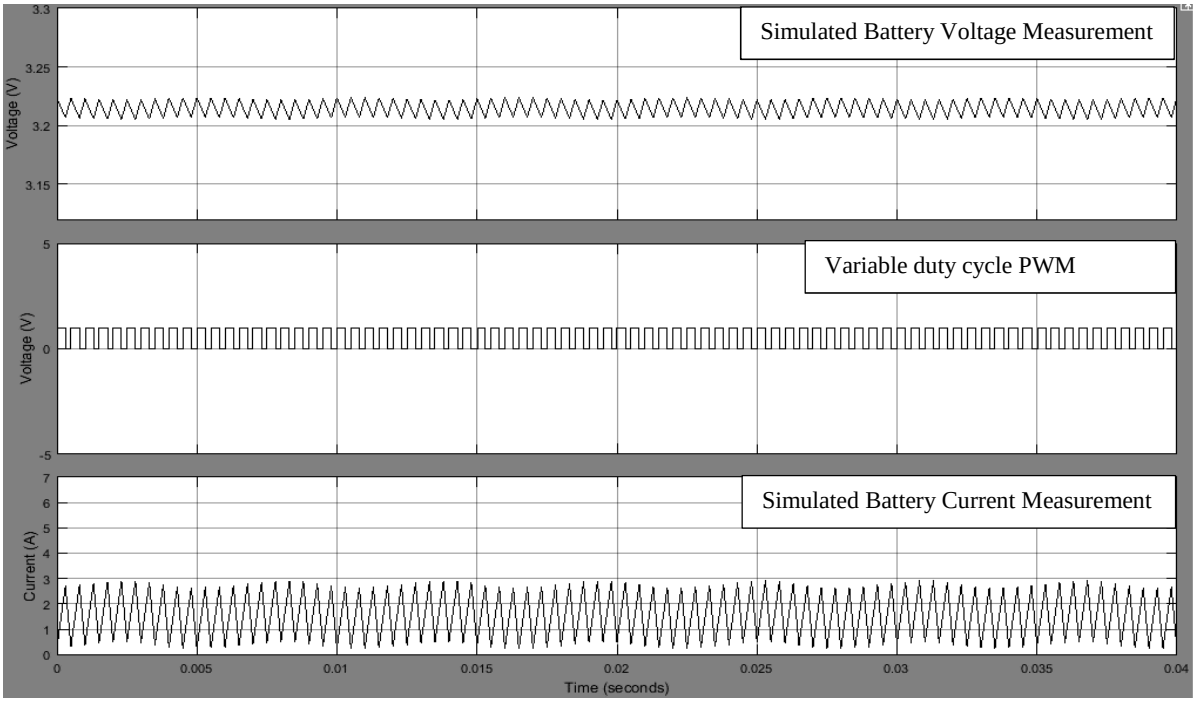

Figure 4-9 : Simulated Li-ion battery Current and Voltage waveforms. The battery is excited with PWM with variable duty cycle at a low frequency of 175Hz with A_d = 0.01.

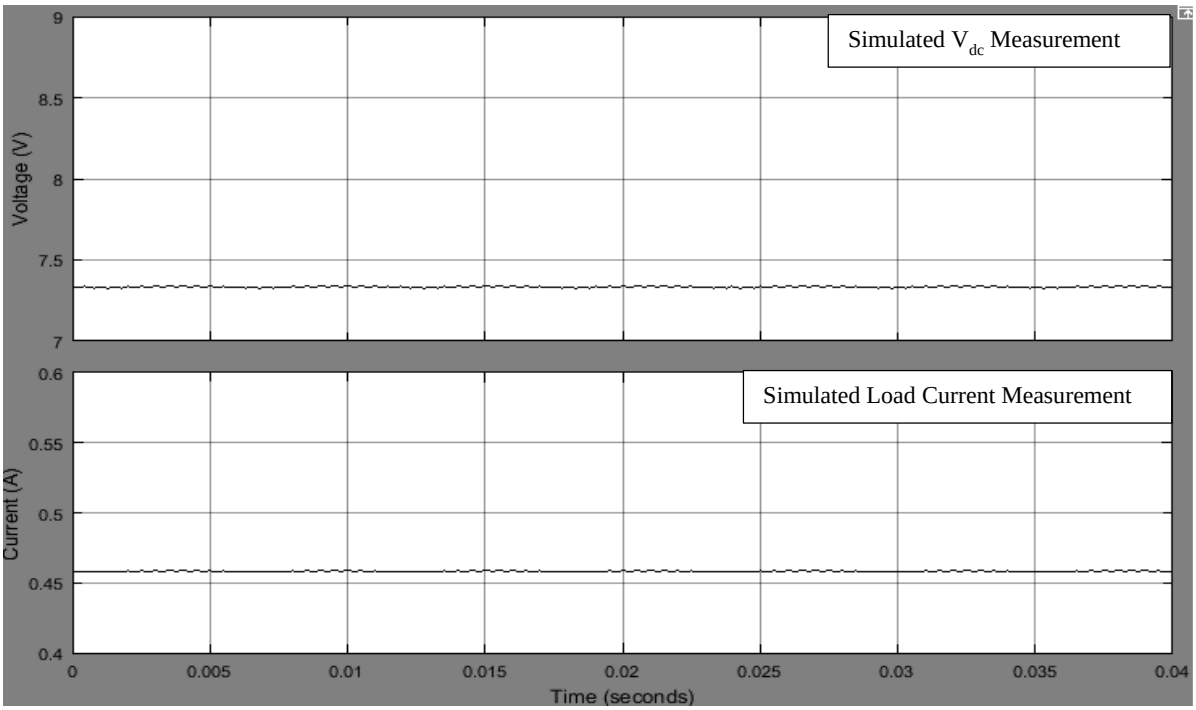

Figure 4-10 : Simulated Load Current and Voltage (Vdc) waveforms. The battery is excited with PWM with variable duty cycle at a low frequency of 175Hz with A_d = 0.01.

Figure 4-11 shows the Fourier analysis of the simulated battery current signal with an injected low frequency component of 125Hz at a switching frequency of 2kHz using the variable duty cycle technique. The simulated current harmonics in Figure 4-11 can be compared to Figure 4-5 with a fixed duty cycle, and show that a low-frequency component has been added.

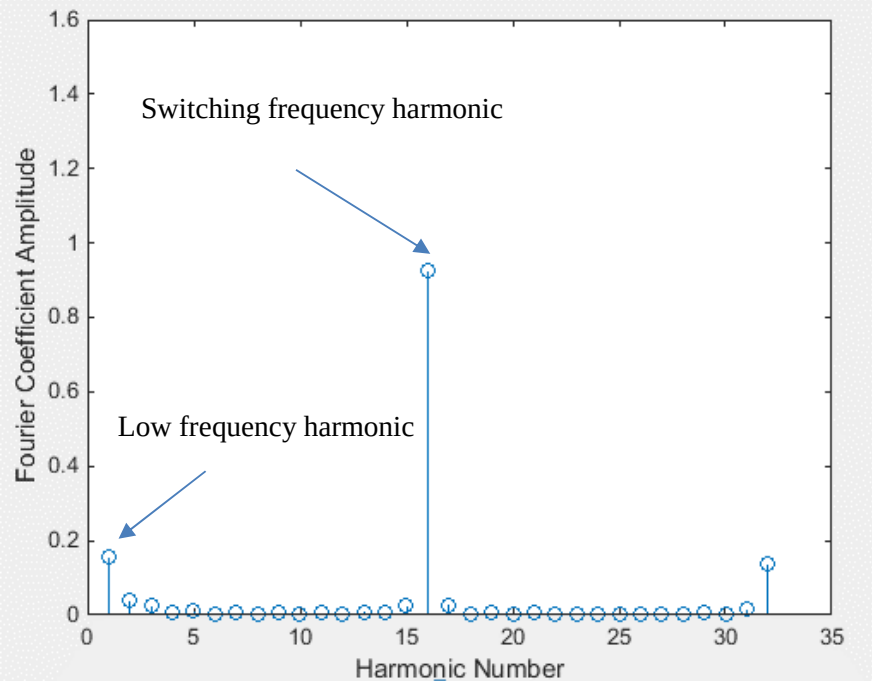

Figure 4-11 : Simulated current harmonics at variable duty cycle of low frequency of 125Hz and switching frequency of 2kHz

These and other results in this chapter will be compared to theory and experimental results in chapter 5, along with more calculated sensitivity studies.

4.3 DC/DC Converter with varying frequency PWM

The same simulated circuit from Figure 4-2 was used with a variable frequency PWM gate drive generated in the gate drive sub-block as shown in Figure 4-12. The variable frequency PWM generator sub block consists of a pulse generator, an integrator block and an external reset point to generate the sawtooth signal as shown in Figure 4-13. The signal from the sawtooth and the duty cycle subtraction is used as an input of the sign block to create a rectangular waveform. The gain and the constant block are used for scaling the created rectangular waveform. The switching frequency of the pulse signal is set to an average value of 2kHz with an added low frequency component.

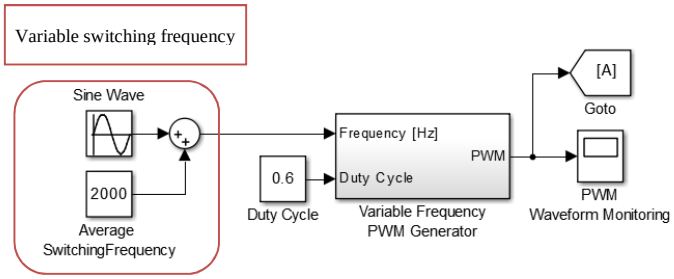

Figure 4-12 : Simulated Variable frequency gate drive control

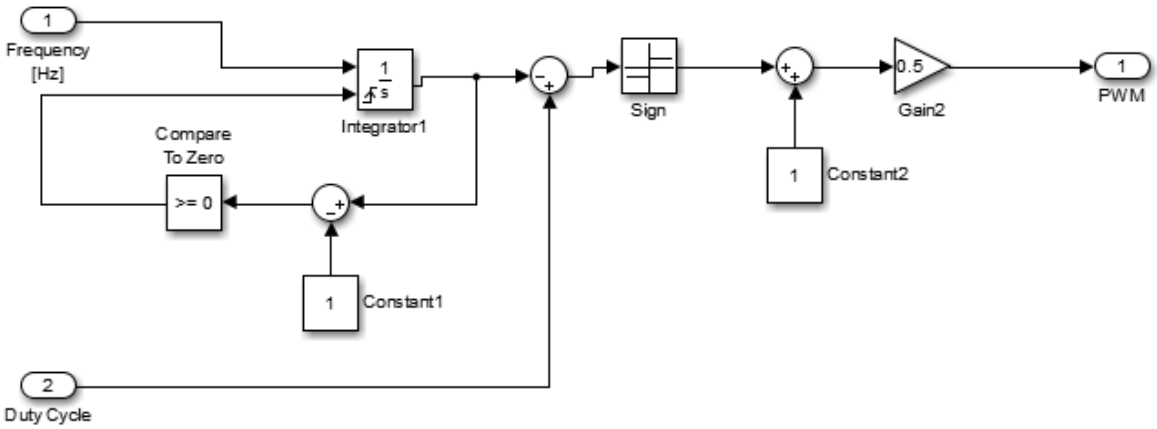

Figure 4-13 : The subsystem model for a variable frequency PWM generator

The circuit was simulated with an average switching frequency of 2kHz with a sine wave of amplitude of A_f = 400 to produce a variable switching frequency signal with a duty cycle of 0.6. The comparison of the simulated circuit data with fixed duty cycle and variable switching frequency at the low-frequencies of 125Hz and 175 Hz are shown in Table 4-6 and Table 4-7 respectively.

Table 4-6: Comparison of simulated results of fixed and variable switching frequency at 125Hz with $A_f = 400$

	Simulation			
	Fixed Duty Cycle		Variable Frequency	
	Average Value	Peak-Peak ripple	Average Value	Peak-Peak ripple
I_{batt}	1.55 A	2.42 A	1.63 A	2.99 A
V_{batt}	3.21 V	16.8 mV	3.21 V	20.7 mV
I_{load}	456 mA	0.7 mA	458 mA	1.4 mA
V_{dc}	7.3 V	11.1 mV	7.3 V	22.1 mV

Table 4-7: Comparison of simulated results of fixed and variable switching frequency at 175Hz with $A_f = 400$

	Simulation			
	Fixed Duty Cycle		Variable frequency	
	Average Value	Peak-Peak ripple	Average Value	Peak-Peak ripple
I_{batt}	1.55 A	2.42 A	1.62 A	2.99 A
V_{batt}	3.21 V	16.8 mV	3.21 V	20.7 mV
I_{load}	456 mA	0.7 mA	459 mA	1.2 mA
V_{dc}	7.3 V	11.1 mV	7.3 V	18.9 mV

Similar to the variable duty cycle technique, the variable switching frequency increases the battery ripple current. The current ripple increased by 24% at both low frequency values as indicated in section 3.3.3 . The variation of the ripple current appears to depend on the amplitude of the sinewave in the excitation signal from Equation 3-52. The V_{dc} average value remains the same as does the boost ratio from the base case circuit.

Figure 4-14 to Figure 4-17 show the simulated battery and load waveforms at the frequencies of 125Hz and 175Hz. The low frequency signal was induced to the system by varying the switching frequency with a sinewave with amplitude of $A_f = 400$. The current ripple waveform shows the change in frequency from low to high as expected from the theory in section 3.3.2. The current ripple increases at the time that the switching frequency of the gate drive is reduced.

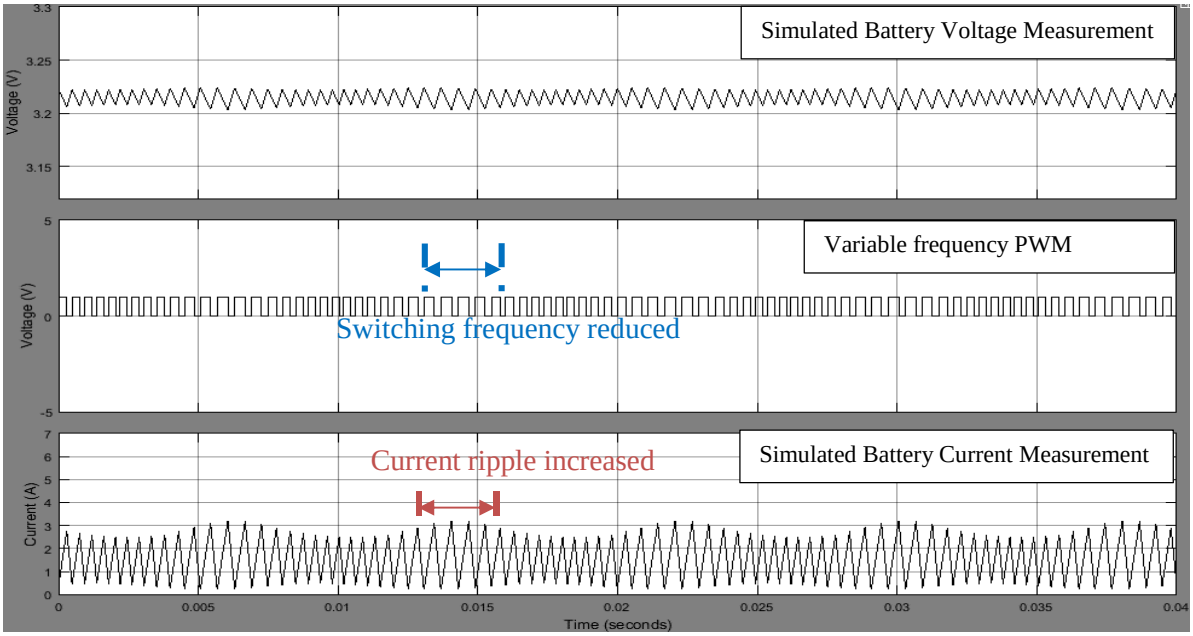

Figure 4-14 : Simulated Li-ion battery Current and Voltage waveforms. The battery is excited with PWM with variable frequency at a low frequency of 125Hz with A_f = 400.

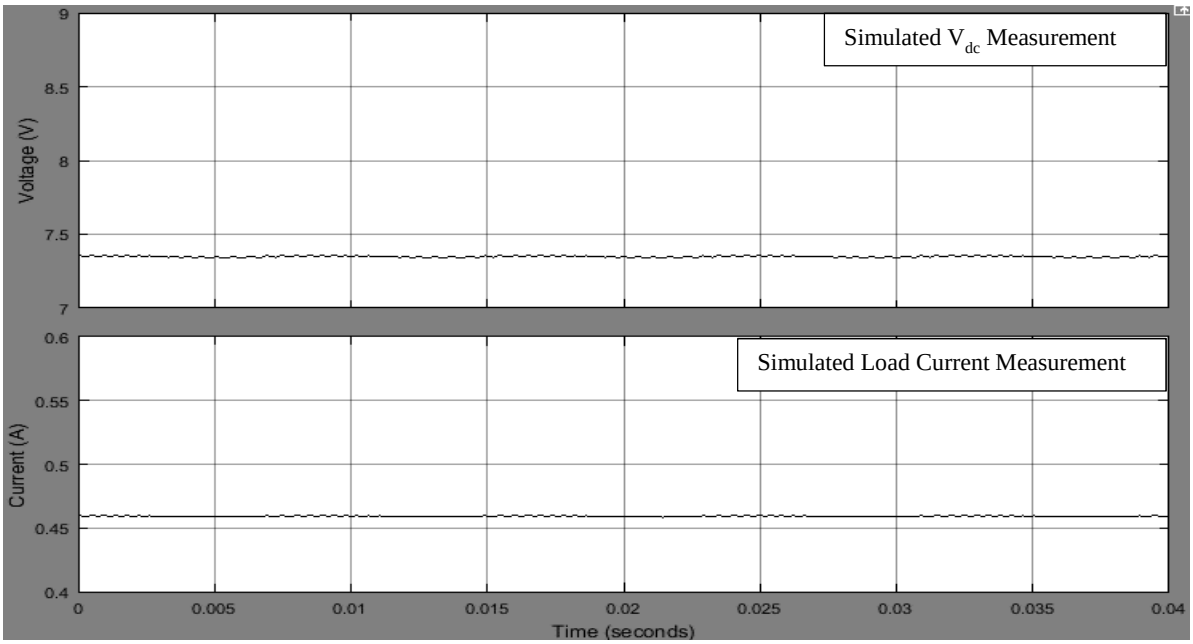

Figure 4-15 : Simulated Load Current and Voltage (Vdc) waveforms. The battery is excited with PWM with variable frequency at a low frequency of 125Hz with A_f = 400.

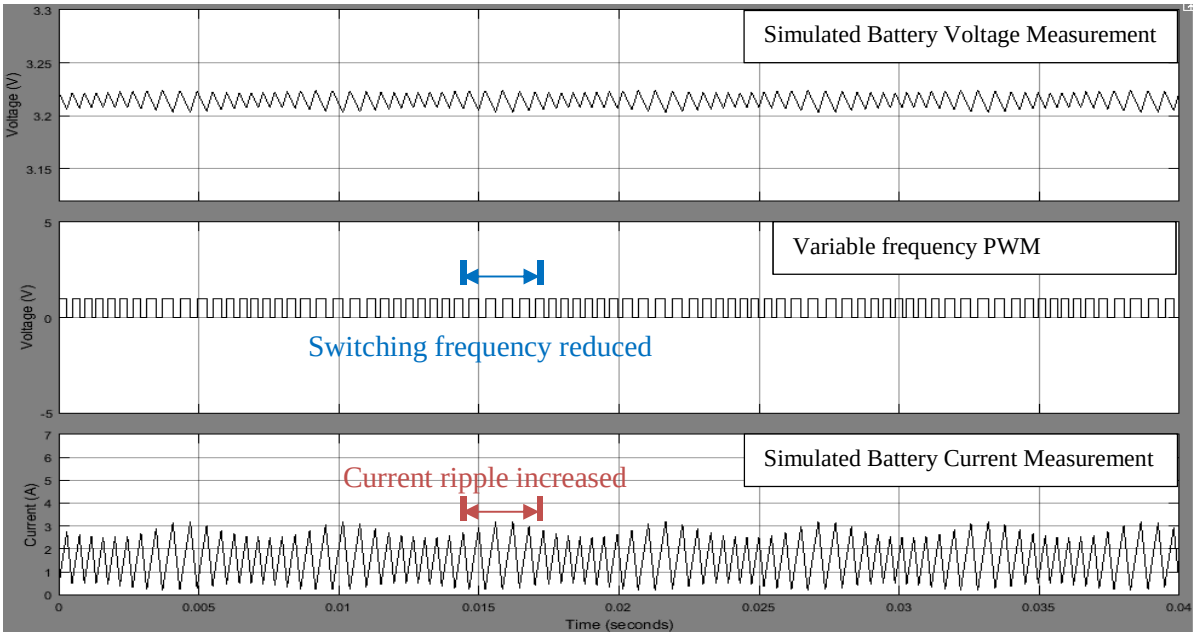

Figure 4-16 : Simulated Li-ion battery Current and Voltage waveforms. The battery is excited with PWM with variable frequency at a low frequency of 175Hz with A_f = 400.

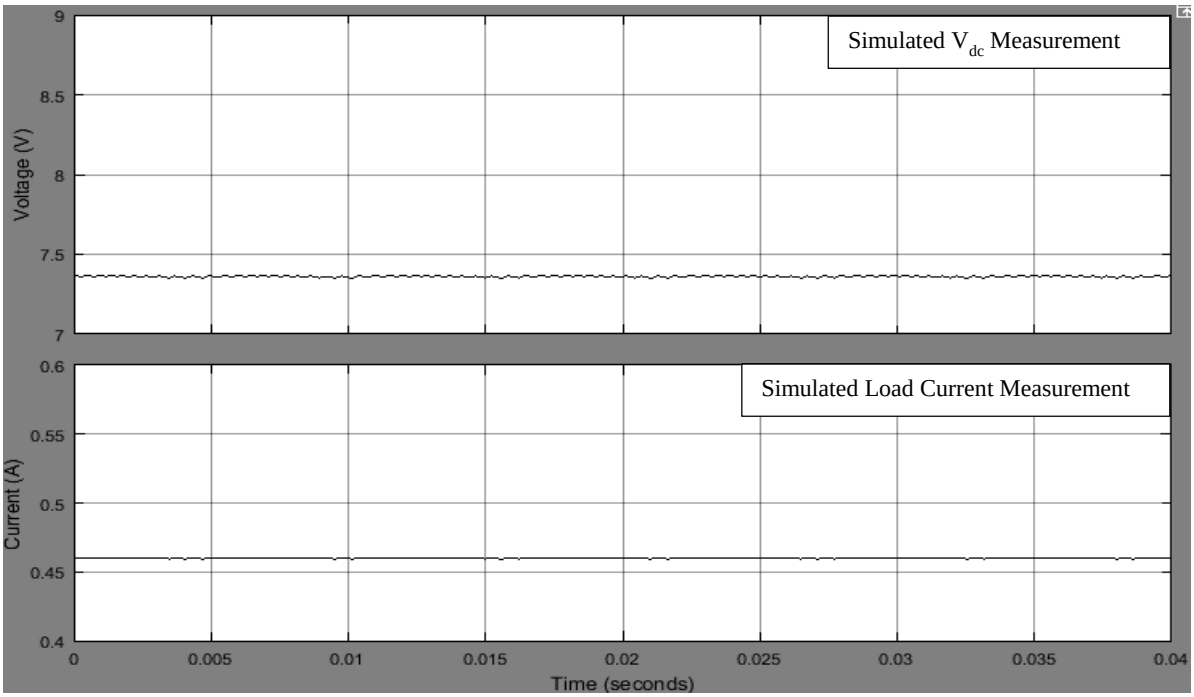

Figure 4-17 : Simulated Load Current and Voltage (Vdc) waveforms. The battery is excited with PWM with variable frequency at a low frequency of 175Hz with A_f = 400.

Figure 4-18 shows the calculated harmonics of the battery current with a low-frequency component of 125Hz and switching frequency of 2kHz with A_f = 400. The amplitude of the current harmonics are smaller than the current harmonic using variable duty cycle technique shown in Figure 4-11. The f_s harmonic is spread across the range between 1600Hz and 2400Hz (e.g. ($f_s \pm A_f$)) as previously mentioned in section 3.3.1. This is not necessarily a desirable characteristic from an EMI perspective.

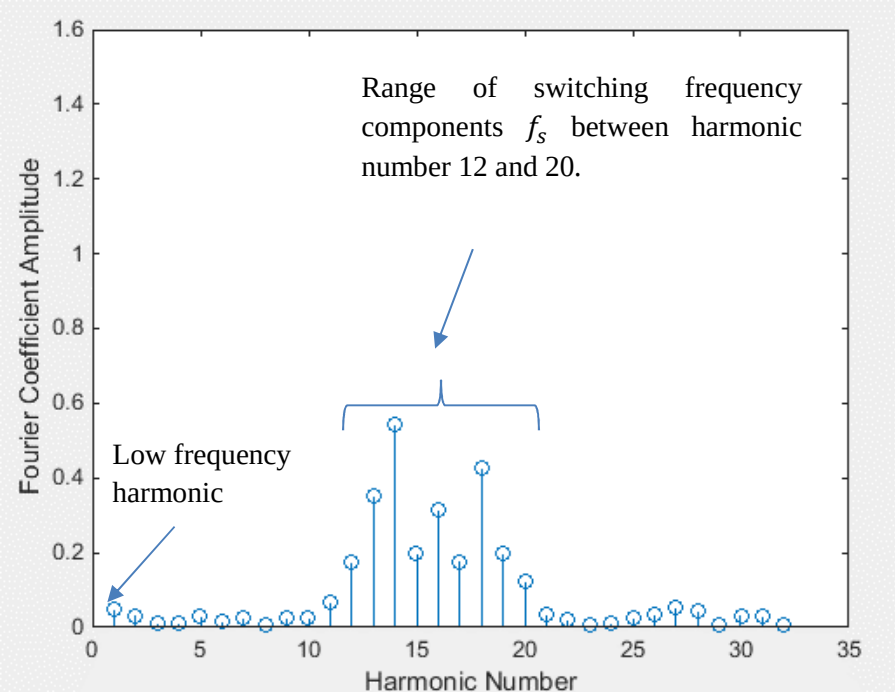

Figure 4-18 : Simulated current ripple at low frequency of 125Hz and switching frequency of 2kHz. A_f = 400.

4.4 DC/DC Converter with variable starting point PWM

In order to induce a low frequency ripple to the battery signals using a variable starting point method, a pulse position modulation (PPM) signal was used. To generate the PPM signal in MATLAB Simulink, a signal generator block was used to generate a saw tooth waveform, a sine wave generator was used to produce sinewave and a rational operator block, and a monostable is used (see Figure 4-20). The rational operator block compares the amplitude of the saw tooth and the sinewave signal. When the value of the sawtooth is bigger than the sinewave the state of the pulse signal is high and when it is lower, the state is low. This generates the pulse width modulation signal. The PPM signal is at high state when the PWM is at low state. This is shown in Figure 4-19. The monostable block is used to generate the PPM signal at the falling edge of the PWM signal and to set the duty cycle of the generated pulse.

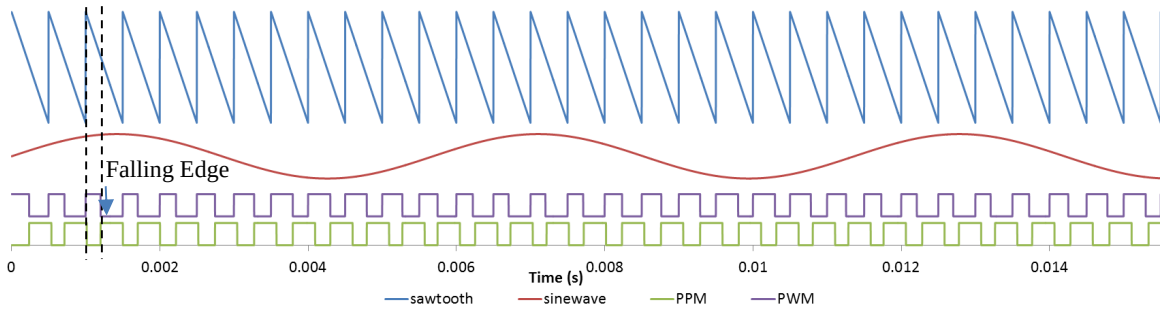

Figure 4-19 : Example showing adding a low frequency variable starting point using a sawtooth waveform with frequency 2kHz and a sinewave with low frequency wave 175Hz, duty cycle = 0.6.

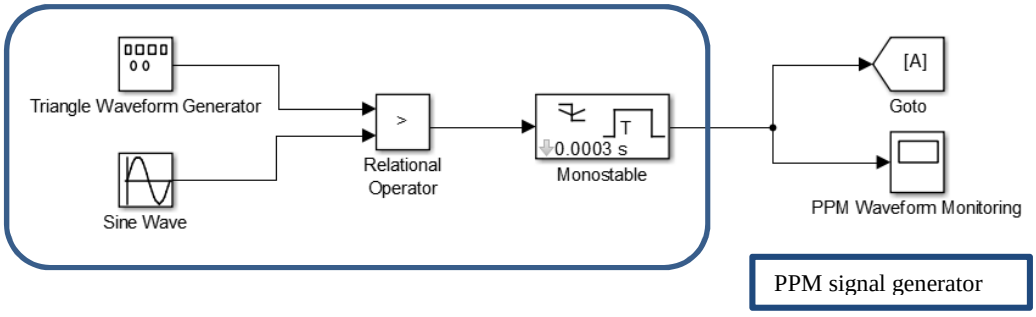

Figure 4-20 : Simulation model of the gate drive circuit to generate a variable starting points pulse

The circuit was simulated under the conditions of continuous mode operation with a switching frequency of 2kHz with an average starting point of 0.00026s and amplitude of variation A_t= 0.00004s to produce a rectangular function with a variable starting point and the duty cycle of 0.6. The comparison of the simulated circuit data with fixed duty cycle and variable starting point at the low frequencies of 125Hz and 175 Hz are shown in Table 4-6 and Table 4-7 respectively.

The average value of load voltage V_{dc} remained the same as does the boost ratio. The current ripple increases by 25% with the addition of the low-frequency ripple with no obvious variation due to low frequency value as described in section 3.4.3 .

Table 4-8: Comparison of simulated PWM with variable starting point at 125Hz effects on Current and Voltage ripple

	Simulation			
	Fixed Duty Cycle		Variable starting point	
	Average Value	Peak-Peak ripple	Average Value	Peak-Peak ripple
I_{batt}	1.55 A	2.42 A	1.58 A	3.02 A
V_{batt}	3.21 V	16.8 mV	3.21 V	21.3 mV
I_{load}	456 mA	0.7 mA	462 mA	2.2 mA
V_{dc}	7.3 V	11.1 mV	7.38 V	35.7 mV

Table 4-9: Comparison of simulated PWM with variable starting point at 175Hz effects on Current and Voltage ripple

	Simulation			
	Fixed Duty Cycle		Variable starting point	
	Average Value	Peak-Peak ripple	Average Value	Peak-Peak ripple
I_{batt}	1.55 A	2.42 A	1.59 A	3.13 A
V_{batt}	3.21 V	16.8 mV	3.2 V	22 mV
I_{load}	456 mA	0.7 mA	465 mA	2.5 mA
V_{dc}	7.3 V	11.1 mV	7.38 V	40.4 mV

Figure 4-21 to Figure 4-24 show the simulated waveforms of the battery and dc/dc converter using the variable starting point method. Similar to waveforms with variable duty cycle, the voltage and current signals have sinusoidal shape. However, the wave shape is distorted. This is believed to be a function of the accuracy by which MATLAB can handle the variable starting position due to the 20µs limitation in accuracy in the controller as described in section 3.5.3.

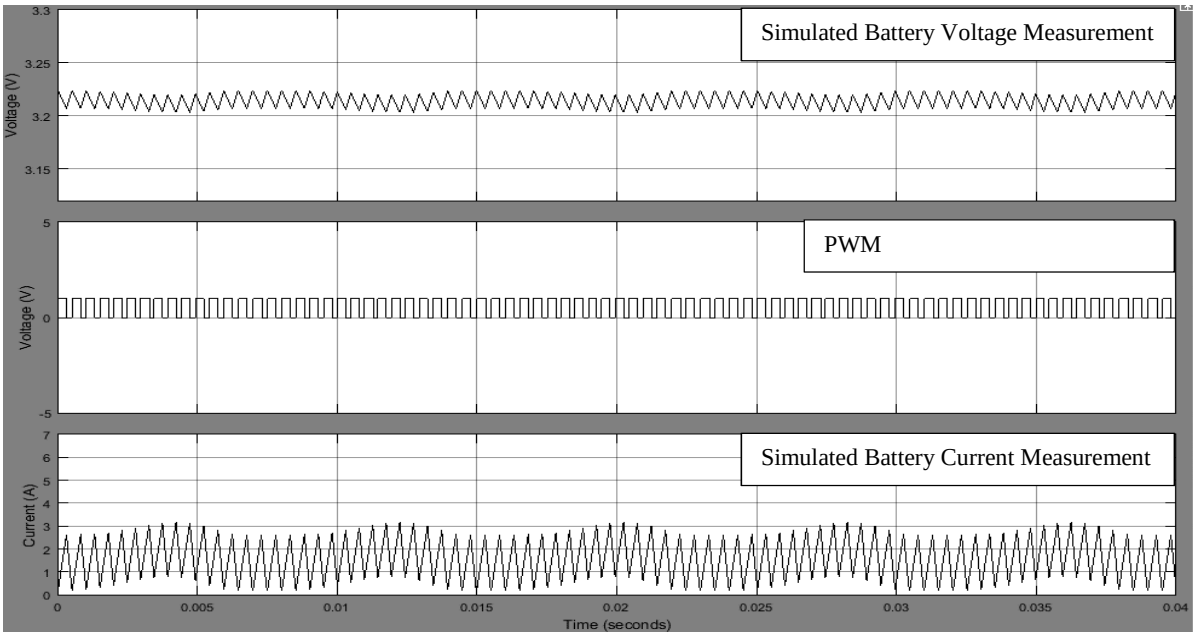

Figure 4-21 : Simulated Li-ion battery Current and Voltage waveforms. The battery is excited with PWM with variable starting point at a low frequency of 125Hz with A_t= 0.00004.

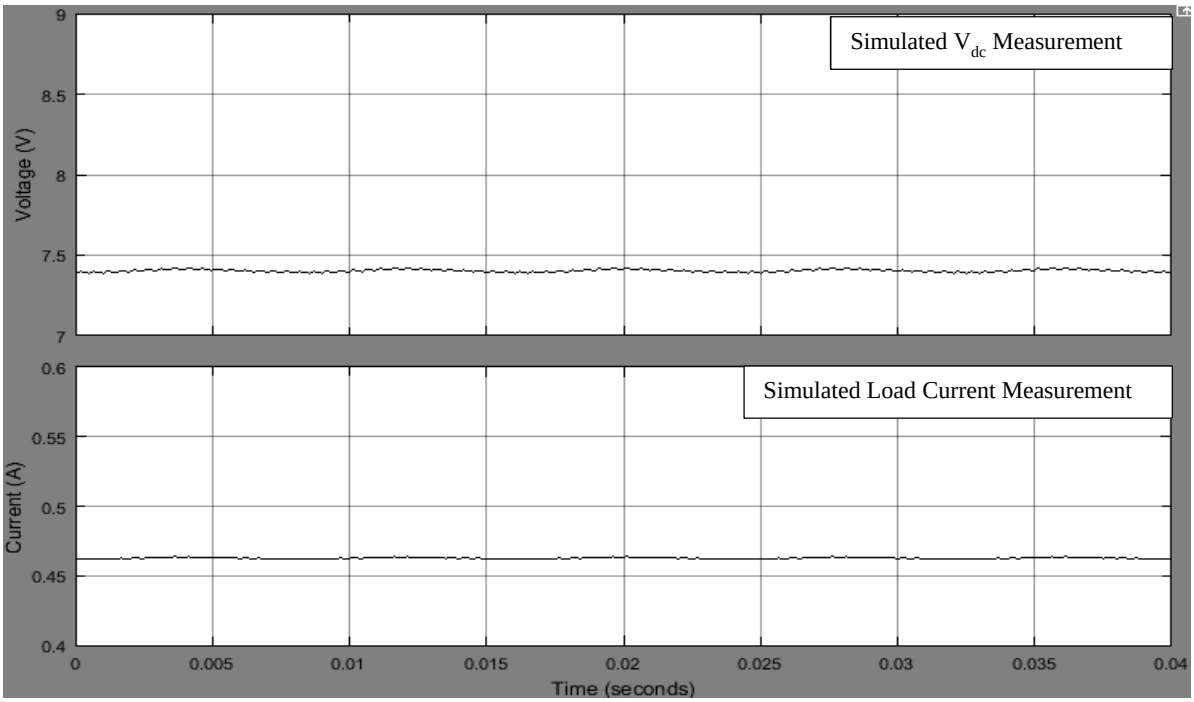

Figure 4-22 : Simulated Load Current and Voltage (Vdc) waveforms. The battery is excited with PWM with variable starting point at a low frequency of 125Hz with A_t= 0.00004.

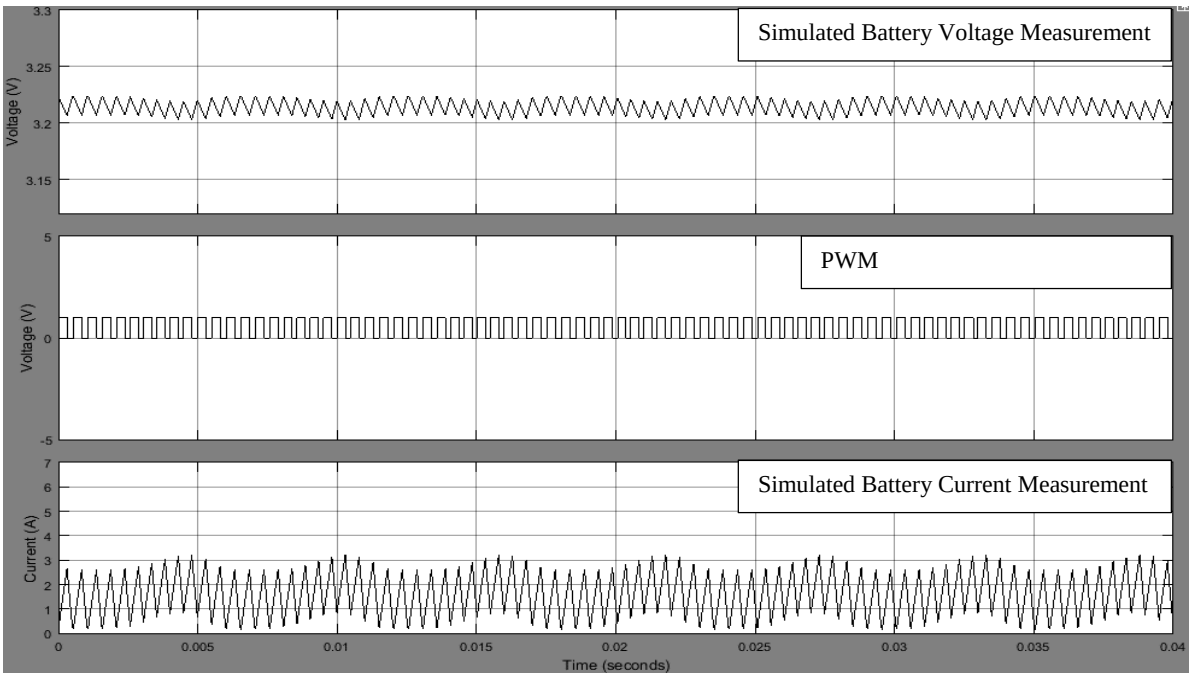

Figure 4-23 : Simulated Li-ion battery Current and Voltage waveforms. The battery is excited with PWM with variable starting point at a low frequency of 175Hz with A_t= 0.00004.

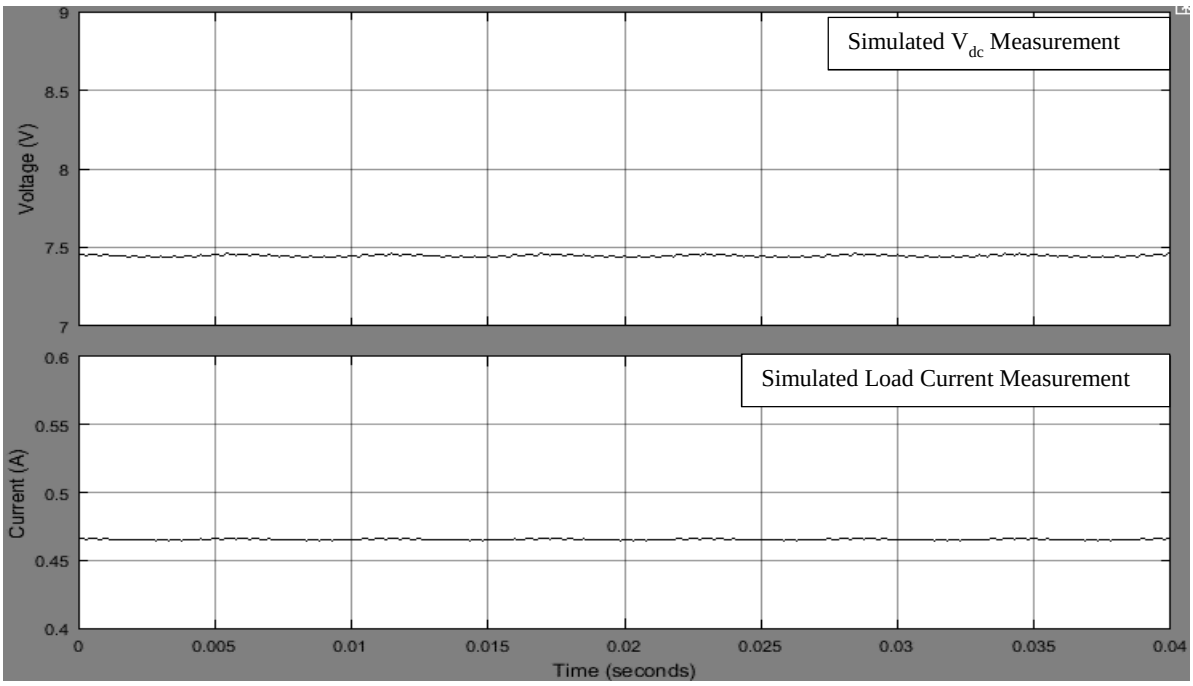

Figure 4-24 : Simulated Load Current and Voltage (Vdc) waveforms. The battery is excited with PWM with variable starting point at a low frequency of 175Hz with A_t= 0.00004.

The battery current harmonic analysis at low-frequency of 125Hz by varying the starting point of the PWM signal with A_t= 0.00004 is shown in Figure 4-25. It is clear that both low frequency 125Hz and the switching frequency of 2kHz harmonics are extracted from the simulated current waveform.

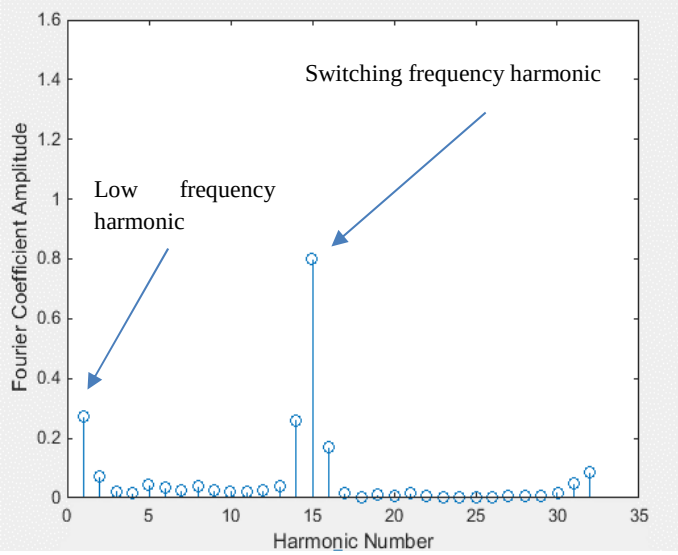

Figure 4-25 : Simulated variable starting point current ripple at low frequency of 125Hz and switching frequency of 2kHz

4.5 DC/DC Converter with an Impulse Function

In the simulation of the boost converter with an Impulse function, two pulse generator blocks were used as shown in Figure 4-26. One of them is used for generating pulse signals with a duty cycle of 0.6 and frequency of 2kHz, the other pulse generator is used to create an impulse signal. A logical operator function block was use to OR the signals from the pulse generator blocks.

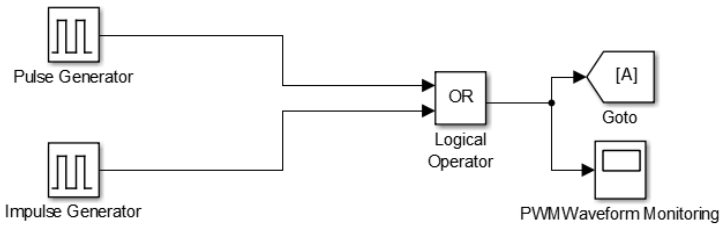

Figure 4-26 : Example showing a simulation model for Impulse function

A fixed time step of 20µs is used in the OpalRT hardware, so the chosen duty cycle and the frequency of the Impulse function must be chosen as a multiple integer of the time step as explained in section 3.5.1. For consistency with section 3.5.1, it is easier to analyse the circuit when the low frequency impulse is an integer multiple of the switching frequency. There are two ways to generate this impulse;

- A small pulse width of 20µs can be used but the start of the pulse needs to be time shifted.
- A pulse of slightly larger width than the 2kHz switching frequency can be used but the start of both pulses needs to be co-incident.

The latter is easier to generate through the OpalRt control so will be used. For example at 125Hz the impulse duty cycle must be chosen such that the impulse width is longer than the switching frequency pulse which is 0.0003s. A duty cycle of 0.04 is used to generate a pulse width of 0.00032s. In this case the low frequency component is then visible to the gate drive after passing through the OR function.

The circuit was simulated under the conditions of continuous mode operation with the average switching frequency of 2kHz and duty cycle of 0.6. The simulation was run for OR combination of the PWM signal and a pulse function with a low-frequency component set to be as an integer value of the switching frequency. The comparison of the simulated circuit data at the low frequencies of 125 Hz with duty cycle of 0.04 and 166.7Hz with duty cycle of 0.06 are shown in Table 4-10 and Table 4-11

respectively. It was chosen not to carry out the second point at 175Hz as this is not an integer of the switching frequency so 166.7Hz was used as the closest integer value.

Table 4-10: Comparison of simulated PWM with Impulse (OR-4 %) at 125Hz effects on Current and Voltage ripple

	Simulation			
	Fixed Duty Cycle		Using impulse function	
	Average Value	Peak-Peak ripple	Average Value	Peak-Peak ripple
I_{batt}	1.55 A	2.42 A	1.56 A	2.7766 A
V_{batt}	3.21 V	16.8 mV	3.21 V	18.2 mV
I_{load}	456 mA	0.7 mA	458.4 mA	1.4 mA
V_{dc}	7.3 V	11.1 mV	7.34 V	22.2 mV

Table 4-11: Comparison of simulated PWM with Impulse (OR-6%) at 166.7Hz effects on Current and Voltage ripple

	Simulation			
	Fixed Duty Cycle		Using impulse function	
	Average Value	Peak-Peak ripple	Average Value	Peak-Peak ripple
I_{batt}	1.55 A	2.42 A	1.56 A	3.43 A
V_{batt}	3.21 V	16.8 mV	3.21 V	22.4 mV
I_{load}	456 mA	0.7 mA	475 mA	2.8 mA
V_{dc}	7.3 V	11.1 mV	7.6 V	45.3 mV

The peak to peak ripple increased with the extra width of the impulse function according to the Equation 3-83. The pulse width at 125Hz increased from 0.0003 to 0.00032s, while the pulse width increased to 0.00036s at 166.7Hz. The ripple and boost ratio of the 166.7Hz impulse function is therefore higher compared to the 125Hz signal as expected, because the circuit is switched on for longer time and therefore the boost ratio of the circuit changes due to the increase in the average duty cycle with time over the T_0 pulses period.

Figure 4-27 to Figure 4-30 illustrate the simulated waveforms of the battery and dc/dc converter for an OR combination of PWM and Impulse signal. The battery current increased at each interval of the f_0 of the low frequency waveform as the switching pulse width, T_i is added as described in section 3.5.4.

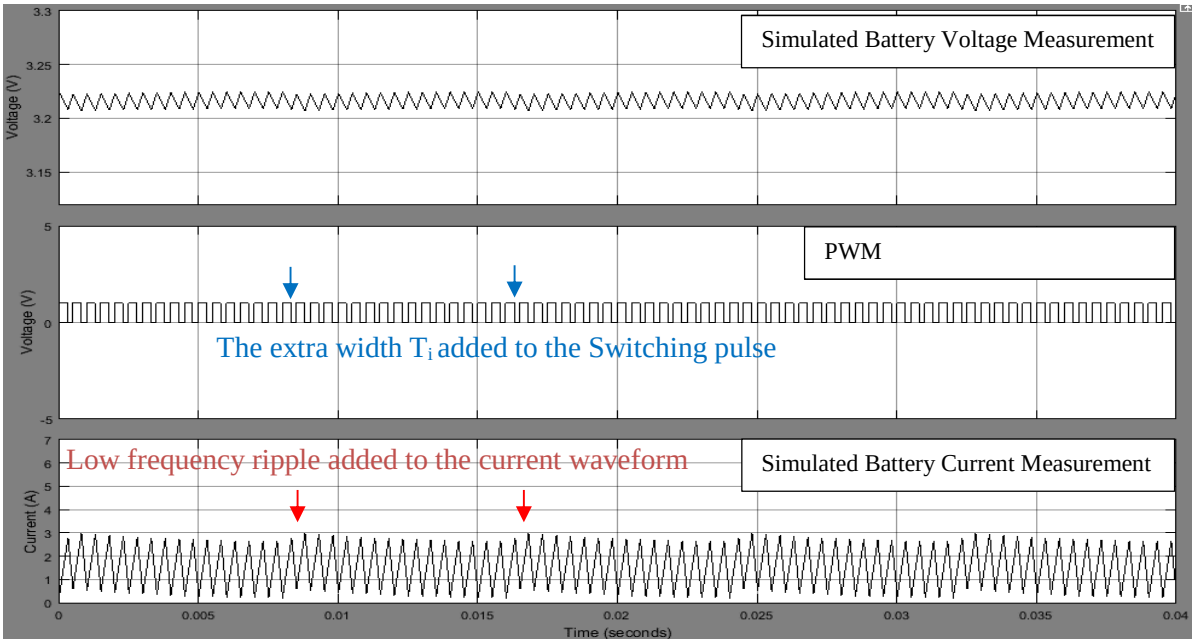

Figure 4-27 : Simulated Li-ion battery Current and Voltage waveforms. The battery is excited with an impulse signal at a low frequency of 125Hz with pulse duty cycle of 0.04.

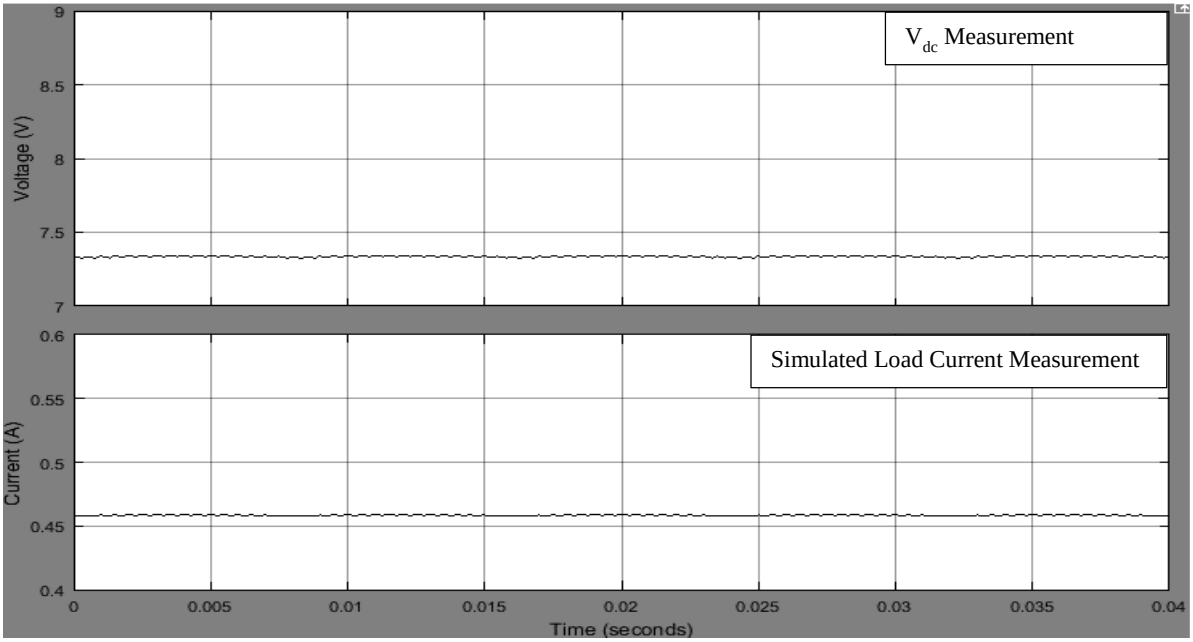

Figure 4-28 : Simulated Load Current and Voltage (Vdc) waveforms. The battery is excited with an impulse signal at a low frequency of 125Hz with pulse duty cycle of 0.04.

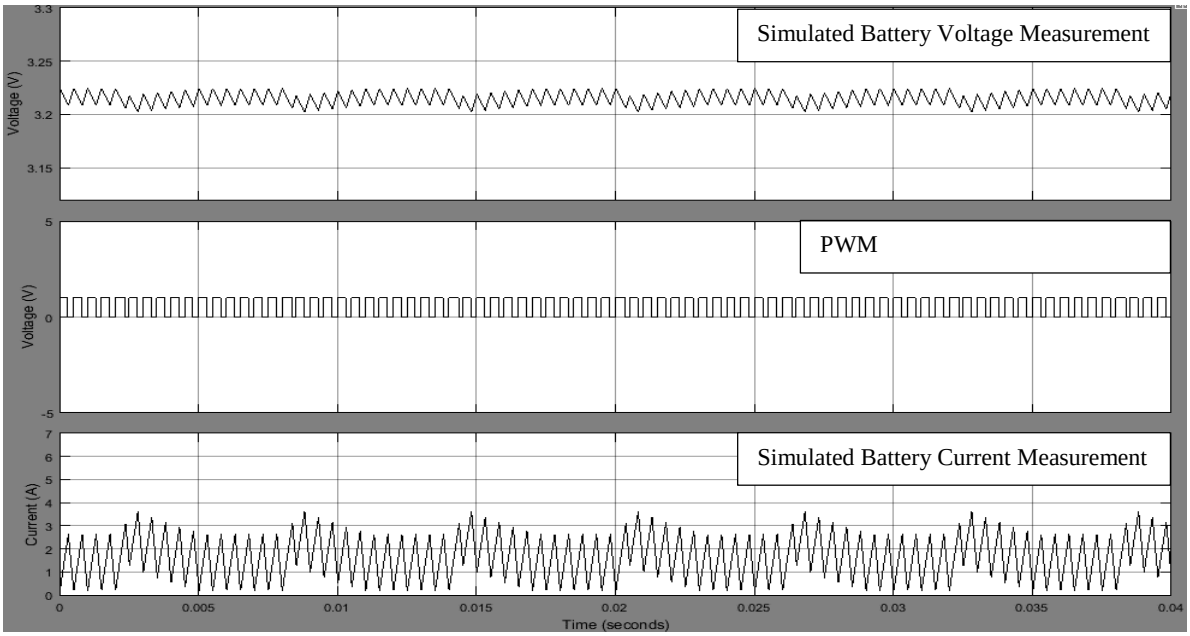

Figure 4-29 : Simulated Li-ion battery Current and Voltage waveforms. The battery is excited with an impulse signal at a low frequency of 166.7Hz with pulse duty cycle of 0.06.

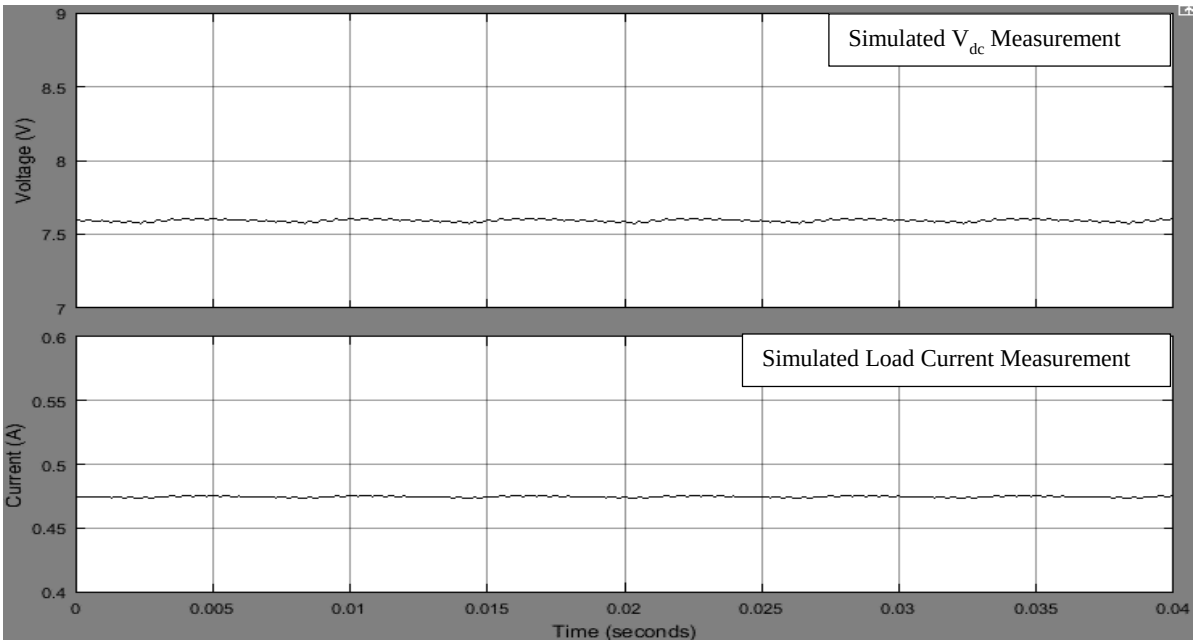

Figure 4-30 : Simulated Load Current and Voltage (Vdc) waveforms. The battery is excited with an impulse signal at a low frequency of 166.7Hz with pulse duty cycle of 0.06.

Figure 4-31 shows the harmonic analysis of the battery current using the Impulse method for $f_0 = 125Hz$ and duty cycle of 0.04.

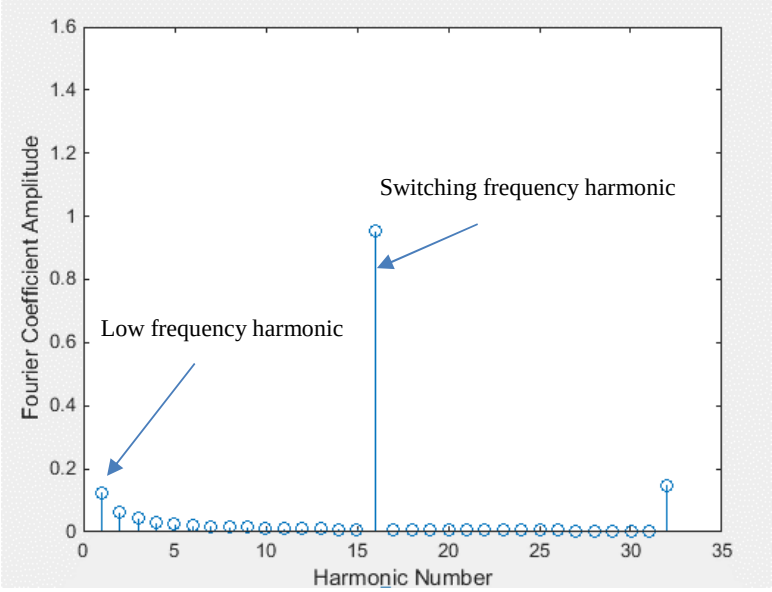

Figure 4-31 : Simulated PWM with an Impulse function current ripple at low frequency of 125Hz with pulse width of 0.0004s and switching frequency of 2kHz

4.6 Battery Balancing

The switched capacitor balancing method is modelled for the balancing of two battery cells. To balance these two cells, four MOSFET switching components with a capacitor are used. For each battery two switches are needed as shown in Figure 4-32. Two pulse generator blocks are used to control the MOSFETs. One pulse generator with a duty cycle of 0.45 controls switches M1 and M3. The other pulse generator controls switches M2 and M4. Because switches M2 and M4 should be turned off while switches M1 and M3 are turned on, a logical operator function block is used to NOT the pulse control signal with the duty cycle of 0.55. So the output signal is a pulse signal with 0.45 duty cycle. A 10mF capacitor was used for the balancing capacitor. As mentioned in section 3.6, the value of this balancing capacitor affects the speed of the balancing time. Some authors [295], [298] also use a series inductance for soft-switching of the battery balancing. They chose the capacitor values based on the resonance circuit design. In this research a series inductance wasn't used, however it would be considered in future work. This method is presented as a proof of concept and the use of the resonance circuit as a balancing method for EIS calculation adds complexity and requires further consideration which is out of scope of this thesis. The model in Figure 4-32 was used. However, using a voltage source within the battery model does not allow the charge transfer to be seen as part of the balancing. To specifically observe this a high value capacitor could be used. One potential disadvantage, is that it may only be possible to detect the low frequency ripple on the batteries waveforms when the batteries are not balanced. This is because when the batteries are balanced there is no current to be shared between the batteries and therefore the low-frequency ripple may not be seen.

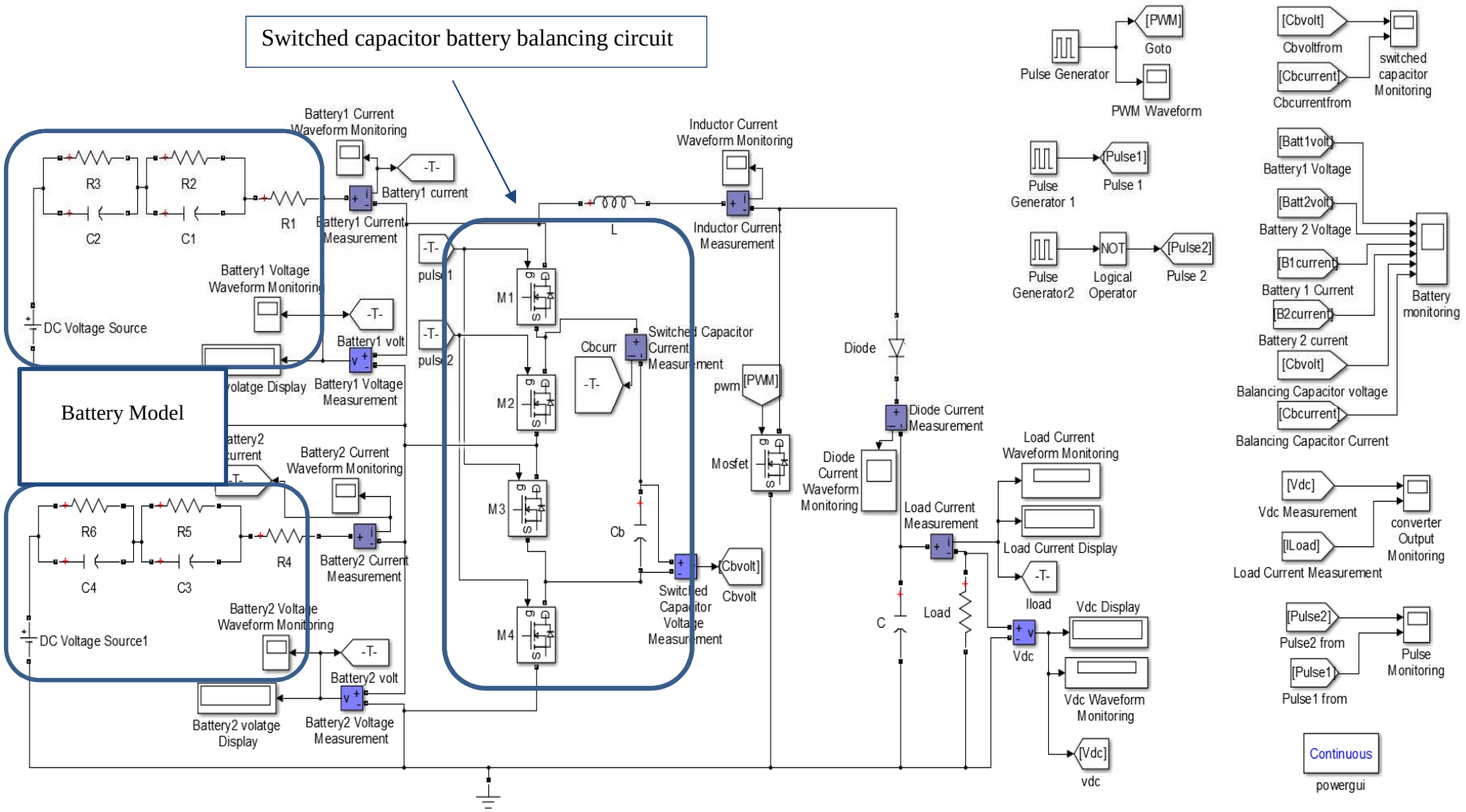

Figure 4-32 : Example showing a simulation model for a switched capacitor battery balancing circuit connected to the converter

To keep consistency with the other methods, the circuit was simulated such that the boost converter is switched at a frequency of 2kHz and a duty cycle of 0.6. The battery balancing is set as two pulse signals with fixed duty cycle of 0.45 at the low-frequency required. The voltage values of the batteries were chosen such that the sum of the two battery voltages has been set to 3.21V to allow comparison with the fixed duty cycle case. Although, these values are smaller than the threshold voltage level of the li-ion battery and are not safe for practical operation as used. The values of the two battery voltages have been offset to simulate the process of balancing, so that current flows through the battery balancing circuit. The comparison of the simulated circuit data with fixed duty cycle and switching frequency at the low frequencies of 125Hz and 166.7Hz are shown in Table 4-12 and Table 4-13 respectively. It was chosen not to carry out the second point at 175Hz as this is not an integer of the switching frequency so 166.7Hz was used as the next closet integer. This is again because of the fixed time step 20µs used by the Opal-rt unit (refer to section 3.5.1).

Table 4-12: Comparison of simulated battery balancing excited signal at 125Hz effects on Current and Voltage ripple

	Simulation			
	Fixed Duty Cycle		Battery with Balancing circuit	
	Average Value	Peak-Peak ripple	Average Value	Peak-Peak ripple
I_L	1.55 A	2.42 A	1.56 A	2.73 A
I_{batt1}	1.55 A	2.42 A	1.8 A	3.51 A
I_{batt2}			1.4 A	3.88 A
V_{batt1}	3.21 V	16.8 mV	1.7 V	25 mV
V_{batt2}			1.51 V	26.7 mV
I_{load}	456 mA	0.7 mA	455 mA	0.8 mA
V_{dc}	7.3 V	11.1 mV	7.3 V	12.5 mV

Table 4-13: Comparison of simulated battery balancing excited signal at 166.7 Hz effects on Current and Voltage ripple

	Simulation			
	Fixed Duty Cycle		Battery with Balancing circuit	
	Average Value	Peak-Peak ripple	Average Value	Peak-Peak ripple
I_L	1.55 A	2.42 A	1.56 A	2.73 A
I_{batt1}	1.55 A	2.42 A	1.86 A	3.49 A
I_{batt2}			1.34 A	3.35 A
V_{batt1}	3.21 V	16.8 mV	1.7 V	24.8 mV
V_{batt2}			1.51 V	24 mV
I_{load}	456 mA	0.7 mA	456 mA	0.8 mA
V_{dc}	7.3 V	11.1 mV	7.3 V	12.1 mV

The boost ratio, load current and voltage remain the same. The ripple in the inductor increases in comparison to the theory because some of the capacitor current passes through the inductor as a function of impedance. The waveform of the batteries and circuit waveforms are shown in Figure 4-33 to Figure 4-36. The waveforms show that the added ripple to the battery waveforms, using the battery balancing method as explained in section 3.6.2, are visible in the simulation. The current in battery 1 and battery 2 is the superposition of the balancing capacitor charging and discharging currents with the boost converter current waveforms (refer to section 3.6.2). When battery 1 is connected and discharging to the balancing capacitor, the current ripple of the battery follows an exponential decay related to the time constant of the circuit until the capacitor is disconnected. In battery 2 which is charging from the capacitor the reciprocal action occurs.

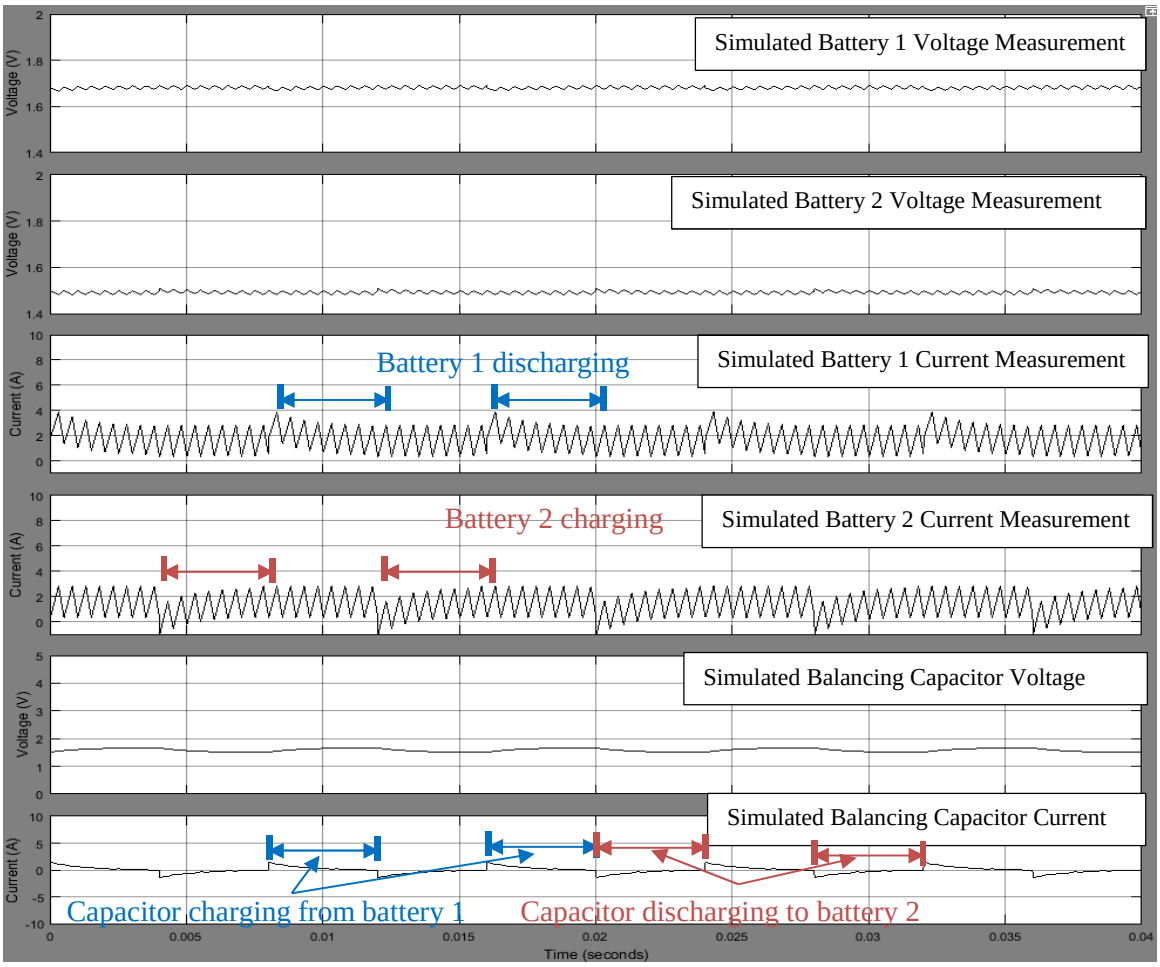

Figure 4-33 : Simulated Li-ion battery Current and Voltage waveforms. The battery is subject to battery balancing at a low frequency of 125Hz.

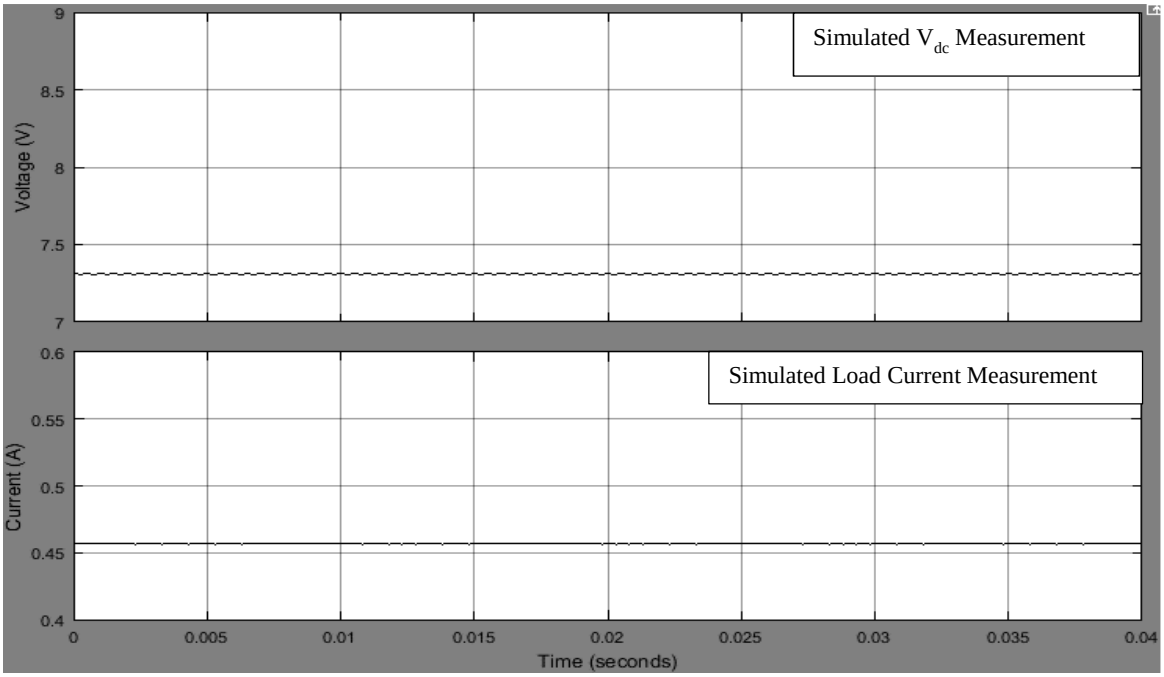

Figure 4-34 : Simulated Load Current and Voltage (Vdc) waveforms. The battery is subject to battery balancing at a low frequency of 125Hz.

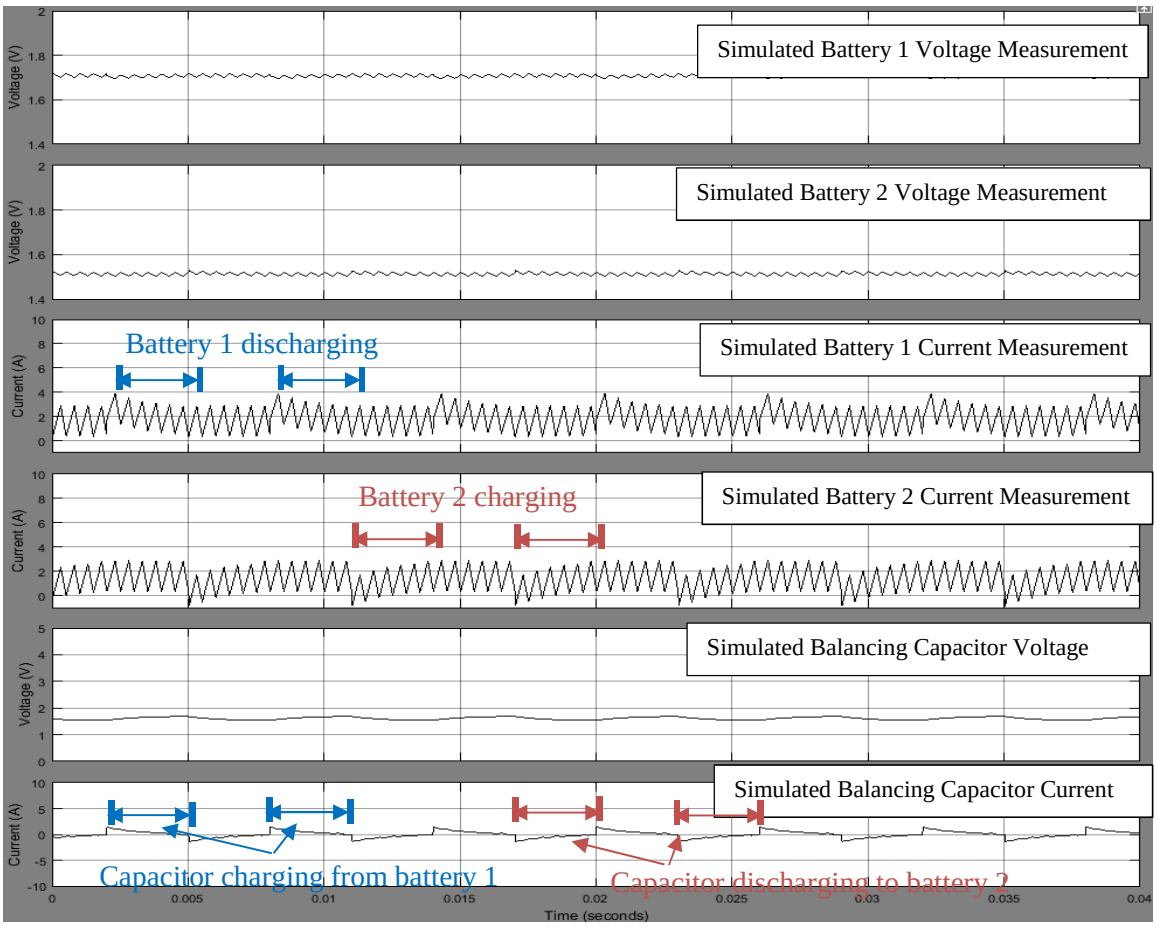

Figure 4-35 : Simulated Li-ion battery Current and Voltage waveforms. The battery is subject to battery balancing at a low frequency of 166.7 Hz.

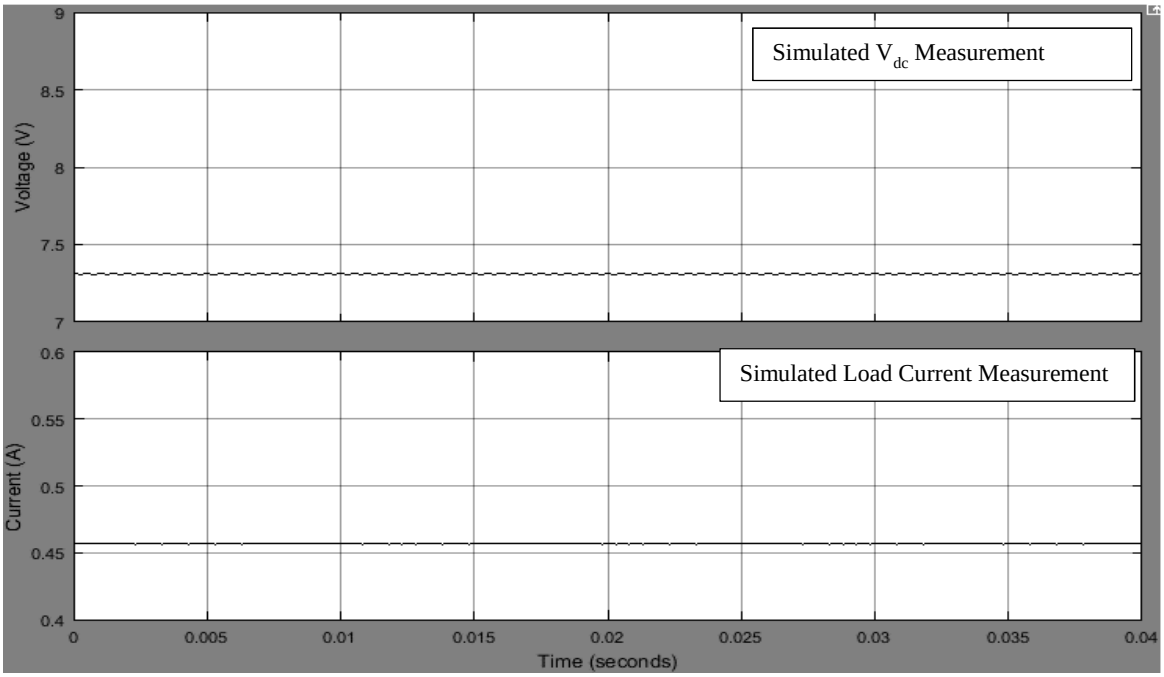

Figure 4-36 : Simulated Load Current and Voltage (Vdc) waveforms. The battery is subject to battery balancing at a low frequency of 175Hz.

This method may not be useful for the batteries when there is a high voltage difference between the two batteries, because this results in a high value of capacitor current. For example, when $V_{batt1} = 3.18V$ and $V_{batt2} = 0.043V$ a large current flows as is shown in Figure 4-37 and Figure 4-38. But the voltage value of 43mV is not practical and safe for li-ion battery. However, this is chosen for proof of concept of the methodology. Additionally the battery low frequency current ripple is not visible when there is a small voltage difference between the two batteries.

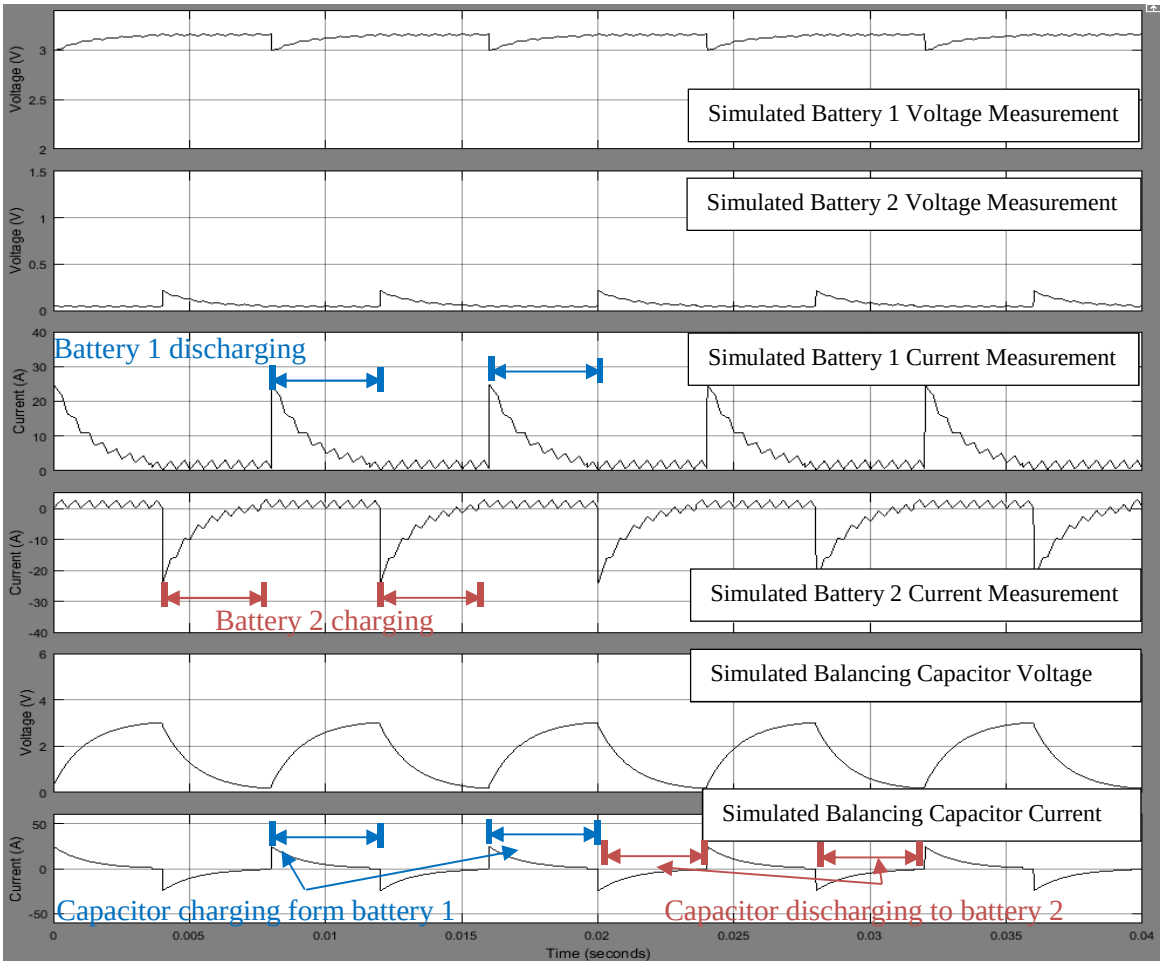

Figure 4-37 : Simulated Li-ion battery Current and Voltage waveforms. The battery is subject to battery balancing at a low frequency of 125Hz. With V_{bat1} =3.18V and V_{bat2} =0.043V

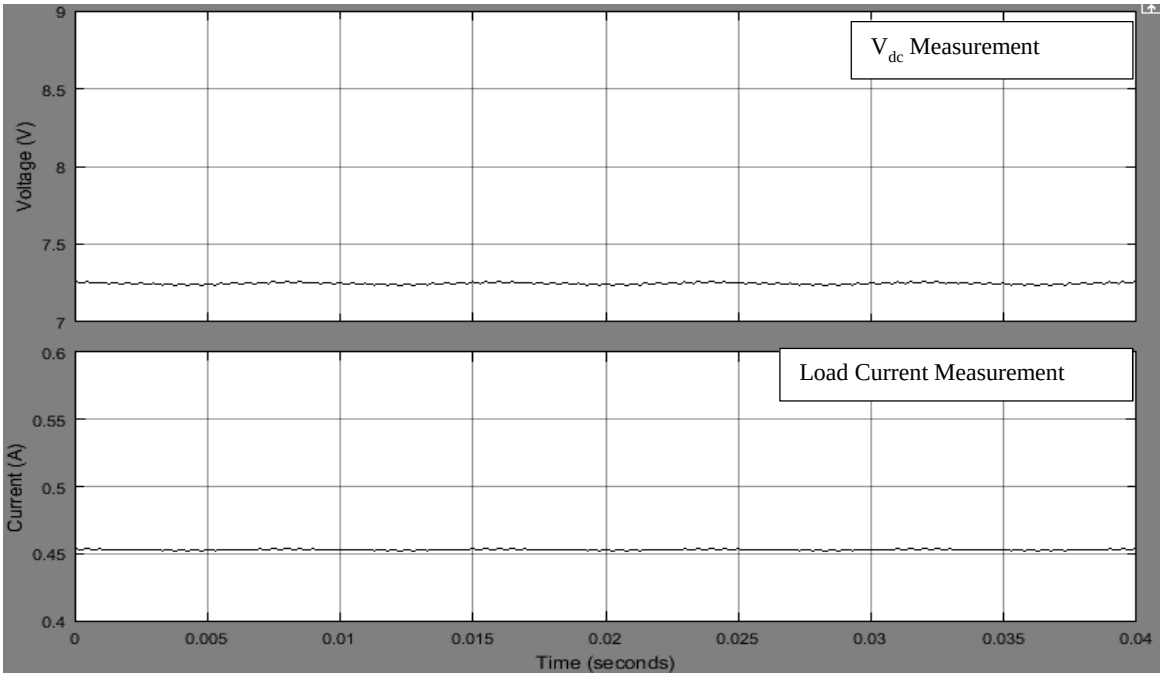

Figure 4-38 : Simulated Load Current and Voltage (Vdc) waveforms. The battery is subject to battery balancing at a low frequency of 125Hz.

Figure 4-39 shows the Fourier analysis of the simulated current of both batteries using the battery balancing circuit at switching frequency of 2kHz and low frequency of the 125Hz. The harmonics of f_0 and f_s are present in the harmonic spectrum of the simulated currents.

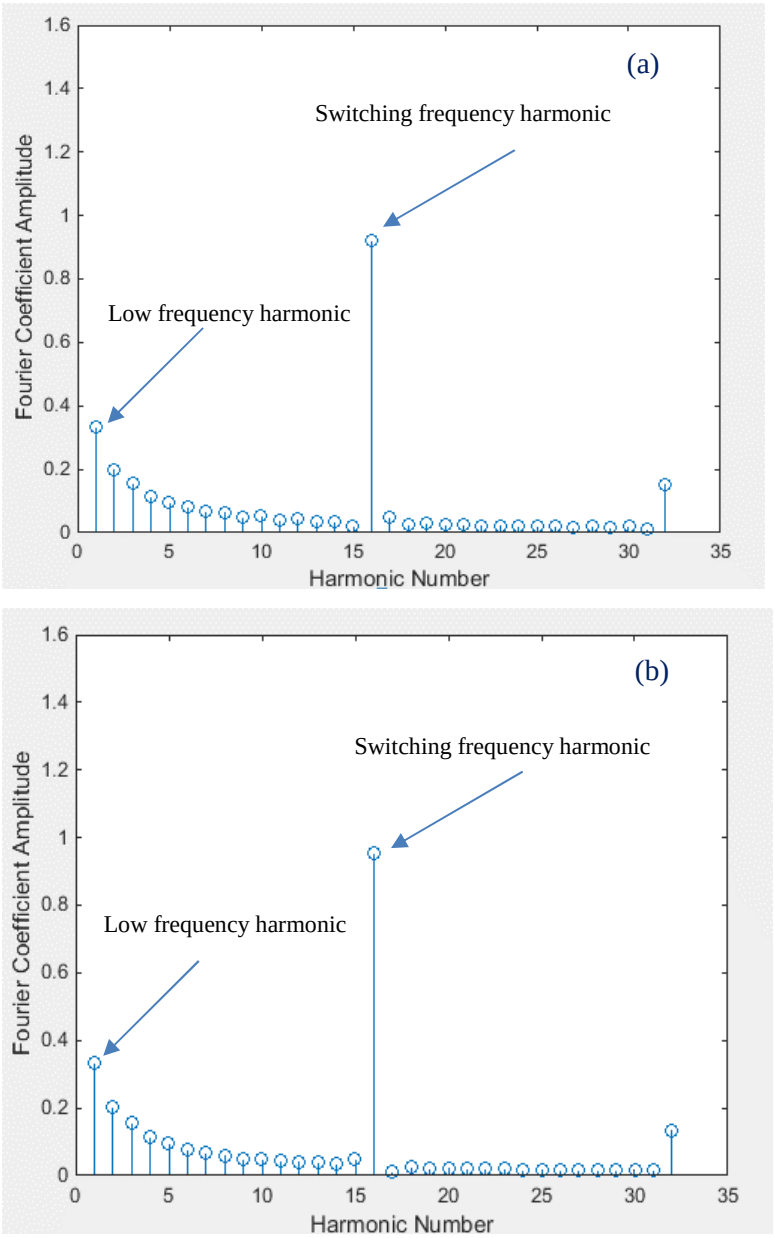

Figure 4-39 : Simulated current ripple at a low frequency of 125Hz and a switching frequency of 2kHz using the battery balancing method. a) Battery 1 current harmonics, b) Battery 2 current harmonics

4.7 Earth Leakage Monitoring

The ELM low-frequency injection technique was simulated in Simulink. The same battery and boost converter models, from section 4.1, were used. The earth leakage monitoring circuit simulation includes two AC voltage sources to inject the low frequency signal, and two ELM resistors and capacitors. The voltage sources are then connected to the battery terminals through the resistors. The AC voltage sources generate low-frequency sinewave signals with the same amplitude of 12V but a 45˚ phase difference with respect to each other. The battery is connected to the boost converter as shown in Figure 4-40.

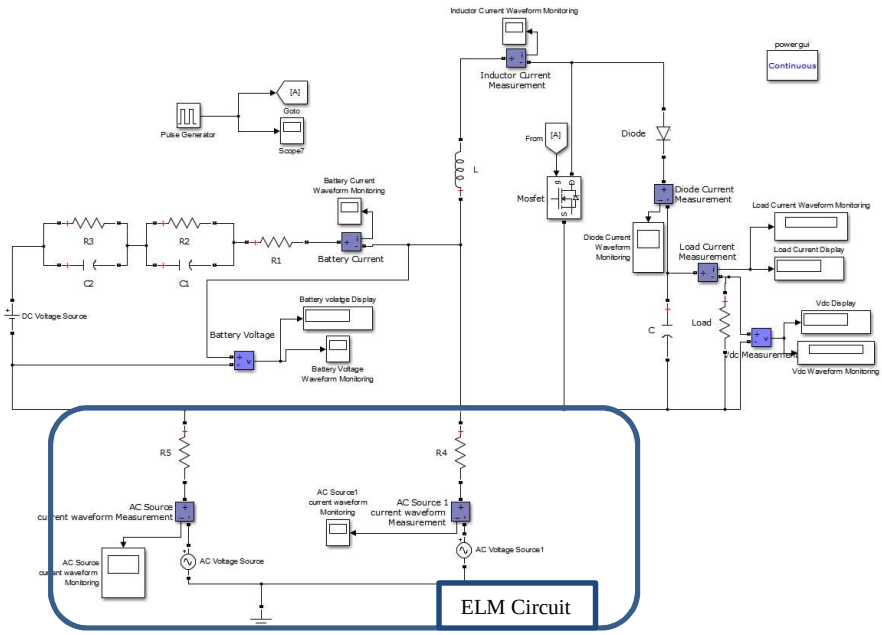

Figure 4-40 : Example showing a simulation model for Earth leakage monitoring battery connected to the converter.

The circuit was simulated with a boost converter switching frequency of 2kHz, a duty cycle of 0.6 and the ELM circuit active. The comparison of the simulated circuit data with fixed duty cycle and switching frequency at the low frequencies of 125Hz and 175 Hz are shown in Table 4-14 and Table 4-15 respectively. The boost ratio and load current and voltage remain the same as the base model. There is no obvious low frequency dependence on ripple, but the indication of increasing frequency giving rise to decreasing ripple, is in keeping with Equation 3-124.

Table 4-14: Comparison of simulated Earth leakage Monitoring excited signal at 125Hz effects on Current and Voltage ripple

	Simulation			
	Fixed Duty Cycle		Earth Leakage connected to the converter	
	Average Value	Peak-Peak ripple	Average Value	Peak-Peak ripple
I_{batt}	1.55 A	2.42 A	1.7 A	3.323 A
V_{batt}	3.21 V	16.8 mV	3.21 V	24.1 mV
I_{load}	456 mA	0.7 mA	455 mA	0.74 mA
V_{dc}	7.3 V	11.1 mV	7.3 V	11.8 mV

Table 4-15: Comparison of simulated Earth leakage Monitoring excited signal at 175Hz effects on Current and Voltage ripple

	Simulation			
	Fixed Duty Cycle		Earth Leakage connected to the converter	
	Average Value	Peak-Peak ripple	Average Value	Peak-Peak ripple
I_{batt}	1.55 A	2.42 A	1.7 A	3.321 A
V_{batt}	3.21 V	16.8 mV	3.21 V	23.9 mV
I_{load}	456 mA	0.7 mA	455 mA	0.71 mA
V_{dc}	7.3 V	11.1 mV	7.3 V	11.4 mV

The waveform of the batteries and circuit waveforms are shown in Figure 4-40 to Figure 4-44. At first glance, the waveforms look similar to the waveforms in the variable duty cycle method. However, they are different, as in this method the sinusoidal waveform is the results of the superposition of the generated ELM current and the boost converter as described in section 3.7.3.

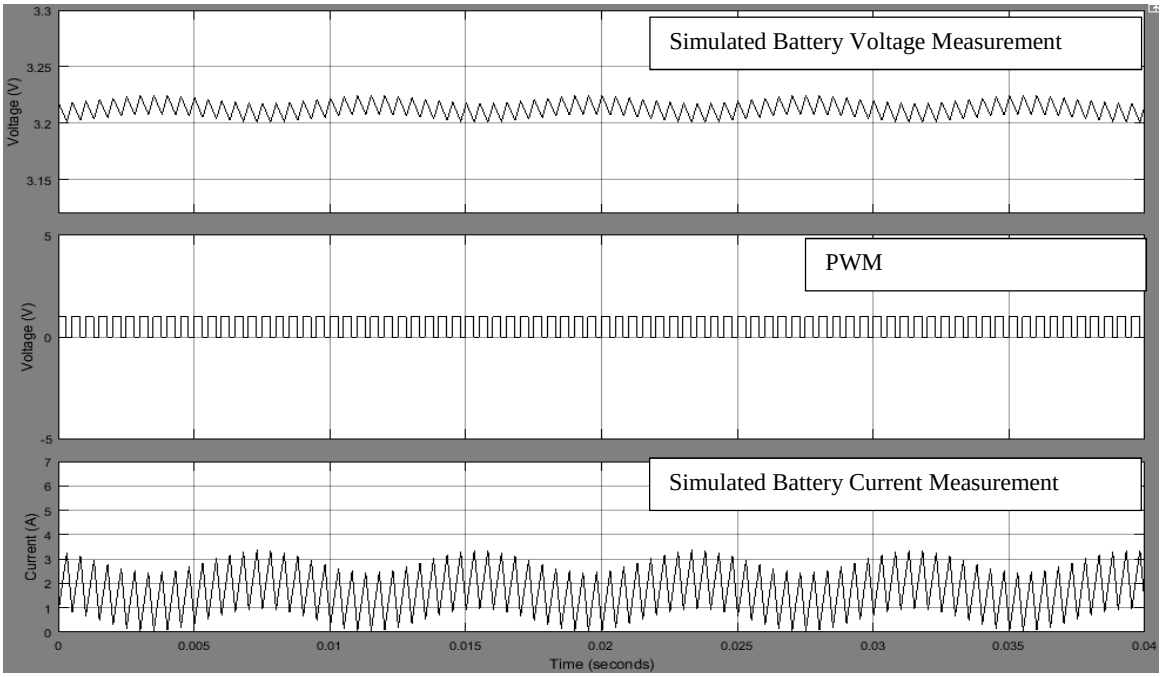

Figure 4-41 : Simulated Li-ion battery Current and Voltage waveforms. The battery is excited with an Earth leakage Monitoring signal at a low frequency of 125Hz.

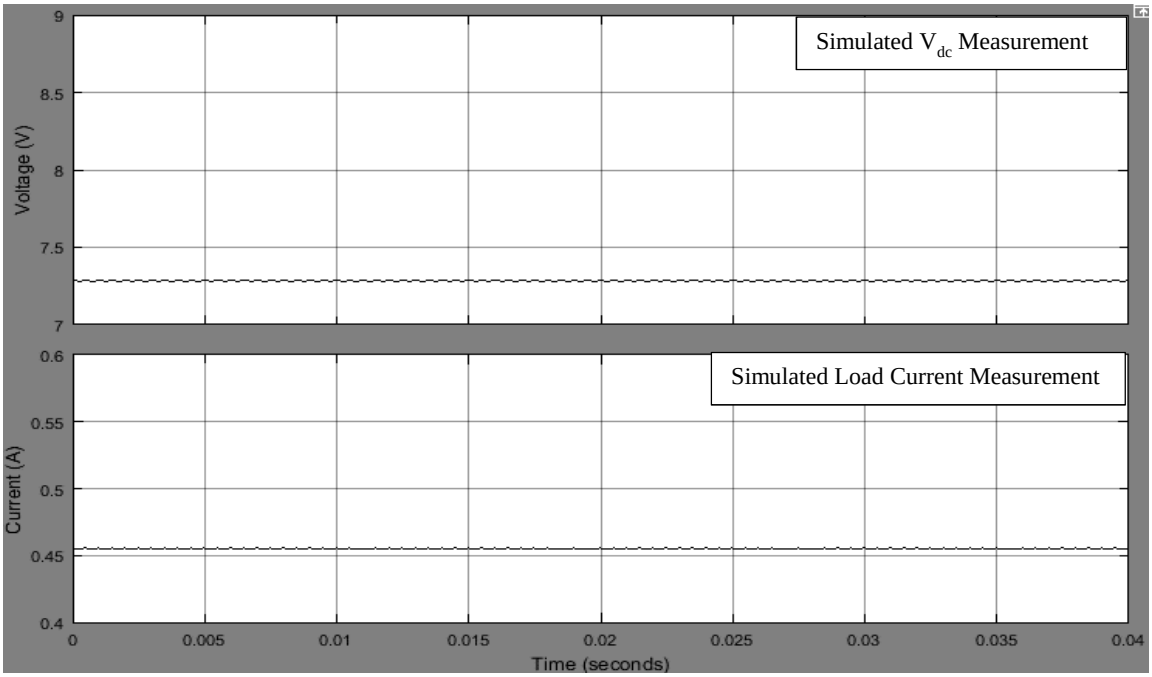

Figure 4-42 : Simulated Load Current and Voltage (Vdc) waveforms. The battery is excited with an Earth leakage Monitoring signal at a low frequency of 125Hz.

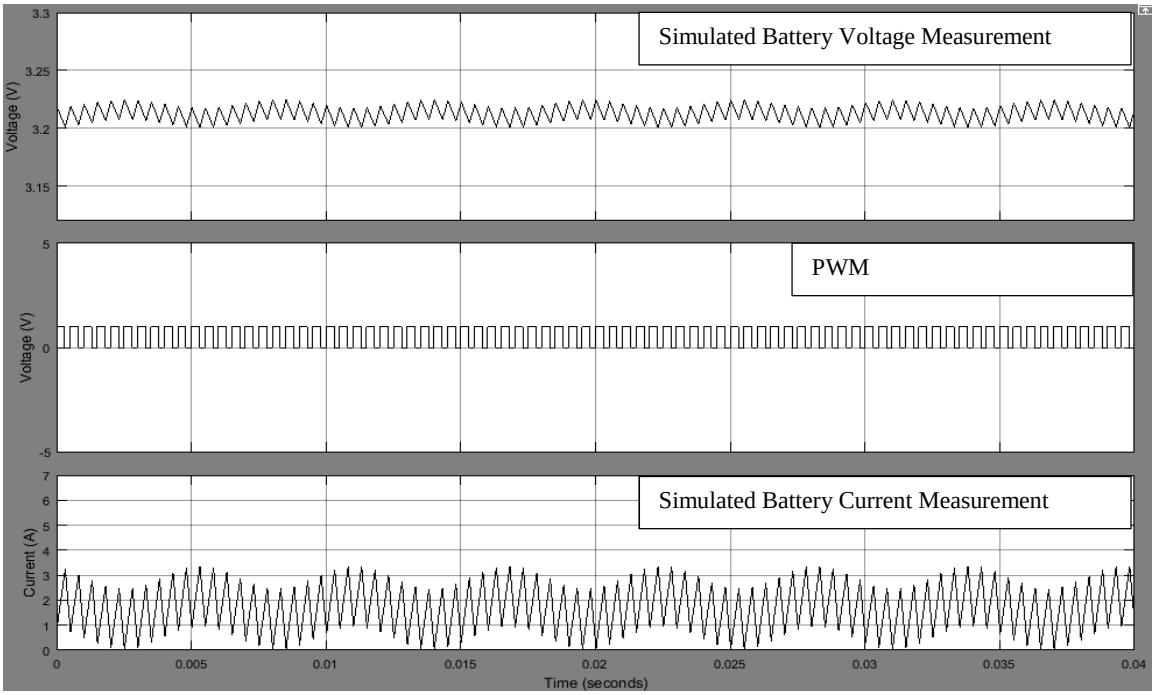

Figure 4-43 : Simulated Li-ion battery Current and Voltage waveforms. The battery is excited with an Earth leakage Monitoring signal at a low frequency of 175Hz.

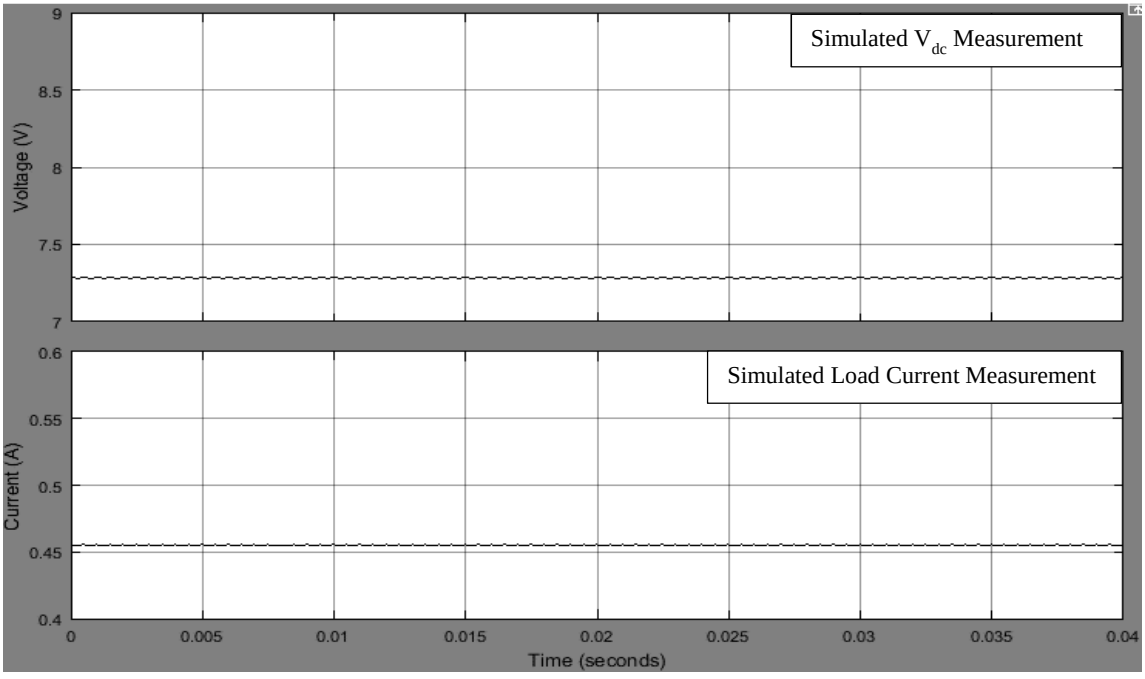

Figure 4-44 : Simulated Load Current and Voltage (Vdc) waveforms. The battery is excited with an Earth leakage Monitoring signal at a low frequency of 175Hz.

Figure 4-45 illustrates the Fourier analysis of the simulated current of the ELM method at a converter switching frequency of 2kHz and a low frequency ELM signal of 125Hz. Both low frequency and switching frequency harmonics are observed in the harmonic spectrum of the simulated current.

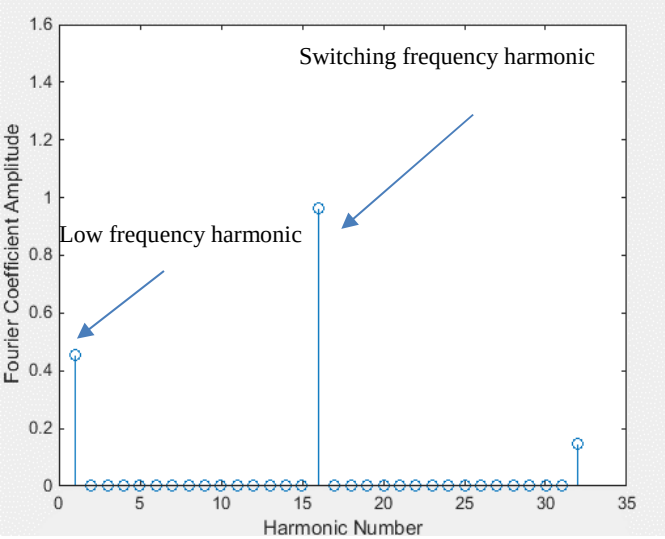

Figure 4-45 : Simulated current harmonics at low frequency of 125Hz and switching frequency of 2kHz using the ELM method

4.8 Summary

This chapter looked at simulating the circuits of the different presented methods for injecting a low frequency harmonic from chapter 3. The DC- DC converter was modelled to operate in continuous mode with a fixed duty cycle and 2kHz switching frequency. The circuit and battery waveforms under the different methods of adding low frequency ripple were obtained through simulation. This chapter also calculated the harmonics of the simulated current through the battery using the Fourier analysis of the simulated battery current using MATLAB. Key results compared to a circuit with no low frequency ripple are summarised in Table 4-16.

In all these methods, the low-frequency component has been detected from the simulated battery waveforms. This indicates the possibility of using the low-frequency excitation signal methods to undertake an on-line EIS measurement. However, there are some issues in using these methods;

- The variable frequency method produces a spread range of switching frequency across the $(f_s \pm A_f)$ range. This may result in EMI/EMC issues.
- In the impulse function, starting position, and battery balancing method, the accuracy of the data is limited by the time step size of 20µs.
- The battery balancing method can't be used when the battery voltages are equalised as the low-frequency ripple is not visible in the waveforms. Also, using the battery balancing may result in an increase in the current ripple when the voltage difference between the batteries is high.

Table 4-16: key results from simulation

Method	Boost ratio compared to base case	Key controlling parameters	Inductor current ripple increase @125Hz	Ripple dependency on frequency	Fourier co-efficient amplitude @125Hz
1- Variable duty cycle	Same	A_d = 0.01 in D = 0.6	12.4%	Yes	0.16
2- Variable frequency	Same	A_f = 400Hz in f_s = 2kHz	20%	Not visible in simulation	0.047
3 – Variable starting point	Same	A_t = 40µs in 260µs	42%	Yes	0.27
4 – Impulse function	Higher	T_i = 0.00002s in a pulse width of 0.0003s	14.7%	Yes – but hardware dependent	0.13
5 – Battery Balancing	Same	voltage difference 0.19V in 3.21V	14% (average)	Not visible in simulation	0.33
6 - ELM	Same	Fixed voltage difference of 9.2V	37%	Not visible in simulation	0.46

Modelling of these circuits for the purposes of understanding their viability as an on-line EIS measurement technique has not previously been published in literature. The techniques for producing the excitation signals through standard control components which are then used in the experimental section can be considered novel for this application. Although simulation is a useful tool, but experimental validation is needed to show full proof of concept.

Chapter 4 looks at validation of these methods through experimental results. The measured data is then compared with the simulated results from this chapter and the theoretical expressions from chapter 3. Chapter 4 also investigates using these techniques to generate an EIS plot by looking at the measured and simulated results over a range of frequencies and comparing this to off-line EIS measurement.

5 Experimental results of on-line EIS techniques

5.1 Experimental setup

This chapter describes the experimental setup used to validate the feasibility of using existing hardware to produce on-line EIS measurement. Figure 5-1 shows the experimental setup used to look at on-line low frequency impedance measurements as described in the theory in Chapter 3 and then simulated in Chapter 4. The components used in the dc/dc boost converter are shown in Table 4-2. The converter and balancing circuit represented in section 5.7 have integrated gate drivers. Each drivers include a driver ic and an isolated dc/dc converter (up to ±15V). An isolated Opto-coupler HCPL 3140 has used to drive the MOSFETs. The opto-coupler can isolate up to 1kV. This driver has a low peak current of 0.4A which can drive a low voltage MOSFETs with a low gate charge. The integrated gate driver is shown in Figure 5-2. The impedance at different frequencies was calculated from a measurement of the battery voltage and current on a lecroy scope using a Lecroy CP031 100MHz current probe and a Tektronix P2220 200MHz voltage probe but IL300 voltage sensor and ACS712 current sensor measurement devices linked to the controller have also been used to get the same results. The manufacturer stated sensitivity of the probes are 10mA/division and 2mV/division. The gate drive signals were derived from an Opal-RT controller with a fixed time step of 20µs.

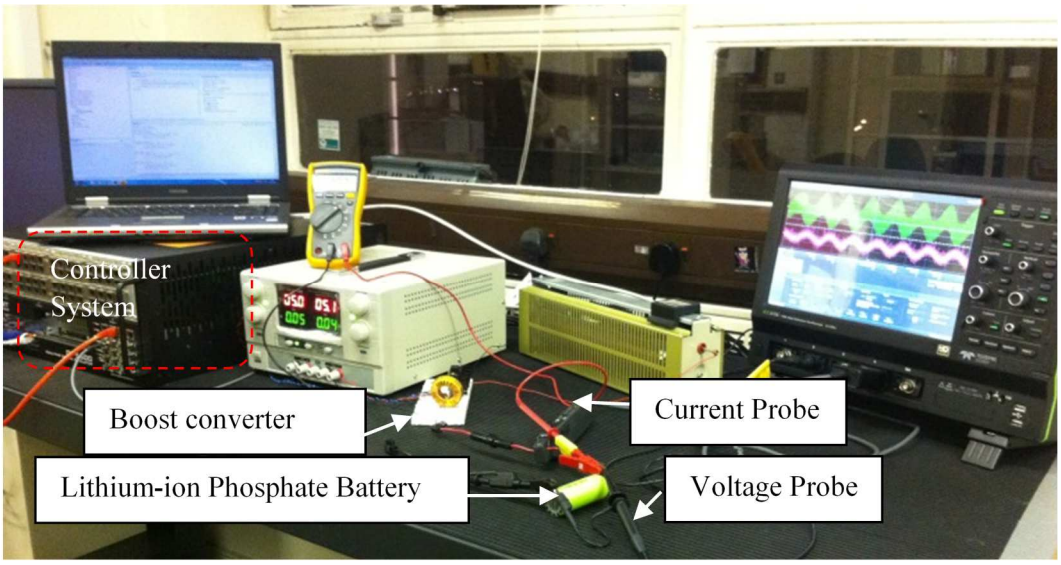

Figure 5-1 : Experimental setup

The methods previously described were applied to a lithium-ion battery to investigate the measured on-line impedance across a range of conditions. The tests were conducted at room temperature in a controlled temperature laboratory and it is assumed this temperature remained

constant through the experimental stages. The battery was started at full state of charge and the tests were conducted as close to this level as possible to guard against variation in impedance due to SOC. To investigate the proposed methods, the calculated battery impedance data from experimental and simulation were compared with offline measured EIS data over a range of frequencies.

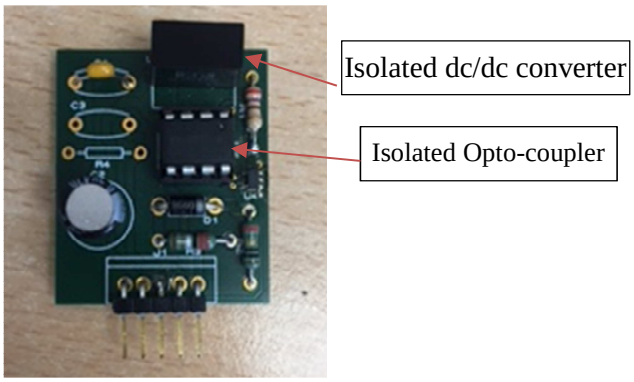

Figure 5-2 : Integrated driver circuit

5.2 DC/DC Converter operating with no low frequency component

5.2.1 Circuit operation

The converter was first operated with a fixed switching frequency of 2kHz, duty cycle of 0.6 and fixed starting position. This was to generate a base set of results from which all the methods of introducing a low frequency excitation signal could be compared against, to allow the impact of each of the methods to be clearly seen. The measured battery current and voltage are shown with the PWM signal in the oscilloscope trace in Figure 5-3 while the load current and voltage are shown in Figure 5-4. The waveforms show the circuit is operating in continuous mode as expected.

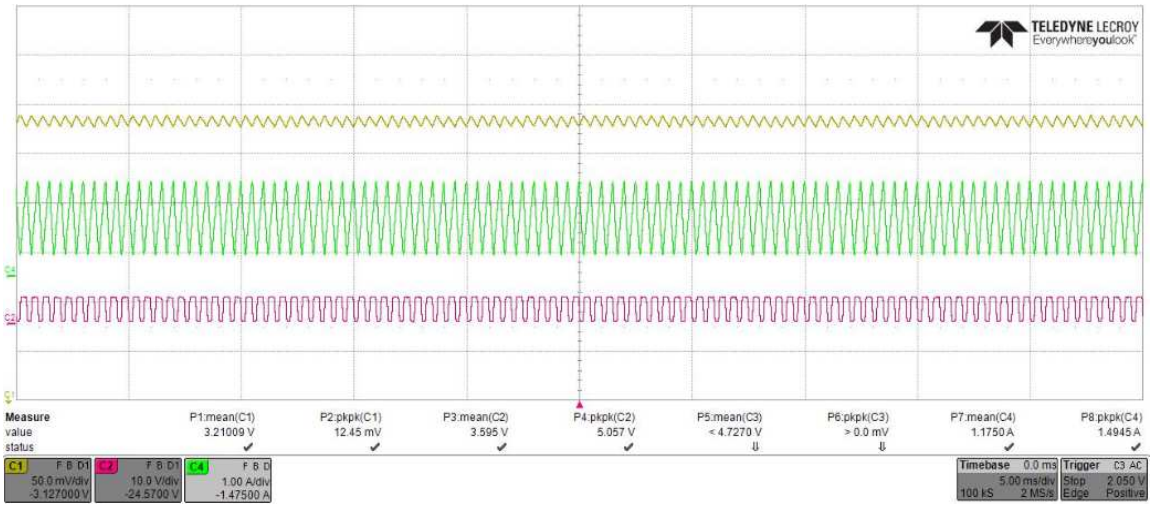

Figure 5-3 : Measured Li-ion battery Current (Green) and Voltage (Yellow) waveforms. The battery is excited with PWM at a fixed duty cycle of 0.6 and switching frequency of 2kHz (red).

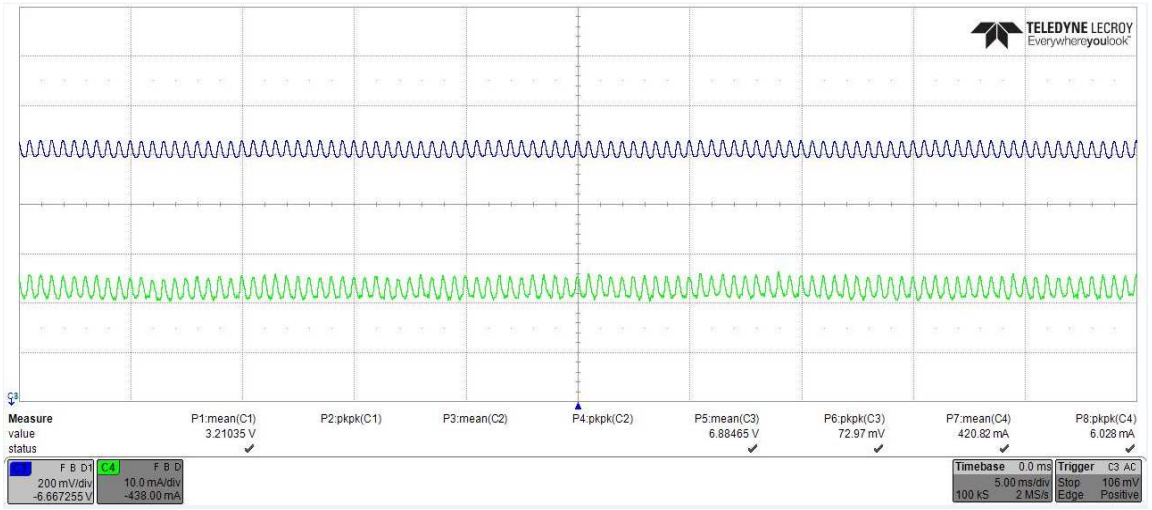

Figure 5-4 : Measured Load Current (Green) and Voltage (Blue) waveforms. The battery is excited with PWM at a fixed duty cycle of 0.6 and switching frequency of 2kHz.

Table 5-1 shows the experimentally measured waveform parameters of the base case circuit. The boost ratio is calculated as 2.14. Compared to the design equations and simulated results in section

4.1, the experimental values of the load output voltage and ripple and the load current and ripple are lower than the design equations and the simulation. Table 4-3 is reproduced in Table 5-2 for comparison purpose. This is primarily as a result of the non-ideal and non-linear components eg diode, mosfet, ESR resistances and leads in the experimental circuit compared to the ideal components used in the theory and simulation chapters. These results are referred to as the "base" results by which the other experimental results from the methods of introducing a low frequency component of ripple will be compared. Table 5-3 shows the simulated waveforms of this base case circuit using non-ideal component. In this model, the circuit boosts at a ratio of 2.12 compared to the experimental, the simulated values of the load output voltage and ripple and the load current and ripple are as per the experimental results.

Table 5-1: Experimental results of fixed duty cycle

	Experimental	
	Fixed Duty Cycle ideal component	
	Average Value	Peak-Peak ripple
I_{batt}	1.18 A	1.49 A
V_{batt}	3.21 V	12.5 mV
I_{load}	420 mA	6 mA
V_{dc}	6.89 V	73 mV

Table 5-2: Simulated results of fixed duty cycle

	Simulation	
	Fixed Duty Cycle ideal component	
	Average Value	Peak-Peak ripple
I_{batt}	1.55 A	2.42 A
V_{batt}	3.21 V	16.8 mV
I_{load}	456 mA	0.7 mA
V_{dc}	7.3 V	11.1 mV

Table 5-3: Simulated results of fixed duty cycle using non-ideal component

	Simulation	
	Fixed Duty Cycle non-ideal component	
	Average Value	Peak-Peak ripple
I_{batt}	1.1 A	2.2 A
V_{batt}	3.21 V	16.8 mV
I_{load}	422 mA	4.5 mA
V_{dc}	6.8 V	72 mV

In comparison with the simulation circuit power losses, the experimental output power loss is higher. This additional loss as a result of the non-ideal components such as the ESR component of the inductor, the switching MOSFET, and the diode can be estimated to aid understanding. The additional power losses in the experimental DC-DC boost converter circuit can be thought of:

- Inductor resistor power loss
- MOSFET switching power loss
- MOSFET conduction power loss
- Diode switching power loss
- Diode conduction power loss

5.2.2 Harmonics

Figure 5-5 shows the harmonic analysis of the experimentally measured inductor current under fixed duty cycle operation of the boost converter using the MATLAB FFT code for 16 cycles of switching frequency. The harmonic spectrum of the current contains only switching frequency harmonics similar to Figure 4-5, which is repeated in Figure 5-5b for comparison purpose.

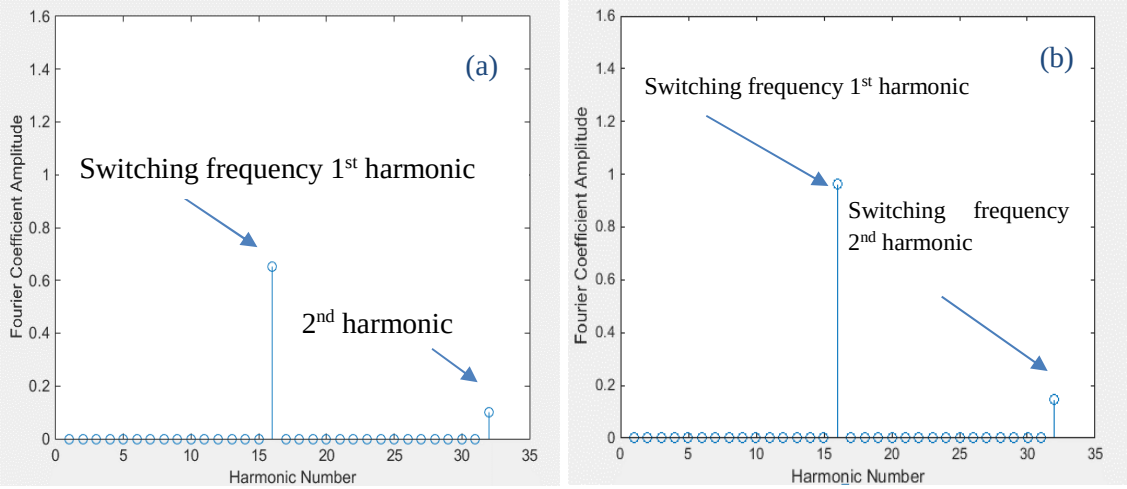

Figure 5-5 : a) Experimentally derived harmonics and b) simulated harmonics of the Li-ion battery current. The battery is excited with PWM at a fixed duty cycle of 0.6 and switching frequency of 2kHz.

5.3 DC/DC Converter with varying duty cycle PWM

The circuit was operated with a varying duty cycle to introduce a low frequency component. The results were then compared to those previously generated by theory and simulation from sections 3.2 and 4.2 respectively.

5.3.1 Circuit Operation

The battery and load voltage and current waveforms for two frequencies, 125Hz and 175Hz, were captured and are shown in Figure 5-6 to Figure 5-9. Two different frequencies are plotted to show the effect of the frequency variation on the key circuit and battery parameters.

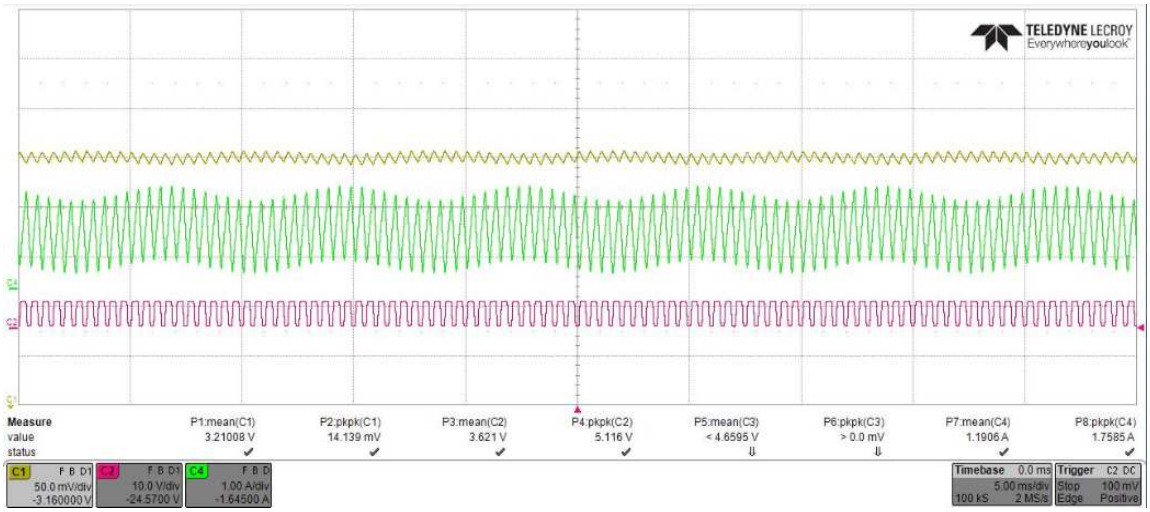

Figure 5-6 : Measured Li-ion battery Current (Green) and Voltage (yellow) waveforms. The battery is excited with PWM with variable duty cycle at a low frequency of 125Hz with A_d = 0.01 (red).

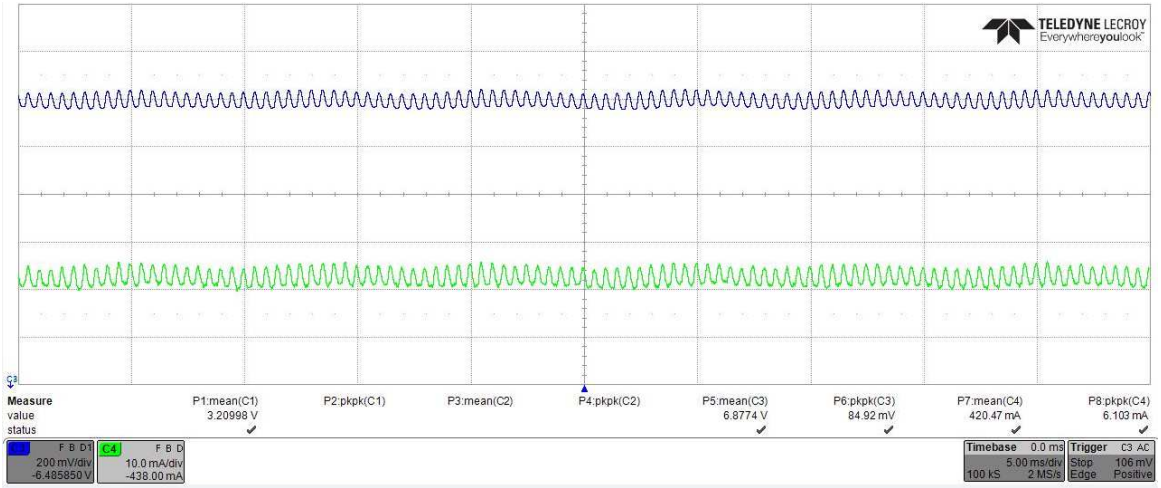

Figure 5-7 : Measured Load Current (Green) and Voltage (Blue) waveforms. The battery is excited with PWM with variable duty cycle at a low frequency of 125Hz with A_d = 0.01.

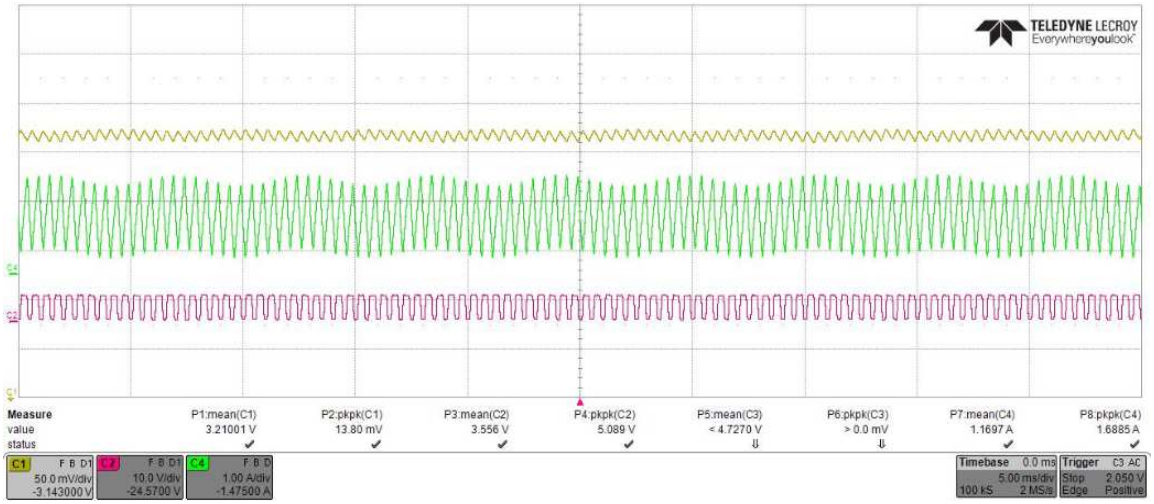

Figure 5-8 : Measured Li-ion battery Current (Green) and Voltage (yellow) waveforms. The battery is excited with PWM with variable duty cycle at a low frequency of 175Hz with A_d = 0.01 (red).

Comparison of the data shows that the experimental model of the converter is performing in a manner similar to the simulation in section 4.2 albeit at a lower battery current indicating an understanding of circuit behaviour. The simulated results from Table 4-4 are replicated in Table 5-6 for comparison purpose. The peak to peak current has increased due to the addition of the low frequency ripple compared to base operation as shown in Figure 5-3. The low-frequency ripple indicates that the low frequency harmonic has been introduced to the system. A comparison of key parameters from these figures compared to the experimental base case is replicated below in Table 5-4 and Table 5-5.

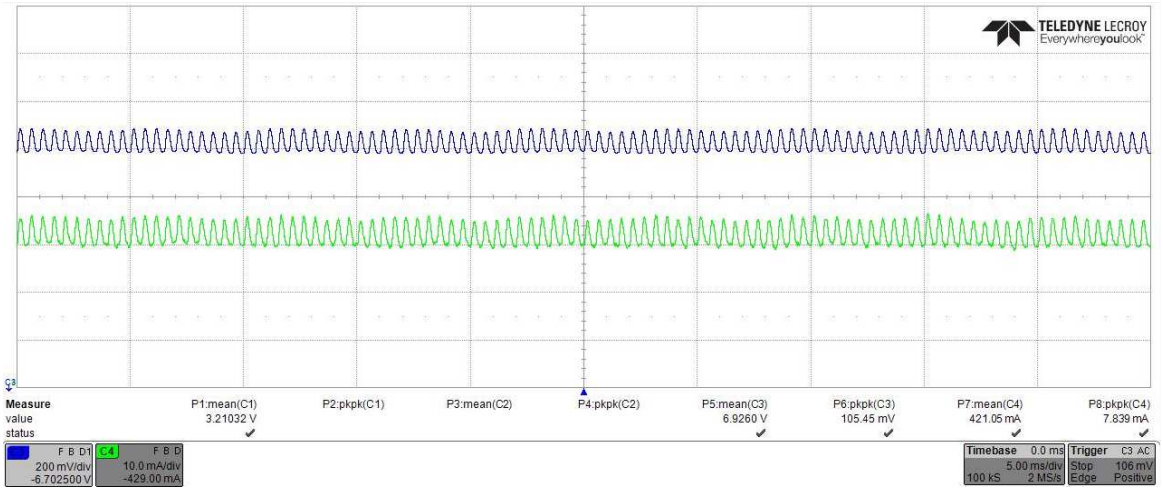

Figure 5-9 : Measured Load Current (Green) and Voltage (Blue) waveforms. The battery is excited with PWM with variable duty cycle at a low frequency of 175Hz with A_d = 0.01.

Table 5-4: Comparison of experimental results of fixed and variable duty cycle at 125Hz with A_d =0.01

	Experimental			
	Fixed Duty Cycle		Variable Duty Cycle	
	Average Value	Peak-Peak ripple	Average Value	Peak-Peak ripple
I_{batt}	1.18 A	1.49 A	1.19 A	1.76 A
V_{batt}	3.21 V	12.45 mV	3.21 V	14.14 mV
I_{load}	420 mA	6 mA	420 mA	6 mA
V_{dc}	6.89 V	73 mV	6.88 V	85 mV

Table 5-5: Comparison of experimental results of fixed and variable duty cycle at 175Hz with A_d = 0.01.

	Experimental			
	Fixed Duty Cycle		Variable Duty Cycle	
	Average Value	Peak-Peak ripple	Average Value	Peak-Peak ripple
I_{batt}	1.18 A	1.49 A	1.17 A	1.69 A
V_{batt}	3.21 V	12.45 mV	3.21 V	13.80 mV
I_{load}	420 mA	6 mA	460 mA	8 mA
V_{dc}	6.89 V	73 mV	6.93 V	105 mV

Table 5-6: Comparison of simulated results of fixed and variable duty cycle at 125Hz with A_d =0.01,

	Simulation			
	Fixed Duty Cycle		Variable Duty Cycle	
	Average Value	Peak-Peak ripple	Average Value	Peak-Peak ripple
I_{batt}	1.55 A	2.42 A	1.55 A	2.72 A
V_{batt}	3.21 V	16.8 mV	3.21 V	18.8 mV
I_{load}	456 mA	0.7 mA	459 mA	1.5 mA
V_{dc}	7.3 V	11.1 mV	7.3 V	23.3 mV

The measurements were undertaken with a fully charged battery. Therefore the average value of the battery voltage and the output voltage and hence the boost ratio of the circuit can be considered to remain the same. The converter boost is the same value as the base circuit in section 5.2. The battery ripple (peak to peak) values have changed because of the injected low frequency ripple. The converter load current ripple have increased as the low-frequency ripple injected to the circuit through the switching signal.

5.3.2 Harmonics

Figure 5-10 shows the FFT analysis of the experimental current waveform with the 125 Hz ripple. Compared to Figure 5-5, the current harmonics show that low-frequency ripple has been added. The low-frequency and switching frequency harmonics of the experimental current is less than that calculated through theory and simulation. As with the base case, this is because of there is a reduction in battery current of the experimental setup due to the non-ideal components.

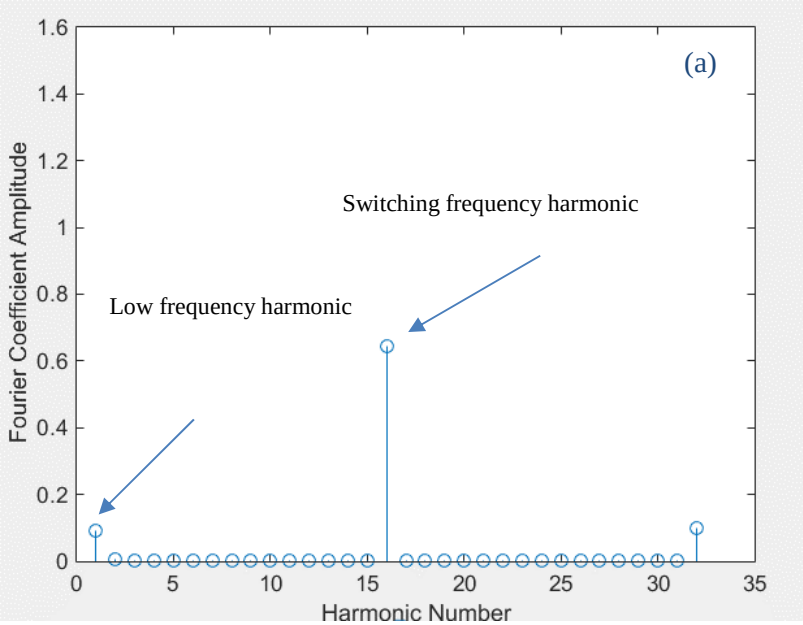

Figure 5-10 : Experimentally derived harmonics of the Li-ion battery current signal with a variable duty cycle at a low frequency of 125Hz with A_d= 0.01.

5.3.3 Inductor Ripple

It is important to understand how the method impacts the ripple current. For example, the ripple current varies as the low frequency value changes as shown in Figure 5-11. The value of A_d is kept fixed but the value Np is reduced from 18 (at 125Hz) to 11.4 (at 175Hz). These values from Table 5-4 and Table 5-5 can be compared against the theoretical increase in ripple from Equation 3-40 as shown in Table 5-7. Additional testing was used to understand the impact of A_d value variation, also shown in Table 5-7 and Figure 5-12 which shows the experimentally captured current ripple variation based on an A_d value variation at a low-frequency of 175Hz.

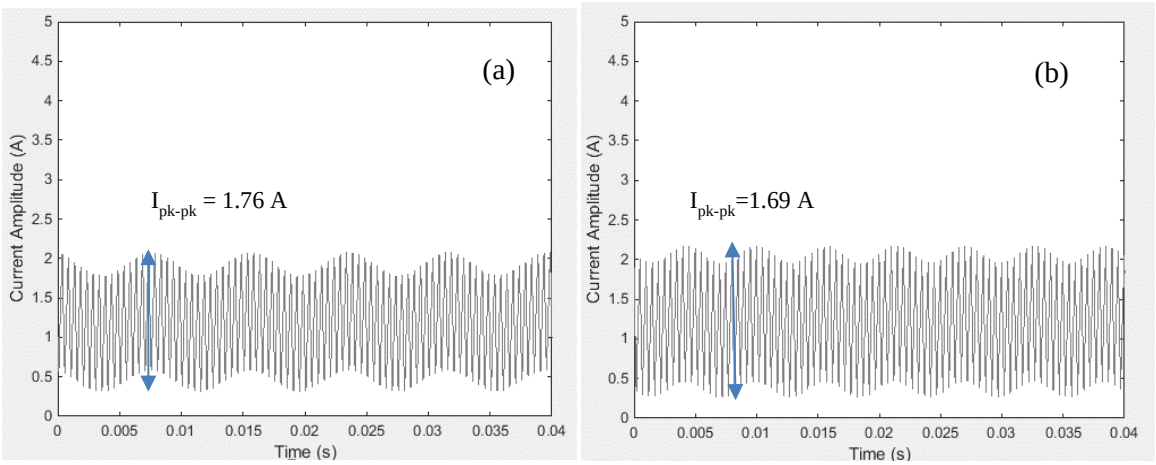

Figure 5-11 : Comparison of the low frequency ripple at different low frequencies (a) f_0 = 125Hz, (b) f_0 = 175Hz, With d_{av} = 0.6 and A_d = 0.01.

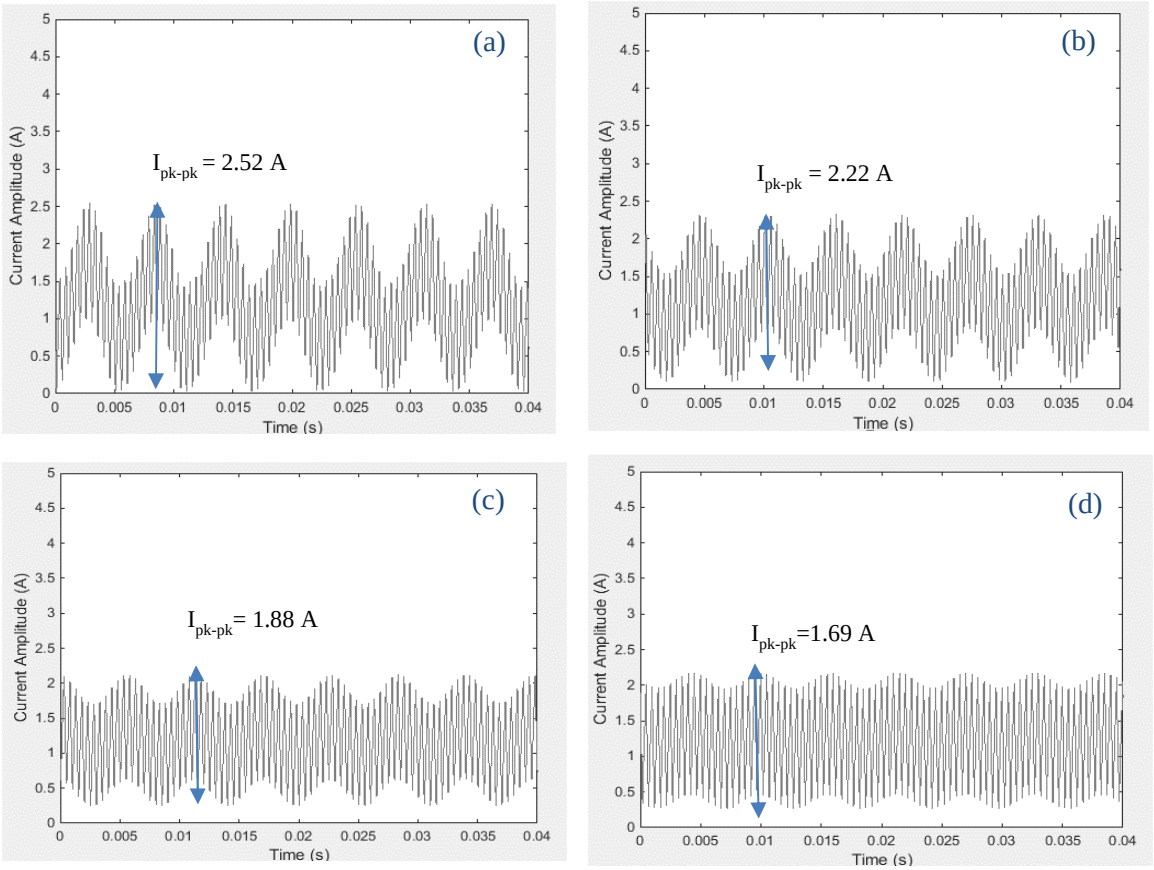

Figure 5-12 : Comparison of the low frequency ripple at different A_d (a) A_d = 0.06, (b) A_d = 0.04, (c) A_d = 0.02, and (d) A_d = 0.01. With d_{av} = 0.6 and f_0 = 175Hz.

The ripple current increases as A_d and N_p increase according to Equation 3-40. A trade off therefore exists between the magnitude of the ripple on the duty cycle and the effectiveness of the instrumentation to measure the maximum and minimum current and voltage ripple on the battery.

Table 5-7: Calculated increase in current ripple as a % with variable duty cycle compared to a fixed duty cycle

Frequency/A_d	Experimental	Simulation	Theoretical
125Hz, A_d = 0.01	118%	115%	121%
175Hz, A_d = 0.01	113%	112%	115%
175Hz, A_d = 0.02	126%	123%	130%
175Hz, A_d = 0.04	149%	140%	160%
175Hz, A_d = 0.06	168%	155%	191%

The experimental results confirm the effect of N_p, the variation of the ratio of the low frequency wave to the high frequency wave on the current ripple. However, the current ripple cannot increase indefinitely as N_p increases in practice. The main reason for this is that the theory is based on an ideal case, whereas the real circuit contains non-ideal components. For example, the ESR of the inductance which would prevent the current from increasing to infinity. The theoretical equations would need to be adapted to deal with this, however this is considered further work beyond the scope of the thesis. Figure 5-13 shows the % variation of the increase of ripple with low frequency component.

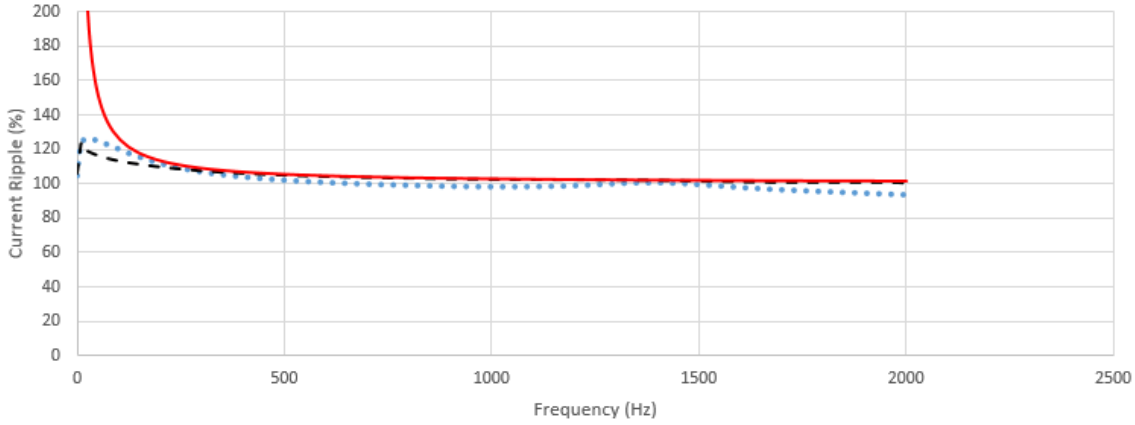

Figure 5-13 : Variation on current ripple with N_p with Theory (red) Simulation (black dash) Experimental (blue dots)

Obviously if the value of A_d gets too large then the circuit enters discontinuous mode as shown in Figure 5-14. Further work is needed to look at the theoretical analysis of a discontinuous circuit as this is considered outside of the scope of this thesis.

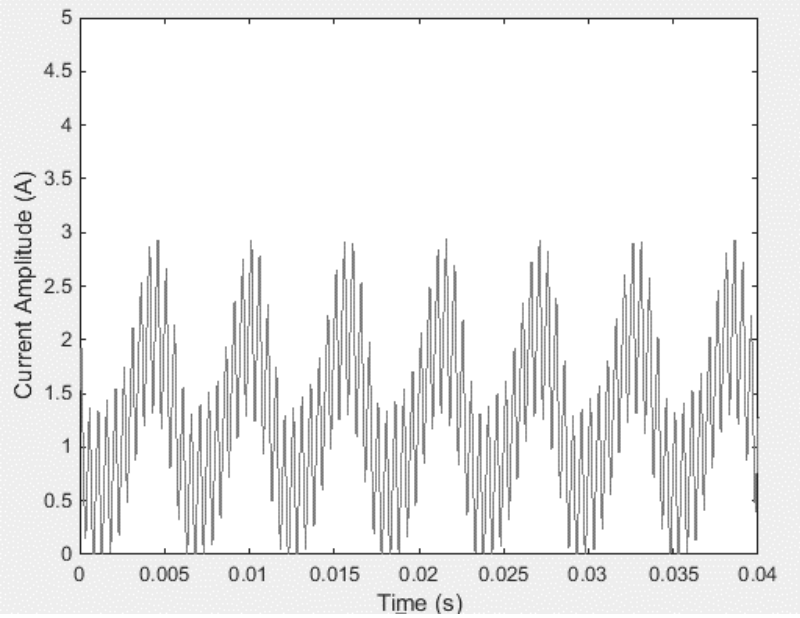

Figure 5-14 : battery current low frequency ripple with A_d = 0.1 at f_0 = 175Hz

5.3.4 EIS Calculation

The main reason for undertaking this work is to investigate if it is possible to use this method to produce an EIS plot of the battery. This method of producing a low frequency excitation signal under different frequencies was used to produce waveforms from which the voltage and current ripple could be measured to determine complex impedance. Figure 5-15 to Figure 5-17 show the calculated complex impedance, amplitude and phase plots of a li-ion battery from offline EIS measured data (in red), experimental test data (in blue dots), and simulation (in black) during discharge mode. The impedance of the battery was calculated for 36 low-frequency points. The battery current and voltage waveforms were measured and captured by the oscilloscope probes at each low-frequency points. The impedance of battery was then calculated by Fourier analysis of the waveforms at each frequency points using the FFT MATLAB code. Results from simulation and experimentally measured data gives values similar to that produced using off-line EIS equipment.

A switching frequency of 2kHz was used while the low frequency signal f_o was varied from 1 to 2kHz. To ensure that the system is always operating in continuous mode a duty cycle of 0.6 with A_d set to 0.01 was used.

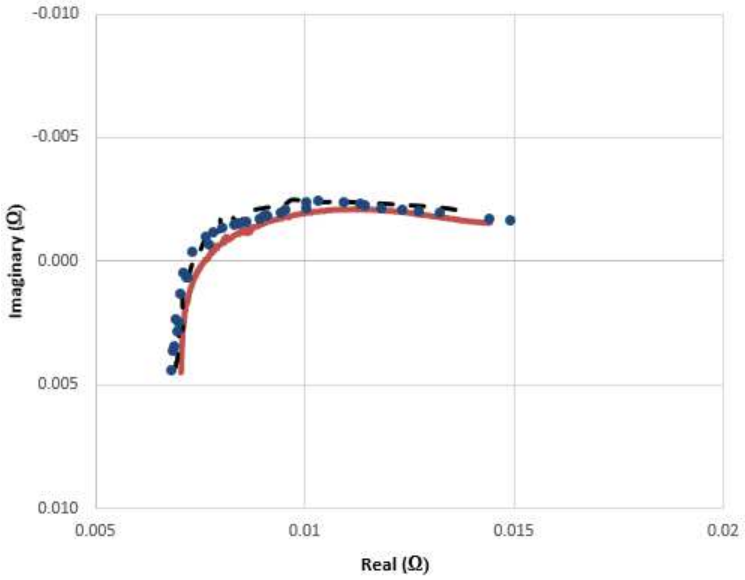

Figure 5-15 : Impedance Nyquist plot of the lithium-ion phosphate battery with EIS (red), Simulation (black dash), and Experimental data (blue dots) for variable duty cycle

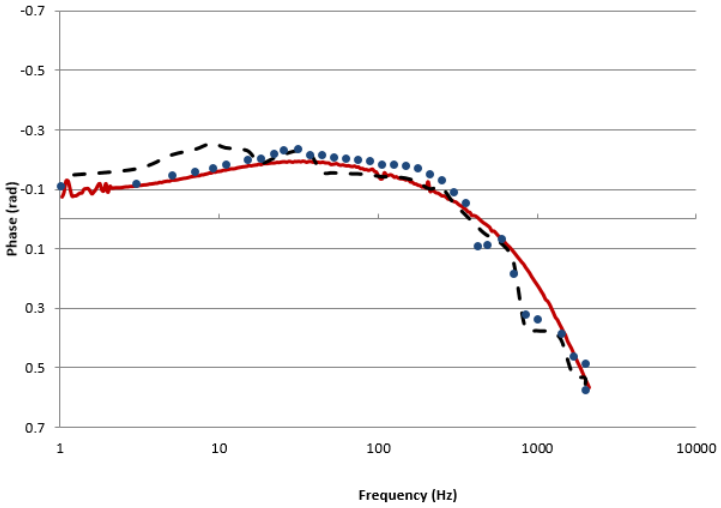

Figure 5-16 : Impedance Bode plot of the lithium-ion phosphate battery with EIS (red), Simulation (black), and Experimental data (blue dots) for variable duty cycle

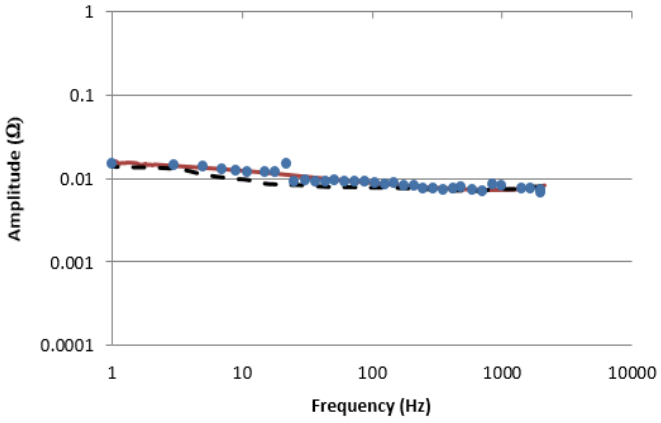

Figure 5-17 : Impedance Bode plot of the lithium-ion phosphate battery with EIS (red), Simulation (black), and Experimental data (blue dots) for variable duty cycle

Figure 5-15 to Figure 5-17 show that it is feasible to use this method to generate an EIS plot of a battery over a range of frequencies designed to characterise the battery.

It is therefore possible to use this method to undertake EIS measurements on-line. This work has extended the preliminary work in this area described in chapter1 to show applicability to EIS.

5.4 DC/DC Converter with variable switching frequency PWM

The circuit was operated with a varying switching frequency to introduce a low frequency component to look more closely at how the circuit behaves in comparison with fixed duty cycle operation and with the theory and simulation of this method from sections 3.3 and 4.3 respectively.

5.4.1 Circuit Operation

The battery and load voltage and current waveforms for the different frequencies of 125Hz and 175Hz were captured and are shown in Figure 5-18 to Figure 5-21. The low frequency signal was induced to the system by varying the switching frequency with a sinewave with amplitude of A_f = 400. Similar to the simulated waveforms in section 4.3, the waveform ripple increases with the injection of the low frequency. This ripple appears approximately constant for different values of low-frequency.

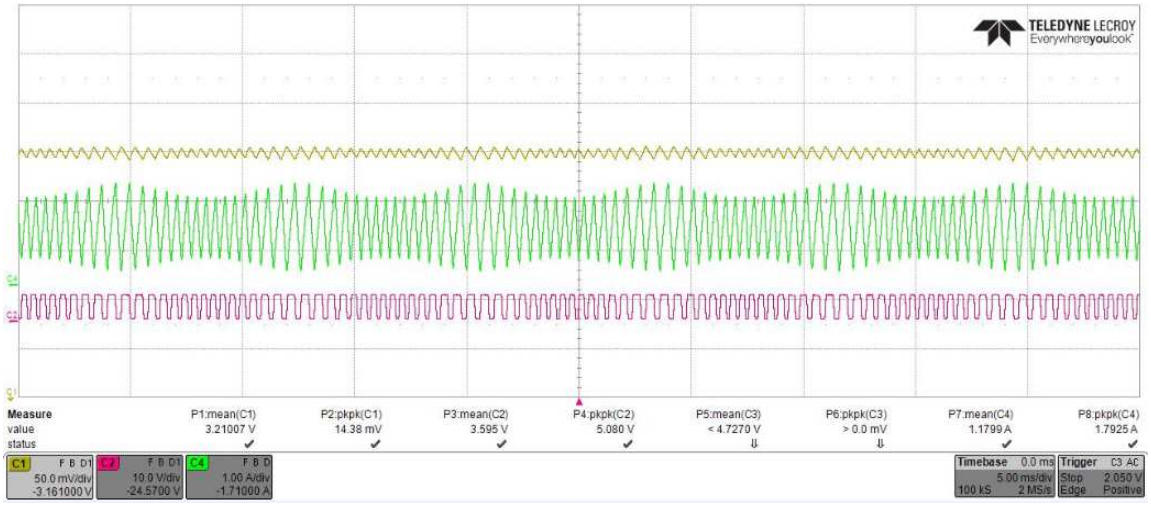

Figure 5-18 : Measured Li-ion battery Current (Green) and Voltage (Yellow) waveforms. The battery is excited with PWM (red) with variable switching frequency at a low frequency of 125Hz and A_f = 400.

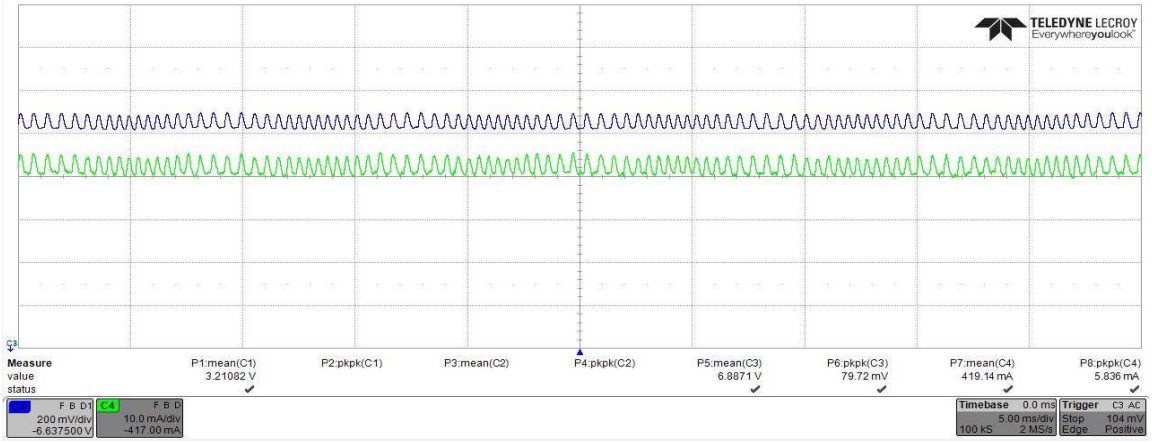

Figure 5-19 : Measured Li-ion Battery setup, Load Current (Green) and Voltage (Blue). The battery is excited with PWM with variable switching frequency at a low frequency of 125Hz and $A_f = 400$.

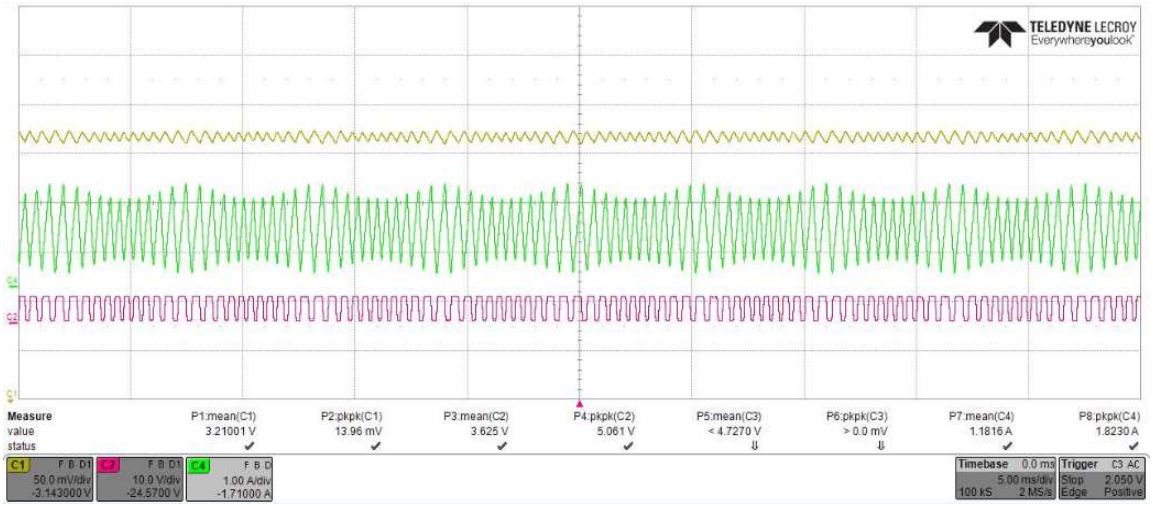

Figure 5-20 : Li-ion battery Current (Green) and Voltage (Yellow) waveforms. Measured Li-ion battery Current (Green) and Voltage (Yellow) waveforms. The battery is excited with PWM (red) with variable switching frequency at a low frequency of 175Hz and $A_f = 400$.

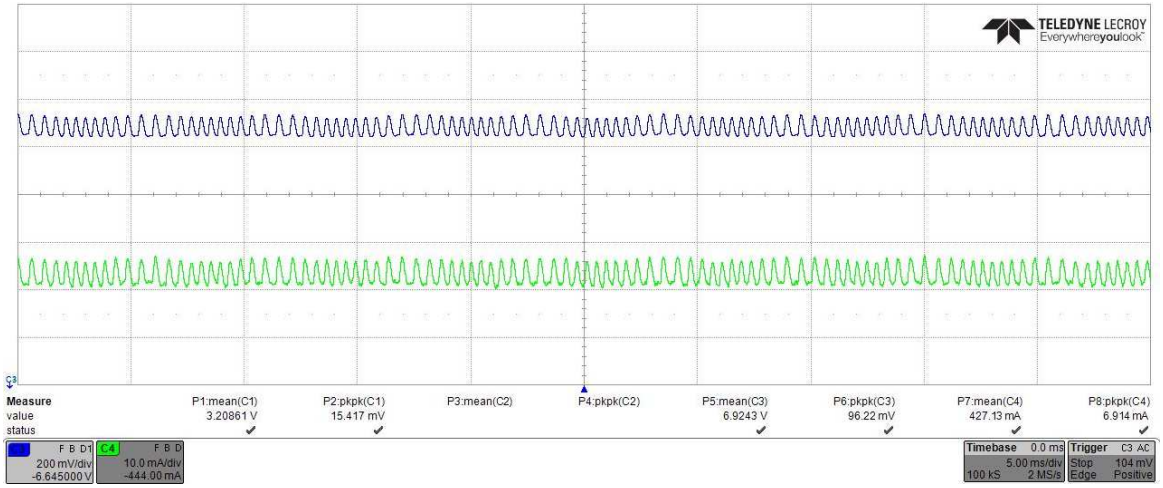

Figure 5-21 : Li-ion Battery setup, Load Current (Green) and Voltage (Blue) waveforms. The battery is excited with PWM with variable switching frequency at a low frequency of 175Hz and $A_f = 400$.

Comparison of the data shows that the experimental model of the converter is performing in a manner similar to the simulation indicating an understanding of circuit behaviour. Compared to the simulated results in section 4.3, the experimental values of the load output voltage and ripple and the load current and ripple are lower than the design equations and the simulation. This is as a result of the non-ideal and non-linear components eg diode, mosfet, and ESR resistances and the voltage drop of the diode in the experimental circuit compared to the ideal components used in the theory and simulation chapters. The peak to peak current is increased due to the addition of the low frequency ripple compared to base case operation as shown in Figure 5-18 and Figure 5-21. The low-frequency ripple clearly shows that the low frequency harmonic has been introduced to the system. A comparison of key parameters from these figures is replicated below in Table 5-8 and Table 5-9.

Table 5-8: Comparison of experimental results of fixed and variable frequency at 125Hz with A_f = 400.

	Experimental			
	Fixed Duty Cycle		Variable Frequency	
	Average Value	Peak-Peak ripple	Average Value	Peak-Peak ripple
I_{batt}	1.18 A	1.49 A	1.18 A	1.79 A
V_{batt}	3.21 V	12.45 mV	3.21 V	14.4 mV
I_{load}	420 mA	10 mA	419 mA	6 mA
V_{dc}	6.89 V	67 mV	6.89 V	80 mV

Table 5-9: Comparison of experimental results of fixed and variable frequency at 175Hz with A_f = 400

	Experimental			
	Fixed Duty Cycle		Variable frequency	
	Average Value	Peak-Peak ripple	Average Value	Peak-Peak ripple
I_{batt}	1.18 A	1.49 A	1.18 A	1.82 A
V_{batt}	3.21 V	12.45 mV	3.21 V	14 mV
I_{load}	420 mA	10 mA	427 mA	7 mA
V_{dc}	6.89 V	67 mV	6.92 V	96 mV

The measurement was undertaken with a fully charged battery. So the average value of the battery voltage, the output voltage and boost ratio of the circuit remain the same and only the ripple peak to peak values increased due to the low frequency excitation.

5.4.2 Harmonics

The Fourier analysis of the experimental and simulated current waveform with the ripple of the 125Hz, switching frequency of 2 kHz, and ripple amplitude of 400 Hz is shown in Figure 5-22. Figure 4-15 is repeated in Figure 5-22b for comparison purpose. The harmonics of the switching frequency is spread over the range of the 1600Hz and 2400Hz as described in section 3.3.1. The magnitude of the current Fourier coefficient using variable switching frequency is very small compared to the current harmonic coefficient in Figure 5-10 from variable duty cycle in section 5.3.2. This indicates that the variation of the frequency added less ripple to the battery signals. Therefore the impedance of the battery cannot be calculated as accurately since the effect of noise from the measurement instrumentation is included in the Fourier coefficient of the battery voltage signal.

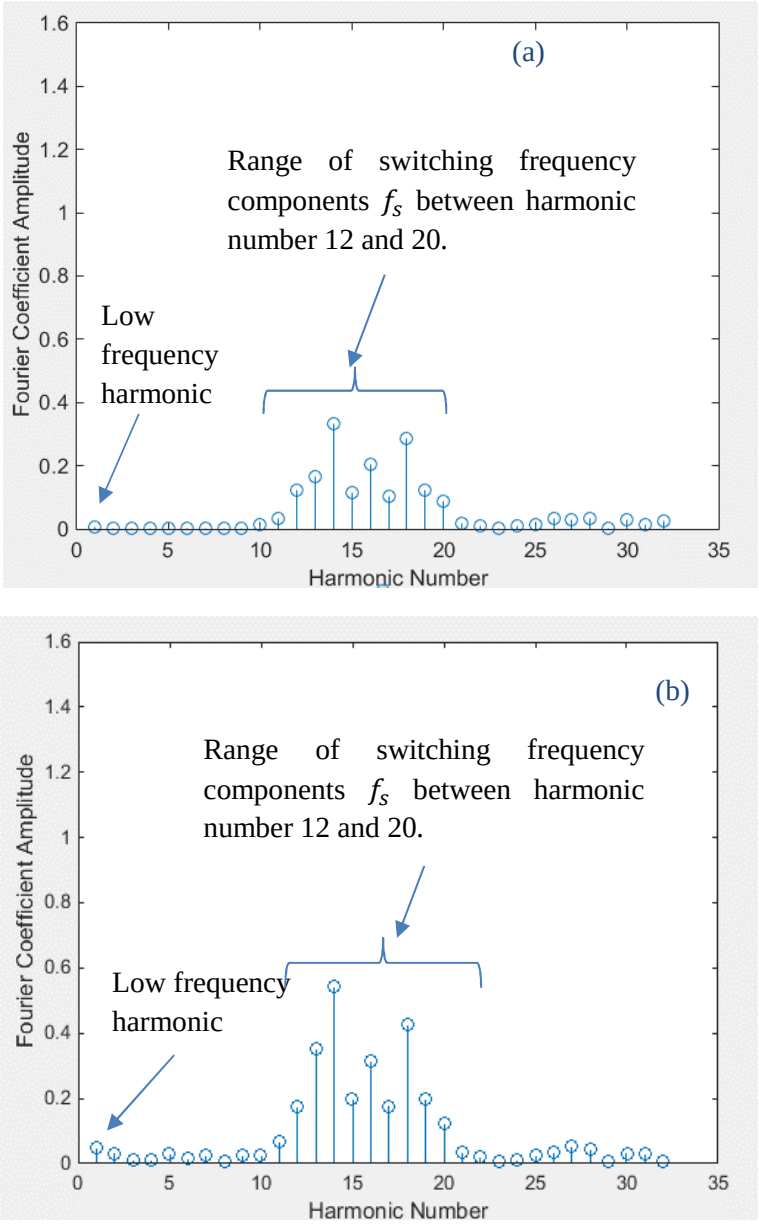

Figure 5-22:a) Experimentally derived harmonics and b) simulated harmonics of the Li-ion battery current signal with a variable frequency at a low frequency of 125Hz with A_f= 400.

5.4.3 Inductor Ripple

The effect of the A_f variation on the added ripple to the current waveform is shown in Figure 5-23. As A_f is increased, the ripple of the waveform is increased. The relationship between ripple increase and theory as per Equation 3-52 is shown in Table 5-10. The data indicates that the circuit waveform ripple depends only on the variation of the injected sine wave amplitude to the switching frequency.

Table 5-10: Calculated increase in current ripple as a % with variable duty cycle compared to a fixed duty cycle

Frequency/A_f	Experimental	Simulation	Theoretical
125Hz, A_f = 400	118%	118%	125%
175Hz, A_f = 400	118%	118%	125%
175Hz, A_f = 600	137%	132%	143%
175Hz, A_f = 200	109%	110%	111%
175Hz, A_f = 100	105%	104%	105%

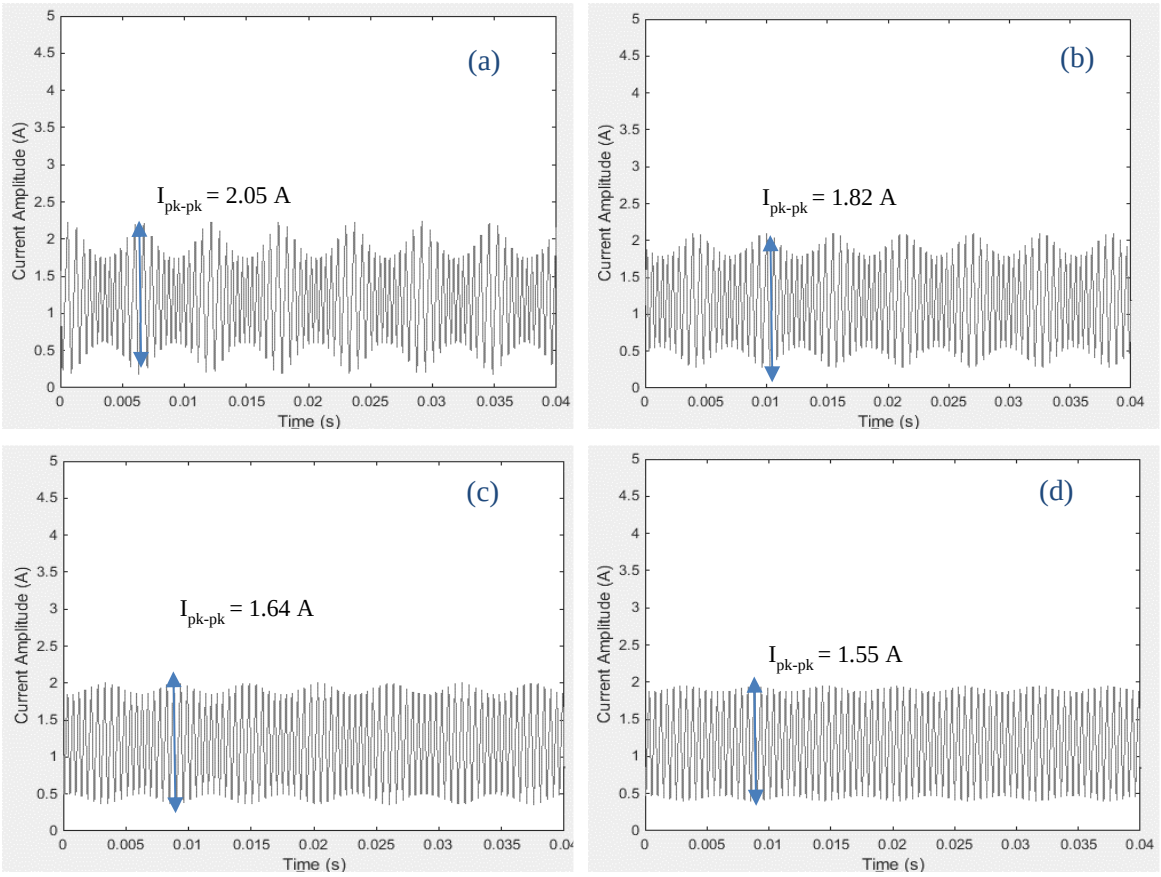

Figure 5-23 : Comparison of the low frequency ripple at different frequency (a) A_f = 600, (b) A_f = 400, (c) A_f = 200, and (d) A_f = 100. With f_{av} = 2kHz and f_0 = 175Hz

Figure 5-24 shows the variation of the signal ripple does not significantly change with low frequency value as expected. From Equation 3-52 the ripple changes remains constant over the range of the low frequency interval. The comparison of experimental, simulation and theoretical calculation of the waveform ripple for the different Np values is shown in Figure 5-25.

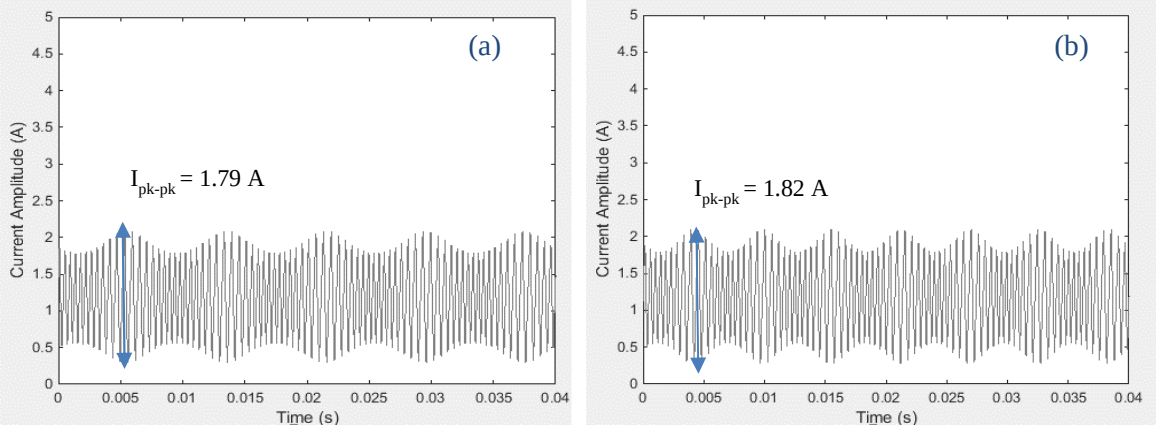

Figure 5-24 : Comparison of the low frequency ripple at different frequencies (a) f_0 = 125Hz, (b) f_0 = 175Hz, With f_{av} = 2kHz and A_f = 400.

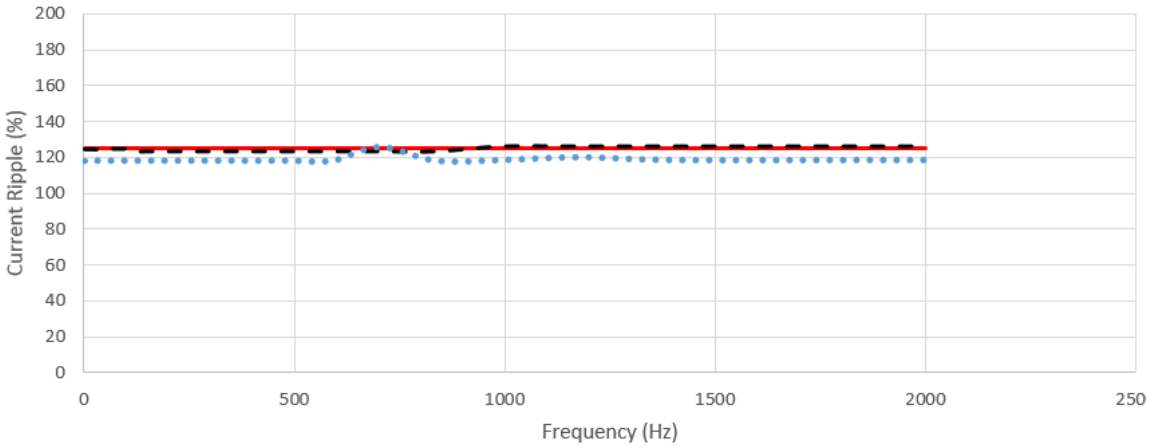

Figure 5-25 : Comparison of the low frequency ripple at different frequencies using theory (Line), Simulation (dash), and Experiment (dots).A_f = 400

When the value of A_f gets too large the battery current peak to peak values inceases and the converter starts operating in discontinuous mode. The battery current waveform is shown in Figure 5-26 at a frequency of 175Hz with $A_f = 1500$.

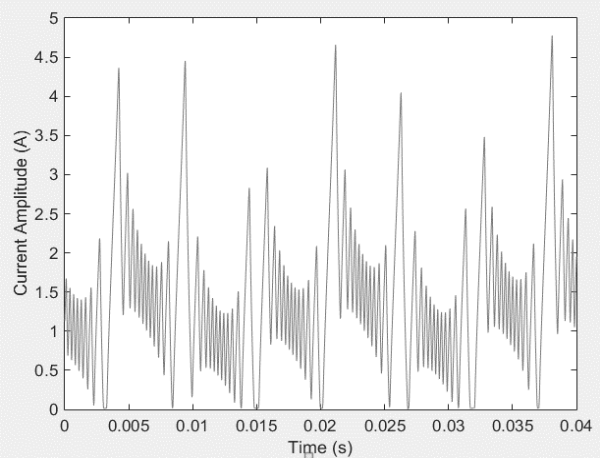

Figure 5-26 : discontinuous battery current low frequency ripple with A_f = 1500 at f_0 = 175Hz

5.4.4 EIS Calculation

In Figure 5-22, the derived value of low frequency harmonic component is very low. This in turn leads to loss of accuracy. The resultant calculated impedance plot based on this measured data is therefore not sufficiently accurate to be useful as a means of looking at on-line battery impedance.

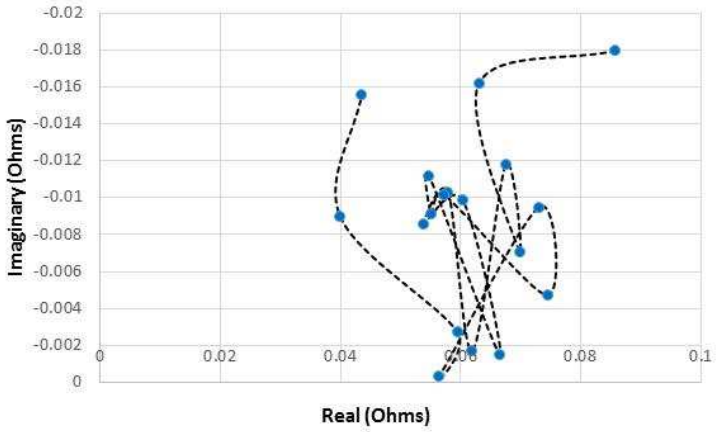

Figure 5-27 : Impedance Nyquist plot of the lithium-ion phosphate battery with Experimentally derived results

This method suffers from issues of accuracy. Therefore it is not recommended as a possible method of undertaking EIS measurement.

5.5 DC/DC Converter with variable starting point PWM

This method looks to vary the starting point of PWM signal within a switching pulse to inject a low frequency component. The circuit was used to experimentally measure voltage and current and to compare these with the base case and with the theory and simulation from sections 3.4 and 4.4 respectively.

5.5.1 Circuit Operation

The battery current, voltage and circuit output voltage and current waveforms for two frequency points of 125 Hz and 175Hz were captured and are shown in Figure 5-28 to Figure 5-31. The low frequency signal was injected into the system by varying the starting point with a sinewave with amplitude of A_t = 0.00004s and an average start time of 0.00026s. The ripple values increased when the low-frequency component was injected.

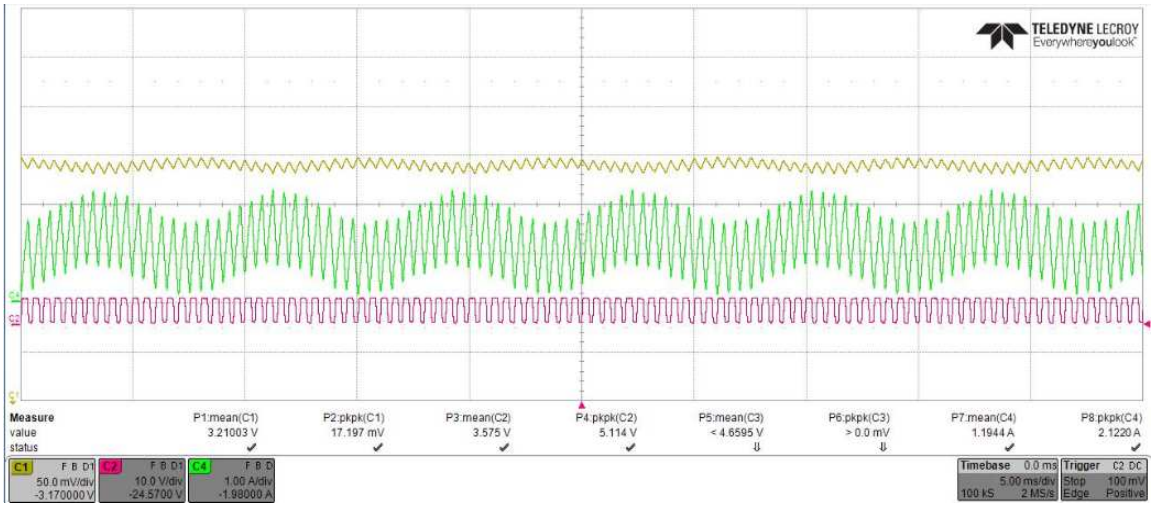

Figure 5-28 : Measured Li-ion battery Current (Green) and Voltage (yellow) waveforms. The battery is excited with PWM (red) with a variable starting point set to a low frequency of 125Hz and A_t = 0.00004s.

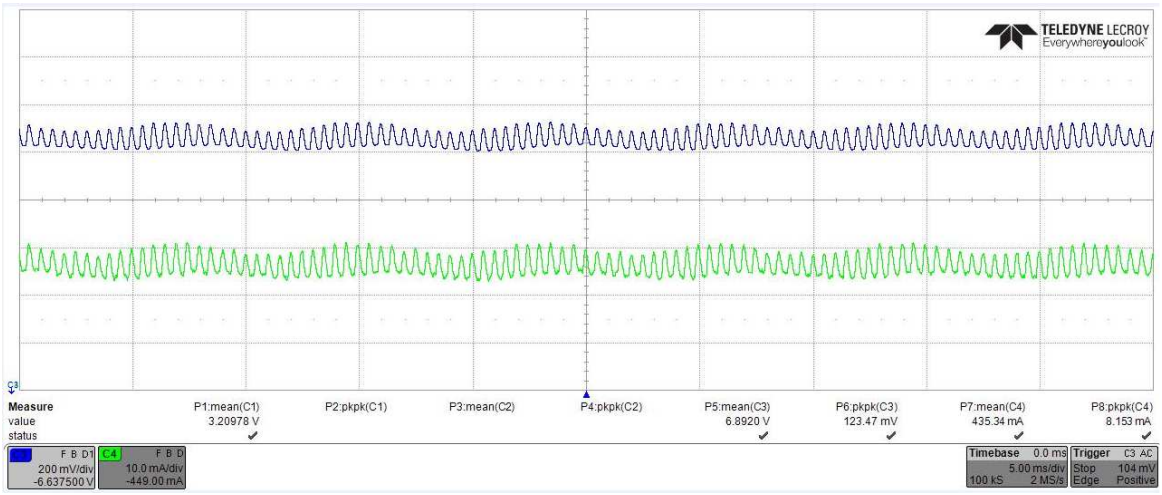

Figure 5-29 : Measured Load Current (Green) and Voltage (Blue) waveforms. The battery is excited with PWM (red) with a variable starting point set to a low frequency of 125Hz and A_t = 0.00004s.

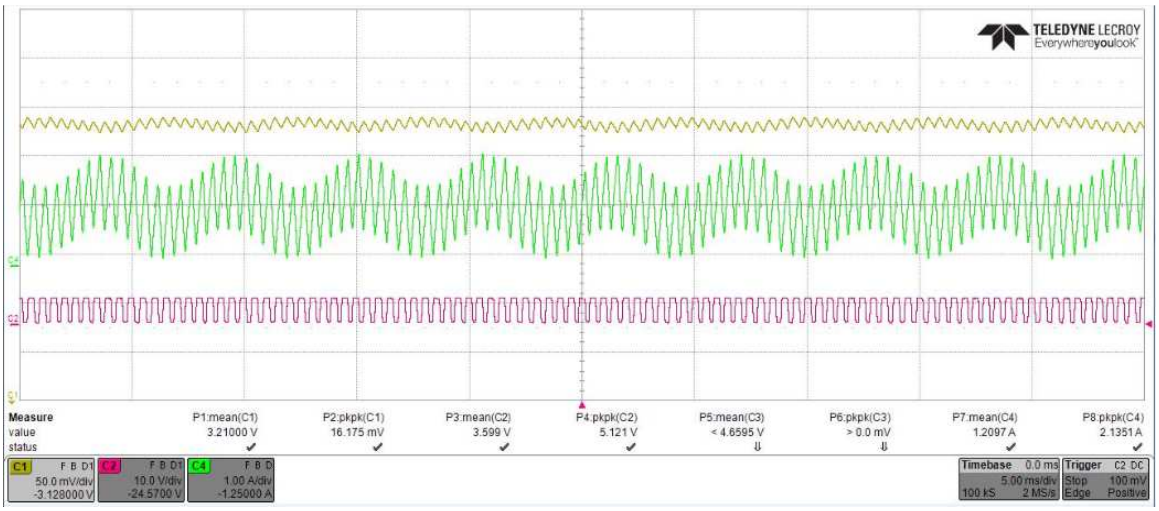

Figure 5-30 : Measured Li-ion battery Current (Green) and Voltage (yellow) waveforms. The battery is excited with PWM (red) with a variable starting point set to a low frequency of 175Hz and A_t = 0.00004s.

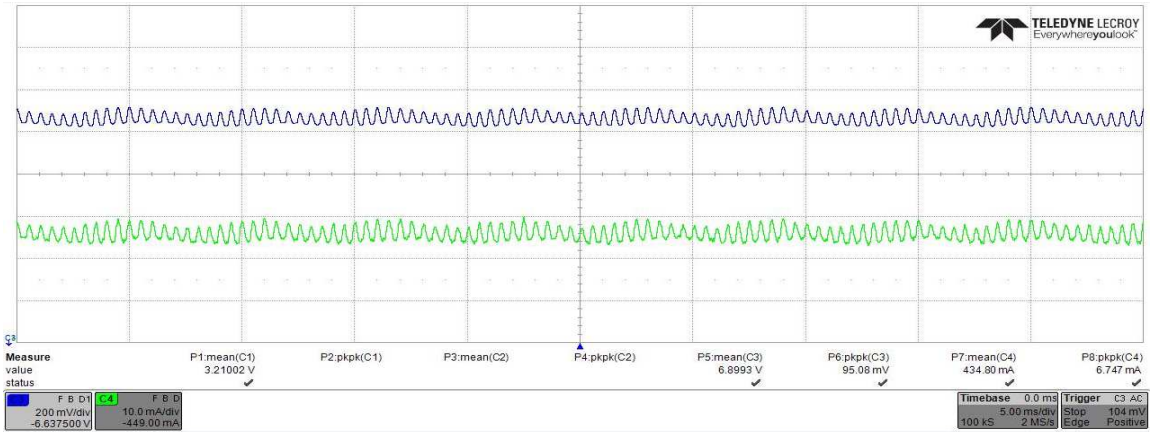

Figure 5-31 : Load Current (Green) and Voltage (Blue) waveforms. The battery is excited with PWM with a variable starting point set to a low frequency of 175Hz and A_t = 0.00004s.

The comparison of results shows that the converter is operating similar to the simulated model in section 4.4. The simulated results from Table 4-8 are replicated in Table 5-13 for comparison purpose. The current ripple is increased as the low frequency ripple is added compared to normal operation as shown in Figure 5-28 and Figure 5-30. The low-frequency ripple clearly shows that the low frequency harmonic has been induced to the system. The key parameters of the experimental results of the variable starting point PWM and the base circuit signal for two low-frequency points of 125Hz and 175Hz are given in Table 5-11 and Table 5-12.

Table 5-11: Comparison of PWM with variable starting point at 125Hz effects on Current and Voltage ripple

	Experimental			
	Fixed Duty Cycle		Variable starting point	
	Average Value	Peak-Peak ripple	Average Value	Peak-Peak ripple
I_{batt}	1.18 A	1.49 A	1.19 A	2.12 A
V_{batt}	3.21 V	12.45 mV	3.21 V	17.2 mV
I_{load}	420 mA	10 mA	435 mA	8 mA
V_{dc}	6.89 V	67 mV	6.94 V	123 mV

Table 5-12: Comparison of PWM with variable starting point at 175Hz effects on Current and Voltage ripple

	Experimental			
	Fixed Duty Cycle		Variable starting point	
	Average Value	Peak-Peak ripple	Average Value	Peak-Peak ripple
I_{batt}	1.18 A	1.49 A	1.21 A	2.14 A
V_{batt}	3.21 V	12.45 mV	3.21 V	16.2 mV
I_{load}	420 mA	10 mA	434 mA	7 mA
V_{dc}	6.89 V	67 mV	6.90 V	95 mV

Table 5-13: Comparison of simulated PWM with variable starting point at 125Hz effects on Current and Voltage ripple

	Simulation			
	Fixed Duty Cycle		Variable starting point	
	Average Value	Peak-Peak ripple	Average Value	Peak-Peak ripple
I_{batt}	1.55 A	2.42 A	1.58 A	3.02 A
V_{batt}	3.21 V	16.8 mV	3.21 V	21.3 mV
I_{load}	456 mA	0.7 mA	462 mA	2.2 mA
V_{dc}	7.3 V	11.1 mV	7.38 V	35.7 mV

The average value of the battery, load voltage and the boost ratio of the circuit remain the same as the base circuit in section 5.2. The ripple values increased as the low-frequency component is induced to the circuit.

5.5.2 Harmonics

Figure 5-32 shows the battery current harmonic analysis at low-frequency of 125Hz by varying the starting point of the PWM signal with A_t= 0.00004. It is clear that both low frequency 125Hz and the switching frequency of 2kHz harmonics can be extracted from the experimental current waveform.

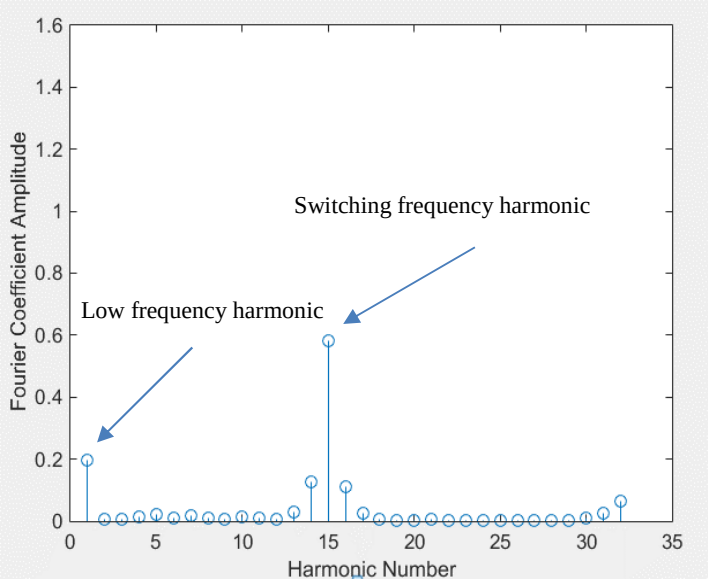

Figure 5-32 : Experimentally derived harmonics of the Li-ion battery current signal with a variable starting position at a low frequency of 125Hz with A_t = 0.00004s.

5.5.3 Inductor ripple

The effect of the A_t variation on the added ripple to the current waveform is shown in Figure 5-33. As A_t increased, the ripple of the waveform is increased. The relationship between ripple increase experimentally, theory, and simulation as per Equation 3-64 is shown in Table 5-14.

Table 5-14: Calculated increase in current ripple as a % with variable starting position compared to a fixed starting position for a switching frequency of 2kHz and a t_{av} = 0.00026

Frequency/A_t	Experimental	Simulation	Theoretical
125Hz, A_t = 0.00004	142%	125%	140%
175Hz, A_t = 0.00004	143%	129%	140%
175Hz, A_t = 0.00005	149%	162%	150%
175Hz, A_t = 0.00008	160%	168%	180%
175Hz, A_t = 0.00002	121%	116%	120%

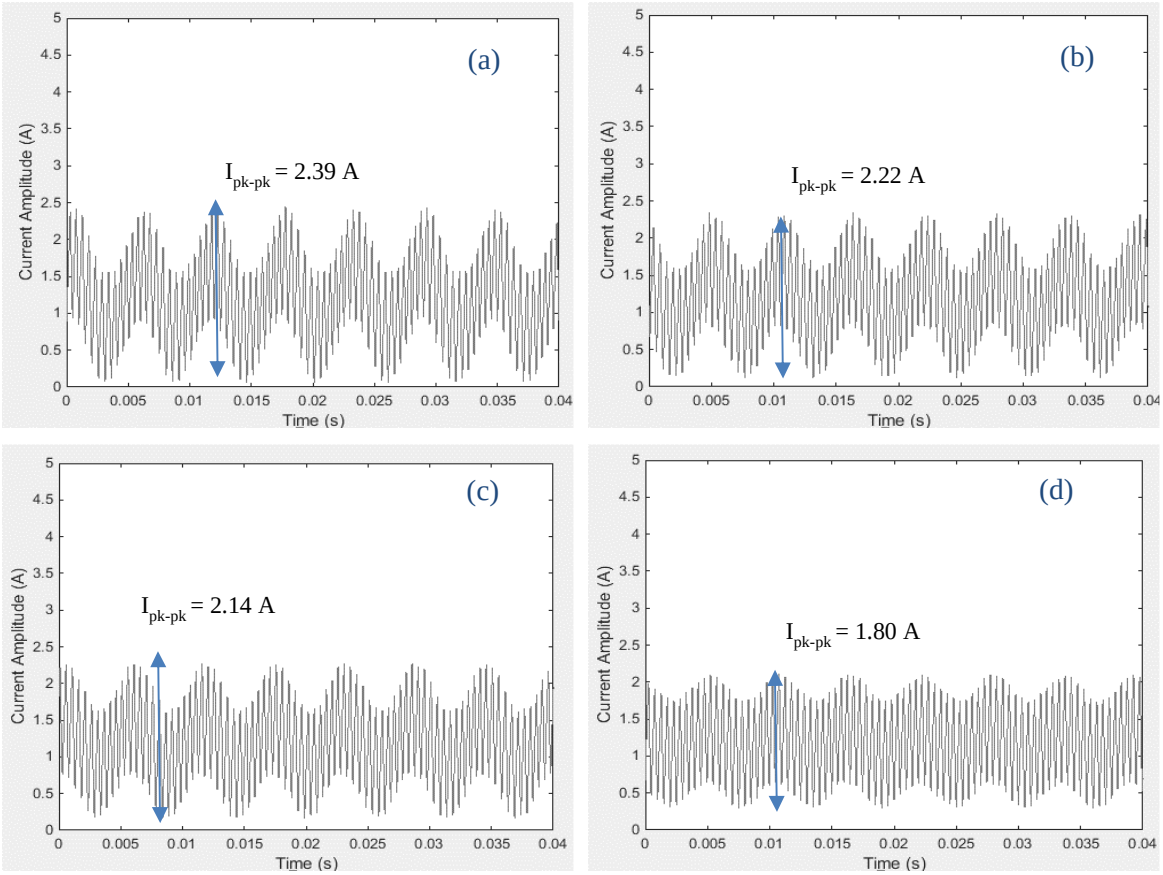

Figure 5-33 : Comparison of the low frequency ripple at different frequency (a)A_t = 0.00008, (b) A_t = 0.00005, (c) A_t = 0.00004, and (d) A_t = 0.00002. With f_s = 2kHz and f_0 = 175Hz

Figure 5-34 shows the current ripple change over the two low-frequency components. From Equation 3-64, the ripple variation depends on the changes of the A_t value and therefore the ripple is expected to remain constant over the low frequency range.

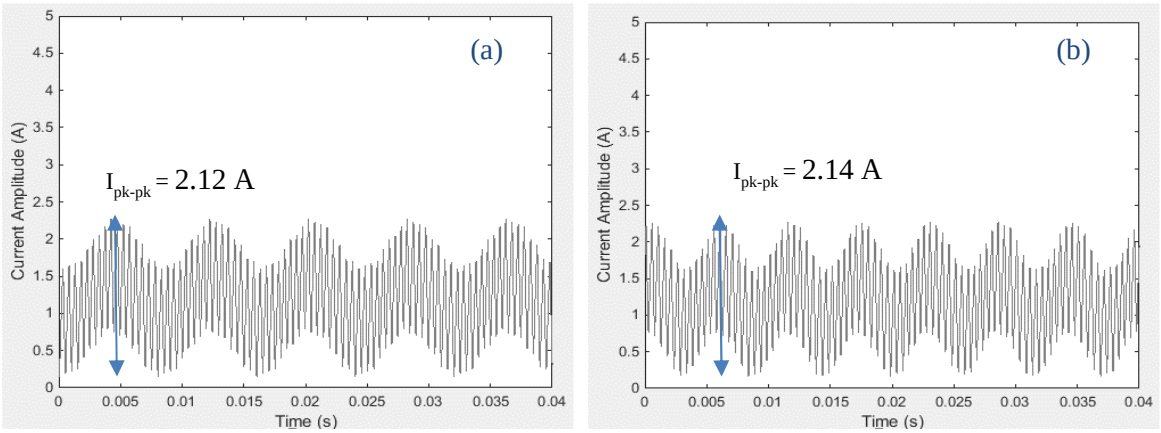

Figure 5-34 : Comparison of the low frequency ripple at different frequency (a) f_0 = 125Hz, (b) f_0 = 175Hz, With t_{av} = 0.00026s and A_t = 0.00004.

Figure 5-35 shows the expected variation of the current ripple value based on Np value variation over the low-frequency range. The data shows that the current ripple value remains approximately constant as the Np value changes. However, the ripple variation is distorted at the lower frequency

points and as the frequency approaches switching frequency as there is little scope to add variation to starting position. This is believed to be a function of the accuracy with which MATLAB can handle the variable starting position due to the 20µs limitation in accuracy in the controller as described in section 3.5.3. This inaccuracy then propagates to influence the ripple component.

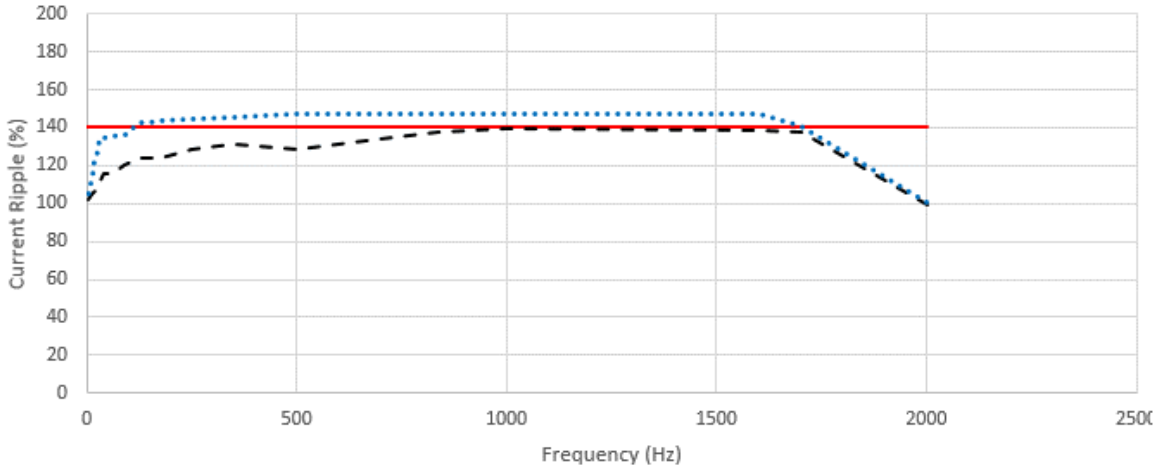

Figure 5-35 : Comparison of the low frequency ripple at different frequencies using theory (Line), Simulation (dash), and Experiment (dots)

As the value of A_t increases, the battery current peak to peak values inceased and converter starts operating in discontinuous mode. The battery current waveform is shown in Figure 5-36 at a frequency of 175Hz with an $A_t = 0.0002$.

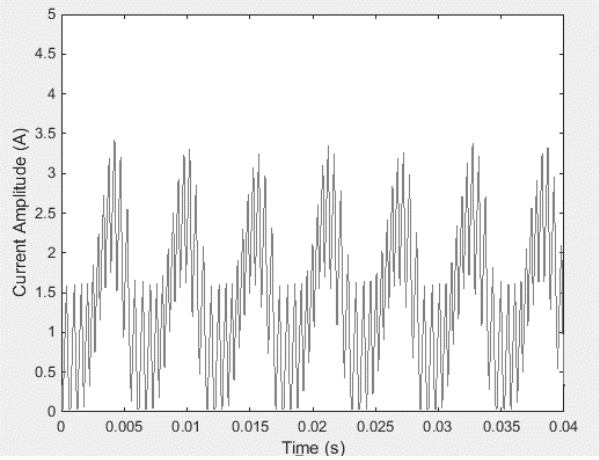

Figure 5-36 : battery current low frequency ripple with A_t = 0.0002 at f_0 = 175Hz.

5.5.4 EIS Calculation

Figure 5-37 to Figure 5-39 show the derived complex impedance, amplitude and phase plots of the li-ion battery from off line EIS measurement equipment (in red), experimentally measured data (in blue dots), and simulation (in black). Experimentally calculated impedance is similar in magnitude to that calculated by offline EIS data. A switching frequency of 2kHz was used while the low

frequency signal f_o was varied from 1 to 2kHz. To ensure that the system is always operating in continuous mode the duty cycle is 0.6 with A_t and t_{av} are set to 0.00004s and 0.00026s for the lithium-ion battery. The impedance of the battery was calculated for 20 low-frequency points. The battery current and voltage waveforms were measured and captured by the oscilloscope probes at each low-frequency points. The impedance of battery was then calculated by Fourier analysis of the waveforms at each frequency points using the FFT MATLAB code.

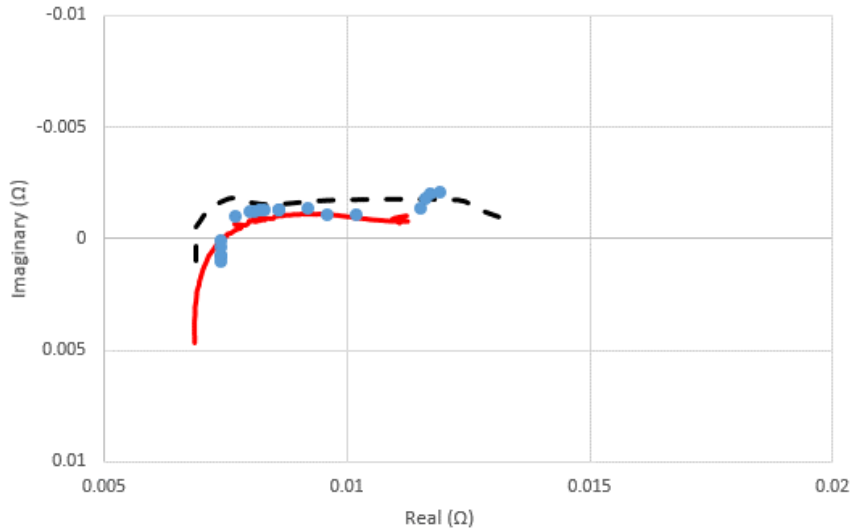

Figure 5-37 : Impedance Nyquist plot of the lithium-ion phosphate battery with EIS (red), Simulation (black), and Experimental data (blue dots)

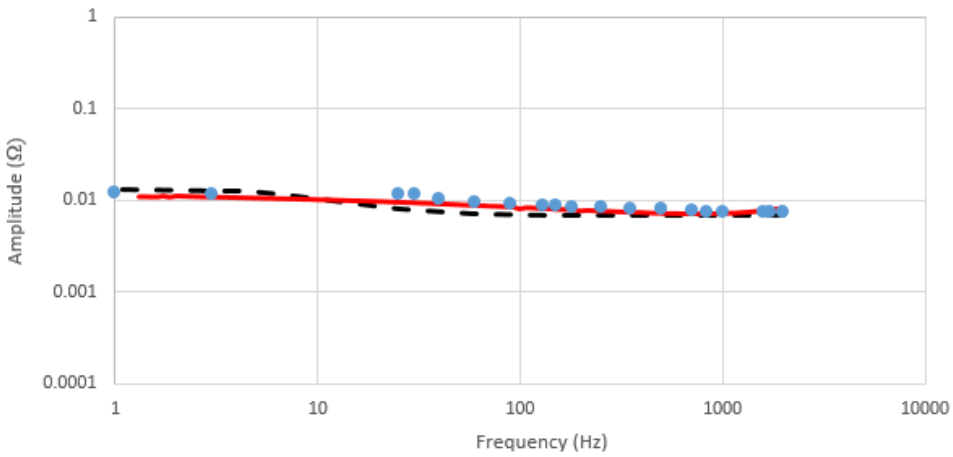

Figure 5-38 : Amplitude bode plot of the lithium-ion phosphate battery with EIS (red), Simulation (black), and Experimental data (blue dots)

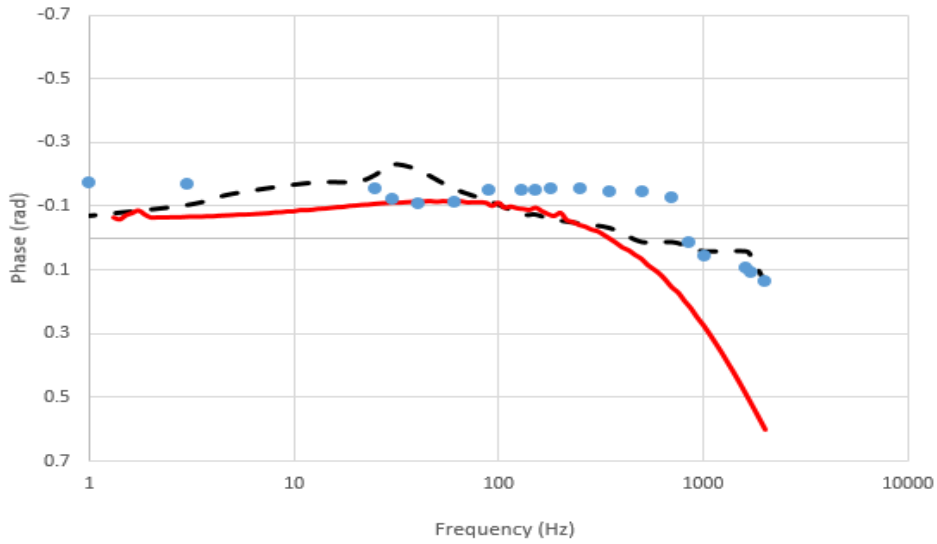

Figure 5-39 : Phase bode plot of the lithium-ion phosphate battery with EIS (red), Simulation (black), and Experimental data (blue dots)

The EIS plot is not as accurate as that produced by the variable duty cycle method. This is thought to be due to the inaccuracy in start position location and its follow on impact on the calculated phase angle of the two waveforms. This method is also more complex to set up with the control system.

5.6 DC/DC Converter with an Impulse Function

The method uses a gate drive signal controlled by a PWM signal with an additional impulse function to induce a low frequency component. The experimentally measured values are compared to the base circuit and with theory and simulation from sections 3.5 and 4.5 respectively. As previously explained, the opal-rt unit runs at a fixed time step of 20µs. A pulse with a pulse width and frequency value that is a multiple integer of the time step as explained in section 3.5.1 was used to allow comparison with theory and simulation.

5.6.1 Circuit Operation

The battery current, voltage and circuit output voltage and current waveforms for two frequency points of 125 Hz and 166.7Hz for a PWM with added impulse signal were captured and are shown in Figure 5-28 to Figure 5-31. A low-frequency of 125Hz with the pulse width of 0.00032s, and 166.7Hz signal with a pulse width of 0.00036s are added to the gate drive PWM signal. The waveform peak to peak value increased with the low-frequency ripple excitation. The ripple values changes at the different frequency because of the need to use different pulse widths. The battery current increased each time an impulse function, T_i is added to the switching pulse width as described in section 3.5.4.

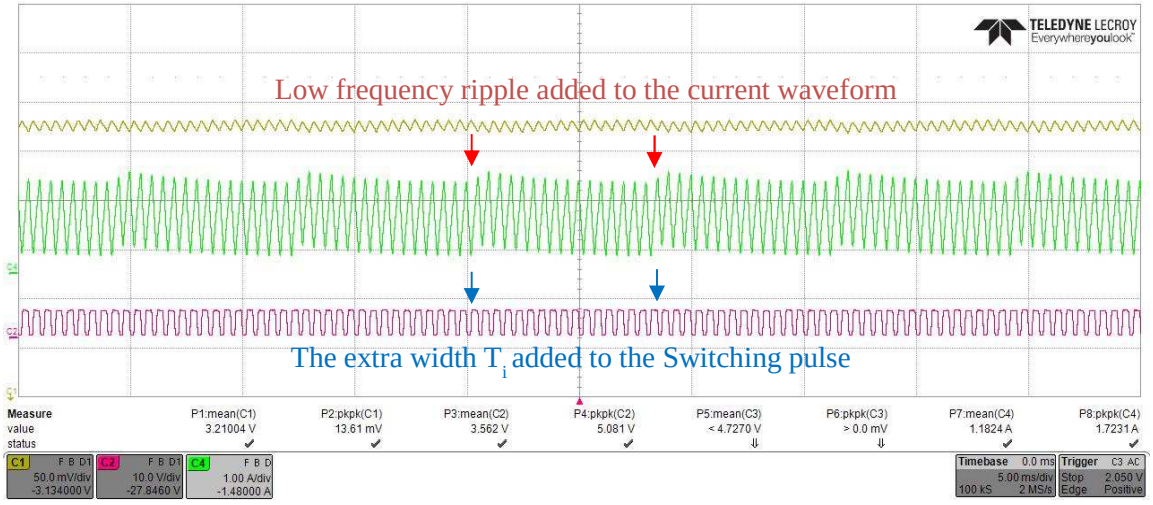

Figure 5-40 : Measured Li-ion battery Current (Green) and Voltage (yellow) waveforms. The battery is excited with a PWM (red) with an impulse function at a Low frequency of 125Hz, with 4% impulse duty cycle.

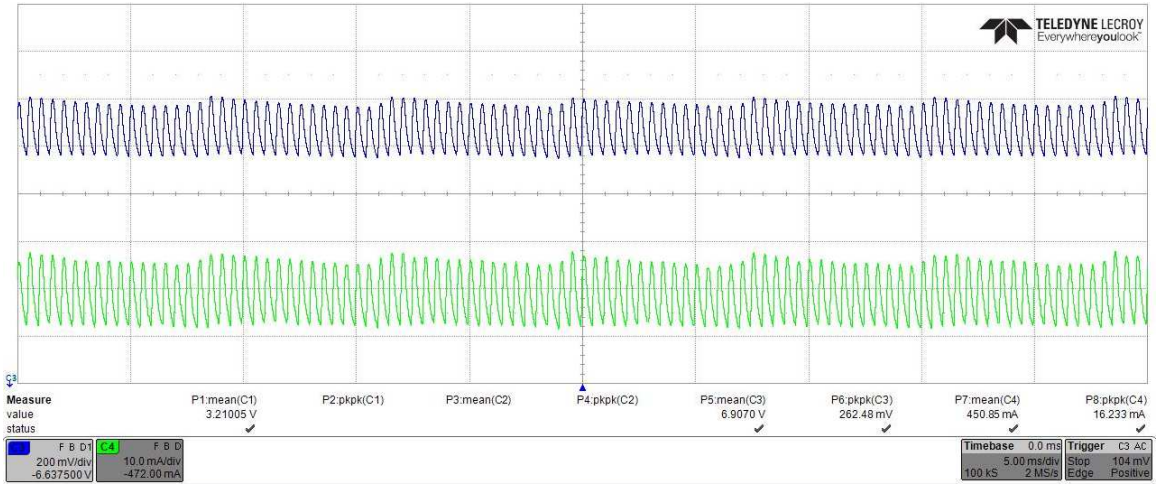

Figure 5-41 : Measured Load Current (Green) and Voltage (Blue) waveforms. The battery is excited with a PWM (red) with an impulse function at a Low frequency of 125Hz, with 4% impulse duty cycle.

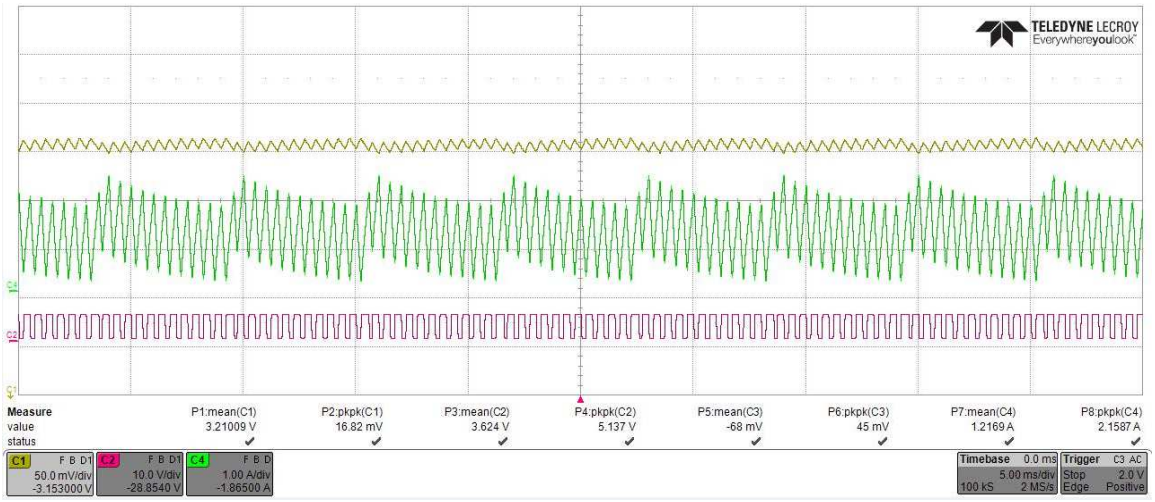

Figure 5-42 : Measured Li-ion battery Current (Green) and Voltage (yellow) waveforms. The battery is excited with a PWM (red) with an impulse function at a Low frequency of 166.7Hz, with 6% impulse duty cycle.

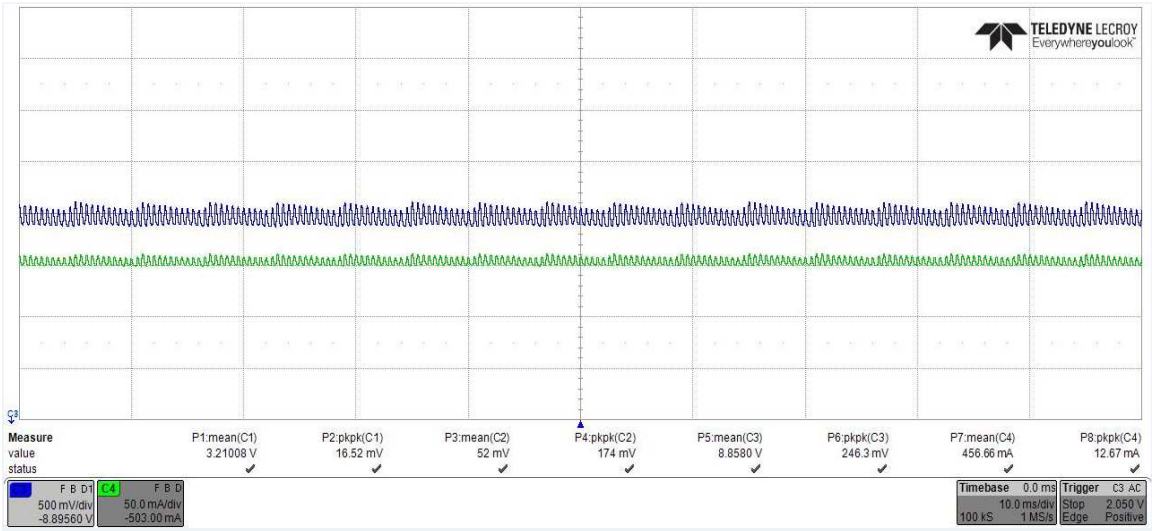

Figure 5-43 : Measured Load Current (Green) and Voltage (Blue) waveforms. The battery is excited with a PWM (red) with an impulse function at a Low frequency of 166.7Hz, with 6% impulse duty cycle.

The converter is operating in a similar manner to the simulated model. The low-frequency ripple shows that a low frequency harmonic has been induced on the system. The experiment was run with combinations of the PWM signal and an impulse function with a low-frequency as an integer value of f_s. The key parameters of the experimental results of the low frequencies of 125 Hz with duty cycle of 0.04 and 166.7Hz with duty cycle of 0.06 are shown in Table 5-11 and Table 5-12.

Table 5-15: Comparison of PWM with Impulse (OR-4%) at 125Hz effects on Current and Voltage ripple

	Experimental			
	Fixed Duty Cycle		Using impulse duty Cycle	
	Average Value	Peak-Peak ripple	Average Value	Peak-Peak ripple
I_{batt}	1.18 A	1.49 A	1.18 A	1.72 A
V_{batt}	3.21 V	12.45 mV	3.21 V	13.6 mV
I_{load}	420 mA	10 mA	450 mA	16 mA
V_{dc}	6.89 V	67 mV	6.91 V	262 mV

Table 5-16: Comparison of PWM with Impulse (OR-6%) at 166.7Hz effects on Current and Voltage ripple

	Experimental			
	Fixed Duty Cycle		Using impulse duty Cycle	
	Average Value	Peak-Peak ripple	Average Value	Peak-Peak ripple
I_{batt}	1.18 A	1.49 A	1.22 A	2.16 A
V_{batt}	3.21 V	12.45 mV	3.21 V	16.9 mV
I_{load}	420 mA	10 mA	460 mA	10 mA
V_{dc}	6.89 V	67 mV	8.86 V	250 mV

The waveform ripple values increase with the T_i value of the pulse function according to the Equation 3-83. The pulse width at 125Hz increased from 0.0003 to 0.00032s, while the pulse width increased to 0.00036s at 166.7Hz. The ripple and boost ratio of the converter on the 166.7Hz pulse function is therefore higher compared to the 125Hz signal as described in section 3.5.3. This is because the circuit is switched on for longer time and therefore the boost ratio of the circuit changes due to the increase in the average duty cycle with time over the T_0 pulses period according to Equation 3-82.

5.6.2 Harmonics

Figure 5-32 shows the battery current harmonic analysis at low-frequency of 125Hz by the pulse function and the PWM signal with duty cycle of 0.04. The harmonic spectrum of the current contains

switching frequency and low frequency component harmonics similar to Figure 4-31, which is repeated in Figure 5-44b for comparison purpose. As it shown the low frequency component is detected in both simulated and experimentally captured waveforms.

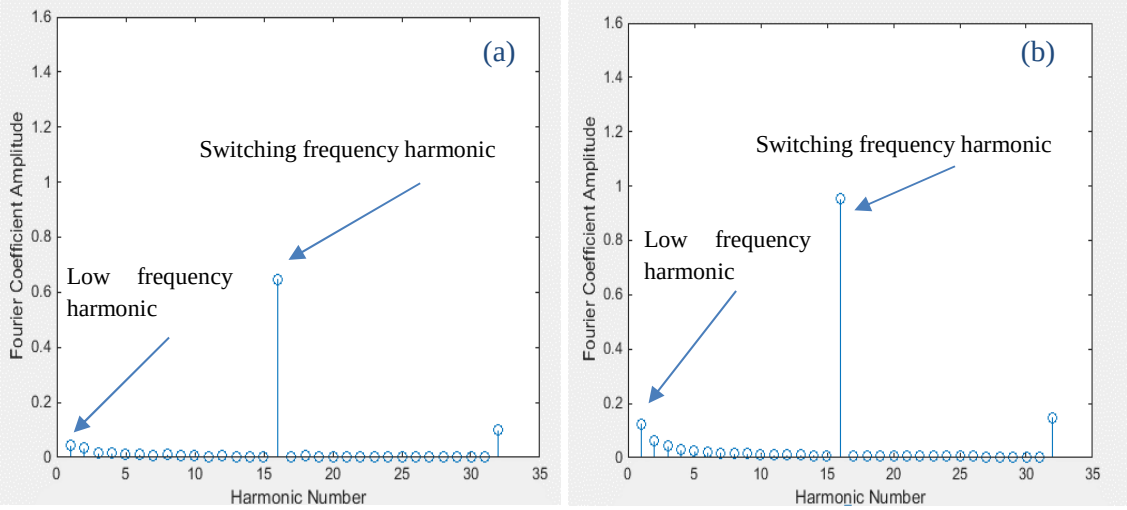

Figure 5-44 : a) Experimentally derived harmonics and b) simulated harmonics of the Li-ion battery current signal with an impulse function at a low frequency of 125Hz with d=4%.

5.6.3 Inductor ripple

The effect of the T_i variation on the added ripple to the current waveform is shown in Figure 5-45. As T_i increased, the ripple of the waveform is increased. Table 5-17 shows the relationship between ripple increases experimentally, simulation, and theoretically as per Equation 3-83.

Table 5-17: Calculated increase in current ripple as a % with pulse function compared to a fixed Pulse for a switching frequency of 2kHz

Frequency/$d_{impulse}$	Experimental	Simulation	Theoretical
125Hz, $d_{impulse}$ = 0.04	115%	116%	107%
166Hz, $d_{impulse}$ = 0.06	144%	142%	120%
166Hz, $d_{timpulse}$= 0.07	194%	200%	140%
166Hz, $d_{impulse}$ = 0.08	222%	232%	160%
166Hz, $d_{impulse}$ = 0.1	244%	249%	300%

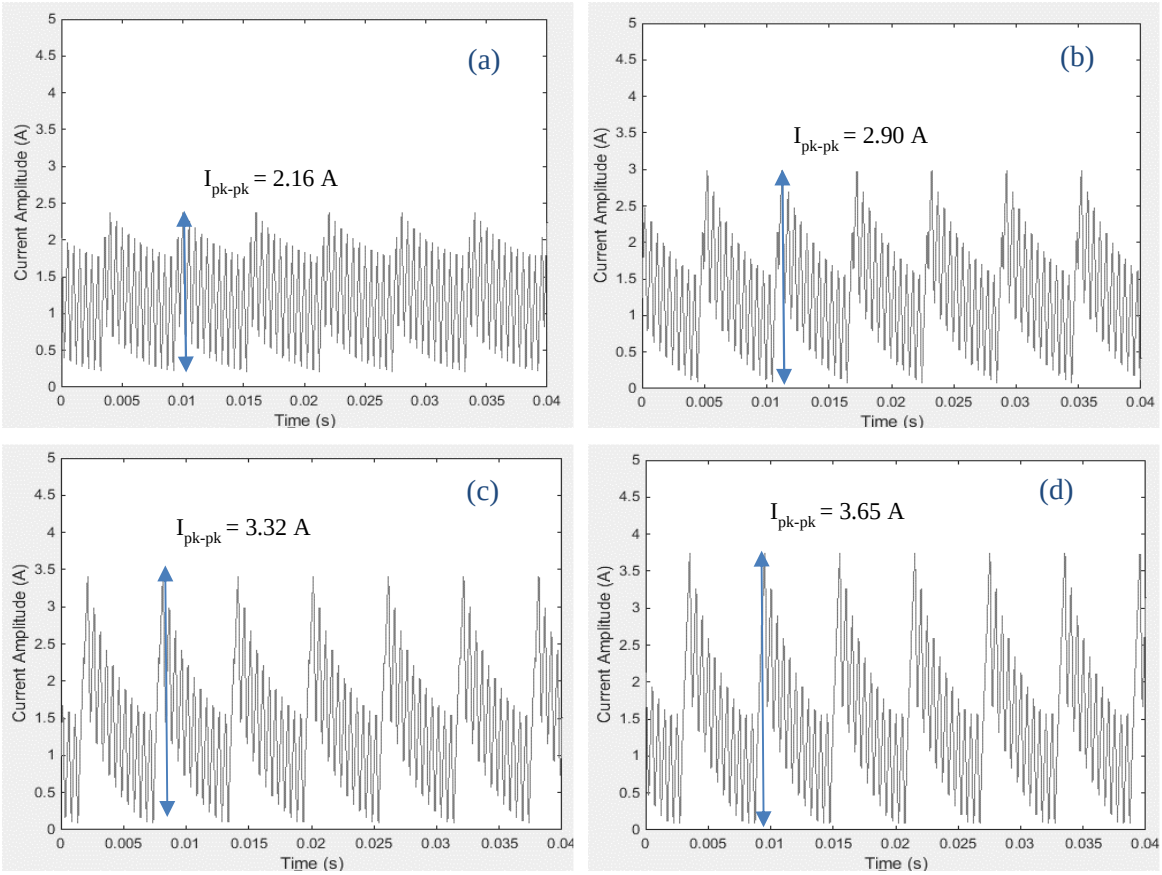

Figure 5-45 : Comparison of the low frequency ripple at different frequency (a) $d_{impulse}$ = 0.06, (b) $d_{impulse}$ = 0.07, (c) $d_{impulse}$ = 0.08, and (d) $d_{impulse}$ = 0.1. With fs = 2kHz and f_0 =166.7Hz

As shown in Figure 5-46, the current ripple changes over the range of the low-frequency components, because of the different duty cycle values of the low-frequency pulse function. As shown in Equation 3-83, the ripple variation depends on the changes of the T_i value and therefore when T_i increases the current ripple value increases.

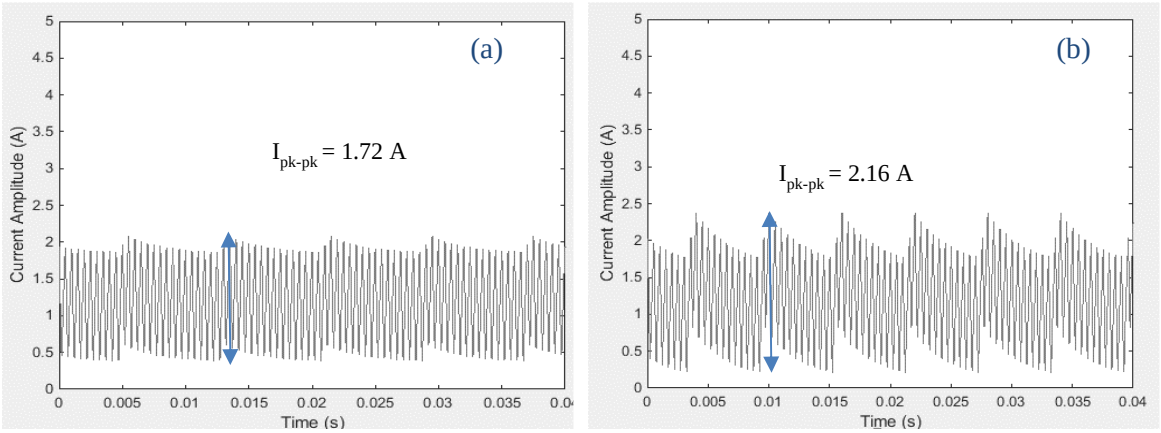

Figure 5-46 : Comparison of the low frequency ripple at different frequency (a) f_0 =125Hz with $d_{impulse}$ = 0.04, (b) f_0 =166.7Hz with $d_{impulse}$ = 0.06 and fs = 2kHz.

Figure 5-47 shows the variation of the current ripple based on the Np value variation over the low-frequency range. Because the different frequencies require a different duty cycle, the graph below only shows those low-frequencies that allow a pulse width of the 0.00032s. The data shows that the current ripple value remains constant as the Np value increases as expected.

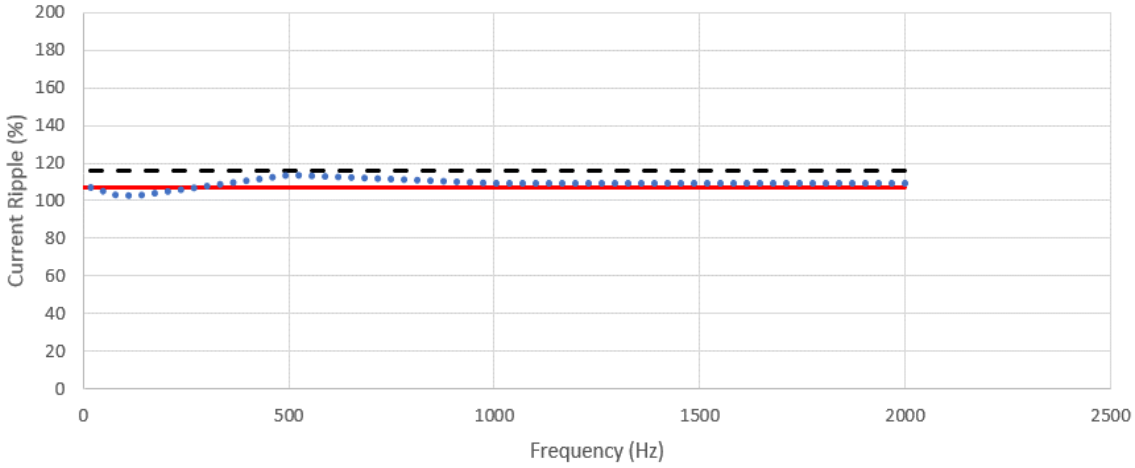

Figure 5-47 : Comparison of the low frequency ripple at different frequencies using theory (Line), Simulation (dash), and Experiment (dots)

5.6.4 EIS Calculation

Figure 5-15 to Figure 5-17 show the calculated complex impedance, amplitude and phase plots of the li-ion battery from off-line EIS measurement equipment (in red), experimentally measured data (in blue dots), and simulation (in black). Results show that on-line measured data has a reasonable correlation with the off-line measurement.

A switching frequency of 2kHz was used while the low frequency signal f_o was varied from 1 to 2kHz. To ensure that the system is always operating in continuous mode the duty cycle is 0.6 during discharge mode. The impedance of the battery was calculated for 22 low-frequency points. The battery current and voltage waveforms were measured and captured by the oscilloscope probes at each low-frequency points. The impedance of battery was then calculated by Fourier analysis of the waveforms at each frequency points using the FFT MATLAB code.

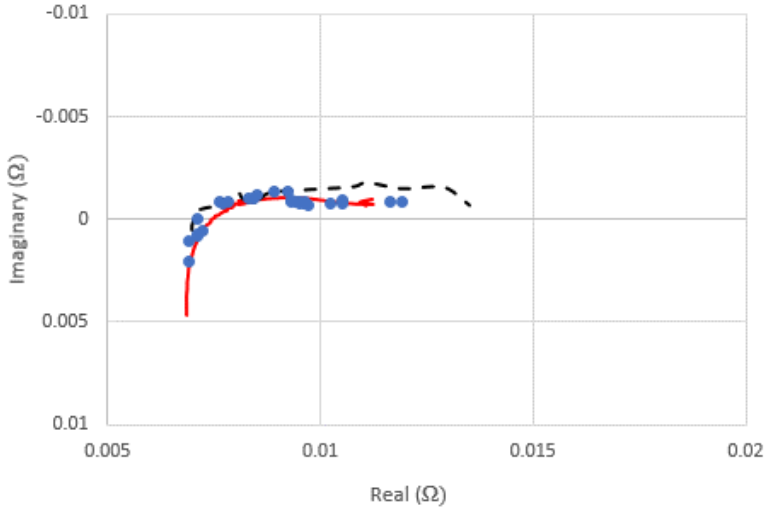

Figure 5-48 : Impedance Nyquist plot of the lithium-ion phosphate battery with EIS (red), Simulation (black), and Experimental data (blue dots)

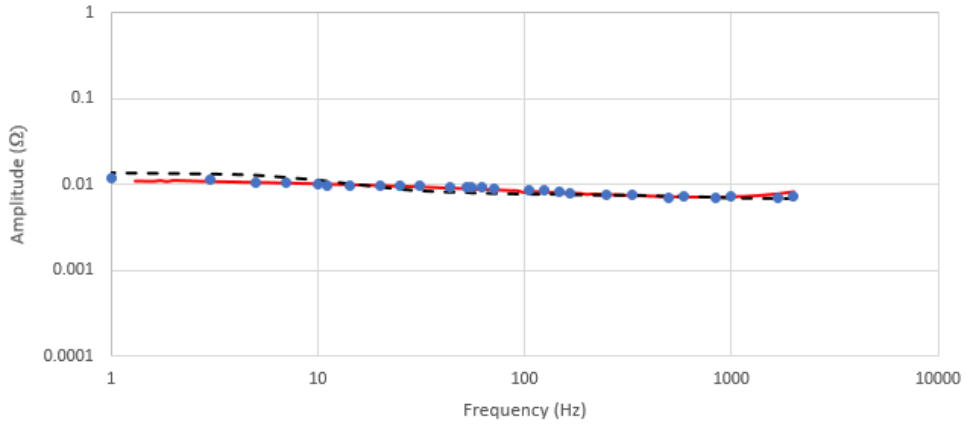

Figure 5-49 : Impedance amplitude bode plot of the lithium-ion phosphate battery with EIS (red), Simulation (black), and Experimental data (blue dots)

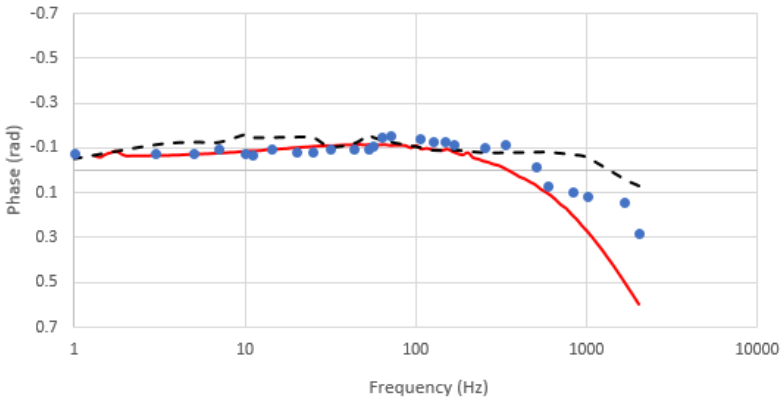

Figure 5-50 : Impedance phase bode plot of the lithium-ion phosphate battery with EIS (red), Simulation (black), and Experimental data (blue dots)

5.7 Battery balancing circuit

In this method, the battery balancing circuit was used to generate a low frequency excitation signal. The battery balancing circuit includes a 10mF capacitor and 4 switch MOSFETs. The Opal-RT was used to generate the two low-frequency PWM signals with the duty cycle of with a duty cycle of 0.45 controls switches M1 and M3. The other pulse generator controls switches M2 and M4. As it mentioned previously in section 4.6, the switches M2 and M4 should be turned off while switches M1 and M3 are turned on, a logical operator function block is used to NOT the pulse control signal with the duty cycle of 0.55. So the output signal is a pulse signal with 0.45 duty cycle. The switches were connected to the opal-rt through the gate drive circuits. A 10mF capacitor was used for the balancing capacitor as previously mentioned in 4.6. The experimental setup is shown in Figure 5-51 and the block diagram is shown in Figure 3-32. The battery balancing circuit was connected to the battery terminals and to the boost converter.

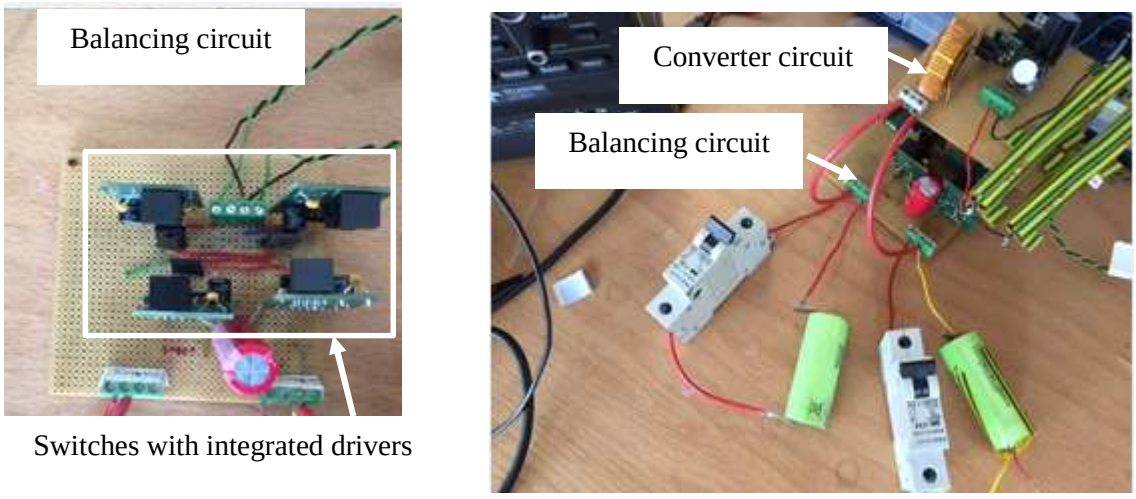

Figure 5-51 : Experimental setup

5.7.1 Circuit Operation

This method is different from those previously described as it doesn't use the power electronic components to generate a low frequency, but instead uses the battery balancing circuit. This makes it harder to directly compare as there are now two batteries in the circuit. The combined battery voltage of the two batteries are set equal to the single battery to allow comparison against the same base case. However this results in the battery SOC being less than the 100% used in other experiments. The EIS measurements of the batteries are run at these reduced values of voltage to try to make the comparison as valid as possible.

The battery currents, voltages and circuit output voltage and current waveforms for two frequency points of 125 Hz and 166Hz for a low frequency excitation signal from with duty cycle of 45% for switches M1 and M3 and 45% for switches M2 and M4 were captured and are shown in Figure 5-52 to Figure 5-55. As mentioned previously in section 4.6, the ripple current in battery 1 and 2 is a result of the superposition of the balancing capacitor charging and discharging currents with the converter sawtooth waveform. The current ripple of both batteries follows an exponential decay related to the time constant of the capacitor balancing circuit.

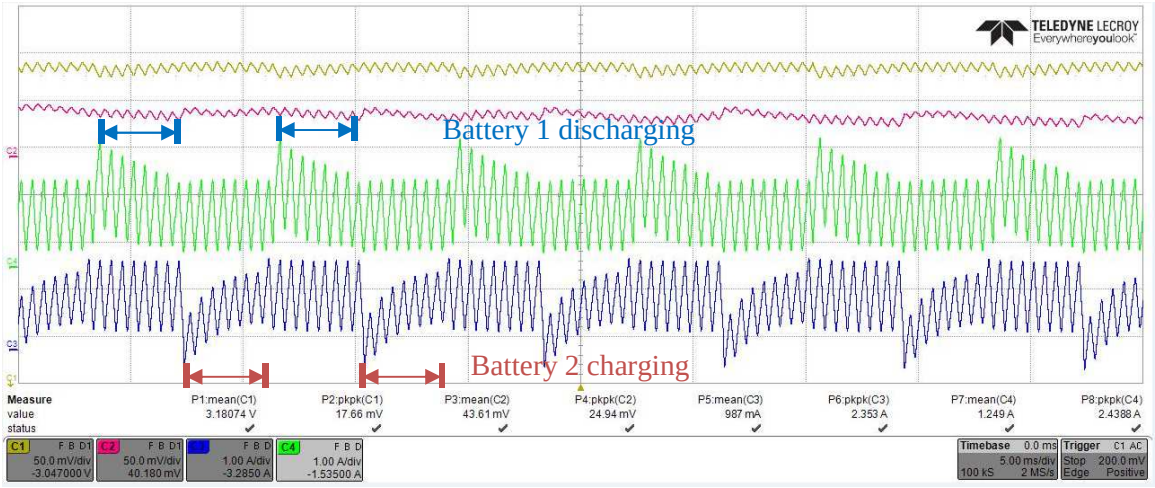

Figure 5-52 : Li-ion battery1 Current (Green), Li-ion battery2 Current (blue), Li-ion battery1 Voltage (yellow), and Li-ion battery2 Voltage (red) waveforms, at Low frequency of 125Hz.

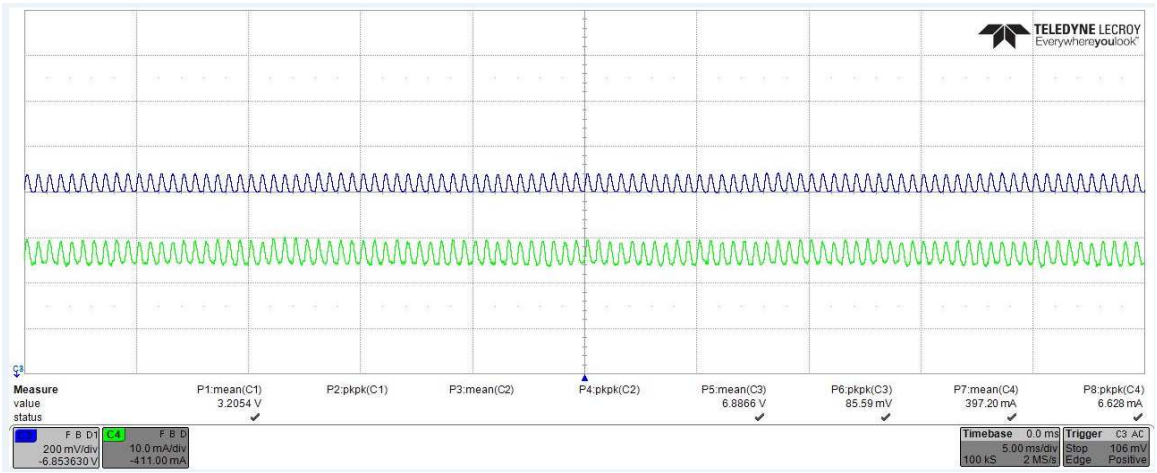

Figure 5-53 : Load Current (Green) and output Voltage (blue) waveforms, the battery is excited at Low frequency of 125Hz. (need to do this again).

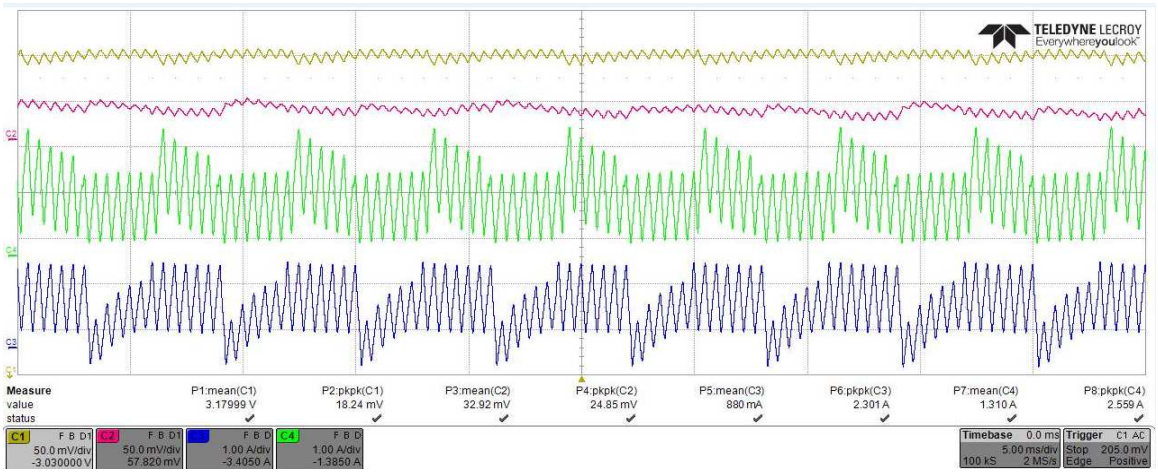

Figure 5-54 : Li-ion battery1 Current (Green), Li-ion battery2 Current (blue), Li-ion battery1 Voltage (yellow), and Li-ion battery2 Voltage (red) waveforms, at Low frequency of 125Hz.

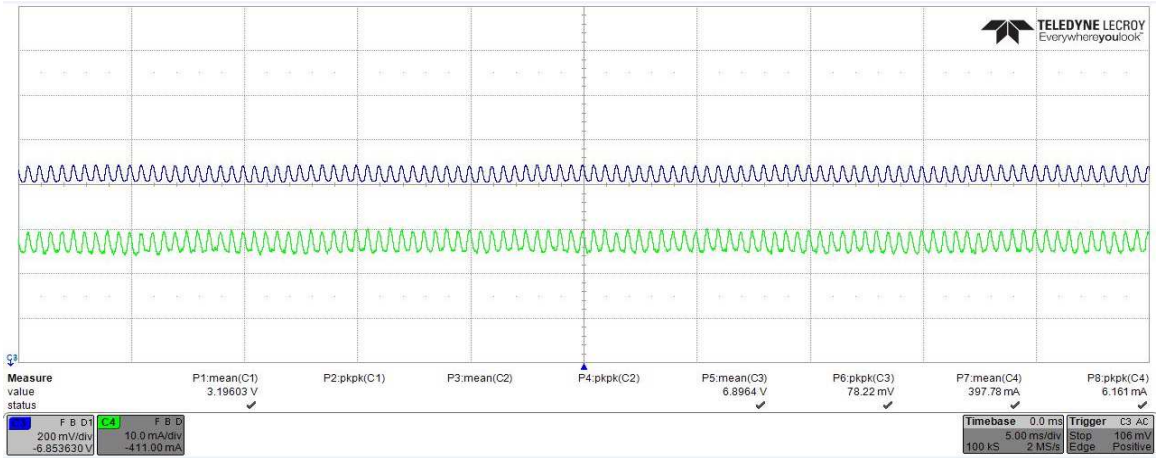

Figure 5-55 : Load Current (Green) and output Voltage (blue) waveforms, the battery is excited at Low frequency of 166Hz.

The circuit was run with a boost converter switching frequency of 2kHz, a duty cycle of 0.6 in continuous mode and the battery balancing circuit active. Table 5-18 and Table 5-19 represents the comparison of the key parameters of the experimental results at the low frequencies of 125 Hz and 166.7Hz. Table 4-12 is reproduced in Table 5-20 for comparison purpose. The results shows that the experimental model of the converter and balancing circuit are performing in a manner similar to the simulation in section 4.6. The average value of the load voltage and current and the boost ratio of the circuit remain the same as the base circuit in section 5.2. The measured data shows that the peak to peak ripple value remained approximately constant at different low-frequency values according to Equation 3-95. In this example, the voltage value of 43.6mV for battery 2 is not practical and safe for the battery and this is only used for proof of concept and requires further consideration.

In order to observe the waveforms, the batteries were set to have a large difference in voltage. This is because the resistance in the experimental circuit is greater than that in simulation which is based on an ideal case and as such Equation 3-85 indicates that charging current will be reduced.

Table 5-18: Comparison of the based circuit data with battery balancing at 125Hz effects on Current and Voltage ripple

	Experimental			
	Fixed Duty Cycle		Battery with Balancing circuit	
	Average Value	Peak-Peak ripple	Average Value	Peak-Peak ripple
I_L	1.18 A	1.49 A	1.18 A	1.59 A
I_{batt1}	1.18 A	1.49 A	1.25 A	2.44 A
I_{batt2}			0.99 A	2.35 A
V_{batt1}	3.21 V	12.45 mV	3.18 V	17.7 mV
V_{batt2}			43.6 mV	26.7 mV
I_{load}	420 mA	10 mA	397 mA	7 mA
V_{dc}	6.89 V	67 mV	6.8 V	86 mV

Table 5-19: Comparison of the based circuit data with battery balancing at 166Hz effects on Current and Voltage ripple

	Experimental			
	Fixed Duty Cycle		Battery with Balancing circuit	
	Average Value	Peak-Peak ripple	Average Value	Peak-Peak ripple
I_L	1.18 A	1.49 A	1.18 A	1.60 A
I_{batt1}	1.18 A	1.49 A	1.31 A	2.56 A
I_{batt2}			0.88 A	2.30 A
V_{batt1}	3.21 V	12.45 mV	3.18 V	18.24 mV
V_{batt2}			33 mV	25 mV
I_{load}	420 mA	10 mA	398 mA	7 mA
V_{dc}	6.89 V	67 mV	6.9 V	78 mV

Table 5-20: Comparison of simulated battery balancing excited signal at 125Hz effects on Current and Voltage ripple

	Simulation			
	Fixed Duty Cycle		Battery with Balancing circuit	
	Average Value	Peak-Peak ripple	Average Value	Peak-Peak ripple
I_L	1.55 A	2.42 A	1.56 A	2.73 A
I_{batt1}	1.55 A	2.42 A	1.8 A	3.51 A
I_{batt2}			1.4 A	3.88 A
V_{batt1}	3.21 V	16.8 mV	1.7 V	25 mV
V_{batt2}			1.51 V	26.7 mV
I_{load}	456 mA	0.7 mA	455 mA	0.8 mA
V_{dc}	7.3 V	11.1 mV	7.3 V	12.5 mV

The sum of the two battery voltages has been set to 3.21V to allow comparison with the base case. The boost ratio, load current and voltage remain the same. The waveforms show that the added ripple to the battery waveforms, using the battery balancing method as explained in section 3.6.2, are visible in the experiment. However, the battery voltage of the second battery is set much lower than that in simulation in order to observe the ripple.

5.7.2 Harmonics

Figure 5-56 shows the battery current harmonic analysis showing the boost converter switching frequency of 2kHz and battery balancing circuit low-frequency of 125Hz. Both low frequency 125Hz and the switching frequency of 2kHz harmonics are extracted from the experimentally measured current waveform.

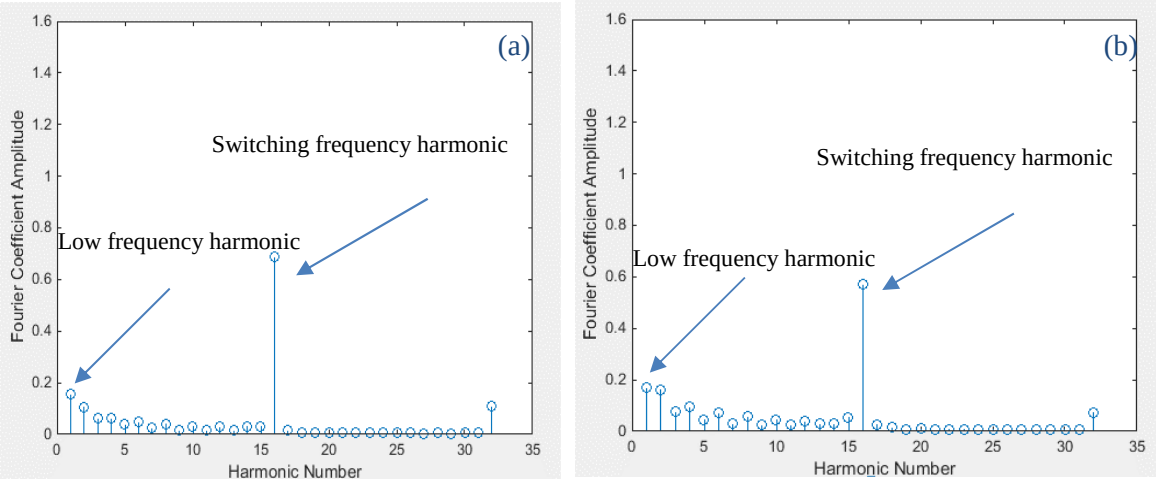

Figure 5-56 : Experimentally derived harmonics of the Li-ion battery current signal with battery balancing at a low frequency of 125Hz (a) battery1 (b) battery2.

5.7.3 Inductor ripple

The effect of the balancing circuit low-frequency variation on the added ripple to the inductor current waveform is shown in Figure 5-57. According to Equation 3-95, the inductor current variation remain constant over the frequency range. As the inductor current ripple is independent of the balancing circuit and the low-frequency component. Table 5-21 gives an estimate of inductor ripple increase above the base case. As it is difficult to match the total voltage the base case current is adjusted in proportion to the total voltage measured against base voltage.

Table 5-21: Calculated increase in current ripple as a % with battery balancing method compared to the base case for a switching frequency of 2kHz

Frequency/V_{diff}	Experimental	Simulation	Theoretical
125Hz, V_{TOTAL} = 3.3V, V_{diff} =3.15 V	104%	100%	100%
166Hz, V_{TOTAL} = 3.3V, V_{diff} =3.15 V	104%	100%	100%
166Hz, V_{TOTAL} = 3.6V, V_{diff} =2.74 V[1]	104%	117%	100%
166Hz, V_{TOTAL} = 3.7V, V_{diff} = 2.67V[1]	102%	116%	100%
166Hz, V_{TOTAL} = 4.0V, V_{diff} = 2.27V[1]	106%	119%	100%

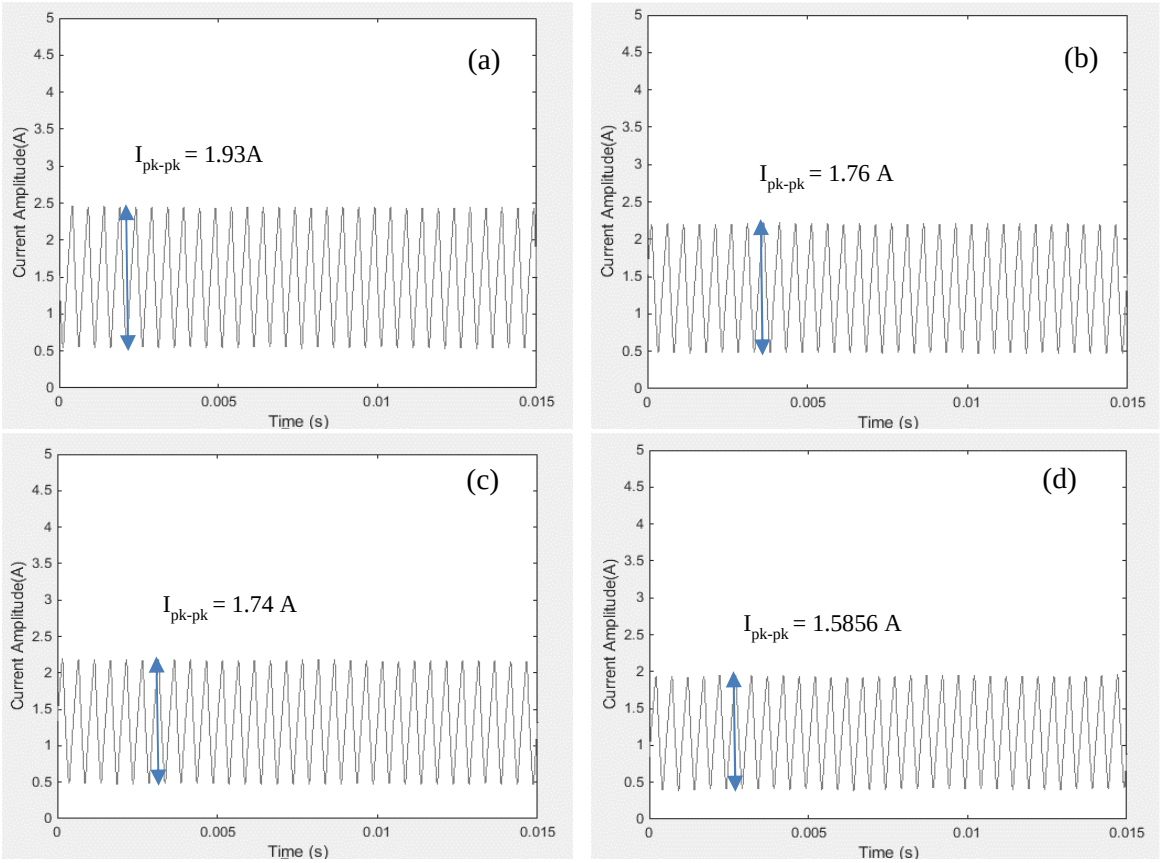

Figure 5-57 : Comparison of the low frequency ripple at different voltage difference (a) V_{diff} = 2.27V, (b) V_{diff} = 2.67V, (c)V_{diff} = 2.74V, and (d) V_{diff} = 3.15V. With f_s = 2kHz and f_0 = 166.7Hz

[1] Battery 1 was kept at constant voltage but battery 2 voltage was increased to reduce the voltage difference. The increase in ripple has been estimated with reference to the increased current by multiplying the base case current by the ratio of $V_{TOTAL}/3.21$ and then calculating measured current as a function of adjusted base current.

Figure 5-58 shows the inductor current ripple appears constant over two different low-frequency values.

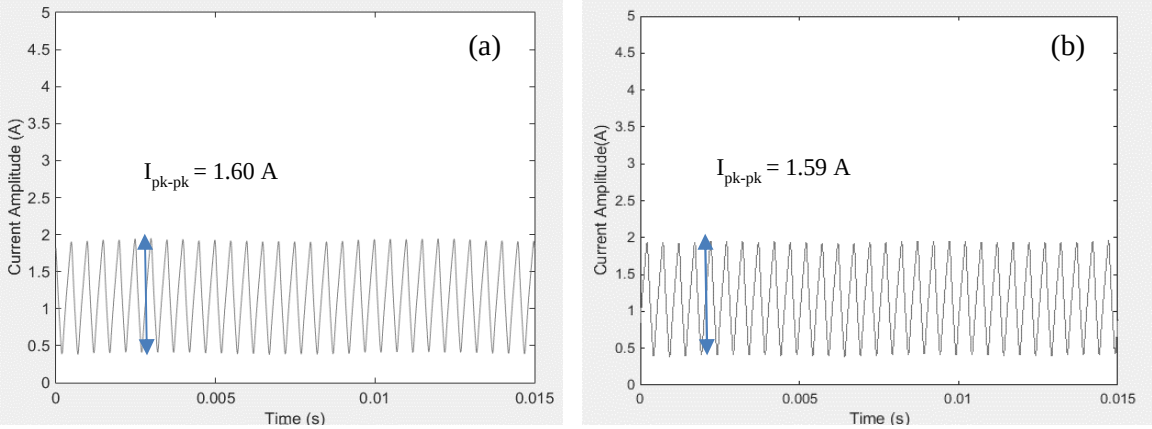

Figure 5-58 : Comparison of the low frequency ripple at different frequency (a) f_0 = 125Hz, (b) f_0 = 166.7Hz, With f_s = 2kHz at V_{diff} = 3.15V

Figure 5-59 shows the variation of the current ripple based on the Np value variation over the low-frequency range. The data shows that the current ripple value remains approximately constant as the Np value increases as expected.

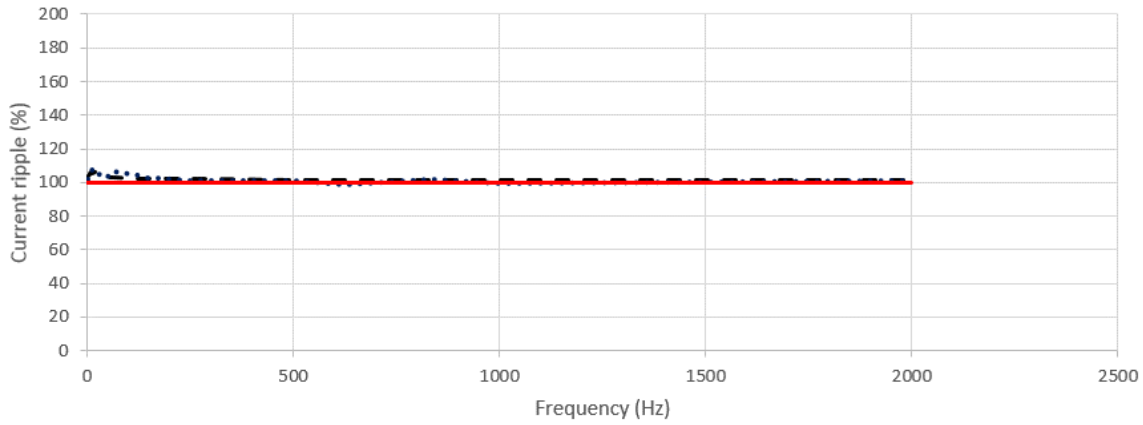

Figure 5-59 : Comparison of the low frequency ripple at different frequencies using theory (Line), Simulation (dash), and Experiment (dots)

5.7.4 EIS Calculation

Figure 5-60 to Figure 5-62 shows the calculated complex impedance, amplitude and phase plots of the li-ion battery from off-line EIS measurement equipment (in red), experimentally measured data (in blue dots), and simulation (in black). Data from experimental tests show similar values compared to the EIS data.

A switching frequency of 2kHz was used while the low frequency signal f_o was varied from 1 to 2kHz. To ensure that the system is always operating in continuous mode the duty cycle was set to

0.6 during discharge mode. The impedance of the battery was calculated for 21 low-frequency points. The battery current and voltage waveforms were measured and captured by the oscilloscope probes at each low-frequency points. The impedance of battery was then calculated by Fourier analysis of the waveforms at each frequency points using the FFT MATLAB code.

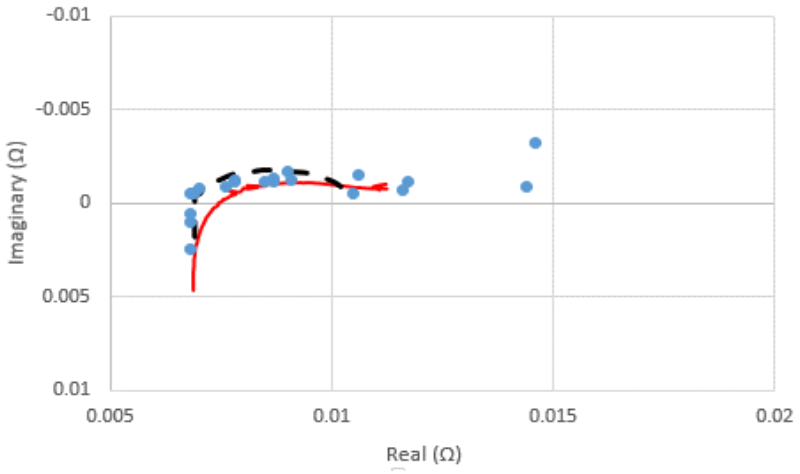

Figure 5-60 : Impedance Nyquist plot of the lithium-ion phosphate battery1 with EIS (red), Simulation (black), and Experimental data (blue dots)

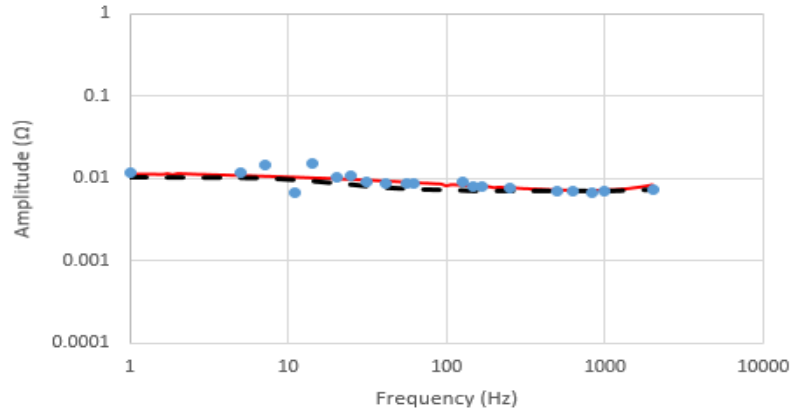

Figure 5-61 : Impedance amplitude bode plot of the lithium-ion phosphate battery1 with EIS (red), Simulation (black), and Experimental data (blue dots)

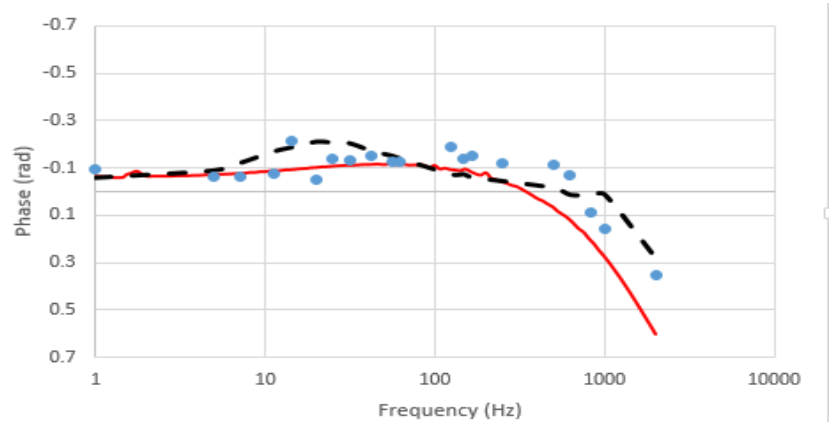

Figure 5-62 : Impedance phase bode plot of the lithium-ion phosphate battery1 with EIS (red), Simulation (black), and Experimental data (blue dots)

As battery 2 was run at a low SOC it was not possible to generate an EIS figure. More works needs to be done on this method to properly appreciate when the balancing circuit is appropriate.

5.8 Earth Leakage monitoring circuit

In this method, the ELM circuit was used to generate a low frequency excitation signal. The ELM circuit includes two ELM loads and a function generator to generate two low-frequency sinewave signals with the same amplitude of 12V but a 45˚ phase difference with respect to each other. The AC signals were generated by using the signal arbitrary function generator (arbstudio 1104). The voltage sources are then connected to the battery terminals through the 10Ω resistors and two capacitors. ELM circuit and the boost converter circuit were connected to the battery terminals. The experimental set-up is shown in Figure 5-63 and the block diagram is shown Figure 3-38.

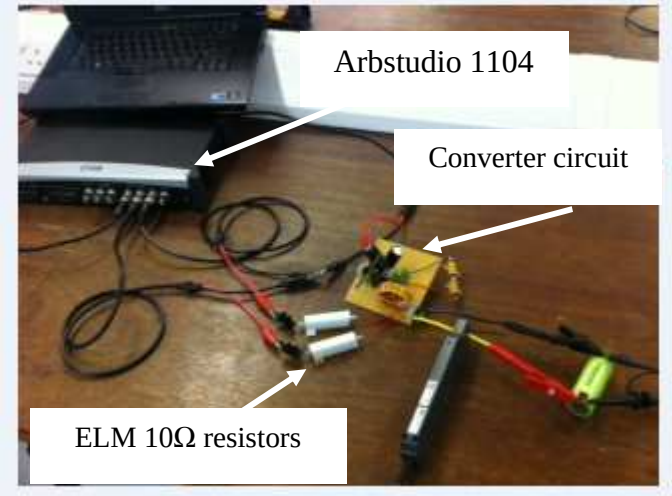

Figure 5-63 : Experimental setup of ELM method

5.8.1 Circuit Operation

The measured battery current, voltage and circuit output voltage and current waveforms for two frequency points of 125 Hz and 175Hz are shown in Figure 5-64 to Figure 5-67. The injected low-frequency using the ELM added a ripple to the battery and circuit waveforms. The resulting waveform is the results of the superposition of the boost converter and the ELM current signals as described in section 3.7.3.

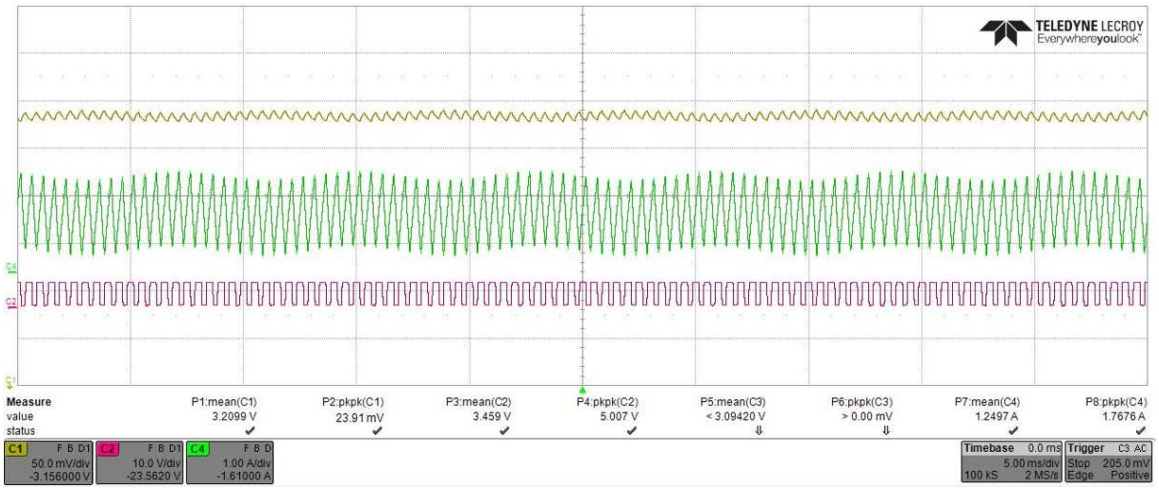

Figure 5-64 : Li-ion battery Current (Green) and Voltage (yellow) waveforms. The battery is excited with fixed duty cycle PWM (red) and a low ELM signal at 125Hz.

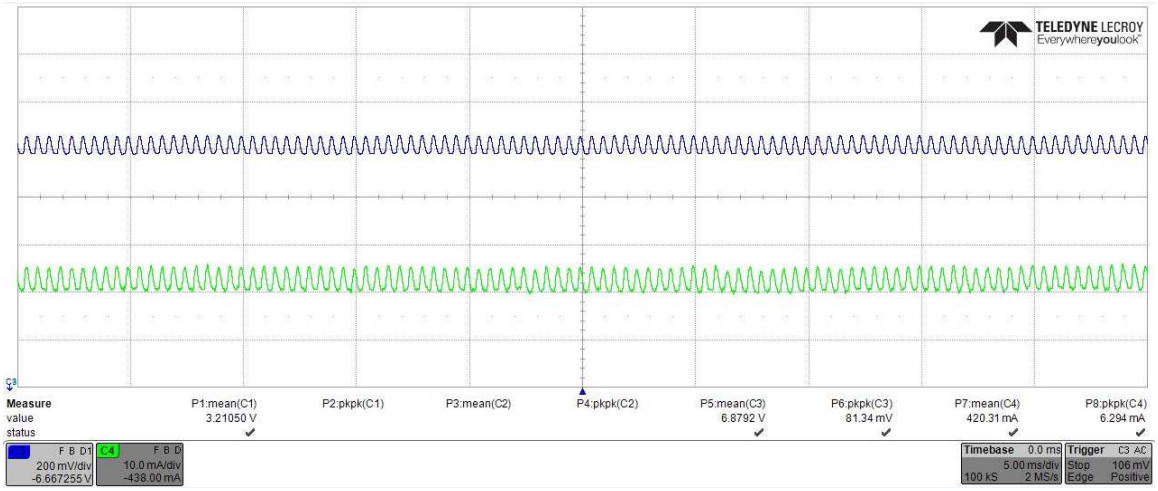

Figure 5-65 : Load Current (Green) and Voltage (blue) waveforms. The battery is excited with fixed duty cycle PWM and a low ELM signal at 125Hz.

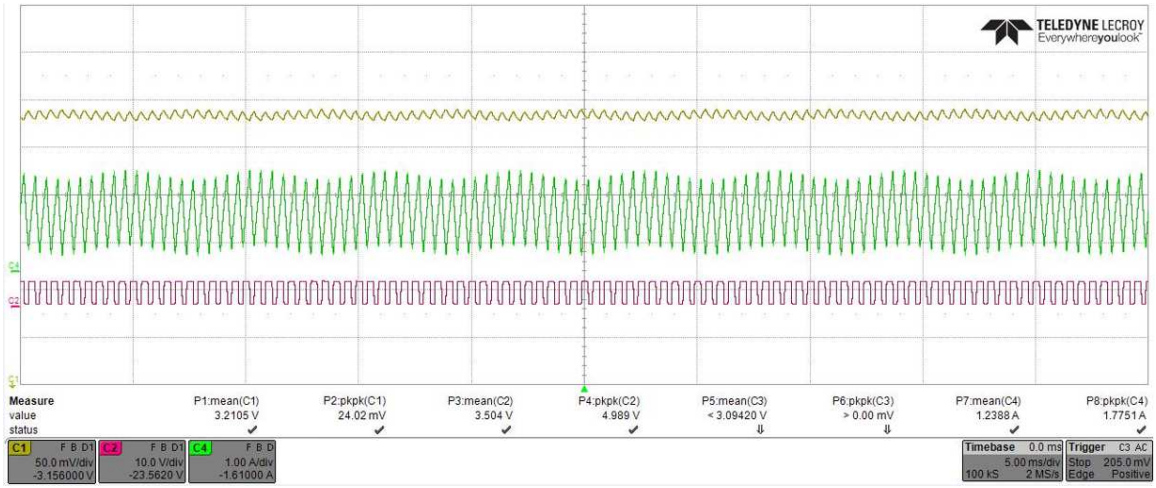

Figure 5-66 : Li-ion battery Current (Green) and Voltage (yellow) waveforms. The battery is excited with fixed duty cycle PWM (red) and a low ELM signal at 175Hz.

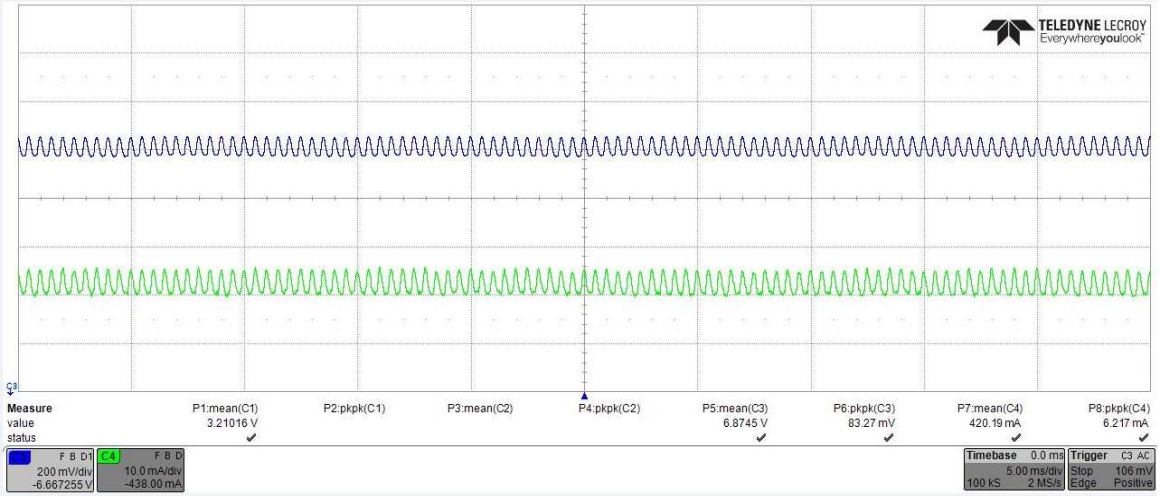

Figure 5-67 : Load Current (Green) and Voltage (blue) waveforms. The battery is excited with fixed duty cycle PWM and a low ELM signal at 175Hz.

The circuit was run with the boost converter switching frequency of 2kHz, a duty cycle of 0.6 in continuous mode and the ELM circuit active. Table 5-11 and Table 5-12 show the comparison of the key parameters of the experimental results at the low-frequencies of 125 Hz and 175Hz. The average value of the load voltage and current and the boost ratio of the circuit remain the same as the base circuit in section 5.2. The peak to peak ripple value remained approximately constant at different low-frequency values as per Equation 3-124.

Table 5-22: Comparison of the based circuit data with the ELM circuit at 125Hz effects on Current and Voltage ripple

	Experimental			
	Fixed Duty Cycle		Earth Leakage connected to the converter	
	Average Value	Peak-Peak ripple	Average Value	Peak-Peak ripple
I_{batt}	1.18 A	1.49 A	1.25 A	1.77 A
V_{batt}	3.21 V	12.45 mV	3.21 V	23.9 mV
I_{load}	420 mA	10 mA	420 mA	6 mA
V_{dc}	6.89 V	67 mV	6.88 V	81 mV

Table 5-23: Comparison of the based circuit data with the ELM 175Hz effects on Current and Voltage ripple

	Experimental			
	Fixed Duty Cycle		Earth Leakage connected to the converter	
	Average Value	Peak-Peak ripple	Average Value	Peak-Peak ripple
I_{batt}	1.18 A	1.49 A	1.24 A	1.78 A
V_{batt}	3.21 V	12.45 mV	3.21 V	24.0 mV
I_{load}	420 mA	10 mA	420 mA	6 mA
V_{dc}	6.89 V	67 mV	6.88 V	83 mV

5.8.2 Harmonics

Figure 5-68 shows the battery current harmonic analysis at the boost converter switching frequency of 2kHz and ELM low-frequency of 125Hz using the ELM circuit method. Both the low frequency 125Hz and the switching frequency of 2kHz harmonics are extracted from the experimental and simulated current waveform. Figure 4-45 is repeated in Figure 5-68b for comparison purpose

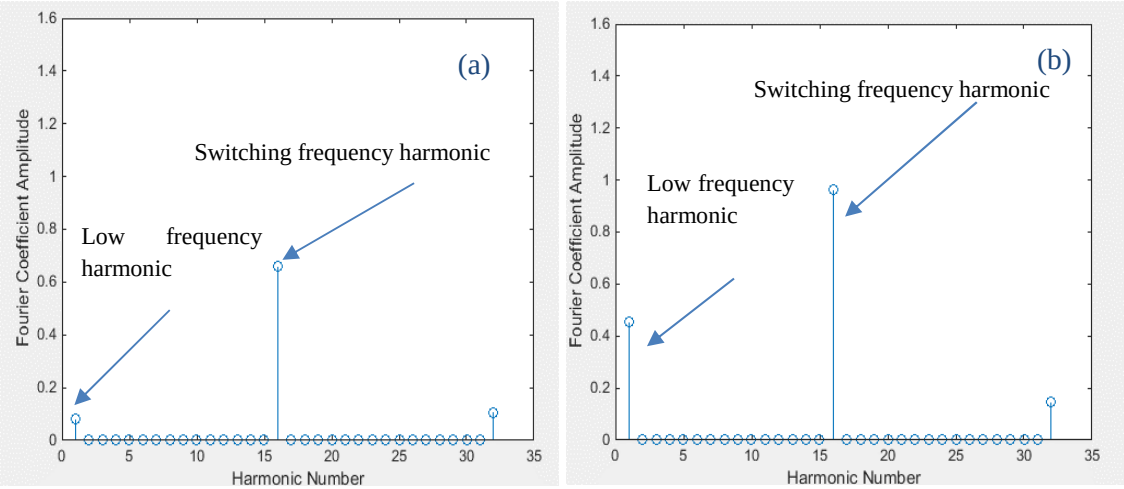

Figure 5-68 :a) Experimentally derived harmonics b)simulated harmonics of the Li-ion battery current signal with an ELM signal at a low frequency of 125Hz

5.8.3 Inductor ripple

The impedance of the power electronics to the ELM circuit is such that the inductor ripple current increase is negligible. The results presented below show the increase on ripple current for the battery as opposed to the ripple on the inductor as this is more useful in this case. The effect of the V_{ELM} amplitude variation on the added ripple to the current waveform is shown in Figure 5-69. As V_{ELM} decreases, the ripple of the waveform is decreased. The relationship between ripple increase experimentally, theory, and simulation as per Equation 3-64 is shown in Table 5-24.

Table 5-24: Calculated increase in current ripple as a % with ELM circuit compared to the base case for a switching frequency of 2kHz

Frequency/ V_{ELM}	Experimental	Simulation	Theoretical
125Hz, V_{ELM} = 12V	103%	117%	118%
175Hz, V_{ELM} = 12V	104%	117%	118%
175Hz, V_{ELM} = 8V	100%	103%	118%
175Hz, V_{ELM} = 5V	98%	102%	118%
175Hz, V_{ELM} = 3.5V	96%	101%	118%

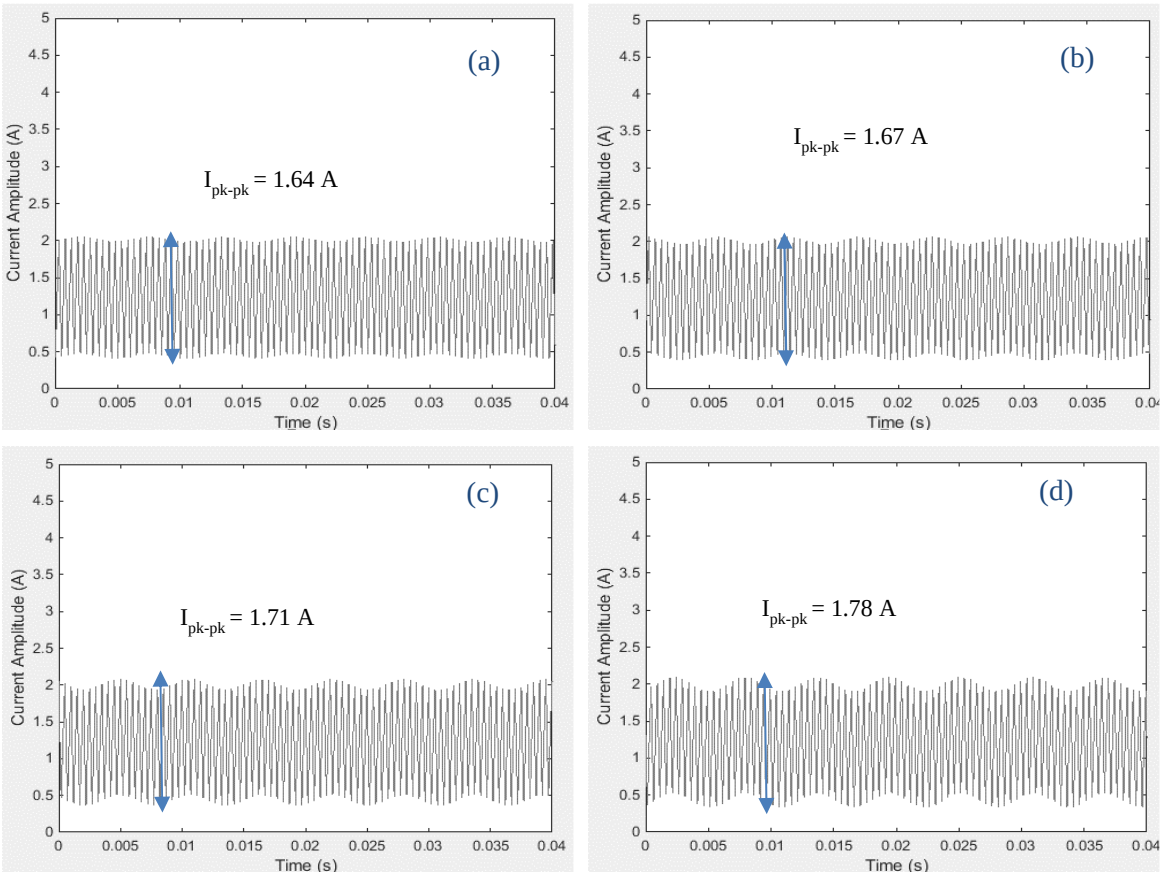

Figure 5-69 : Comparison of the low frequency ripple at different frequency (a)V_{ELM} = 3.5V, (b)V_{ELM} = 5V, (c) V_{ELM} = 8V, and (d) V_{ELM} = 12V. With f_s = 2kHz and f_0 = 175Hz

Figure 5-70 shows the current ripple for two low-frequency components. As determined in Equation 3-124, the ripple variation depends on many factors of $z_{ELM}, z_{PE}, V_{bat}, z_{bat}, L$, and dT_s values and therefore is less easy to predict the experimental outcome.

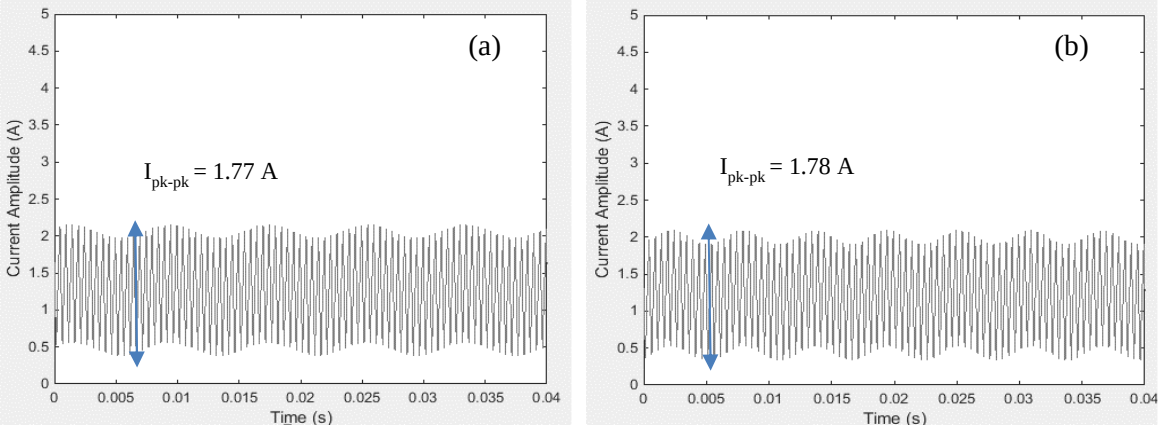

Figure 5-70 : Comparison of the low frequency ripple at different frequency (a) f_0 = 125Hz, (b) f_0 = 175Hz

Figure 5-71 shows the variation of the current ripple value based on Np value variation over the low-frequency range experimentally, theory using Equation 3-124, and simulation. The value of z_{PE} and z_{bat} changes depending on the variation of the frequency. The impedance of the battery and power electronics is calculated for different low-frequency points to calculate the battery current ripple theoretically. The data shows that the ripple mostly remains constant and the effect of the low frequency value on ripple variation is small.

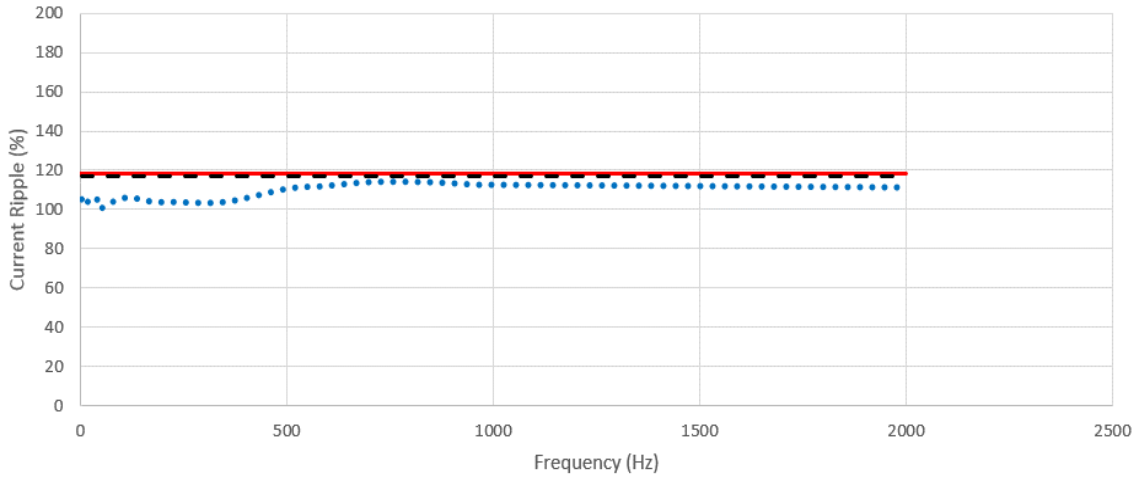

Figure 5-71 : Comparison of the low frequency ripple at different frequencies using theory (Line), Simulation (dash), and Experiment (dots)

5.8.4 EIS Calculation

Figure 5-72 to Figure 5-74 show the calculated complex impedance, amplitude and phase plots of the li-ion battery from off-line EIS measurement equipment (in red), experimentally measured data (in blue dots), and simulation (in black). Data from experimental tests show similar values compared to the EIS data.

A switching frequency of 2kHz was used while the low frequency signal f_o was varied from 1 to 2kHz. To ensure that the system is always operating in continuous mode the duty cycle was set to 0.6 and V_{ELM} was set to 12V. The method could be suitable for implementation. The impedance of the battery was calculated for 23 low-frequency points. The battery current and voltage waveforms were measured and captured by the oscilloscope probes at each low-frequency points. The impedance of battery was then calculated by Fourier analysis of the waveforms at each frequency points using the FFT MATLAB code.

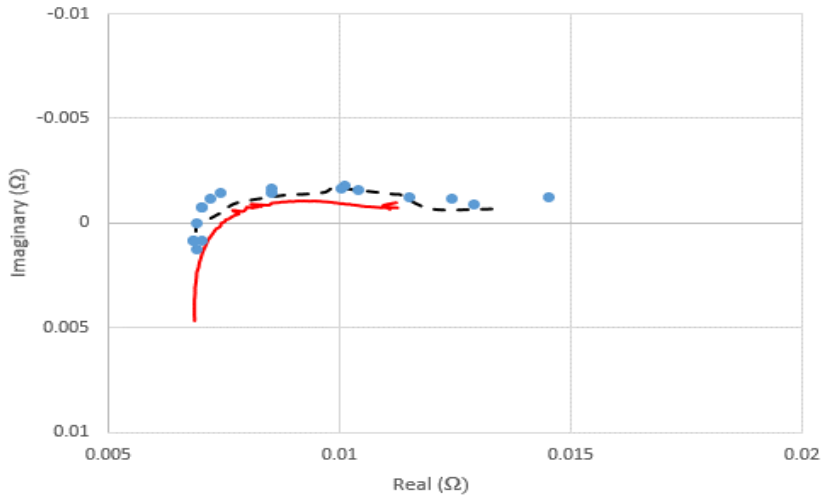

Figure 5-72 : Impedance Nyquist plot of the lithium-ion phosphate battery with EIS (red), Simulation (black), and Experimental data (blue dots)

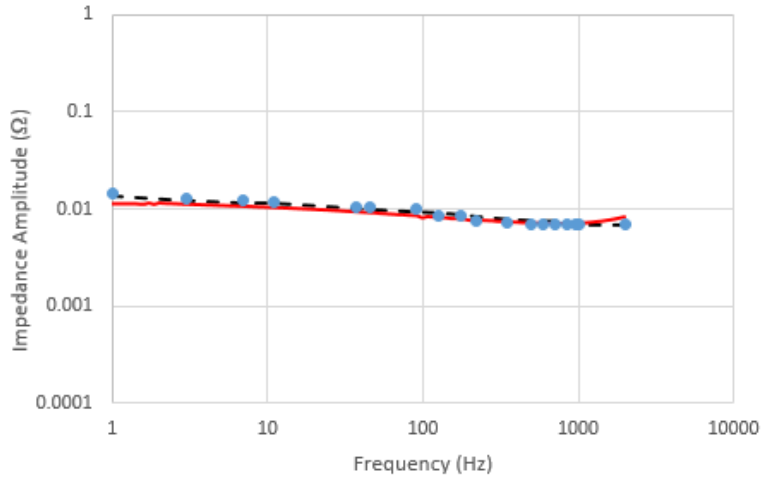

Figure 5-73 : Impedance amplitude bode plot of the lithium-ion phosphate battery with EIS (red), Simulation (black), and Experimental data (blue dots)

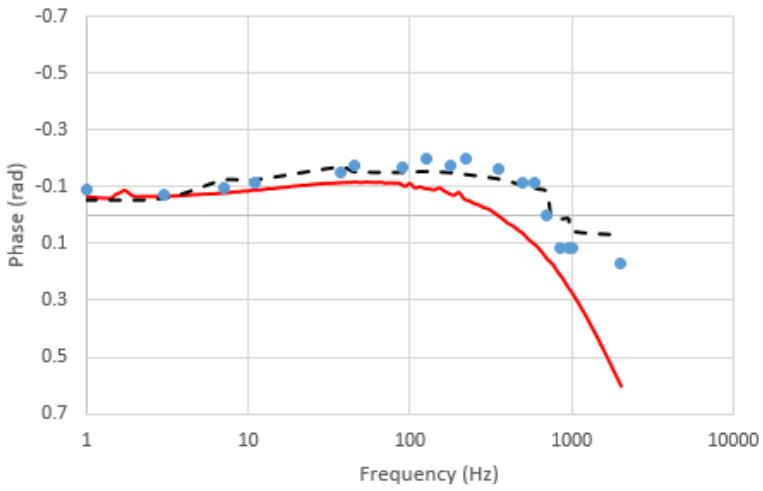

Figure 5-74 : Impedance phase bode plot of the lithium-ion phosphate battery with EIS (red), Simulation (black), and Experimental data (blue dots)

5.9 Summary

This chapter looked at implementing the methods of inducing a low frequency excitation signal in hardware. The measurements were used to look at the different circuit operations, the ripple current increase and its dependency on other variables. Finally the circuits were used to generate an EIS plot by sweeping the frequency across a range from 1Hz to 2kHz to try and understand the suitability of each method to be further investigated as an on-line measurement technique.

These methods of using the existing hardware in the power electronics to produce an on-line EIS measurement have not previously been reported and shown at this level of detail and is a contribution of this thesis to knowledge in the area. Key results of the experimental data are shown in Table 5-25. Comparison with Table 4-16 show that the simulated and experimental results follow the same trends. The simulation has been carried out with ideal components and therefore the battery current is lower in the experimental setup than that in simulation.

Table 5-25: key results from experimentally derived data

Method	Boost ratio compared to base case	Inductor current ripple increase @125Hz	Inductor current ripple increase @125Hz	Fourier co-efficient amplitude @125Hz	Ripple dependency on frequency	Suitability for On-line EIS
3- Variable duty cycle	Same	A_d = 0.01 in D = 0.6	17.7%	0.09	Yes	yes
4- Variable frequency	Same	A_f = 400Hz in f_s = 2kHz	19.7%	0.013	Not visible in experiment	no
3 – Variable starting point	Same	A_t = 40µs in 260µs	41.8%	0.2	Yes	yes
4 – Impulse function	Higher	T_i = 0.00002s in a pulse width of 0.0003s	15.1%	0.45	Yes – but hardware dependent	yes
5 – Battery Balancing	Same	voltage difference 0.19V in 3.21V	0%	0.16	Not visible in experiment	maybe
6 - ELM	Same	Fixed voltage difference of 9.2V	0%	0.081	Not visible in experiment	yes

The work contained with Chapters 3-4 looks at the methods of introducing a low frequency component into the battery circuit and deriving and validating the impact that this has on the circuit behaviour. This chapter has gone beyond that initial work and has looked at using the low frequency signals to generate an EIS type plot. However, this has been done under ideal conditions (fixed battery voltage and oscilloscope data capture using an open-loop control system and a fixed load).

Chapter 5 looks at expanding on this work to firstly investigate if this work can be used for different battery chemistries and also if it has a use within other fields such as solar power generation. Chapter 5 then goes on to explore the practical limitations of an on-line system based on these methods.

6 Practical implementation issues

6.1 Introduction

The work in chapters 2-4 has concentrated on proving the feasibility of different methods of EIS measurement for consideration towards on-line techniques. These were undertaken with a single battery chemistry under controlled conditions at a fixed SOC using a high speed oscilloscope. This chapter builds on the feasibility studies to look at other issues including:

- Applicability to different battery chemistries
- Applicability to different devices characterised by EIS
- Working towards a practical on-line scheme including issues with
    - Instrumentation
    - Variable SOC
    - Data processing
    - Multiple cells

6.2 Applicability to other battery types

The variable duty cycle method was applied to measure the impedance of a 1.5V Ansmann rechargeable AA NiMH (nickel-metal hybrid) battery with 2.86Ah capacity. The same circuit design as presented in chapter 4, was used for the impedance calculation of the NiMH battery.

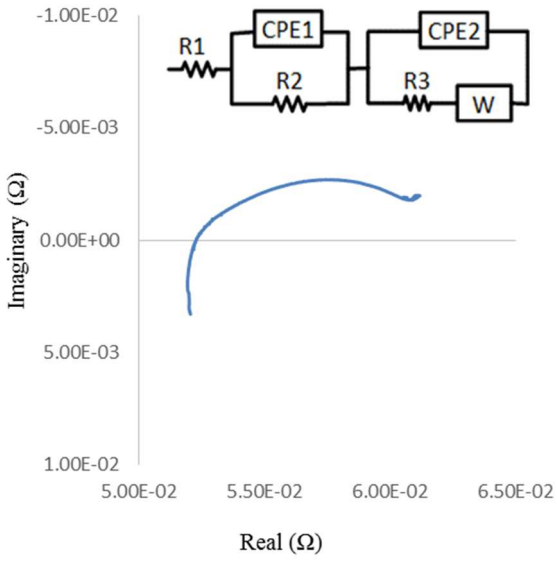

Figure 6-1 : NiMH battery EIS impedance plot and equivalent circuit model

The equivalent circuit used is shown in Figure 6-1, which is the closest and most common representation for the Nickel Metal Hybrid (NiMH) [227] Table 6-1 represents the estimated values of these components for use in simulation.

Table 6-1: Battery Model component specifications

Components	Ni-MH Battery
$R_1(\Omega)$	0.052
$R_2(\Omega)$	0.0041
$R_3(\Omega)$	0.0051
CPE_1(S)	6.43
CPE_2(S)	11.28

Using the variable duty cycle method, Figure 6-2 to Figure 6-4 show the calculated complex impedance, amplitude and phase plots of the NiMH battery from offline EIS measured data (in red), experimental test data (in blue dots), and simulation (in black). Results from simulation and experimentally measured data give values similar to that produced using the off-line EIS equipment.

A switching frequency of 2kHz was used while the low frequency signal f_o was varied from 1 to 2kHz. To ensure that the system is always operating in continuous mode the duty cycle is increased to 0.7 (as the voltage of the NiMH battery is lower), with an A_d of 0.01.

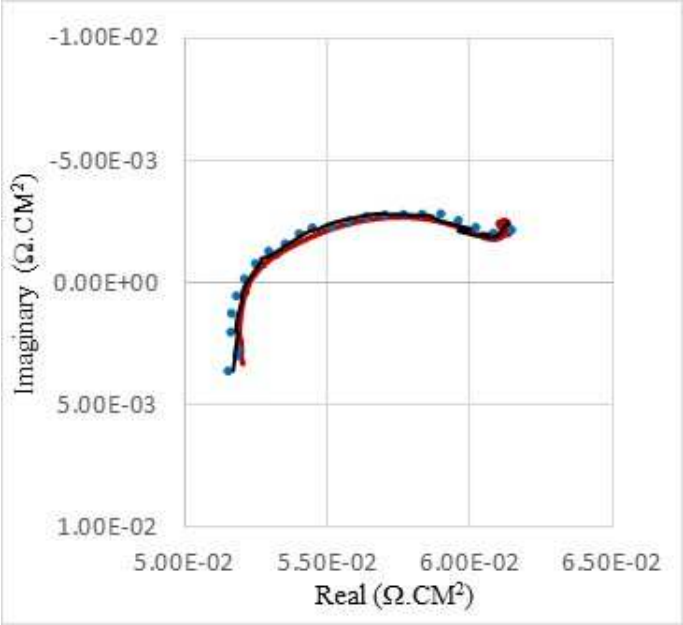

Figure 6-2 : Impedance Nyquist plot of the NiMH battery with EIS (red), Simulation (black), and Experimental Validation (blue dots)

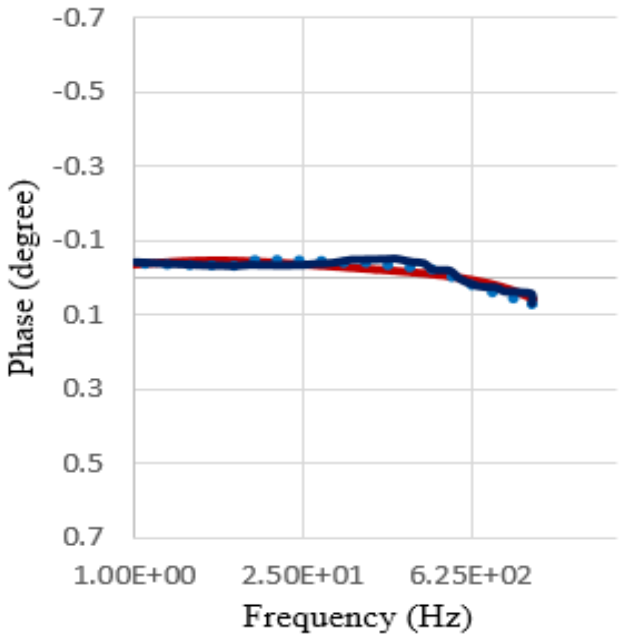

Figure 6-3 : Impedance Bode plot of the NiMH battery with EIS (red), Simulation (black), and Experimental Validation (blue dots)

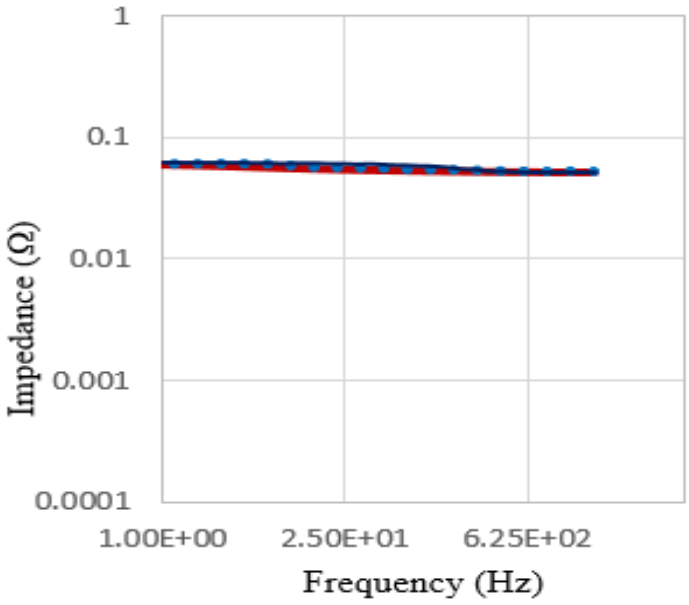

Figure 6-4 : Impedance Bode plot of the NiMH battery with EIS (red), Simulation (black), and Experimental Validation (blue dots)

The results indicate that this method is appropriate for consideration with other battery chemistries.

6.3 Applicability to PV panels

To undertake analysis of a solar panel, two operational conditions were chosen as shown in Figure 6-5 the maximum power point (MPP) and Point A was chosen as alternative operating points by way of comparison. Point A also lies on a more linear part of the I-V curve, such that a small perturbation of current will result in a linear perturbation of voltage about this operating point [330].

An off-the shelf multicomp polycrystalline 800mW Solar Panel was used in these experiments. The solar equivalent circuit parameters were obtained using the EIS impedance analyser (solatron 1260 and 1287) as shown in Figure 6-6. The impedance of the solar cell was excited by 73mA Ac current and a dc discharge current of 140mA in the frequency interval of (500Hz to 100 kHz). The dc discharge current value was chosen to match the inductor current of the converter under later experimental conditions. The useful EIS data is contained over a much higher frequency range than for a battery so an increased switching range needs to be considered.

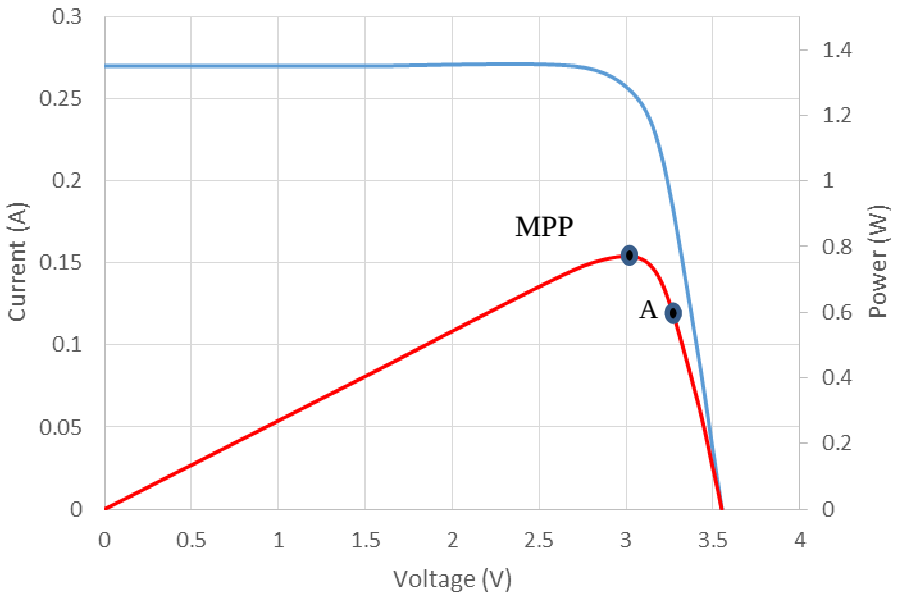

Figure 6-5: Solar Panel current (blue) and power rating (red) characteristic

The Nyquist diagram of the solar panel comprises a semicircle (represented as a parallel resistor and constant phase element, CPE, due to impurity in capacitor behaviour [143]) and a series resistor [243][331]. Table 6-2 shows the EIS derived values of these components under the two operating points.

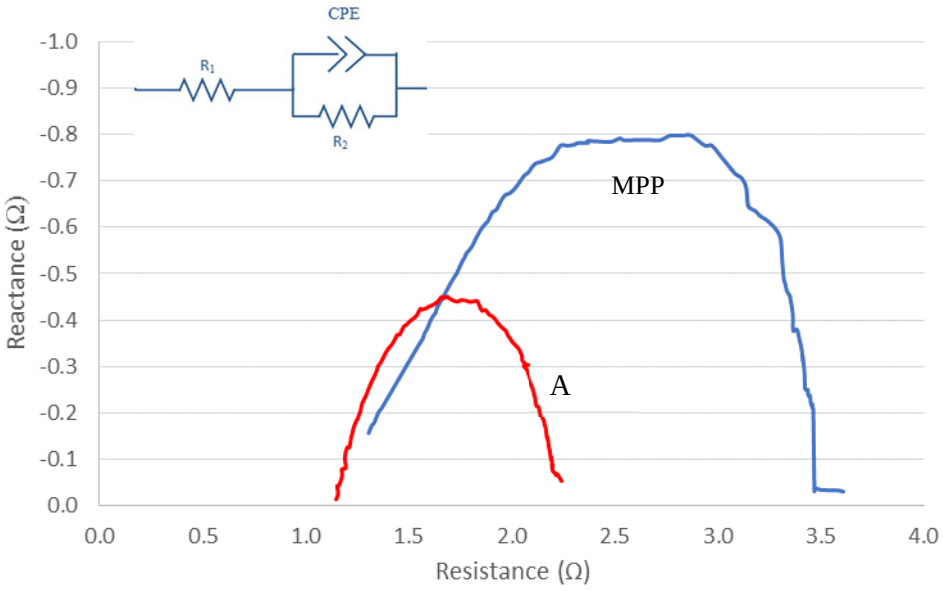

Figure 6-6 : Photovoltaic solar panel EIS impedance plot and equivalent circuit model

Table 6-2: Solar panel Equivalent Circuit Model component specifications

Components	Photovoltaic solar panel
MPP operation	
R_1(Ω)	1.372
R_2(Ω)	2.26
CPE_1(F)	8.67e-5
Point A operation	
R_1(Ω)	1.163
R_2(Ω)	1.077
CPE_1(F)	6.404E-5

In order to generate a set of comparable simulation results the PV panel and boost converter are modelled using Matlab Simulink software. The component values in the simulation model are based on the experimental hardware components. The component values of the converter were selected to ensure that for the purposes of the continuous mode operation of the converter at a duty cycle of 0.5 at 100 kHz frequency.

The 0.8W polycrystalline solar panel was operated with an output voltage of 3.4V. The dc-dc converter was used to boost this to 7.19V with a corresponding load output current of $6.8\,mA$. The hardware setup was set to always operate the converter in continuous mode with a boost ratio of 2. Converter components were calculated according to this assumption. An HER204G Rectifier Diode with maximum 2A forward current was used. The specifications of the components are summarised in Table 6-3.

Table 6-3: Boost converter component specifications

Components	Specifications
Inductance	360µH, 20 A, Toroidal
Capacitance	470µF, 16V Electrolytic
Load	1kΩ Resistor
Switch MOSFET	FDPF045N10A, 100 V, 67 A, 4.5 mΩ

The experimental setup is shown in Figure 6-7 panel voltage and current are measured every time that the low frequency is changed for impedance measurement in the low frequency range. The voltage and current were measured using a Lecroy 100MHz current probe and a Tektronix P2220 200MHz voltage probe The gate drive signals were derived from a signal generator because of high frequency switching.

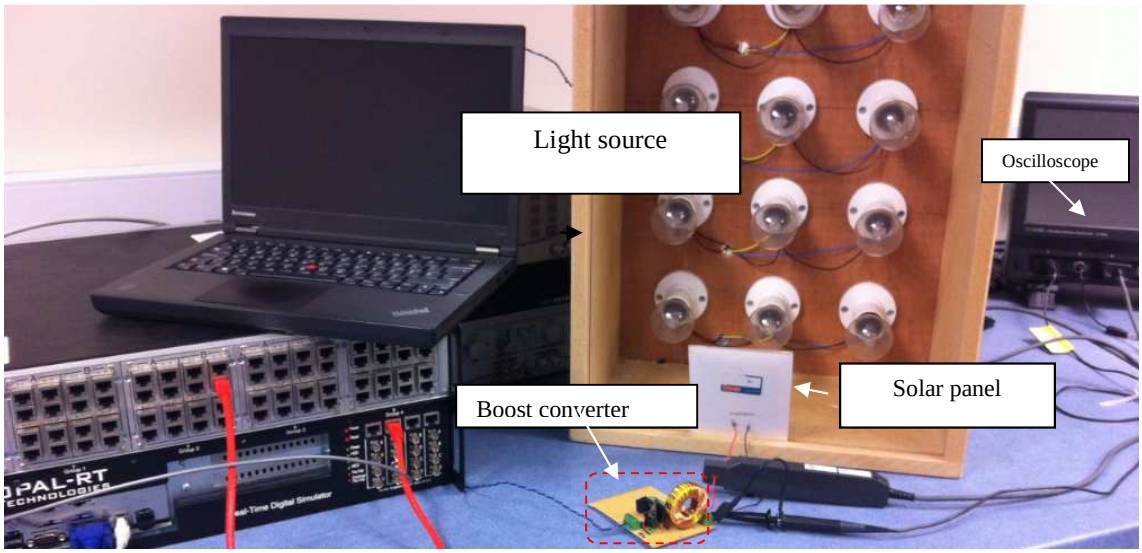

Figure 6-7 : Solar panel Experimental Set Up

The methodology was applied to a photovoltaic panel to investigate the impedance across a range of low frequencies. The low frequencies were chosen in the frequency range of 500Hz to 90 kHz to tie up with the EIS results. The tests were conducted under constant luminance with a fixed light source in a dark room. The solar cell was operated at point A and MPP on its operational voltage and current curve. The maximum measured power of the solar panel occurs at point MPP on the operating chart. This occurs with a load resistance of 1kΩ and an equivalent power of 0.798W under the same illumination as the experiments above. This is close to the published manufacturers data. The short circuit current was measured at 0.270 mA and the open circuit voltage was 3.6V.

Issues with the solar panel are that the relevant frequency range containing useful information is much higher and therefore to cover this range a much faster switching frequency is required for the dc/dc converter. The switching frequency is therefore chosen to be 100 kHz while the low frequency signal f_o was varied from 500Hz to 90kHz. To ensure that the system is always operating in continuous mode the duty cycle is set to 0.5 with an A_d= 0.012 for the solar panel. This increase in switching frequency makes it difficult for other methods such as varying the start position to be used as the control equipment generating the pulses will struggle with the high level of fidelity needed.

Figure 6-8 and Figure 6-9 show the experimentally captured I and V waveform with a variable duty cycle including a low-frequency ripple of 10 kHz and a fixed duty cycle.

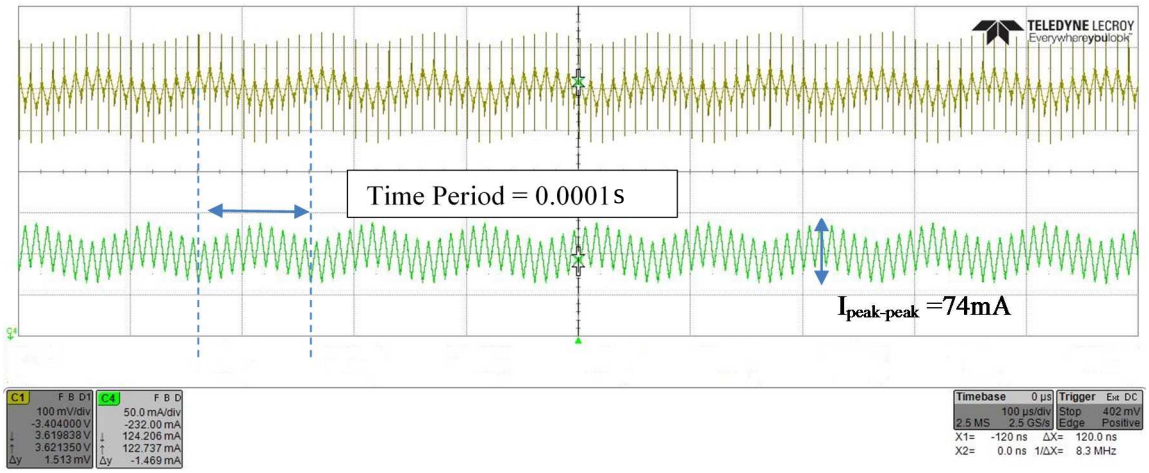

Figure 6-8 : Solar Current (Green) and Voltage (yellow) waveforms, the panel is excited with variable duty cycle with a low frequency component of 10 kHz, A_d= 0.012.

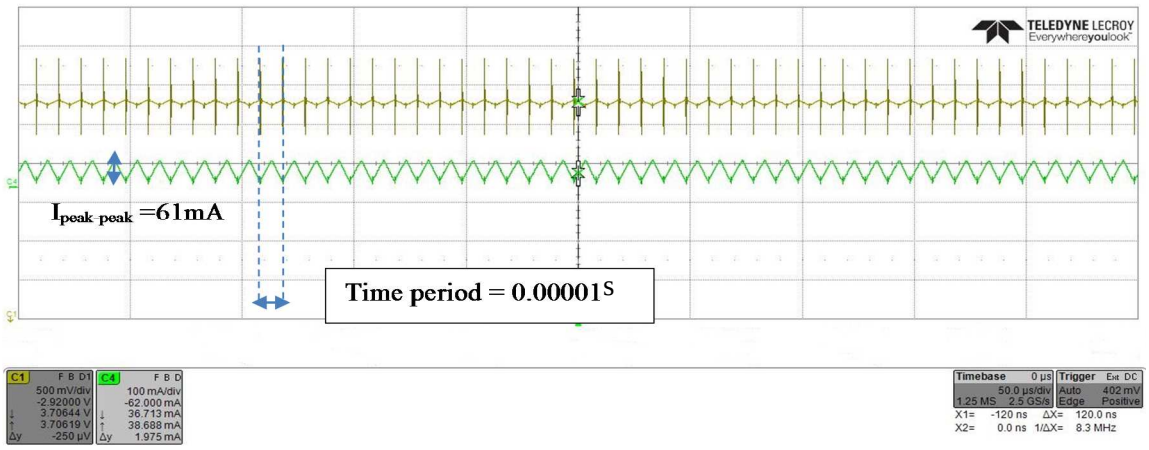

Figure 6-9 : Solar Current (Green) and Voltage (yellow) waveforms, the panel is excited with constant duty cycle (no low frequency ripple is included)

The experimental results show a component of low frequency ripple has been added to the solar panel increasing the peak to peak ripple. A full comparison of the key parameters using a fixed duty cycle and variable duty cycle under experimental and simulated conditions at 10kHz low frequency ripple are shown in Table 6-4.

Table 6-4: Comparison of fixed duty cycle with variable duty cycle at 10 kHz effects on Current and Voltage ripple

	Experimental			
	Fixed Duty Cycle		Variable Duty Cycle	
	Average Value	Peak –Peak value	Average Value	Peak –Peak value
P_{in}	486 mW		490 mW	
I_{solar}	135 mA	61 mA	140 mA	74 mA
V_{solar}	3.6 V		3.5 V	
I_{load}	6.7 mA		6.9 mA	
V_{dc}	7.19 V		7 V	
P_{out}	48.17 mW		48.3 mW	
	Simulation			
	Fixed Duty Cycle		Variable Duty Cycle	
	Average Value	Peak –Peak value	Average Value	Peak –Peak value
P_{in}	459 mW		476 mW	
I_{solar}	135.2 mA	57.1 mA	140.2 mA	68.4 mA
V_{solar}	3.4V		3.4 V	
I_{load}	6.8 mA		6.75 mA	
V_{dc}	6.8 V		6.75 V	
P_{out}	46.24 mW		45.88 mW	

Table 6-4 shows the values of the input and output current, voltage and power of the boost converter measured from simulation model and experiments. Comparison of the data shows that the simulation model of the converter is performing in a manner similar to the experimental data indicating a good understanding of circuit behaviour and the validity of the EIS impedance in the simulation.

The peak to peak current is increased due to the low frequency ripple. The pu increase in ripple between variable and fixed duty cycle is 1.2 which is slightly higher than the calculated increase from Equation 3-40 of 1.15. To verify the proposed method the calculated solar impedance data from experimental and simulation was compared with the measured EIS data. Impedance data is presented in three typical impedance formats; amplitude, phase, and complex plots in Figure 6-10 to Figure 6-13 EIS measurement equipment (in blue), experimental test (in red dots), and simulation (in black). These show the measured complex impedance of the PV panel from EIS measurement equipment (in blue), experimental test (in red dots), and simulation (in black).

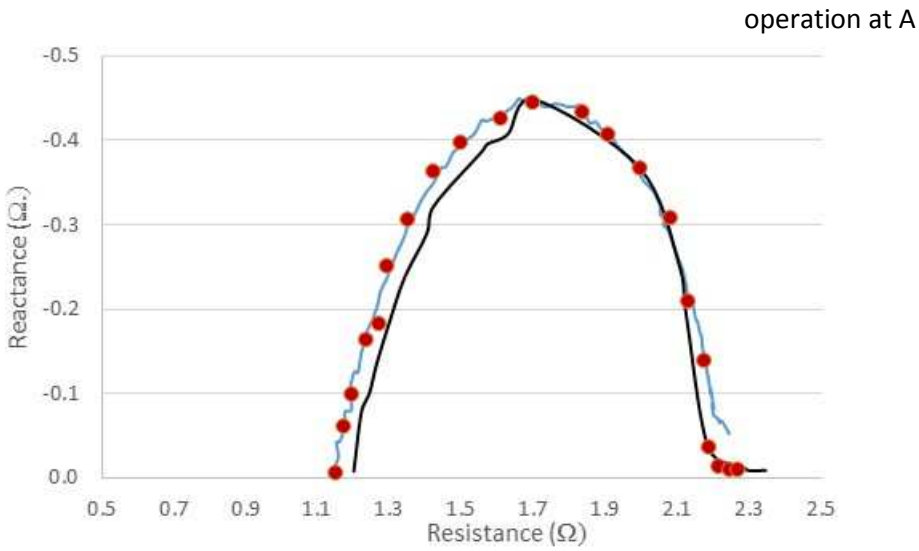

Figure 6-10 : Impedance Nyquist plot of solar panel with EIS (blue), Simulation (black), and Experimental Validation (red dots) operation at A

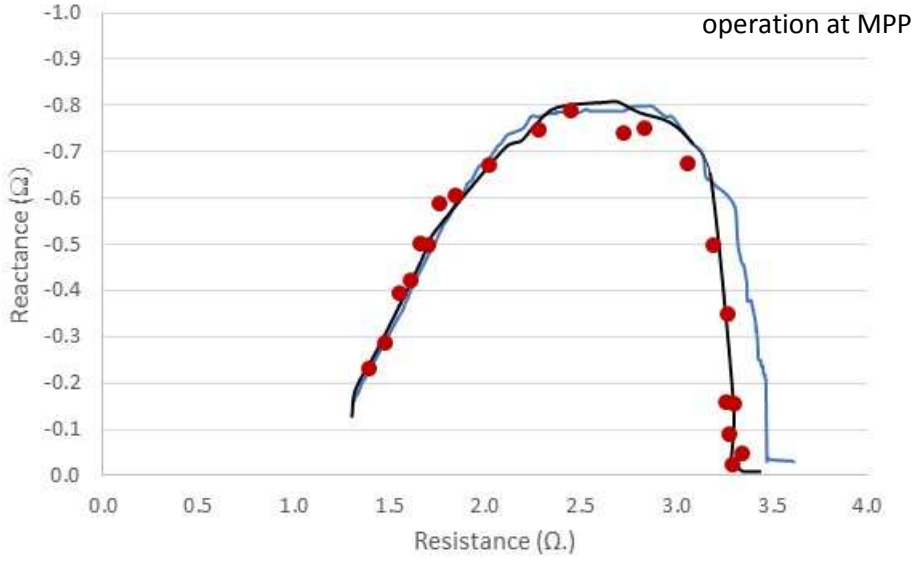

Figure 6-11 : Impedance Nyquist plot of solar panel with EIS (blue), Simulation (black), and Experimental Validation (red dots). operation at MPP

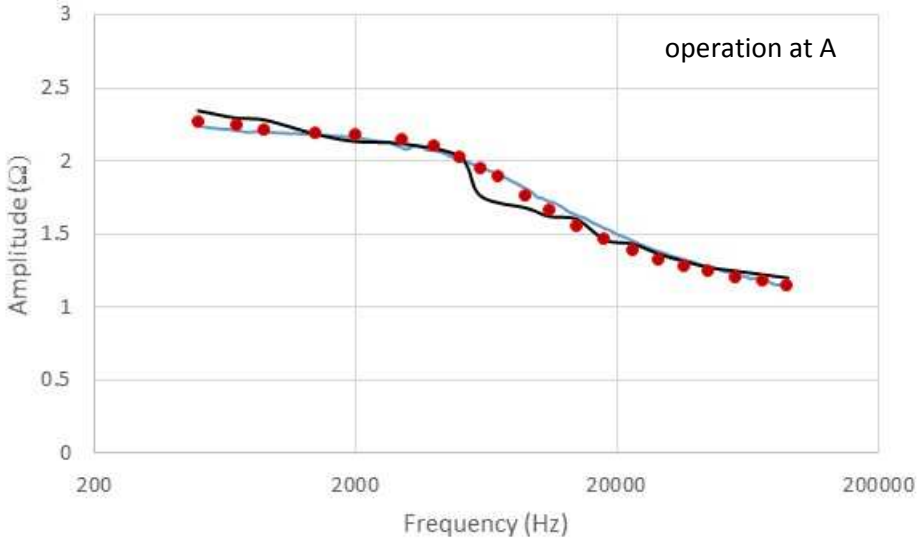

Figure 6-12 : Impedance phase Bode plots of solar panel with EIS (blue), Simulation (black), and Experimental Validation (red dots) operation at A

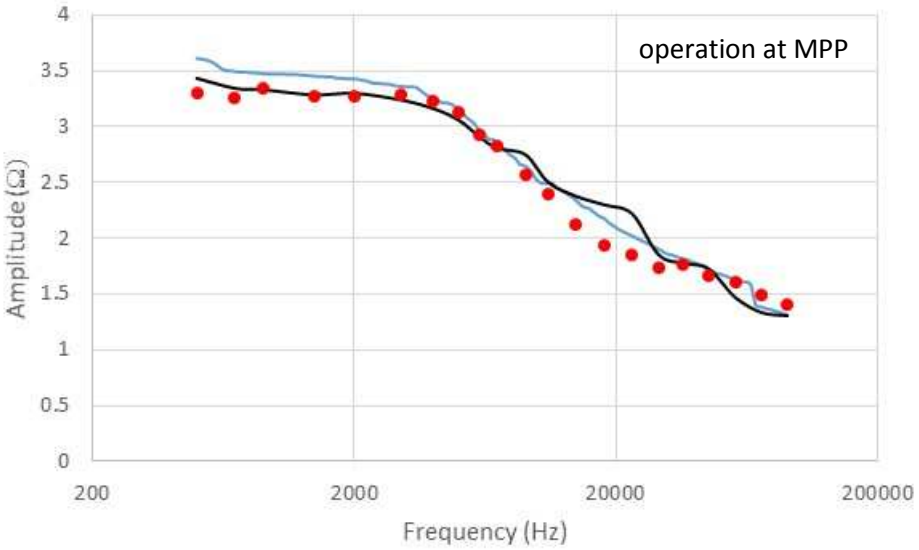

Figure 6-13 : Impedance Amplitude Bode plots of solar panel with EIS (blue), Simulation (black), and Experimental Validation (red dots) operation at MPP

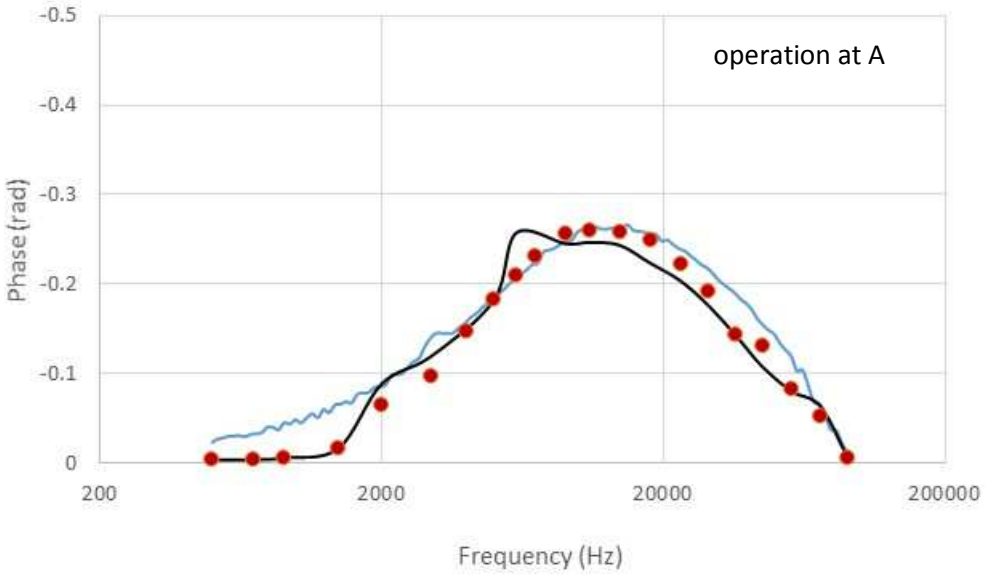

Figure 6-14: Impedance phase Bode plots of solar panel with EIS (blue), Simulation (black), and Experimental Validation (red dots) operation at A

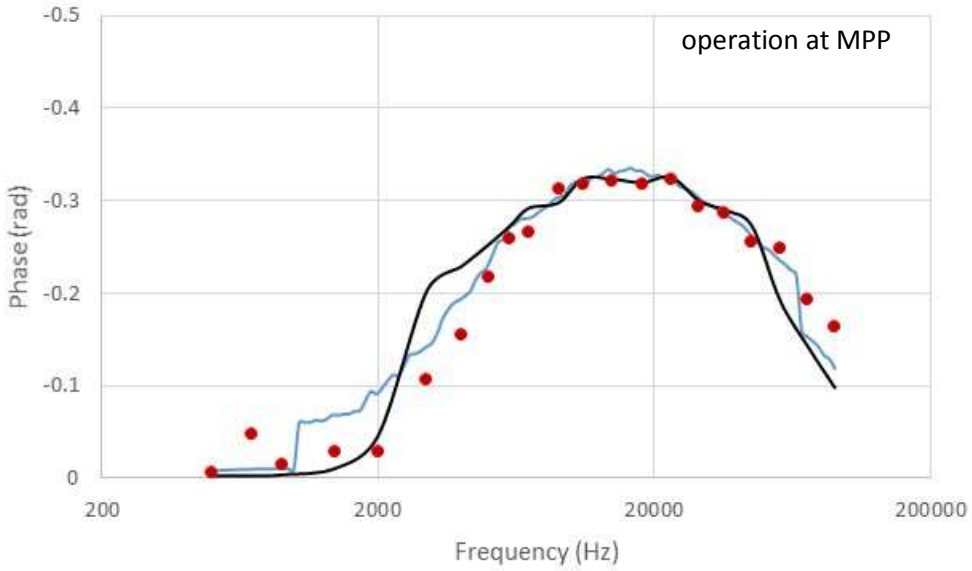

Figure 6-15 : Impedance phase Bode plots of solar panel with EIS (blue), Simulation (black), and Experimental Validation (red dots) operation at MPP

The key result is that the on-line method of producing Impedance spectroscopy through the power electronics switching can give comparable results to off-line measurements under similar conditions and that circuit simulations using an equivalent circuit derived from these values performs in a similar manner. This means there is scope to use this methodology in conjunction with other devices which may benefit from EIS analysis and it allows the impact of degradation to be observed in real time in a visual manner.

6.4 Measurements over variable SOC

A practical on-line EIS technique needs to take data from the battery under any condition using low cost instrumentation and then turn this into useful data which can be used by the controller, BMS or battery system operator. The EIS techniques described in this thesis produces measured data which needs to be analysed and turned into useful information. It is suggested that a process similar to that shown below is employed to do this. Due to the complexity of such a system it is beyond the scope of this thesis to implement the full system in hardware. This chapter provides pointers as to the key considerations that would be needed to be undertaken to produce a realisable and commercial system. A full second life battery system, for example similar to that described in ref [332] uses batteries of different capacities, SOC and SOH in a cascaded dc/dc system. The system controls the import and export of power to and from the batteries based on the relative estimated states of the batteries. The data from a real time EIS measurement could potentially provide an indication as to which batteries should be charged/discharged and to what level.

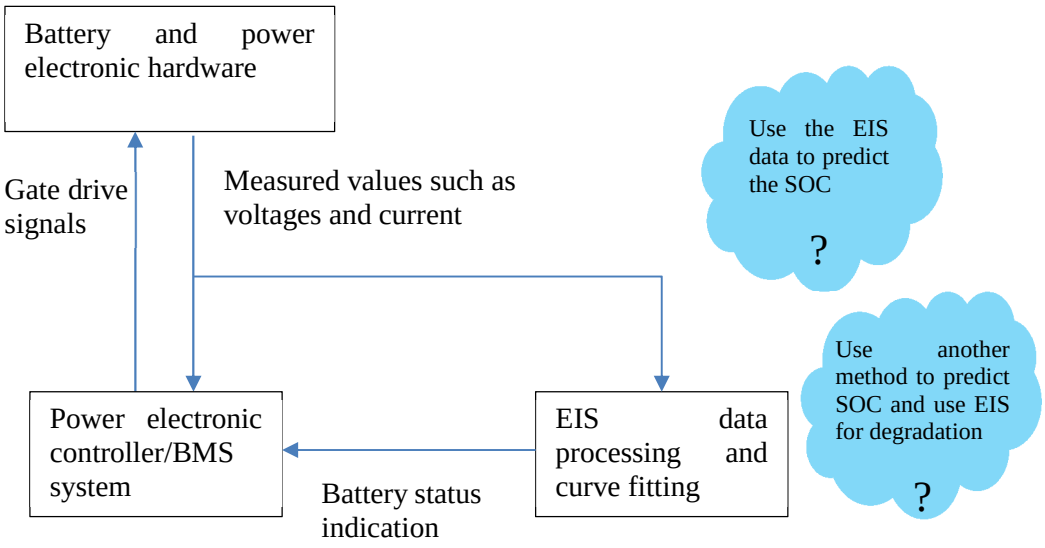

Figure 6-16 : Path of measured values to information

Although it is possible to take an EIS measurement at full SOC only, it is more desirable to have a continuous real time indication of the battery under any SOC and, if possible to use the EIS data to predict the SOC. Providing a real time indication of the battery condition using EIS is complicated as the EIS impedance curves change with both temperature and SOC [161], [163]. The EIS method could therefore be used to predict the SOC or an alternative method of predicting SOC could be used to allow the EIS to predict the degradation at a known SOC. Various methods of predicting SOC of batteries have been presented in Chapter 1. EIS measures impedance data of the battery over a

frequency range using different charge/discharge current rate. The measured impedance values of an equivalent circuit model are correlated to the known impedance at different SOC levels [161], [168]. However, the accuracy of this method is affected by temperature variation and its not clear what impact capacity changes have. In this thesis, it was felt that it was better to estimate SOC by alternative means and then continuously sweep the low frequency EIS excitation to generate a set of curves which go from fully charged to fully discharged. A simplification of this can be seen in Figure 6-17 which shows each low frequency exciation sweep as a different colour, but the impedance curves are changing dynamically as the SOC continuously changes.

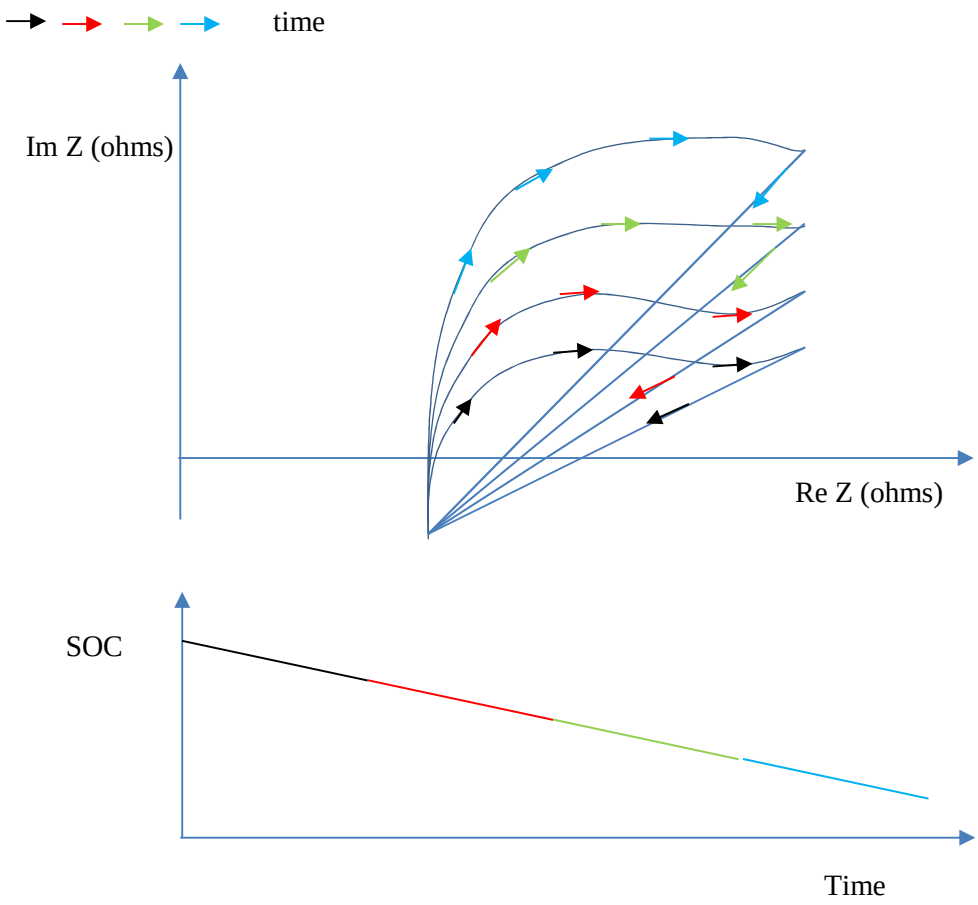

Figure 6-17 : Real time EIS data continuously changes over a low frequency excitation sweep

In this experiment the 100% SOC was set to 3.2V the maximum possible charging value to start. The battery was discharged continuously with a constant discharge current of 1.18A using the variable duty cycle method till it reached 2.7V SOC. The current and voltage of the battery were measured over the frequency range at a sweep time interval of 3min. The impedance of the battery over the range of the frequencies were calculated using the measured voltage and current data. Figure

6-18 to Figure 6-20 show the calculated impedance of the battery from the experimentally measured data at the different frequency sweep conditions. The curves show that battery EIS impedance changes as the battery SOC changes, so as the SOC of the battery reduced the impedance of the battery increased. The process is continuous in real life and therefore the next section discusses how best to understand this changing data.

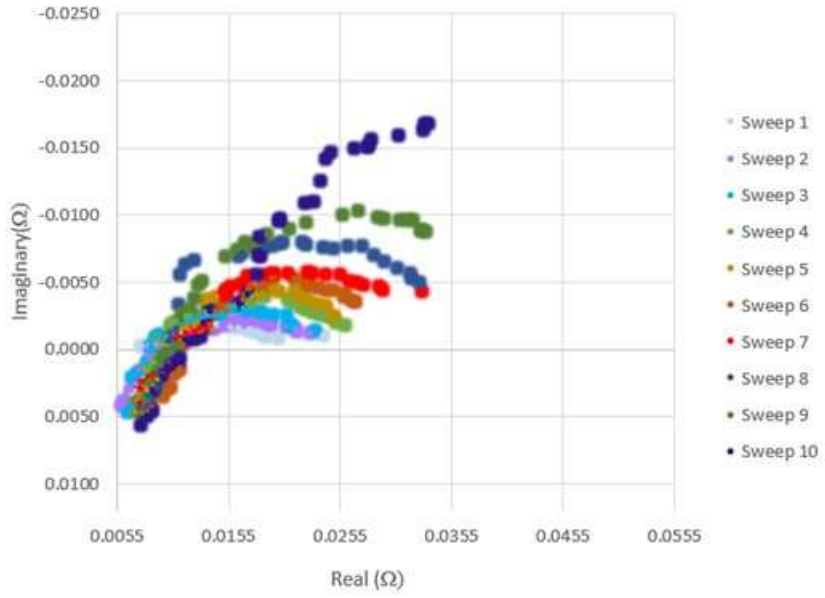

Figure 6-18 : Battery Impedance Nyquist plot for different state of charge

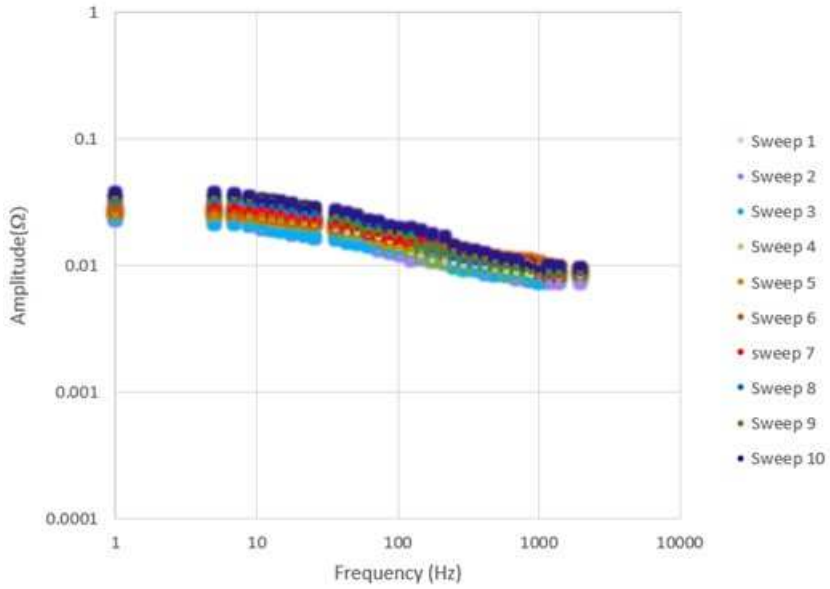

Figure 6-19 : Battery Impedance Amplitude bode plot for different state of charge

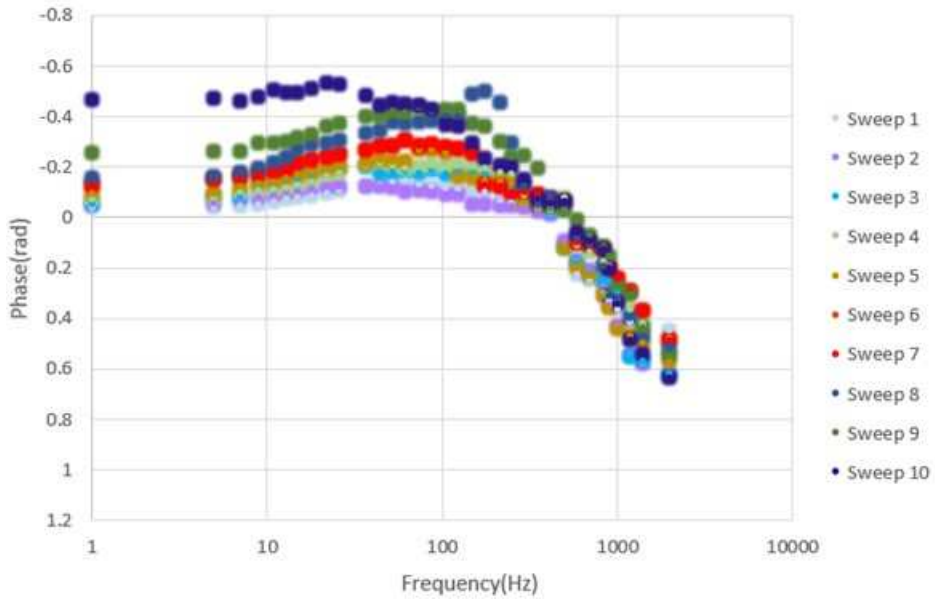

Figure 6-20 : Battery Impedance Phase bode plot for different state of charge

6.5 Integrating into a battery management strategy

Calculation of equivalent circuit parameters using curve fitting gives useful values which can be used by the BMS/power electronic controller. The impedance data of the battery can be used as a basis to curve fitting battery model parameters. An equivalent circuit of the battery impedance curve is used to fit the impedance data over the frequency domain. In this work, an equivalent circuit the same as shown in Figure 4-1 in section 4.1 is used. The circuit includes two parallel RCPE components (R_2CPE_1, R_3CPE_2) in series with R_1. To simplifying the model, capacitor components are used instead of CPE components. The transfer function from the presented equivalent circuit can be written as:

$$y(s) = \frac{v(s)}{i(s)} = R_1 + \frac{R_2}{1+sR_2C_3} + \frac{R_3}{1+sR_3C_2} = \quad \text{Equation 6-1}$$

Simplifying the Z(s) we have:

$$y(s) = \frac{R_1+R_2+R_3+s(R_1R_2C_1+R_1R_3C_2+R_2R_3C_2+R_2R_3C_1)+s^2R_1R_2C_1R_3C_2}{1+s(R_3C_2+R_2C_1)+s^2R_2C_1R_3C_2} \quad \text{Equation 6-2}$$

Substituting s=jω in Equation 6-2:

$$y(j\omega) = \frac{R_1+R_2+R_3+j\omega(R_1R_2C_1+R_1R_3C_2+R_2R_3C_2+R_2R_3C_1)+j\omega^2R_1R_2C_1R_3C_2}{1+j\omega(R_3C_2+R_2C_1)+j\omega^2R_2C_1R_3C_2} \quad \text{Equation 6-3}$$

A complex nonlinear least square method was undertaken to predict the parameter values of the battery equivalent circuit to match the measured impedance data [141]–[145]. This method

minimizes the error between the measured data and the estimated data using a set of battery model parameters. The impedance of the battery model in Figure 4-1 can be written as:

$$Z(j\omega) = f(j\omega, \theta_i)$$ **Equation 6-4**

Where $\theta_i = R_1, R_2, C_1, R_3, C_2$ are the equivalent circuit parameter of the lithium-ion battery, and can be calculated from:

$$\Phi = \sum_{i=0}^{n} [Re(y_i - Z_i)^2 + Im(y_i - Z_i)^2]$$ **Equation 6-5**

Where y_i is the measured impedance from the experiment data, and $Z_i$is the calculated impedance data. In this method a Taylor series method was used to predict the parameters. In the Taylor series, the impedance value can be calculated from its previous value and the variation of its approximation parameters. By defining the approximation values of the parameters with Δ and using Taylor series the below expression can be represented as:

$$Z(j\omega)_{j+1} = Z(j\omega)_j + \frac{\partial Z(\omega)_j}{\partial \theta_i} \Delta\theta_i$$ **Equation 6-6**

Where the value of $\Delta\theta_i$ can be calculated from the following expression:

$$\Delta\theta_i = \alpha^{-1} G$$ **Equation 6-7**

Where α and G can be calculated as:

$$\alpha = [(Z_{Re})^T Z_{Re} + (Z_{Im})^T Z_{Im}]$$ **Equation 6-8**

$$G = [(Z_{Re})^T \Delta y_{Re} + (Z_{Im})^T \Delta y_{Im}]$$ **Equation 6-9**

$$[Z_{Re}]_{ij} = Re\left(\frac{\partial Z_i}{\partial \theta_i}\right); \qquad [Z_I]_{ij} = Im\left(\frac{\partial Z_i}{\partial \theta_i}\right)$$ **Equation 6-10**

$$\left[\Delta y_{Re}\right]_j = Re\,(y_i - Z_i)\ ; \qquad \left[\Delta y_{Im}\right]_j = Im\,(y_i - Z_i)$$

The above process was performed using Excel on the generated data from the measured experiments impedance data. The first value of the Φ was generated using the initial value of the approximated equivalent circuits components and updates of the value of the components for the next repetition. The different estimation data of the battery model parameters is shown in Figure 6-21 and Table 6-5.

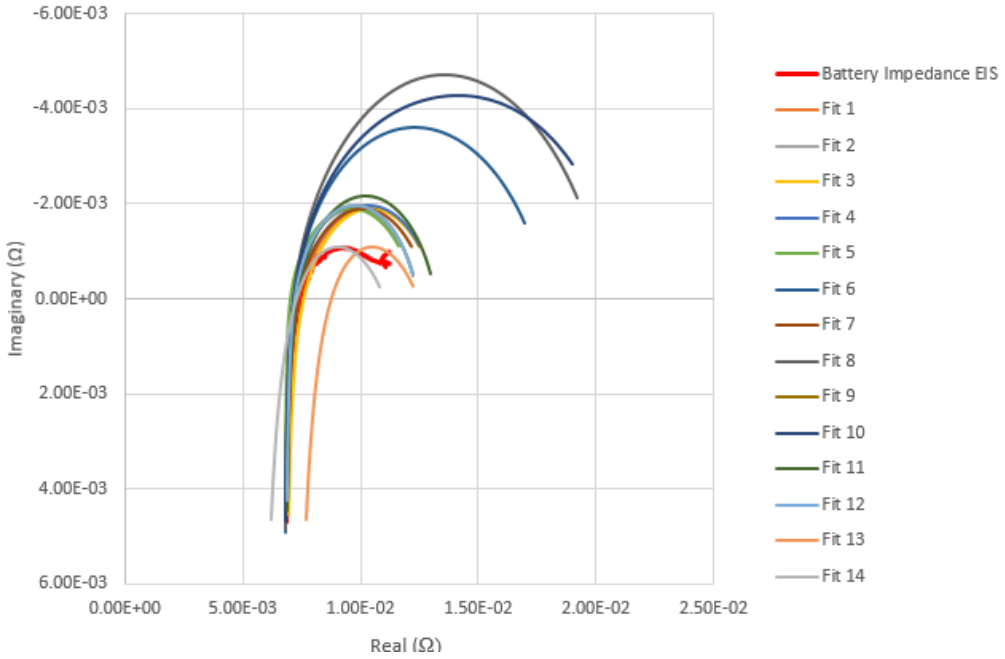

Figure 6-21 : comparison of different fitting curves

Table 6-5: Equivalent circuit components variation

Components	Values from	To
R_2	1.18 Ω	0.0081 Ω
R_3	0.0000026 Ω	0.00095 Ω
C_1	0.02 F	3.8 F
C_2	6.65 F	45.7 F

Converting the measured data into useful information is computationally complex and requires data to go through an FFT process followed by a curve fitting process. Before these methods can be adapted large scale low cost means of undertaking these calculation online must be realised.

6.6 Investigating a degraded battery in a series battery connection

In most practical systems there is more than one battery cell depending on the type of application many battery cells may be connected in series and/or parallel. This leads to the possibility of mismatch between different battery cells in a battery bank based on different temperature conditions and variation on the batteries impedance, capacity and etc. Battery charge and/or discharge imbalance may result in over charging or over discharging of the cells with lower capacity. This research uses the on-line EIS method to generate impedance traces of each of the two cells one with low capacity and the other with high capacity to consider if the variation of cell impedance allows the detection of the battery cell with the higher capacity from the impedance data of the battery cells. The batteries were connected in series and connected to the DC-DC converter from section 5. The joint measured impedance data of these two battery cells was then compared with the measured data using the laboratory EIS equipment. The calculated complex impedance, amplitude and phase plots of the li-ion battery cells from offline EIS measured data (in red battery with higher capacity, black battery with lower capacity, and yellow two battery cells in series) and experimental test data (in blue dots) is shown in Figure 6-22 to Figure 6-24. Results from experimentally measured data gives values similar to that produced using off-line EIS equipment. However, it is unlikely there is sufficient information to detect the battery with smaller capacitor and requires further work considered outside the scope of this thesis.

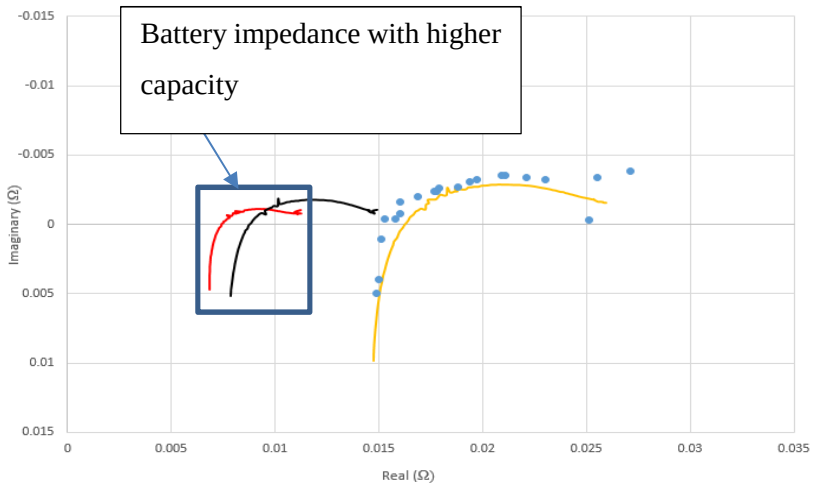

Figure 6-22 : Battery Impedance Nyquist plot, impedance of two batteries in series connection experiment (blue dots), EIS of two batteries in series (red line), EIS of degraded battery (black dash), EIS of new battery (yellow dash)

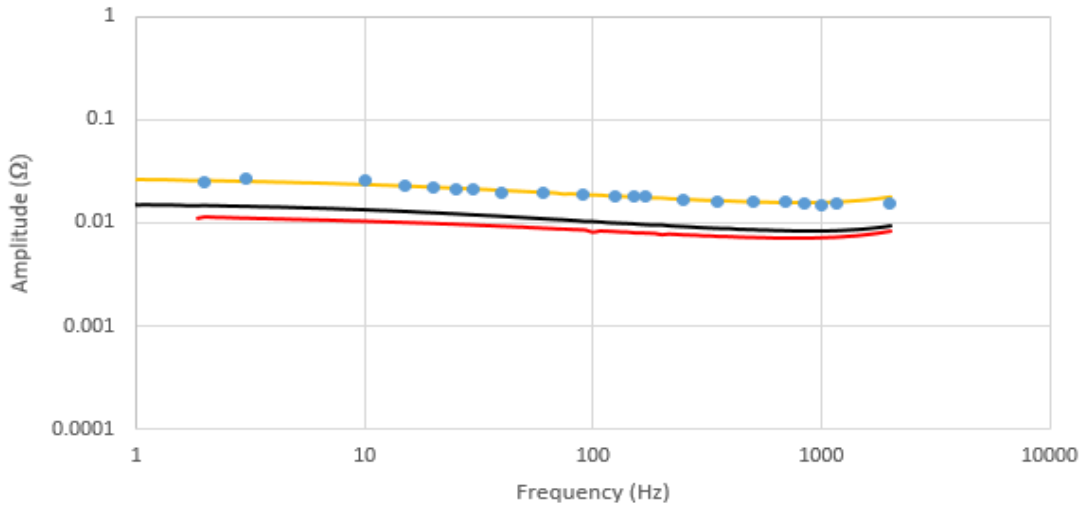

Figure 6-23 : Battery Impedance Amplitude bode plot of two batteries in series connection experiment (blue dots), EIS of two batteries in series (yellow line), EIS of degraded battery (black line), EIS of new battery (yellow line)

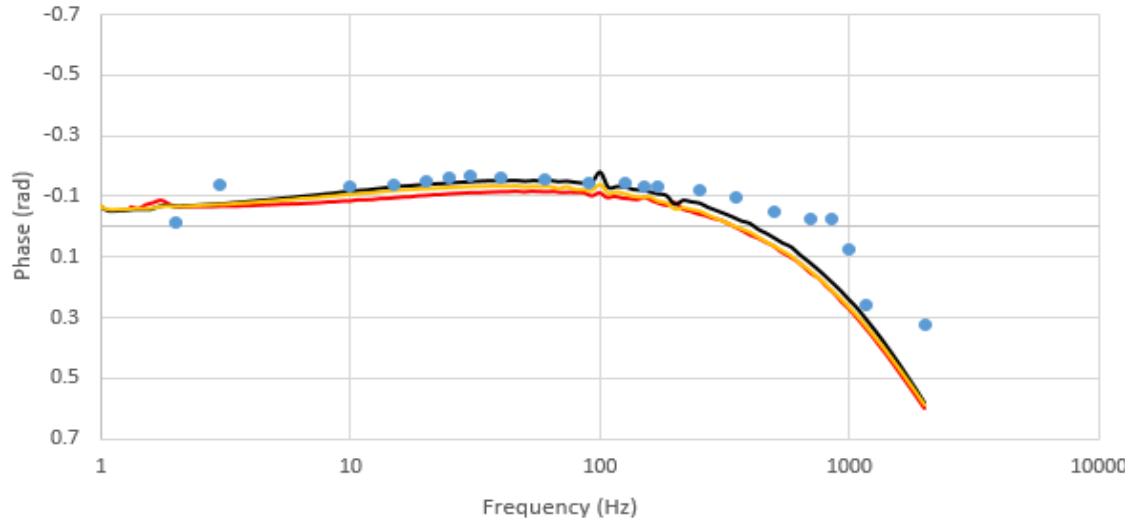

Figure 6-24 : Battery Impedance Phase bode plot of two batteries in series connection experiment (blue dots), EIS of two batteries in series (yellow line), EIS of degraded battery (black line), EIS of new battery (yellow line)

6.7 Closed loop control model

It is typical to control the output voltage across the capacitor to a fixed value and to control the inductor current with a faster inner control loop. By adjusting the duty cycle to give a variable ripple on the inductor at a slow speed there is the danger that the control system can negate the impact of this by re-adjusting the average duty cycle more quickly. A closed loop control system was added to the boost converter to investigate this. A typical current and voltage control system of a boost converter is shown in Figure 6-25.

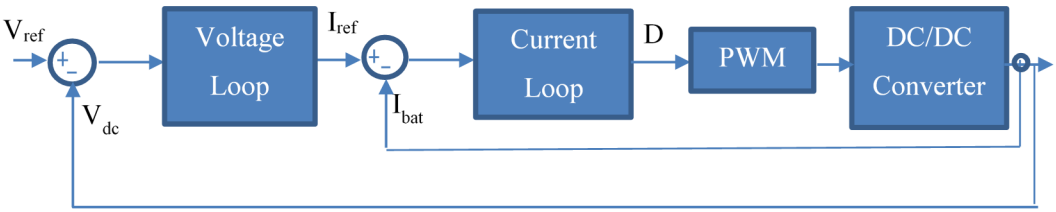

Figure 6-25 :Typical control system model

Figure 6-27 shows that a low frequency ripple is still presented in the battery current indicating that, undertaking this technique in closed loop control is feasible. However the impact on the excitation current needs further work.

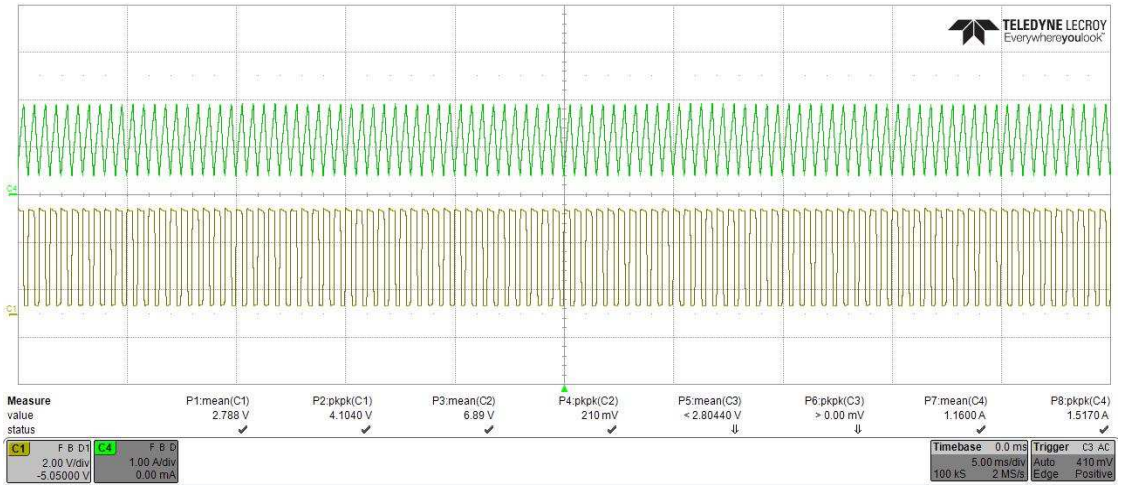

Figure 6-26 : Current (Green), PWM signal (yellow), fixed duty cycle and switching frequency using closed loop control

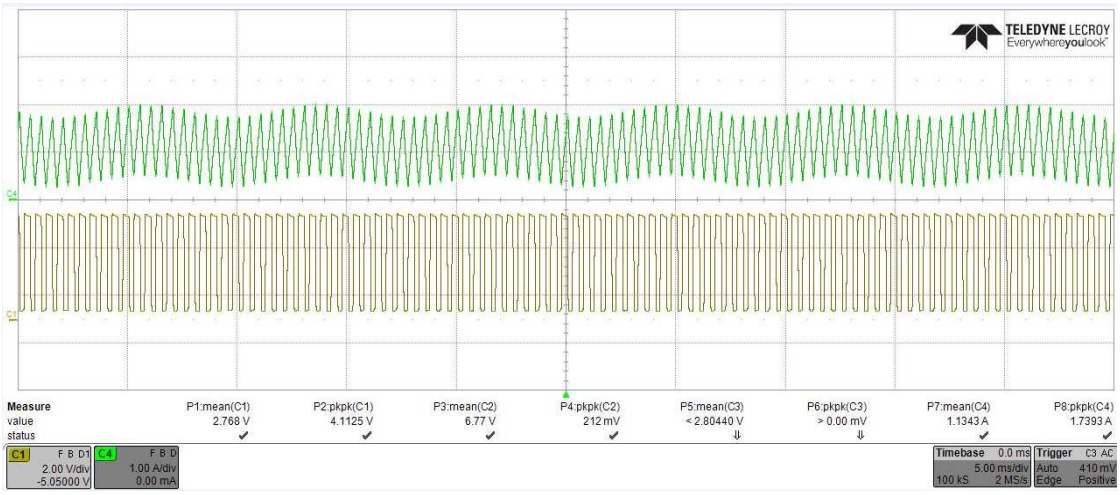

Figure 6-27 : Current (Green), PWM signal (yellow), variable duty cycle at low frequency of 125Hz using closed loop control

6.8 Summary

This chapter looked at the complexity of taking forward the development of these new techniques towards a practical real time solution for use with a real system. Key areas that need investigation include;

Instrumentation over different voltage and current ranges to a suitable level of accuracy to allow work on all sizes of systems. Having measured the data it is necessary to undertake a time consuming FFT process to access the voltage and current measurement for use. There is very little literature on undertaking real time FFT and what there is suggests that this is complex. In this work the OpalRT controller was used to undertake this process but this is not practical in a real system because of its expense. Therefore a separate controller, will be needed to undertake these intensive calculations before feeding the results back to the system Power Electronic/BMS controller. The data itself is changing in real time and is a function of temperature and SOC. Although lookup tables can be generated to help understand what the data is referring to, it is not clear how these tables would change with aging and degradation.

There are still many areas to be solved within this thesis which is beyond the scope of this thesis. Chapter 6 provides a summary of all the work completed and also provides a summary of the future work needed to arrive at a commercially useful system.

7 Conclusions and Future Work

A key challenge in a battery energy storage system is understanding the availability and reliability of the system from the perspective of the end customer. This thesis started by taking a look at data collected as part of the FALCON project in particular the difference that a battery maintenance cycle can make to the availability of a battery. [*The presented results represent a contribution to knowledge of this thesis*]. A key task of a battery system is recognising when a battery or a module within a system starts to degrade and then mitigating against this using the control system or battery management system. Battery characterisation parameters such as internal impedance and state of health and state of charge of the battery are a useful representation of the battery conditions. These representations can be used to estimate the battery remaining lifetime, energy storage capacity, and degradation. Recent work in published literature has started to investigate the feasibility of performing Electrochemical Impedance Spectroscopy methods online to generate an understanding of battery impedance. In order to perform an EIS measurement, an excitation signal of fixed frequency must be generated and the voltage and current measured and used to calculate the impedance. The work in this thesis has been undertaken in parallel to most of the published literature in this field. However, because of the rapid independent development of knowledge in this area, the techniques developed in parallel have been categorised according to their hardware and control. [*The categorisation of different on-line EIS methods represents a contribution to knowledge of this thesis*]

This thesis proposed different methods of generating a low-frequency excitation signal using hardware found in most battery systems to extract the harmonic impedance of a battery cell to allow low cost on-line impedance estimation. This work focuses on producing impedance spectroscopy measurements through the power electronics system, a battery balancing system and the earth leakage monitoring system to attempt to get comparable results to off-line measurements under similar conditions.

The proposed methods included: a) using DC-DC converter hardware with variable duty cycle, b) using DC-DC converter hardware with variable switching frequency, c) using DC-DC converter hardware with variable pulse starting position, d) using DC-DC converter hardware with an added impulse function, e) using capacitive battery balancing hardware, and f) using Earth Leakage Monitoring hardware. In all these methods, the DC-DC converter operated in continuous mode with a fixed duty cycle and load to allow comparable analysis between the techniques. Although utilising variable duty cycle to generate a harmonic impedance has been previously published in literature, the other techniques analysed within this these have not previously been considered. [*Five new proposed methods of on-line EIS methods represents a contribution to knowledge of this thesis*]

Chapter 3 focused on the theoretical aspects of the proposed methods. This included looking at the waveforms that would be generated by changing the switching of the power electronics, the battery balancing or the earth leakage monitoring and then using these waveforms to determine the harmonic current in the battery using Fourier analysis to understand how much excitation current would be available [*The analysis of the harmonics in the battery current waveform to show that an excitation signal has been generated represents a contribution to knowledge in this thesis*]

Explicit equations were derived to try to understand the increase in ripple current on the inductor – such that these can be used at a design phase prior to component choice to understand the impact on the inductor. [*The derivation of explicit equations to describe the increase in inductor current ripple for each power electronic hardware based method represents a contribution to knowledge of this thesis*]

The key conclusions from this chapter are that the theoretical results indicate that all methods have the capability to generate a low frequency perturbation signal to undertake on-line EIS measurement. However, there are potential trade-offs. They key trade-off is the increase in ripple current through the battery and possibly the inductor (depending on method). The methods that used the power electronics to generate the excitation signal all saw an increase ripple on the battery which was matched by an increase in inductor ripple. The methods of using a variable starting point had the potential to generate less excitation current.

Chapter 4 looked at using an equivalent circuit of the battery to allow each method to be simulated and analysed with a DC- DC converter circuit. The simulation of the proposed methods for injecting a low frequency harmonic were undertaken while the converter was deemed to be operating in a continuous mode with a fixed duty cycle and 2kHz switching frequency. The harmonics of the simulated current through the battery using the Fourier analysis of the simulated battery current using MATLAB were calculated. The detected low-frequency component from the harmonic spectrum of the simulated battery current matched that found in the Chapter 2.

As part of this work it was necessary within simulation to determine how to generate the signals needed to induce the excitation signals developed in chapter 2. [*The method of producing the control signals needed to generate the low frequency excitation of 3 of these methods (variable starting point, capacitive balancing and earth leakage monitoring) represents a contribution to knowledge of this thesis*].

The key conclusions from this chapter can be represented as:

- In the impulse function method, the boost ratio of the DC-DC converter increased depending on the pulse width of the impulse function injected to the gate drive PWM. Therefore, the duty

ratio of the impulse function may need to be adjusted. However, in other methods the boost ratio of the converter remains the same as base case circuit.

- The current ripple of the impulse function with the gate drive PWM signal highly depends on hardware and frequency.
- The variation of the current ripple in variable duty cycle and variable starting position depends on the injected low frequency signal. But dependency of the ripple variation on the low frequency on methods of battery balancing, variable frequency, and ELM is not visible in simulated current.
- The inductor current ripple variation in ELM method and battery balancing method is negligible over the low-frequency change, however the excitation ripple can be seen in the battery current.
- There were issues identified through simulation of these methods;
    - The accuracy of the data is limited by the time step size of 20µs for methods of impulse function, starting position, and battery balancing method.
    - In the battery balancing method, when the battery voltages are equal then there is negligible low-frequency ripple on the battery waveforms. Also, a high voltage difference between the batteries results in an increase in the battery current ripple.
    - The variable frequency method produces a spread range of switching frequency across the ($f_s \pm A_f$) range. This may result in EMI/EMC issues.

[*The observations from the simulations on each method and the realisation of the dependency of inductor current with the frequency of the applied ripple current in some methods is a contribution to knowledge of this thesis*]

All the proposed methods of inducing a low-frequency excitation signal were implemented in hardware in chapter 5. The measurements were used to look at the different circuit operations, the ripple current increase and its dependency on other variables. Finally, the hardware was used to generate an EIS plot by sweeping the frequency across a frequency range to investigate the suitability of each method. The experimental setup was run under conditions of fixed battery voltage and fixed load and duty cycle to tie in with simulations as far as possible. The key results of the experimental data are:

- The experimental results follow the same trends as the simulated results. However, the battery current in the experimental setup is lower. This is because the simulation has been carried out with ideal components.
- In all the proposed methods, the low-frequency component has been detected from the measured battery waveforms from the experimental setup. This indicates the possibility of using these methods to undertake and implement an on-line EIS measurement.

- The generated EIS results from the experimentally measured data indicates that the variable duty cycle, addition of an impulse function, battery balancing method and the ELM can be considered suitable as measurement to take forward for further testing. The variable switching frequency method was less suitable and did not generate good EIS results.

[*The use of all these methods to produce or otherwise an on-line EIS plot of comparable quality to off-line techniques is a contribution of this thesis to knowledge*]

Chapter 6 looked at expanding on the knowledge around the experimental testing to further the understanding on practical implementation issues. The key summaries of this chapter include:

- These new techniques are applicable to other battery types and different devices characterised by EIS such as a solar cell was investigated. There is only a small body of previously published work on using this technique to look at solar cells and none of these considered an on-line condition [*The use of all on-line EIS techniques to solar cells is a contribution of this thesis to knowledge*]
- Instrumentation over different voltage and current ranges was undertaken to work towards a practical on-line scheme, and the measured by sensors shows good accuracy of the measurement instruments.
- This methodology can be used to provide a real time indication of the battery SOC by measuring the impedance of the battery over the different frequency sweep interval. However, the impact of the temperature variation on the battery capacity and the impedance changes is not clear.
- The least square method was undertaken to predict the battery model components values which is useful for battery condition estimation.
- The data from the online method was used to see if it was possible to detect a degraded cell in series with a normal cell. However this was not immediately possible and would require further work.

To summarise, 1 previously published and 5 new methods of performing on-line impedance spectroscopy using existing hardware in the system have been proposed and analysed. This represents a significant novel change in the knowledge in this field.

7.1 Future work

This work proposed different online impedance measurement methods. However, because of the novelty of the proposed methods, there are still many areas to be solved within this topic area. The following list gives a selection of ideas for consideration for further work:

Theoretical analysis

- In the variable duty cycle method, the current ripple is defined as a function of N_p . However, this value cannot increase indefinitely as N_p increases in practice. This is because the theory analysis is based on an ideal case, whereas the real circuit contains non-ideal components. Further theoretical analysis needs to be adapted to deal with the circuit nonlinearity.

- There is a need to extend the analysis to investigate the analysis and impact of the discontinuous mode operation of the DC-DC converter on the current ripple variation over the frequency ranges.

- The harmonic analysis showed that some of the methods were producing signals at multiple low frequency components. This could be utilised to reduce the sweep time of a signal and look at more than one harmonic at a time.

Simulation

- The simulation looked at ideal components to allow easy comparison with the theory. The next step would be to look at the simulation with non-ideal components in both boost and buck mode.

Other hardware Systems

- Only a limited amount of research was done on battery balancing. There is scope for future work to look at other alternative battery balancing methods than published methods to produce a low-frequency excitation signal for impedance measurement.

- In the same way – there are many published dc/dc converter systems and implementing the methodologies on different circuit eg the flyback converter could generate further means of on-line analysis and extend its applicability.

- In a switched capacitor balancing circuit, a series resonant inductor may be considered for soft switching. Further work is required to look into the effect of the resonant switched capacitor balancing circuit to produce a perturbation signal.

- The battery balancing used in this work needed a clear voltage difference between two battery cells to detect a signal. Alternative balancing circuit need to investigate the effect of low battery voltage differences on the battery and inductor current ripple variation.

- The battery balancing circuit was designed to balance two battery cell. A more sufficient circuit design for balancing more battery cells is needed.

Implementation issues

- The hardware and control system lack accuracy especially for variable switching frequency and variable starting pulse position. Further work is required to look at alternative controllers and control methods to improve the system accuracy.

- The proposed methods were applied on one and two battery cells. An improved hardware system needs to be adapted for bigger battery system. This will have implications for the I/O control count needed if all measurements if each battery is monitored independently or the ability to use the method to pick out a degrade cell needs to be refined.

- Improvements to the design of the DC-DC converter such that the switching frequency is increased to allow operation at higher frequency points would allow the system to be applied to different applications.

- In this research, it was difficult to implement full system in hardware to calculate the state of the battery. The full implementation of the system would be needed to be undertaken to produce an online realisable and commercial system for battery states calculation.

- This research assumes the constant room temperature for the battery impedance and SOC estimation. Including the temperature variation effects explicitly into the online techniques analysis is required.

- The impedance data itself is changing in real time as a function of SOC. Although lookup tables can be generated to help understand what the data is referring to, it is not clear how these tables would change with aging and degradation.

- New measurement devices and controller need to be specified, purchased and tested as part of the next level demonstration. This is because OpalRt controller is a rapid prototyping system and unsuitable for a normal system. This would be replaced by a more standard microprocessor or FPGA solution and an additional low cost controller may be needed to be added to deal with the measurement signals and produce a valid output to the FPGA card to allow it to use the results of the measurement within its control. The reason for a separate controller is because the low frequency signal needs to be extracted from the measurements by FFT which are dominated by the switching frequency produced ripple.

8 References

[1] IEA, “Energy, Climate Change and Environment 2016 Insights,” 2016.

[2] U. C. on C. C. (DECC), “Reducing the UK’s carbon footprint Progress meeting carbon budgets Advice requested by Government.” 2013.

[3] UK Committee on Climate Change (DECC), “TIMELINE FOR THE DEPLOYMENT OF NUCLEAR POWER IN THE UK.” 2009.

[4] Carbon Trust, “Energy Storage Report: Can storage help reduce the cost of a future UK electricity system?” 2016.

[5] P. Taylor, R. Bolton, X.-P. Zhang, C. Martin, P. Upham, Y. Li, R. Porter, and E. Pereira Bonvallet, “Pathways for energy storage in the UK,” 2012.

[6] T. M. Masaud, K. L. K. Lee, and P. K. Sen, “An overview of energy storage technologies in electric power systems: What is the future?,” in *North American Power Symposium NAPS 2010*, 2010, pp. 1–6.

[7] J. C. Beardsall, C. A. Gould, and M. Al-Tai, “Energy storage systems: A review of the technology and its application in power systems,” in *2015 50th International Universities Power Engineering Conference (UPEC)*, 2015, pp. 1–6.

[8] IEC, “Electrical Energy Storage.” .

[9] S. Dechert, “The top 10 energy storage countries are… : Renew Economy.” [Online]. Available: http://reneweconomy.com.au/the-top-10-energy-storage-countries-are-66261/. [Accessed: 12-Apr-2017].

[10] Department of Energy USA (DOE), “DOE Global Energy Storage Database.” [Online]. Available: https://www.energystorageexchange.org/. [Accessed: 12-Apr-2017].

[11] OFGEM, “Low Carbon Networks Fund | Ofgem.” [Online]. Available: https://www.ofgem.gov.uk/electricity/distribution-networks/network-innovation/low-carbon-networks-fund. [Accessed: 12-Apr-2017].

[12] EA Technology, “Energy Storage Operators’ Forum.” [Online]. Available: https://www.eatechnology.com/projects/energy-storage-operators-forum/. [Accessed: 12-Apr-2017].

[13] WPD Innovation project close down report, “Project FALCON Energy storage,” 2015.

[14] M. A. Varnosfaderani, D. Strickland, and C. Harrap, “Experience of availability of sodium-nickel based energy storage,” in *IET International Conference on Resilience of Transmission and Distribution Networks (RTDN) 2015*, 2015, p. 30 (6 .)-30 (6 .).

[15] D. Strickland, C. Harrap, and M. Abedi Varnosfaderani, “Measuring the impact of energy storage on the Network,” in *UKES2015*, 2015.

[16] X. Bai, M. Abedi Varnosfaderani, and D. Strickland, “Energy Storage Trial Operation Experience on the 11kV Distribution Network,” in *UKES2014*, 2014.

[17] N. Mukherjee and D. Strickland, “Modular ESS with second life batteries operating in grid independent mode,” in *2012 3rd IEEE International Symposium on Power Electronics for Distributed Generation Systems (PEDG)*, 2012, pp. 653–660.

[18] D. Strickland, M. A. Varnosfederani, J. Scott, P. Quintela, A. Duran, R. Bravery, A. Corliss, K. Ashworth, and S. Blois-Brooke, “A review of community electrical energy systems,” in *2016 IEEE International Conference on Renewable Energy Research and Applications (ICRERA)*, 2016, pp. 49–54.

[19] “ABB and partners to evaluate the reuse of the Nissan LEAF battery for commercial purposes.” [Online]. Available: http://www.abb.co.uk/cawp/seitp202/a2b2d2aff96520bec1257989004e62ae.aspx. [Accessed: 13-Apr-2017].

[20] “Energy Storage Journal.” [Online]. Available: http://www.energystoragejournal.com/second-life/. [Accessed: 13-Apr-2017].

[21] W.-Y. Chang, “The State of Charge Estimating Methods for Battery: A Review,” *ISRN Appl. Math.*, vol. 2013, p. 7, 2013.

[22] S. Park, A. Savvides, and M. Srivastava, “Battery capacity measurement and analysis using lithium coin cell battery,” in *Proceedings of the 2001 international symposium on Low power electronics and design*, 2001, pp. 382–387.
[23] L. W. Juang, P. J. Kollmeyer, T. M. Jahns, and R. D. Lorenz, “Implementation of online battery state-of-power and state-of-function estimation in electric vehicle applications,” in *2012 IEEE Energy Conversion Congress and Exposition (ECCE)*, 2012, pp. 1819–1826.
[24] P. J. van Bree, A. Veltman, W. H. A. Hendrix, and P. P. J. van den Bosch, “Prediction of Battery Behavior Subject to High-Rate Partial State of Charge,” *IEEE Trans. Veh. Technol.*, vol. 58, no. 2, pp. 588–595, Feb. 2009.
[25] G. L. Plett, “High-Performance Battery-Pack Power Estimation Using a Dynamic Cell Model,” *IEEE Trans. Veh. Technol.*, vol. 53, no. 5, pp. 1586–1593, Sep. 2004.
[26] E. Meissner and G. Richter, “Battery Monitoring and Electrical Energy Management,” *J. Power Sources*, vol. 116, no. 1–2, pp. 79–98, Jul. 2003.
[27] S. Piller, M. Perrin, and A. Jossen, “Methods for state-of-charge determination and their applications,” *J. Power Sources*, vol. 96, no. 1, pp. 113–120, 2001.
[28] N. Kong-Soon, H. Yao-Feng, M. Chin-Sien, and H. Yao-Ching, “An enhanced coulomb counting method for estimating state-of-charge and state-of-health of lead-acid batteries,” in *Telecommunications Energy Conference, 2009. INTELEC 2009. 31st International*, 2009, pp. 1–5.
[29] J. Yong-Min, C. Yong-Ki, A. Jung-Hoon, R. Seung-Hee, and L. Byoung-Kuk, “Enhanced Coulomb counting method with adaptive SOC reset time for estimating OCV,” in *Energy Conversion Congress and Exposition (ECCE), 2014 IEEE*, 2014, pp. 1313–1318.
[30] E. Leksono, I. N. Haq, M. Iqbal, F. X. N. Soelami, and I. G. N. Merthayasa, “State of charge (SoC) estimation on LiFePO4 battery module using Coulomb counting methods with modified Peukert,” in *Rural Information & Communication Technology and Electric-Vehicle Technology (rICT & ICeV-T), 2013 Joint International Conference on*, 2013, pp. 1–4.
[31] A. Purwadi, A. Rizqiawan, A. Kevin, and N. Heryana, “State of Charge estimation method for lithium battery using combination of Coulomb Counting and Adaptive System with considering the effect of temperature,” in *Power Engineering and Renewable Energy (ICPERE), 2014 International Conference on*, 2014, pp. 91–95.
[32] A. Nugroho, E. Rijanto, F. D. Wijaya, and P. Nugroho, “Battery state of charge estimation by using a combination of Coulomb Counting and dynamic model with adjusted gain,” in *Sustainable Energy Engineering and Application (ICSEEA), 2015 International Conference on*, 2015, pp. 54–58.
[33] L. W. Juang, P. J. Kollmeyer, R. Zhao, T. M. Jahns, and R. D. Lorenz, “Coulomb counting state-of-charge algorithm for electric vehicles with a physics-based temperature dependent battery model,” in *IEEE Energy Conversion Congress and Exposition (ECCE)*, 2015, pp. 5052–5059.
[34] T. Kim, W. Qiao, and L. Qu, “Real-time state of charge and electrical impedance estimation for lithium-ion batteries based on a hybrid battery model,” in *2013 28th IEEE Applied Power Electronics Conference and Exposition*, 2013, pp. 563–568.
[35] S. J. Lee, J. H. Kim, J. M. Lee, and B. H. Cho, “The State and Parameter Estimation of an Li-Ion Battery Using a New OCV-SOC Concept,” in *Power Electronics Specialists Conference, 2007. PESC 2007. IEEE*, 2007, pp. 2799–2803.
[36] S. Santhanagopalan and R. E. White, “Online estimation of the state of charge of a lithium ion cell,” *J. Power Sources*, vol. 161, no. 2, pp. 1346–1355, 2006.
[37] C.-J. Chiang, J.-L. Yang, and W.-C. Cheng, “Temperature and state-of-charge estimation in ultracapacitors based on extended Kalman filter,” *J. Power Sources*, vol. 234, no. 0, pp. 234–243, 2013.
[38] C. Chang Yoon, S. Gab-Su, Y. Sung Hyun, and C. Bo-Hyung, “State-of-charge estimation for lithium-ion battery pack using reconstructed open-circuit-voltage curve,” in *Power Electronics Conference (IPEC-Hiroshima 2014 - ECCE-ASIA), 2014 International*, 2014, pp. 2272–2276.
[39] T. Gallien and G. Brasseur, “State of charge estimation of a LiFePO4 battery: A dual estimation approach incorporating open circuit voltage hysteresis,” in *IEEE International*

Instrumentation and Measurement Technology Conference Proceedings, 2016, pp. 1–6.
[40] S. Nejad, D. T. Gladwin, and D. A. Stone, "Enhanced state-of-charge estimation for lithium-ion iron phosphate cells with flat open-circuit voltage curves," in *Industrial Electronics Society, IECON 2015 - 41st Annual Conference of the IEEE*, 2015, pp. 003187–003192.
[41] H. Wang, Y. Liu, H. Fu, and G. Li, "Estimation of state of charge of batteries for electric vehicles," *Int. J. Control Autom.*, vol. 6, no. 2, pp. 185–194, 2013.
[42] H.-G. Schweiger, O. Obeidi, O. Komesker, A. Raschke, M. Schiemann, C. Zehner, M. Gehnen, M. Keller, and P. Birke, "Comparison of several methods for determining the internal resistance of lithium ion cells," *Sensors*, vol. 10, no. 6, pp. 5604–5625, 2010.
[43] Y. K. Cho, Y. M. Jeong, J. H. Ahn, S. H. Ryu, and B. K. Lee, "A new SOC estimation algorithm without integrated error using DCIR repetitive calculation," in *Electrical Machines and Systems (ICEMS), 2014 17th International Conference*, 2014, pp. 865–870.
[44] Y. Li, B. Zhang, M. Chen, D. Yang, and J. Liu, "Investigation of the internal resistance in LiFePO4 cells for battery energy storage system," in *2014 9th IEEE Conference on Industrial Electronics and Applications*, 2014, pp. 1596–1600.
[45] S. Sato and A. Kawamura, "A new estimation method of state of charge using terminal voltage and internal resistance for lead acid battery," in *Power Conversion Conference, 2002. PCC-Osaka 2002. Proceedings of the*, 2002, vol. 2, pp. 565–570 vol.2.
[46] H. Lee, J. Park, and J. Kim, "Comparative analysis of the SOH estimation based on various resistance parameters for LiCoO2 cells," in *2016 IEEE Transportation Electrification Conference and Expo*, 2016, pp. 788–792.
[47] T. Goh, D. Kim, J. J. Jeong, M. Park, and S. W. Kim, "Robust observer for state-of-charge estimation of li-ion battery with uncertainties," in *Control Conference (ASCC), 2015 10th Asian*, 2015, pp. 1–6.
[48] M. V Micea, L. Ungurean, G. N. Cârstoiu, and V. Groza, "Online State-of-Health Assessment for Battery Management Systems," *IEEE Trans. Instrum. Meas.*, vol. 60, no. 6, pp. 1997–2006, Jun. 2011.
[49] P. K. I, D. B. Rao Professor SOIS, and A. Sharma, "Estimation of SOC and SOH of Li-Ion Batteries," *Int. J. Comput. Appl.*, vol. 104, no. 4, pp. 975–8887, 2014.
[50] V. Pop, H. J. Bergveld, P. H. L. Notten, and P. P. L. Regtien, "State-of-the-art of battery state-of-charge determination," *Meas. Sci. Technol.*, vol. 16, no. 12, pp. R93–R110, Dec. 2005.
[51] N. Watrin, B. Blunier, and A. Miraoui, "Review of adaptive systems for lithium batteries State-of-Charge and State-of-Health estimation," in *Transportation Electrification Conference and Expo (ITEC), 2012 IEEE*, 2012, pp. 1–6.
[52] N. Watrin, H. Ostermann, B. Blunier, and A. Miraoui, "Multiphysical Lithium-Based Battery Model for Use in State-of-Charge Determination," *IEEE Trans. Veh. Technol.*, vol. 61, no. 8, pp. 3420–3429, Oct. 2012.
[53] R. Koch, R. Kuhn, I. Zilberman, and A. Jossen, "Electrochemical impedance spectroscopy for online battery monitoring - power electronics control," in *Power Electronics and Applications (EPE'14-ECCE Europe), 2014 16th European Conference on*, 2014, pp. 1–10.
[54] A. Rahmoun and H. Biechl, "Modelling of Li-ion batteries using equivalent circuit diagrams," *Prz. Elektrotechniczny*, vol. 2, no. 7, pp. 152–156, 2012.
[55] M. Galád, P. Špánik, M. Cacciato, and G. Nobile, "Comparison of common and combined state of charge estimation methods for VRLA batteries," in *2016 ELEKTRO*, 2016, pp. 220–225.
[56] M. Bayya, U. M. Rao, B. V. S. S. N. Prabhakara, and N. Moorthy Muthukrishnan, "Online battery monitoring using model based approach - impedance," in *Industrial Instrumentation and Control (ICIC), 2015 International Conference on*, 2015, pp. 1630–1634.
[57] J. Kim, S. Lee, and B. H. Cho, "Complementary cooperation algorithm based on DEKF combined with pattern recognition for SOC/capacity estimation and SOH prediction," *IEEE Trans. Power Electron.*, vol. 27, no. 1, pp. 436–451, 2012.
[58] H. Dai, X. Wei, and Z. Sun, "State and Parameter Estimation of a HEV Li-ion Battery Pack Using Adaptive Kalman Filter with a New SOC-OCV Concept," in *Measuring Technology and Mechatronics Automation, 2009. ICMTMA '09. International Conference on*, 2009, vol. 2, pp. 375–380.

[59] D. Dinh Vinh, C. Forgez, K. El Kadri Benkara, and G. Friedrich, “Impedance Observer for a Li-Ion Battery Using Kalman Filter,” *Veh. Technol. IEEE Trans.*, vol. 58, no. 8, pp. 3930–3937, 2009.
[60] F. Sun, X. Hu, Y. Zou, and S. Li, “Adaptive unscented Kalman filtering for state of charge estimation of a lithium-ion battery for electric vehicles,” *Energy*, vol. 36, no. 5, pp. 3531–3540, 2011.
[61] T. Dragicevic, S. Sucic, and J. M. Guerrero, “Battery state-of-charge and parameter estimation algorithm based on Kalman filter,” in *EUROCON, 2013 IEEE*, 2013, pp. 1519–1525.
[62] G. L. Plett, “Extended Kalman filtering for battery management systems of LiPB-based HEV battery packs: Part 1. Background,” *J. Power Sources*, vol. 134, no. 2, pp. 252–261, 2004.
[63] A. Vasebi, S. M. T. Bathaee, and M. Partovibakhsh, “Predicting state of charge of lead-acid batteries for hybrid electric vehicles by extended Kalman filter,” *Energy Convers. Manag.*, vol. 49, no. 1, pp. 75–82, 2008.
[64] G. L. Plett, “Sigma-point Kalman filtering for battery management systems of LiPB-based HEV battery packs: Part 1: Introduction and state estimation,” *J. Power Sources*, vol. 161, no. 2, pp. 1356–1368, 2006.
[65] M. Mastali, J. Vazquez-Arenas, R. Fraser, M. Fowler, S. Afshar, and M. Stevens, “Battery state of the charge estimation using Kalman filtering,” *J. Power Sources*, vol. 239, no. 0, pp. 294–307, 2013.
[66] J. Chenguang, A. Taylor, D. Chen, and K. Bai, “Extended Kalman Filter based battery state of charge(SOC) estimation for electric vehicles,” in *Transportation Electrification Conference and Expo (ITEC), 2013 IEEE*, 2013, pp. 1–5.
[67] K. W. E. Cheng, B. P. Divakar, H. Wu, K. Ding, and H. F. Ho, “Battery-management system (BMS) and SOC development for electrical vehicles,” *IEEE Trans. Veh. Technol.*, vol. 60, no. 1, pp. 76–88, 2011.
[68] K. Jonghoon and B. H. Cho, “State-of-Charge Estimation and State-of-Health Prediction of a Li-Ion Degraded Battery Based on an EKF Combined With a Per-Unit System,” *Veh. Technol. IEEE Trans.*, vol. 60, no. 9, pp. 4249–4260, 2011.
[69] M. W. Yatsui and H. Bai, “Kalman filter based state-of-charge estimation for lithium-ion batteries in hybrid electric vehicles using pulse charging,” in *IEEE Vehicle Power and Propulsion Conference*, 2011, pp. 1–5.
[70] M. Knauff, C. Dafis, and D. Niebur, “A new battery model for use with an extended Kalman filter state of charge estimator,” in *American Control Conference (ACC), 2010*, 2010, pp. 1991–1996.
[71] C. Taborelli and S. Onori, “State of charge estimation using extended Kalman filters for battery management system,” in *Electric Vehicle Conference (IEVC), 2014 IEEE International*, 2014, pp. 1–8.
[72] D. Di Domenico, G. Fiengo, and A. Stefanopoulou, “Lithium-ion battery state of charge estimation with a Kalman Filter based on a electrochemical model,” in *Control Applications, 2008. CCA 2008. IEEE International Conference on*, 2008, pp. 702–707.
[73] M. M. Ismail and M. A. M. Hassan, “The state of charge estimation for rechargeable batteries based on artificial neural network techniques,” in *Control, Decision and Information Technologies (CoDIT), 2013 International Conference on*, 2013, pp. 733–739.
[74] M. Charkhgard and M. Farrokhi, “State-of-Charge Estimation for Lithium-Ion Batteries Using Neural Networks and EKF,” *IEEE Trans. Ind. Electron.*, vol. 57, no. 12, pp. 4178–4187, 2010.
[75] X. Chen, W. Shen, M. Dai, Z. Cao, J. Jin, and A. Kapoor, “Robust Adaptive Sliding-Mode Observer Using RBF Neural Network for Lithium-Ion Battery State of Charge Estimation in Electric Vehicles,” *IEEE Trans. Veh. Technol.*, vol. 65, no. 4, pp. 1936–1947, 2016.
[76] F. Husnayain, A. R. Utomo, and P. S. Priambodo, “State of charge estimation for a lead-acid battery using backpropagation neural network method,” in *Electrical Engineering and Computer Science (ICEECS), 2014 International Conference*, 2014, pp. 274–278.
[77] M. Charkhgard and M. Farrokhi, “State-of-Charge Estimation for Lithium-Ion Batteries Using Neural Networks and EKF,” *IEEE Trans. Ind. Electron.*, vol. 57, no. 12, pp. 4178–

4187, 2010.
[78] I. Anand and B. L. Mathur, “State of charge estimation of lead acid batteries using neural networks,” in *2013 International Conference on Circuits, Power and Computing Technologies (ICCPCT)*, 2013, pp. 596–599.
[79] F. Liu, T. Liu, and Y. Fu, “An Improved SoC Estimation Algorithm Based on Artificial Neural Network,” in *2015 8th International Symposium on Computational Intelligence and Design (ISCID)*, 2015, vol. 2, pp. 152–155.
[80] A. a. Hussein, “Capacity fade estimation in electric vehicles Li-ion batteries using artificial neural networks,” *2013 IEEE Energy Convers. Congr. Expo.*, no. 2, pp. 677–681, 2013.
[81] P. Singh, R. Vinjamuri, X. Wang, and D. Reisner, “Design and implementation of a fuzzy logic-based state-of-charge meter for Li-ion batteries used in portable defibrillators,” *J. Power Sources*, vol. 162, no. 2, pp. 829–836, 2006.
[82] P. Singh, R. Vinjamuri, X. Wang, and D. Reisner, “Fuzzy logic modeling of EIS measurements on lithium-ion batteries,” *Electrochim. Acta*, vol. 51, no. 8–9, pp. 1673–1679, 2006.
[83] A. Zenati, P. Desprez, H. Razik, and S. Rael, “Impedance measurements combined with the fuzzy logic methodology to assess the SOC and SOH of lithium-ion cells,” in *Vehicle Power and Propulsion Conference (VPPC), 2010 IEEE*, 2010, pp. 1–6.
[84] A. Zenati, P. Desprez, and H. Razik, “Estimation of the SOC and the SOH of li-ion batteries, by combining impedance measurements with the fuzzy logic inference,” in *IECON 2010 - 36th Annual Conference on IEEE Industrial Electronics Society*, 2010, pp. 1773–1778.
[85] N. L. Diaz, T. Dragicevic, J. C. Vasquez, and J. M. Guerrero, “Fuzzy-logic-based gain-scheduling control for state-of-charge balance of distributed energy storage systems for DC microgrids,” in *Applied Power Electronics Conference and Exposition (APEC), 2014 Twenty-Ninth Annual IEEE*, 2014, pp. 2171–2176.
[86] J. Du, Z. Liu, Y. Wang, and C. Wen, “A fuzzy logic-based model for Li-ion battery with SOC and temperature effect,” in *Control & Automation (ICCA), 11th IEEE International Conference on*, 2014, pp. 1333–1338.
[87] K. Jonghoon and D. Nikitenkov, “Fuzzy logic-controlled online state-of-health (SOH) prediction in large format LiMn2O4 cell for energy storage system (ESS) applications,” in *Industrial Technology (ICIT), 2014 IEEE International Conference on*, 2014, pp. 474–479.
[88] V. S. Donepudi, “Electrochemical Calorimetry of the Zinc and Bromine Electrodes in Zinc-Bromine and Zinc-Air Batteries,” *J. Electrochem. Soc.*, vol. 131, no. 7, pp. 1477–1485, 1984.
[89] T. T. de Sousa, V. T. Arioli, C. S. Vieira, S. Rocha dos Santos, and A. P. Franca, “Comparison of different approaches for lead acid battery state of health estimation based on artificial neural networks algorithms,” in *2016 IEEE Conference on Evolving and Adaptive Intelligent Systems (EAIS)*, 2016, pp. 79–84.
[90] J. Zhou, Z. He, M. Gao, and Y. Liu, “Battery state of health estimation using the generalized regression neural network,” in *2015 8th International Congress on Image and Signal Processing (CISP)*, 2015, pp. 1396–1400.
[91] S. Nejad, D. T. Gladwin, and D. A. Stone, “On-chip implementation of Extended Kalman Filter for adaptive battery states monitoring,” in *IECON 2016 - 42nd Annual Conference of the IEEE Industrial Electronics Society*, 2016, pp. 5513–5518.
[92] T. Kim, Y. Wang, H. Fang, Z. Sahinoglu, T. Wada, S. Hara, and W. Qiao, “Model-Based Condition Monitoring for Lithium-ion Batteries.”
[93] Jonghoon Kim and D. Nikitenkov, “Fuzzy logic-controlled online state-of-health (SOH) prediction in large format LiMn2O4 cell for energy storage system (ESS) applications,” in *2014 IEEE International Conference on Industrial Technology (ICIT)*, 2014, pp. 474–479.
[94] P. Singh and D. Reisner, “Fuzzy logic-based state-of-health determination of lead acid batteries,” in *24th Annual International Telecommunications Energy Conference*, pp. 583–590.
[95] M. Shahriari and M. Farrokhi, “State of health estimation of VRLA batteries using fuzzy logic,” in *2010 18th Iranian Conference on Electrical Engineering*, 2010, pp. 629–634.
[96] B. Mo, J. Yu, D. Tang, H. Liu, and J. Yu, “A remaining useful life prediction approach for lithium-ion batteries using Kalman filter and an improved particle filter,” in *2016 IEEE*

International Conference on Prognostics and Health Management (ICPHM), 2016, pp. 1–5.
[97] P.-H. Michel and V. Heiries, "An Adaptive Sigma Point Kalman Filter Hybridized by Support Vector Machine Algorithm for Battery SoC and SoH Estimation," in *2015 IEEE 81st Vehicular Technology Conference (VTC Spring)*, 2015, pp. 1–7.
[98] Fei Zhang, Guangjun Liu, and Lijin Fang, "Battery state estimation using Unscented Kalman Filter," in *2009 IEEE International Conference on Robotics and Automation*, 2009, pp. 1863–1868.
[99] M. Cacciato, G. Nobile, G. Scarcella, and G. Scelba, "Real-Time Model-Based Estimation of SOC and SOH for Energy Storage Systems," *IEEE Trans. Power Electron.*, vol. 32, no. 1, pp. 794–803, Jan. 2017.
[100] T. Kim, "Model-Based Condition Monitoring and Power Management for Rechargeable Electrochemical Batteries."
[101] T. Kim, W. Qiao, and L. Qu, "Online SOC and SOH estimation for multicell lithium-ion batteries based on an adaptive hybrid battery model and sliding-mode observer," in *2013 IEEE Energy Conversion Congress and Exposition*, 2013, pp. 292–298.
[102] L. D. Couto, J. Schorsch, M. M. Nicotra, and M. Kinnaert, "SOC and SOH estimation for Li-ion batteries based on an equivalent hydraulic model. Part I: SOC and surface concentration estimation," in *2016 American Control Conference (ACC)*, 2016, pp. 4022–4028.
[103] T.-H. Wu, J.-K. Wang, C.-S. Moo, and A. Kawamura, "State-of-charge and state-of-health estimating method for lithium-ion batteries," in *2016 IEEE 17th Workshop on Control and Modeling for Power Electronics (COMPEL)*, 2016, pp. 1–6.
[104] Min Zhu, Wensong Hu, and N. C. Kar, "The SOH estimation of LiFePO4 battery based on internal resistance with Grey Markov Chain," in *2016 IEEE Transportation Electrification Conference and Expo (ITEC)*, 2016, pp. 1–6.
[105] K.-H. Tseng, J.-W. Liang, W. Chang, and S.-C. Huang, "Regression Models Using Fully Discharged Voltage and Internal Resistance for State of Health Estimation of Lithium-Ion Batteries," *Energies*, vol. 8, no. 4, pp. 2889–2907, Apr. 2015.
[106] K. S. Ng, C. S. Moo, Y. P. Chen, and Y. C. Hsieh, "Enhanced coulomb counting method for estimating state-of-charge and state-of-health of lithium-ion batteries," *Appl. Energy*, vol. 86, no. 9, pp. 1506–1511, 2009.
[107] D. Liu, J. Zhou, D. Pan, Y. Peng, and X. Peng, "Lithium-ion battery remaining useful life estimation with an optimized Relevance Vector Machine algorithm with incremental learning," *Measurement*, vol. 63, no. 63, pp. 143–151, Mar. 2015.
[108] J. Zhou, D. Liu, Y. Peng, and X. Peng, "Dynamic battery remaining useful life estimation: An on-line data-driven approach," in *2012 IEEE International Instrumentation and Measurement Technology Conference Proceedings*, 2012, pp. 2196–2199.
[109] J. Z. Sikorska, M. Hodkiewicz, and L. Ma, "Prognostic modelling options for remaining useful life estimation by industry," *Mech. Syst. Signal Process.*, vol. 25, no. 5, pp. 1803–1836, Jul. 2011.
[110] Q. Miao, L. Xie, H. Cui, W. Liang, and M. Pecht, "Remaining useful life prediction of lithium-ion battery with unscented particle filter technique," *Microelectron. Reliab.*, vol. 53, no. 6, pp. 805–810, 2013.
[111] S. Tang, C. Yu, X. Wang, X. Guo, and X. Si, "Remaining Useful Life Prediction of Lithium-Ion Batteries Based on the Wiener Process with Measurement Error," *Energies*, vol. 7, no. 2, pp. 520–547, Jan. 2014.
[112] A. Harris, P. O'Connor, and R. W. Cox, "A time-domain approach for monitoring battery state of health (SOH) and remaining useful life (RUL)," in *IECON 2014 - 40th Annual Conference of the IEEE Industrial Electronics Society*, 2014, pp. 3083–3087.
[113] L. W. Juang, P. J. Kollmeyer, T. M. Jahns, and R. D. Lorenz, "Improved nonlinear model for electrode voltage-current relationship for more consistent online battery system identification," in *2011 IEEE Energy Conversion Congress and Exposition*, 2011, pp. 2628–2634.
[114] N. Karami, H. El-Sheikh, and N. Moubayed, "Evaluation study of different useful life estimation techniques of lithium-ion battery," in *2016 Third International Conference on Electrical, Electronics, Computer Engineering and their Applications (EECEA)*, 2016, pp.

77–82.
[115] A. Guha, A. Patra, and K. V Vaisakh, “Remaining useful life estimation of lithium-ion batteries based on the internal resistance growth model,” in *2017 Indian Control Conference (ICC)*, 2017, pp. 33–38.
[116] Fengchun Sun, R. Xiong, H. He, W. Li, and J. E. E. Aussems, “Model-based dynamic multi-parameter method for peak power estimation of lithium–ion batteries, Applied Energy,” vol. 96, pp. 378–386, 2012.
[117] R. Xiong, H. He, F. Sun, and K. Zhao, “Online Estimation of Peak Power Capability of Li-Ion Batteries in Electric Vehicles by a Hardware-in-Loop Approach,” *Energies*, vol. 5, no. 12, pp. 1455–1469, May 2012.
[118] C. Zhang, C. Zhang, and S. M. Sharkh, “Estimation of Real-Time Peak Power Capability of a Traction Battery Pack Used in an HEV,” in *2010 Asia-Pacific Power and Energy Engineering Conference*, 2010, pp. 1–6.
[119] R. Xiong, H. He, F. Sun, X. Liu, and Z. Liu, “Model-based state of charge and peak power capability joint estimation of lithium-ion battery in plug-in hybrid electric vehicles,” *J. Power Sources*, vol. 229, pp. 159–169, 2013.
[120] W. Waag, C. Fleischer, and D. U. Sauer, “On-line estimation of lithium-ion battery impedance parameters using a novel varied-parameters approach,” *J. Power Sources*, vol. 237, pp. 260–269, 2013.
[121] L. W. Juang, P. J. Kollmeyer, T. M. Jahns, and R. D. Lorenz, “Implementation of online battery state-of-power and state-of-function estimation in electric vehicle applications,” in *2012 IEEE Energy Conversion Congress and Exposition (ECCE)*, 2012, pp. 1819–1826.
[122] R. D. Anderson, Yanan Zhao, Xu Wang, Xiao Guang Yang, and Yonghua Li, “Real time battery power capability estimation,” in *2012 American Control Conference (ACC)*, 2012, pp. 592–597.
[123] L. Pei, C. Zhu, T. Wang, R. Lu, and C. C. Chan, “Online peak power prediction based on a parameter and state estimator for lithium-ion batteries in electric vehicles,” *Energy*, vol. 66, pp. 766–778, 2014.
[124] N. Watrin, B. Blunier, and A. Miraoui, “Review of adaptive systems for lithium batteries State-of-Charge and State-of-Health estimation,” in *2012 IEEE Transportation Electrification Conference and Expo (ITEC)*, 2012, pp. 1–6.
[125] S. Lee, J. Kim, J. Lee, and B. H. Cho, “State-of-charge and capacity estimation of lithium-ion battery using a new open-circuit voltage versus state-of-charge,” *J. Power Sources*, vol. 185, no. 2, pp. 1367–1373, 2008.
[126] Y. Xing, W. He, M. Pecht, and K. L. Tsui, “State of charge estimation of lithium-ion batteries using the open-circuit voltage at various ambient temperatures,” *Appl. Energy*, vol. 113, pp. 106–115, 2014.
[127] C. Hu, B. D. Youn, and J. Chung, “A multiscale framework with extended Kalman filter for lithium-ion battery SOC and capacity estimation,” *Appl. Energy*, vol. 92, pp. 694–704, 2012.
[128] R. Xiong, H. He, F. Sun, and K. Zhao, “Evaluation on State of Charge Estimation of Batteries With Adaptive Extended Kalman Filter by Experiment Approach,” *IEEE Trans. Veh. Technol.*, vol. 62, no. 1, pp. 108–117, 2013.
[129] K. S. Ng, C.-S. Moo, Y.-P. Chen, and Y.-C. Hsieh, “Enhanced coulomb counting method for estimating state-of-charge and state-of-health of lithium-ion batteries,” *Appl. Energy*, vol. 86, no. 9, pp. 1506–1511, 2009.
[130] X. Feng, J. Li, M. Ouyang, L. Lu, J. Li, and X. He, “Using probability density function to evaluate the state of health of lithium-ion batteries,” *J. Power Sources*, vol. 232, pp. 209–218, 2013.
[131] L. Wang, C. Pan, L. Liu, Y. Cheng, and X. Zhao, “On-board state of health estimation of LiFePO4 battery pack through differential voltage analysis,” *Appl. Energy*, vol. 168, pp. 465–472, 2016.
[132] P. Keil and A. Jossen, “Calendar Aging of NCA Lithium-Ion Batteries Investigated by Differential Voltage Analysis and Coulomb Tracking,” *J. Electrochem. Soc.*, vol. 164, no. 1, pp. A6066–A6074, Oct. 2017.
[133] C. Weng, J. Sun, and H. Peng, “A unified open-circuit-voltage model of lithium-ion batteries

for state-of-charge estimation and state-of-health monitoring," *J. Power Sources*, vol. 258, pp. 228–237, 2014.
[134] A. Farmann, W. Waag, A. Marongiu, and D. U. Sauer, "Critical review of on-board capacity estimation techniques for lithium-ion batteries in electric and hybrid electric vehicles," *J. Power Sources*, vol. 281, pp. 114–130, 2015.
[135] W. F. Bentley, "Cell balancing considerations for lithium-ion battery systems," *Twelfth Annu. Batter. Conf. Appl. Adv.*, pp. 223–226, 1997.
[136] M. Daowd, N. Omar, P. Van Den Bossche, and J. Van Mierlo, "Passive and active battery balancing comparison based on MATLAB simulation," in *2011 IEEE Vehicle Power and Propulsion Conference, VPPC 2011*, 2011.
[137] J. Cao, N. Schofield, and A. Emadi, "Battery balancing methods: A comprehensive review," in *2008 IEEE Vehicle Power and Propulsion Conference, VPPC 2008*, 2008.
[138] R. Koch, C. Riebel, and A. Jossen, "On-line electrochemical impedance spectroscopy implementation for telecommunication power supplies," in *2015 IEEE International Telecommunications Energy Conference (INTELEC)*, 2015, pp. 1–6.
[139] P. Medina, a. W. Bizuayehu, J. P. S. Catalao, E. M. G. Rodrigues, and J. Contreras, "Electrical Energy Storage Systems: Technologies' State-of-the-Art, Techno-economic Benefits and Applications Analysis," *2014 47th Hawaii Int. Conf. Syst. Sci.*, pp. 2295–2304, 2014.
[140] E. Din, C. Schaef, K. Moffat, and J. T. Stauth, "A Scalable Active Battery Management System With Embedded Real-Time Electrochemical Impedance Spectroscopy," *IEEE Trans. Power Electron.*, vol. 32, no. 7, pp. 5688–5698, 2017.
[141] T.-T. Nguyen, V.-L. Tran, and W. Choi, "Development of the intelligent charger with battery State-Of-Health estimation using online impedance spectroscopy," in *2014 IEEE 23rd International Symposium on Industrial Electronics (ISIE)*, 2014, pp. 454–458.
[142] E. Din, C. Schaef, K. Moffat, and J. Stauth, "A Scalable Active Battery Management System with Embedded Real-Time Electrochemical Impedance Spectroscopy," *IEEE Trans. Power Electron.*, vol. PP, no. 99, 2016.
[143] A. Lasia, "Electrochemical Impedance Spectroscopy and its Applications," in *Modern Aspects of Electrochemistry*, vol. 32, B. E. Conway, J. O. Bockris, and R. White, Eds. Springer US, 2002, pp. 143–248.
[144] M. E. Orazem and B. Tribollet, *Electrochemical impedance spectroscopy*, vol. 48. John Wiley & Sons, 2011.
[145] V. F. Lvovich, *Impedance Spectroscopy: Applications to Electrochemical and Dielectric Phenomena*. 2012.
[146] B. Saha, K. Goebel, and J. Christophersen, "Comparison of prognostic algorithms for estimating remaining useful life of batteries," *Trans. Inst. Meas. Control*, vol. 31, no. 3–4, pp. 293–308, Jun. 2009.
[147] R. Dietz and A. Mertens, "Grid impedance estimation in inductive-resistive distributed power networks using particle filtering," in *2016 18th European Conference on Power Electronics and Applications (EPE'16 ECCE Europe)*, 2016, pp. 1–8.
[148] K. Goebel, B. Saha, A. Saxena, J. Celaya, and J. Christophersen, "Prognostics in Battery Health Management," *IEEE Instrum. Meas. Mag.*, vol. 11, no. 4, pp. 33–40, Aug. 2008.
[149] W. Xian, B. Long, M. Li, and H. Wang, "Prognostics of Lithium-Ion Batteries Based on the Verhulst Model, Particle Swarm Optimization and Particle Filter," *IEEE Trans. Instrum. Meas.*, vol. 63, no. 1, pp. 2–17, Jan. 2014.
[150] X. Hu, S. Li, and H. Peng, "A comparative study of equivalent circuit models for Li-ion batteries," *J. Power Sources*, vol. 198, pp. 359–367, 2012.
[151] C. Zhang, K. Li, S. Mcloone, and Z. Yang, "Battery modelling methods for electric vehicles - A review," in *2014 European Control Conference (ECC)*, 2014, pp. 2673–2678.
[152] K. Bundy, M. Karlsson, G. Lindbergh, and A. Lundqvist, "An electrochemical impedance spectroscopy method for prediction of the state of charge of a nickel-metal hydride battery at open circuit and during discharge," *J. Power Sources*, vol. 72, no. 2, pp. 118–125, 1998.
[153] A. Eddahech, O. Briat, N. Bertrand, J.-Y. Delétage, and J.-M. Vinassa, "Behavior and state-of-health monitoring of Li-ion batteries using impedance spectroscopy and recurrent neural

networks," *Int. J. Electr. Power Energy Syst.*, vol. 42, no. 1, pp. 487–494, 2012.
[154] X. Wang, X. Wei, H. Dai, and Q. Wu, "State Estimation of Lithium Ion Battery Based on Electrochemical Impedance Spectroscopy with On-Board Impedance Measurement System," in *Vehicle Power and Propulsion Conference (VPPC), 2015 IEEE*, 2015, pp. 1–5.
[155] A. Densmore and M. Hanif, "Determining battery SoC using Electrochemical Impedance Spectroscopy and the Extreme Learning Machine," in *Future Energy Electronics Conference (IFEEC), 2015 IEEE 2nd International*, 2015, pp. 1–7.
[156] H. Blanke, O. Bohlen, S. Buller, R. W. De Doncker, B. Fricke, A. Hammouche, D. Linzen, M. Thele, and D. U. Sauer, "Impedance measurements on lead–acid batteries for state-of-charge, state-of-health and cranking capability prognosis in electric and hybrid electric vehicles," *J. Power Sources*, vol. 144, no. 2, pp. 418–425, 2005.
[157] N. D. C. and N. J. Evans, "An Introduction to Electrochemical Impedance Measurement," no. 05/May/1999. 1999.
[158] E. Barsoukov and J. R. Macdonald, *Impedance spectroscopy : theory, experiment, and applications*, 2nd ed. /. Hoboken, N.J.: [Chichester] : Wiley-Interscience, 2005.
[159] N. D. Cogger and N. J. Evans, "An Introduction to Electrochemical Impedance Measurement," 1999. [Online]. Available: http://www.korozja.pl/html/eis/technote06.pdf.
[160] A. M. Kauffman, "Understanding electrochemical cell," 1997. [Online]. Available: http://www.korozja.pl/html/eis/technote17.pdf.
[161] J. Xu, C. C. Mi, B. Cao, and J. Cao, "A new method to estimate the state of charge of lithium-ion batteries based on the battery impedance model," *J. Power Sources*, vol. 233, no. 0, pp. 277–284, 2013.
[162] R. Li, J. Wu, H. Wang, and G. Li, "Prediction of state of charge of Lithium-ion rechargeable battery with electrochemical impedance spectroscopy theory," in *Industrial Electronics and Applications (ICIEA), 2010 the 5th IEEE Conference on*, 2010, pp. 684–688.
[163] O. S. Mendoza-Hernandez, H. Ishikawa, Y. Nishikawa, Y. Maruyama, Y. Sone, and M. Umeda, "State of Charge Dependency of Graphitized-Carbon-Based Reactions in a Lithium-ion Secondary Cell Studied by Electrochemical Impedance Spectroscopy," *Electrochim. Acta*, vol. 131, no. 0, pp. 168–173, 2014.
[164] L. Wang, J. Zhao, X. He, J. Gao, J. Li, C. Wan, and C. Jiang, "Electrochemical Impedance Spectroscopy (EIS) Study of LiNi1/3Co1/3Mn1/3O2 for Li-ion Batteries," *Int. J. Electrochem. Sci.*, vol. 7, p. 345, 2012.
[165] M. Swierczynski, D. I. Stroe, A. I. Stan, R. Teodorescu, and D. U. Sauer, "Selection and Performance-Degradation Modeling of LiMO2Li4Ti5O12 and LiFePO4 Battery Cells as Suitable Energy Storage Systems for Grid Integration With Wind Power Plants: An Example for the Primary Frequency Regulation Service," *Sustain. Energy, IEEE Trans.*, vol. 5, no. 1, pp. 90–101, 2014.
[166] H. Li, X. Huang, and L. Chen, "Electrochemical impedance spectroscopy study of SnO and nano-SnO anodes in lithium rechargeable batteries," *J. Power Sources*, vol. 81–82, no. 0, pp. 340–345, 1999.
[167] U. Tröltzsch, O. Kanoun, and H.-R. Tränkler, "Characterizing aging effects of lithium ion batteries by impedance spectroscopy," *Electrochim. Acta*, vol. 51, no. 8–9, pp. 1664–1672, 2006.
[168] B.-L. He, B. Dong, and H.-L. Li, "Preparation and electrochemical properties of Ag-modified TiO2 nanotube anode material for lithium–ion battery," *Electrochem. commun.*, vol. 9, no. 3, pp. 425–430, 2007.
[169] D. Andre, M. Meiler, K. Steiner, C. Wimmer, T. Soczka-Guth, and D. U. Sauer, "Characterization of high-power lithium-ion batteries by electrochemical impedance spectroscopy. I. Experimental investigation," *J. Power Sources*, vol. 196, no. 12, pp. 5334–5341, 2011.
[170] S. Tippmann, D. Walper, L. Balboa, B. Spier, and W. G. Bessler, "Low-temperature charging of lithium-ion cells part I: Electrochemical modeling and experimental investigation of degradation behavior," *J. Power Sources*, vol. 252, no. 0, pp. 305–316, 2014.
[171] P. S. Attidekou, S. Lambert, M. Armstrong, J. Widmer, K. Scott, and P. A. Christensen, "A study of 40 Ah lithium ion batteries at zero percent state of charge as a function of

temperature," *J. Power Sources*, vol. 269, no. 0, pp. 694–703, 2014.
[172] Z.-Q. Huo, Y.-T. Cui, D. Wang, Y. Dong, and L. Chen, "The influence of temperature on a nutty-cake structural material: LiMn1−xFexPO4 composite with LiFePO4 core and carbon outer layer for lithium-ion battery," *J. Power Sources*, vol. 245, no. 0, pp. 331–336, 2014.
[173] J. Vetter, P. Novák, M. R. Wagner, C. Veit, K. C. Möller, J. O. Besenhard, M. Winter, M. Wohlfahrt-Mehrens, C. Vogler, and A. Hammouche, "Ageing mechanisms in lithium-ion batteries," *J. Power Sources*, vol. 147, no. 1–2, pp. 269–281, 2005.
[174] J. Shim, R. Kostecki, T. Richardson, X. Song, and K. A. Striebel, "Electrochemical analysis for cycle performance and capacity fading of a lithium-ion battery cycled at elevated temperature," *J. Power Sources*, vol. 112, no. 1, pp. 222–230, 2002.
[175] L. Liao, P. Zuo, Y. Ma, X. Chen, Y. An, Y. Gao, and G. Yin, "Effects of temperature on charge/discharge behaviors of LiFePO4 cathode for Li-ion batteries," *Electrochim. Acta*, vol. 60, no. 0, pp. 269–273, 2012.
[176] D. Aurbach, B. Markovsky, Y. Talyossef, G. Salitra, H.-J. Kim, and S. Choi, "Studies of cycling behavior, ageing, and interfacial reactions of LiNi0.5Mn1.5O4 and carbon electrodes for lithium-ion 5-V cells," *J. Power Sources*, vol. 162, no. 2, pp. 780–789, 2006.
[177] M. Mirzaeian and P. J. Hall, "Characterizing capacity loss of lithium oxygen batteries by impedance spectroscopy," *J. Power Sources*, vol. 195, no. 19, pp. 6817–6824, 2010.
[178] D. Andre, M. Meiler, K. Steiner, H. Walz, T. Soczka-Guth, and D. U. Sauer, "Characterization of high-power lithium-ion batteries by electrochemical impedance spectroscopy. II: Modelling," *J. Power Sources*, vol. 196, no. 12, pp. 5349–5356, 2011.
[179] D. Andre, C. Appel, T. Soczka-Guth, and D. U. Sauer, "Advanced mathematical methods of SOC and SOH estimation for lithium-ion batteries," *J. Power Sources*, vol. 224, no. 0, pp. 20–27, 2013.
[180] J. Li, J. Klee Barillas, C. Guenther, and M. A. Danzer, "A comparative study of state of charge estimation algorithms for LiFePO4 batteries used in electric vehicles," *J. Power Sources*, vol. 230, no. 0, pp. 244–250, 2013.
[181] F. Sun, R. Xiong, and H. He, "Estimation of state-of-charge and state-of-power capability of lithium-ion battery considering varying health conditions," *J. Power Sources*, vol. 259, no. 0, pp. 166–176, 2014.
[182] F. Xu, C. Liu, W. Feng, J. Nie, H. Li, X. Huang, and Z. Zhou, "Molten salt of lithium bis(fluorosulfonyl)imide (LiFSI)-potassium bis(fluorosulfonyl)imide (KFSI) as electrolyte for the natural graphite/LiFePO4 lithium-ion cell," *Electrochim. Acta*, vol. 135, no. 0, pp. 217–223, 2014.
[183] M. Umeda, K. Dokko, Y. Fujita, M. Mohamedi, I. Uchida, and J. R. Selman, "Electrochemical impedance study of Li-ion insertion into mesocarbon microbead single particle electrode: Part I. Graphitized carbon," *Electrochim. Acta*, vol. 47, no. 6, pp. 885–890, 2001.
[184] K. Dokko, Y. Fujita, M. Mohamedi, M. Umeda, I. Uchida, and J. R. Selman, "Electrochemical impedance study of Li-ion insertion into mesocarbon microbead single particle electrode: Part II. Disordered carbon," *Electrochim. Acta*, vol. 47, no. 6, pp. 933–938, 2001.
[185] M. Kerlau, M. Marcinek, V. Srinivasan, and R. M. Kostecki, "Studies of local degradation phenomena in composite cathodes for lithium-ion batteries," *Electrochim. Acta*, vol. 52, no. 17, pp. 5422–5429, 2007.
[186] N.-S. Choi, J.-S. Kim, R.-Z. Yin, and S.-S. Kim, "Electrochemical properties of lithium vanadium oxide as an anode material for lithium-ion battery," *Mater. Chem. Phys.*, vol. 116, no. 2–3, pp. 603–606, 2009.
[187] G. Ning, B. Haran, and B. N. Popov, "Capacity fade study of lithium-ion batteries cycled at high discharge rates," *J. Power Sources*, vol. 117, no. 1–2, pp. 160–169, 2003.
[188] K. Asakura, M. Shimomura, and T. Shodai, "Study of life evaluation methods for Li-ion batteries for backup applications," *J. Power Sources*, vol. 119–121, no. 0, pp. 902–905, 2003.
[189] Y. Zhang, C.-Y. Wang, and X. Tang, "Cycling degradation of an automotive LiFePO4 lithium-ion battery," *J. Power Sources*, vol. 196, no. 3, pp. 1513–1520, 2011.
[190] B. V Ratnakumar, M. C. Smart, and S. Surampudia, "Electrochemical impedance

spectroscopy and its applications to lithium ion cells," in *Battery Conference on Applications and Advances, 2002. The Seventeenth Annual*, 2002, pp. 273–277.
[191] H. Wang, L. He, J. Sun, S. Liu, and F. Wu, "Study on correlation with SOH and EIS model of Li-ion battery," in *Strategic Technology (IFOST), 2011 6th International Forum on*, 2011, vol. 1, pp. 261–264.
[192] Q.-C. Zhuang, T. Wei, L.-L. Du, Y.-L. Cui, L. Fang, and S.-G. Sun, "An Electrochemical Impedance Spectroscopic Study of the Electronic and Ionic Transport Properties of Spinel LiMn2O4," *J. Phys. Chem. C*, vol. 114, no. 18, pp. 8614–8621, 2010.
[193] J. P. Christophersen, J. L. Morrison, and W. H. Morrison, "Acquiring impedance spectra from diode-coupled primary batteries to determine health and state of charge," in *Aerospace Conference, 2013 IEEE*, 2013, pp. 1–10.
[194] J. P. Christophersen, C. D. Ho, and J. L. Morrison, "Rapid Impedance Spectrum Measurement for Onboard State-of-Health Applications," in *45th Power Sources Conference Proceedings*, 2012.
[195] S. Wang, J. Zhang, and C. Chen, "Fe3O4 submicron spheroids as anode materials for lithium-ion batteries with stable and high electrochemical performance," *J. Power Sources*, vol. 195, no. 16, pp. 5379–5381, 2010.
[196] C. H. Chen, J. Liu, and K. Amine, "Symmetric cell approach and impedance spectroscopy of high power lithium-ion batteries," *J. Power Sources*, vol. 96, no. 2, pp. 321–328, 2001.
[197] R. Ruffo, S. S. Hong, C. K. Chan, R. A. Huggins, and Y. Cui, "Impedance Analysis of Silicon Nanowire Lithium Ion Battery Anodes," *J. Phys. Chem. C*, vol. 113, no. 26, pp. 11390–11398, 2009.
[198] N. Dimov, S. Kugino, and M. Yoshio, "Carbon-coated silicon as anode material for lithium ion batteries: advantages and limitations," *Electrochim. Acta*, vol. 48, no. 11, pp. 1579–1587, 2003.
[199] M. Takahashi, S. Tobishima, K. Takei, and Y. Sakurai, "Reaction behavior of LiFePO4 as a cathode material for rechargeable lithium batteries," *Solid State Ionics*, vol. 148, no. 3–4, pp. 283–289, 2002.
[200] F. Nobili, F. Croce, B. Scrosati, and R. Marassi, "Electronic and Electrochemical Properties of LixNi1-yCoyO2 Cathodes Studied by Impedance Spectroscopy," *Chem. Mater.*, vol. 13, no. 5, pp. 1642–1646, 2001.
[201] F. Gao and Z. Tang, "Kinetic behavior of LiFePO4/C cathode material for lithium-ion batteries," *Electrochim. Acta*, vol. 53, no. 15, pp. 5071–5075, 2008.
[202] J. Y. Song, H. H. Lee, Y. Y. Wang, and C. C. Wan, "Two- and three-electrode impedance spectroscopy of lithium-ion batteries," *J. Power Sources*, vol. 111, no. 2, pp. 255–267, 2002.
[203] A.-K. Hjelm and G. Lindbergh, "Experimental and theoretical analysis of LiMn2O4 cathodes for use in rechargeable lithium batteries by electrochemical impedance spectroscopy (EIS)," *Electrochim. Acta*, vol. 47, no. 11, pp. 1747–1759, 2002.
[204] P. P. Prosini, R. Mancini, L. Petrucci, V. Contini, and P. Villano, "Li4Ti5O12 as anode in all-solid-state, plastic, lithium-ion batteries for low-power applications," *Solid State Ionics*, vol. 144, no. 1–2, pp. 185–192, 2001.
[205] D. Zhang, B. S. Haran, A. Durairajan, R. E. White, Y. Podrazhansky, and B. N. Popov, "Studies on capacity fade of lithium-ion batteries," *J. Power Sources*, vol. 91, no. 2, pp. 122–129, 2000.
[206] M. V Reddy, R. Jose, A. Le Viet, K. I. Ozoemena, B. V. R. Chowdari, and S. Ramakrishna, "Studies on the lithium ion diffusion coefficients of electrospun Nb2O5 nanostructures using galvanostatic intermittent titration and electrochemical impedance spectroscopy," *Electrochim. Acta*, vol. 128, no. 0, pp. 198–202, 2014.
[207] Q.-C. Zhuang, S. Xu, X. Qiu, Y. Cui, L. Fang, S. Sun, and 孙世刚, "Diagnosis of electrochemical impedance spectroscopy in lithium-ion batteries," *Prog. Chem*, vol. 22, p. 1044, 2010.
[208] J. G. Zhu, Z. C. Sun, X. Z. Wei, and H. F. Dai, "A new lithium-ion battery internal temperature on-line estimate method based on electrochemical impedance spectroscopy measurement," *J. Power Sources*, vol. 274, pp. 990–1004, 2015.

[209] W. C. ltd, “Battery and Energy Technologies,” 2005. [Online]. Available: http://www.mpoweruk.com/life.htm.
[210] S. M. Rezaei Niya, M. Hejabi, and F. Gobal, “Estimation of the kinetic parameters of processes at the negative plate of lead-acid batteries by impedance studies,” *J. Power Sources*, vol. 195, no. 17, pp. 5789–5793, 2010.
[211] M. Hejabi, A. Oweisi, and N. Gharib, “Modeling of kinetic behavior of the lead dioxide electrode in a lead–acid battery by means of electrochemical impedance spectroscopy,” *J. Power Sources*, vol. 158, no. 2, pp. 944–948, 2006.
[212] A. Li, Y. Cheni, H. Chen, D. Shu, W. Li, H. Wang, C. Dou, W. Zhang, and S. Chen, “Electrochemical behavior and application of lead–lanthanum alloys for positive grids of lead-acid batteries,” *J. Power Sources*, vol. 189, no. 2, pp. 1204–1211, 2009.
[213] C. V D’Alkaine, P. Mengarda, and P. R. Impinnisi, “Discharge mechanisms and electrochemical impedance spectroscopy measurements of single negative and positive lead-acid battery plates,” *J. Power Sources*, vol. 191, no. 1, pp. 28–35, 2009.
[214] W. Pin-Chien, H. Wen-Chien, and C. Jiann-Fuh, “Detection on SOC of VRLA battery with EIS,” in *Future Energy Electronics Conference (IFEEC), 2013 1st International*, 2013, pp. 897–902.
[215] N. Thanh-Tuan, T. Van-Long, and C. Woojin, “Development of the intelligent charger with battery State-Of-Health estimation using online impedance spectroscopy,” in *Industrial Electronics (ISIE), 2014 IEEE 23rd International Symposium on*, 2014, pp. 454–458.
[216] E. Karden, S. Buller, and R. W. De Doncker, “A method for measurement and interpretation of impedance spectra for industrial batteries,” *J. Power Sources*, vol. 85, no. 1, pp. 72–78, 2000.
[217] A. J. Salkind, P. Singh, A. Cannone, T. Atwater, X. Wang, and D. Reisner, “Impedance modeling of intermediate size lead–acid batteries,” *J. Power Sources*, vol. 116, no. 1–2, pp. 174–184, 2003.
[218] A. Kirchev, A. Delaille, M. Perrin, E. Lemaire, and F. Mattera, “Studies of the pulse charge of lead-acid batteries for PV applications: Part II. Impedance of the positive plate revisited,” *J. Power Sources*, vol. 170, no. 2, pp. 495–512, 2007.
[219] B. Hong, L. Jiang, H. Xue, F. Liu, M. Jia, J. Li, and Y. Liu, “Characterization of nano-lead-doped active carbon and its application in lead-acid battery,” *J. Power Sources*, vol. 270, no. 0, pp. 332–341, 2014.
[220] R. De Marco, A. Lowe, M. Sercombe, and P. Singh, “An electrochemical impedance spectroscopy and scanning electron microscopy study of the influence of positive plate compression on the electrochemical behaviour of lead-acid batteries,” *Electrochim. Acta*, vol. 51, no. 10, pp. 2088–2095, 2006.
[221] B. Yang, Z. Yang, Z. Peng, and Q. Liao, “Effect of silver additive on the electrochemical performance of ZnAl-layered double hydroxide as anode material for nickel-zinc rechargeable batteries,” *Electrochim. Acta*, vol. 132, no. 0, pp. 83–90, 2014.
[222] C. Khaldi, S. Boussami, M. Tliha, S. Azizi, N. Fenineche, O. El-Kedim, H. Mathlouthi, and J. Lamloumi, “The effect of the temperature on the electrochemical properties of the hydrogen storage alloy for nickel–metal hydride accumulators,” *J. Alloys Compd.*, vol. 574, no. 0, pp. 59–66, 2013.
[223] J. Li, E. Shangguan, D. Guo, Q. Li, Z. Chang, X.-Z. Yuan, and H. Wang, “Calcium metaborate as a cathode additive to improve the high-temperature properties of nickel hydroxide electrodes for nickel–metal hydride batteries,” *J. Power Sources*, vol. 263, no. 0, pp. 110–117, 2014.
[224] S. Cheng, J. Zhang, M. Zhao, and C. Cao, “Electrochemical impedance spectroscopy study of Ni/MH batteries,” *J. Alloys Compd.*, vol. 293–295, no. 0, pp. 814–820, 1999.
[225] S. N. Begum, V. S. Muralidharan, and C. A. Basha, “Electrochemical investigations and characterization of a metal hydride alloy (MmNi3.6Al0.4Co0.7Mn0.3) for nickel metal hydride batteries,” *J. Alloys Compd.*, vol. 467, no. 1–2, pp. 124–129, 2009.
[226] S. R. Nelatury and P. Singh, “Equivalent circuit parameters of nickel/metal hydride batteries from sparse impedance measurements,” *J. Power Sources*, vol. 132, no. 1–2, pp. 309–314, 2004.

[227] N. Cui, J. L. Luo, and K. T. Chuang, “Nickel–metal hydride (Ni–MH) battery using Mg2Ni-type hydrogen storage alloy,” *J. Alloys Compd.*, vol. 302, no. 1–2, pp. 218–226, 2000.
[228] O. Aaboubi, J. Amblard, J. P. Chopart, and A. Olivier, “A Temperature and Electrochemical Impedance Spectroscopy Analysis of Nickel Electrocrystallization from a Watts Solution,” *J. Phys. Chem. B*, vol. 105, no. 30, pp. 7205–7210, 2001.
[229] L. F. Q. P. Marchesi, F. R. Simões, L. A. Pocrifka, and E. C. Pereira, “Investigation of Polypyrrole Degradation Using Electrochemical Impedance Spectroscopy,” *J. Phys. Chem. B*, vol. 115, no. 31, pp. 9570–9575, 2011.
[230] M. Galeotti, C. Giammanco, L. Cina, S. Cordiner, and A. Di Carlo, “Diagnostic methods for the evaluation of the state of health (SOH) of NiMH batteries through electrochemical impedance spectroscopy,” in *Industrial Electronics (ISIE), 2014 IEEE 23rd International Symposium on*, 2014, pp. 1641–1646.
[231] A. Hammouche, E. Karden, and R. W. De Doncker, “Monitoring state-of-charge of Ni–MH and Ni–Cd batteries using impedance spectroscopy,” *J. Power Sources*, vol. 127, no. 1–2, pp. 105–111, 2004.
[232] Y. Xu, “The electrochemical behavior of Ni–MH battery, Ni(OH)2 electrode and metal hydride electrode,” *Int. J. Hydrogen Energy*, vol. 29, no. 7, pp. 749–757, 2004.
[233] E. Ferg, C. Rossouw, and P. Loyson, “The testing of batteries linked to supercapacitors with electrochemical impedance spectroscopy: A comparison between Li-ion and valve regulated lead acid batteries,” *J. Power Sources*, vol. 226, no. 0, pp. 299–305, 2013.
[234] S. Buller, E. Karden, D. Kok, and R. W. De Doncker, “Modeling the dynamic behavior of supercapacitors using impedance spectroscopy,” in *Industry Applications Conference, 2001. Thirty-Sixth IAS Annual Meeting. Conference Record of the 2001 IEEE*, 2001, vol. 4, pp. 2500–2504.
[235] S. Buller, M. Thele, R. W. A. De Doncker, and E. Karden, “Impedance-based simulation models of supercapacitors and Li-ion batteries for power electronic applications,” *Ind. Appl. IEEE Trans.*, vol. 41, no. 3, pp. 742–747, 2005.
[236] A. Hammar, P. Venet, R. Lallemand, G. Coquery, and G. Rojat, “Study of Accelerated Aging of Supercapacitors for Transport Applications,” *Ind. Electron. IEEE Trans.*, vol. 57, no. 12, pp. 3972–3979, 2010.
[237] K. Sang-Hyun and C. Woojin, “A method for performance evaluation and optimal sizing of the supercapacitor module by the Electrochemical Impedance Spectroscopy,” in *Telecommunications Energy Conference, 2009. INTELEC 2009. 31st International*, 2009, pp. 1–6.
[238] R. A. Kumar, M. S. Suresh, and J. Nagaraju, “Facility to measure solar cell ac parameters using an impedance spectroscopy technique,” *Rev. Sci. Instrum.*, vol. 72, no. 8, pp. 3422–3426, 2001.
[239] F. Fabregat-Santiago, J. Bisquert, E. Palomares, S. A. Haque, and J. R. Durrant, “Impedance spectroscopy study of dye-sensitized solar cells with undoped spiro-OMeTAD as hole conductor,” *J. Appl. Phys.*, vol. 100, no. 3, pp. 34510–34517, 2006.
[240] F. Fabregat-Santiago, J. Bisquert, G. Garcia-Belmonte, G. Boschloo, and A. Hagfeldt, “Influence of electrolyte in transport and recombination in dye-sensitized solar cells studied by impedance spectroscopy,” *Sol. Energy Mater. Sol. Cells*, vol. 87, no. 1–4, pp. 117–131, 2005.
[241] H. Seo, M.-K. Son, J.-K. Kim, J. Choi, S. Choi, S.-K. Kim, and H.-J. Kim, “Analysis of current loss from a series-parallel combination of dye-sensitized solar cells using electrochemical impedance spectroscopy,” *Photonics Nanostructures - Fundam. Appl.*, vol. 10, no. 4, pp. 568–574, 2012.
[242] M. Lohrasbi, P. Pattanapanishsawat, M. Isenberg, and S. S. C. Chuang, “Degradation study of dye-sensitized solar cells by electrochemical impedance and FTIR spectroscopy,” in *Energytech, 2013 IEEE*, 2013, pp. 1–4.
[243] M. Shanmugam and M. F. Baroughi, “Characterization of interfacial charge transport and recombination by impedance spectroscopy on SiO2 coated TiO2 based dye sensitized solar cells,” in *Photovoltaic Specialists Conference (PVSC), 2011 37th IEEE*, 2011, pp. 2656–2660.

[244] Y. Zhang, L. Li, S. Yuan, G. Li, and W. Zhang, “Electrical properties of the interfaces in bulk heterojunction organic solar cells investigated by electrochemical impedance spectroscopy,” *Electrochim. Acta*, vol. 109, no. 0, pp. 221–225, 2013.
[245] E. Parvazian, F. Karimzadeh, and M. H. Enayati, “Photovoltaic Characterization and Electrochemical Impedance Spectroscopy Analysis of Dye-Sensitized Solar Cells Based on Composite TiO2–MWCNT Photoelectrodes,” *J. Electron. Mater.*, vol. 43, no. 5, pp. 1450–1459, 2014.
[246] P. Hartmann, N. Zamel, and D. Gerteisen, “Position dependent analysis of membrane electrode assembly degradation of a direct methanol fuel cell via electrochemical impedance spectroscopy,” *J. Power Sources*, vol. 241, no. 0, pp. 127–135, 2013.
[247] H. Ping Wu, L. Lin Li, C. Chon Chen, and E. W. Guang Diau, “Anodic TiO2 Nanotube Arrays for Dye-Sensitized Solar Cells Characterized by Electrochemical Impedance Spectroscopy,” *Ceram. Int.*, vol. 38, no. 8, pp. 6253–6266, 2012.
[248] S. Sarker, H. W. Seo, and D. M. Kim, “Electrochemical impedance spectroscopy of dye-sensitized solar cells with thermally degraded N719 loaded TiO2,” *Chem. Phys. Lett.*, vol. 585, no. 0, pp. 193–197, 2013.
[249] C. Justin Raj, S. N. Karthick, A. Dennyson Savariraj, K. V Hemalatha, S.-K. Park, H.-J. Kim, and K. Prabakar, “Electrochemical properties of TiO2 encapsulated ZnO nanorod aggregates dye sensitized solar cells,” *J. Alloys Compd.*, vol. 537, no. 0, pp. 159–164, 2012.
[250] C. He, L. Zhao, Z. Zheng, and F. Lu, “Determination of Electron Diffusion Coefficient and Lifetime in Dye-Sensitized Solar Cells by Electrochemical Impedance Spectroscopy at High Fermi Level Conditions,” *J. Phys. Chem. C*, vol. 112, no. 48, pp. 18730–18733, 2008.
[251] A. Hauch and A. Georg, “Diffusion in the electrolyte and charge-transfer reaction at the platinum electrode in dye-sensitized solar cells,” *Electrochim. Acta*, vol. 46, no. 22, pp. 3457–3466, 2001.
[252] H.-L. Lu, T. F. R. Shen, S.-T. Huang, Y.-L. Tung, and T. C. K. Yang, “The degradation of dye sensitized solar cell in the presence of water isotopes,” *Sol. Energy Mater. Sol. Cells*, vol. 95, no. 7, pp. 1624–1629, 2011.
[253] N. Kato, Y. Takeda, K. Higuchi, A. Takeichi, E. Sudo, H. Tanaka, T. Motohiro, T. Sano, and T. Toyoda, “Degradation analysis of dye-sensitized solar cell module after long-term stability test under outdoor working condition,” *Sol. Energy Mater. Sol. Cells*, vol. 93, no. 6–7, pp. 893–897, 2009.
[254] F. Fabregat-Santiago, G. Garcia-Belmonte, I. Mora-Seró, and J. Bisquert, “Characterization of nanostructured hybrid and organic solar cells by impedance spectroscopy,” *Phys. Chem. Chem. Phys.*, vol. 13, no. 20, pp. 9083–9118, 2011.
[255] D. A. Howey, P. D. Mitcheson, V. Yufit, G. J. Offer, and N. P. Brandon, “Online Measurement of Battery Impedance Using Motor Controller Excitation,” *Veh. Technol. IEEE Trans.*, vol. 63, no. 6, pp. 2557–2566, 2014.
[256] H. Wangxin and J. A. Qahouq, “An Online Battery Impedance Measurement Method Using DC-DC Power Converter Control,” *Ind. Electron. IEEE Trans.*, vol. 61, no. 11, pp. 5987–5995, 2014.
[257] J. A. A. Qahouq, “Online Battery Impedance Spectrum Measurement Method,” in *2016 IEEE Applied Power Electronics Conference and Exposition (APEC)*, 2016, pp. 3611–3615.
[258] D. Depernet, O. Ba, and A. Berthon, “Online impedance spectroscopy of lead acid batteries for storage management of a standalone power plant,” *J. Power Sources*, vol. 219, pp. 65–74, 2012.
[259] P. Neti and S. Grubic, “Online broadband insulation spectroscopy of induction machines using signal injection,” in *2014 IEEE Energy Conversion Congress and Exposition (ECCE)*, 2014, pp. 630–637.
[260] L. Zhao, Q. Fu, and Z. Liu, “An electrochemical impedance spectroscopy measurement system for electric vehicle batteries,” in *2016 35th Chinese Control Conference (CCC)*, 2016, pp. 5050–5055.
[261] X. Wang, X. Wei, H. Dai, and Q. Wu, “State Estimation of Lithium Ion Battery Based on Electrochemical Impedance Spectroscopy with On-Board Impedance Measurement System,” in *2015 IEEE Vehicle Power and Propulsion Conference (VPPC)*, 2015, pp. 1–5.

[262] L.-R. Chen, S.-L. Wu, D.-T. Shieh, and T.-R. Chen, “Sinusoidal-Ripple-Current Charging Strategy and Optimal Charging Frequency Study for Li-Ion Batteries,” *IEEE Trans. Ind. Electron.*, vol. 60, no. 1, pp. 88–97, Jan. 2013.
[263] S.-Y. Cho, I.-O. Lee, J.-I. Baek, and G.-W. Moon, “Battery Impedance Analysis Considering DC Component in Sinusoidal Ripple-Current Charging,” *IEEE Trans. Ind. Electron.*, vol. 63, no. 3, pp. 1561–1573, Mar. 2016.
[264] U. Tröltzsch and O. Kanoun, “Miniaturized Impedance Measurement System for Battery Diagnosis,” in *Proceedings SENSOR 2009, Volume I*, 2009, pp. 251–256.
[265] A. J. Fairweather, M. P. Foster, and D. A. Stone, “VRLA battery parameter identification using pseudo random binary sequences (PRBS),” in *Power Electronics, Machines and Drives (PEMD 2010), 5th IET International Conference on*, 2010, pp. 1–6.
[266] M. Ranieri, D. Alberto, H. Piret, and V. Cattin, “Electronic module for the thermal monitoring of a Li-ion battery cell through the electrochemical impedance estimation,” in *2016 22nd International Workshop on Thermal Investigations of ICs and Systems (THERMINIC)*, 2016, pp. 294–297.
[267] E. Din, C. Schaef, K. Moffat, and J. T. Stauth, “Online spectroscopic diagnostics implemented in an efficient battery management system,” in *2015 IEEE 16th Workshop on Control and Modeling for Power Electronics, COMPEL 2015*, 2015.
[268] N. Katayama and S. Kogoshi, “Real-Time Electrochemical Impedance Diagnosis for Fuel Cells Using a DC-DC Converter,” *IEEE Trans. Energy Convers.*, vol. 30, no. 2, pp. 707–713, Jun. 2015.
[269] J. A. Abu Qahouq and Z. Xia, “Single-Perturbation-Cycle Online Battery Impedance Spectrum Measurement Method with Closed-Loop Control of Power Converter,” *IEEE Trans. Ind. Electron.*, pp. 1–1, 2017.
[270] J. Groot, “State-of-health estimation of Li-ion batteries: cycle life test methods,” Chalmers University of technology, 2012.
[271] U. Tröltzsch, O. Kanoun, and H.-R. Tränkler, “Characterizing aging effects of lithium ion batteries by impedance spectroscopy,” *Electrochim. Acta*, vol. 51, no. 8–9, pp. 1664–1672, 2006.
[272] B. S. Haran, P. Ramadass, R. E. W. And, and B. N. Popov, “Capacity fade of Li-ion cells cycled at different temperaturesNo Title,” in *Seventeenth Annual Battery Conference on Applications and Advances*, 2002, pp. 13–18.
[273] Abraham, D.P.Knuth, J.L.Dees, D.W.Bloom, and J. P. I.Christophersen, “Performance degradation of high-power lithium-ion cells—Electrochemistry of harvested electrodes,” *J. Power Sources*, vol. 170, no. 2, pp. 465–475, 2007.
[274] E. V. Thomas, I. Bloom, J. P. Christophersen, and V. S. Battaglia, “Statistical methodology for predicting the life of lithium-ion cells via accelerated degradation testing,” *Power source*, vol. 184, no. 1, pp. 312–317, 2008.
[275] C. A. N. Published, C. Life, C. Be, U. To, E. Pv, and B. Life, “CHOOSING THE RIGHT BATTERY THE IMPORTANCE OF TESTING PV BATTERIES TO THE IEC 61427 STANDARD.”
[276] IEA PVPS, “Testing of batteries used in Stand Alone PV Power Supply Systems,” 2002.
[277] B. Y. Liaw, E. P. Roth, R. G. Jungst, G. Nagasubramanian, H. L. Case, and D. H. Doughty, “Correlation of Arrhenius behaviors in power and capacity fades with cell impedance and heat generation in cylindrical lithium-ion cells.”
[278] N. Ogihara, Y. Igarashi, A. Kamakura, K. Naoi, Y. Kusachi, and K. Utsugi, “Disordered carbon negative electrode for electrochemical capacitors and high-rate batteries,” *Electrochim. Acta*, vol. 52, pp. 1713–1720, 2006.
[279] British. Standard. BS. 7671., *Requirements for Electrical Installations. IET Wiring Regulations*, 17th ed. 2008.
[280] *IEEE Recommended Practice for Grounding of Industrial and Commercial Power Systems - Redline*. IEEE Std 142-2007 (Revision of IEEE Std 142-1991) - Redline, 2007.
[281] Herve Nyirinkwaya, “Low voltage high resistance grounding system basics, C-HRG technical information, and adjustment procedure,” 2014.
[282] P. Argo Dahono, A. Purwadi, and T. Kataoka, “A new approach for harmonic analysis of

three-phase current-type PWM converters," in *IAS '97. Conference Record of the 1997 IEEE Industry Applications Conference Thirty-Second IAS Annual Meeting*, vol. 2, pp. 1487–1495.
[283] "9 Basic dc to dc converter circuits."
[284] P. P. Biringer and M. A. Slonim, "Determination of Harmonics of Converter Current and/or Voltage Waveforms (New Method for Fourier Coefficient Calculations), Part I: Fourier Coefficients of Homogeneous Functions," *IEEE Trans. Ind. Appl.*, vol. IA-16, no. 2, pp. 242–247, Mar. 1980.
[285] M. A. Slonim and P. P. Biringer, "Determination of Harmonics of Converter Current and/or Voltage Waveforms (New Method for Fourier Coefficient Calculations), Part II: Fourier Coefficients of Nonhomogeneous Functions," *IEEE Trans. Ind. Appl.*, vol. IA-16, no. 2, pp. 248–253, Mar. 1980.
[286] J. Belanger, P. Venne, and J.-N. Paquin, "The What, Where and Why of Real-Time Simulation," *Planet RT*, vol. 1, no. 0, pp. 37–49, 2010.
[287] H. W. Dommel, "Digital Computer Solution of Electromagnetic Transients in Single-and Multiphase Networks," *IEEE Trans. Power Appar. Syst.*, vol. PAS-88, no. 4, pp. 388–399, 1969.
[288] A. C. Baisden and A. Emadi, "ADVISOR-based model of a battery and an ultra-capacitor energy source for hybrid electric vehicles," *IEEE Trans. Veh. Technol.*, vol. 53, no. 1, pp. 199–205, Jan. 2004.
[289] S. M. Lukic, J. Cao, R. C. Bansal, F. Rodriguez, and A. Emadi, "Energy storage systems for automotive applications," *IEEE Transactions on Industrial Electronics*, vol. 55, no. 6. pp. 2258–2267, 2008.
[290] K. Vitols, "Redesign of passive balancing battery management system to active balancing with integrated charger converter," in *Electronic Conference (BEC), 2014 14th Biennial Baltic*, 2014, pp. 241–244.
[291] T. Blank, C. Lipps, W. Ott, P. Hoffmann, and M. Weber, "Influence of environmental conditions on the sensing accuracy of Li-Ion battery management systems with passive charge balancing," in *Power Electronics and Applications (EPE'15 ECCE-Europe), 2015 17th European Conference*, 2015, pp. 1–9.
[292] W. C. Lee, D. Drury, and P. Mellor, "Comparison of passive cell balancing and active cell balancing for automotive batteries," in *2011 IEEE Vehicle Power and Propulsion Conference, VPPC 2011*, 2011.
[293] M. Daowd, N. Omar, P. van den Bossche, and J. van Mierlo, "Capacitor based battery balancing system," *World Electr. Veh. J.*, vol. 5, no. 2, pp. 385–393, 2012.
[294] M. Daowd, M. Antoine, N. Omar, P. Lataire, P. Van Den Bossche, and J. Van Mierlo, "Battery Management System—Balancing Modularization Based on a Single Switched Capacitor and Bi-Directional DC/DC Converter with the Auxiliary Battery," *Energies*, vol. 7, no. 5, p. 2897, 2014.
[295] A. Ahmed, "Series Resonant Switched Capacitor Converter for Electric Vehicle Lithium-Ion Battery Cell Voltage Equalization," Concordia University, 2012.
[296] C. Pascual and P. T. Krein, "Switched capacitor system for automatic series battery equalization," *Proc. APEC 97 - Appl. Power Electron. Conf.*, vol. 2, pp. 848–854, 1997.
[297] S. West and P. T. Krein, "Equalization of valve-regulated lead-acid batteries: issues and life test results," *Telecommun. Energy Conf. 2000. INTELEC. Twenty-second Int.*, pp. 439–446, 2000.
[298] Y. Yuanmao, K. W. E. Cheng, and Y. P. B. Yeung, "Zero-current switching switched-capacitor zero-voltage-gap automatic equalization system for series battery string," *IEEE Trans. Power Electron.*, vol. 27, no. 7, pp. 3234–3242, 2012.
[299] L.-R. Chen, C.-M. Young, N.-Y. Chu, C.-C. Li, and Y.-C. Hsiao, "A battery-balancing seven-level inverter," in *Sustainable Energy Technologies (ICSET), 2012 IEEE Third International Conference on*, 2012, pp. 211–216.
[300] Z.-Y. Chiou, C.-H. Lee, and C. Y. Wu, "Balancing Strategies for an Unbalanced LiFePO4 Battery Pack," in *2016 International Symposium on Computer, Consumer and Control (IS3C)*, 2016, pp. 204–207.
[301] V.-L. Pham, T.-T. Nguyen, D.-H. Tran, V.-B. Vu, and W. Choi, "A new cell-to-cell fast

balancing circuit for Lithium-Ion batteries in Electric Vehicles and Energy Storage System," in *Power Electronics and Motion Control Conference (IPEMC-ECCE Asia), 2016 IEEE 8th International*, 2016, pp. 2461–2465.

[302] L. Mathe, P. D. Burlacu, E. Schaltz, and R. Teodorescu, "Battery pack state of charge balancing algorithm for cascaded H-Bridge multilevel converters," in *2016 IEEE 16th International Conference on Environment and Electrical Engineering (EEEIC)*, 2016, pp. 1–6.

[303] K. Nishijima, H. Sakamoto, and K. Harada, "A PWM controlled simple and high performance battery balancing system," *IEEE Power Electron. Spec. Conf.*, vol. 1, no. c, pp. 517–520, 2000.

[304] B. Gerislioglu, F. Ozturk, A. E. Sanli, and G. Gunlu, "The multi-windings forward structure battery balancing," in *Electronics, Computer and Computation (ICECCO), 2014 11th International Conference*, 2014, pp. 1–4.

[305] S. Li, C. C. Mi, and M. Zhang, "A high-efficiency active battery-balancing circuit using multiwinding transformer," *IEEE Trans. Ind. Appl.*, vol. 49, no. 1, pp. 198–207, 2013.

[306] L. Wang, L. Wang, C. Liao, and J. Liu, "Research on battery balance system applied on HEV," in *5th IEEE Vehicle Power and Propulsion Conference, VPPC '09*, 2009, pp. 1788–1791.

[307] J. Ewanchuk and J. Salmon, "A modular balancing bridge for series connected voltage sources," *IEEE Trans. Power Electron.*, vol. 29, no. 9, pp. 4712–4722, 2014.

[308] T. H. Phung, A. Collet, and J. C. Crebier, "An optimized topology for next-to-next balancing of series-connected lithium-ion cells," *IEEE Trans. Power Electron.*, vol. 29, no. 9, pp. 4603–4613, 2014.

[309] Y. C. Hsieh, C. S. Moo, I. S. Tsai, and J. C. Cheng, "Dynamic charge equalization for series-connected batteries," in *Proceedings of the IEEE International Conference on Industrial Technology*, 2002, vol. 1, pp. 444–449.

[310] J. W. Shin, G. S. Seo, C. Y. Chun, and B. H. Cho, "Selective Flyback balancing circuit with improved balancing speed for series connected Lithium-ion batteries," in *2010 International Power Electronics Conference - ECCE Asia -, IPEC 2010*, 2010, pp. 1180–1184.

[311] H. S. Park, C. E. Kim, C. H. Kim, G. W. Moon, and J. H. Lee, "A modularized charge equalizer for an HEV lithium-ion battery string," *IEEE Trans. Ind. Electron.*, vol. 56, no. 5, pp. 1464–1476, 2009.

[312] M. Caspar, T. Eiler, and S. Hohmann, "Comparison of active battery balancing systems," in *2014 IEEE Vehicle Power and Propulsion Conference, VPPC 2014*, 2015.

[313] Z. G. Kong, C. B. Zhu, R. G. Lu, and S. K. Cheng, "Comparison and evaluation of charge equalization technique for series connected batteries," in *PESC Record - IEEE Annual Power Electronics Specialists Conference*, 2006.

[314] C. D. Rahn and C.-Y. Wang, *Battery Systems Engineering*. 2013.

[315] Y.-S. L. Y.-S. Lee, C.-Y. D. C.-Y. Duh, G.-T. C. G.-T. Chen, and S.-C. Y. S.-C. Yang, "Battery Equalization Using Bi-directional Cuk Converter in DCVM Operation," *2005 IEEE 36th Power Electron. Spec. Conf.*, pp. 765–771, 2005.

[316] W. Hong, K. S. Ng, J. H. Hu, and C. S. Moo, "Charge equalization of battery power modules in series," in *2010 International Power Electronics Conference - ECCE Asia -, IPEC 2010*, 2010, pp. 1568–1572.

[317] C. S. Moo, K. S. Ng, and Y. C. Hsieh, "Parallel operation of battery power modules," *IEEE Trans. Energy Convers.*, vol. 23, no. 2, pp. 701–707, Jun. 2008.

[318] M. Uno and K. Tanaka, "Single-switch cell voltage equalizer using multistacked buck-boost converters operating in discontinuous conduction mode for series-connected energy storage cells," *IEEE Trans. Veh. Technol.*, vol. 60, no. 8, pp. 3635–3645, Oct. 2011.

[319] C. H. Kim, H. S. Park, C. E. Kim, G. W. Moon, and J. H. Lee, "Individual charge equalization converter with parallel primary winding of transformer for series connected Lithium-Ion battery strings In an hev," *J. Power Electron.*, vol. 9, no. 3, pp. 472–480, May 2009.

[320] S. Chakraborty, a K. Jain, and N. Mohan, "Novel converter topology and algorithm for simultaneous charging and individual cell balancing of multiple Li-ion batteries," *INTELEC 2004 26th Annu. Int. Telecommun. Energy Conf.*, pp. 248–253, 2004.

[321] T. Gottwald, Z. Ye, and T. Stuart, “Equalization of EV and HEV batteries with a ramp converter,” *IEEE Trans. Aerosp. Electron. Syst.*, vol. 33, no. 1, pp. 307–312, 1997.
[322] M. Tang and T. Stuart, “Selective buck-boost equalizer for series battery packs,” *IEEE Trans. Aerosp. Electron. Syst.*, vol. 36, no. 1, pp. 201–211, 2000.
[323] “Eaton EMR4-R Earth Leakage Monitor.” [Online]. Available: http://www.moeller.net/en/products_solutions/motor_applications/control/measuring_relay/earth_leakage_monitor.jsp.
[324] “Bender Earth leakage monitoring.” [Online]. Available: http://www.bender.org/products/iso685/.
[325] “Thiim earth leakage monitor.” [Online]. Available: http://thiim.com/datasheets/ddea.pdf.
[326] B. Hirschorn, M. E. Orazem, B. Tribollet, V. Vivier, I. Frateur, and M. Musiani, “Determination of effective capacitance and film thickness from constant-phase-element parameters,” *Electrochim. Acta*, vol. 55, no. 21, pp. 6218–6227, 2010.
[327] J. Valsa and J. Vlach, “RC models of a constant phase element,” *Int. J. Circuit Theory Appl.*, vol. 41, no. 1, pp. 59–67, 2013.
[328] J.-B. Jorcin, M. E. Orazem, N. Pébère, and B. Tribollet, “CPE analysis by local electrochemical impedance spectroscopy,” *Electrochim. Acta*, vol. 51, no. 8–9, pp. 1473–1479, 2006.
[329] B. Hauke, “Basic Calculation of a Boost Converter’s Power Stage,” 2009.
[330] S. Armstrong, C. K. Lee, and W. G. Hurley, “Investigation of the harmonic response of a photovoltaic system with a solar emulator,” in *2005 European Conference on Power Electronics and Applications*, 2005, p. 8–P.8.
[331] B. Romero, G. del Pozo, B. Arredondo, J. P. Reinhardt, M. Sessler, W. U, x00Fc, and rfel, “Circuital Model Validation for S-Shaped Organic Solar Cells by Means of Impedance Spectroscopy,” *IEEE J. Photovoltaics*, vol. 5, no. 1, pp. 234–237, 2015.
[332] D. Strickland, L. Chittock, D. A. Stone, M. P. Foster, and B. Price, “Estimation of Transportation Battery Second Life for Use in Electricity Grid Systems,” *IEEE Trans. Sustain. Energy*, vol. 5, no. 3, pp. 795–803, Jul. 2014.
[333] M.-F. S. Yue -Li Shi Shou-Dong Xu, Xiang-Yun Qiu, Li Jiang, Ying-Huai Qiang, Quan-Chao Zhuang, Shi- Gang Sun, “Electrochemical Impedance Spectroscopic Study of the Electronic and Ionic Transport Properties of NiF2/C Composite,” *Int. J. Electrochem. Sci.*, vol. 6, no. 11 July 2011, p. 17, 2011.
[334] G. Instrument, “Basics of Electrochemical Impedance Spectroscopy.” [Online]. Available: https://www.gamry.com/application-notes/EIS/basics-of-electrochemical-impedance-spectroscopy/.
[335] E. T. H. Zürich, “ELECTROCHEMICAL IMPEDANCE SPECTROSCOPY.” [Online]. Available: www.nonmet.mat.ethz.ch/education/courses/ceramic2/EIS.ppt.
[336] “EIS 101,” *Diffusion and the Warburg Impedance*. [Online]. Available: http://www.lucasbard.com/eis101/08_warburg.html.
[337] J. Bisquert, G. Garcia-Belmonte, P. Bueno, E. Longo, and L. O. S. Bulhões, “Impedance of constant phase element (CPE)-blocked diffusion in film electrodes,” *J. Electroanal. Chem.*, vol. 452, no. 2, pp. 229–234, 1998.
[338] “EIS 101,” *Constant Phase Elements*. [Online]. Available: http://www.lucasbard.com/eis101/09_cpe.html.
[339] S. Buller, E. Karden, D. Kok, and R. W. De Doncker, “Modeling the dynamic behavior of supercapacitors using impedance spectroscopy,” *Ind. Appl. IEEE Trans.*, vol. 38, no. 6, pp. 1622–1626, 2002.
[340] E. Barsoukov and J. R. Macdonald, “Impedance spectroscopy : theory, experiment, and applications,” 2nd ed., Hoboken, N.J.: [Chichester] : Wiley-Interscience, 2005, p. 445.

Appendix A- Battery Nyquist plots

Despite dissimilarity in chemistry between different batteries, there are key common elements; porous electrodes, electrolyte and separator. Generally, porous electrodes comprise the energy storage materials and a conductive additive. The study of impedance of batteries based on their kinetics can give a precise evaluation of impedance response of components and comparison of different chemistries [158]. The kinetic steps of batteries were originally introduced for lithium ion batteries [158], [207], [333]. These steps are shown in Figure A1-1 and can be separated into six areas:

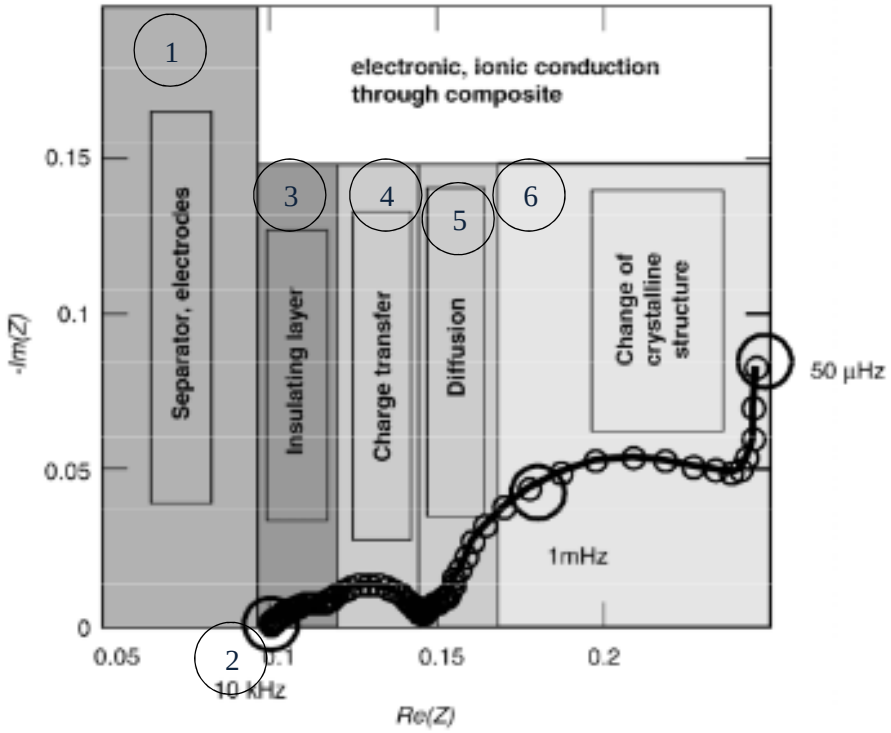

Figure A1-1 : Typical Impedance spectra of electrode intercalation by Barsoukov et al [340], [207].

1. After electrode excitation, the separated charges move into the conductive section of the active particle and ionized charges move into the active layer of the particles. This results in high frequency performance of the material above 10 kHz.
2. A factor of inductive behaviour of electrodes winding occurs at higher frequency above 10kHz.

3. The conducted ions diffuse via the insulated surface of the particles layer.
4. The electron charges transfer from the active material layer because of electrochemical reaction in active particles surface.
5. Ions diffuse into the solid phase and cause phase-transfer where a capacitive behaviour is presented. This reaction presented as a semicircle and a straight line in frequency range of 0.15 kHz - 1mHz.
6. Creation of the crystalline layer in the battery due to phase-transfer from 1mHz to 50μHz.

The key components in the Nyquist plot may include the following;

Inductor: At high frequency, the electrochemical impedance of the cell appears inductive. In some EIS analysis, it is described as an inductive behaviour of the system and in others, it is presented as an error in measurement due to non-ideal perturbation signal and measurement errors [334].

Charge Transfer Resistor: This is also called faradaic resistor, R_{ct}. This resistor represents the interface between the electrolyte and the working electrode (WE). In an equivalent circuit, it is generally presented in a parallel connection with a double layer capacitor.

Double Layer Capacitor: When the electrode is dipped into an electrolyte, the positive and negative charge separate, due to effect of the electrolyte atoms. A fixed layer of positive ions cover the electrode surface. In the electrolyte, negative ions attract to the bare surface and form a layer near the electrode bar. The interface between the fixed layer of the electrode surface and the diffused layer characterises a double layer capacitor C_{dl}.

Impedance of Electrolyte: Generally in the battery electrolyte, conductive salts are used to increase the conductivity. Within the EIS process, conductivity of the electrolyte and its impedance is small and is presented as a series resistor in the high frequency region. This is due to adsorption of ions in the charge and discharge reaction and the thin layer of electrolyte. To measure the conductivity and impedance of electrolyte excluding electrode effects, the four-terminal connection measurement techniques should be implemented.

Surface Impedance: Particle surface impedance involves a double layer formation, adsorption, and electrochemical reaction. Because of the limit in adsorbed material diffusion inside active materials especially in metal anodes [158], it is suggested that the Warburg impedance be used to present the adsorption effect. The Warburg impedance is a frequency dependant impedance created by the effect of diffusion. It appears as a line with a phase shift and slope of 45° in bode and complex plot. The impedance is very small at high frequency and can only be observed at low frequency [157], [335]. If the diffusion has an infinite thickness in its layer the impedance is an infinite Warburg impedance.

Diffusion Impedance: Crystals of the batteries materials are less active, compared to the material surface because of their dense structure. Ions can easily exchange within the open crystalline structure. Further, solid-state diffusion is proposed to protect the crystalline structure from the compress form and control the ion transfer inside the crystal. In other word diffusion is presented as a result of the species concentration at the electrolyte/electrode interface (depending on applied potential). It is generally followed by a resistor (i.e. represent the charge transfer process between electrode and solution) in series in equivalent circuits. In case of semi-infinite diffusion; the impedance of the diffusion is represented as positive real and negative imaginary part with same magnitude and phase angle of -45˚.

Corrosion: In electrochemical characterisation of the power system/batteries, some heterogeneity in behaviour can be observed. This heterogeneity occurs at the termination of the impedance curve and looks like a negative resistor mode as the frequency decreases. This is due to sudden dissolution and conduction of the mobile ions in electrolyte and electrode surface, which leads to the low current flow through the solution. This chemical process can be defined as a result of three corrosion effect mechanisms.

Table A-1: Description of different cause of corrosion

Corrosion types	Description
Active dissolution	This mechanism appeared when the metal dissolves into the solution and electrolyte.
Active-Passive Transition	The active/passive mechanism generally happens when the electrode-electrolyte interface of a battery is abounded and covered by the product of corrosion. So the charge conduction into the electrolyte is blocked and a passive layer due to the concentration of the charges is created.
Passive State	Because of electrical potential and concentration of mobile ions/charges; the ions from the metal-solution interfaces into the electrolyte though the corroding surface exchange instantly.

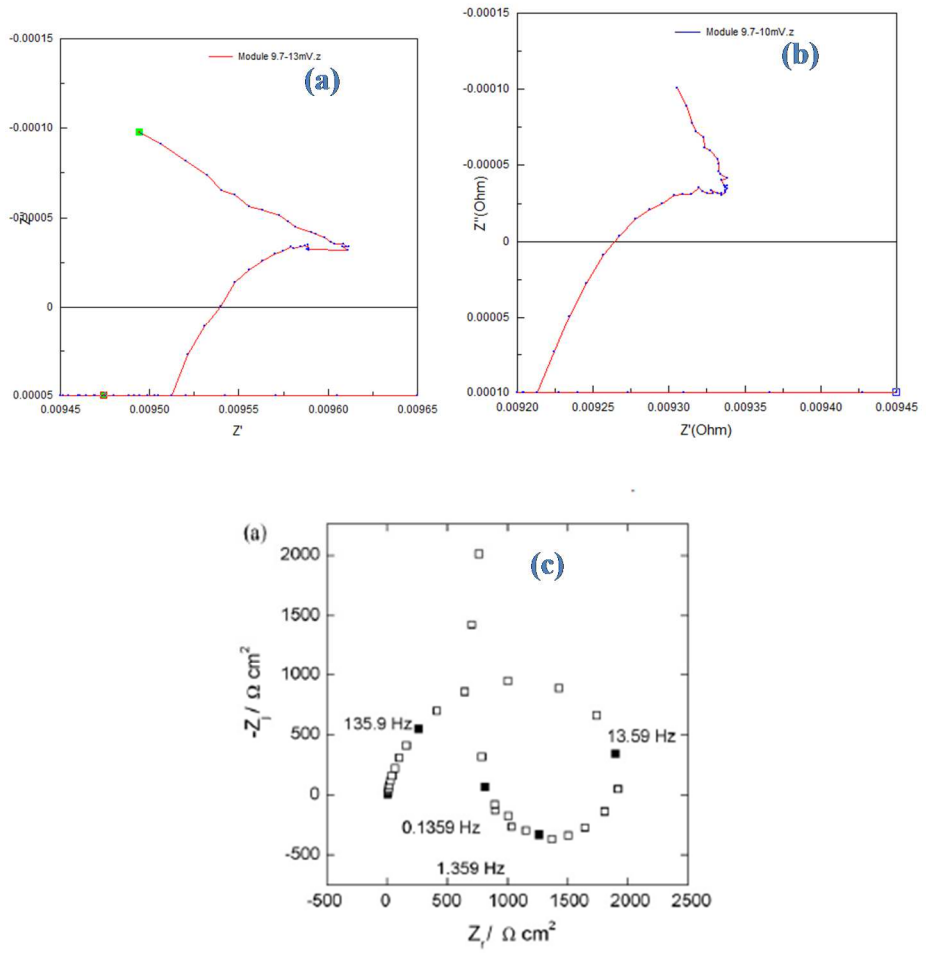

Figure A-2 : Example of corrosion effects (a), (b) impedance from EIS experiment on Lithium-ion battery (c) impedance spectra of an electrode in NH4F solution presented by [326]

Constant Phase Element: Constant phase element (CPE) is an equivalent circuit that is used for impedance data fitting in EIS. It is used to represent the imperfection behaviour of the impedance spectra which cannot be described by the simple electric circuit elements such as capacitance, resistance, and inductance. The heterogeneity of impedance can attribute to the boundary effects such as current and potential distribution, inhomogeneity in variation of the electrode surface thickness, and time constant distribution.

Element	Example of Nyquist plot
R and C in series $Z_t = R + {}^{1}/_{j\omega C}$	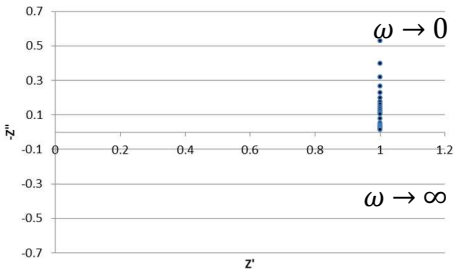 $Z_t \to R$ when $\omega \to \infty$
R and L in series $Z_t = R + j\omega L$	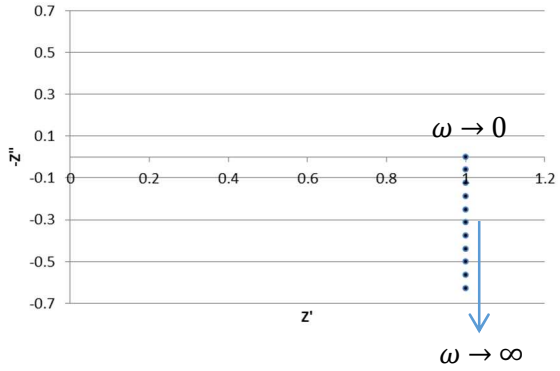 $Z_t \to \infty$ when $\omega \to \infty$
R and C in parallel 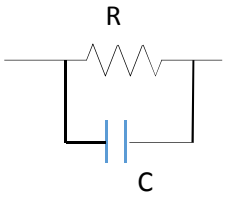 $\lvert Z_t \rvert = \frac{\sqrt{R^2 + (\omega C R^2)^2}}{\omega^2 R^2 C^2 + 1}$	The impedance spectrum of parallel resistor and pure capacitance trace out a semicircle When $\omega \to \infty$ the total impedance goes to zero when $\omega \to 0$the total impedance becomes real; $Z_t = Z_R$ 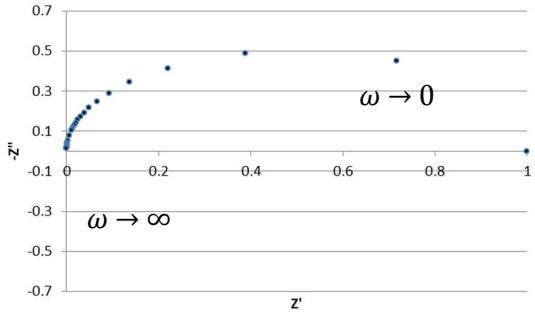

Two or more R and C in parallel

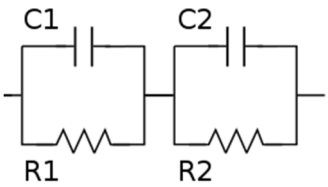

$$Z_t = \frac{1}{j\omega\tau_2 + \frac{R_1}{R_2}} + \frac{1}{j\omega\tau_1 + 1}$$

Where $\tau_1 = C_1R_1$ and $\tau_2 = C_2R_2$

An alternative is a nested circuit

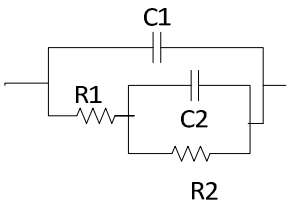

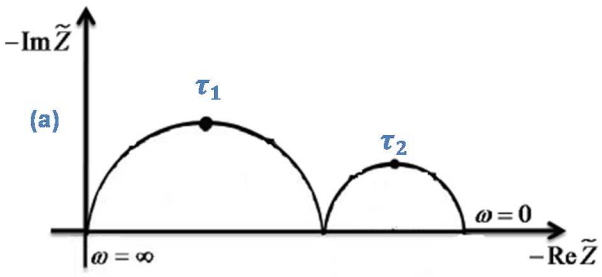

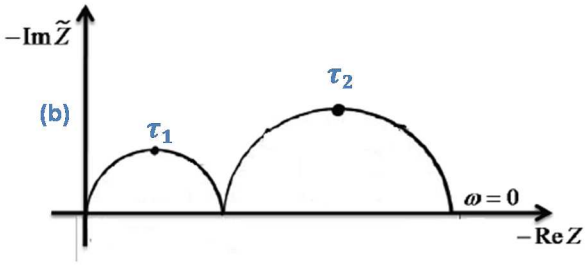

Series Connection of Two Parallel RC, (a) when $\boldsymbol{C_1R_1}$ reaction speed is faster than $\boldsymbol{C_2R_2}$, (b) $\boldsymbol{C_1R_1}$ reaction speed is slower than $\boldsymbol{C_2R_2}$, (c) $\boldsymbol{C_1R_1}$ reaction speed is the same as $\boldsymbol{C_2R_2}$, [143].

When the values of the resistors and capacitors (time constants) merge, the two separate semicircles also merge resulting in a large semicircle which behaves similar to one parallel RC circuit

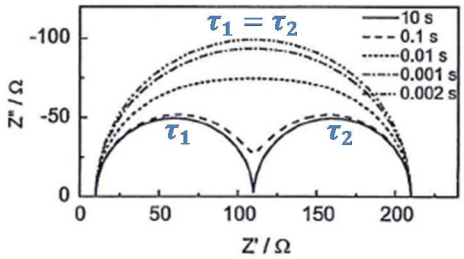

Parallel RC in series with RC

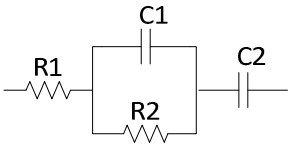

$$\tilde{Z} = \frac{1}{1 + j\omega\tau_1} + \frac{1}{j\omega\tau_2}$$

Where, $\tau_1 = C_1R_2$, $\tau_2 = C_2R_2$

$$\tilde{Z} = \begin{cases} 1 + \frac{1}{i\omega\tau_2} & for \quad \omega \ll \frac{1}{\tau_2} \\ \frac{1}{1 + j\omega\tau_1} & for \quad \frac{1}{\tau_2} \ll \omega \ll \frac{1}{\tau_1} \end{cases}$$

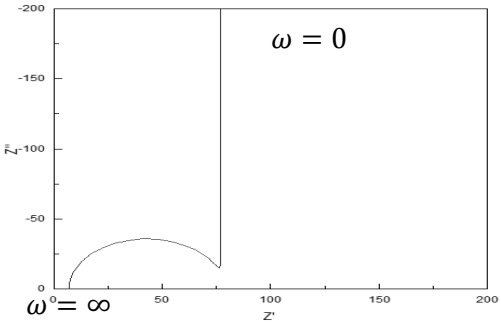

The resistor R_2 and capacitor C_1 produce a semicircle from high to low frequencies. At low frequencies the impedance (Z_{im}) of the circuit goes to negative infinity because the C_2 blocks the dc current flow through the circuit.

Parallel RC with diffusion effect

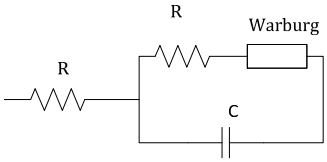

$$Z_t = R + \frac{1}{j\omega C + {}^{1}/_{(Z_w + R_1)}}$$

Alternative diffusion effect representations [336].

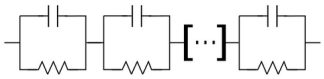

[337]

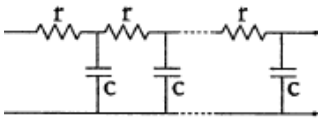

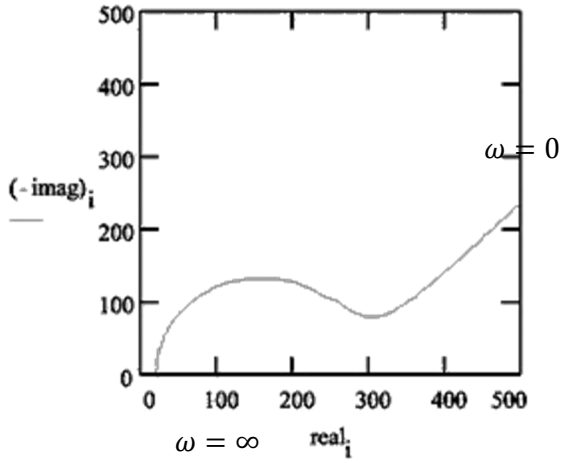

This effect can be represented by a circuit element called the Warburg impedance. The total impedance is illustrated as a combination of a semicircle due to parallel connection of RC and an inclined line with a slope of 45° caused by the diffusion impedance in the low frequency region in complex plot.

Parallel R and CPE

$$Z_t = R + \frac{R_1}{1 + Z_{CPE} R_1}$$

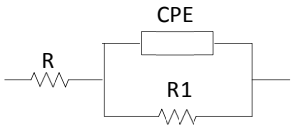

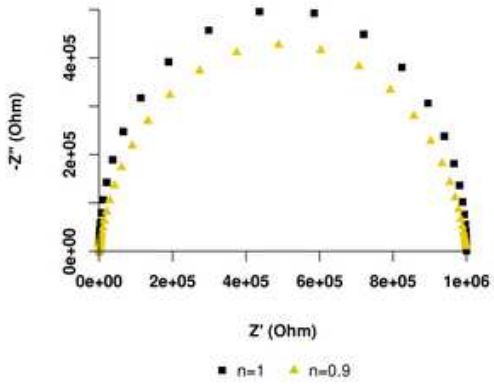

Constant phase element (CPE) components are used instead of capacitors to represent the impurity in capacitance behaviour and frequency distribution that are presented in the impedance data [143]. This component only acts as pure capacitor when its constant number is 1, and for the values between 0 and 1 shows imperfect behavior [338].

Appendix B – Gate drive signal Fourier analysis

Fourier analysis of PWM function with varying duty cycle

Functions to be analysed

The function set to be analysed is a set of square pulses with period T_o and varying pulse widths which tie up with the varying duty cycle.

$$f_0(t) = \begin{cases} A & 0 < t \leq \tau_0 \\ 0 & \tau_0 < t \leq T_s \end{cases}$$ **Equation B-1**

$$f_1(t) = \begin{cases} A & T_s < t \leq \tau_1 + T_s \\ 0 & \tau_1 + T_s < t \leq 2T_s \end{cases}$$ **Equation B-2**

$$f_2(t) = \begin{cases} A & 2T_s < t \leq \tau_2 + 2T_s \\ 0 & \tau_2 + 2T_s < t \leq 3T_s + 2T_s \end{cases}$$ **Equation B-3**

.

$$f_k(t) = \begin{cases} A & kT_s < t \leq \tau_k + kT_s \\ 0 & \tau_k + kT_s < t \leq (k+1)T_s \end{cases}$$ **Equation B-4**

.

$$f_{N_p-1}(t) = \begin{cases} A & (N_p - 1)T_s < t \leq \tau_{N_p-1} + (N_p - 1)T_s \\ 0 & \tau_{N_p-1} + (N_p - 1)T_s < t \leq N_p T_s \end{cases}$$ **Equation B-5**

Fourier co-efficient calculation for first function

$$a_{0,0} = \frac{2}{T_0}\left[\int_0^{\tau_0} A\, dt + \int_{\tau_0}^{T_s} 0\, dt\right]$$ **Equation B-6**

$$a_{0,0} = \frac{2}{T_0}\left[\int_0^{\tau_0} A\, dt\right]$$ **Equation B-7**

$$a_{0,0} = \frac{2}{T_0}[A\tau_0]$$ **Equation B-8**

$$a_{0,0} = \frac{2A\tau_0}{T_0}$$ Equation B-9

$$a_{n,0} = \frac{2}{T_0}\left[\int_0^{\tau_0} A\cos n\omega_0 t\, dt + \int_{\tau_0}^{T_s} 0\cos n\omega_0 t\ dt\right]$$ Equation B-10

$$a_{n,0} = \frac{2}{T_0}\left[\int_0^{\tau_0} A\ \cos n\omega_0 t\, dt\right]$$ Equation B-11

$$a_{n,0} = \frac{2}{T_0}\left[\frac{A}{n\omega_0}\sin n\omega_0\tau_0\right]$$ Equation B-12

$$a_{n,0} = \frac{2A}{n\omega_0 T_0}\sin n\omega_0\tau_0$$ Equation B-13

Fourier coefficient calculation for the kth function

Where k goes from 1to N_p-1

$$a_{0,k} = \frac{2}{T_0}\left[\int_{kT_s}^{\tau_k+kT_s} A\, dt + \int_{\tau_k+kT_s}^{(k+1)T_s} 0\, dt\right]$$ Equation B-14

$$a_{0,k} = \frac{2}{T_0}\left[\int_{(k)T_s}^{\tau_k+(k)T_s} A\, dt\right]$$ Equation B-15

$$a_{0,k} = \frac{2}{T_0}\left[A\tau_k + A(k)T_s - A(k)T_s\right]$$ Equation B-16

$$a_{0,k} = \frac{2A\tau_k}{T_0}$$ Equation B-17

$$a_{n,k} = \frac{2}{T_0}\left[\int_{(k)T_s}^{\tau_k+(k)T_s} A\cos n\omega_0 t\, dt + \int_{\tau_k+(k)T_s}^{(k+1)T_s} 0\cos n\omega_0 t\ dt\right]$$ Equation B-18

$$a_{n,k} = \frac{2}{T_0}\left[\int_{(k)T_s}^{\tau_k+(k)T_s} A\ \cos n\omega_0 t\, dt\right]$$ Equation B-19

$$a_{n,k} = \frac{2}{T_0}\left[\frac{A}{n\omega_0}\sin n\omega_0(\tau_k + (k)T_s) - \frac{A}{n\omega_0}\sin n\omega_0(k)T_s\right]$$ Equation B-20

$$a_{n,k} = \left(\frac{2A}{n\omega_0 T_0}\right)e^{-jn\omega_0(k)T_s}\sin n\omega_0\tau_k$$ Equation B-21

$$b_{n,k} = \frac{2}{T_0}\left[\int_{(k)T_s}^{\tau_k+(k)T_s} A\sin n\omega_0 t\, dt + \int_{\tau_k+(k)T_s}^{(k+1)T_s} 0\sin n\omega_0 t\ dt\right]$$ Equation B-22

$$b_{n,k} = \frac{2}{T_0}\left[\int_{(k)T_s}^{\tau_k+(k)T_s} A\ \sin n\omega_0 t\, dt\right]$$ Equation B-23

$$b_{n,k} = \frac{2}{T_0}\left[\frac{-A}{n\omega_0}\cos n\omega_0(\tau_k + (k)T_s) + \frac{A}{n\omega_0}\cos n\omega_0(k)T_s\right]$$ **Equation B-24**

$$b_{n,k} = \left(\frac{2A}{n\omega_0 T_0}\right)e^{-jn\omega_0(k)T_s}(1 - \cos n\omega_0\tau_k)$$ **Equation B-25**

Total coefficients

$$a_0 = \sum_{k=0}^{N_p-1}\frac{2A\tau_k}{T_0}$$ **Equation B-26**

$$a_n = \sum_{k=0}^{N_p-1}\left(\frac{2A}{n\omega_0 T_0}\right)e^{-jn\omega_0(k)T_s}\sin n\omega_0\tau_k$$ **Equation B-27**

$$b_n = \sum_{k=0}^{N_p-1}\left(\frac{2A}{n\omega_0 T_0}\right)e^{-jn\omega_0(k)T_s}(1 - \cos n\omega_0\tau_k)$$ **Equation B-28**

$$c_n = \sum_{k=0}^{N_p-1}\frac{2A}{n\omega_0 T_0}(\sin n\omega_0\tau_k - j(1 - \cos n\omega_0\tau_k))e^{-jn\omega_0(k)T_s}$$ **Equation B-29**

Fourier analysis of PWM function with varying frequency

Functions to be analysed

The function set to be analysed is a set of square pulses with period T_o and varying pulse widths which tie up with the varying frequency at a fixed duty cycle.

$$f_0(t) = \begin{cases} A & 0 < t \leq \tau_0 \\ 0 & \tau_0 < t \leq T_{s0} \end{cases}$$ **Equation B-30**

$$f_1(t) = \begin{cases} A & T_{s0} < t \leq \tau_1 + T_{s0} \\ 0 & \tau_1 + T_{s0} < t \leq T_{s0} + T_{s1} \end{cases}$$ **Equation B-31**

$$f_2(t) = \begin{cases} A & T_{s0} + T_{s1} < t \leq \tau_2 + T_{s0} + T_{s1} \\ 0 & \tau_2 + T_{s0} + T_{s1} < t \leq T_{s0} + T_{s1} + T_{s2} \end{cases}$$ **Equation B-32**

.

$$f_k(t) = \begin{cases} A & \sum_{m=0}^{k-1} T_{sm} < t \leq \tau_k + \sum_{m=0}^{k-1} T_{sm} \\ 0 & \tau_k + \sum_{m=0}^{k-1} T_{sm} < t \leq \sum_{m=0}^{k} T_{sm} \end{cases}$$ **Equation B-33**

.

$$f_{N_p-1}(t) = \begin{cases} A & \sum_{m=0}^{N_p-2} T_{sm} < t \leq \tau_{N_p-1} + \sum_{m=0}^{N_p-2} T_{sm} \\ 0 & \tau_{N_p-1} + \sum_{m=0}^{N_p-2} T_{sm} < t \leq \sum_{m=0}^{N_p-1} T_{sm} \end{cases}$$ **Equation B-34**

Fourier co-efficient calculation for first function

$$a_{0,0} = \frac{2}{T_0}\left[\int_0^{\tau_0} A\, dt + \int_{\tau_0}^{T_{s0}} 0\, dt\right]$$ **Equation B-35**

$$a_{0,0} = \frac{2}{T_0}\left[\int_0^{\tau_0} A\, dt\right]$$ **Equation B-36**

$$a_{0,0} = \frac{2}{T_0}[A\tau_0]$$ **Equation B-37**

$$a_{0,0} = \frac{2A\tau_0}{T_0}$$ **Equation B-38**

$$a_{n,0} = \frac{2}{T_0}\left[\int_0^{\tau_0} A\cos n\omega_0 t\, dt + \int_{\tau_0}^{T_{s0}} 0\cos n\omega_0 t\ dt\right]$$ **Equation B-39**

$$a_{n,0} = \frac{2}{T_0}\left[\int_0^{\tau_0} A\ \cos n\omega_0 t\ dt\right]$$ Equation B-40

$$a_{n,0} = \frac{2}{T_0}\left[\frac{A}{n\omega_0}\sin n\omega_0\tau_0\right]$$ Equation B-41

$$a_{n,0} = \frac{2A}{n\omega_0 T_0}\sin n\omega_0\tau_0$$ Equation B-42

$$b_{n,0} = \frac{2}{T_0}\left[\int_0^{\tau_0} A\sin n\omega_0 t\ dt + \int_{\tau_0}^{T_{s0}} 0\sin n\omega_0 t\ \ dt\right]$$ Equation B-43

$$b_{n,0} = \frac{2}{T_0}\left[\int_0^{\tau_0} A\ \sin n\omega_0 t\ dt\right]$$ Equation B-44

$$b_{n,0} = \frac{2}{T_0}\left[\frac{-A}{n\omega_0}\cos n\omega_0\tau_0 + \frac{A}{n\omega_0}\right]$$ Equation B-45

$$b_{n,0} = \frac{2A}{n\omega_0 T_0} - \frac{2A}{n\omega_0 T_0}\cos n\omega_0\tau_0$$ Equation B-46

Fourier coefficient calculation for the kth function

$$a_{0,k} = \frac{2}{T_0}\left[\int_{\sum_{m=0}^{k-1} T_{sm}}^{\tau_k+\sum_{m=0}^{k-1} T_{sm}} A\ dt + \int_{\tau_k+\sum_{m=0}^{k-1} T_{sm}}^{\sum_{m=0}^{k} T_{sm}} 0\ dt\right]$$ Equation B-47

$$a_{0,k} = \frac{2}{T_0}\left[\int_{\sum_{m=0}^{k-1} T_{sm}}^{\tau_k+\sum_{m=0}^{k-1} T_{sm}} A\ dt\right]$$ Equation B-48

$$a_{0,k} = \frac{2}{T_0}\left[A\tau_k + A\sum_{m=0}^{k-1} T_{sm} - A\sum_{m=0}^{k-1} T_{sm}\right]$$ Equation B-49

$$a_{0,k} = \frac{2A\tau_k}{T_0}$$ Equation B-50

$$a_{n,k} = \frac{2}{T_0}\left[\int_{\sum_{m=0}^{k-1} T_{sm}}^{\tau_k+\sum_{m=0}^{k-1} T_{sm}} A\cos n\omega_0 t\ dt + \int_{\tau_{k+\sum_{m=0}^{k-1} T_{sm}}}^{\sum_{m=0}^{k} T_{sm}} 0\cos n\omega_0 t\ \ dt\right]$$ Equation B-51

$$a_{n,k} = \frac{2}{T_0}\left[\int_{\sum_{m=0}^{k-1} T_{sm}}^{\tau_k+\sum_{m=0}^{k-1} T_{sm}} A\ \cos n\omega_0 t\ dt\right]$$ Equation B-52

$$a_{n,k} = \frac{2}{T_0}\left[\frac{A}{n\omega_0}\sin n\omega_0(\tau_k + \sum_{m=0}^{k-1} T_{sm}) - \frac{A}{n\omega_0}\sin n\omega_0\sum_{m=0}^{k-1} T_{sm}\right]$$ Equation B-53

$$a_{n,k} = \left(\frac{2A}{n\omega_0 T_0}\right) \sin n\omega_0(\tau_k + \sum_{m=0}^{k-1} T_{sm}) - \left(\frac{2A}{n\omega_0 T_0}\right) \sin n\omega_0 \sum_{m=0}^{k-1} T_{sm}$$ Equation B-54

$$a_{n,k} = \left(\frac{2A}{n\omega_0 T_0}\right) e^{-jn\omega_0 \sum_{m=0}^{k-1} T_{sm}} \sin n\omega_0 \tau_k$$ Equation B-55

$$b_{n,k} = \frac{2}{T_0}\left[\int_{\sum_{m=0}^{k-1} T_{sm}}^{\tau_k + \sum_{m=0}^{k-1} T_{sm}} A \sin n\omega_0 t \, dt + \int_{\tau_k + \sum_{m=0}^{k-1} T_{sm}}^{\sum_{m=0}^{k} T_{sm}} 0 \sin n\omega_0 t \; dt\right]$$ Equation B-56

$$b_{n,k} = \frac{2}{T_0}\left[\int_{\sum_{k=0}^{k-1} T_{sk}}^{\tau_k + \sum_{m=0}^{k-1} T_{sm}} A \; \sin n\omega_0 t \, dt\right]$$ Equation B-57

$$b_{n,k} = \frac{2}{T_0}\left[\frac{-A}{n\omega_0} \cos n\omega_0(\tau_k + \sum_{m=0}^{k-1} T_{sm}) + \frac{A}{n\omega_0} \cos n\omega_0 \sum_{m=0}^{k-1} T_{sm}\right]$$ Equation B-58

$$b_{n,k} = \left(\frac{2A}{n\omega_0 T_0}\right) e^{-jn\omega_0 \sum_{m=0}^{k-1} T_{sm}} (1 - \cos n\omega_0 \tau_k)$$ Equation B-59

Total coefficients

$$a_0 = \sum_{k=0}^{N_p - 1} \frac{2A\tau_k}{T_0}$$ Equation B-60

$$a_n = \frac{2A}{n\omega_0 T_0} \sin n\omega_0 \tau_0 + \sum_{k=1}^{N_p - 1} \left(\frac{2A}{n\omega_0 T_0}\right) e^{-jn\omega_0 \sum_{m=0}^{k-1} T_{sm}} \sin n\omega_0 \tau_k$$ Equation B-61

$$b_n = \frac{2A}{n\omega_0 T_0} - \frac{2A}{n\omega_0 T_0} \cos n\omega_0 \tau_0 + \sum_{k=1}^{N_p - 1} \left(\frac{2A}{n\omega_0 T_0}\right) e^{-jn\omega_0 \sum_{m=0}^{k-1} T_{sm}} (1 - \cos n\omega_0 \tau_k)$$ Equation B-62

$$c_n = \frac{2A}{n\omega_0 T_0} (\sin n\omega_0 \tau_0 - j\,(1 - \cos n\omega_0 \tau_0)) + \sum_{k=1}^{N_p - 1} \frac{2A}{n\omega_0 T_0} (\sin n\omega_0 \tau_k - j(1 - \cos n\omega_0 \tau_k)) e^{-jn\omega_0 \sum_{m=0}^{k-1} T_{sm}}$$ Equation B-63

Fourier analysis of PWM function with varying starting location

Functions to be analysed

The function set to be analysed is a set of square pulses with period T_o and fixed pulse width but starting at different times. The first function is defined to start when the wave switches on rather than at time t=0

$$f_0(t) = \begin{cases} A & t_{ph0} < t \leq \tau + t_{ph0} \\ 0 & \tau + t_{ph0} < t \leq T_s + t_{ph1} \end{cases}$$ **Equation B-64**

$$f_1(t) = \begin{cases} A & T_s + t_{ph1} < t \leq \tau + t_{ph1} + T_s \\ 0 & \tau + t_{ph1} + T_s < t \leq 2T_s + t_{ph2} \end{cases}$$ **Equation B-65**

$$f_2(t) = \begin{cases} A & 2T_s + t_{ph2} < t \leq \tau + t_{ph2} + 2T_s \\ 0 & \tau + t_{ph2} + 2T_s < t \leq 3T_s + t_{ph3} \end{cases}$$ **Equation B-66**

.

$$f_{Np-1}(t) =$$ **Equation B-67**

$$\begin{cases} A & (Np-1)T_s + t_{ph(Np-1)} < t \leq \tau + t_{ph(Np-1)} + (Np-1)T_s \\ 0 & \tau + t_{ph(Np-1)} + (Np-1)T_s < t \leq NpT_s + t_{ph0} \end{cases}$$

Fourier co-efficient calculation for first function

$$a_{0,0} = \frac{2}{T_0}\left[\int_{t_{ph0}}^{\tau+t_{ph0}} A\, dt + \int_{\tau+t_{ph0}}^{T_s+t_{ph0}} 0\, dt\right]$$ **Equation B-68**

$$a_{0,0} = \frac{2}{T_0}\left[\int_{t_{ph0}}^{\tau+t_{ph0}} A\, dt\right]$$ **Equation B-69**

$$a_{0,0} = \frac{2}{T_0}\left[A(\tau + t_{ph0}) - At_{ph0}\right]$$ **Equation B-70**

$$a_{0,0} = \frac{2A\tau}{T_0}$$ **Equation B-71**

$$a_{n,0} = \frac{2}{T_0}\left[\int_{t_{ph0}}^{\tau+t_{ph0}} A\cos n\omega_0 t\, dt + \int_{\tau+t_{ph0}}^{T_s+t_{ph0}} 0\cos n\omega_0 t\ dt\right]$$ **Equation B-72**

$$a_{n,0} = \frac{2}{T_0}\left[\int_{t_{ph0}}^{\tau+t_{ph0}} A\ \cos n\omega_0 t\, dt\right]$$ **Equation B-73**

$$a_{n,0} = \frac{2}{T_0}\left[\frac{A}{n\omega_0}\sin n\omega_0(\tau + t_{ph0}) - \frac{A}{n\omega_0}\sin n\omega_0 t_{ph0}\right]$$ Equation B-74

$$a_{n,0} = \frac{2A}{n\omega_0 T_0}\sin n\omega_0(\tau + t_{ph0}) - \frac{2A}{n\omega_0 T_0}\sin n\omega_0(t_{ph0})$$ Equation B-75

$$a_{n,0} = \frac{2A}{n\omega_0 T_0}e^{-jn\omega_0 t_{ph0}}\sin n\omega_0\tau$$ Equation B-76

$$b_{n,0} = \frac{2}{T_0}\left[\int_{t_{ph0}}^{\tau+t_{ph0}} A\sin n\omega_0 t\, dt + \int_{\tau+t_{ph0}}^{T_s+t_{ph0}} 0\sin n\omega_0 t\ dt\right]$$ Equation B-77

$$b_{n,0} = \frac{2}{T_0}\left[\int_{t_{ph0}}^{\tau+t_{ph0}} A\ \sin n\omega_0 t\, dt\right]$$ Equation B-78

$$b_{n,0} = \frac{2}{T_0}\left[\frac{-A}{n\omega_0}\cos n\omega_0(\tau + t_{ph0}) + \frac{A}{n\omega_0}\cos n\omega_0 t_{ph0}\right]$$ Equation B-79

$$b_{n,0} = \frac{2A}{n\omega_0 T_0}\cos n\omega_0 t_{ph0} - \frac{2A}{n\omega_0 T_0}\cos n\omega_0(\tau + t_{ph0})$$ Equation B-80

$$b_{n,0} = \frac{2A}{n\omega_0 T_0}e^{-jn\omega_0 t_{ph0}}(1 - \cos n\omega_0\tau)$$ Equation B-81

Fourier coefficient calculation for the kth function

$$a_{0,k} = \frac{2}{T_0}\left[\int_{(k)T_s+t_{phk}}^{\tau+t_{phk}+(k)T_s} A\, dt + \int_{\tau+t_{phk}+(k)T_s}^{(k+1)T_s+t_{phk+1}} 0\, dt\right]$$ Equation B-82

$$a_{0,k} = \frac{2}{T_0}\left[\int_{(k)T_s+t_{phk}}^{\tau+t_{phk}+(k)T_s} A\, dt\right]$$ Equation B-83

$$a_{0,k} = \frac{2}{T_0}\left[A(\tau + t_{phk} + (k)T_s) - A((k)T_s + t_{phk})\right]$$ Equation B-84

$$a_{0,k} = \frac{2A\tau}{T_0}$$ Equation B-85

$$a_{n,k} = \frac{2}{T_0}\left[\int_{(k)T_s+t_{phk}}^{\tau+t_{phk}+(k)T_s} A\cos n\omega_0 t\, dt + \int_{\tau+t_{phk}+(k)T_s}^{(k+1)T_s+t_{phk+1}} 0\cos n\omega_0 t\ dt\right]$$ Equation B-86

$$a_{n,k} = \frac{2}{T_0}\left[\int_{(k)T_s+t_{phk}}^{\tau+t_{phk}+(k)T_s} A\ \cos n\omega_0 t\, dt\right]$$ Equation B-87

$$a_{n,k} = \frac{2}{T_0}\left[\frac{A}{n\omega_0}\sin n\omega_0(\tau + t_{phk} + (k)T_s) - \frac{A}{n\omega_0}\sin n\omega_0((k)T_s + t_{phk})\right]$$ Equation B-88

$$a_{n,k} = \left(\frac{2A}{n\omega_0 T_0}\right)\sin n\omega_0(\tau + t_{phk} + (k)T_s) - \left(\frac{2A}{n\omega_0 T_0}\right)\sin n\omega_0\left((k)T_s + t_{phk}\right)$$ Equation B-89

$$a_{n,k} = \left(\frac{2A}{n\omega_0 T_0}\right) e^{-jn\omega_0((k)T_s + t_{phk})} \sin n\omega_0\tau$$ Equation B-90

$$b_{n,k} = \frac{2}{T_0}\left[\int_{(k)T_s + t_{phk-1}}^{\tau + t_{phk} + (k)T_s} A \sin n\omega_0 t\, dt + \int_{\tau + t_{phk} + (k)T_s}^{(k+1)T_s + t_{phk+1}} 0 \sin n\omega_0 t\ dt\right]$$ Equation B-91

$$b_{n,k} = \frac{2}{T_0}\left[\int_{(k)T_s + t_{phk}}^{\tau + t_{phk} + (k)T_s} A\ \sin n\omega_0 t\, dt\right]$$ Equation B-92

$$b_{n,k} = \frac{2}{T_0}\left[\frac{-A}{n\omega_0}\cos n\omega_0(\tau + t_{phk} + (k)T_s) + \frac{A}{n\omega_0}\cos n\omega_0((k)T_s + t_{phk})\right]$$ Equation B-93

$$b_{n,k} = \left(\frac{2A}{n\omega_0 T_0}\right)\cos n\omega_0((k)T_s + t_{phk}) - \left(\frac{2A}{n\omega_0 T_0}\right)\cos n\omega_0(\tau + t_{phk} + (k)T_s)$$ Equation B-94

$$b_{n,k} = \left(\frac{2A}{n\omega_0 T_0}\right) e^{-jn\omega_0(t_{phk} + (k)T_s)}(1 - \cos n\omega_0\tau)$$ Equation B-95

Total coefficients

$$a_0 = \sum_{k=0}^{N_p - 1} \frac{2A\tau}{T_0}$$ Equation B-96

$$a_n = \sum_{k=0}^{N_p - 1} \left(\frac{2A}{n\omega_0 T_0}\right) e^{-jn\omega_0((k)T_s + t_{phk})} \sin n\omega_0\tau$$ Equation B-97

$$b_n = \sum_{k=0}^{N_p - 1} \left(\frac{2A}{n\omega_0 T_0}\right) e^{-jn\omega_0(t_{phk} + (k)T_s)}(1 - \cos n\omega_0\tau)$$ Equation B-98

$$c_n = \sum_{k=0}^{N_p - 1} \frac{2A}{n\omega_0 T_0}(\sin n\omega_0\tau - j(1 - \cos n\omega_0\tau)) e^{-jn\omega_0(t_{phk} + (k)T_s)}$$ Equation B-99

Fourier analysis of PWM function including an impulse function

Functions to be analysed

The function set to be analysed is a set of square pulses with period T_o and the first function has an increased pulse width while the other functions have the same pulse width.

$$f_0(t) = \begin{cases} A & 0 < t \leq \tau_{or} \\ 0 & \tau_{or} < t \leq T_s \end{cases}$$ **Equation B-100**

$$f_1(t) = \begin{cases} A & T_s < t \leq \tau + T_s \\ 0 & \tau + T_s < t \leq 2T_s \end{cases}$$ **Equation B-101**

$$f_2(t) = \begin{cases} A & 2T_s < t \leq \tau + 2T_s \\ 0 & \tau + 2T_s < t \leq 3T_s \end{cases}$$ **Equation B-102**

.

$$f_{N_p-1}(t) = \begin{cases} A & (N_p - 1)T_s < t \leq \tau + (N_p - 1)T_s \\ 0 & \tau + (N_p - 1)T_s < t \leq N_p T_s \end{cases}$$ **Equation B-103**

Fourier co-efficient calculation for first function

$$a_{0,0} = \frac{2}{T_0}\left[\int_0^{\tau_{or}} A\, dt + \int_{\tau_{or}}^{T_s} 0\, dt\right]$$ **Equation B-104**

$$a_{0,0} = \frac{2}{T_0}\left[\int_0^{\tau_{or}} A\, dt\right]$$ **Equation B-105**

$$a_{0,0} = \frac{2}{T_0}[A\tau_{or}]$$ **Equation B-106**

$$a_{0,0} = \frac{2A\tau_{or}}{T_0}$$ **Equation B-107**

$$a_{n,0} = \frac{2}{T_0}\left[\int_0^{\tau_{or}} A\cos n\omega_0 t\, dt + \int_{\tau_{or}}^{T_s} 0\cos n\omega_0 t\ dt\right]$$ **Equation B-108**

$$a_{n,0} = \frac{2}{T_0}\left[\int_0^{\tau_{or}} A\ \cos n\omega_0 t\, dt\right]$$ **Equation B-109**

$$a_{n,0} = \frac{2}{T_0}\left[\frac{A}{n\omega_0}\sin n\omega_0\tau_{or}\right]$$ Equation B-110

$$a_{n,0} = \frac{2A}{n\omega_0 T_0}\sin n\omega_0\tau_{or}$$ Equation B-111

$$b_{n,0} = \frac{2}{T_0}\left[\int_0^{\tau_{or}} A\sin n\omega_0 t\, dt + \int_{\tau_{or}}^{T_s} 0\sin n\omega_0 t\ dt\right]$$ Equation B-112

$$b_{n,0} = \frac{2}{T_0}\left[\int_0^{\tau_{or}} A\ \sin n\omega_0 t\, dt\right]$$ Equation B-113

$$b_{n,0} = \frac{2}{T_0}\left[\frac{-A}{n\omega_0}\cos n\omega_0\tau_{or} + \frac{A}{n\omega_0}\right]$$ Equation B-114

$$b_n, 0 = \frac{2A}{n\omega_0 T_0}(1 - \cos n\omega_0\tau_{or})$$ Equation B-115

Fourier coefficient calculation for the kth function

$$a_{0,k} = \frac{2}{T_0}\left[\int_{(k)T_s}^{\tau+(k)T_s} A\, dt + \int_{\tau+(k)T_s}^{(k+1)T_s} 0\, dt\right]$$ Equation B-116

$$a_{0,k} = \frac{2}{T_0}\left[\int_{(k)T_s}^{\tau+(k)T_s} A\, dt\right]$$ Equation B-117

$$a_{0,k} = \frac{2}{T_0}[A(\tau + (k)T_s) - A((k)T_s)]$$ Equation B-118

$$a_{0,k} = \frac{2A\tau}{T_0}$$ Equation B-119

$$a_{n,k} = \frac{2}{T_0}\left[\int_{(k)T_s}^{\tau+(k)T_s} A\cos n\omega_0 t\, dt + \int_{\tau+(k)T_s}^{(k+1)T_s} 0\cos n\omega_0 t\ dt\right]$$ Equation B-120

$$a_{n,k} = \frac{2}{T_0}\left[\int_{(k)T_s}^{\tau+(k)T_s} A\ \cos n\omega_0 t\, dt\right]$$ Equation B-121

$$a_{n,k} = \frac{2}{T_0}\left[\frac{A}{n\omega_0}\sin n\omega_0(\tau + (k)T_s) - \frac{A}{n\omega_0}\sin n\omega_0(k)T_s\right]$$ Equation B-122

$$a_{n,k} = \left(\frac{2A}{n\omega_0 T_0}\right)\sin n\omega_0(\tau + (k)T_s) - \left(\frac{2A}{n\omega_0 T_0}\right)\sin n\omega_0(k)T_s$$ Equation B-123

$$a_{n,k} = \left(\frac{2A}{n\omega_0 T_0}\right)e^{-jn\omega_0(k)T_s}\sin n\omega_0\tau$$ Equation B-124

$$b_{n,k} = \frac{2}{T_0}\left[\int_{(k)T_s}^{\tau+(k)T_s} A \sin n\omega_0 t \, dt + \int_{\tau+(k)T_s}^{(k+1)T_s} 0 \sin n\omega_0 t \; dt\right]$$ Equation B-125

$$b_{n,k} = \frac{2}{T_0}\left[\int_{(k)T_s}^{\tau+(k)T_s} A \; \sin n\omega_0 t \, dt\right]$$ Equation B-126

$$b_{n,k} = \frac{2}{T_0}\left[\frac{-A}{n\omega_0}\cos n\omega_0(\tau + (k)T_s) + \frac{A}{n\omega_0}\cos n\omega_0(k)T_s\right]$$ Equation B-127

$$b_{n,k} = \left(\frac{2A}{n\omega_0 T_0}\right) e^{-jn\omega_0(k)T_s}(1 - \cos n\omega_0\tau)$$ Equation B-128

Total coefficients

$$a_0 = \frac{2A\tau_{or}}{T_0} + \sum_{k=1}^{N_p-1} \frac{2A\tau}{T_0}$$ Equation B-129

$$a_n = \frac{2A}{n\omega_0 T_0}\sin n\omega_0\tau_{or} + \sum_{k=1}^{N_p-1}\left(\frac{2A}{n\omega_0 T_0}\right) e^{-jn\omega_0(k)T_s}\sin n\omega_0\tau$$ Equation B-130

$$b_n = \frac{2A}{n\omega_0 T_0}(1 - \cos n\omega_0\tau_{or}) + \sum_{k=1}^{N_p-1}\left(\frac{2A}{n\omega_0 T_0}\right) e^{-jn\omega_0(k)T_s}(1 - \cos n\omega_0\tau)$$ Equation B-131

$$c_n = \frac{2A}{\omega_0 T_0}\left(\sin n\omega_0\tau_{or} - j(1 - \cos n\omega_0\tau_{or})\right) + \frac{2A}{n\omega_0 T_0}\sum_{k=1}^{N_p-1}(\sin n\omega_0\tau - j(1 - \cos n\omega_0\tau))e^{-jn\omega_0(k)T_s}$$ Equation B-132

Appendix C – Battery current Fourier analysis

Fourier Analysis of Sawtooth wave with varying duty cycle

Functions to be analysed

$$f_0(t) = \begin{cases} u_0 + m_{on}t & 0 < t \le \tau_0 \\ v_0 + m_{off}(t-\tau_0) & \tau_0 < t \le T_s \end{cases}$$ Equation C-1

$$f_1(t) = \begin{cases} u_1 + m_{on}(t-T_s) & T_s < t \le \tau_1 + T_s \\ v_1 + m_{off}(t-\tau_1-T_s) & \tau_1 - T_s < t \le 2T_s \end{cases}$$ Equation C-2

$$f_2(t) = \begin{cases} u_2 + m_{on}(t-2T_s) & 2T_s < t \le \tau_2 + 2T_s \\ v_2 + m_{off}(t-\tau_2-2T_s) & \tau_2 + 2T_s < t \le 3T_s \end{cases}$$ Equation C-3

.

$$f_k(t) = \begin{cases} u_k + m_{on}(t-(k)T_s) & (k)T_s < t \le \tau_k + (k)T_s \\ v_k + m_{off}(t-\tau_k-(k)T_s) & \tau_k + (k)T_s < t \le (k+1)T_s \end{cases}$$ Equation C-4

.

$$f_{N_p-1}(t) =$$ Equation C-5

$$\begin{cases} u_{N_p-1} + m_{on}\left(t-(N_p-1)T_s\right) & (N_p-1)T_s < t \le \tau_{N_p-1} + (N_p-1)T_s \\ v_{N_p-1} + m_{off}\left(t-\tau_{N_p-1}-(N_p-1)T_s\right) & \tau_{N_p-1} + (N_p-1)T_s < t \le (N_p)T_s \end{cases}$$

Fourier co-efficient calculation for first function

$$a_{0,0} = \frac{2}{T_0}\left[\int_0^{\tau_0} u_0\,dt + \int_0^{\tau_0} m_{on}t\,dt + \int_{\tau_0}^{T_s} v_0\,dt - \int_{\tau_0}^{T_s} m_{off}t\,dt + \int_{\tau_0}^{T_s} m_{off}\tau_0\,dt\right]$$ Equation C-6

$$a_{0,0} = \frac{2}{T_0}\left[u_0\tau_0 + \frac{m_{on}}{2}{\tau_0}^2 + v_0(T_s-\tau_0) - \frac{m_{off}}{2}\left({T_s}^2 - {\tau_0}^2\right) + m_{off}\tau_0(T_s-\tau_0)\right]$$ Equation C-7

$$a_{0,0} = \frac{2u_0\tau_0}{T_0} + \frac{m_{on}}{T_0}{\tau_0}^2 + \frac{2v_0(T_s-\tau_0)}{T_0} - \frac{m_{off}}{T_0}\left({T_s}^2 - {\tau_0}^2\right) + \frac{2m_{off}}{T_0}\tau_0(T_s-\tau_0)$$ Equation C-8

$$a_{0,0} = \frac{2}{T_0}\left[\int_0^{\tau_0} u_0 + m_{on}t\,dt + \int_{\tau_0}^{T_s} v_0 - m_{off}(t-\tau_0)\,dt\right]$$ Equation C-9

$$a_{n,0} = \frac{2}{T_0}\left[\int_0^{\tau_0}(u_0 + m_{on}t)\cos n\omega_0 t\,dt + \int_{\tau_0}^{T_s}\left(v_0 + m_{off}(t-\tau_0)\right)\cos n\omega_0 t\;dt\right]$$ **Equation C-10**

$$a_{n,0} = \frac{2}{T_0}\left[\int_0^{\tau_0} u_0\;\cos n\omega_0 t\,dt + \int_0^{\tau_0} m_{on}t\;\cos n\omega_0 t\,dt + \int_{\tau_0}^{T_s} v_0\;\cos n\omega_0 t\,dt + \int_{\tau_0}^{T_s} m_{off}t\;\cos n\omega_0 t\,dt - \int_{\tau_0}^{T_s} m_{off}\tau_0\;\cos n\omega_0 t\,dt\right]$$ **Equation C-11**

$$a_{n,0} = \frac{2}{T_0}\left[\frac{u_0}{n\omega_0}\sin n\omega_0\tau_0 + \frac{m_{on}}{n\omega_0}\tau_0\sin n\omega_0\tau_0 - \frac{m_{on}}{n\omega_0}\int_0^{\tau_0}\sin n\omega_0 t\,dt + \frac{v_0}{n\omega_0}\sin n\omega_0 T_s - \frac{v_0}{n\omega_0}\sin n\omega_0\tau_0 + \frac{m_{off}}{n\omega_0}\;T_s\sin n\omega_0 T_s - \frac{m_{off}}{n\omega_0}\;\tau_0\sin n\omega_0\tau_0 - \frac{m_{off}}{n\omega_0}\int_{\tau_0}^{T_s}\;\sin n\omega_0 t\,dt + \frac{m_{off}}{n\omega_0}\tau_0\sin n\omega_0 T_s - \frac{m_{off}}{n\omega_0}\tau_0\sin n\omega_0\tau_0\right]$$ **Equation C-12**

$$a_{n,0} = \frac{2}{T_0}\left[\frac{u_0}{n\omega_0}\sin n\omega_0\tau_0 + \frac{m_{on}}{n\omega_0}\tau_0\sin n\omega_0\tau_0 + \frac{m_{on}}{n^2{\omega_0}^2}\cos n\omega_0\tau_0 - \frac{m_{on}}{n^2{\omega_0}^2} + \frac{v_0}{n\omega_0}\sin n\omega_0 T_s - \frac{v_0}{n\omega_0}\sin n\omega_0\tau_0 + \frac{m_{off}}{n\omega_0}\;T_s\sin n\omega_0 T_s - \frac{m_{off}}{n\omega_0}\;\tau_0\sin n\omega_0\tau_0 - \frac{m_{off}}{n^2{\omega_0}^2}\cos n\omega_0 T_s + \frac{m_{off}}{n^2{\omega_0}^2}\cos n\omega_0\tau_0 + \frac{m_{off}}{n\omega_0}\tau_0\sin n\omega_0 T_s - \frac{m_{off}}{n\omega_0}\tau_0\sin n\omega_0\tau_0\right]$$ **Equation C-13**

$$a_{n,0} = \frac{2u_0}{n\omega_0 T_0}\sin n\omega_0\tau_0 + \frac{2m_{on}}{n\omega_0 T_0}\tau_0\sin n\omega_0\tau_0 + \frac{2m_{on}}{n^2{\omega_0}^2 T_0}\cos n\omega_0\tau_0 - \frac{2m_{on}}{n^2{\omega_0}^2 T_0} + \frac{2v_0}{n\omega_0 T_0}\sin n\omega_0 T_s - \frac{2v_0}{n\omega_0 T_0}\sin n\omega_0\tau_0 + \frac{2m_{off}}{n\omega_0 T_0}\;T_s\sin n\omega_0 T_s - \frac{2m_{off}}{n\omega_0 T_0}\;\tau_0\sin n\omega_0\tau_0 - \frac{2m_{off}}{n^2{\omega_0}^2 T_0}\cos n\omega_0 T_s + \frac{2m_{off}}{n^2{\omega_0}^2 T_0}\cos n\omega_0\tau_0 + \frac{2m_{off}}{n\omega_0 T_0}\tau_0\sin n\omega_0 T_s - \frac{2m_{off}}{n\omega_0 T_0}\tau_0\sin n\omega_0\tau_0$$ **Equation C-14**

$$a_{n,0} = \frac{-2m_{on}}{n^2{\omega_0}^2 T_0} + \left(\frac{2u_0}{n\omega_0 T_0} + \frac{2m_{on}}{n\omega_0 T_0}\tau_0 - \frac{2v_0}{n\omega_0 T_0}\right)\sin n\omega_0\tau_0 + \left(\frac{2m_{on}}{n^2{\omega_0}^2 T_0} + \frac{2m_{off}}{n^2{\omega_0}^2 T_0}\right)\cos n\omega_0\tau_0 + \left(\frac{2v_0}{n\omega_0 T_0} - \frac{2m_{off}}{n\omega_0 T_0}\right)\sin n\omega_0 T_s + \frac{2m_{off}}{n^2{\omega_0}^2 T_0}\cos n\omega_0 T_s$$ **Equation C-15**

$$a_n = \frac{-2m_{on}}{n^2{\omega_0}^2 T_0} + \left(\frac{2u_0}{n\omega_0 T_0} + \frac{2m_{on}}{n\omega_0 T_0}\tau_0 - \frac{2v_0}{n\omega_0 T_0}\right)\sin n\omega_0\tau_0 + \left(\frac{2v_0}{n\omega_0 T_0} + \frac{2m_{off}}{n\omega_0 T_0}\;(T_s - \tau_0)\right)\sin n\omega_0 T_s - \frac{2m_{off}}{n^2{\omega_0}^2 T_0}\cos n\omega_0 T_s$$ **Equation C-16**

$$b_{n,0} = \frac{2}{T_0}\left[\int_0^{\tau_0} u_0\;\sin n\omega_0 t\,dt + \int_0^{\tau_0} m_{on}t\;\sin n\omega_0 t\,dt + \int_{\tau_0}^{T_s} v_0\;\sin n\omega_0 t\,dt + \int_{\tau_0}^{T_s} m_{off}t\;\sin n\omega_0 t\,dt - \int_{\tau_0}^{T_s} m_{off}\tau_0\;\sin n\omega_0 t\,dt\right]$$ **Equation C-17**

$$b_{n,0} = \frac{2}{T_0}\left[\frac{-u_0}{n\omega_0}\cos n\omega_0\tau_0 + \frac{u_0}{n\omega_0} - \frac{m_{on}}{n\omega_0}\tau_0\cos n\omega_0\tau_0 + \frac{m_{on}}{n\omega_0}\int_0^{\tau_0}\cos n\omega_0 t\,dt - \frac{v_0}{n\omega_0}\cos n\omega_0 T_s + \frac{v_0}{n\omega_0}\cos n\omega_0\tau_0 - \frac{m_{off}}{n\omega_0}\;T_s\cos n\omega_0 T_s + \frac{m_{off}}{n\omega_0}\;\tau_0\cos n\omega_0\tau_0 + \frac{m_{off}}{n\omega_0}\int_{\tau_0}^{T_s}\;\cos n\omega_0 t\,dt + \frac{m_{off}}{n\omega_0}\tau_0\cos n\omega_0 T_s - \frac{m_{off}}{n\omega_0}\tau_0\cos n\omega_0\tau_0\right]$$ **Equation C-18**

$$b_{n,0} = \frac{2}{T_0}\left[\frac{-u_0}{n\omega_0}\cos n\omega_0\tau_0 + \frac{u_0}{n\omega_0} - \frac{m_{on}}{n\omega_0}\tau_0\cos n\omega_0\tau_0 + \frac{m_{on}}{n^2{\omega_0}^2}\sin n\omega_0\tau_0 - \right.$$
$$\frac{v_0}{n\omega_0}\cos n\omega_0 T_s + \frac{v_0}{n\omega_s}\cos n\omega_0\tau_0 - \frac{m_{off}}{n\omega_0}\,T_s\cos n\omega_0 T_s +$$
$$\frac{m_{off}}{n\omega_0}\,\tau_0\cos n\omega_0\tau_0 + \frac{m_{off}}{n^2{\omega_0}^2}\sin n\omega_0 T_s - \frac{m_{off}}{n^2{\omega_0}^2}\sin n\omega_0\tau_0 +$$
$$\left.\frac{m_{off}}{n\omega_0}\tau_0\cos n\omega_0 T_s - \frac{m_{off}}{n\omega_0}\tau_0\cos n\omega_0\tau_0\right]$$

Equation C-19

$$b_{n,0} = \frac{-2u_0}{n\omega_0 T_0}\cos n\omega_0\tau_0 + \frac{2u_0}{n\omega_0 T_0} - \frac{2m_{on}}{n\omega_0 T_0}\tau_0\cos n\omega_0\tau_0 + \frac{2m_{on}}{n^2{\omega_0}^2 T_0}\sin n\omega_0\tau_0 -$$
$$\frac{2v_0}{n\omega_0 T_0}\cos n\omega_0 T_s + \frac{2v_0}{n\omega_0 T_0}\cos n\omega_0\tau_0 - \frac{2m_{off}}{n\omega_0 T_0}\,T_s\cos n\omega_0 T_s +$$
$$\frac{2m_{off}}{n\omega_0 T_0}\,\tau_0\cos n\omega_0\tau_0 - \frac{2m_{off}}{n^2{\omega_0}^2 T_0}\sin n\omega_0 T_s - \frac{2m_{off}}{n^2{\omega_0}^2 T_0}\sin n\omega_0\tau_0 +$$
$$\frac{2m_{off}}{n\omega_0 T_0}\tau_0\cos n\omega_0 T_s - \frac{2m_{off}}{n\omega_0 T_0}\tau_0\cos n\omega_0\tau_0$$

Equation C-20

$$b_{n,0} = \frac{2u_0}{n\omega_0 T_0} + \left(\frac{2v_0}{n\omega_0 T_0} - \frac{2u_0}{n\omega_0 T_0} - \frac{2m_{on}}{n\omega_0 T_0}\tau_0\right)\cos n\omega_0\tau_0 + \left(\frac{2m_{on}}{n^2{\omega_0}^2 T_0} -\right.$$
$$\left.\frac{2m_{off}}{n^2{\omega_0}^2 T_0}\right)\sin n\omega_0\tau_0 - \frac{2m_{off}}{n^2{\omega_0}^2 T_0}\sin n\omega_0 T_s + \left(-\frac{2m_{off}}{n\omega_0 T_0}(T_s - \tau_0)\right. - \left.\frac{2v_0}{n\omega_0 T_0}\right)\cos n\omega_0 T_s$$

Equation C-21

Fourier coefficient calculation for the kth function

$$a_{0,k} = \frac{2}{T_0}\left[\int_{kT_s}^{\tau_k + kT_s} u_k + m_{on}(t - kT_s)\,dt + \int_{\tau_{k1} + kT_s}^{(k+1)T_s} v_k + m_{off}(t - (\tau_k + kT_s))\,dt\right]$$

Equation C-22

$$a_{0,k} = \frac{2}{T_0}\left[-m_{on}kT_s\tau_k + \frac{m_{on}}{2}((\tau_k + kT_s)^2 - k^2T_s^2) + u_k\tau_k + \frac{m_{off}}{2}\,(((k+1)T_s)^2 - (\tau_k + kT_s)^2) + v_k((k+1)T_s - (\tau_k + kT_s)) + m_{off}(-\tau_k - kT_s)((k+1)T_s - \tau_k + kT_s)\right]$$

Equation C-23

$$a_{n,k} = \frac{2}{T_0}\left[\int_{kT_s}^{\tau_k + kT_s}(u_k + m_{on}(t - kT_s))\cos n\omega_0 t\,dt + \int_{\tau_k + kT_s}^{(k+1)T_s}\left(v_k + m_{off}(t - (\tau_k + kT_s))\right)\cos n\omega_0 t\;dt\right]$$

Equation C-24

$$a_{n,k} = \frac{2}{T_0}\left[\frac{\sin(n\omega_0(\tau_k+kT_s))nm_{on}\omega_0\tau_k+u_k\sin\left(n\omega_0(\tau_k+kT_s)\right)\omega_0 n-u_k\sin(n\omega_0 kT_s)\omega_0 n}{n^2{\omega_0}^2}+\right.$$

$$\frac{\cos(n\omega_0(\tau_k+kT_s))m_{on}-\cos(n\omega_0 kT_s)m_{on}+n^2T_s{\omega_0}^2v_k-n^2{\omega_0}^2\tau_k v_k}{n^2{\omega_0}^2}+$$

$$\frac{\sin(n\omega_0(k+1)T_s)nT_s m_{off}\omega_0-\sin(n\omega_0(k+1)T_s)nm_{off}\omega_0\tau_k}{n^2{\omega_0}^2}+$$

$$\left.\frac{\cos\left(n\omega_0(k+1)T_s\right)m_{off}-\cos(n\omega_0(\tau_k+kT_s))m_{off}}{n^2{\omega_0}^2}\right]$$

Equation C-25

$$b_{n,k} = \frac{2}{T_0}\left[\int_{kT_s}^{\tau_k+kT_s}(u_k + m_{on}(t-kT_s))\sin n\omega_0 t\,dt + \int_{\tau_k+kT_s}^{(k+1)T_s}\left(v_k + m_{off}(t-\right.\right.$$

$$\left.\left.(\tau_k + kT_s))\right)\sin n\omega_0 t\ dt\right]$$

Equation C-26

$$b_n, k = \frac{2}{T_0}\left[\frac{-\cos\left(n\omega_0(\tau_k+kT_s)\right)nm_{on}\omega_0\tau_k-u_k\cos\left(n\omega_0(\tau_k+kT_s)\right)\omega_0 n}{n^2{\omega_0}^2}+\right.$$

$$\frac{u_k\cos(n\omega_0 kT_s)\omega_0 n+\sin(n\omega_0(\tau_k+kT_s))m_{on}-\sin(n\omega_0 kT_s)m_{on}}{n^2{\omega_0}^2}+$$

$$\frac{n^2T_s{\omega_0}^2v_k-n^2{\omega_0}^2\tau_k v_k-cos(n\omega_0(k+1)T_s)nT_s m_{off}\omega_0+cos(n\omega_0(k+1)T_s)nm_{off}\omega_0\tau_k}{n^2{\omega_0}^2}+$$

$$\left.\frac{\sin\left(n\omega_0(k+1)T_s\right)m_{off}-\sin(n\omega_0(\tau_k+kT_s))m_{off}}{n^2{\omega_0}^2}\right]$$

Equation C-27

Total coefficients

$$a_0 = \sum_{k=0}^{N_p-1} a_{0,k}$$

Equation C-28

$$a_n = \sum_{k=0}^{N_p-1} a_{n,k}$$

Equation C-29

$$b_n = \sum_{k=0}^{N_p-1} b_{n,k}$$

Equation C-30

$$c_n = \sum_{k=0}^{N_p-1} \begin{matrix}\frac{1}{2}\left(a_{n,k} - ib_{n,k}\right)(n \geq 1)\\ \frac{1}{2}\left(a_{n,k} + ib_{n,k}\right)(n \leq 1)\end{matrix}$$

Equation C-31

Fourier Analysis of Sawtooth wave with varying frequency

Functions to be analysed

$$f_0(t) = \begin{cases} u_0 + m_{on}t & 0 < t \le \tau_0 \\ v_0 + m_{off}(t - \tau_0) & \tau_0 < t \le T_{s0} \end{cases}$$ **Equation C-32**

$$f_1(t) = \begin{cases} u_1 + m_{on}(t - T_{s0}) & T_{s0} < t \le \tau_1 + T_{s0} \\ v_1 + m_{off}(t - (\tau_1 + T_{s0})) & \tau_1 + T_{s0} < t \le T_{s0} + T_{s1} \end{cases}$$ **Equation C-33**

$$f_2(t) = \begin{cases} u_2 + m_{on}(t - (T_{s0} + T_{s1})) & T_{s0} + T_{s1} < t \le \tau_2 + T_{s0} + T_{s1} \\ v_2 + m_{off}\left(t - (\tau_2 + T_{s0} + T_{s1})\right) & \tau_2 + T_{s0} + T_{s1} < t \le T_{s0} + T_{s1} + T_{s2} \end{cases}$$ **Equation C-34**

.

$$f_k(t) = \begin{cases} u_k + m_{on}\left(t - \sum_{k=0}^{k-1} T_{sk}\right) & \sum_{k=0}^{k-1} T_{sk} < t \le \tau_k + \sum_{k=0}^{k-1} T_{sk} \\ v_k + m_{off}\left(t - (\tau_k + \sum_{k=0}^{k-1} T_{sk})\right) & \tau_k + \sum_{k=0}^{k-1} T_{sk} < t \le \sum_{k=0}^{k} T_{sk} \end{cases}$$ **Equation C-35**

Fourier co-efficient calculation for first function

$$a_{0,0} = \frac{2}{T_0}\left[\int_0^{\tau_0} u_0 + m_{on}t\, dt + \int_{\tau_0}^{T_{s0}} v_0 + m_{off}(t - \tau_0)\, dt\right]$$ **Equation C-36**

$$a_{0,0} = \frac{2}{T_0}\left[\int_0^{\tau_0} u_0\, dt + \int_0^{\tau_0} m_{on}t\, dt + \int_{\tau_0}^{T_{s0}} v_0\, dt + \int_{\tau_0}^{T_{s0}} m_{off}t\, dt - \int_{\tau_0}^{T_{s0}} m_{off}\tau_0\, dt\right]$$ **Equation C-37**

$$a_{0,0} = \frac{2}{T_0}\left[u_0\tau_0 + \frac{m_{on}}{2}{\tau_0}^2 + v_0(T_{s0} - \tau_0) + \frac{m_{on}}{2}\left({T_{s0}}^2 - {\tau_0}^2\right) - m_{off}\tau_0(T_{s0} - \tau_0)\right]$$ **Equation C-38**

$$a_{0,0} = \frac{2u_0\tau_0}{T_0} + \frac{m_{on}{\tau_0}^2}{T_0} + \frac{2v_0(T_{s0} - \tau_0)}{T_0} + \frac{m_{off}}{T_0}\left({T_{s0}}^2 - {\tau_0}^2\right) - \frac{2m_{off}}{T_0}\tau_0(T_{s0} - \tau_0)$$ **Equation C-39**

$$a_{n,0} = \frac{2}{T_0}\left[\int_0^{\tau_0}(u_0 + m_{on}t)\cos n\omega_0 t\, dt + \int_{\tau_0}^{T_{s0}}\left(v_0 + m_{off}(t - \tau_0)\right)\cos n\omega_0 t\, dt\right]$$ **Equation C-40**

$$a_{n,0} = \frac{2}{T_0}\left[\int_0^{\tau_0} u_0 \cos n\omega_0 t\, dt + \int_0^{\tau_0} m_{on} t \cos n\omega_0 t\, dt + \int_{\tau_0}^{T_{s0}} v_0 \cos n\omega_0 t\, dt + \int_{\tau_0}^{T_{s0}} m_{off} t \cos n\omega_0 t\, dt - \int_{\tau_0}^{T_{s0}} m_{off}\tau_0 \cos n\omega_0 t\, dt\right]$$ Equation C-41

$$a_{n,0} = \frac{2}{T_0}\left[\frac{u_0}{n\omega_0}\sin n\omega_0\tau_0 + \frac{m_{on,0}}{n\omega_0}\tau_0 \sin n\omega_0\tau_0 - \frac{m_{on,0}}{n\omega_0}\int_0^{\tau_0}\sin n\omega_0 t\, dt + \frac{v_0}{n\omega_0}\sin n\omega_0 T_{s0} - \frac{v_0}{n\omega_0}\sin n\omega_0\tau_0 + \frac{m_{off,0}}{n\omega_0} T_{s0}\sin n\omega_0 T_{s0} - \frac{m_{off,0}}{n\omega_0}\tau_0 \sin n\omega_0\tau_0 - \frac{m_{off,0}}{n\omega_0}\int_{\tau_0}^{T_{s0}} \sin n\omega_0 t\, dt - \frac{m_{off,0}}{n\omega_0}\tau_0 \sin n\omega_0 T_{s0} + \frac{m_{off,0}}{n\omega_0}\tau_0 \sin n\omega_0\tau_0\right]$$ Equation C-42

$$a_{n,0} = \frac{2}{T_0}\left[\frac{u_0}{n\omega_0}\sin n\omega_0\tau_0 + \frac{m_{on}}{n\omega_0}\tau_0 \sin n\omega_0\tau_0 + \frac{m_{on}}{n^2{\omega_0}^2}\cos n\omega_0\tau_0 - \frac{m_{on}}{n^2{\omega_0}^2} + \frac{v_0}{n\omega_0}\sin n\omega_0 T_{s0} - \frac{v_0}{n\omega_0}\sin n\omega_0\tau_0 + \frac{m_{off}}{n\omega_0} T_{s0}\sin n\omega_0 T_{s0} - \frac{m_{off}}{n\omega_0}\tau_0 \sin n\omega_0\tau_0 + \frac{m_{off}}{n^2{\omega_0}^2}\cos n\omega_0 T_{s0} - \frac{m_{off}}{n^2{\omega_0}^2}\cos n\omega_0\tau_0 - \frac{m_{off}}{n\omega_0}\tau_0 \sin n\omega_0 T_{s0} + \frac{m_{off}}{n\omega_0}\tau_0 \sin n\omega_0\tau_0\right]$$ Equation C-43

$$a_{n,0} = \frac{2u_0}{n\omega_0 T_0}\sin n\omega_0\tau_0 + \frac{2m_{on}}{n\omega_0 T_0}\tau_0 \sin n\omega_0\tau_0 + \frac{2m_{on}}{n^2{\omega_0}^2 T_0}\cos n\omega_0\tau_0 - \frac{2m_{on}}{n^2{\omega_0}^2 T_0} + \frac{2v_0}{n\omega_0 T_0}\sin n\omega_0 T_{s0} - \frac{2v_0}{n\omega_0 T_0}\sin n\omega_0\tau_0 + \frac{2m_{off}}{n\omega_0 T_0} T_{s0}\sin n\omega_0 T_{s0} - \frac{2m_{off}}{n\omega_0 T_0}\tau_0 \sin n\omega_0\tau_0 + \frac{2m_{off}}{n^2{\omega_0}^2 T_0}\cos n\omega_0 T_{s0} - \frac{2m_{off}}{n^2{\omega_0}^2 T_0}\cos n\omega_0\tau_0 - \frac{2m_{off}}{n\omega_0 T_0}\tau_0 \sin n\omega_0 T_{s0} + \frac{2m_{off}}{n\omega_0 T_0}\tau_0 \sin n\omega_0\tau_0$$ Equation C-44

$$a_{n,0} = \frac{-2m_{on}}{n^2{\omega_0}^2 T_0} + \left(\frac{2u_0}{n\omega_0 T_0} + \frac{2m_{on}}{n\omega_0 T_0}\tau_0 - \frac{2v_0}{n\omega_0 T_0}\right)\sin n\omega_0\tau_0 + \left(\frac{2m_{on}}{n^2{\omega_0}^2 T_0} - \frac{2m_{off}}{n^2{\omega_0}^2 T_0}\right)\cos n\omega_0\tau_0 + \left(\frac{2v_0}{n\omega_0 T_0} + \frac{2m_{off}}{n\omega_0 T_0}\right)\sin n\omega_0 T_{s0} + \frac{2m_{off}}{n^2{\omega_0}^2 T_0}\cos n\omega_0 T_{s0}$$ Equation C-45

$$b_{n,0} = \frac{2}{T_0}\left[\int_0^{\tau_0}(u_0 + m_{on}t)\sin n\omega_0 t\, dt + \int_{\tau_0}^{T_{s0}}\left(v_0 + m_{off}(t - \tau_0)\right)\sin n\omega_0 t\ dt\right]$$ Equation C-46

$$b_{n,0} = \frac{2}{T_0}\left[\int_0^{\tau_0} u_0 \sin n\omega_0 t\, dt + \int_0^{\tau_0} m_{on} t \sin n\omega_0 t\, dt + \int_{\tau_0}^{T_{s0}} v_0 \sin n\omega_0 t\, dt + \int_{\tau_0}^{T_{s0}} m_{off} t \sin n\omega_0 t\, dt - \int_{\tau_0}^{T_{s0}} m_{off}\tau_0 \sin n\omega_0 t\, dt\right]$$ Equation C-47

$$b_{n,0} = \frac{2}{T_0}\left[\frac{-u_0}{n\omega_0}\cos n\omega_0\tau_0 + \frac{u_0}{n\omega_0} - \frac{m_{on}}{n\omega_0}\tau_0\cos n\omega_0\tau_0 + \right.$$
$$\frac{m_{on}}{n\omega_0}\int_0^{\tau_0}\cos n\omega_0 t\,dt - \frac{v_0}{n\omega_0}\cos n\omega_0 T_{s0} + \frac{v_0}{n\omega_0}\cos n\omega_0\tau_0 -$$
$$\frac{m_{off}}{n\omega_0}\,T_{s0}\cos n\omega_0 T_{s0} + \frac{m_{off}}{n\omega_0}\,\tau_0\cos n\omega_0\tau_0 + \frac{m_{off}}{n\omega_0}\int_{\tau_0}^{T_{s0}}\cos n\omega_0 t\,dt +$$
$$\left.\frac{m_{off}}{n\omega_0}\tau_0\cos n\omega_0 T_{s0} - \frac{m_{off}}{n\omega_0}\tau_0\cos n\omega_0\tau_0\right]$$

Equation C-48

$$b_{n,0} = \frac{2}{T_0}\left[\frac{-u_0}{n\omega_0}\cos n\omega_0\tau_0 + \frac{u_0}{n\omega_0} - \frac{m_{on}}{n\omega_0}\tau_0\cos n\omega_0\tau_0 + \frac{m_{on}}{n^2{\omega_0}^2}\sin n\omega_0\tau_0 - \right.$$
$$\frac{v_0}{n\omega_0}\cos n\omega_0 T_{s0} + \frac{v_0}{n\omega_s}\cos n\omega_0\tau_0 - \frac{m_{off}}{n\omega_0}\,T_{s0}\cos n\omega_0 T_{s0} +$$
$$\frac{m_{off}}{n\omega_0}\,\tau_0\cos n\omega_0\tau_0 + \frac{m_{off}}{n^2{\omega_0}^2}\sin n\omega_0 T_{s0} - \frac{m_{off}}{n^2{\omega_0}^2}\sin n\omega_0\tau_0 +$$
$$\left.\frac{m_{off}}{n\omega_0}\tau_0\cos n\omega_0 T_{s0} - \frac{m_{off}}{n\omega_0}\tau_0\cos n\omega_0\tau_0\right]$$

Equation C-49

$$b_{n,0} = \frac{-2u_0}{n\omega_0 T_0}\cos n\omega_0\tau_0 + \frac{2u_0}{n\omega_0 T_0} - \frac{2m_{on}}{n\omega_0 T_0}\tau_0\cos n\omega_0\tau_0 +$$
$$\frac{2m_{on}}{n^2{\omega_0}^2 T_0}\sin n\omega_0\tau_0 - \frac{2v_0}{n\omega_0 T_0}\cos n\omega_0 T_{s0} + \frac{2v_0}{n\omega_0 T_0}\cos n\omega_0\tau_0 -$$
$$\frac{2m_{off}}{n\omega_0 T_0}\,T_{s0}\cos n\omega_0 T_{s0} + \frac{2m_{off}}{n\omega_0 T_0}\,\tau_0\cos n\omega_0\tau_0 - \frac{2m_{off}}{n^2{\omega_0}^2 T_0}\sin n\omega_0 T_{s0} -$$
$$\frac{2m_{off}}{n^2{\omega_0}^2 T_0}\sin n\omega_0\tau_0 + \frac{2m_{off}}{n\omega_0 T_0}\tau_0\cos n\omega_0 T_{s0} - \frac{2m_{off}}{n\omega_0 T_0}\tau_0\cos n\omega_0\tau_0$$

Equation C-50

$$b_{n,0} = \frac{2u_0}{n\omega_0 T_0} + \left(\frac{2v_0}{n\omega_0 T_0} - \frac{2u_0}{n\omega_0 T_0} - \frac{2m_{on}}{n\omega_0 T_0}\tau_0\right)\cos n\omega_0\tau_0 + \left(\frac{2m_{on}}{n^2{\omega_0}^2 T_0} - \right.$$
$$\left.\frac{2m_{off}}{n^2{\omega_0}^2 T_0}\right)\sin n\omega_0\tau_0 - \frac{2m_{off}}{n^2{\omega_0}^2 T_0}\sin n\omega_0 T_{s0} - \left(\frac{2m_{off}}{n\omega_0 T_0}(T_{s0} - \tau_0) + \frac{2v_0}{n\omega_0 T_0}\right)\cos n\omega_0 T_{s0}$$

Equation C-51

Fourier coefficient calculation for the kth function

$$a_{0,k} = \frac{2}{T_0}\left[\int_{\sum_{k=0}^{k-1}T_{sk}}^{\tau_k+\sum_{k=0}^{k-1}T_{sk}} u_k + m_{on}\left(t - \sum_{k=0}^{k-1}T_{sk}\right)dt + \int_{\tau_k+\sum_{k=0}^{k-1}T_{sk}}^{\sum_{k=0}^{k}T_{sk}} v_k + \right.$$
$$\left.m_{off}\left(t - \left(\tau_k + \sum_{k=0}^{k-1}T_{sk}\right)\right)dt\right]$$

Equation C-52

$$a_{0,k} = \frac{2}{T_0}\left[\frac{1}{2}m_{off}\tau_k^2 + \frac{1}{2}m_{on}\tau_k^2 - m_{off}\tau_k T_{sk} + \frac{1}{2}m_{off}T_{sk}^2 + v_k\tau_k - \right.$$
$$\left.v_k T_{sk} - u_k\tau_k\right]$$

Equation C-53

Equation C-54

$$a_{n,k} = \frac{2}{T_0}\left[\int_{\sum_{k=0}^{k-1} T_{sk}}^{\tau_k+\sum_{k=0}^{k-1} T_{sk}} \left(u_k + m_{on}\left(t - \sum_{k=0}^{k-1} T_{sk}\right)\right)\cos(n\omega_0 t)dt + \int_{\tau_k+\sum_{k=0}^{k-1} T_{sk}}^{\sum_{k=0}^{k} T_{sk}} \left(v_k + m_{off}\left(t - \left(\tau_k + \sum_{k=0}^{k-1} T_{sk}\right)\right)\right)\cos(n\omega_0 t)\, dt\right]$$

Equation C-55

$$a_{n,k} = \frac{1}{T_0}\left[2\left(\frac{1}{n^2\omega_0^2}\left(\tau_k n m_{on}\omega_0 sin\left(\left(\sum_{k=0}^{k-1} T_{sk}\right)n\omega_0\right)cos(n\omega_0\tau_k) + \tau_k n m_{on}\omega_0 cos\left(\left(\sum_{k=0}^{k-1} T_{sk}\right)n\omega_0\right)sin(n\omega_0\tau_k) + u_k n\omega_0 sin\left(\left(\sum_{k=0}^{k-1} T_{sk}\right)n\omega_0\right)cos(n\omega_0\tau_k) + u_k n\omega_0 cos\left(\left(\sum_{k=0}^{k-1} T_{sk}\right)n\omega_0\right)sin(n\omega_0\tau_k) - u_k n\omega_0 sin\left(\left(\sum_{k=0}^{k-1} T_{sk}\right)n\omega_0\right) + m_{on}cos\left(\left(\sum_{k=0}^{k-1} T_{sk}\right)n\omega_0\right)cos(n\omega_0\tau_k) - m_{on}sin\left(\left(\sum_{k=0}^{k-1} T_{sk}\right)n\omega_0\right)sin(n\omega_0\tau_k) - m_{on}cos\left(\left(\sum_{k=0}^{k-1} T_{sk}\right)n\omega_0\right)\right)\right) + \frac{1}{n^2\omega_0^2}\left(-v_k n\omega_0 sin\left(\left(\sum_{k=0}^{k-1} T_{sk}\right)n\omega_0\right)cos(n\omega_0\tau_k) - v_k n\omega_0 cos\left(\left(\sum_{k=0}^{k-1} T_{sk}\right)n\omega_0\right)sin(n\omega_0\tau_k) - \tau_k n\omega_0 m_{off} sin\left(\left(\sum_{k=0}^{k} T_{sk}\right)n\omega_0\right) - n\omega_0 m_{off}\left(\sum_{k=0}^{k-1} T_{sk}\right)sin\left(\left(\sum_{k=0}^{k} T_{sk}\right)n\omega_0\right) + n\omega_0 m_{off}\left(\sum_{k=0}^{k} T_{sk}\right)sin\left(\left(\sum_{k=0}^{k} T_{sk}\right)n\omega_0\right) + v_k n\omega_0 sin\left(\left(\sum_{k=0}^{k} T_{sk}\right)n\omega_0\right) - m_{off}cos\left(\left(\sum_{k=0}^{k-1} T_{sk}\right)n\omega_0\right)cos(n\omega_0\tau_k) + m_{off}sin\left(\left(\sum_{k=0}^{k-1} T_{sk}\right)n\omega_0\right)sin(n\omega_0\tau_k) + m_{off}cos\left(\left(\sum_{k=0}^{k} T_{sk}\right)n\omega_0\right)\right)\right]$$

Equation C-56

$$b_{n,k} = \frac{2}{T_0}\left[\int_{\sum_{k=0}^{k-1} T_{sk}}^{\tau_k+\sum_{k=0}^{k-1} T_{sk}} \left(u_k + m_{on}\left(t - \sum_{k=0}^{k-1} T_{sk}\right)\right)\sin(n\omega_0 t)dt + \int_{\tau_k+\sum_{k=0}^{k-1} T_{sk}}^{\sum_{k=0}^{k} T_{sk}} \left(v_k + m_{off}\left(t - \left(\tau_k + \sum_{k=0}^{k-1} T_{sk}\right)\right)\right)\sin(n\omega_0 t)\, dt\right]$$

Equation C-57

$$b_{n,k} = \frac{1}{T_0}\left[2\left(-\frac{1}{n^2\omega_0^2}\left(\tau_k n m_{on}\omega_0 cos\left(\left(\sum_{k=0}^{k-1} T_{sk}\right)n\omega_0\right)cos(n\omega_0\tau_k) - \right.\right.\right.$$
$$\tau_k n m_{on}\omega_0 sin\left(\left(\sum_{k=0}^{k-1} T_{sk}\right)n\omega_0\right)sin(n\omega_0\tau_k) +$$
$$u_k n\omega_0 cos\left(\left(\sum_{k=0}^{k-1} T_{sk}\right)n\omega_0\right)cos(n\omega_0\tau_k) -$$
$$u_k n\omega_0 sin\left(\left(\sum_{k=0}^{k-1} T_{sk}\right)n\omega_0\right)sin(n\omega_0\tau_k) -$$
$$u_k n\omega_0 cos\left(\left(\sum_{k=0}^{k-1} T_{sk}\right)n\omega_0\right) - m_{on}sin\left(\left(\sum_{k=0}^{k-1} T_{sk}\right)n\omega_0\right)cos(n\omega_0\tau_k) -$$
$$\left.\left.\left.m_{on}cos\left(\left(\sum_{k=0}^{k-1} T_{sk}\right)n\omega_0\right)sin(n\omega_0\tau_k) + m_{on}sin\left(\left(\sum_{k=0}^{k-1} T_{sk}\right)n\omega_0\right)\right)\right) -$$
$$\frac{1}{n^2\omega_0^2}\left(-v_k n\omega_0 cos\left(\left(\sum_{k=0}^{k-1} T_{sk}\right)n\omega_0\right)cos(n\omega_0\tau_k) + \right.$$
$$v_k n\omega_0 sin\left(\left(\sum_{k=0}^{k-1} T_{sk}\right)n\omega_0\right)sin(n\omega_0\tau_k) -$$
$$\tau_k n\omega_0 m_{off} cos\left(\left(\sum_{k=0}^{k} T_{sk}\right)n\omega_0\right) -$$
$$n\omega_0 m_{off}\left(\sum_{k=0}^{k-1} T_{sk}\right)cos\left(\left(\sum_{k=0}^{k} T_{sk}\right)n\omega_0\right) +$$
$$n\omega_0 m_{off}\left(\sum_{k=0}^{k} T_{sk}\right)cos\left(\left(\sum_{k=0}^{k} T_{sk}\right)n\omega_0\right) +$$
$$v_k n\omega_0 cos\left(\left(\sum_{k=0}^{k} T_{sk}\right)n\omega_0\right) + m_{off}sin\left(\left(\sum_{k=0}^{k-1} T_{sk}\right)n\omega_0\right)cos(n\omega_0\tau_k) +$$
$$\left.m_{off}cos\left(\left(\sum_{k=0}^{k-1} T_{sk}\right)n\omega_0\right)sin(n\omega_0\tau_k) - m_{off}sin\left(\left(\sum_{k=0}^{k} T_{sk}\right)n\omega_0\right)\right)\Bigg]$$

Total coefficients

Equation C-58

$$a_0 = \sum_{k=0}^{N_p-1} a_{0,k}$$

Equation C-59

$$a_n = \sum_{k=0}^{N_p-1} a_{n,k}$$

Equation C-60

$$b_n = \sum_{k=0}^{N_p-1} b_{n,k}$$

Equation C-61

$$c_n = \sum_{k=0}^{N_p-1} \begin{matrix} \frac{1}{2}(a_{n,k} - ib_{n,k})(n \geq 1) \\ \frac{1}{2}(a_{n,k} + ib_{n,k})(n \leq 1) \end{matrix}$$

Fourier Analysis of Sawtooth wave with varying starting position

Functions to be analysed

$$f_0(t) = \begin{cases} u_0 + m_{on}(t - t_{ph0}) & t_{ph0} < t \le \tau + t_{ph0} \\ v_0 + m_{off}(t - \tau - t_{ph0}) & \tau + t_{ph0} < t \le T_s + t_{ph1} \end{cases}$$ Equation C-62

$$f_1(t) = \begin{cases} u_1 + m_{on}(t - T_s - t_{ph1}) & T_s + t_{ph1} < t \le \tau + t_{ph1} + T_s \\ v_1 + m_{off}(t - \tau - t_{ph1} - T_s) & \tau + t_{ph1} + T_s < t \le 2T_s + t_{ph2} \end{cases}$$ Equation C-63

$$f_2(t) = \begin{cases} u_2 + m_{on}(t - 2T_s - t_{ph2}) & 2T_s + t_{ph2} < t \le \tau + t_{ph2} + 2T_s \\ v_2 + m_{off}(t - \tau - t_{ph2} - 2T_s) & \tau + t_{ph2} + 2T_s < t \le 3T_s + t_{ph3} \end{cases}$$ Equation C-64

.

.

$$f_{Np-1}(t) =$$ Equation C-65

$$\begin{cases} u_{Np-1} + m_{on}(t - (Np-1)T_s - t_{phNp-1}) & (Np-1)T_s + t_{phNp-1} < t < \tau + t_{phNp-1} + (Np-1)T_s \\ v_{Np-1} + m_{off}(t - \tau - t_{phNp-1} - (k-1)T_s) & \tau + t_{phNp-1} + (Np-1)T_s < t < NpT_s + t_{ph0} \end{cases}$$

Fourier co-efficient calculation for first function

$$a_{0,0} = \frac{2}{T_0}\left[\int_{t_{ph0}}^{\tau+t_{ph0}} u_0 + m_{on}(t - t_{ph0})\,dt + \int_{\tau+t_{ph0}}^{T_s+t_{ph0}} v_0 + m_{off}(t - \tau - t_{ph0})\,dt\right]$$ Equation C-66

$$a_{0,0} = \frac{2}{T_0}\left[\int_{t_{ph0}}^{\tau+t_{ph0}} u_0\,dt + \int_{t_{ph0}}^{\tau+t_{ph0}} m_{on}t\,dt - \int_{t_{ph0}}^{\tau+t_{ph0}} m_{on}t_{ph0}\,dt + \int_{\tau+t_{ph0}}^{T_s+t_{ph0}} v_0\,dt + \int_{\tau+t_{ph0}}^{T_s+t_{ph0}} m_{off}t\,dt - \int_{\tau+t_{ph0}}^{T_s+t_{ph0}} m_{off}(\tau + t_{ph0})dt\right]$$ Equation C-67

$$a_{0,0} = \frac{2}{T_0}\left[u_0(\tau + t_{ph0}) - u_0 t_{ph0} + \frac{m_{on}}{2}(\tau + t_{ph0})^2 - \frac{m_{on}}{2}(t_{ph0})^2 + v_0(T_s + t_{ph0}) - v_0(\tau + t_{ph0}) + \frac{m_{off}}{2}(T_s + t_{ph0})^2 - \frac{m_{off}}{2}(\tau + t_{ph0})^2 - m_{off}(\tau + t_{ph0})(T_s + t_{ph0}) + m_{off}(\tau + t_{ph0})^2\right]$$ Equation C-68

$$a_{0,0} = \frac{2}{T_0}\left[u_0\tau + \frac{m_{on}}{2}\tau^2 + v_0T_s - v_0\tau + \frac{m_{off}}{2}T_s^2 - \frac{m_{off}}{2}\tau^2 - m_{off}\tau T_s + m_{off}\tau^2\right]e^{-jn\omega_0 t_{ph0}}$$ Equation C-69

$$a_{0,0} = (\frac{2u_0\tau}{T_0} + \frac{m_{on}\tau^2}{T_0} + \frac{2v_0(T_s-\tau)}{T_0} + \frac{m_{off}}{T_0}\left({T_s}^2 - \tau^2\right) - \frac{2m_{off}}{T_0}\tau(T_s - \tau))e^{-jn\omega_0 t_{ph0}}$$ Equation C-70

$$a_{n,0} = \frac{2}{T_0}\left[\int_{t_{ph0}}^{\tau+t_{ph0}}\left(u_0 + m_{on}(t-t_{ph0})\right)\cos n\omega_0 t\, dt + \int_{\tau+t_{ph0}}^{T_s+t_{ph0}}\left(v_0 + m_{off}(t-\tau-t_{ph0})\right)\cos n\omega_0 t\ dt\right]$$ Equation C-71

$$a_{n,0} = \frac{2}{T_0}\left[\int_{t_{ph0}}^{\tau+t_{ph0}} u_0\ \cos n\omega_0 t\, dt + \int_{t_{ph0}}^{\tau+t_{ph0}} m_{on}(t-t_{ph0})\ \cos n\omega_0 t\, dt + \int_{\tau+t_{ph0}}^{T_s+t_{ph0}} v_0\ \cos n\omega_0 t\, dt + \int_{\tau+t_{ph0}}^{T_s+t_{ph0}} m_{off} t\ \cos n\omega_0 t\, dt - \int_{\tau+t_{ph0}}^{T_s+t_{ph0}} m_{off}(\tau + t_{ph0})\ \cos n\omega_0 t\, dt\right]$$ Equation C-72

$$a_{n,0} = \frac{2}{T_0}\left[\frac{u_0}{n\omega_0}\sin n\omega_0(\tau+t_{ph0}) - \frac{u_0}{n\omega_0}\sin n\omega_0 t_{ph0} + \frac{m_{on}}{n\omega_0}\left(\tau + t_{ph0}\right)\sin n\omega_0(\tau+t_{ph0}) - \frac{m_{on}}{n\omega_0}t_{ph0}\sin n\omega_0 t_{ph0} - \frac{m_{on}}{n\omega_0}\int_{t_{ph0}}^{\tau+t_{ph0}}\sin n\omega_0 t\, dt + \frac{v_0}{n\omega_0}\sin n\omega_0\left(T_s + t_{ph0}\right) - \frac{v_0}{n\omega_0}\sin n\omega_0(\tau + t_{ph0}) + \frac{m_{off}}{n\omega_0}\ (T_s + t_{ph0})\sin n\omega_0\left(T_s + t_{ph0}\right) - \frac{m_{off}}{n\omega_0}\ (\tau + t_{ph0})\sin n\omega_0(\tau + t_{ph0}) - \frac{m_{off}}{n\omega_0}\int_{\tau+t_{ph0}}^{T_s+t_{ph0}}\ \sin n\omega_0 t\, dt - \frac{m_{off}}{n\omega_0}(\tau + t_{ph0})\sin n\omega_0(T_s + t_{ph0}) + \frac{m_{off}}{n\omega_0}(\tau + t_{ph0})\sin n\omega_0(\tau + t_{ph0})\right]$$ Equation C-73

$$a_{n,0} = \frac{2}{T_0}\left[\frac{u_0}{n\omega_0}\sin n\omega_0(\tau+t_{ph0}) - \frac{u_0}{n\omega_0}\sin n\omega_0 t_{ph0} + \frac{m_{on}}{n\omega_0}\left(\tau + t_{ph0}\right)\sin n\omega_0\left(\tau+t_{ph0}\right) - \frac{m_{on}}{n\omega_0}t_{ph0}\sin n\omega_0 t_{ph0} + \frac{m_{on}}{n^2{\omega_0}^2}\cos n\omega_0(\tau + t_{ph0}) - \frac{m_{on}}{n^2{\omega_0}^2}\cos n\omega_0 t_{ph0} + + \frac{v_0}{n\omega_0}\sin n\omega_0\left(T_s + t_{ph0}\right) - \frac{v_0}{n\omega_0}\sin n\omega_0(\tau + t_{ph0}) + \frac{m_{off}}{n\omega_0}\ (T_s + t_{ph0})\sin n\omega_0\left(T_s + t_{ph0}\right) - \frac{m_{off}}{n\omega_0}\ (\tau + t_{ph0})\sin n\omega_0(\tau + t_{ph0}) + \frac{m_{off}}{n^2{\omega_0}^2}\cos n\omega_0(T_s + t_{ph0}) - \frac{m_{off}}{n^2{\omega_0}^2}\cos n\omega_0(\tau + t_{ph0}) - \frac{m_{off}}{n\omega_0}(\tau + t_{ph0})\sin n\omega_0(T_s + t_{ph0}) + \frac{m_{off}}{n\omega_0}(\tau + t_{ph0})\sin n\omega_0(\tau + t_{ph0})\right]$$ Equation C-74

$$a_{n,0} = \frac{2u_0}{n\omega_0 T_0}\sin n\omega_0(\tau+t_{ph0}) - \frac{u_0}{n\omega_0 T_0}\sin n\omega_0 t_{ph0} + \frac{2m_{on}}{n\omega_0 T_0}\left(\tau + t_{ph0}\right)\sin n\omega_0\left(\tau+t_{ph0}\right) - \frac{m_{on}}{n\omega_0 T_0}t_{ph0}\sin n\omega_0 t_{ph0} + \frac{2m_{on}}{n^2{\omega_0}^2 T_0}\cos n\omega_0(\tau +$$ Equation C-75

$$t_{ph0}) - \frac{2m_{on}}{n^2\omega_0{}^2T_0}\cos n\omega_0 t_{ph0} + \frac{2v_0}{n\omega_0 T_0}\sin n\omega_0\left(T_s + t_{ph0}\right) -$$

$$\frac{2v_0}{n\omega_0 T_0}\sin n\omega_0(\tau + t_{ph0}) + \frac{2m_{off}}{n\omega_0 T_0}\ (T_s + t_{ph0})\sin n\omega_0\left(T_s + t_{ph0}\right) -$$

$$\frac{2m_{off}}{n\omega_0 T_0}\ (\tau + t_{ph0})\sin n\omega_0(\tau + t_{ph0}) + \frac{2m_{off}}{n^2\omega_0{}^2T_0}\cos n\omega_0(T_s + t_{ph0}) -$$

$$\frac{2m_{off}}{n^2\omega_0{}^2T_0}\cos n\omega_0(\tau + t_{ph0}) - \frac{2m_{off}}{n\omega_0 T_0}(\tau + t_{ph0})\sin n\omega_0(T_s + t_{ph0}) +$$

$$\frac{2m_{off}}{n\omega_0 T_0}(\tau + t_{ph0})\sin n\omega_0(\tau + t_{ph0})$$

$$a_{n,0} = (\frac{2u_0}{n\omega_0 T_0}\sin n\omega_0\tau + \frac{2m_{on}}{n\omega_0 T_0}\tau\sin n\omega_0\tau + \frac{2m_{on}}{n^2\omega_0{}^2T_0}\cos n\omega_0\tau - \frac{2m_{on}}{n^2\omega_0{}^2T_0} + \quad \text{Equation C-76}$$

$$\frac{2v_0}{n\omega_0 T_0}\sin n\omega_0 T_s - \frac{2v_0}{n\omega_0 T_0}\sin n\omega_0\tau + \frac{2m_{off}}{n\omega_0 T_0}\ T_s\sin n\omega_0 T_s -$$

$$\frac{2m_{off}}{n\omega_0 T_0}\ \tau\sin n\omega_0\tau + \frac{2m_{off}}{n^2\omega_0{}^2T_0}\cos n\omega_0 T_s - \frac{2m_{off}}{n^2\omega_0{}^2T_0}\cos n\omega_0\tau -$$

$$\frac{2m_{off}}{n\omega_0 T_0}\tau\sin n\omega_0 T_s + \frac{2m_{off}}{n\omega_0 T_0}\tau\sin n\omega_0\tau)e^{-jn\omega_0 t_{ph0}}$$

$$a_{n,0} = (\frac{-2m_{on}}{n^2\omega_0{}^2T_0} + \left(\frac{2u_0}{n\omega_0 T_0} + \frac{2m_{on}}{n\omega_0 T_0}\tau - \frac{2v_0}{n\omega_0 T_0}\right)\sin n\omega_0\tau + \left(\frac{2m_{on}}{n^2\omega_0{}^2T_0} - \quad \text{Equation C-77}$$

$$\frac{2m_{off}}{n^2\omega_0{}^2T_0}\right)\cos n\omega_0\tau + \left(\frac{2v_0}{n\omega_0 T_0} + \frac{2m_{off}}{n\omega_0 T_0}(T_s - \tau)\ \right)\sin n\omega_0 T_s +$$

$$\frac{2m_{off}}{n^2\omega_0{}^2T_0}\cos n\omega_0 T_s)e^{-jn\omega_0 t_{ph0}}$$

$$b_{n,0} = \frac{2}{T_0}\left[\int_{t_{ph0}}^{\tau+t_{ph0}}\left(u_0 + m_{on}(t - t_{ph0})\right)\sin n\omega_0 t\ dt + \int_{\tau+t_{ph0}}^{T_s+t_{ph0}}\left(v_0 + \right.\right. \quad \text{Equation C-78}$$

$$\left.\left.m_{off}(t - \tau - t_{ph0})\right)\sin n\omega_0 t\ \ dt\right]$$

$$b_{n,0} = \frac{2}{T_0}\left[\int_{t_{ph0}}^{\tau+t_{ph0}} u_0\ \sin n\omega_0 t\ dt + \int_{t_{ph0}}^{\tau+t_{ph0}} m_{on}(t - t_{ph0})\ \sin n\omega_0 t\ dt + \right. \quad \text{Equation C-79}$$

$$\int_{\tau+t_{ph0}}^{T_s+t_{ph0}} v_0\ \sin n\omega_0 t\ dt + \int_{\tau+t_{ph0}}^{T_s+t_{ph0}} m_{off}t\ \sin n\omega_0 t\ dt - \int_{\tau+t_{ph0}}^{T_s+t_{ph0}} m_{off}(\tau + $$

$$\left.t_{ph0})\sin n\omega_0 t\ dt\right]$$

$$b_{n,0} = \frac{2}{T_0}\left[\frac{-u_0}{n\omega_0}\cos n\omega_0(\tau + t_{ph0}) + \frac{u_0}{n\omega_0} - \frac{m_{on}}{n\omega_0}(\tau + t_{ph0})\cos n\omega_0(\tau + \right. \quad \text{Equation C-80}$$

$$t_{ph0}) + \frac{m_{on}}{n\omega_0\tau_0}\int_0^{\tau+t_{ph0}}\cos n\omega_0 t\ dt - \frac{v_0}{n\omega_0}\cos n\omega_0\left(T_s + t_{ph0}\right) +$$

$$\frac{v_0}{n\omega_0}\cos n\omega_0(\tau + t_{ph0}) - \frac{m_{off}}{n\omega_0}\ \left(T_s + t_{ph0}\right)\cos n\omega_0\left(T_s + t_{ph0}\right) + \frac{m_{off}}{n\omega_0}\ (\tau +$$

$$t_{ph0})\cos n\omega_0(\tau + t_{ph0}) + \frac{m_{off,}}{n\omega_0}\int_{\tau+t_{ph0}}^{T_{s0}} \cos n\omega_0 t\, dt + \frac{m_{off}}{n\omega_0}(\tau +$$

$$t_{ph0})\cos n\omega_0(T_s + t_{ph0}) - \frac{m_{off}}{n\omega_0}(\tau + t_{ph0})\cos n\omega_0(\tau + t_{ph0})\Big]$$

$$b_{n,0} = \frac{2}{T_0}\left[\frac{-u_0}{n\omega_0}\cos n\omega_0(\tau + t_{ph0}) + \frac{u_0}{n\omega_0}\cos n\omega_0(t_{ph0}) - \frac{m_{on}}{n\omega_0}(\tau + \right. \quad \text{Equation C-81}$$

$$t_{ph0})\cos n\omega_0(\tau + t_{ph0}) + \frac{2m_{on}}{n\omega_0 T_0}(t_{ph0})\cos n\omega_0(t_{ph0}) + \frac{m_{on}}{n^2{\omega_0}^2}\sin n\omega_0(\tau +$$

$$t_{ph0}) - \frac{v_0}{n\omega_0}\cos n\omega_0(T_s + t_{ph0}) + \frac{v_0}{n\omega_s}\cos n\omega_0(\tau + t_{ph0}) - \frac{m_{off}}{n\omega_0}(T_s +$$

$$t_{ph0})\cos n\omega_0(T_s + t_{ph0}) + \frac{m_{off}}{n\omega_0}(\tau + t_{ph0})\cos n\omega_0(\tau + t_{ph0}) +$$

$$\frac{m_{off}}{n^2{\omega_0}^2}\sin n\omega_0(T_s + t_{ph0}) - \frac{m_{off}}{n^2{\omega_0}^2}\sin n\omega_0(\tau + t_{ph0}) + \frac{m_{off}}{n\omega_0}(\tau +$$

$$\left. t_{ph0})\cos n\omega_0(T_s + t_{ph0}) - \frac{m_{off}}{n\omega_0}(\tau + t_{ph0})\cos n\omega_0(\tau + t_{ph0})\right]$$

$$b_{n,0} = \frac{-2u_0}{n\omega_0 T_0}\cos n\omega_0(\tau + t_{ph0}) + \frac{2u_0}{n\omega_0 T_0}\cos n\omega_0(t_{ph0}) - \frac{2m_{on}}{n\omega_0 T_0}(\tau + \quad \text{Equation C-82}$$

$$t_{ph0})\cos n\omega_0(\tau + t_{ph0}) + \frac{2m_{on}}{n\omega_0 T_0}(t_{ph0})\cos n\omega_0(t_{ph0}) + \frac{2m_{on}}{n^2{\omega_0}^2 T_0}\sin n\omega_0(\tau +$$

$$t_{ph0}) - \frac{2v_0}{n\omega_0 T_0}\cos n\omega_0(T_s + t_{ph0}) + \frac{2v_0}{n\omega_0 T_0}\cos n\omega_0(\tau + t_{ph0}) - \frac{2m_{off}}{n\omega_0 T_0}(T_s +$$

$$t_{ph0})\cos n\omega_0(T_s + t_{ph0}) + \frac{2m_{off}}{n\omega_0 T_0}(\tau + t_{ph0})\cos n\omega_0(\tau + t_{ph0}) -$$

$$\frac{2m_{off}}{n^2{\omega_0}^2 T_0}\sin n\omega_0(T_s + t_{ph0}) - \frac{2m_{off}}{n^2{\omega_0}^2 T_0}\sin n\omega_0(\tau + t_{ph0}) + \frac{2m_{off}}{n\omega_0 T_0}(\tau +$$

$$t_{ph0})\cos n\omega_0(T_s + t_{ph0}) - \frac{2m_{off}}{n\omega_0 T_0}(\tau + t_{ph0})\cos n\omega_0(\tau + t_{ph0})$$

$$\begin{aligned} b_{n,0} = (&\frac{-2u_0}{n\omega_0 T_0}\cos n\omega_0\tau + \frac{2u_0}{n\omega_0 T_0} - \frac{2m_{on}}{n\omega_0 T_0}\tau\cos n\omega_0\tau + \frac{2m_{on}}{n^2{\omega_0}^2 T_0}\sin n\omega_0\tau \\ &- \frac{2v_0}{n\omega_0 T_0}\cos n\omega_0 T_s + \frac{2v_0}{n\omega_0 T_0}\cos n\omega_0\tau - \frac{2m_{off}}{n\omega_0 T_0}\,T_s\cos n\omega_0 T_s \\ &+ \frac{2m_{off}}{n\omega_0 T_0}\,\tau\cos n\omega_0\tau - \frac{2m_{off}}{n^2{\omega_0}^2 T_0}\sin n\omega_0 T_s - \frac{2m_{off}}{n^2{\omega_0}^2 T_0}\sin n\omega_0\tau \\ &+ \frac{2m_{off}}{n\omega_0 T_0}\tau\cos n\omega_0 T_s - \frac{2m_{off}}{n\omega_0 T_0}\tau\cos n\omega_0\tau\,)e^{-jn\omega_0 t_{ph0}} \end{aligned} \quad \text{Equation C-83}$$

$$\begin{aligned} b_{n,0} = (&\frac{2u_0}{n\omega_0 T_0} + \left(\frac{2v_0}{n\omega_0 T_0} - \frac{2u_0}{n\omega_0 T_0} - \frac{2m_{on}}{n\omega_0 T_0}\tau\right)\cos n\omega_0\tau \\ &+ \left(\frac{2m_{on}}{n^2{\omega_0}^2 T_0} - \frac{2m_{off}}{n^2{\omega_0}^2 T_0}\right)\sin n\omega_0\tau - \frac{2m_{off}}{n^2{\omega_0}^2 T_0}\sin n\omega_0 T_s \\ &- (\frac{2m_{off}}{n\omega_0 T_0}(T_s - \tau) + \frac{2v_0}{n\omega_0 T_0})\cos n\omega_0 T_s)e^{-jn\omega_0 t_{ph0}} \end{aligned} \quad \text{Equation C-84}$$

Fourier coefficient calculation for the kth function

$$a_{0,k} = \frac{2}{T_0}\left[\int_{(k)T_s+t_{phk}}^{\tau+t_{phk}+(k)T_s} u_k + m_{on}(t - kT_s - t_{phk})\,dt + \int_{\tau+t_{phk-2}+(k)T_s}^{(k+1)T_s+t_{phk+1}} v_k + m_{off}(t - \tau - -kT_s - t_{phk})\,dt\right]$$

Equation C-85

$$a_{0,k} = -\frac{1}{T_0}\left[-2m_{off}{t_{phk}}^2 + 2m_{off}t_{phk}t_{phk+1} - 2m_{off}t_{phk}\tau + 2m_{off}t_{phk}T_s - m_{off}{t_{phk+1}}^2 + 2m_{off}t_{phk+1}\tau - 2m_{off}t_{phk+1}T_s - m_{off}\tau^2 - m_{on}\tau^2 + 2m_{off}\tau T_s - m_{off}{T_s}^2 + 2v_k t_{phk+1} + 2v_k\tau - 2v_k T_s - 2u_k\tau\right]$$

Equation C-86

$$a_{n,k} = \frac{2}{T_0}\left[\int_{(k)T_s+t_{phk}}^{\tau+t_{phk}+(k)T_s} u_k + m_{on}(t - kT_s - t_{phk})\,\cos n\omega_0 t\,dt + \int_{\tau+t_{phk-2}+(k)T_s}^{(k+1)T_s+t_{phk+1}} v_k + m_{off}(t - \tau - -kT_s - t_{phk})\,\cos n\omega_0 t\,dt\right]$$

Equation C-87

and

$$b_{n,k} = \frac{2}{T_0}\left[\int_{(k)T_s+t_{phk}}^{\tau+t_{phk}+(k)T_s} u_k + m_{on}(t - kT_s - t_{phk})\,\sin n\omega_0 t\,dt + \int_{\tau+t_{phk-2}+(k)T_s}^{(k+1)T_s+t_{phk+1}} v_k + m_{off}(t - \tau - -kT_s - t_{phk})\,\sin n\omega_0 t\,dt\right]$$

Equation C-88

$$a_{n,k} =$$ **Equation C-89**

$$
\begin{aligned}
&-\frac{1}{T_0\, n^2\, \omega_0^2}\Big(2\left(u(k)\, n\, \omega_0 \sin\left(k\, T_s\, n\, \omega_0\right) \cos\left(n\, \omega_0\, tph(k)\right)\right.\\
&+ u(k)\, n\, \omega_0 \cos\left(k\, T_s\, n\, \omega_0\right) \sin\left(n\, \omega_0\, tph(k)\right)\\
&- n\, \tau\, m_{on}\, \omega_0 \sin\left(k\, T_s\, n\, \omega_0\right) \cos\left(n\, \omega_0\, tph(k)\right) \cos\left(n\, \omega_0\, \tau\right)\\
&+ n\, \tau\, m_{on}\, \omega_0 \sin\left(k\, T_s\, n\, \omega_0\right) \sin\left(n\, \omega_0\, tph(k)\right) \sin\left(n\, \omega_0\, \tau\right)\\
&- n\, \tau\, m_{on}\, \omega_0 \cos\left(k\, T_s\, n\, \omega_0\right) \sin\left(n\, \omega_0\, tph(k)\right) \cos\left(n\, \omega_0\, \tau\right)\\
&- n\, \tau\, m_{on}\, \omega_0 \cos\left(k\, T_s\, n\, \omega_0\right) \cos\left(n\, \omega_0\, tph(k)\right) \sin\left(n\, \omega_0\, \tau\right)\\
&+ tph(k)\, n\, m_{off} \omega_0 \sin\left(k\, T_s\, n\, \omega_0\right) \cos\left(n\, T_s\, \omega_0\right) \cos\left(n\, \omega_0\, tph(k+1)\right)\\
&- tph(k)\, n\, m_{off} \omega_0 \sin\left(k\, T_s\, n\, \omega_0\right) \sin\left(n\, T_s\, \omega_0\right) \sin\left(n\, \omega_0\, tph(k+1)\right)\\
&+ tph(k)\, n\, m_{off} \omega_0 \cos\left(k\, T_s\, n\, \omega_0\right) \sin\left(n\, T_s\, \omega_0\right) \cos\left(n\, \omega_0\, tph(k+1)\right)\\
&+ tph(k)\, n\, m_{off} \omega_0 \cos\left(k\, T_s\, n\, \omega_0\right) \cos\left(n\, T_s\, \omega_0\right) \sin\left(n\, \omega_0\, tph(k+1)\right) - tph(k\\
&+ 1)\, n\, m_{off} \omega_0 \sin\left(k\, T_s\, n\, \omega_0\right) \cos\left(n\, T_s\, \omega_0\right) \cos\left(n\, \omega_0\, tph(k+1)\right) + tph(k\\
&+ 1)\, n\, m_{off} \omega_0 \sin\left(k\, T_s\, n\, \omega_0\right) \sin\left(n\, T_s\, \omega_0\right) \sin\left(n\, \omega_0\, tph(k+1)\right) - tph(k\\
&+ 1)\, n\, m_{off} \omega_0 \cos\left(k\, T_s\, n\, \omega_0\right) \sin\left(n\, T_s\, \omega_0\right) \cos\left(n\, \omega_0\, tph(k+1)\right) - tph(k\\
&+ 1)\, n\, m_{off} \omega_0 \cos\left(k\, T_s\, n\, \omega_0\right) \cos\left(n\, T_s\, \omega_0\right) \sin\left(n\, \omega_0\, tph(k+1)\right)\\
&+ n\, \tau\, m_{off} \omega_0 \sin\left(k\, T_s\, n\, \omega_0\right) \cos\left(n\, T_s\, \omega_0\right) \cos\left(n\, \omega_0\, tph(k+1)\right)\\
&- n\, \tau\, m_{off} \omega_0 \sin\left(k\, T_s\, n\, \omega_0\right) \sin\left(n\, T_s\, \omega_0\right) \sin\left(n\, \omega_0\, tph(k+1)\right)\\
&+ n\, \tau\, m_{off} \omega_0 \cos\left(k\, T_s\, n\, \omega_0\right) \sin\left(n\, T_s\, \omega_0\right) \cos\left(n\, \omega_0\, tph(k+1)\right)\\
&+ n\, \tau\, m_{off} \omega_0 \cos\left(k\, T_s\, n\, \omega_0\right) \cos\left(n\, T_s\, \omega_0\right) \sin\left(n\, \omega_0\, tph(k+1)\right)\\
&- n\, T_s\, m_{off} \omega_0 \sin\left(k\, T_s\, n\, \omega_0\right) \cos\left(n\, T_s\, \omega_0\right) \cos\left(n\, \omega_0\, tph(k+1)\right)\\
&+ n\, T_s\, m_{off} \omega_0 \sin\left(k\, T_s\, n\, \omega_0\right) \sin\left(n\, T_s\, \omega_0\right) \sin\left(n\, \omega_0\, tph(k+1)\right)\\
&- n\, T_s\, m_{off} \omega_0 \cos\left(k\, T_s\, n\, \omega_0\right) \sin\left(n\, T_s\, \omega_0\right) \cos\left(n\, \omega_0\, tph(k+1)\right)\\
&- n\, T_s\, m_{off} \omega_0 \cos\left(k\, T_s\, n\, \omega_0\right) \cos\left(n\, T_s\, \omega_0\right) \sin\left(n\, \omega_0\, tph(k+1)\right)\\
&+ m_{on} \cos\left(k\, T_s\, n\, \omega_0\right) \cos\left(n\, \omega_0\, tph(k)\right) - m_{on} \sin\left(k\, T_s\, n\, \omega_0\right) \sin\left(n\, \omega_0\, tph(k)\right)\\
&- u(k)\, n\, \omega_0 \sin\left(k\, T_s\, n\, \omega_0\right) \cos\left(n\, \omega_0\, tph(k)\right) \cos\left(n\, \omega_0\, \tau\right)\\
&+ u(k)\, n\, \omega_0 \sin\left(k\, T_s\, n\, \omega_0\right) \sin\left(n\, \omega_0\, tph(k)\right) \sin\left(n\, \omega_0\, \tau\right)\\
&- u(k)\, n\, \omega_0 \cos\left(k\, T_s\, n\, \omega_0\right) \sin\left(n\, \omega_0\, tph(k)\right) \cos\left(n\, \omega_0\, \tau\right)\\
&- u(k)\, n\, \omega_0 \cos\left(k\, T_s\, n\, \omega_0\right) \cos\left(n\, \omega_0\, tph(k)\right) \sin\left(n\, \omega_0\, \tau\right)\\
&+ v(k)\, n\, \omega_0 \sin\left(k\, T_s\, n\, \omega_0\right) \cos\left(n\, \omega_0\, tph(k)\right) \cos\left(n\, \omega_0\, \tau\right)\\
&- v(k)\, n\, \omega_0 \sin\left(k\, T_s\, n\, \omega_0\right) \sin\left(n\, \omega_0\, tph(k)\right) \sin\left(n\, \omega_0\, \tau\right)\\
&+ v(k)\, n\, \omega_0 \cos\left(k\, T_s\, n\, \omega_0\right) \sin\left(n\, \omega_0\, tph(k)\right) \cos\left(n\, \omega_0\, \tau\right)\\
&+ v(k)\, n\, \omega_0 \cos\left(k\, T_s\, n\, \omega_0\right) \cos\left(n\, \omega_0\, tph(k)\right) \sin\left(n\, \omega_0\, \tau\right)\\
&- m_{on} \cos\left(k\, T_s\, n\, \omega_0\right) \cos\left(n\, \omega_0\, tph(k)\right) \cos\left(n\, \omega_0\, \tau\right)\\
&+ m_{on} \cos\left(k\, T_s\, n\, \omega_0\right) \sin\left(n\, \omega_0\, tph(k)\right) \sin\left(n\, \omega_0\, \tau\right)\\
&+ m_{on} \sin\left(k\, T_s\, n\, \omega_0\right) \sin\left(n\, \omega_0\, tph(k)\right) \cos\left(n\, \omega_0\, \tau\right)\\
&+ m_{on} \sin\left(k\, T_s\, n\, \omega_0\right) \cos\left(n\, \omega_0\, tph(k)\right) \sin\left(n\, \omega_0\, \tau\right)\\
&+ m_{off} \cos\left(k\, T_s\, n\, \omega_0\right) \cos\left(n\, \omega_0\, tph(k)\right) \cos\left(n\, \omega_0\, \tau\right)\\
&- m_{off} \cos\left(k\, T_s\, n\, \omega_0\right) \sin\left(n\, \omega_0\, tph(k)\right) \sin\left(n\, \omega_0\, \tau\right)\\
&- m_{off} \sin\left(k\, T_s\, n\, \omega_0\right) \sin\left(n\, \omega_0\, tph(k)\right) \cos\left(n\, \omega_0\, \tau\right)\\
&- m_{off} \sin\left(k\, T_s\, n\, \omega_0\right) \cos\left(n\, \omega_0\, tph(k)\right) \sin\left(n\, \omega_0\, \tau\right)\\
&- m_{off} \cos\left(k\, T_s\, n\, \omega_0\right) \cos\left(n\, T_s\, \omega_0\right) \cos\left(n\, \omega_0\, tph(k+1)\right)\\
&+ m_{off} \cos\left(k\, T_s\, n\, \omega_0\right) \sin\left(n\, T_s\, \omega_0\right) \sin\left(n\, \omega_0\, tph(k+1)\right)\\
&+ m_{off} \sin\left(k\, T_s\, n\, \omega_0\right) \sin\left(n\, T_s\, \omega_0\right) \cos\left(n\, \omega_0\, tph(k+1)\right)\\
&+ m_{off} \sin\left(k\, T_s\, n\, \omega_0\right) \cos\left(n\, T_s\, \omega_0\right) \sin\left(n\, \omega_0\, tph(k+1)\right)\\
&- v(k)\, n\, \omega_0 \sin\left(k\, T_s\, n\, \omega_0\right) \cos\left(n\, T_s\, \omega_0\right) \cos\left(n\, \omega_0\, tph(k+1)\right)\\
&+ v(k)\, n\, \omega_0 \sin\left(k\, T_s\, n\, \omega_0\right) \sin\left(n\, T_s\, \omega_0\right) \sin\left(n\, \omega_0\, tph(k+1)\right)\\
&- v(k)\, n\, \omega_0 \cos\left(k\, T_s\, n\, \omega_0\right) \sin\left(n\, T_s\, \omega_0\right) \cos\left(n\, \omega_0\, tph(k+1)\right)\\
&- v(k)\, n\, \omega_0 \cos\left(k\, T_s\, n\, \omega_0\right) \cos\left(n\, T_s\, \omega_0\right) \sin\left(n\, \omega_0\, tph(k+1)\right)\Big)\Big)
\end{aligned}
$$

Equation C-90

$$
\begin{aligned}
b_{n,k} = \frac{1}{T_0}\Bigg(2\Bigg(&-\frac{1}{n^2\omega_0^2}\left(n\,\tau\,m_{on}\,\omega_0\cos\left(k\,T_s\,n\,\omega_0\right)\cos\left(n\,\omega_0\,tph(k)\right)\cos\left(n\,\omega_0\,\tau\right)\right.\\
&-n\,\tau\,m_{on}\,\omega_0\sin\left(k\,T_s\,n\,\omega_0\right)\cos\left(n\,\omega_0\,tph(k)\right)\sin\left(n\,\omega_0\,\tau\right)\\
&-n\,\tau\,m_{on}\,\omega_0\sin\left(k\,T_s\,n\,\omega_0\right)\sin\left(n\,\omega_0\,tph(k)\right)\cos\left(n\,\omega_0\,\tau\right)\\
&-n\,\tau\,m_{on}\,\omega_0\cos\left(k\,T_s\,n\,\omega_0\right)\sin\left(n\,\omega_0\,tph(k)\right)\sin\left(n\,\omega_0\,\tau\right)\\
&+u(k)\,n\,\omega_0\cos\left(k\,T_s\,n\,\omega_0\right)\cos\left(n\,\omega_0\,tph(k)\right)\cos\left(n\,\omega_0\,\tau\right)\\
&-u(k)\,n\,\omega_0\sin\left(k\,T_s\,n\,\omega_0\right)\cos\left(n\,\omega_0\,tph(k)\right)\sin\left(n\,\omega_0\,\tau\right)\\
&-u(k)\,n\,\omega_0\sin\left(k\,T_s\,n\,\omega_0\right)\sin\left(n\,\omega_0\,tph(k)\right)\cos\left(n\,\omega_0\,\tau\right)\\
&-u(k)\,n\,\omega_0\cos\left(k\,T_s\,n\,\omega_0\right)\sin\left(n\,\omega_0\,tph(k)\right)\sin\left(n\,\omega_0\,\tau\right)\\
&-u(k)\,n\,\omega_0\cos\left(k\,T_s\,n\,\omega_0\right)\cos\left(n\,\omega_0\,tph(k)\right)+u(k)\,n\,\omega_0\sin\left(k\,T_s\,n\,\omega_0\right)\sin\left(n\,\omega_0\,tph(k)\right)\\
&-m_{on}\sin\left(k\,T_s\,n\,\omega_0\right)\cos\left(n\,\omega_0\,tph(k)\right)\cos\left(n\,\omega_0\,\tau\right)\\
&-m_{on}\cos\left(k\,T_s\,n\,\omega_0\right)\cos\left(n\,\omega_0\,tph(k)\right)\sin\left(n\,\omega_0\,\tau\right)\\
&-m_{on}\cos\left(k\,T_s\,n\,\omega_0\right)\sin\left(n\,\omega_0\,tph(k)\right)\cos\left(n\,\omega_0\,\tau\right)\\
&+m_{on}\sin\left(k\,T_s\,n\,\omega_0\right)\sin\left(n\,\omega_0\,tph(k)\right)\sin\left(n\,\omega_0\,\tau\right)+m_{on}\sin\left(k\,T_s\,n\,\omega_0\right)\cos\left(n\,\omega_0\,tph(k)\right)\\
&\left.+m_{on}\cos\left(k\,T_s\,n\,\omega_0\right)\sin\left(n\,\omega_0\,tph(k)\right)\right)\\
&+\frac{1}{n^2\omega_0^2}\left(m_{off}\sin\left(k\,T_s\,n\,\omega_0\right)\cos\left(n\,T_s\,\omega_0\right)\cos\left(n\,\omega_0\,tph(k+1)\right)\right.\\
&-m_{off}\sin\left(k\,T_s\,n\,\omega_0\right)\sin\left(n\,T_s\,\omega_0\right)\sin\left(n\,\omega_0\,tph(k+1)\right)\\
&+m_{off}\cos\left(k\,T_s\,n\,\omega_0\right)\sin\left(n\,T_s\,\omega_0\right)\cos\left(n\,\omega_0\,tph(k+1)\right)\\
&+m_{off}\cos\left(k\,T_s\,n\,\omega_0\right)\cos\left(n\,T_s\,\omega_0\right)\sin\left(n\,\omega_0\,tph(k+1)\right)\\
&-m_{off}\sin\left(k\,T_s\,n\,\omega_0\right)\cos\left(n\,\omega_0\,tph(k)\right)\cos\left(n\,\omega_0\,\tau\right)\\
&+m_{off}\sin\left(k\,T_s\,n\,\omega_0\right)\sin\left(n\,\omega_0\,tph(k)\right)\sin\left(n\,\omega_0\,\tau\right)\\
&-m_{off}\cos\left(k\,T_s\,n\,\omega_0\right)\sin\left(n\,\omega_0\,tph(k)\right)\cos\left(n\,\omega_0\,\tau\right)\\
&-m_{off}\cos\left(k\,T_s\,n\,\omega_0\right)\cos\left(n\,\omega_0\,tph(k)\right)\sin\left(n\,\omega_0\,\tau\right)\\
&+v(k)\,n\,\omega_0\cos\left(k\,T_s\,n\,\omega_0\right)\cos\left(n\,\omega_0\,tph(k)\right)\cos\left(n\,\omega_0\,\tau\right)\\
&-v(k)\,n\,\omega_0\cos\left(k\,T_s\,n\,\omega_0\right)\sin\left(n\,\omega_0\,tph(k)\right)\sin\left(n\,\omega_0\,\tau\right)\\
&-v(k)\,n\,\omega_0\sin\left(k\,T_s\,n\,\omega_0\right)\sin\left(n\,\omega_0\,tph(k)\right)\cos\left(n\,\omega_0\,\tau\right)\\
&-v(k)\,n\,\omega_0\sin\left(k\,T_s\,n\,\omega_0\right)\cos\left(n\,\omega_0\,tph(k)\right)\sin\left(n\,\omega_0\,\tau\right)\\
&+tph(k)\,n\,m_{off}\,\omega_0\cos\left(k\,T_s\,n\,\omega_0\right)\cos\left(n\,T_s\,\omega_0\right)\cos\left(n\,\omega_0\,tph(k+1)\right)\\
&-tph(k)\,n\,m_{off}\,\omega_0\cos\left(k\,T_s\,n\,\omega_0\right)\sin\left(n\,T_s\,\omega_0\right)\sin\left(n\,\omega_0\,tph(k+1)\right)\\
&-tph(k)\,n\,m_{off}\,\omega_0\sin\left(k\,T_s\,n\,\omega_0\right)\sin\left(n\,T_s\,\omega_0\right)\cos\left(n\,\omega_0\,tph(k+1)\right)\\
&-tph(k)\,n\,m_{off}\,\omega_0\sin\left(k\,T_s\,n\,\omega_0\right)\cos\left(n\,T_s\,\omega_0\right)\sin\left(n\,\omega_0\,tph(k+1)\right)-tph(k\\
&+1)\,n\,m_{off}\,\omega_0\cos\left(k\,T_s\,n\,\omega_0\right)\cos\left(n\,T_s\,\omega_0\right)\cos\left(n\,\omega_0\,tph(k+1)\right)+tph(k\\
&+1)\,n\,m_{off}\,\omega_0\cos\left(k\,T_s\,n\,\omega_0\right)\sin\left(n\,T_s\,\omega_0\right)\sin\left(n\,\omega_0\,tph(k+1)\right)+tph(k\\
&+1)\,n\,m_{off}\,\omega_0\sin\left(k\,T_s\,n\,\omega_0\right)\sin\left(n\,T_s\,\omega_0\right)\cos\left(n\,\omega_0\,tph(k+1)\right)\\
&+v(k)\,n\,\omega_0\sin\left(k\,T_s\,n\,\omega_0\right)\cos\left(n\,T_s\,\omega_0\right)\sin\left(n\,\omega_0\,tph(k+1)\right)+tph(k\\
&+1)\,n\,m_{off}\,\omega_0\sin\left(k\,T_s\,n\,\omega_0\right)\cos\left(n\,T_s\,\omega_0\right)\sin\left(n\,\omega_0\,tph(k+1)\right)\\
&+n\,\tau\,m_{off}\,\omega_0\cos\left(k\,T_s\,n\,\omega_0\right)\cos\left(n\,T_s\,\omega_0\right)\cos\left(n\,\omega_0\,tph(k+1)\right)\\
&-n\,\tau\,m_{off}\,\omega_0\cos\left(k\,T_s\,n\,\omega_0\right)\sin\left(n\,T_s\,\omega_0\right)\sin\left(n\,\omega_0\,tph(k+1)\right)\\
&-n\,\tau\,m_{off}\,\omega_0\sin\left(k\,T_s\,n\,\omega_0\right)\sin\left(n\,T_s\,\omega_0\right)\cos\left(n\,\omega_0\,tph(k+1)\right)\\
&-n\,\tau\,m_{off}\,\omega_0\sin\left(k\,T_s\,n\,\omega_0\right)\cos\left(n\,T_s\,\omega_0\right)\sin\left(n\,\omega_0\,tph(k+1)\right)\\
&-n\,T_s\,m_{off}\,\omega_0\cos\left(k\,T_s\,n\,\omega_0\right)\cos\left(n\,T_s\,\omega_0\right)\cos\left(n\,\omega_0\,tph(k+1)\right)\\
&+n\,T_s\,m_{off}\,\omega_0\cos\left(k\,T_s\,n\,\omega_0\right)\sin\left(n\,T_s\,\omega_0\right)\sin\left(n\,\omega_0\,tph(k+1)\right)\\
&+n\,T_s\,m_{off}\,\omega_0\sin\left(k\,T_s\,n\,\omega_0\right)\sin\left(n\,T_s\,\omega_0\right)\cos\left(n\,\omega_0\,tph(k+1)\right)\\
&+n\,T_s\,m_{off}\,\omega_0\sin\left(k\,T_s\,n\,\omega_0\right)\cos\left(n\,T_s\,\omega_0\right)\sin\left(n\,\omega_0\,tph(k+1)\right)\\
&-v(k)\,n\,\omega_0\cos\left(k\,T_s\,n\,\omega_0\right)\cos\left(n\,T_s\,\omega_0\right)\cos\left(n\,\omega_0\,tph(k+1)\right)\\
&+v(k)\,n\,\omega_0\cos\left(k\,T_s\,n\,\omega_0\right)\sin\left(n\,T_s\,\omega_0\right)\sin\left(n\,\omega_0\,tph(k+1)\right)\\
&\left.+v(k)\,n\,\omega_0\sin\left(k\,T_s\,n\,\omega_0\right)\sin\left(n\,T_s\,\omega_0\right)\cos\left(n\,\omega_0\,tph(k+1)\right)\right)\Bigg)\Bigg)
\end{aligned}
$$

Total coefficients

$$a_0 = \sum_{k=0}^{N_p-1} a_{0,k}$$ Equation C-91

$$a_n = \sum_{k=0}^{N_p-1} a_{n,k}$$ Equation C-92

$$b_n = \sum_{k=0}^{N_p-1} b_{n,k}$$ Equation C-93

$$c_n = \sum_{k=0}^{N_p-1} \begin{matrix} \frac{1}{2}\left(a_{n,k} - ib_{n,k}\right)(n \geq 1) \\ \frac{1}{2}\left(a_{n,k} + ib_{n,k}\right)(n \leq 1) \end{matrix}$$ Equation C-94

Fourier Analysis of Sawtooth wave with an impulse function

Functions to be analysed

$$f_0(t) = \begin{cases} u_0 + m_{on}t & 0 < t \le \tau_{or} \\ v_0 + m_{off}(t - \tau_{or}) & \tau_{or} < t \le T_s \end{cases}$$ Equation C-95

$$f_1(t) = \begin{cases} u_1 + m_{on}(t - T_s) & T_s < t \le \tau + T_s \\ v_1 + m_{off}(t - \tau - T_s) & \tau + T_s < t \le 2T_s \end{cases}$$ Equation C-96

$$f_2(t) = \begin{cases} u_2 + m_{on}(t - 2T_s) & 2T_s < t \le \tau + 2T_s \\ v_2 + m_{off}(t - \tau - 2T_s) & \tau + 2T_s < t \le 3T_s \end{cases}$$ Equation C-97

.

.

$$f_k(t) = \begin{cases} u_k + m_{on}(t - (k)T_s) & (k)T_s < t \le \tau + (k)T_s \\ v_k + m_{off}(t - \tau - (k)T_s) & \tau + (k)T_s < t \le (k+1)T_s \end{cases}$$ Equation C-98

Fourier co-efficient calculation for first function

$$a_{0,0} = \frac{2}{T_0}\left[\int_0^{\tau_{0r}} u_0 + m_{on}t\, dt + \int_{\tau_{0r}}^{T_s} v_0 + m_{off}(t - \tau_{or})\, dt\right]$$ Equation C-99

$$a_{0,0} = \frac{2}{T_0}\left[\int_0^{\tau_{0r}} u_0\, dt + \int_0^{\tau_{0r}} m_{on}t\, dt + \int_{\tau_0 r}^{T_s} v_0\, dt + \int_{\tau_{0r}}^{T_s} m_{off}t\, dt - \int_{\tau_{0r}}^{T_s} m_{off}\tau_{or}\, dt\right]$$ Equation C-100

$$a_{0,0} = \frac{2}{T_0}\left[u_0\tau_{or} + \frac{m_{on}}{2\tau_{or}}{\tau_{or}}^2 + v_0(T_s - \tau_{or}) + \frac{m_{off}({T_s}^2 - {\tau_0}^2)}{2} - m_{off}\tau_{or}(T_s - \tau_{or})\right]$$ Equation C-101

$$a_{n,0} = \frac{2}{T_0}\left[\int_0^{\tau_{0r}} (u_0 + m_{on}t)\cos n\omega_0 t\, dt + \int_{\tau_{0r}}^{T_s} \left(v_0 + m_{off}(t - \tau_{or})\right)\cos n\omega_0 t\ dt\right]$$ Equation C-102

$$a_{n,0} = \frac{2}{T_0}\left[\int_0^{\tau_{0r}} u_0 \cos n\omega_0 t\, dt + \int_0^{\tau_{0r}} m_{on} t \cos n\omega_0 t\, dt + \int_{\tau_{0r}}^{T_s} v_0 \cos n\omega_0 t\, dt + \int_{\tau_{0r}}^{T_s} m_{off} t \cos n\omega_0 t\, dt - \int_{\tau_{0r}}^{T_s} m_{off}\tau_{or} \cos n\omega_0 t\, dt\right]$$ Equation C-103

$$a_{n,0} = \frac{2}{T_0}\left[\frac{u_0}{n\omega_0}\sin n\omega_0\tau_{or} + \frac{m_{on}}{n\omega_0}\tau_{or}\sin n\omega_0\tau_{or} - \frac{m_{on}}{n\omega_0}\int_0^{\tau_{0r}}\sin n\omega_0 t\, dt + \frac{v_0}{n\omega_0}\sin n\omega_0 T_s - \frac{v_0}{n\omega_0}\sin n\omega_0\tau_{or} + \frac{m_{off}}{n\omega_0} T_s \sin n\omega_0 T_s - \frac{m_{off}}{n\omega_0}\tau_{or}\sin n\omega_0\tau_{or} - \frac{m_{off}}{n\omega_0}\int_{\tau_{0r}}^{T_s}\sin n\omega_0 t\, dt - \frac{m_{off}}{n\omega_0}\tau_{or}\sin n\omega_0 T_s + \frac{m_{off}}{n\omega_0}\tau_{or}\sin n\omega_0\tau_{or}\right]$$ Equation C-104

$$a_{n,0} = \frac{2}{T_0}\left[\frac{u_0}{n\omega_0}\sin n\omega_0\tau_{or} + \frac{m_{on}}{n\omega_0}\tau_{or}\sin n\omega_0\tau_{or} + \frac{m_{on}}{n^2{\omega_0}^2}\cos n\omega_0\tau_{or} + \frac{v_0}{n\omega_0}\sin n\omega_0 T_s - \frac{v_0}{n\omega_0}\sin n\omega_0\tau_{or} + \frac{m_{off}}{n\omega_0} T_s \sin n\omega_0 T_s - \frac{m_{off}}{n\omega_0}\tau_{or}\sin n\omega_0\tau_{or} + \frac{m_{off}}{n^2{\omega_0}^2}(\cos n\omega_0 T_s - \cos n\omega_0\tau_{or}) - \frac{m_{off}}{n\omega_0}\tau_{or}\sin n\omega_0 T_s + \frac{m_{off}}{n\omega_0}\tau_{or}\sin n\omega_0\tau_{or}\right]$$ Equation C-105

$$b_{n,0} = \frac{2}{T_0}\left[\int_0^{\tau_{0r}}(u_0 + m_{on}t)\sin n\omega_0 t\, dt + \int_{\tau_{0r}}^{T_s}\big(v_0 + m_{off}(t - \tau_{or})\big)\sin n\omega_0 t\, dt\right]$$ Equation C-106

$$b_{n,0} = \frac{2}{T_0}\left[\int_0^{\tau_{0r}} u_0 \sin n\omega_0 t\, dt + \int_0^{\tau_{0r}} m_{on} t \sin n\omega_0 t\, dt + \int_{\tau_{0r}}^{T_s} v_0 \sin n\omega_0 t\, dt + \int_{\tau_{0r}}^{T_s} m_{off} t \sin n\omega_0 t\, dt - \int_{\tau_{0r}}^{T_s} m_{off}\tau_{or} \sin n\omega_0 t\, dt\right]$$ Equation C-107

$$b_{n,0} = \frac{2}{T_0}\left[-\frac{u_0}{n\omega_0}\cos n\omega_0\tau_{or} - \frac{m_{on}}{n\omega_0}\tau_{or}\cos n\omega_0\tau_{or} + \frac{m_{on}}{n\omega_0}\int_0^{\tau_{0r}}\cos n\omega_0 t\, dt - \frac{v_0}{n\omega_0}\cos n\omega_0 T_s + \frac{v_0}{n\omega_0}\cos n\omega_0\tau_{or} - \frac{m_{off}}{n\omega_0} T_s \cos n\omega_0 T_s + \frac{m_{off}}{n\omega_0}\tau_{or}\cos n\omega_0\tau_{or} + \frac{m_{off}}{n\omega_0}\int_{\tau_{0r}}^{T_s}\cos n\omega_0 t\, dt + \frac{m_{off}}{n\omega_0}\tau_{or}\cos n\omega_0 T_s - \frac{m_{off}}{n\omega_0}\tau_{or}\cos n\omega_0\tau_{or}\right]$$ Equation C-108

$$b_{n,0} = \frac{2}{T_0}\left[-\frac{u_0}{n\omega_0}\cos n\omega_0\tau_{or} - \frac{m_{on}}{n\omega_0}\tau_{or}\cos n\omega_0\tau_{or} + \frac{m_{on}}{n^2{\omega_0}^2}\sin n\omega_0\tau_{or} - \right.$$
$$\frac{v_0}{n\omega_0}\cos n\omega_0 T_s + \frac{v_0}{n\omega_0}\cos n\omega_0\tau_{or} - \frac{m_{off}}{n\omega_0}\,T_s\cos n\omega_0 T_s +$$
$$\frac{m_{off}}{n\omega_0}\,\tau_{or}\cos n\omega_0\tau_{or} + \frac{m_{off}}{n^2{\omega_0}^2}(\sin n\omega_0 T_s - \sin n\omega_0\tau_{or}) +$$
$$\left.\frac{m_{off}}{n\omega_0}\tau_{or}\cos n\omega_0 T_s - \frac{m_{off}}{n\omega_0}\tau_{or}\cos n\omega_0\tau_{or}\right] \qquad \text{Equation C-109}$$

Fourier coefficient calculation for the kth function

$$a_{0,k} = \frac{2}{T_0}\left[\int_{kT_s}^{kT_s+\tau} u_k + m_{on}(t - kT_s)\,dt + \int_{kT_s+\tau}^{(k+1)T_s} v_k + m_{off}(t - kT_s - \tau)\,dt\right] \qquad \text{Equation C-110}$$

$$a_{0,k} = \frac{2}{T_0}\left[\int_{kT_s}^{kT_s+\tau} u_k\,dt + \int_{kT_s}^{kT_s+\tau} m_{on}t\,dt - \int_{kT_s}^{kT_s+\tau} m_{on}kT_s\,dt + \int_{kT_s+\tau}^{(k+1)T_s} v_k\,dt + \int_{kT_s+\tau}^{(k+1)T_s} m_{off}t\,dt - \int_{kT_s+\tau}^{(k+1)T_s} m_{off}kT_s\,dt - \int_{kT_s+\tau}^{(k+1)T_s} m_{off}\tau\,dt\right] \qquad \text{Equation C-111}$$

$$a_{0,k} = \frac{2}{T_0}\left[u_k\tau + \frac{m_{on}}{2}\tau^2 - \frac{m_{on}kT_s}{2}\tau + v_k(T_s - \tau) + \frac{m_{off}}{2}\left(T_s^2 + 2kT_s{}^2 - 2kT_s\tau - \tau^2\right) - m_{off}kT_s(T_s - \tau) - m_{off}\tau(T_s - \tau)\right] \qquad \text{Equation C-112}$$

$$a_{n,k} = \frac{2}{T_0}\left[\int_{kT_s}^{kT_s+\tau}(u_k + m_{on}(t - kT_s))\cos n\omega_0 t\;dt + \int_{kT_s+\tau}^{(k+1)T_s}(v_k + m_{off}(t - kT_s - \tau))\cos n\omega_0 t\;dt\right] \qquad \text{Equation C-113}$$

$$b_{n,k} = \frac{2}{T_0}\left[\int_{kT_s}^{kT_s+\tau}(u_k + m_{on}(t - kT_s))\sin n\omega_0 t\;dt + \int_{kT_s+\tau}^{(k+1)T_s}(v_k + m_{off}(t - kT_s - \tau))\sin n\omega_0 t\;dt\right] \qquad \text{Equation C-114}$$

$a_{n,k} =$ **Equation C-115**

$$
\begin{aligned}
&-\frac{1}{T_0\, n^2\, \omega_0^2}\Big(2\Big(-n\,\tau\, m_{on}\,\omega_0 \sin\left(k\,T_s\,n\,\omega_0\right)\cos\left(n\,\omega_0\,\tau\right) - n\,\tau\, m_{on}\,\omega_0\cos\left(k\,T_s\,n\,\omega_0\right)\sin\left(n\,\omega_0\,\tau\right)\\
&\quad + n\,\tau\, m_{off}\omega_0\cos\left(k\,T_s\,n\,\omega_0\right)\sin\left(n\,\omega_0\,T_s\right) - n\,T_s\,m_{off}\omega_0\cos\left(k\,T_s\,n\,\omega_0\right)\sin\left(n\,\omega_0\,T_s\right)\\
&\quad + n\,\tau\, m_{off}\omega_0\sin\left(k\,T_s\,n\,\omega_0\right)\cos\left(n\,\omega_0\,T_s\right) - n\,T_s\,m_{off}\omega_0\sin\left(k\,T_s\,n\,\omega_0\right)\cos\left(n\,\omega_0\,T_s\right)\\
&\quad + v(k)\,n\,\omega_0\sin\left(k\,T_s\,n\,\omega_0\right)\cos\left(n\,\omega_0\,\tau\right) + v(k)\,n\,\omega_0\cos\left(k\,T_s\,n\,\omega_0\right)\sin\left(n\,\omega_0\,\tau\right)\\
&\quad - v(k)\,n\,\omega_0\cos\left(k\,T_s\,n\,\omega_0\right)\sin\left(n\,\omega_0\,T_s\right) - v(k)\,n\,\omega_0\sin\left(k\,T_s\,n\,\omega_0\right)\cos\left(n\,\omega_0\,T_s\right)\\
&\quad - u(k)\,n\,\omega_0\sin\left(k\,T_s\,n\,\omega_0\right)\cos\left(n\,\omega_0\,\tau\right) - u(k)\,n\,\omega_0\cos\left(k\,T_s\,n\,\omega_0\right)\sin\left(n\,\omega_0\,\tau\right)\\
&\quad + u(k)\sin\left(k\,T_s\,n\,\omega_0\right)n\,\omega_0 + m_{off}\cos\left(k\,T_s\,n\,\omega_0\right)\cos\left(n\,\omega_0\,\tau\right)\\
&\quad - m_{on}\cos\left(k\,T_s\,n\,\omega_0\right)\cos\left(n\,\omega_0\,\tau\right) - m_{off}\sin\left(k\,T_s\,n\,\omega_0\right)\sin\left(n\,\omega_0\,\tau\right)\\
&\quad + m_{on}\sin\left(k\,T_s\,n\,\omega_0\right)\sin\left(n\,\omega_0\,\tau\right) - m_{off}\cos\left(k\,T_s\,n\,\omega_0\right)\cos\left(n\,\omega_0\,T_s\right)\\
&\quad + m_{off}\sin\left(k\,T_s\,n\,\omega_0\right)\sin\left(n\,\omega_0\,T_s\right) + \cos\left(k\,T_s\,n\,\omega_0\right)m_{on}\Big)\Big)
\end{aligned}
$$

$b_{n,k}=$ **Equation C-116**

$$
\begin{aligned}
&\frac{1}{T_0\, n^2\, \omega_0^2}\Big(2\Big(-n\,\tau\, m_{on}\,\omega_0\cos\left(k\,T_s\,n\,\omega_0\right)\cos\left(n\,\omega_0\,\tau\right) + n\,\tau\, m_{on}\,\omega_0\sin\left(k\,T_s\,n\,\omega_0\right)\sin\left(n\,\omega_0\,\tau\right)\\
&\quad + n\,\tau\, m_{off}\omega_0\cos\left(k\,T_s\,n\,\omega_0\right)\cos\left(n\,\omega_0\,T_s\right) - n\,T_s\,m_{off}\omega_0\cos\left(k\,T_s\,n\,\omega_0\right)\cos\left(n\,\omega_0\,T_s\right)\\
&\quad - n\,\tau\, m_{off}\omega_0\sin\left(k\,T_s\,n\,\omega_0\right)\sin\left(n\,\omega_0\,T_s\right) + n\,T_s\,m_{off}\omega_0\sin\left(k\,T_s\,n\,\omega_0\right)\sin\left(n\,\omega_0\,T_s\right)\\
&\quad + v(k)\,n\,\omega_0\cos\left(k\,T_s\,n\,\omega_0\right)\cos\left(n\,\omega_0\,\tau\right) - v(k)\,n\,\omega_0\sin\left(k\,T_s\,n\,\omega_0\right)\sin\left(n\,\omega_0\,\tau\right)\\
&\quad - v(k)\,n\,\omega_0\cos\left(k\,T_s\,n\,\omega_0\right)\cos\left(n\,\omega_0\,T_s\right) + v(k)\,n\,\omega_0\sin\left(k\,T_s\,n\,\omega_0\right)\sin\left(n\,\omega_0\,T_s\right)\\
&\quad - u(k)\,n\,\omega_0\cos\left(k\,T_s\,n\,\omega_0\right)\cos\left(n\,\omega_0\,\tau\right) + u(k)\,n\,\omega_0\sin\left(k\,T_s\,n\,\omega_0\right)\sin\left(n\,\omega_0\,\tau\right)\\
&\quad + \cos\left(k\,T_s\,n\,\omega_0\right)u(k)\,n\,\omega_0 - m_{off}\sin\left(k\,T_s\,n\,\omega_0\right)\cos\left(n\,\omega_0\,\tau\right)\\
&\quad + m_{on}\sin\left(k\,T_s\,n\,\omega_0\right)\cos\left(n\,\omega_0\,\tau\right) - m_{off}\cos\left(k\,T_s\,n\,\omega_0\right)\sin\left(n\,\omega_0\,\tau\right)\\
&\quad + m_{on}\cos\left(k\,T_s\,n\,\omega_0\right)\sin\left(n\,\omega_0\,\tau\right) + m_{off}\cos\left(k\,T_s\,n\,\omega_0\right)\sin\left(n\,\omega_0\,T_s\right)\\
&\quad + m_{off}\sin\left(k\,T_s\,n\,\omega_0\right)\cos\left(n\,\omega_0\,T_s\right) - \sin\left(k\,T_s\,n\,\omega_0\right)m_{on}\Big)\Big)
\end{aligned}
$$

Total coefficients

$$a_0 = \sum_{k=0}^{N_p-1} a_{0,k}$$ Equation C-117

$$a_n = \sum_{k=0}^{N_p-1} a_{n,k}$$ Equation C-118

$$b_n = \sum_{k=0}^{N_p-1} b_{n,k}$$ Equation C-119

$$c_n = \sum_{k=0}^{N_p-1} \begin{matrix} \frac{1}{2}\left(a_{n,k} - ib_{n,k}\right)(n \geq 1) \\ \frac{1}{2}\left(a_{n,k} + ib_{n,k}\right)(n \leq 1) \end{matrix}$$ Equation C-120

Fourier Analysis of Sawtooth wave with Battery Balancing

Functions to be analysed

This is a combination of the sawtooth function

$$f_0(t) = \begin{cases} u_0 + m_{on}t & 0 < t \leq \tau \\ v_0 + m_{off}(t-\tau) & \tau < t \leq T_s \end{cases}$$ Equation C-121

And the battery balancing circuit equations

$$f_1(t) = \begin{cases} \frac{-CV_{diff}}{\tau_c}(e^{-t/\tau_c}) & 0 < t \leq 0.45T_0 \\ 0 & 0.45T_0 < t \leq T_0 \end{cases}$$ Equation C-122

Fourier co-efficient calculation for first function

$$a_0 = \frac{2}{T_s}\left[\int_0^{\tau} u + m_{on}t\, dt + \int_{\tau}^{T_s} v + m_{on}(t-\tau)\, dt\right]$$ Equation C-123

$$a_0 = \frac{2}{T_s}\left[\int_0^{\tau} u\, dt + \int_0^{\tau} m_{on}t\, dt + \int_{\tau}^{T_s} v\, dt + \int_{\tau}^{T_s} m_{off}t\, dt - \int_{\tau}^{T_s} m_{off}\tau dt\right]$$ Equation C-124

$$a_0 = \frac{2}{T_s}\left[u(\tau) + \frac{m_{on}}{2}(\tau)^2 + vT_s - v\tau + \frac{m_{off}}{2}{T_s}^2 - \frac{m_{off}}{2}\tau^2 - m_{off}\tau T_s + m_{off}\tau^2\right]$$ Equation C-125

$$a_0 = \frac{2}{T_s}\left[u\tau + \frac{m_{on}}{2}\tau^2 + vT_s - v\tau + \frac{m_{off}}{2}{T_s}^2 - \frac{m_{off}}{2}\tau^2 - m_{off}\tau T_s + m_{off}\tau^2\right]$$ Equation C-126

$$a_0 = \frac{2u\tau}{T_s} + \frac{m_{on}\tau^2}{T_s} + \frac{2v(T_s-\tau)}{T_s} + \frac{m_{off}}{T_s}\left({T_s}^2 - \tau^2\right) - \frac{2m_{off}}{T_s}\tau(T_s - \tau)$$ Equation C-127

$$a_n = \frac{2}{T_s}\left[\int_0^{\tau}(u + m_{on}t)\cos n\omega_s t\, dt + \int_{\tau}^{T_s}\left(v + m_{off}(t-\tau)\right)\cos n\omega_s t\ dt\right]$$ Equation C-128

$$a_n = \frac{2}{T_s}\left[\int_0^{\tau} u\ \cos n\omega_s t\, dt + \int_0^{\tau} m_{on}t\ \cos n\omega_s t\, dt + \int_{\tau}^{T_s} v\ \cos n\omega_s t\, dt + \int_{\tau}^{T_s} m_{off}t\ \cos n\omega_s t\, dt - \int_{\tau}^{T_s} m_{off}\tau\ \cos n\omega_s t\, dt\right]$$ Equation C-129

$$a_n = \frac{2}{T_s}\left[\frac{u}{n\omega_s}\sin n\omega_s(\tau) + \frac{m_{on}}{n\omega_s}(\tau)\sin n\omega_s(\tau) + \frac{m_{on}}{n^2{\omega_s}^2}\cos n\omega_s(\tau) - \frac{m_{on}}{n^2{\omega_s}^2} + + \frac{v}{n\omega_s}\sin n\omega_s(T_s) - \frac{v}{n\omega_s}\sin n\omega_s(\tau) + \frac{m_{off}}{n\omega_s}(T_s)\sin n\omega_s(T_s) -$$ Equation C-130

$$\frac{m_{off}}{n\omega_s}(\tau)\sin n\omega_s(\tau) + \frac{m_{off}}{n^2{\omega_s}^2}\cos n\omega_s(T_s) - \frac{m_{off}}{n^2{\omega_s}^2}\cos n\omega_s(\tau) -$$
$$\frac{m_{off}}{n\omega_s}(\tau)\sin n\omega_s(T_s) + \frac{m_{off}}{n\omega_s}(\tau)\sin n\omega_s(\tau)\Big]$$

$$a_n = \frac{2u}{n\omega_s T_s}\sin n\omega_s(\tau) + \frac{2m_{on}}{n\omega_s T_s}(\tau)\sin n\omega_s(\tau) + \frac{2m_{on}}{n^2{\omega_s}^2 T_s}\cos n\omega_s(\tau) - \quad \text{Equation C-131}$$
$$\frac{2m_{on}}{n^2{\omega_s}^2 T_s} + \frac{2v}{n\omega_s T_s}\sin n\omega_s(T_s) - \frac{2v}{n\omega_s T_s}\sin n\omega_s(\tau) + \frac{2m_{off}}{n\omega_s T_s}(T_s)\sin n\omega_s(T_s) -$$
$$\frac{2m_{off}}{n\omega_s T_s}(\tau)\sin n\omega_s(\tau) + \frac{2m_{off}}{n^2{\omega_s}^2 T_s}\cos n\omega_s(T_s) - \frac{2m_{off}}{n^2{\omega_s}^2 T_s}\cos n\omega_s(\tau) -$$
$$\frac{2m_{off}}{n\omega_s T_s}(\tau)\sin n\omega_s(T_s) + \frac{2m_{off}}{n\omega_s T_s}(\tau)\sin n\omega_s(\tau)$$

$$a_n = \left(\frac{-2m_{on}}{n^2{\omega_s}^2 T_s} + \left(\frac{2u}{n\omega_s T_s} + \frac{2m_{on}}{n\omega_s T_s}\tau - \frac{2v}{n\omega_s T_s}\right)\sin n\omega_s\tau + \left(\frac{2m_{on}}{n^2{\omega_s}^2 T_s} - \right. \quad \text{Equation C-132}$$
$$\left.\frac{2m_{off}}{n^2{\omega_0}^2 T_0}\right)\cos n\omega_0\tau + \left(\frac{2v}{n\omega_s T_s} + \frac{2m_{off}}{n\omega_s T_s}(T_s - \tau)\right)\sin n\omega_0 T_s +$$
$$\frac{2m_{off}}{n^2{\omega_s}^2 T_s}\cos n\omega_s T_s)$$

$$b_n = \frac{2}{T_s}\left[\int_0^\tau (u + m_{on}(t))\sin n\omega_s t\, dt + \int_\tau^{T_s}\left(v + m_{off}(t - \right. \quad \text{Equation C-133}$$
$$\left.\tau)\right)\sin n\omega_s t\ dt\Big]$$

$$b_n = \frac{2}{T_s}\left[\int_0^\tau u\ \sin n\omega_s t\, dt + \int_0^\tau m_{on}(t)\ \sin n\omega_s t\, dt + \int_\tau^{T_s} v\ \sin n\omega_s t\, dt + \right. \quad \text{Equation C-134}$$
$$\left.\int_\tau^{T_s} m_{off} t\ \sin n\omega_s t\, dt - \int_\tau^{T_s} m_{off}(\tau)\sin n\omega_s t\, dt\right]$$

$$b_n = \frac{2}{T_s}\left[\frac{-u}{n\omega_s}\cos n\omega_s(\tau) + \frac{u}{n\omega_s} - \frac{m_{on}}{n\omega_s}(\tau)\cos n\omega_s(\tau) + \right. \quad \text{Equation C-135}$$
$$\frac{m_{on}}{n\omega_s}\int_0^\tau \cos n\omega_s t\, dt - \frac{v}{n\omega_s}\cos n\omega_s(T_s) + \frac{v}{n\omega_s}\cos n\omega_s(\tau) -$$
$$\frac{m_{off}}{n\omega_s}(T_s)\cos n\omega_s(T_s) + \frac{m_{off}}{n\omega_s}(\tau)\cos n\omega_s(\tau) + \frac{m_{off}}{n\omega_s}\int_\tau^{T_s}\cos n\omega_s t\, dt +$$
$$\left.\frac{m_{off}}{n\omega_s}(\tau)\cos n\omega_s(T_s) - \frac{m_{off}}{n\omega_s}(\tau)\cos n\omega_s(\tau)\right]$$

$$b_n = \frac{2}{T_s}\left[\frac{-u}{n\omega_s}\cos n\omega_s(\tau) + \frac{u}{n\omega_s} - \frac{m_{on}}{n\omega_s}(\tau)\cos n\omega_s(\tau) + \right. \quad \text{Equation C-136}$$
$$+\frac{m_{on}}{n^2{\omega_s}^2}\sin n\omega_s(\tau) - \frac{v}{n\omega_s}\cos n\omega_s(T_s) + \frac{v}{n\omega_s}\cos n\omega_s(\tau) -$$
$$\frac{m_{off}}{n\omega_s}(T_s)\cos n\omega_s(T_s) + \frac{m_{off}}{n\omega_s}(\tau)\cos n\omega_s(\tau) + \frac{m_{off}}{n^2{\omega_s}^2}\sin n\omega_s(T_s) -$$
$$\left.\frac{m_{off}}{n^2{\omega_s}^2}\sin n\omega_s(\tau) + \frac{m_{off}}{n\omega_s}(\tau)\cos n\omega_s(T_s) - \frac{m_{off}}{n\omega_s}(\tau)\cos n\omega_s(\tau)\right]$$

$$b_n = \frac{-2u}{n\omega_s T_s}\cos n\omega_s(\tau) + \frac{2u}{n\omega_s T_s} - \frac{2m_{on}}{n\omega_s T_s}(\tau)\cos n\omega_s(\tau) + \frac{2m_{on}}{n^2{\omega_s}^2 T_s}\sin n\omega_s(\tau) - \frac{2v}{n\omega_s T_s}\cos n\omega_s(T_s) + \frac{2v}{n\omega_s T_s}\cos n\omega_s(\tau) - \frac{2m_{off}}{n\omega_s T_s}(T_s)\cos n\omega_s(T_s) + \frac{2m_{off}}{n\omega_s T_s}(\tau)\cos n\omega_s(\tau) - \frac{2m_{off}}{n^2{\omega_s}^2 T_s}\sin n\omega_s(T_s) - \frac{2m_{off}}{n^2{\omega_s}^2 T_s}\sin n\omega_s(\tau) + \frac{2m_{off}}{n\omega_s T_s}(\tau)\cos n\omega_s(T_s) - \frac{2m_{off}}{n\omega_s T_s}(\tau)\cos n\omega_s(\tau)$$

Equation C-137

$$b_n = \left(\frac{2u}{n\omega_s T_s} + \left(\frac{2v}{n\omega_s T_s} - \frac{2u}{n\omega_s T_s} - \frac{2m_{on}}{n\omega_s T_s}\tau\right)\cos n\omega_s\tau + \left(\frac{2m_{on}}{n^2{\omega_s}^2 T_s} - \frac{2m_{off}}{n^2{\omega_s}^2 T_s}\right)\sin n\omega_s\tau - \frac{2m_{off}}{n^2{\omega_s}^2 T_s}\sin n\omega_0 T_s - \left(\frac{2m_{off}}{n\omega_s T_s}(T_s - \tau) + \frac{2v}{n\omega_s T_s}\right)\cos n\omega_s T_s\right)$$

Equation C-138

Fourier coefficient calculation for the second function

$$a_{0,1} = \frac{2}{T_0}\int_0^{0.45T_0}\left(-\frac{CV_{diff}}{\tau_c}\left(e^{-t/\tau_c}\right)\right)dt$$

Equation C-139

$$a_{0,1} = -\frac{2CV_{diff}}{T_0{\tau_c}^2}\left(1 - \left(e^{-0.45T_o/\tau_c}\right)\right)$$

Equation C-140

$$a_{n,1} = \frac{2}{T_0}\int_0^{0.45T_0}\left(-\frac{CV_{diff}}{\tau_c}\left(e^{-t/\tau_c}\right)\right)\cos n\omega_0 t\,dt$$

Equation C-141

$$a_{n,1} = -\frac{2CV_{diff}}{T_0\left(n^2\omega_0^2{\tau_c}^2+1\right)}\left(\sin(0.45n\omega_0 T_0)\,n\omega_0\tau_c e^{-0.45T_o/\tau_c} + 1 - \cos(0.45n\omega_0 T_0)e^{-0.45T_o/\tau_c}\right)$$

Equation C-142

$$b_{n,1} = \frac{2}{T_0}\int_0^{0.45T_0}\left(-\frac{CV_{diff}}{\tau_c}\left(e^{-t/\tau_c}\right)\right)\sin n\omega_0 t\,dt$$

Equation C-143

$$b_{n,1} = \frac{2CV_{diff}}{T_0\left(n^2\omega_0^2{\tau_c}^2+1\right)}\left(e^{-0.45T_o/\tau_c}\cos(0.45n\omega_0 T_0)\,n\omega_0\tau_c - n\omega_0\tau_c + \sin(0.45n\omega_0 T_0)e^{-0.45T_o/\tau_c}\right)$$

Equation C-144

Total coefficients

$$a_0 = \sum_{k=0}^{1} a_{0,k}$$ Equation C-145

$$a_n = \sum_{k=0}^{1} a_{n,k}$$ Equation C-146

$$b_n = \sum_{k=0}^{1} b_{n,k}$$ Equation C-147

$$c_n = \sum_{k=0}^{1} \frac{1}{2}\left(a_{n,k} - ib_{n,k}\right)(n \geq 1) \\ \frac{1}{2}\left(a_{n,k} + ib_{n,k}\right)(n \leq 1)$$ Equation C-148

Fourier Analysis of Sawtooth wave with ELM

Functions to be analysed

This is a combination of the sawtooth function (similar to the battery balancing method)

$$f_0(t) = \begin{cases} u_0 + m_{on}t & 0 < t \leq \tau \\ v_0 + m_{off}(t-\tau) & \tau < t \leq T_s \end{cases}$$ Equation C-149

And the ELM sine wave

$$f_1(t) \approx \frac{9.2}{Z_{bat}+20}\sin(\omega_o t) \qquad 0 < t \leq T_0$$ Equation C-150

Fourier co-efficient calculation for first function

As per the battery balancing method

Fourier co-efficient calculation for second function

The magnitude of the sine wave for the $b_{n,1}$ component only

Total coefficients

$$a_0 = a_{0,k}$$ Equation C-151

$$a_n = a_{n,k}$$ Equation C-152

$$b_n = \sum_{k=0}^{1} b_{n,k}$$ Equation C-153

$$c_n = \sum_{k=0}^{1} \frac{1}{2}\left(a_{n,k} - ib_{n,k}\right)(n \geq 1) \; \frac{1}{2}\left(a_{n,k} + ib_{n,k}\right)(n \leq 1)$$ Equation C-154